polymers

Special Issue Reprint

Advances in Biocompatible and Biodegradable Polymers, 4th Edition

Edited by
José Miguel Ferri, Vicent Fombuena Borrás and María Fernanda López Pérez

mdpi.com/journal/polymers

MDPI

Advances in Biocompatible and Biodegradable Polymers, 4th Edition

Advances in Biocompatible and Biodegradable Polymers, 4th Edition

Guest Editors

José Miguel Ferri
Vicent Fombuena Borrás
María Fernanda López Pérez

MDPI

Basel • Beijing • Wuhan • Barcelona • Belgrade • Novi Sad • Cluj • Manchester

Guest Editors

José Miguel Ferri
University Institute of Materials Technology (IUTM)
Universitat Politècnica de València
Alcoy
Spain

Vicent Fombuena Borrás
University Institute of Materials Technology (IUTM)
Universitat Politècnica de València
Alcoy
Spain

María Fernanda López Pérez
Research Institute for Industrial, Radiophysical and Environmental Safety (ISIRYM)
Universitat Politècnica de València
Alcoy
Spain

Editorial Office

MDPI AG
Grosspeteranlage 5
4052 Basel, Switzerland

This is a reprint of the Special Issue, published open access by the journal *Polymers* (ISSN 2073-4360), freely accessible at: https://www.mdpi.com/journal/polymers/special_issues/M1PZE06G1W.

For citation purposes, cite each article independently as indicated on the article page online and as indicated below:

Lastname, A.A.; Lastname, B.B. Article Title. *Journal Name* **Year**, *Volume Number*, Page Range.

ISBN 978-3-7258-6376-1 (Hbk)
ISBN 978-3-7258-6377-8 (PDF)
https://doi.org/10.3390/books978-3-7258-6377-8

Contents

About the Editors

José Miguel Ferri

José Miguel Ferri is an associate professor of Mechanical Engineering and has been engaged as a technician at the Department of Nuclear and Chemical Engineering of the Universitat Politècnica de València (UPV), Alcoy, Spain. He joined the University Institute of Materials Technology (IUTM) in 2014 and his primary interests are related to the development of new metallic materials (Mg foams for the medical sector), polymeric materials (improvement of thermal, mechanical, and processing properties of biodegradable polymers) and composite materials (metallic matrices for the electronics and aeronautics sectors, and polymeric matrices for the aeronautics and construction sectors).

Vicent Fombuena Borrás

Vicent Fombuena Borrás is a full professor of the Department of Nuclear and Chemical Engineering at the Universitat Politècnica de València (UPV), Alcoy, Spain. He joined the University Institute of Materials Technology (IUTM) in 2008, and his primary interests are related to the implementation of a circular economy model in the polymer industry. He has focused his efforts on obtaining multiple active compounds from seeds and agroforestry residues to be applied in thermoplastic and thermosetting polymers. In addition, he has extensive experience in techniques related to the chemical, thermal, and mechanical characterization of materials.

María Fernanda López Pérez

María Fernanda López Pérez is a professor at the Department of Nuclear and Chemical Engineering of the Universitat Politècnica de València (UPV), Alcoy, Spain. She is a member of the Instituto Universitario de Investigación de Seguridad Industrial, Radiofísica y Medioambiental (ISIRYM). Her primary interests are in biologically advanced oxidation processes and membrane technologies for water treatment, contributing to sustainable solutions for pollutant removal and resource recovery. One of her current areas of focus is the generation of biopolymers such as PHB from urban waste and the extraction of polyphenols from biomass waste for use in key sectors such as pharmaceuticals and polymers.

polymers

MDPI

Review

Advanced Biocompatible and Biodegradable Polymers: A Review of Functionalization, Smart Systems, and Sustainable Applications

Latifat Abdulsalam [1], Sadam Abubakar [1], Ikfa Permatasari [1], Anas Abdulwahab Lawal [1], Shihab Uddin [1], Saleem Ullah [2] and Irshad Ahmad [1,3,*]

[1] Department of Bioengineering, King Fahd University of Petroleum and Minerals (KFUPM), Dhahran 31261, Saudi Arabia; g202210360@kfupm.edu.sa (L.A.); g202315670@kfupm.edu.sa (S.A.); g202215280@kfupm.edu.sa (I.P.); g202404880@kfupm.edu.sa (A.A.L.); shihab.uddin@kfupm.edu.sa (S.U.)
[2] VTT Technical Research Centre of Finland Ltd., Tekniikantie 21, 02150 Espoo, Finland; saleem.ullah@vtt.fi
[3] Interdisciplinary Research Center for Membranes and Water Security, King Fahd University of Petroleum and Minerals (KFUPM), Dhahran 31261, Saudi Arabia
* Correspondence: irshad@kfupm.edu.sa; Tel.: +966-13-8608393

Abstract

The growing dependence on plastics is driving a sharp increase in environmental pollution, posing serious risks to human health. This issue necessitates immediate attention and proactive measures to mitigate its impact on both individuals and the broader ecosystem. From this viewpoint, biocompatible and biodegradable polymers, both synthetic and natural, have emerged as vital materials for applications in biomedicine, packaging, and environmental sustainability. The main advantages of biodegradable polymer materials lie in conserving fossil fuel resources, utilizing inedible biomass, and enabling environmentally friendly production processes. In this context, this review thoroughly discusses the categorization of biocompatible and biodegradable polymers into natural and synthetic types, detailing their structural characteristics, mechanisms of biodegradation, and compatibility matrices appropriate for biomedical, environmental, and industrial uses. It also addresses recent advancements in polymer synthesis technology, highlighting significant progress in polymer functionalization, responsiveness to stimuli, and environmentally friendly biobased synthesis methods. Additionally, it identifies challenges such as mechanical constraints, control over degradation, and expense, while also discussing future opportunities in the field of polymer science.

Keywords: biocompatible polymers; biodegradable polymers; drug delivery; tissue engineering; sustainable materials; smart polymers

1. Introduction

Since the 1950s, the study and commercial application of polymers have grown significantly, becoming essential in almost every facet of everyday life. By the late 1980s, worldwide polymer production had exceeded that of steel, and it now totals approximately 413.8 million tons each year [1]. The biggest portion is allocated for packaging (exceeding 30%), while the building and construction sector follows closely with over 20%. The automotive, electrical, and electronic sectors each represent 7% to 10%. The medical

industry utilizes less than 2% by weight, which is split between packaging materials (like prefilled syringes and blood bags) and medical devices [1,2].

The extensive application of polymers can be credited to their distinctive characteristics, such as ease of production, low weight, flexibility in mechanics, chemical resilience (especially at low temperatures), and affordability. However, these benefits have also led to considerable environmental issues. Globally, only around 9% of plastic waste is recycled, with the majority either going to landfills or being incinerated, while plastic's total greenhouse gas emissions from production to disposal were estimated to be 1.8 gigatons of CO_2 equivalent in 2019, making up roughly 3.4% of the worldwide figure. Incineration of waste is one of the most emission-heavy methods of disposal, and unmanaged leakage continues to negatively impact ecosystems. These challenges have prompted a move toward circular strategies in the realms of design, manufacturing, usage, and final disposal [3].

In response to these issues, both research and industry have sped up the creation of alternatives that minimize hazards, energy use, and waste production. One key approach focuses on the advancement of bio-based and biodegradable polymers intended to perform efficiently for a specified time before decomposing into simpler substances that can be managed and disposed of more easily through regulated methods [4]. It is estimated that in 2022, the production of bioplastic reached 2.22 million tons, with approximately 1.1 million tons (about 51%) categorized as biodegradable plastics, including polylactic acid (PLA), polyhydroxyalkanoates (PHAs), starch blends, polybutylene adipate terephthalate (PBAT), cellulose films, and polybutylene succinate (PBS). Additionally, nearly 1.1 million tons (roughly 49%) consisted of non-biodegradable polymers sourced from biological materials, primarily featuring bio-based polyethylene (PE), polyethylene terephthalate (PET), polyamides (PA), and polypropylene (PP), among others [5].

Biodegradable polymers are widely applied in biomedical fields, including tissue engineering, regenerative medicine, urology, controlled drug delivery, cardiac surgery, dentistry, and orthopedics, among others [6]. Literature reviews have highlighted the increasing utilization of these materials in controlled drug delivery systems, temporary implants, tissue scaffolds, and resorbable devices, where the polymer chemistry, processing methods, and microstructure are tailored to meet specific biocompatibility and degradation requirements [7–9].

This article explores the key properties of polymers, including their degradation mechanisms, biocompatibility, and mechanical and thermal characteristics, and categorizes polymers based on their origin as either natural or synthetic. The manuscript highlights recent technological advancements aimed at improving polymer interactions with biological systems, enhancing functional performance, and promoting sustainable, bio-based synthesis methods. Additionally, it examines the critical roles of polymers in medical, environmental, and industrial applications. Finally, the article addresses current challenges, limitations, and potential directions for future research in the field.

2. Key Properties and Classification of Biopolymers

2.1. Key Physicochemical and Biological Properties

The successful application of biopolymers in environmental and biomedical settings relies heavily on a thorough understanding of their physicochemical and biological properties. These properties influenced how they interact and degrade under different conditions. The key properties that are pivotal for the application of biopolymers include degradation mechanism, biocompatibility, and mechanical and thermal properties.

2.1.1. Degradation Mechanisms

The pathways of polymer degradation are crucial factors that shape their performance in environmental and biomedical applications. Biopolymers mainly degrade through hydrolytic and enzymatic degradation pathways, although other mechanisms, particularly photodegradation, are also possible.

In hydrolytic degradation, water molecules often cleave the bonds that join the monomeric units in polymers. A typical example is the cleavage of the ester bonds in PLA by a water molecule [10].

Various factors, including humidity, temperature, and catalyst availability, greatly influence the hydrolytic degradation pathways of biopolymers. For example, the hydrolysis rate of PLA can increase by 30–50% when the temperature is raised by 50 °C under humidity above 90%, compared to the hydrolysis rate at normal environmental conditions. Similarly, the presence of 0.5% by weight of $SnCl_2$ has been shown to accelerate PLA hydrolysis by approximately 40% relative to pure PLA, under the same environmental temperature and humidity conditions [11].

Enzymatic degradation occurs due to the action of enzymes that cleave the bonds joining the monomeric units in the polymer backbone. For example, the enzymatic cleavage of α-1,4-glycosidic linkages in starch-based polymers. Specifically, enzymes such as β-glucosidase and α-amylase act on the α-1,4-glycosidic linkages in starch-based polymers, whereas enzymes such as lipases, proteases, and esterases act on the ester bonds in PLA [10]. Similarly to hydrolytic degradation pathways, the enzymatic degradation of polymer can also be strongly influenced by factors such as temperature and humidity. A typical example shows how the rate of enzymatic degradation is accelerated by raising the temperature from 30 °C to 50 °C and maintaining humidity above 80% [12].

Overall, both hydrolytic and enzymatic degradation mechanisms play significant roles in determining the lifespan and stability of biopolymers in environmental and biomedical applications.

2.1.2. Biocompatibility Metrics

The thorough assessment of the biocompatibility of biodegradable and biocompatible polymers is essential. This is particularly important when these biopolymers are intended to be used in human beings. Biomaterials are typically evaluated for toxicity, allergic potential, and immunogenicity to prevent adverse events and ensure patient safety. Additionally, several regulatory bodies require rigorous biocompatibility testing before such materials are commercialized for consumer or clinical applications. Biocompatibility evaluation involves multiple aspects, including the careful selection of test types, choice of relevant cell lines or tissues, and performance assays tailored to the intended function of the biomaterials [13].

While most biopolymers discussed are generally regarded as biocompatible, a long-term biocompatibility assessment remains crucial. For example, PEG has traditionally been considered a non-immunogenic and biocompatible biomaterial. However, Chen et al. (2025) [14] reported the presence of anti-PEG antibodies, either pre-existing or induced by PEGylated vaccines and medicine, that may compromise the safety and efficacy of nanomedicines. These antibodies can alter the biodistribution of nanocarriers, stimulate undesirable inflammatory and hypersensitivity responses, and destabilize lipid formulations [14]. Similarly, PLA is also regarded as a biomaterial with good biocompatibility. However, when applied in vivo, it can provoke an inflammatory reaction and adverse tissue responses. Liu et al. (2024) reported that PLA-based microspheres modified with short-chain PEG exhibited enhanced histocompatibility [15].

2.1.3. Mechanical and Thermal Characteristics

The mechanical and thermal properties of biopolymers are crucial factors to consider for their suitability, especially for biomedical applications. From a mechanical characteristics perspective, the inherent biodegradability and biocompatibility properties of polymers render them suitable for use in bone tissue engineering and wound healing. For example, natural polymers such as collagen, alginate, and chitosan offer unique biocompatibility and biodegradability properties. They also promote cell proliferation and adhesion because of their structural similarities to the extracellular matrix (ECM). However, their practical applications, especially in load-bearing applications such as scaffolds for bone healing, are limited due to their low mechanical strength. As such, natural biopolymers are often blended with synthetic polymers or reinforced with inorganic substances such as calcium phosphates to improve their mechanical properties [16,17].

Conversely, synthetic polymers, particularly PLA and PCL, often exhibit impressive tunability and favorable mechanical properties. These properties allow synthetic polymers to be more suitable for long-term load-bearing applications compared to natural biopolymers. However, their lack of natural bioactivity often limits broader biomedical applications. As such, to improve their bioactivity for cell attachment and osteoconductivity, synthetic biopolymers are usually modified by combining them with bioactive materials [17].

Other important properties for biomedical and environmental applications of biopolymers beyond mechanical properties are the thermal properties. For example, the suitability of a biopolymer-based packaging film in food storage and preservation largely depends on its thermal stability. This ensures that the polymeric material maintains both its functional and structural integrity within a range of temperatures. As such, thermal stability prevents the premature degradation of polymeric packaging films, ensuring adequate protection of food products during processing, transportation, and storage.

To assess the thermal properties, analytical techniques such as differential scanning calorimetry (DSC), thermogravimetric analysis (TGA), and thermomechanical analysis are often invaluable. These techniques provide detailed insight into the relationship between polymeric packaging films and their thermal behavior and material structure, including crystallinity, chemical arrangements, morphology, and the role of nano-reinforcements in enhancing the thermal stability of polymeric films [18]. A notable study introduces PCL into PLA/PCL blends at varying ratios, which has been shown to influence the thermal properties, degradation rate, and flexibility of a 3D printed scaffold, demonstrating the importance and potential of this blend in tailoring material properties for specific tissue engineering applications [19].

Following this comprehensive overview of the fundamental physicochemical and biological properties that influence the behaviors of biopolymers, we next discuss the classification of natural and synthetic polymers. Throughout, we emphasize comparative performance, limitations, and specific design considerations, with concise summaries in Table 1 (natural polymers) and Table 2 (synthetic polymers).

2.2. Natural and Synthetic Polymers

Biodegradable polymers refer to polymeric materials that can be decomposed or disintegrated primarily through the enzymatic action of microorganisms into useful environmental products, such as water, methane, biomass, and carbon dioxide. On the other hand, other polymeric materials are considered biocompatible, meaning they do not elicit toxic, inflammatory, or immunogenic responses, particularly when used as biomaterials in humans. Both biodegradable and biocompatible polymers are used in diverse sectors, including biomedical devices and drug delivery, sustainable packaging, and agriculture [13,20–22].

For clarity, in this review, polymers are classified as natural or synthetic based on their source, irrespective of whether they are biodegradable, biocompatible, or both.

Natural polymers, as the name suggests, are derived from natural sources (Figure 1), while synthetic polymers are artificially synthesized to meet a particular need (Figure 2). This classification provides the framework for comparing the performance, limitations, and design considerations of each polymer across the two subclasses.

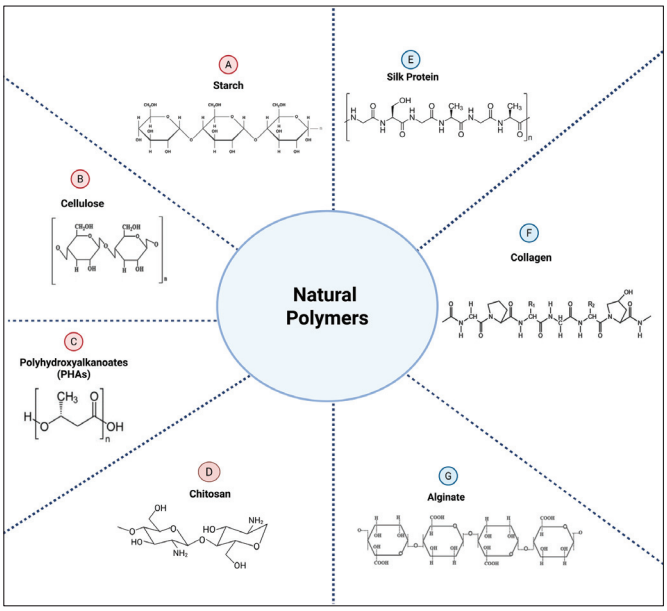

Figure 1. Representative structures of natural polymers. Illustration showing the chemical structures of common natural polymers, including starch, cellulose, PHAs, chitosan, silk protein, collagen, and alginate. Created with Biorender.com.

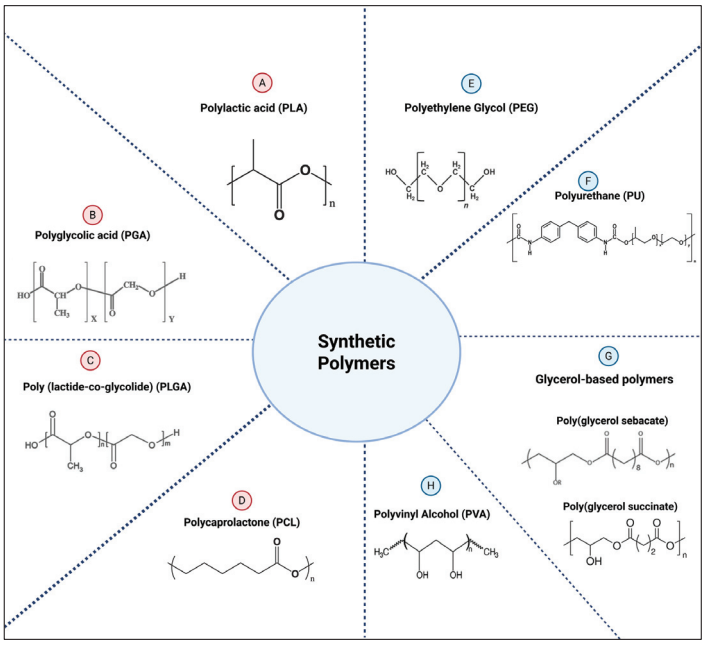

Figure 2. Representative structures of synthetic polymers. Illustration showing the chemical structures of common synthetic polymers, including PGA, PLGA, PLA, PEG, PU, glycerol-based polymers, PVA and PCL. Created with Biorender.com.

2.2.1. Natural Polymers

- Starch

Starch is one of the most abundant and inexpensive biodegradable polymers. It is a low-cost hydrophilic polysaccharide produced in the form of granules by several crops. The main crops from which starch is extracted include corn, rice, potatoes, and wheat. Chemically, starch is composed of amylose (linear) and amylopectin (branching) poly-(1,4)-α-glucose, and its physicochemical properties are strongly influenced by the amylose-to-amylopectin ratio [23]. Starch is poorly soluble in water at ambient temperature. However, the solubility of starch largely depends on the relative proportions of amylose to amylopectin [24–26].

However, some drawbacks of starch for broad applications include water sensitivity, brittleness, poor mechanical strength, and low impact resistance. Consequently, it is a common practice to chemically or physically modify starch to enhance its properties for a specific application. Due to their renewability, excellent oxygen barrier properties, and high biodegradability, starch-based biopolymers are utilized in various applications, including biomedical, packaging, agricultural, and adhesives [27]. These properties make starch-based films attractive for niche packaging applications, such as pouches, single-use wraps, and coating layers for vegetables, fruits, or snacks [28].

Despite the promising potential of starch-based films, the brittleness and high moisture absorption ability of starch impair its film-forming capacity. These limitations are often addressed by incorporating plasticizers into the starch matrix to enhance the water resistance and flexibility. However, adding plasticizers such as fructose and glycerol to starch-based films typically enhances ductility and water stability at the expense of mechanical strength. For instance, with the addition of 35% fructose, the tensile strength of wheat starch films decreases from 38.7 MPa to 7.6 MPa [29,30].

Recent reviews highlight the application of starch-based hydrogels (SBHs) in cutting-edge fields, including drug delivery, flexible sensors, wound dressings, tissue engineering, food packaging, soil protection, and wastewater treatment [31]. As a biomedical application example, a pH-responsive starch/PVA/g-C_3N_4 nanocarrier hydrogel has been shown to enhance doxorubicin delivery to cancer tumors or in vitro breast cancer cells, indicating the potential of SBHs for targeted therapy [32]. However, the weak mechanical properties of pure starch-based hydrogels have prompted the need for innovative strategies to enhance them. This is commonly achieved through the addition of nanofibers, inorganic fillers, or various crosslinking methods [33].

Table 1. Comparison of key properties of natural polymers.

Polymer	Mechanical Strength	Degradation Rate	Biocompatibility and Biodegradability	Key Limitations	References
Starch	Poor mechanical strength; reinforced with fiber matrix or by chemical or physical modification	Fast; temperature dependent	Biocompatible and biodegradable	Moisture absorbance and mechanical failure	[10,27]
Cellulose	Mechanical property weakened by moisture absorption; improved by chemical modification	Fast; temperature and environmental factors dependent	Biocompatible and biodegradable	Moisture absorbance and deterioration of mechanical properties	[10,27]
Polyhydroxyalkanoates (PHAs)	Weak mechanical property. Brittle.	Relatively fast, depending on HV content	Biocompatible and biodegradable	Commercially available PHAs are still brittle	[27,34,35]
Chitosan	Moderate mechanical properties, 10–60 MPa	Tunable degradation rate, Days-Months	Biocompatible and biodegradable	Poor water resistance, non-thermoplastic	[7,36–38]
Silk protein	0.74–1.65 GPa tensile strength (native silk fibers)	Weeks–months; tunable	Biocompatible	Brittle when dry, recombinant yield is low	[39–41]

Table 1. *Cont.*

Polymer	Mechanical Strength	Degradation Rate	Biocompatibility and Biodegradability	Key Limitations	References
Collagen	50–150 MPa tensile strength, 0.3–1.2 GPa Young's modulus	Weeks–months (native); days–weeks (marine)	fully biodegradable and highly biocompatible	May be immunogenic and pathogens contaminated	[42–47]
Alginate	Poor mechanical properties; may be improved by crosslinking with multivalent cations.	Fast at high temperatures	Biocompatible and biodegradable	Poor stability and mechanical properties. Difficulty in customization.	[48]

Graft engineering can also influence the properties of starch. For instance, a starch-based hydrogel produced by grafting polylactic acid and acrylamide onto starch exhibits antibacterial properties against both Gram-negative and Gram-positive bacteria. In addition, the synthesized hydrogel not only exhibits improved thermal and mechanical properties but is also biodegradable and non-toxic, making it an excellent material for wound dressings [49]. Despite the reported improvement, the long-term stability of grafted SBHs remains unclear and requires further research [33].

Apart from biomedicine, starch and starch-based materials are increasingly used as adsorbents for removing heavy metals and emerging pollutants, including pesticides and antibiotics, in addition to their roles in drug delivery and imaging. However, the promising removal of several pollutants by starch-based absorbents does not signify high selectivity for a specific pollutant. Therefore, the development of pollutant-specific starch-based absorbents remains an area of future research [50].

- Cellulose

Cellulose is a common organic polymer found in the cell walls of organisms from distinct biological groups, including algae, green plants, and bacteria. Chemically, cellulose is composed mainly of glucose monomers linked by β-1,4-glycosidic bonds, in contrast to the α-glycosidic bonds found in starch, a related biopolymer. It can be sourced from natural biological materials, particularly wood, cotton, hemp, and other fibrous plants. Both cellulose and its derivatives are considered eco-friendly materials due to their compatibility with various materials, regenerative properties, and ability to degrade. In addition, cellulose exhibits excellent rigidity, tensile strength, and mechanical properties [27,51].

The favorable mechanical properties of cellulose are associated with its ability to provide structural support, enabling plants to resist mechanical stress [52]. The tensile strength of cellulose-based films ranges from 30 to 50 MPa, while that of starch ranges only from 15 to 40 MPa [53].

However, the mechanical properties of cellulose may be compromised by moisture due to its hydrophilic nature. A common cellulose modification strategy involves the introduction of a specific reagent that reacts with its hydroxyl groups to reduce its hydrophilicity and enhance its mechanical and solubility properties [54].

Both cellulose and its derivatives have been widely applied in various sectors, including pharmaceutical, textile, wood, and fiber industries. A recent study highlights the potential of cellulose as a drug carrier, enhancing both the release of drugs and inhibiting the ability of several bacterial species to form biofilms [51,55]. Despite their promising potential, cellulose-based materials face challenges, including long-term durability, variability in properties, high production costs, and the need to tailor properties for specific applications [56].

- Polyhydroxyalkanoates (PHAs)

Polyhydroxyalkanoates (PHAs) belong to the family of aliphatic biopolyesters that accumulate inside microbial cells as intracellular granules (carbonosomes). When carbon-rich, low-value, or waste substrates are available and other nutrients are limiting (typically

nitrogen), some microorganisms can synthesize and store PHAs that are equivalent to 30% to 80% of their cellular dry mass [23,57].

PHAs are thermoplastic, generally biocompatible, and biodegradable biopolymers derived from several renewable feedstocks [58].

PHAs are increasingly considered an innovative alternative to non-degradable plastics such as polypropylene and polyethylene. PHAs are often considered a model for biologically sourced polyesters due to their chemical tunability, benign (non-toxic) degradation byproducts, and robust biocompatibility [27,59]. Although PHAs are produced through purely microbial synthesis, their large-scale commercialization is hindered by the lack of environmentally friendly, cost-effective downstream recovery methods, which can make them less competitive than chemically synthesized polyesters [60].

PHAs can biodegrade effectively without specific temperature requirements, similar to other biopolymers, in landfills and in environments unfavorable to degradation, such as freshwater and marine ecosystems [61,62]. However, PHAs have slower degradation kinetics than other biopolymers, such as cellulose, which can affect their potential as a sustainable material. A common strategy to increase the degradation rate of PHAs is to blend them with cellulose, which enhances water accessibility and facilitates enzymatic degradation [63].

Beyond environmental sustainability, their favorable biocompatibility and non-toxicity make PHAs promising candidates for biomedical applications, particularly in tissue engineering [34]. This explains the recent surge of interest in research on the biomedical applications of PHAs in regenerative engineering, with a strong emphasis on bone regeneration [35].

Among PHAs, poly(3-hydroxybutyrate) (PHB), a natural polymer typically derived from specific bacterial species, receives significant attention. It is an eco-friendly biopolymer that can be obtained from low-cost, renewable feedstocks and can be degraded both aerobically and anaerobically without the release of harmful byproducts [27].

Beyond the simple homopolymers, PHAs copolymers are attracting interest for their tunable properties. By altering the composition of their comonomer, their thermal and mechanical properties can be tailored [35]. A copolymer of economic significance, poly(3-hydroxybutyrate-co-3-hydroxyvalerate (PHBV), is well known for its versatility. PHBV is a high-crystalline copolymer of 3-hydroxybutyrate (3HB) and 3-hydroxyvalerate (3HV). Its impact strength increases with an increase in its 3HV content. However, higher 3HV levels reduce crystallinity, tensile strength, melting points (Tm), and the glass transition temperature (Tg) [64,65] Notably, PHBV exhibits superior flexibility to PHB, although it has been shown that its composites with PLA improved its stiffness property, comparable to poly(ethylene terephthalate) (PET) [66]. Therefore, manipulating the ratio of 3HB and 3HV monomers or blending PHBV with other biopolymers can enable the development of PHBV materials with desired properties, ranging from more ductile films to stiffer molded objects, thereby expanding their application range [34,66,67].

Nevertheless, Jin et al. (2023) noted that commercially available PHBV has a lower 3HV content, which confers brittleness and limits broader use [35]. To address this issue, several studies have shown that blending PHBV with other polymers, particularly PCL, PLA, PBAT, and polybutylene succinate (PBS), produces composites with targeted properties for environmental, packaging, and biomedical applications [35].

- Chitosan

Chitosan is a non-synthetic, biocompatible biopolymer that is often considered the second-most-abundant natural biopolymer after cellulose. Chitosan mainly originates from the deacetylation of chitin, the structural component that forms the exoskeleton of many

invertebrate organisms. The deacetylation process of chitin typically occurs in a strong alkaline environment, although it can also be achieved through enzymatic hydrolysis [68].

Based on structural similarities, chitosan is closely related to cellulose and chitin, and it stands out as the only known cationic polysaccharide. It consists mainly of β-(1-4) linked glucosamine units, with a variable proportion of N-acetylglucosamine residues. Unlike cellulose, the cationic character of chitosan allows its electrostatic interaction with other negatively charged biomolecules. These properties not only broaden chitosan's biomedical applications but also render its behavior strictly pH-dependent, which can be harnessed for the design of chitosan-based materials [36,69].

The presence of amino and hydroxyl groups in chitosan confers it with exceptional biological functionalities and chemical properties. Chitosan is relatively soluble in various media, interacts with microbial cell walls, exhibits viscosity, film-forming capacity, and has unique optical properties [36]. In biomedical research and applications, chitosan has been extensively studied for use in tissue engineering. The biomedical application of chitosan results from its consideration as a biopolymer that is non-toxic, biodegradable, biocompatible, and exhibits antimicrobial properties [7]. However, a practical challenge with chitosan is its limited solubility in body fluids, which restricts its broad application for drug delivery [70]. One key strategy to address chitosan's limited solubility is to blend it with hydrophilic plasticizers to enhance its moisture-absorption capacity [37].

In the context of sustainability, chitosan has also received growing interest for use in sustainable food packaging, mainly due to its multifunctional properties. Its intrinsic antimicrobial properties, combined with its barrier properties, make it a promising material for biodegradable food packaging films. Chitosan can also be particularly useful when combined with several additives, particularly bioactive compounds, polymers, and nanoparticles, which enhance its thermal, mechanical, and functional properties. Although the addition of plasticizers (such as PEG and glycerol) can improve the mechanical properties of chitosan composite films, the hydrophilicity of these plasticizers often results in increased moisture absorption, thereby compromising the chitosan barrier property [37].

Nevertheless, chitosan composite films can represent a biodegradable alternative to non-degradable petroleum-based plastics for packaging. They have been shown to have the ability to preserve perishable foods, including meat, dairy products, and seafood, thereby reducing spoilage and extending their shelf life [71].

In addition to food packaging, chitosan-based bionanocomposites are emerging as a cost-effective and highly efficient adsorbent for removing highly toxic contaminants in wastewater purification. However, the adsorption efficiency largely depends on the type of grafted solid materials on the chitosan composite, notably activated carbon, clays, and metals [72]. These studies bolstered the versatility of chitosan and chitosan-based materials for applications in biomedicine, packaging, and environmental sustainability.

- Silk Protein

Silk Protein is a natural polymeric material primarily produced by certain members of the phylum *Arthropoda*, including silkworms, spiders, fleas, and mites [39]. Although silk protein has received less attention than other biocompatible polymers, its favorable mechanical properties and controlled degradability have sustained scientific interest in its biomedical applications [40].

Silk possesses distinctive properties that continue to attract scientific interest. Its composition, structure, and properties differ depending on the source species, resulting in variations in environmental adaptability and functional roles [41]. Variation in the sequence of amino acids in the silk protein produced by different silkworm species results in distinct chemical, biological, and physical properties [73]. Among these species, *Bombyx*

mori silk protein stands out for its excellent properties and is the most widely studied for biomedical applications [74].

Silk protein is widely considered a biocompatible and less immunogenic material with impressive mechanical properties. These properties have supported its growing applications in biomedicine. Silk protein has been applied particularly in the development of nanospheres, microspheres, and membranes for therapeutic purposes [75]. However, silk protein (specifically silk fibroin) has a relatively slow degradation rate, which may negatively impact some biological applications. To address this issue, silk fibroin is enzymatically cross-linked with genipin or other materials to modify its stiffness, making it customizable for specific biological applications [40].

Recent studies have highlighted how the two main components of silk protein (sericin and fibroin), when combined with nanoplatforms, are emerging as effective materials for wound repair [76]. Another area of growing interest is the development of silk protein-based hydrogels, as they integrate well into tissue, exhibit lower immunogenicity, and are degradable, making them suitable candidates for wound dressings [77].

Silk protein-based composites are also being increasingly explored for their strong potential in bone tissue repair and regeneration. These silk-based protein composites are reported to exhibit favorable physicochemical properties and osteogenic signaling capabilities. This makes silk protein-based composites promising in bone tissue regeneration [78]. Despite the favorable mechanical and biocompatible properties of silk protein, the rearing of its insect producers requires the use of non-renewable energy sources, which has a negative environmental impact [79].

Apart from biomedical uses, silk protein is also being explored as a green and sustainable material. Silk protein has expanded potential because it can be used alone or in combination with other polymers, thereby broadening its potential as an advanced material [80]. The incorporation of low-cost polymers, particularly cellulose or starch, into silk protein composites may not only enhance their economic feasibility but also modify their degradability and flexibility for applications in various fields.

- Collagen

Collagen represents a principal fibrous structural protein often considered the most highly distributed and abundant protein in the animal body. It has impressive mechanical properties, which are strongly influenced by its triple-helical structure, composed of intertwined polypeptide chains. Each of the polypeptide chains is composed of a unique repeating sequence of glycine, proline, and hydroxyproline amino acids, which reinforces the helical structure of the protein. These properties impart collagen with strength and resilience, allowing it to perform structural functions in various tissues of the body. In addition to its structural properties, collagen is inherently biocompatible and low-immunogenic, increasing its potential breadth for biomedical applications.

However, gels derived from native collagen (especially marine) often exhibit insufficient mechanical properties for certain load-bearing applications [45]. Like other natural polymers with low mechanical properties, improved collagen mechanical properties can be achieved with crosslinking with chemical agents. However, the use of a chemical crosslinking agent, such as formaldehyde or glutaraldehyde, may induce toxicity [45].

Collagen can be obtained from various sources, each with its own advantages and disadvantages. Collagen sourced from the Achilles tendon, pig, and sheep skin raises concerns about pathogen transmission and immunogenicity, which necessitate the exploration of safer alternatives, such as marine and recombinant collagen [42,43,46].

Some of the advantages of marine collagen over mammalian collagens include simpler extraction methods, lower denaturation temperatures, minimal inflammatory response, and

overall safety. However, marine collagen is also limited by variability in structure owing to differences in source species, environmental conditions, and other factors. Such differences make it difficult for batch standardization and reproducibility, which are necessary for regulatory approval in biomedical applications [45].

Still, collagen and its derivatives are being developed in various forms, including hydrogels, scaffolds, sponges, and thin films for applications in tissue engineering, wound healing, regenerative medicine, and drug delivery [81]. For example, collagen-based nanofibers, owing to their bioactivity and structural similarities with the extracellular matrix, provide essential support for wound repair by stimulating cell adhesion, proliferation, migration, and differentiation.

Outside the biomedical field, collagen is also explored as a sustainable, environmentally friendly material for food packaging and other environmental applications. A recent study on collagen fiber film (CFF) derived from *Halocynthia roretzi* reported good tensile, water resistance, and biodegradability properties, coupled with a positive preservation effect on strawberries and pork when combined with chitosan [47].

Collagen packaging films have relatively favorable mechanical properties compared to other biopolymers, owing to collagen's unique triple-helical structure, which influences the film density. Despite these potentials, the broad application of collagen-based films, especially those derived from safer marine collagen, is limited by the brittleness of collagen, its high water solubility, and high production costs [45]. A more effective approach to addressing this issue could be to explore highly thermally stable collagen sourced from marine species, as chemical crosslinking may increase toxicity.

- Alginate

Alginate is a natural anionic, linear biopolymer commonly obtained from brown algae (such as bladderwrack, kelp, and sargassum) and certain bacteria (such as Pseudomonas aeruginosa). Structurally, alginate consists of α-mannuronic acid (M) and β-guluronic acid (G) linked by 1,4-glycosidic bonds. Alginate physicochemical properties are largely determined by its composition and the G-to-M ratio, which is primarily determined by the source species and geographical origin. Alginate has been explored for various human applications due to its favorable properties [82]. However, reproducibility and standardization remain challenging, as variability in alginate composition is influenced by factors such as species, season, and geographical origin [82].

Alginate exhibits beneficial properties, including biodegradability, biocompatibility, ease of gelation, non-toxicity, and high water absorption, rendering it a promising material for various biomedical uses [82]. For example, the biocompatibility and water retention ability of alginate-based microcapsules or nanoparticles offer them the ability to protect the drug constituent from gastric acid damage through controlled release, resulting in a better absorption rate [83,84]. However, alginate hydrogels exhibit poor mechanical integrity, and under physiological conditions, their stability can be compromised by their insufficient moisture barrier properties [85].

In wound dressings, alginate-based hydrogels exhibit good biocompatibility and are associated with minimal inflammatory reactions in the targeted areas of bone and joint injuries [86]. However, due to its high moisture absorbance capacity, an alginate/chitosan composite is typically developed not only to reduce moisture permeability but also to bestow it with additional antimicrobial and enhanced mechanical properties [82].

From sustainability perspectives, the multifaceted properties of alginate have gained growing scientific interest for its consideration in sustainable food packaging. For example, alginate-based films can prolong the freshness and reduce the spoilage of perishable foods such as meats, fruits, and vegetables. These films function by inhibiting microbial growth

while maintaining the oxygen level and moisture content of the preserved foods. Based on these combined effects, alginate-based films can maintain food quality and offer a promising, eco-friendly alternative to conventional plastic packaging [85]. Despite the progress made with regard to alginate-based packaging films, certain challenges remain for practical applications. These include large moisture absorption, which can impair food quality and the mechanical integrity of the film, as well as difficulty in scaling up packaging film production [85].

2.2.2. Synthetic Polymers

- Polylactic acid (PLA)

Polylactic acid (PLA) is widely recognized for its distinct advantage of being synthesized from renewable materials, such as rice bran, corn, and potato starch [27]. It is a linear aliphatic polyester chain that can be synthesized through the polycondensation or ring-opening polymerization of lactic acid monomers [55].

PLA is extensively used in the development of medical devices and sustainable packaging, owing to its well-known biocompatibility and biodegradability [27,55]. However, the inherent stiffness of PLA, which can make it unsuitable for certain load-bearing applications, necessitates blending it with other polymers to enhance its performance [19].

Table 2. Comparison of key properties of synthetic polymers.

Polymer	Mechanical Strength	Degradation Rate	Biocompatibility and Biodegradability	Key Limitations	References
Polylactic acid (PLA)	Satisfactory; depends on stereoisomer distribution.	Accelerated at high temperature and humidity	Biocompatible and biodegradable	Weak mechanical properties	[11]
Polyglycolic acid (PGA)	~31 MPa (pure PGA), 4–5% elongation	90% mass loss in 20 days (70 °C, water)	Biocompatible and biodegradable	High crystallinity leads to low elongation (≈4–5%), limiting flexibility.	[27,87]
Poly (lactide-co-glycolide) (PLGA)	High (up to 2× with HA/β-TCP); load bearing	Tunable (1–6 months)	Biocompatible and biodegradable	Burst release, acidic microenvironment, brittleness	[10,20,54]
Polycaprolactone (PCL)	~23 MPa (bulk), 2.5 MPa (electrospun), ~700% elongation	4.8% mass loss (32 weeks), full resorption ≈14 months	Biocompatible and biodegradable	Slow degradation and hydrophobicity	[27,88–90]
Polyethylene glycol (PEG)	Flexible and elastic, 1.24–1.44 Mpa (PVA-PEG-CNF hydrogel)	Very slow; partial degradation in blends after 35–45 days	Biocompatible	Poor biodegradability, moisture instability, and MW variability	[91,92]
Polyurethane (PU)	10–40 MPa (bio-based PU); up to 1000% elongation	Weeks to months (depending on structure and environment)	Biocompatible and biodegradable	Isocyanate toxicity, poor biodegradability, and recycling limits	[93–95]
Polyvinyl Alcohol	High (adjustable via crosslinking and FT cycles)	Weeks–months; accelerated by ester copolymerization	Biocompatible	Non-degradability, swelling, process sensitivity	[96–98]

Therefore, in addition to its intrinsic properties, PLA is commonly improved for several applications. For example, the mechanical and degradation properties of PLA were tuned in a 3D-printed PLA/PCL scaffold by varying the PLA/PCL ratio, providing invaluable insights for the development of custom scaffolds to meet specific needs. However, for such blends to be put to practical use, they may need to be optimized for a specific application. For example, an increased PLA content in the blend may make the composite more appropriate in applications where rapid degradation is necessary (e.g., soft tissue implants). On the other hand, a load-bearing application with the PLA/PCL blend scaffold will require a higher PCL content for long-term structural support [19].

In another study, PLA's tensile and thermal performance has been shown to improve significantly through filler hybridization derived from rice husk and biocarbon, resulting in a composite suitable for structural applications and enhancing sustainability. However, a high concentration of the biocarbon results in poor matrix interaction, signifying a challenge that needs to be addressed for large-scale manufacturing [99].

In addition, a compostable composite based on a PLA/polybutylene adipate-co-terephthalate (PBAT) blend with ε-poly-L-lysine (ε-PL) was developed to impart antimicrobial properties, yielding an antimicrobial packaging film that enhances food safety and increases shelf life. Despite the impressive advances, the study highlighted impairments in the mechanical and moisture-barrier properties of the composite due to the hydrophilic nature of the ε-PL, which decreases the crystallinity of the material [100]. Therefore, a critical challenge remains in developing PLA-based composites with suitable antimicrobial properties without compromising their mechanical or barrier properties.

- Polyglycolic acid (PGA)

Polyglycolic acid (PGA) is a synthetic, thermoplastic, biodegradable polymer based on a linear aliphatic polyester. PGA is synthesized by the polymerization of ring-opening of cyclic glycolide monomers [101]. The two-step process of PGA degradation involves the initial penetration of water into the amorphous region, where ester bonds break, followed by the hydrolytic cleavage of the crystalline regions [102].

Despite the biodegradability of PGA and its structural similarities to PLA, it is known for its favorable barrier properties, high mechanical properties, and heat resistance compared to PLA [103].

Consequently, PGA has been applied in various fields of biomedicine, including drug delivery, tissue engineering, and biomedical devices [55]. Despite its potential, PGA has disadvantages, including rapid hydrolytic degradation and poor toughness, which can limit its long-term mechanical stability. As such, PGA is blended with other polymers to enhance its mechanical properties. The water resistance and mechanical properties of PGA can also be enhanced through graft or chain-extension reactions with chemicals such as glycidyl methacrylate [103].

Beyond biomedicine, a PBAT/PGA blend film exhibits enhanced mechanical properties and biodegradability in ambient environments, highlighting the potential of PBAT/PGA films as a sustainable material for packaging applications. However, a thorough investigation of the performance of PBAT/PGA under different environmental conditions and an evaluation of the migration behavior of the PBAT/PGA component under various conditions are necessary before practical packaging applications.

- Poly (lactide-co-glycolide) (PLGA)

Poly (lactide-co-glycolate) (PLGA) is synthesized by the copolymerization of glycolic acid (GA) monomers with L-lactide and LD-lactide (LA). Its physical form, whether largely amorphous or more crystalline, depends on the molar ratio of lactide to glycolide in the copolymer. The variation in this ratio also governs the degradation rate [104]. The adjustment of these proportions often provides an opportunity for fine-tuning the chemical and mechanical properties of PLGA for specific applications [54].

PLGA is a crucial biopolymer in drug delivery and regenerative medicine. It has increasingly been considered for these purposes owing to its tunable degradation properties, biocompatibility, and ability to sustain and localize drug release. However, for orthopedic or certain applications that require mechanical and thermal stability, PLGA is typically reinforced or grafted with other chemicals. Some key PLGA reinforcement agents include hydroxyapatite and β-tricalcium phosphate (β-TCP), which enhance its structural integrity in a wet environment and improve mechanical strength. [20].

A typical example of a sustained-release study is one in which a peptide-loaded PLGA microsphere exhibits an enhanced release profile and significantly reduced burst release. This provides insight into the efficient preparation of microspheres for drug delivery using a microfluidic device [105]. Although such studies may serve as a benchmark for preparing peptide-loaded microspheres, rigorous optimization studies are needed to achieve consis-

tent encapsulation efficiency and reproducible performance under physiological conditions before clinical translation.

- Polycaprolactone (PCL)

Polycaprolactone (PCL) is a synthetic, biodegradable, linear aliphatic polyester produced by the ring-opening polymerization of caprolactone monomers in the presence of a metal anion catalyst. Its tensile stress ranges from 12 to 30 MPa, with elongation at break between 400% and 900% [106].

The melting point of PCL ranges from 58 to 60 °C. Some properties that support its biomedical applications include its low cost, high toughness, and solubility in most organic solvents. Although both aerobic and anaerobic microorganisms can degrade PCL, the crystallinity and molecular weight of PCL may influence the rate of degradation. In addition, its poor biological activity due to its hydrophobic structure and slow degradation rates are factors that could limit its extensive applications [27].

The complete degradation of PCL can take 2 to 3 years, making it unsuitable for applications that require rapid degradation, particularly in drug delivery. The degradability issue of PCL can be addressed by blending it with degradable materials, particularly PLA and PGA, thereby reducing its crystallinity. PCL can also be blended with biological materials, particularly collagen and hydroxyapatite, to enhance its biological properties for specific applications, such as craniofacial tissue regeneration [89].

A growing number of studies have shown that PCL properties can be improved by producing its composites with other polymers for specific applications. For instance, a new biodegradable and biocompatible PCL-PU-semi-IPNs scaffold was developed, supporting the attachments and proliferation of cells, highlighting an advanced material for skin tissue engineering applications.

In another study, electrospun PCL-based membranes were developed, demonstrating promising properties for localized drug delivery, tissue regeneration, with mechanical properties comparable to those of commercially available guided bone regeneration (GBR) and guided tissue regeneration (GTR) membranes. Although these studies are promising, there are still biocompatibility and safety concerns, especially regarding degradation products that may stimulate an inflammatory response. Additional in vivo studies are also needed to assess the clinical applicability, biocompatibility, long-term stability, and consistent therapeutic potential of the incorporated agents before practical applications [90].

- Polyethylene Glycol (PEG)

Polyethylene Glycol (PEG) is a synthetic and hydrophilic polymeric material widely recognized for its versatility. It can also be distinguished by its several end functional groups and varying chain lengths [107]. PEG can be synthesized either through the polycondensation polymerization of ethylene glycol or through the ring-opening polymerization of ethylene oxide [91].

Some of the distinct physicochemical properties of PEG, particularly its good water solubility, inherent biocompatibility, and tunable molecular structure, have placed it as one of the most widely applied synthetic polymers across pharmaceuticals, biomedicine, and related fields. In addition, PEG can be customized through molecular modifications and polymer design to suit specific applications in tissue engineering, drug delivery, and food packaging. Despite the enormous potential of PEG, its broad biomedical application is limited by its potential toxicity and limited biodegradability [91].

An expanding area of PEG application in biomedicine is the development of PEG-based hydrogels and drug delivery technologies. PEG-based hydrogels continue to be applied for the treatment of various wound injuries due to their responsiveness

to environmental stimuli and controlled drug release to a specific target area, thereby minimizing off-target effects and enhancing the success of chemotherapy [108].

In the context of food packaging and preservation, PEG-based nanocomposite films combined with antimicrobials have been shown to improve food quality, thereby mitigating spoilage and extending shelf life. However, despite PEG's benefits, its hydrophilicity could, in the long term, affect food quality and the mechanical integrity of packaging films. Additionally, strict consideration of dosage is necessary for its safe use [91]. Nevertheless, these advances underscore the potential of PEG-based materials not only in biomedicine but also in the production of food packaging and solutions.

- Polyurethane (PU)

Polyurethane (PU) is an important synthetic polymeric material, mainly distinguished by its urethane bonds. The synthesis of PU occurs through the process of addition reactions between isocyanates and alcohols [94]. Based on its structural composition, PU is divided into hard and soft segments. The hard segments are typically composed of isocyanates and chain extenders, while the soft segments are derived from polyols. By adjusting the ratio, structure, and molecular distribution of these segments, PU can be engineered into functional materials with antibacterial, self-healing, anti-aging, and anticoagulating properties [93].

The growing interest in the use of PU in biomedical applications can be associated with its low cytotoxicity, inherent chemical stability, and biocompatibility. Recent reviews, especially the work of Cui et al. (2023) [93], have comprehensively emphasized the growing interest in the application of PU in orthopedics, biosensors, wound dressings, and cardiovascular applications, reflecting the growing importance of PU in biomedical innovations. However, an active area of research is ensuring PU stability to prevent undesired degradation and aging for long-term applications. Also, for short-term applications, efforts are being made to tailor the PU degradation rate so that it does not degrade too fast, releasing a product that may stimulate inflammatory reactions, or too slow, delaying patient recovery and causing undesired damage [93].

From a sustainability perspective, efforts have been focused on bio-based PU materials derived from renewable sources, such as vegetable oils, polysaccharides, and lignin, to reduce the environmental challenges posed by PU production and may open new avenues for its commercialization. Although bio-based PU materials offer numerous advantages, achieving PU materials with satisfactory mechanical properties for the desired application is still challenging. Efforts have been made to reinforce PU-based materials with fillers, especially chitosan, to produce bio-composites with suitable properties for long-term use. Still, scalability and economic feasibility continue to limit large-scale production of PU-based materials [95].

- Polyvinyl Alcohol (PVA)

Polyvinyl Alcohol (PVA) is a biodegradable polymeric material that has attracted considerable attention in recent years. The strong interest in PVA stems from its favorable properties, including hydrophilicity, biocompatibility, non-toxicity, and mechanical performance. PVA is mainly synthesized through the hydrolysis of poly(vinyl acetate) (PVAc), which is formed via the polymerization of vinyl acetate monomers [97].

PVA has been considered for many biomedical applications. However, it is particularly valuable in the production of PVA-based hydrogels. The strong interest in PVA-based hydrogels stems from their combination of favorable properties, including good mechanical strength, suitable water content, and excellent biocompatibility. However, when specific mechanical properties are desired, such as in tissue engineering, filtration, or membrane

production, the inherent mechanical properties of PVA are often insufficient and have to be improved through various crosslinking strategies [96].

Consequently, with advances in synthesis and crosslinking strategies, PVA-based materials, such as PVA-based hydrogels, have the potential to become promising materials for various biomedical applications. Advanced cross-linking strategies using cross-linking agents often yield PVA with enhanced flexibility, cytocompatibility, and antimicrobial properties, thereby expanding their potential applications in areas such as drug delivery, regenerative medicine, contact lenses, and related biomedical fields. On the other hand, the improved mechanical and thermal properties achieved by crosslinking often reduce the PVA biodegradation rate, a drawback which is particularly undesirable in drug delivery systems. As a result, even with significant progress in developing PVA materials, particularly PVA-based hydrogels, they have not yet reached an appropriate level for large-scale production [96,109].

In the context of environmental sustainability and green packaging, PVA is also receiving considerable attention as a green packaging material. Trigui et al. (2025) developed a PVA-based packaging film reinforced with nanofibril fillers, demonstrating improved barrier performance, thermomechanical stability, and mechanical strength, highlighting the potential of PVA-based materials as an environmentally friendly packaging alternative [110]. However, further optimization of the coating process on both plastic and paper packaging films is still needed before practical applications [110].

- Glycerol-based polyesters

Glycerol-based polyesters have emerged as a promising class of biodegradable and biocompatible materials, particularly for biomedical applications. These polymers are typically synthesized via polycondensation of glycerol with non-toxic dicarboxylic acids, producing materials with tunable mechanical and degradation properties. Among these, poly(glycerol sebacate) (PGS) is the most extensively studied, followed by poly(glycerol succinate) (PGSu), which has shown emerging potential in related fields.

Poly(glycerol sebacate) (PGS) was first reported in 2002 in the context of tissue engineering, as a tough biodegradable polyester synthesized for soft tissue engineering [111,112]. PGS is relatively inexpensive, exhibits thermoset elastomeric properties, and is bioresorbable, meaning it degrades in vivo, with its degradation products eliminated via natural metabolic pathways. Moreover, its mechanical properties and degradation rates can be tailored to meet specific application requirements [113].

The common starting materials for PGS synthesis are glycerol and sebacic acid. Glycerol is a basic building block of lipids, while sebacic acid, a natural metabolic intermediate in the ω-oxidation of medium- to long-chain fatty acids, is chosen for its favorable toxicological and polymer chemistry profile. Both monomers are considered safe: the U.S. Food and Drug Administration (FDA) has approved glycerol for use as a humectant in foods, and polymers containing sebacic acid are also considered safe [114].

The synthesis of PGS is guided by five key criteria based on its intended use: Hydrolytic degradation is preferred to reduce variability from enzyme-based degradation, and ester bonds are included to enable hydrolysis. The polymer should have a low degree of cross-linking, which must be hydrolysable and chemically identical to the backbone to ensure uniform degradation. The starting materials must be non-toxic, with at least one being trifunctional and one supplying hydroxyl groups for hydrogen bonding (as mentioned above, the starting materials glycerol and sebacic acid meet this criterion) [115]. The conventional method for synthesizing PGS, i.e., polycondensation synthesis, involves a two-step procedure that incorporates a pre-polymerization step to form low-molecular-weight polymers/oligomers, followed by a curing step to cross-link these products and

shape the final material [116,117]. Alternative synthesis methods have also been explored, including microwave-assisted processes, catalytic or enzymatic synthesis (e.g., using lipase), photopolymerization, and urethane cross-linking [118,119].

PGS is characterized as a transparent, nearly colorless polyester with mechanical behavior similar to soft biological tissues such as the cornea, arteries, spinal cord, and some muscle types. Structurally, hydroxyl groups on the carbon backbone enhance the hydrophilicity of the polymer [120]. PGS exhibits nonlinear stress–strain behavior, typical of soft elastomeric materials. As a partially semicrystalline polymer, its thermal properties are influenced by both its glass transition temperature (Tg) and melting temperature (Tm). PGS remains stable up to 250 °C and exhibits a single weight loss step between 320 °C and 475 °C [121].

Poly(glycerol succinate) (PGSu) is another glycerol-based polyester that can be synthesized via the polycondensation of glycerol with succinic acid, a dicarboxylic acid similar to adipic and sebacic acids [121]. Succinic acid is derived from the fermentation of biomass and is now produced at an industrial scale. The synthesis of PGSu typically involves bulk polycondensation in the absence of solvent and catalyst, without generating toxic byproducts [122]. PGSu macromolecules can adopt various architectures, including dendrimers, branched, highly branched, and hyperbranched polymers. The synthesis conditions significantly affect the physical and mechanical properties of hyperbranched polyesters (HBPEs), due to variations in molecular weight, cross-linking density, and degree of branching. However, compared to PGS, there is currently limited data available on the mechanical properties of PGSu [123].

Poly(glycerol succinate) has been used as an accelerant for poly(caprolactone) degradation, promoting moisture penetration into hydrophobic matrices. Furthermore, hydrophilic PGSu oligomers can be functionalized with fatty alkyl chains to form amphiphilic structures, which may serve as bio-based surfactants in various personal care and household products, such as shampoos, body washes, and kitchen cleaners. These bio-based surfactants could reduce the skin and hair damage associated with synthetic detergents [124]. PGSu shares similarities with PGS, particularly in its potential for tissue engineering applications. PGSu has been proposed as a scaffold material or scaffold additive for cardiac, bone, cartilage, nerve, and corneal tissue regeneration [125].

Despite the many advantageous properties of glycerol-based polymers, continued research is needed to enhance their performance and functionality for clinical use. Further development and modification strategies are essential to fully realize their potential, especially in the regeneration of damaged tissues and the treatment of various diseases.

3. Recent Technological Advancements

3.1. Surface Modification and Functionalization

A significant drawback of many inexpensive polymers is their resistance to various chemical treatments, which is a result of their naturally low surface energy. Even though their bulk properties, including density, chemical resistance, and mechanical flexibility or rigidity, may satisfy the needs for different applications, their surface qualities frequently fall short [126]. This concern is especially significant in biomedical applications, where materials need to interact well with water-based environments. For example, since biological processes take place in liquid mediums, the polymers used in these applications must demonstrate adequate wettability. If this property is lacking, biological fluids like blood can form droplets and slide off the surface, which obstructs proper functionality. Therefore, polymer-based biomedical devices intended for handling liquids must undergo surface treatment or functionalization to attain the required wettable properties [127].

Currently, conventional techniques for altering the surfaces of polymeric substrates involve either attaching polyethylene glycol chains to the polymers, particularly those used in drug and gene delivery, or chemically treating the polymer to introduce functional groups, nanoparticles, and other polymers (both natural and synthetic) [128]. Conversely, methods based on plasma and irradiation can enhance the chemistry and physical characteristics of the BC in a single step while preserving its inherent bulk properties. We will elaborate on each of these techniques in more detail in this section.

3.1.1. PEGylation

PEGylation is the process of attaching polyethylene glycol (PEG) chains to various biomolecules, including hydrophobic polymers, drugs, nanoparticles, proteins, and peptides, to improve their therapeutic effectiveness while minimizing the associated toxicity [129]. The idea of PEGylation was first introduced by Davis and Abuchowski in 1970, when they successfully altered albumin and catalase using PEG. Since then, the technology has been extensively advanced and broadly utilized by various biomedical research and therapeutics [130]. PEG can be applied to nanoparticle (NP) surfaces using three primary strategies, namely covalent grafting to form a stable chemical bond, physical adsorption through electrostatic or hydrophobic interactions, and conjugation with hydrophobic molecules to create macromolecules that self-assemble with other compounds, resulting in PEGylated NPs in solution [131].

PEGylation has been widely utilized in biomedical applications to improve the stability and performance of nanomaterials [132]. For instance, PEGylation has been demonstrated to enhance the stability of micelles, liposomes, dendrimers, gold nanoshells, quantum dots, and polymeric nanoparticles (NPs) in vivo, thereby improving therapeutic efficacy [133]. PEG-modified NPs exhibit increased hydrophilicity and near-neutral zeta potential, reducing protein adsorption (opsonization) and subsequent clearance by the mononuclear phagocyte system [134]. Additionally, the hydrated PEG chains increase the hydrodynamic size of NPs, providing steric shielding that reduces renal filtration and limits degradation by enzymes and antibodies. This prolongs circulation time and supports more efficient, localized drug release [135].

To date, over 20 PEGylated liposomal or RNA-based formulations have received approval from the United States Food and Drug Administration, including Doxil® and Macugen®, which are employed in the treatment of cancer and neovascular age-related macular degeneration, respectively [136,137]. Beyond drug delivery, PEGylation also enhances the stability and biocompatibility of nanomaterials such as graphene, without compromising their intrinsic properties [136–139]. For instance, PEG coatings have been shown to improve the solubility and stability of graphene and extend the circulation time of PEGylated PLGA nanoparticles by reducing their immunogenicity and resistance to immune clearance [140].

3.1.2. Chemical and Plasma Treatments

- Chemical treatments

The chemical modification of polymer surfaces is an important area where traditional physical methods fall short or are unsuitable for industrial needs, particularly in biomedical applications, where improved properties are necessary without changing the surface texture. Many chemical surface treatment techniques utilize wet processes, where the polymer is submerged or coated/sprayed with a solution to improve its surface characteristics and eliminate debris and microbes, creating a sterile environment appropriate for biomedical use [141]. Chemical treatments rely on the reactive sites or functional groups found on polymer chains. Typically, these processes are conducted in a watery environment (wet

chemical etching), which enhances the number of functional groups on the surface. These functional groups are then activated and later interact with other molecules present in the solution [127].

Although wet chemical treatments offer a diverse array of reagents for selectively treating polymers at scale and low cost, they necessitate a careful approach, since the reaction rate is influenced by the reagent's strength, the composition of the material, and the duration of treatment. Furthermore, additional steps such as rinsing, washing, and drying are necessary before any further processing of the polymer, which inevitably leads to an increase in the amount of hazardous waste produced during a single surface treatment operation. Consequently, surface modification via wet chemical methods is advantageous if the application is non-invasive and poses minimal side effects, with proactive etching and alterations in the material's bulk crystalline phase being of lesser significance for the intended application. For instance, biomedical implants demand both elasticity and strength alongside surface modifications to enhance functionality and affect bio-interactions with surfaces [141].

Various approaches for altering the chemistry of polymers include substituting the existing functional groups on the polymer, such as replacing the hydroxyl groups in the polymer with different functional groups [142,143], crosslinking with other polymer materials through either covalent or non-covalent bonds [144], or creating physically attached composites with polymers that exhibit improved characteristics [145,146]. The creation of composites involving metal or metal chalcogenide nanomaterials, along with the integration of carbon-based nanocomposites, has been well established [145]. The key benefit of developing nanocomposites by incorporating metals or metal chalcogenides is that the resulting polymer can merge the properties of multiple materials, thereby enhancing both the mechanical characteristics and functionalities beyond those of the individual composites alone. Although chemical treatment is an easy way to render a polymer wettable, this process is declining due to the ecological impact caused by the use of excessive organic solvents and other toxic chemicals [2].

- Plasma treatment

Plasma is a partially ionized gas composed of free electrons, ions, radicals, and neutral molecules or atoms. It can be generated through several techniques, including direct current (DC), alternating current (AC), and radiofrequency (RF) discharge. In these processes, gases are excited into energetic states by means of radio-frequency waves, microwaves, or electrons emitted from a heated filament discharge [147]. The plasmas most commonly used for surface treatment are cold non-equilibrium plasmas, in which the electrons possess much higher translational energies (1–10 eV) than the ions, molecules, or radicals (around 0.025 eV, corresponding to 298 K). Only a small fraction of the gas molecules are ionized under these conditions. Low-pressure plasmas, typically operated at 0.1–10 Pa, are especially effective for such applications, as the reduced pressure allows the plasma to penetrate more deeply into materials while minimizing surface damage [148].

In low-pressure plasmas, particles exhibit a longer mean free path, allowing them to travel greater distances before colliding with gas molecules or surfaces. As a result, the plasma can penetrate more effectively and interact with materials at deeper levels, leading to enhanced surface modifications [126]. For large-scale surface modifications, atmospheric-pressure plasmas are often preferred because they operate at or near room temperature and do not require a vacuum system. These plasmas are sustained by gas mixtures capable of maintaining a discharge at atmospheric pressure, eliminating the need for costly vacuum chambers. This makes it possible to treat extensive surface areas

efficiently, thereby overcoming a key limitation of vacuum-dependent surface modification processes in industrial applications [149].

Plasma treatment provides enhanced flexibility and typically utilizes environmentally friendly substances such as noble gases, oxygen, and nitrogen, along with minimal amounts of organic precursors, and requires relatively straightforward equipment, which includes a vacuum chamber, a plasma source to create the discharge, gas supplies to fuel the plasma, and vacuum equipment like vacuum pumps [150]. When a surface is exposed to plasma, two primary types of modifications can occur. (i) Functionalization by reactive species: inert gases activated in the plasma can generate reactive species that interact with the polymer surface. For example, oxygen plasma can introduce hydroxyl groups through surface hydroxylation. (ii) Deposition of polymeric films: when organic molecules such as saturated or unsaturated hydrocarbons are used to generate plasma, thin polymeric coatings can be deposited onto the surface [127].

The effect of plasma treatment on surface characteristics depends strongly on the type of gas and the plasma conditions. Oxygen plasma introduces carboxyl and hydroxyl groups, while hydrogen plasma primarily yields hydroxyl groups through single-bond formation. Ammonia and nitrogen plasmas generate nitrogen-containing functional groups on the surface, whereas water plasma treatment results in the incorporation of hydroxyl groups [151]. Although plasma treatment offers several benefits, the effects are typically temporary, causing the altered surfaces to slowly regain their original wetting and adhesion characteristics. Recent studies have shown that integrating plasma treatment with approaches such as PEG silane treatment can lead to a lasting hydrophilic modification and enhance the durability of the polymer surface [152].

3.2. Stimuli-Responsive Polymers

The ability to respond to external stimuli is a characteristic frequently observed in living organisms. Nature necessitates finely tuned assemblies and interfaces capable of reacting to changes in the environment to sustain biological processes. For instance, certain plants can fold their leaves to trap insects when touched, such as the Mimosa pudica and the Venus flytrap (Dionaea muscipula), which begins to close when its trigger hairs are mechanically stimulated [153]. Drawing inspiration from how nature responds and functions, scientists across the globe have been working on innovative functional materials to create actuators that can perform tasks in reaction to changes in their physical and chemical surroundings [154]. The capacity to tune polymer properties in response to external stimuli enables the design of intelligent materials with applications in controlled drug delivery, bio-separation, biosensing, biomimetic actuators, and immobilized biocatalysis, among others [155].

Stimuli-responsive polymers can be derived from either natural or synthetic sources or by integrating a responsive element or function into the existing structure of a polymer. Polymeric nanocarriers, particularly those designed for the delivery of bioactive substances, can be adapted into stimuli-responsive systems based on the mechanism of release triggered by specific stimuli, which can be either endogenous (such as pH, enzymes, temperature, redox potential, hypoxia, glucose concentration) or exogenous (including light, magnetism, ultrasound, or electrical impulses) to ensure effective biodistribution and controlled release of drugs or genes at designated locations [153,156].

3.2.1. Temperature-Responsive Polymers

Temperature-responsive polymers, or thermoresponsive polymers, represent one of the most extensively studied classes of smart materials. They are generally categorized

into two groups based on their temperature-dependent phase behavior: lower critical solution temperature (LCST) and upper critical solution temperature (UCST) types. The LCST corresponds to the temperature at which the binodal, or coexistence curve, reaches its minimum in the phase diagram, while the concentration at this minimum is referred to as the lower critical solution concentration (LCSC) [157]. Temperature-responsive polymers exhibiting a lower critical solution temperature (LCST) remain soluble in water (or organic solvents) when the temperature is below the LCST. Above this threshold, however, they become hydrophobic due to intensified hydrophobic interactions both within and between polymer chains. This reversible solubility transition has been widely exploited in diverse applications, including model protein design, triggers for self-assembly, "on–off" switches for protein functionality, cell sheet engineering, drug delivery carriers, chromatography, sensors, and adsorption materials [158].

The first polymer reported to exhibit LCST behavior was poly(N-isopropylacrylamide) (PNIPAM) in aqueous solution. Since its discovery, PNIPAM has become the most extensively studied thermoresponsive polymer, largely because its phase transition occurs near physiological conditions, at approximately 32 °C. This transition, which lies between room and body temperature, makes PNIPAM particularly attractive for biomedical applications [159]. To broaden the range of applications, several LCST-type water-soluble polymers have been identified [160]. Among these is Poly-N-vinylcaprolactam (PNVCL), a synthetic, non-ionic, water-soluble, thermoresponsive polymer that can shift from a liquid state to a gel state when the temperature exceeds its lower critical solution temperature (LCST), typically reported within the physiological range of 34–37 °C. In summary, PNVCL is an affordable and widely utilized polymer due to its low cytotoxicity, making it suitable for use in the biomedical sector for purposes such as wound healing, drug delivery, and tissue engineering [161]. Another example is poly(2-chloroethyl vinyl ether-alt-maleic anhydride), which displays LCST-type thermoresponsive phase behavior in selected organic solvents under mild conditions [162,163].

In contrast to LCST polymers, UCST polymers are soluble in solvents at temperatures above the UCST and become insoluble when the temperature drops below this threshold [164]. Specifically, increasing the temperature beyond the transition point leads to solubilization that is driven by enthalpy, as the interactions among polymer chains are diminished in favor of interactions between the polymer and the solvent [165]. This phenomenon arises due to particular interactions like hydrogen bonding and electrostatic interactions. The capability of UCST polymers to experience phase transitions triggered by temperature changes offers potential for a variety of applications, including insulating materials, catalysis, the assembly of nanomaterials, sensors, and protein separations [166]. At present, the most extensively studied UCST polymers include poly(sulfobetaine), poly(acrylic acid), and poly(acrylamide), all of which exhibit phase transitions in aqueous media under practical conditions [159].

Typically, temperature-sensitive homopolymers exhibit two main changes in properties: a shift from hydrophilicity to hydrophobicity, and the onset of aggregation/precipitation due to hydrophobic interactions once the concentrations exceed the critical aggregation concentration. Depending on their design, polymers containing two temperature-sensitive segments covalently linked at each end of the chain can exhibit dual temperature-responsive behavior as a result of conformational changes. Such dual responsiveness can be engineered by combining segments with LCST and UCST characteristics—for example, LCST–LCST, UCST–UCST, or LCST–UCST arrangements, with the latter tailored according to whether the LCST is higher or lower than the UCST. Polymers exhibiting multi-temperature responsiveness with three, four, or even more temperature-responsive characteristics have also

been documented. Such polymers are capable of undergoing highly intricate, programmed structural transformations in aqueous solutions. In recent years, these multi-temperature-responsive properties have also been incorporated into other polymeric systems, including gels and nanoparticles [167].

3.2.2. pH-Responsive Polymers

pH-sensitive polymers are a type of intelligent material that experiences significant physical and chemical transformations in response to minor changes in pH levels. These polymers comprise ionizable functional groups that can either take up or release protons, leading to reversible shifts between their charged and neutral forms [168]. pH serves as one of the most frequently utilized stimuli for drug delivery, targeting specific organs (such as the vagina or gastrointestinal tract) or organelles (including lysosomes, Golgi apparatus, and endosomes). It has also been employed to release drug components in response to changed pathological states, such as cancer, inflammation, or ischemia, which are associated with significant shifts in pH levels [169]. In cancer treatment, this characteristic is particularly advantageous because the extracellular environment of tumors is more acidic compared to normal tissues and blood. This acidity results from the hallmark of cancer cells, which is rapid tumor proliferation driven by glycolysis, allowing for the regulated release of drugs [170]. Typically, the pH of tumors falls between 5.8 and 7.8 (with an average of approximately 6.0), while intracellular compartments have even lower pH values (lysosomes: 4.0–5.0; endosomes: 5.0–6.0). As a result, pH-responsive polymeric micelles (PMs) can enhance cellular uptake, boost anticancer effectiveness, and allow for controlled drug release through pH-triggered structural changes within the acidic environment of tumors [171].

The most frequently encountered pH-sensitive structures consist of: (i) chemical bonds that tend to remain quite stable in neutral or alkaline environments but become unstable and susceptible to hydrolysis or cleavage when exposed to acidic conditions. For instance, stimuli-responsive polymer dots can be modified with boronic acid and catechol groups to establish a pH-responsive mechanism, enhanced by reversible diol–diol crosslinking at different pH levels. The pH-sensitive boronate esters display exceptional responsiveness to variations in acidity, rendering them suitable for customized interactions with the acidic tumor microenvironment, thereby facilitating targeted sensing [172]; (ii) polymers that modify their charge characteristics with variations in pH; and (iii) specialized pH-responsive polymers possessing distinctive structural attributes. As these materials change their structure or properties in response to the surrounding pH, the nanocarriers that include them also experience rearrangement, expansion, or breakdown. This mechanism aids in controlled drug release, the removal of protective layers, and disintegration near target locations, ultimately improving drug delivery effectiveness and therapeutic results [173].

Polymeric systems that demonstrate swelling dependent on pH show increased swelling in a simulated fluid with a pH of approximately 7.4, while they exhibit minimal swelling in a pH 1.2 environment. These types of polymeric nanomaterials play a crucial role in creating a gastroretentive drug delivery system designed to allow controlled drug release, reduce gastric side effects, and lower the frequency of administration [174].

Natural PRPs can be categorized based on their source, distinguishing them from synthetic variants. A notable characteristic of many biopolymers is their ability to undergo pH-responsive conformational changes, which often lead to variations in solubility. Natural polymers are often preferred because of their abundance, biodegradability, non-toxicity, biocompatibility, and ease of chemical modification. Representative natural PRPs include hyaluronic acid, alginic acid, heparin, and cellulose derivatives such as carboxymethylcel-

lulose and carboxymethyldextran [175]. Natural polymers are highly regarded for their availability, ability to decompose naturally, compatibility with biological systems, and potential for modification. At the same time, synthetic polypeptide derivatives (PRPs) have been created and are applied in various fields. One notable example is poly(L-glutamic acid) (PGA) [176] and poly(aspartic acid) (PASA) represent biocompatible and degradable pH-sensitive polymers [177,178]. These intelligent polymers have been effectively utilized to create smart active packaging systems that alter the microenvironment for food storage. For example, during fruit storage, acidic compounds such as oxalic acid and carbonic acid may form, causing a decrease in pH. In addition, spoilage-related microorganisms produce acidic metabolites that further lower the pH. pH-sensitive polymers can be designed to respond to these changes by releasing active substances in a controlled manner when needed [177].

3.2.3. Redox-Sensitive Systems

The fundamental concept behind redox-responsive polymeric systems is to exploit the unique variations in redox potentials found between tumor tissues and healthy tissues [179]. Cellular redox homeostasis pertains to the continual balance between oxidizing and reducing agents in cells, which are essential for survival, growth, differentiation, and aging. An excess of reactive oxygen species (ROS) and reactive nitrogen species (RNS) induces oxidative stress, a condition associated with aging and the onset of diseases such as neurodegeneration, cardiovascular disorders, and cancer [180]. Cancer cells exhibit markedly higher levels of reactive oxygen species (ROS) than normal cells. While these elevated ROS contribute to tumor progression, supporting initiation, angiogenesis, and metastasis. Excessive ROS levels beyond a critical threshold can also trigger cytotoxic effects. ROS are mainly produced in the mitochondria via the electron transport chain (primarily Complexes I and III), NADPH oxidases (NOX family), peroxisomes, and enzymes related to the endoplasmic reticulum. The types of ROS produced encompass both free radicals (such as O^{2-}, •OH, RO•, ROO•) and nonradicals (like H_2O_2, $^1O_2$, O_3, ROOH, HOCl, HOBr). Normally, cells maintain redox homeostasis through antioxidant mechanisms such as catalase, superoxide dismutase (SOD), glutathione peroxidase (GSH-Px), and the reduced glutathione (GSH)/oxidized glutathione (GSSG) system. Conversely, in tumors, this balance is frequently disturbed, with increased levels of ROS met with heightened antioxidant responses, especially GSH [180].

The altered redox state leads to significant therapeutic implications. While excessive production of reactive oxygen species (ROS) contributes to oxidative damage to DNA, activation of oncogenes, and disruption of DNA repair processes, thereby promoting cancer development, the imbalance in redox status also makes tumor cells susceptible to increased ROS levels or depletion of GSH, creating a therapeutic opportunity for targeted treatments. Redox-sensitive nanocarriers are developed to take advantage of the heightened intracellular concentrations of GSH, allowing for the controlled release of drugs. This approach raises the levels of drugs within the cells post-treatment, thus improving therapeutic effectiveness while reducing the systemic side effects associated with the original medications [181].

Many redox-sensitive nanocarriers utilize disulfide or diselenide bonds as cleavable connections. Of these, disulfide bonds are the most commonly utilized because of their biocompatibility and reduced toxicity in comparison to selenium-containing groups. Disulfide linkages are frequently incorporated into linker molecules that covalently attach therapeutic agents to the components of the nanocarrier [182]. When high levels of intracellular GSH are present, a thiol–disulfide exchange reaction occurs, causing bond rupture, disassembly of particles, and release of the drug. Although this reaction is thermodynamically

favorable ($\Delta G < 0$), it proceeds more slowly than thiol–diselenide exchange, indicating that careful management of disulfide exchange kinetics could enhance drug delivery and improve therapeutic results. In a proof-of-concept study, Dabas and Kanaly (2024) demonstrated that monomers containing disulfide groups, which were specifically designed for the production of nanogels, facilitated the controlled release of the antioxidative enzyme paraoxonase-1 under physiological GSH conditions [182]. Additionally, they maintained the enzymatic activity of the protein payload in stimulated RAW 264.7 macrophages, highlighting that cationic polymeric materials linked by disulfide bonds can act as effective redox-responsive carriers for protein-based therapies, achieving a balance between colloidal stability, encapsulation efficiency, and the preservation of bioactivity [182].

A significant drawback of these systems is their inability to distinguish between cancerous and healthy cells, as both types contain reductive cytosols with millimolar concentrations of GSH. To tackle this issue, the use of tumor-targeting ligands in surface engineering has been suggested to enhance selectivity and reduce off-target repercussions. For instance, angiopep2-aPD-L1@PTX nano-micelles (A2-APM) were recently created by crosslinking anti-PD-L1 antibodies (aPD-L1) and attaching paclitaxel (PTX) to PEG-PLL. The addition of angiopep-2 peptides improved penetration through the blood–tumor barrier, while the reductive microenvironment of GBM triggered the cleavage of the crosslinker and the selective release of aPD-L1 without damaging its structure. At the same time, the dissociation of micelles sped up the release of PTX, which not only caused direct cytotoxic effects but also promoted immunogenic cell death, making tumors more responsive to PD-1/PD-L1 blockade [183].

Cationic polymers, a type of polymeric vector, have garnered considerable interest due to their biodegradability, biocompatibility, and ease of modification when compared to conventional liposomes. By incorporating ROS/GSH-cleavable linkages, redox-responsive polymer nanoparticles (NPs) create a flexible platform for the delivery of intracellular nucleic acids, improving the precision of therapeutics while reducing off-target effects. According to earlier studies, a research team developed a superior polymer called Cys8E, noted for its favorable biocompatibility and responsive nature to GSH, to transport the THZ1 (a covalent inhibitor specific to CDK7). This nanoparticle drug conjugate significantly enhanced THZ1 aggregation and its antitumor efficacy against prostate cancer. In addition, the nanoparticle demonstrated high drug-loading efficiency, excellent stability, and remarkable release capability [184].

Redox-responsive polymers can be utilized to create wound-dressing materials that possess antimicrobial properties and promote wound healing. These materials include redox-responsive degradable hydrogels that are designed by incorporating stimuli-responsive components into the backbone of gel-forming macromonomers. Such hydrogels undergo degradation in response to elevated levels of glutathione (GSH) or reactive oxygen species (ROS), which are typically present at wound sites, in inflamed tissues, or in regions affected by bacterial infections and biofilms. In these environments, the redox imbalance can simultaneously trigger hydrogel degradation and the controlled release of therapeutic agents. Recently, various redox-responsive hydrogels acting as disulfide bond reservoirs have been developed to enhance wound healing, particularly for the topical delivery of therapeutic agents, especially proteins. The inclusion of disulfide bonds in the hydrogel framework offers several advantages: (i) eventual degradation and removal of the hydrogel without inflicting secondary harm to the wound, (ii) provision of dynamic bonds that allow for self-healing, and (iii) regulation of ROS levels in the wound to mediate redox potential and achieve improved wound healing effectiveness. In one study, a redox-degradable hydrogel loaded with the antibacterial peptide vancomycin was synthe-

sized through a straightforward Gram-scale process. The hydrogel structure was based on hyperbranched polyglycerol containing disulfide bonds (SS-hPG), cross-linked with 4-arm polyethylene glycol-thiol (4-arm PEG-SH). Both in vitro and in vivo evaluations confirmed that the vancomycin-loaded hydrogel functioned as an effective antibacterial barrier for wound dressings and significantly accelerated the healing of infected wounds in a mouse model [185].

Despite promising results in preclinical studies, the clinical application of redox-responsive nanomedicines is still limited. While several candidates have entered clinical trials, obtaining regulatory approval remains rare. Two primary obstacles impede translation: (i) their in vivo effectiveness often shows little significant improvement compared to current formulations, and (ii) their intricate design makes large-scale production and quality assurance challenging. Consequently, future research should aim to optimize and streamline nanocarrier design, ensuring reproducibility without sacrificing therapeutic effectiveness, to facilitate broader clinical implementation of stimuli-responsive nanomedicines [186].

3.3. Bio-Based and Green Synthesis

3.3.1. Renewable Sources

The concept of biopolymers has developed and now includes materials produced by the polymerization of natural and renewable resources, the polymerization of monomers derived from these resources, or the direct utilization of sustainable macromolecules and their derivatives. These materials come from living organisms like plants, animals, and microorganisms, and they can be acquired either straight from cells or through the chemical synthesis of polymers using bio-based monomers. Biopolymers sourced from plants, such as cellulose, lignin, starch, and hemicellulose, are plentiful and adaptable [187]. These polymers are sourced from a variety of plants, including wheat, rice, and potatoes, among others. For instance, lignin and cellulose are primarily obtained from the agro-industrial waste of lignocellulosic sources. The lignin component of this biomass has been investigated as a starting material for biopolymers such as polyhydroxyalkanoates, polyesters, polyurethanes, and more. On the carbohydrate side, cellulose serves as a significant renewable resource for functional materials. As a homopolymer composed of glucose connected by β (1→4) glycosidic bonds, cellulose exhibits considerable resistance, crystallinity, and mechanical strength. Consequently, much of the research focuses on developing more sustainable extraction methods, followed by physicochemical alterations and modifications, including nano-structuring, to create new functional materials like hydrogels, films, membranes, and coatings [188]. Thanks to their features like biodegradability, biocompatibility, and the ability to customize functionalities, plant-derived biopolymers are gaining popularity in various sectors such as packaging, agriculture, personal care, and biomedical uses.

Microbial pathways produce polymers that naturally biodegrade and have adjustable characteristics, such as polyhydroxyalkanoates (PHAs, with polyhydroxybutyrate, PHB, as a prominent example), polylactic acid (PLA), and bacterial cellulose. These biopolymers are increasingly used in various sectors, including food packaging, medical applications, cosmetics, agriculture, wastewater management, and industrial processes. For example, microalgae are promising raw materials for bioplastic production due to their rapid growth to substantial biomass, lack of direct competition with food crops, and ability to flourish in non-arable conditions like wastewater. They absorb inorganic nutrients to generate proteins, carbohydrates, and lipids, which can be transformed into polymer precursors or extracted as algal polysaccharides for use in bioplastics such as alginate, carrageenan,

and agar. Microalgae present an eco-friendly alternative for the commercial production of biopolymers, either through controlled cultivation or harvesting from natural ecosystems. The conversion of algal biomass into bioplastics typically involves several steps, including fermentation, plasticization, blending, and compatibilization.

Microalgae-derived plastics, in particular, are regarded as cost-effective, recyclable, biocompatible, biodegradable, energy-efficient, and flexible. They also offer a reduced carbon footprint and produce minimal toxic by-products, thereby supporting the transition toward a more circular economy. Nevertheless, many existing bioplastics tend to be brittle, exhibiting low melt strength and inadequate barrier properties. Polylactic acid is commonly utilized in the automotive industry because of its mechanical strength [189].

A diverse range of microorganisms—including bacteria, fungi, and yeast—can be engineered to synthesize polymers from renewable carbon sources. A prominent example is polyhydroxyalkanoates (PHAs), biodegradable polyesters produced through microbial fermentation of renewable feedstocks such as sugars and lipids [190].

3.3.2. Green Solvents and Catalysis

In order to prepare standard polymers, a significant amount of fossil fuels, including natural gas and oil, is typically needed as raw materials. This not only strains the finite supply of fossil energy but also increases resource consumption. Furthermore, a significant amount of waste materials is produced during the production and use of traditional polymers, and these wastes are frequently not adequately handled or recycled, leading to significant pollution and adverse environmental effects. Thus, a sustainable and environmentally friendly method of producing biobased polymers is required [189]. The 12 principles of green chemistry were first introduced by Paul Anastas and John Warner in 1998. One of these principles emphasizes minimizing the use of hazardous solvents in chemical processes and preventing the generation of solvent-related waste [185,191].

Growing environmental concerns and the need to create sustainable and green products as alternatives to fossil fuels have led to an increase in the synthesis of bio-based polymers and chemicals in recent years. Making bio-based polymers minimizes reliance on non-renewable feedstocks and maximizes the use of renewable resources. Under the right biological or composting conditions, many bio-based polymers can be made to break down into harmless compounds, reducing pollution and environmental persistence. Sustainability is further improved by designing and creating closed-loop polymers from bio-based materials, which allow for chemical recycling or depolymerization back to monomers. Research on closed-loop, recyclable polymers made from bio-based ingredients has increased recently.

On the other hand, widespread usage of edible biomass feedstocks, including vegetable oils, might put food sources in competition and cause issues with food security. Prioritizing non-food feedstocks and residues, such as lignocellulosic biomass, waste oils and fats, algae, or specialized non-food crops, is one mitigation strategy. To prevent burden shifting, benefits are validated by life-cycle assessment [192]. Utilization of these resources can be greatly improved by employing them as renewable feedstocks, applying targeted chemical modifications, and introducing degradable or dynamically cross-linkable functional groups. These strategies transform them into high-value functional materials and chemicals for research and industrial applications. For example, a study explored non-isocyanate polyurethane (NIPU) precursors derived from non-food aromatics and non-edible oils, Cardanol. This cashew nut shell-liquid derivative combines a flexible C15 aliphatic chain, a rigid aromatic ring, and useful functional groups such as a phenolic hydroxyl and unsaturation. These features enable higher glass transition temperatures and

improved thermal stability while maintaining toughness, and cardanol has been widely explored in epoxy, phenolic, benzoxazine, and polyurethane systems [193].

Biopolymers such as polylactic acid (PLA) are inherently flammable and therefore require flame retardants to improve their fire safety. Intumescent flame retardants (IFRs), which typically consist of acid, gas, and carbon sources, are well known for providing effective thermal insulation and smoke suppression. Its flame-retardant effect arises from the formation of an expanded carbonaceous layer during combustion, which further acts as a physical barrier, reducing heat transfer and limiting oxygen penetration, thereby inhibiting the burning of the underlying polymer. From a sustainability perspective, bio-based flame retardants derived from renewable biomass can maintain PLA's environmentally friendly characteristics and also improve its flame resistance. In one study, a green strategy was developed to enhance both the flame retardancy and toughness of PLA by employing a pH-induced gelling process in water. This approach enabled the deposition of natural latex onto a bio-based core–shell flame retardant (CSFR), yielding a bio-based flame-retardant/natural rubber inorganic–organic hybrid (CSFR-NR) [194].

3.3.3. Eco-Friendly Processing Techniques

Aliphatic polyesters such as poly(butylene succinate) (PBS) and poly(lactic acid) (PLA) are often limited by brittleness, arising from their high crystallinity and susceptibility to thermal degradation. These drawbacks restrict their broader application. Traditional modification strategies frequently employ solution casting with solvents such as chloroform, which raises sustainability concerns [195]. A more sustainable alternative is the incorporation of aromatic units into the polymer backbone, which enhances chain rigidity and thereby improves thermal stability and mechanical performance. This can be accomplished through solvent-free techniques like extrusion, an environmentally friendly and scalable process compatible with high-throughput manufacturing [196].

Solvent-free synthesis methods have also been successfully employed to produce biostable and cytocompatible shape memory polymers, particularly segmented thermoplastic polyurethanes (STPUs) with adjustable thermomechanical properties [197]. STPU synthesis typically involves three key components: small-molecule chain extenders (hard segments), long-chain hydroxyl-terminated macromonomers (soft segments), and coupling agents. The macromonomers provide flexibility, while the chain extenders, upon reaction with coupling agents, form rigid domains stabilized by hydrogen bonding. In solvent-free approaches, STPUs can be synthesized using hexamethylene diisocyanate (HDI), polypropylene glycol (PPG), and triethylene glycol (TEG), eliminating the need for organic solvents such as tetrahydrofuran. This strategy is both straightforward and user-friendly, as it avoids additional titration and strict stoichiometric balancing steps. Moreover, the one-pot reaction setup minimizes preparation time compared with conventional solvent-based methods, offering a more efficient and sustainable pathway to advanced polyurethanes [197].

Despite the benefits of solvent-free synthesis, thermal control remains a key challenge, as managing the heat released during polymerization is difficult, particularly for temperature-sensitive monomers and polymers. This highlights the need to enhance the processability of biobased polymers by broadening their processing window to avoid thermal degradation. A recent study addressed this issue by preparing blends of atactic poly(3-hydroxybutyrate) (a-P3HB) with isotactic poly(3-hydroxybutyrate) (i-P3HB) and poly(3-hydroxybutyrate-co-4-hydroxybutyrate) (P34HB) through solvent-free extrusion. These blends demonstrated an extended processing window, with processing temperatures reduced to 150–160 °C—well below the decomposition onset of i-P3HB—thereby prevent-

ing thermal degradation. Moreover, their crystallinity could be tuned between 17% and 70% by adjusting polymer ratios, enabling the fabrication of materials with customizable mechanical properties and elongation at break values of up to 600%. Overall, these results underscore the promise of such blends as sustainable alternatives to conventional plastics, with compatibility across diverse processing techniques including injection molding, extrusion, and fiber spinning [196].

Another eco-friendly strategy for polymer synthesis is enzymatic or organocatalyzed solution polymerization. Enzyme-catalyzed polymerization employs biocatalysts such as lipases, peroxidases, and laccases, while organocatalysis often relies on catalysts such as N, N-dimethyl-4-aminopyridine (DMAP) and N, N′-diisopropylcarbodiimide (DIC). Both approaches operate under mild conditions, typically at ambient temperature and pressure, offering advantages in environmental compatibility and reduced energy consumption. For instance, immobilized Candida antarctica lipase B (iCALB) has been successfully applied as a biocatalyst in the synthesis of 2,5-bis(hydroxymethyl)furan (BHMF), a sustainable rigid furanic compound structurally similar to 2,5-furandicarboxylic acid (FDCA). BHMF serves as a promising biobased building block for the preparation of aliphatic–aromatic polymers, broadening the toolkit of renewable monomers available for sustainable polymer development [198]. However, in this study, only a limited molecular weight was achieved (2100–3100 g mol^{-1}).

In a separate study, the copolymerization of BHMF and FDCA, catalyzed either by iCALB or by the combination of DMAP and DIC, resulted in polymers with slightly higher molecular weights [199]. In a more recent study, BHMF was polymerized in bulk for the first time using either the enzyme iCALB or the commercially available catalyst dibutyltin (IV) oxide (DBTO). The resulting BHMF-based polyesters, produced via this solvent-free and sustainable approach, were biodegradable, and their thermal and rheological properties could be tuned by adjusting the number of methylene groups in the aliphatic segment. Despite these advances, challenges remain in maintaining enzyme activity and stability during large-scale production, which continues to hinder broader industrial adoption [195]. Moreover, the high cost of enzyme production and purification further constrains the economic viability of this method for large-scale applications.

Other eco-friendly approaches for the synthesis of polymers include Photopolymerization, Atom Ring-Opening Polymerization (ROP), Transfer Radical Polymerization (ATRP), and click chemistry, which have been reviewed in the literature [190].

4. Applications in Key Sectors

Due to their versatility in biocompatibility and biodegradability, the development and use of biopolymers have been expanding to multiple domains where performance, safety, and sustainability are critical. The tunable physicochemical properties and advancement in functionalization strategies have enabled biopolymers to be integrated into biomedical applications, their primary application, and other key sectors, such as environmental, industrial, agricultural, and manufacturing additive applications (Figure 3 and Table 3). This section provides an overview of the most prominent applications, particularly biomedical, sustainability-oriented uses for the environment, and industries, and additive manufacturing technologies.

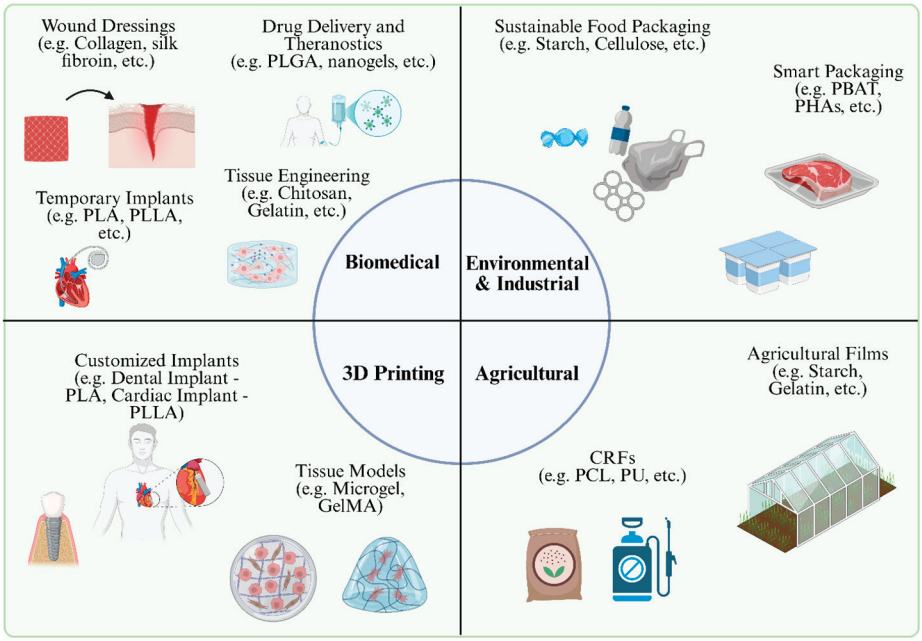

Figure 3. Application of biodegradable and biocompatible polymers in key sectors. Created with Biorender.com.

4.1. Biomedical Applications

4.1.1. Drug Delivery Vehicles and Diagnostics

Biodegradable and biocompatible polymers have become central to the development of advanced drug delivery and diagnostic systems. Their ability to degrade into nontoxic byproducts, combined with highly tunable physicochemical properties and modifiable surfaces, provides opportunities for sustained release, site-specific targeting, and multifunctional applications. These characteristics position biopolymers as essential materials in the design of controlled delivery vehicles and emerging theranostic platforms [200,201].

Drug release from polymeric systems is governed by polymer erosion, hydrolytic degradation, and diffusion of therapeutic agents through the carrier matrix. More recent innovations have focused on stimuli-responsive materials that respond to pH, redox potential, temperature, enzymatic activity, or light to trigger site-specific release. Such strategies exploit pathological microenvironments, particularly in cancer, to improve drug bioavailability at diseased sites while minimizing systemic exposure and toxicity [202,203].

Among available materials, poly(lactic-co-glycolic acid) (PLGA) remains the most widely used biodegradable polymer due to its FDA approval, tunable degradation rates, and compatibility with diverse therapeutic agents, ranging from small molecules to nucleic acids [204–207]. Alongside PLGA, smart nanogels represent a new generation of carriers capable of combining the hydrophilicity and flexibility of hydrogels with nanoparticle targeting and release properties. These nanogels can respond dynamically to internal or external stimuli and have shown particular promise in both cancer drug delivery and diagnostic imaging [202].

Surface functionalization strategies, including PEGylation, ligand conjugation, and incorporation of responsive groups, further enhance circulation time, tissue penetration, and cellular uptake [201]. Building on these approaches, recent studies emphasize how chemophysical tuning of polymer architecture and surface chemistry dictates the biological fate of nanocarriers in vivo. Subtle adjustments to polymer rigidity, hydrophobic-hydrophilic balance, and segmental density can minimize protein adsorption and improve endothe-

lial transport, thereby enhancing pharmacokinetics and biodistribution [208]. In parallel, stealth and pseudo-stealth coatings, including hydrophilic brushes, zwitterionic polymers, and biomimetic coronas derived from albumin or cellular membranes, suppress opsonization and clearance by the reticuloendothelial system [209]. This prolongs systemic circulation and promotes selective accumulation of therapeutic payloads at pathological sites.

At the molecular level, polymer functionalization with stimuli-responsive linkers enables drug release triggered by local pH, enzyme activity, or redox gradients, providing spatially controlled delivery in tumor or inflammatory microenvironments. Meanwhile, optimization of amphiphilic block-copolymer composition and surface charge enhances colloidal stability and interstitial transport, while specific ligand or antibody conjugation promotes receptor-mediated uptake and cellular internalization. Collectively, these molecular-design and surface-engineering strategies integrate polymer chemistry with biological performance to achieve long circulation, predictable biodistribution, active targeting, and controlled release, maximizing therapeutic efficacy and minimizing off-target toxicity [208,209].

The clinical applications of biopolymer-based systems are broad and span oncology, ophthalmology, respiratory medicine, and neurology. In cancer therapy, polymeric nanoparticles, micelles, dendrimers, and drug conjugates have been extensively investigated for both passive accumulation in tumors via the enhanced permeability and retention effect and active targeting through the attachment of ligands such as antibodies, peptides, or folic acid. Multifunctional designs have enabled the co-delivery of cytotoxic drugs with imaging probes, bridging therapy with real-time monitoring and paving the way for personalized theranostics [210–212]. In ocular drug delivery, biodegradable microspheres and implants have addressed challenges of rapid clearance from the eye, maintaining therapeutic concentrations in both anterior and posterior segments without repeated invasive procedures [200]. In pulmonary drug delivery, inhalable nanoparticles based on PLGA provide controlled release while protecting drugs from enzymatic degradation, whereas in neurological applications, biopolymer nanoparticles engineered with surface modifications can cross the blood–brain barrier to deliver drugs for neurodegenerative disorders [213–217].

Biopolymer systems, such as multifunctional nanoparticles, have received increasing attention due to their performance, which integrates therapeutic payloads with imaging agents such as fluorescent probes or quantum dots, allowing for simultaneous treatment and disease monitoring. This integration supports early detection, image-guided therapy, and real-time assessment of treatment outcomes, which are critical in advancing precision medicine [202,212].

4.1.2. Tissue Engineering Scaffolds

Biodegradable and biocompatible polymers are pivotal in scaffold-based tissue engineering, where they serve as temporary extracellular matrix (ECM) analogues to support cell adhesion, proliferation, differentiation, and matrix deposition until natural tissue regenerates. These polymers can be natural (e.g., collagen, gelatin, hyaluronic acid, chitosan, alginate) or synthetic (e.g., polylactic acid [PLA], polyglycolic acid [PGA], polycaprolactone [PCL], polylactic-co-glycolic acid [PLGA], polyurethanes, polyphosphazenes). Natural polymers provide intrinsic bioactivity and mimicry of ECM, while synthetic polymers offer tunable degradation, reproducibility, and mechanical strength [218–222]. Increasingly, hybrid and nanocomposite scaffolds combine these advantages, while advanced fabrication methods such as electrospinning, 3D printing, and phase separation yield tailored architectures [223–225].

- Bone Tissue Engineering

Bone tissue engineering requires scaffolds with high compressive strength, osteoconductivity, and controlled biodegradation. Synthetic aliphatic polyesters such as PLLA [226,227], PLA, PGA, PLGA, and PCL are widely applied [228–230] but often combined with ceramics such as hydroxyapatite (HA) or β-tricalcium phosphate (β-TCP) to mimic bone's mineralized ECM and to buffer acidic degradation by-products [231,232]. Advanced fabrication strategies, including additive manufacturing and electrospinning, enable scaffolds with interconnected porosity that support vascularization [233,234]. Poly(glycerol sebacate) (PGS) has also been explored for hard-tissue applications through composite formation, where PGS-Bioglass and PGS-HA scaffolds exhibit improved osteoconductivity, enhanced mechanical stiffness (≈0.5 MPa), and support osteoblast proliferation and matrix mineralization while maintaining biodegradability [113]. Nanocomposites, such as PVA, alginate scaffolds reinforced with TiO_2 nanoparticles, further demonstrate potential for osteogenic induction, antimicrobial activity, and fibroblast viability [235]. Smart scaffolds incorporating bioactive molecules or controlled drug release systems provide multifunctionality for bone regeneration and infection control [236].

- Cartilage Tissue Engineering

Cartilage scaffolds must reproduce viscoelastic properties, nutrient permeability, and the proteoglycan-rich ECM environment [237]. Hydrogels derived from natural polymers such as collagen, agarose, and hyaluronic acid promote chondrocyte phenotype maintenance [238], while PLGA and PCL improve mechanical stability [239]. PGA–hyaluronan scaffolds seeded with mesenchymal stem cells have shown significant chondrogenic stimulation in vivo, making them promising for cartilage repair [240]. The elastomeric and hydrophilic nature of poly(glycerol sebacate) (PGS) facilitates chondrocyte adhesion and extracellular matrix deposition, indicating its suitability for cartilage repair, particularly when blended with natural polymers such as chitosan or collagen. Its moderate degradation rate (≈8–12 weeks) corresponds well with cartilage-regeneration timelines [113]. Advanced strategies, such as electrospun fibers with zonal orientation, replicate the anisotropy of native cartilage, and peptide-functionalized scaffolds enhance glycosaminoglycan and collagen type II synthesis [241,242].

- Neural Tissue Engineering

Neural scaffolds must be soft, elastic, and conductive to guide axonal growth and restore connectivity [243]. PCL and PLGA scaffolds functionalized with conductive polymers, such as polypyrrole, enhance neurite outgrowth and neurocompatibility [244,245]. PGS-based nerve-guidance conduits have shown effective support for Schwann-cell migration and axonal elongation due to their low modulus and hydroxyl-rich surface that favors neural adhesion. Their microporous architecture improves nutrient diffusion and waste removal, reducing inflammation and enhancing axonal regeneration [113]. Hydrogels, due to their hydrated and ECM-like microenvironment, further support neurite extension and synapse formation [246]. Smart biomaterials, including shape-memory and electroactive scaffolds, are being developed to provide electrical stimulation and dynamic cues for neural regeneration [247]. Chitosan derivatives, such as chitooligosaccharides, have also been shown to enhance Schwann cell activity and facilitate nerve regeneration [248,249].

- Skin and Wound Healing

Skin scaffolds are designed to accelerate wound closure, angiogenesis, and re-epithelialization. Natural polymers such as collagen, chitosan, and alginate provide bioactivity and hemostatic properties [250], while PLA and PCL nanofibers fabricated via electrospinning enhance tensile strength and surface area for fibroblast adhesion [251,252]. Hydrogel dressings composed of gelatin, hyaluronic acid, or alginate maintain a moist

healing environment and can be engineered for controlled drug delivery [253]. Smart hydrogel scaffolds responsive to environmental cues such as pH and temperature allow on-demand antimicrobial release [254].

In addition to chitosan- and collagen-based systems, glycerol-derived elastomers such as poly(glycerol sebacate) (PGS) and poly(glycerol succinate) (PGSuc) provide biocompatible and flexible platforms for wound dressings and soft-tissue regeneration. Their hydroxyl-functional surfaces enhance fibroblast adhesion and angiogenesis, while their controlled degradation maintains mechanical integrity during the healing process [113]. PGS-based wound dressings and adhesives also exhibit conformal contact with irregular wound geometries and strong wet adhesion inspired by gecko-like mechanics, making them suitable for hemostatic or post-surgical applications. Such PGS membranes act as temporary epidermal barriers, preventing infection and dehydration while promoting re-epithelialization [113].

- Vascular and Cardiac Tissue Engineering

Vascular scaffolds require compliance and anisotropy to prevent thrombosis and intimal hyperplasia [255]. Electrospun fibrous tubes of PLLA support endothelialization, while anticoagulant-functionalized lumens enhance hemocompatibility [256]. In cardiac tissue engineering, scaffolds must withstand cyclic strain and fatigue while supporting synchronized cardiomyocyte contraction [257]. Conductive elastomers and hydrogels promote electrical coupling and pacing [258,259]. Shape-memory polymers are also explored for minimally invasive vascular stents and cardiac patches that expand in situ [260].

Beyond conventional polyesters, PGS and PGSA (poly(glycerol sebacate acrylate)) have emerged as benchmark elastomers for cardiac and vascular scaffolds. PGS exhibits mechanical compliance and elasticity comparable to native myocardium (0.05–1.2 MPa modulus, >300% elongation), enabling cyclic deformation without mechanical failure. Porous "accordion-like" honeycomb PGS architectures mimic the anisotropy of the heart wall and support spontaneous, synchronous beating of cultured cardiomyocytes [113]. Its hydrolytic degradation yields nontoxic products, while hydroxyl-rich surfaces promote endothelialization and integration. For small-diameter vascular grafts, PGS's compliance minimizes stress mismatch, and PGSA's UV-curable chemistry allows precision micropatterning and rapid scaffold fabrication for 3D printing and photo-curing processes [113].

- Other Soft Tissue Applications

In bladder and urethral scaffolds, elastomeric polymers such as poly(glycerol sebacate) and polyurethanes replicate compliance and resilience [261,262]. For tendon and ligament repair, aligned fibrous scaffolds made from PLGA and PLLA guide fibroblast orientation and new collagen deposition [263,264]. Corneal scaffolds require transparency and hydration, achieved with hydrogels engineered for refractive clarity and biocompatibility [265].

Glycerol-based aliphatic polyesters, particularly poly(glycerol sebacate) (PGS) and poly(glycerol succinate) (PGSuc), form a distinctive subgroup of biodegradable polyesters used in soft-tissue engineering. Their elastomeric and compliant nature allows close replication of soft-organ mechanics, making them attractive for bladder, urethral, and skin substitutes as well as flexible nerve and ligament supports. These polymers degrade gradually into biocompatible products, minimizing inflammation and eliminating the need for device removal. Their cross-linked structures can be tuned by curing temperature and time to match the stiffness or resilience required for different soft tissues [113]. Beyond musculoskeletal tissues, PGS thin films have been employed in tympanic membrane and retinal tissue reconstruction, where optical transparency and flexibility support epithelial attachment and light transmission, highlighting the polymer's potential in ophthalmic and auditory repair [113].

- Smart and Stimuli-Responsive Scaffolds

Recent research highlights "smart" scaffolds with shape-memory, electroactivity, and stimuli-responsiveness (pH, temperature, magnetic, or electrical cues). These scaffolds not only act as ECM analogues but also deliver dynamic signals, minimally invasive deployment, and controlled drug release [266,267].

Recent advances have extended glycerol-based polyesters into stimuli-responsive and smart scaffolds. Functionalizing PGS and poly(glycerol succinate) (PGSuc) backbones with photo-crosslinkable or thermoresponsive moieties enables shape-memory behavior, electrical conductivity, and on-demand degradation for next-generation biomedical devices. Related short-chain diol-dicarboxylic acid polyesters, such as poly(glycerol adipate) and poly(glycerol azelate), provide intermediate stiffness and faster resorption rates, bridging the mechanical gap between rigid thermoplastics and hydrogels [113].

In parallel, linear aliphatic polyesters derived from short-chain diols and dicarboxylic acids, such as poly(butylene succinate) (PBS), poly(butylene adipate) (PBA), and poly(ethylene succinate) (PESu) exhibit tunable stiffness, crystallinity, and degradation rates depending on the monomer chain length. These materials hydrolytically degrade into biocompatible diols and acids (e.g., succinic, adipic) and have been employed in resorbable sutures, fixation pins, and slow-release coatings [113]. Their higher crystallinity and mechanical stability (modulus $\approx$ 200–400 MPa) make them suitable for structural or load-bearing applications, whereas PGS-type triol systems provide complementary elasticity for soft-tissue scaffolds.

4.1.3. Temporary Implants and Wound-Healing Materials

Biodegradable polymers underpin the design of temporary implants and wound healing systems, enabling devices that provide transient structural or biological support before degrading safely in vivo. This reduces the need for secondary removal surgeries, lowers complication risks, and allows controlled synchronization of device degradation with the tissue regeneration timeline [7,268]. The progression from inert to bioactive biomaterials has expanded the potential of polymers to actively participate in healing rather than simply acting as passive supports [269].

- Temporary Implants

In orthopedics, biodegradable polymers are central to temporary fixation devices such as plates, screws, rods, sutures, and stents [270]. Polyesters including PLA, PLLA, PGA, PLGA, and PCL, are the most widely applied, with elastic moduli closer to bone than metals, reducing stress shielding while ensuring gradual transfer of load to regenerating tissue [271–274]. PLA in particular demonstrates excellent biocompatibility, degrading into lactic acid that is safely metabolized or excreted [275]. Its resorption rate can be tuned Via stereochemistry (L-, D-, DL-forms) and copolymerization (PLGA), aligning degradation kinetics with bone or soft tissue healing [276].

Composites such as PLA-hydroxyapatite (HA) and PLLA-HA demonstrate improved mechanical properties and osteoconductivity, promoting bone integration while maintaining degradability [277,278]. Injectable thermosensitive implants based on mPEG–PLGA copolymers form gels in situ at body temperature, enabling localized and sustained release of proteins or drugs, expanding the role of implants beyond mechanics to controlled therapy [279].

Biodegradable implants such as screws, plates, and pins achieve effective fixation with fewer long-term complications compared to permanent metal devices [280,281]. Short-term host responses resemble those of inert implants, but inflammation resolves as the polymer degrades, unlike metallic systems that may cause ion release and chronic tissue

reactions [282]. Rare complications, such as foreign-body responses or osteolysis, are more commonly associated with fast-degrading PGA, whereas PLA-based implants exhibit better long-term tolerance [283].

- Wound-Healing Materials

Polymer-based wound dressings now function as bioactive interfaces with the wound bed. Hydrogels, nanofibrous mats, foams, and films provide moisture retention, exudate absorption, and antimicrobial barriers while promoting cell adhesion, angiogenesis, and re-epithelialization [284–287]. Natural polymers demonstrate inherent biocompatibility and bioactivity but consistently exhibit poor mechanical properties that necessitate blending with synthetic polymers. ECM with PEUU fibers achieved 80–187 kPa tensile strength, while PVA–hydroxyapatite composites improved mechanical properties by up to 64% [288,289]. Stimulus-responsive and smart hydrogels, which perform self-healing, conductive, or responsive to pH, temperature, and ions, are emerging, and can dynamically adapt to wound microenvironments. Self-healing hydrogels and bioadhesives, including cyanoacrylate blends, provide alternatives to sutures by offering conformal closure and antibacterial activity [290].

4.2. Environmental and Industrial Uses

4.2.1. Sustainable Packaging Alternatives

The global packaging sector, dominated by petroleum-derived plastics, is a primary contributor to environmental pollution, greenhouse gas emissions, and the generation of persistent microplastics [291]. Conventional plastics such as polyethylene, polypropylene, and polystyrene provide excellent mechanical and barrier properties but resist degradation for centuries, disrupting terrestrial and aquatic ecosystems [292]. Biodegradable and biocompatible polymers present a sustainable alternative by offering comparable packaging performance while degrading under controlled conditions into harmless by-products such as carbon dioxide, water, and biomass [293].

- Natural Biopolymers for Packaging

Natural polymers, including starch, cellulose, chitosan, alginate, carrageenan, pectin, and proteins such as gelatin and casein, are renewable, biodegradable, and biocompatible. They can be processed into edible films, coatings, and biodegradable packaging materials with inherent bioactivity [294]. Edible films and coatings made from proteins and lipids add functionality by improving sensory quality and acting as carriers for antioxidants and antimicrobials, reducing the need for synthetic additives [295–297]. Starch remains the most widely used due to its abundance and low cost, though native starch films are brittle and moisture sensitive. Converting starch into thermoplastic starch (TPS) through plasticization improves flexibility and processability, positioning TPS as a scalable replacement for single-use plastics [298,299]. Cellulose derivatives yield transparent and strong films [300,301], while chitosan-based materials provide intrinsic antimicrobial activity and valorize seafood industry waste streams [302,303]. Alginate continues to expand its role in edible and biodegradable food coatings [304].

- Synthetic Biodegradable Polyesters

Polylactic acid (PLA), polycaprolactone (PCL), and poly(butylene adipate terephthalate) (PBAT) are among the most widely commercialized [305–307]. PLA, derived from lactic acid, is the most established, offering mechanical and optical properties similar to polyethylene terephthalate (PET), though limited by brittleness and thermal instability [308]. Blending PLA with PET decreases tear strength and increases impact strength, while increasing color and decreasing transparency [309]. PCL offers flexibility and compatibility with blends, though it is slow in degradation [310,311].

- Blends, Composites, and Compatibilization

The inherent weaknesses of pure biopolymers, such as low mechanical strength, poor thermal stability, and weak barrier properties, are addressed through blending, compatibilization, and composite strategies. PLA–starch and PBAT–TPS blends, when compatibilized, exhibit improved strength and flexibility [312,313]. Lignocellulosic fillers (coffee grounds, nanocellulose, date stones) and nanoclays enhance tensile properties, reduce permeability, and improve thermal stability [314–317]. Eco-friendly surface modifications with rosin or stearic acid improve filler–matrix compatibility while retaining biodegradability [318,319]. Nanocomposites, particularly those incorporating nanoclays, silica, and graphene derivatives, significantly improve oxygen and water vapor barrier performance, making biopolymer films more competitive with petrochemical plastics [320–322].

- Active, Antioxidant, and Smart Packaging

Packaging is increasingly designed to extend shelf life and ensure food safety. Active packaging integrates antimicrobial or antioxidant agents directly into films. Biopolymer matrices embedded with nanoparticles (silver, TiO_2, ZnO) inhibit microbial growth [323], while natural additives such as essential oils, phenolic compounds, and plant extracts reduce spoilage [324–327]. PLA films enriched with tocopherol or olive leaf extract exemplify antioxidant-active packaging, controlling oxidative degradation and extending freshness [328,329]. Smart packaging incorporates pH- or temperature-sensitive indicators, conductive hydrogels, and self-healing materials to monitor food quality and freshness in real time [330–332].

- Industrial Applications and Cross-Sector Relevance

Food packaging remains the most extensive application area, with biodegradable films already commercialized in modified atmosphere packaging (MAP) systems [333]. In pharmaceuticals, biodegradable polymers such as starch, PLA, and gelatin provide safe, non-toxic, and protective packaging [334]. Industrial applications extend beyond food and medicine to include agricultural films, disposable containers, and eco-friendly paperboard coatings [335–337].

Beyond biomedical applications, short-chain diol-dicarboxylic acid polyesters such as poly(butylene succinate) (PBS), poly(ethylene succinate) (PESu), and poly(butylene adipate) (PBA) have attracted attention as renewable and biodegradable thermoplastics. They are synthesized via condensation of bio-derived monomers, such as succinic acid from microbial fermentation and 1,4-butanediol from glucose hydrogenation. These polymers combine thermal processability, mechanical strength, and controlled biodegradation [113].

PBS and PESu exhibit semicrystalline structures and hydrolytic degradation into non-toxic small molecules, making them suitable for biomedical devices and sustainable packaging. Their mechanical moduli (200–400 MPa) exceed those of PGS-type elastomers, enabling their use in rigid containers, resorbable plates, and eco-friendly films. Furthermore, integrating diol-based polyesters into PLA or starch blends enhances flexibility and compostability, bridging the gap between high-performance biomedical polymers and environmentally sustainable materials [113].

4.2.2. Agricultural Applications

Agriculture is a major consumer of plastics and chemical inputs, contributing to plastic pollution, inefficient nutrient use, and soil and water degradation [338]. Biodegradable and biocompatible polymers have emerged as key tools to address these challenges, offering applications ranging from mulch films and crop covers to controlled-release fertilizers and pesticides, superabsorbents, and nanocarriers [339]. These innovations reduce environmen-

tal impact, improve input-use efficiency, and align with policy and sustainability targets for climate-smart agriculture [340].

- Biodegradable Mulch Films and Crop Covers

Mulching improves soil temperature regulation, moisture retention, and weed suppression [341,342]. Conventional polyethylene films, however, accumulate as persistent waste in soil [343–345]. Biodegradable mulch films based on starch, cellulose, PLA, PHAs, and their blends degrade naturally without leaving toxic residues, making them attractive alternatives [346,347]. Field studies show that these films improve crop yields, water-use efficiency, and soil structure while reducing the need for herbicides [341]. Beyond mulching, biopolymer-based crop covers and greenhouse films provide protection while mitigating microplastic pollution [348–350].

- Controlled- and Slow-Release Fertilizers

Over-application of fertilizers leads to nutrient leaching, runoff, and volatilization, causing eutrophication and greenhouse gas emissions [351]. Biodegradable polymers are used as coatings or carriers in controlled-release fertilizers (CRFs), synchronizing nutrient delivery with crop demand [352]. Starch-based hydrogels form three-dimensional networks that absorb water and gradually release nitrogen, phosphorus, and potassium, also acting as soil conditioners [353–355]. Coatings made of polyvinyl alcohol (PVA), PLA, gelatin, or gum arabic significantly reduce nutrient losses, enhance microbial biomass, and improve yields in maize and other crops [356]. Electrospun PVA/PLA core–shell nanofibers encapsulating NPK have demonstrated efficient nutrient release and improved growth in lettuce under field conditions [357].

Stimuli-responsive coatings represent a new generation of CRFs. Temperature-sensitive polyurethanes derived from polycaprolactone (PCL) regulate nitrogen release depending on soil conditions [358]. Similarly, bio-based coatings that are responsive to pH, enzymatic activity, or moisture enhance nutrient-use efficiency while minimizing environmental leakage [359,360]. Comparative studies distinguish between slow-release fertilizers (SRFs), which release nutrients gradually, and CRFs, which synchronize release with physiological crop needs, both of which benefit from biodegradable polymer matrices [361,362].

4.3. Additive Manufacturing and 3D Printing

Additive manufacturing (AM), commonly referred to as 3D printing, has transformed biomedical engineering by enabling the production of customized, patient-specific implants, scaffolds, and tissue models with unprecedented precision [363]. Unlike traditional subtractive manufacturing, AM constructs objects layer by layer, allowing intricate geometries, controlled porosity, and integration of bioactive agents. Biodegradable and biocompatible polymers, particularly PLA, PCL, and hydrogel-based systems, are central to these advances due to their tunable mechanics, processability, and safe degradation pathways [364,365].

4.3.1. Custom Implants

PLA and PCL dominate as thermoplastic feedstocks in fused deposition modeling (FDM) and selective laser sintering (SLS) [366,367]. PLA offers rigidity, biodegradability, and printability, making it suitable for craniofacial plates, dental implants, and fixation devices, though it degrades relatively quickly [368]. PCL, with slower degradation and higher elasticity, is employed in load-bearing applications, cartilage substitutes, and bone scaffolds, where gradual resorption is advantageous [369,370]. PLA/PCL composites reinforced with bioactive fillers such as hydroxyapatite (HA) or bioglass enhance osteocon-

ductivity and integration, addressing the limitations of pure polymers [371,372]. Custom implants fabricated via AM have shown promising outcomes in orthopedics, including hip, knee, and spinal implants, offering lightweight, porous structures that mimic trabecular bone and improve osteointegration [373–375].

4.3.2. Dental and Craniofacial Applications

AM has also advanced dental and oral regeneration. Biodegradable polymers such as PLA, PCL, and PLGA, often combined with hydrogels or ceramics (e.g., nano-HA), are used to produce 3D-printed constructs for periodontal, alveolar bone, and pulp regeneration [376–378]. Multi-material strategies allow region-specific repair, such as scaffolds supporting both pulp regeneration and alveolar bone healing, leading to multifunctional constructs with enhanced regenerative efficacy [379].

4.3.3. Tissue Models and Hydrogel Bioinks

Hydrogel-based polymers serve as the backbone of bioprinting tissue models. Materials such as gelatin methacryloyl (GelMA), alginate, hyaluronic acid, collagen, and PEG derivatives replicate extracellular matrix (ECM) properties, providing cell-encapsulating environments for constructing vascularized tissues, cartilage replacements, and organ-on-chip systems [380–383]. Despite their bioactivity, hydrogels often lack mechanical strength, necessitating hybrid approaches where PLA or PCL frameworks provide structural stability while hydrogels supply biological functionality [384–387].

4.3.4. Advanced Additive Manufacturing Technologies

Different AM technologies cater to specific biomedical needs. FDM is widely used for thermoplastics like PLA [388], while stereolithography (SLA) and digital light processing (DLP) enable high-resolution printing of photo-crosslinkable hydrogels [389,390]. Selective laser sintering (SLS) produces porous implants with controlled architecture, and binder jetting allows large-scale customization of surgical models [391]. Advances in photoinitiator chemistry have improved the safety and resolution of hydrogel-based printing for tissue engineering [392]. Furthermore, multi-material additive manufacturing (MMAM) enables the simultaneous fabrication of composites, yielding multifunctional implants [393–395].

4.3.5. Stimuli-Responsive and 4D Printing

Recent developments in stimuli-responsive polymers (SRPs) have introduced 4D printing, where constructs change properties or geometry over time in response to external triggers such as temperature, pH, or light [396–398]. PLA and PCL have been functionalized with shape-memory capabilities [399], while hydrogels provide swelling/shrinking responses, opening opportunities for dynamic tissue scaffolds and smart implants that adapt in vivo [400].

Table 3. Applications of polymers in diverse sectors: medicine, agriculture, and environment.

Biopolymer (Family)	Key Property	Typical Forms	Representative Application	References
		Medicine		
PLGA, PEG, nanogels, PEGylated carriers	Biocompatible, biodegradable, tunable degradation and surface chemistry, stimuli-responsive	Nanoparticles, micelles, dendrimers, nanogels	Drug delivery and theranostics (cancer, ocular, pulmonary, neurological)	[200–215]
Collagen, gelatin, hyaluronic acid, chitosan, alginate (natural); PLA, PGA, PCL, PLGA, PU, polyphosphazenes (synthetic)	Support cell adhesion, tunable degradation, and mechanical strength	Hydrogels, electrospun fibers, 3D-printed scaffolds, nanocomposites	Tissue engineering (bone, cartilage, neural, skin, vascular, cardiac)	[216,217,219–223]
PLA, PLLA, PGA, PLGA, PCL, PGS, PGSuc, short-chain diol-dicarboxylic acid polyesters (PBS, PESu, PBA)	Biodegradable and biocompatible; tunable stiffness and elasticity; hydrolytic degradation into non-toxic by-products	Composite scaffolds, fixation plates and screws, nanocomposites, elastomeric films	Temporary implants (orthopedic, dental) and hard/soft-tissue scaffolds (bone, cartilage, cardiac)	[113,224–236]
PGS, PGSuc, PU, collagen, chitosan, gelatin, alginate, silk fibroin, PVA composites	Elastomeric, bioactive, hemostatic, flexible; tunable cross-linking and hydroxyl-functional surfaces	Hydrogels, foams, nanofibrous mats, bio adhesives, and elastomeric membranes	Wound healing and soft-tissue regeneration (skin, vascular, cardiac, bladder, neural)	[113,237–243]
Starch, cellulose, chitosan, alginate, carrageenan, gelatin, casein, PESu, PBS blends	Renewable, biodegradable, edible, antimicrobial; tunable crystallinity and processability	Films, coatings, TPS blends, edible composites	Sustainable food packaging (active, antioxidant, smart films)	[113,244–257]
PLA, PCL, PBAT, PHAs, PBS, PESu, and blends	Biodegradable synthetic polyesters with tunable mechanics and barrier properties	Blends, composites, and nanocomposites for thermal and mechanical stability	Packaging (eco-friendly, industrial, agricultural, pharmaceutical)	[7,113,258–270]
Starch, cellulose, PVA, PLA, chitosan, gelatin, gum Arabic, PU, PCL coatings	Moisture retention, nutrient-controlled release, soil biodegradability	Mulch films, hydrogels, coatings, nanocarriers	Agricultural films, controlled-release fertilizers, pesticide carriers, biosorbents	[272–281,283–296,338–362]
PLA, PCL, PLGA, PGS, PGSuc, PBS, GelMA, alginate, collagen, PEG derivatives	Printable, biocompatible, degradable; photo-/thermo-crosslinkable	FDM filaments, hydrogel bioinks, composites for 3D/4D printing	Additive manufacturing (implants, dental, tissue models, 4D printing)	[227,273,297–313,315–332]
		Environment		
Chitosan	Cationic, chelating, antimicrobial	Beads, powders, membranes	Waste water treatment (dyes, heavy metals), antimicrobial food wraps	[401]
Alginate	Gel-forming, non-toxic, high water absorption	Beads, films, hydrogels	Heavy metal removal, encapsulation of microbes, food packaging	[402,403]
Starch-based blends,	Biodegradable, renewable, adhesive	Films, foams, hydrogels, composites	Controlled-release fertilizers/urea, compostable packaging, bioplastic blends	[404]
Silk fibroin	Amphiphilic, High mechanical strength	Membrane, films, gels, films, composites	Heavy-metal adsorption membranes; water purification	[405]
PHA, PCL	Fully biodegradable, thermoplastic	Films, fibers, molded parts	Biodegradable packaging, soil-biodegradable plastics, mulch films	[406,407]
		Industry		
Starch/PVA	Adhesive, high tensile strength, hydrophobicity, flexibility	Pastes, glues	Paper, food packaging adhesives, corrugation	[408–410]
PLA	Thermoplastic, compostable, high tensile strength	Films, fibers, molded parts	Packaging, bioplastic, 3D printing filaments	[411,412]
PHA	Versatile thermoplastics	Films, fibers, composites	Bioplastics, single-use items, paper coatings	[413]
Cellulose derivatives	Renewable, water-soluble	Films, fibers, membranes, composites	Packaging, textile finishing, paper coatings	[414,415]
Polyurethane	Adhesive, flexible, high mechanical strength	Foams, composites	Coatings, furniture	[416,417]

5. Challenges and Limitations

Polymers are unique and constantly developing materials that have gained significant attention because of their advantageous mechanical and physicochemical properties, such as tensile strength, mechanical modulus, and degradation rate, all of which can be customized for specific applications by varying polymerization conditions [418]. Nonetheless, despite these advantages, a few challenges remain associated with their use, which impose significant constraints.

5.1. Mechanical Property Enhancement

One of the most persistent disadvantages of biodegradable polymers is their lower mechanical strength as compared to conventional, petroleum-derived alternatives. To make

biodegradable composites feasible for practical applications, studies have stressed the urgent need for enhanced mechanical reinforcement and better management of structure-property interactions [5]. In biomedical settings, such limitations translate into implants or scaffolds that lose strength too quickly, while in packaging they lead to short shelf-life under humid or mechanical stress conditions.

For instance, PLA shows good tensile strength but breaks at under 10% elongation, reflecting its brittle nature. That is why various research have explored things like adding cellulose nanocrystals or plasticizers to boost flexibility with one study reporting improvement in elongation from 6% to 140–190% [419]. Even so, the mechanical properties of PLA do not always match those of fossil-based polymers, and its excessive brittleness can make performance difficult to accurately predict [420]. To mitigate this, a promising approach in recent experiment used the reactive compatibilization of PLA with ductile polymers like PBAT or PCL using epoxy chain extenders (e.g., Joncryl) to chemically bond phases and enhance toughness [421].

It has also been shown that the incorporation of natural fibers into PLA can enhance mechanical strength, but the resulting composites exhibit pronounced sensitivity to hydrothermal aging [422]. In a study analyzing PLA/flax bio composites, specimens immersed at 20 °C, 35 °C, and 50 °C for up to 51 days showed that while low-temperature exposure induced primarily reversible swelling and plasticization effects, higher temperature conditions triggered irreversible molecular degradation, marked by hydrolysis, increased crystallinity, crack formation, and a sharp decline in mechanical integrity. Notably, a 10 wt % fiber addition extended the effective lifespan by approximately 230 percent at 50 °C, although longer exposure ultimately accelerated deterioration [423]. To counteract these effects, experimental work now focuses on fiber surface modifications, such as silane coupling agents, plasma treatments, or hydrophobic sizing to strengthen interfacial adhesion and limit moisture uptake, thereby reducing property loss during aging [424].

A persistent gap remains between laboratory advances and consistent performance under physiological or service conditions. A fundamental issue is mechanical robustness versus degradability: materials engineered to erode or resorb frequently lose load-bearing capacity or barrier function before the application timeline is complete. This trade-off is evident in biomedical contexts (e.g., vascular scaffolds and temporary implants) where stiffness retention and fatigue resistance are as critical as bioresorption kinetics, and in packaging where oxygen/water vapor barriers degrade as crystallinity or morphology evolves during use. Current literature highlights that addressing these challenges will likely require higher crystallinity, strategic blending, and optimized nanofiller loading to achieve a practical balance between strength and biodegradability [425,426].

5.2. Degradation Kinetics and By-Products

Another critical limitation is the difficulty of precisely controlling degradation rates. In drug delivery or tissue engineering, premature loss of mechanical integrity can compromise clinical outcomes, while delayed degradation can trigger chronic inflammation or necessitate surgical retrieval. PLGA undergoes autocatalytic hydrolysis, and during this process, ester bond cleavage produces lactic acid and glycolic acid monomers that accumulate within the bulk of the material [427]. These acidic by-products lower the local pH, which in turn accelerates further hydrolysis, creating a self-reinforcing degradation cycle [428].

The biological consequences of these by-products are significant. Accumulation of lactic and glycolic acid has been shown to recruit immune cells, polarize macrophages toward a pro-inflammatory (M1) phenotype, and trigger localized irritation in surround-

ing tissues [429]. In tissue engineering applications, this can compromise scaffold integration or prolong inflammatory phases of wound healing. Similarly, in drug delivery systems, acidic microenvironments may destabilize sensitive drugs, altering release profiles and efficacy [428]. Recent studies show that incorporating mild basic buffers such as magnesium hydroxide ($Mg(OH)_2$) or calcium carbonate within the matrix can neutralize acidic oligomers in situ and markedly reduce local pH drops without compromising polymer integrity [430].

By-product hazards extend beyond biomedical uses to the environmental setting. While polymers such as PLA or PHAs are marketed as biodegradable, their breakdown in real-world conditions frequently yields oligomers, organic acids, or microplastic particles that may survive and interact with ecosystems. [431]. Limited composting infrastructure and changing environmental conditions exacerbate degradation, creating concerns about the ecological safety of these materials [431]. For example, in the case of biodegradable mulch films, typical biodegradability testing procedures have significant drawbacks because they are frequently performed under controlled laboratory conditions and rely on indirect metrics that do not account for soil properties. Field performance is heavily impacted by pH, moisture, salinity, and microbial diversity; hence, laboratory findings may not adequately reflect actual degradation behavior. Even when polymers breakdown in soil, the long-term consequences of remainder matter remain largely unknown, emphasizing the necessity for field-based testing methodologies that mirror actual circumstances and account for any residual impacts [432].

Bio-based polyesters degrade slowly in packaging applications, and structural modification through techniques such as copolymerization or mixing can be a useful way to speed breakdown. These efforts can result in biodegradable polymers under mild conditions, such as home composting or direct soil burial [335].The current study also reveals that introducing pro-oxidants or natural polymers can improve anaerobic and aerobic degradation, whereas pre-treatment with UV radiation, heat, or light accelerates the breakdown. However, a few researchers have described how efficiently such approaches increase the degradation rates of regularly used polymers like PLA and PGA, leaving significant data gaps [433].

These findings highlight the importance of understanding not only degradation kinetics, but also the nature, accumulation, and impact of byproducts in order to advance both biological safety and environmental sustainability.

5.3. Scalability and Cost

Even when the performance requirements are reached, scaling up manufacturing remains a major problem. Biodegradable polymers such as PLA, PHA, and PCL are currently more expensive to manufacture than their petroleum-based counterparts, largely due to higher feedstock costs and energy-intensive fermentation or processing requirements [434]. Techno-economic analyses (TEA) indicate that feedstock cost and downstream recovery dominate the cost of biopolyesters. For PHA, raw materials typically account for over 40% of the total production cost [435]. Consequently, scale-up strategies now emphasize the use of low-cost renewable substrates such as agricultural wastes or industrial side-streams, improved microbial productivities, and simplified extraction and purification steps to achieve market competitiveness [435].

Industrial adaptation is further slowed by incompatibility with existing processing lines, meaning costly modifications to equipment are often necessary [5]. For packaging and agriculture, cost competitiveness is paramount; without significant reductions, adoption beyond niche applications will remain limited. For example, in agriculture, biodegradable

mulch films have been developed as alternatives to polyethylene; however, their large-scale use remains limited because they are expensive, difficult to manage, and often require specialized equipment for application [432].

Despite reports of rapid growth in the amount of biodegradable plastics that are being produced (about 1.1 million tons in 2022), they are still comparatively expensive and hard to scale to match fossil-derived plastics [5]. Schick et al. outlined how biopolymers are not yet translating into widely available products. It points to economic pressures, ecological concerns, and the need for "degradation by design" approaches, where the manufacturing process and degradation behavior are planned hand in hand [434]. Innovative approaches, such as energy-efficient processing technologies, including out-of-autoclave (OoA) methods, are proposed as viable pathways to reduce environmental impact while supporting circular economy adoption [436].

Nonetheless, despite these promising advances, scaling such techniques remains a significant challenge, underscoring the need for systemic solutions that integrate technical innovation with economic feasibility. Poly(glycerol sebacate) (PGS) serves as a key example in this regard. Recent progress in the scalable synthesis of PGS demonstrates how process optimization, particularly catalyst-assisted and mathematically optimized synthesis methods can substantially reduce production time and energy consumption, offering a promising pathway for industrial-scale polymer manufacturing [437]. Economic feasibility analyses of biodegradable mulch films further emphasize this challenge, indicating that widespread adoption may only be possible with government intervention through subsidies, incentives, or targeted marketing programs to support farmers [432].

5.4. Regulatory and Standardization Issues

Regulatory frameworks and standardized testing remain critical yet underdeveloped for both biodegradable and biocompatible polymers. In the environmental sector, several internationally recognized specifications exist, including ASTM D6400 [ASTM D6400 12; Standard Specification for Labeling of Plastics Designed to be Aerobically Composted in Municipal or Industrial Facilities. ASTM International: West Conshohocken, PA, USA, 2012.], which sets criteria for biodegradability based on the requirement that 90% of carbon atoms must be mineralized to CO_2 within 180 days [438,439]. This standard is supported by a suite of related ASTM protocols, that test biodegradability under aerobic, anaerobic, and composting conditions. They include [439]:

- D5209 [ASTM D5209-92; Standard Test Method for Determining the Aerobic Biodegradation of Plastic Materials in the Presence of Municipal Sewage Sludge (Withdrawn 2004). ASTM International: West Conshohocken, PA, USA, 1996–2025],
- D5338 [ASTM D5338-21; Standard Test Method for Determining Aerobic Biodegradation of Plastic Materials Under Controlled Composting Conditions. ASTM International: West Conshohocken, PA, USA, 2021],
- D6002 [Standard Guide for Assessing the Compostability of Environmentally Degradable Plastics. ASTM International: West Conshohocken, PA, USA, 1996],
- D5988-03 [Standard Test Method for Determining Aerobic Biodegradation of Plastic Materials in Soil of Plastic Materials or Residual Plastic Materials After Composting. ASTM International: West Conshohocken, PA, USA, 2003], and
- D6954 [Standard Guide for Exposing and Testing Plastics That Degrade in the Environment by a Combination of Oxidation and Biodegradation. ASTM International: West Conshohocken, PA, USA, 2018].

Comparable frameworks have been developed by the Bureau of Indian Standards

(BIS) and the International Organization for Standardization (ISO), with specifications adopted across countries to harmonize evaluation methods [438]:

- ISO 14851 [Determination of the Ultimate Aerobic Biodegradability of Plastic Materials in an Aqueous Medium—Method by Measuring the Oxygen Demand in a Closed Respirometer. International Organization for Standardization: Geneva, Switzerland, 2019],
- ISO 14852 [Determination of the Ultimate Aerobic Biodegradability of Plastic Materials in an Aqueous Medium—Method by Analysis of Evolved Carbon Dioxide. International Organization for Standardization: Geneva, Switzerland, 2021],
- ISO 14853 [Determination of the Ultimate Anaerobic Biodegradability of Plastic Materials in an Aqueous System—Method by Measurement of Biogas Production. International Organization for Standardization: Geneva, Switzerland, 2016], and
- EN 13432 [EN 13432:2000; Packaging—Requirements for packaging recoverable through composting and biodegradation—Test scheme and evaluation criteria for the final acceptance of packaging. European Committee for Standardization: Brussels, Belgium, 2000.]. Despite these advances, implementation remains inconsistent across regions. These gaps highlight that even when test methods exist, enforcement and harmonization lag behind scientific progress. However, third-party auditing and dissemination of guidelines through both policy and academic channels are now the strategy used to ensure compliance and public accountability [439].

In the biomedical domain, the regulatory landscape is equally complex. Standards such as ISO 10993 [Biological Evaluation of Medical Devices—Part 1: Evaluation and Testing within a Risk Management Process. International Organization for Standardization: Geneva, Switzerland, 2018] provide guidance on cytotoxicity, sensitization, irritation, and implantation testing, but these remain largely device-oriented rather than material-oriented, meaning that even "proven" biomaterials must be re-evaluated when introduced in new devices [440]. Agencies including the FDA, EMA, and ASTM are actively developing regulatory frameworks for biomaterials, but the rapid pace of innovation in drug delivery systems, tissue engineering scaffolds, and minimally invasive implants creates challenges for approval pathways [441]. Issues such as long-term toxicity, foreign body responses, protein adsorption, and inflammatory reactions remain difficult to capture fully in preclinical testing, highlighting the need for more rigorous and degradation-aware biocompatibility assessments [442,443]. Establishing harmonized global standards for both biodegradable and biocompatible polymers is therefore essential, not only to accelerate clinical and industrial translation but also to build public trust in these materials.

6. Future Prospects

Advances in key areas will shape the future of biodegradable and biocompatible polymers, including the design of smart, multi-responsive materials, integration with bioelectronics and sensors, strategies for clinical translation and industrial scalability, and the adoption of circular economy principles to improve recyclability and sustainability.

6.1. Smart and Multi-Responsive Polymers

The next generation of polymer science is being shaped by "smart" polymers: materials engineered to respond dynamically to environmental cues. In agriculture, for example, stimuli-responsive starch-based coatings are being designed for controlled-release fertilizers (CRFs), where nutrient delivery is coupled with soil triggers such as pH, temperature, moisture, ionic strength, and enzymatic activity. By tailoring starch's biodegradable backbone through chemical modification, coatings can control nutrient release via mecha-

nisms like ionization-driven swelling, enzyme-mediated scission, and thermally induced coil–globule transitions. These innovations promise to synchronize fertilizer release with crop demand, reduce leaching, and improve soil health under realistic field conditions [444]. In biomedical and industrial packaging contexts, similar principles are being applied to develop polymers that can adaptively release therapeutic agents, maintain product integrity, or resist environmental stressors [445,446]. These advances reflect the growing recognition that multi-responsive polymers can couple biodegradability with precise, real-world functionality.

At the same time, future directions for smart polymers must also emphasize biocompatibility to ensure safe and sustained integration with biological systems. Stimuli-sensitive polymers used in medical applications are required to be non-toxic, non-mutagenic, and responsive to diverse physiological cues [447]. Considerable progress has been made in light-, ultrasound-, and redox-responsive polymers, particularly for drug delivery, but challenges remain in tissue penetration, reproducibility, and controlling the diversity of degradation products [448]. Multi-responsive or dual-responsive polymers, which can respond to combinations of external stimuli, are gaining momentum because they provide higher accuracy and controllability. The integration of two or more responsive materials can generate mismatch strain within 3D-printed structures, introducing multidimensional cues for tissue regeneration. Such systems create multifunctional constructs with more favorable mechanical characteristics, and examples include thermo-photo, thermo-magnetic, and thermo-pH polymers that have already shown promise in real physiological environments [449].

Looking ahead, smart biomedical polymer materials are being designed to go beyond passive responsiveness by enabling intelligent functions such as controlled drug release, self-repair, and dynamic tissue support. Therefore, their integration with artificial intelligence and machine learning is expected to optimize responsiveness and improve personalized therapeutic outcomes [450]. Importantly, ongoing research is expanding beyond small molecule drugs toward immunotherapy and regenerative medicine, with polymers being explored as carriers for cells, antibodies, and other biotherapeutics [448]. Taken together, these developments point toward a future in which smart polymers are not only biodegradable and environmentally sustainable but also biocompatible, enabling applications that span agriculture, packaging, and advanced biomedical therapies.

6.2. Integration with Bioelectronics and Sensors

A growing area of interest is the integration of biodegradable polymers with bioelectronics, creating transient sensors and devices that function during a therapeutic window before safely degrading [451]. Such systems, including resorbable pressure monitors and smart wound dressings, combine the biocompatibility of polymers with advances in flexible electronics components [452]. Beyond medicine, similar principles could underpin environmental sensors that monitor soil health or pollutant levels and then safely disappear. Trends in this field are advancing quickly, with PLLA (a PLA variant) emerging as a functional material for sensors, implants, or IoT (Internet of Things) devices [453]. Studies across materials science and bioelectronics emphasize design principles for biodegradable, conductive, and elastomeric matrices, including the use of conductive hydrogel interfaces, and component-level strategies (substrates, encapsulants, interconnects) compatible with physiological environments. The key challenges center on preserving conductivity during hydration and degradation, maintaining mechanical compliance with soft tissues, and ensuring that breakdown products are non-toxic [454,455].

With the rise of wearable medical technologies, biomedical polymer materials that are flexible, lightweight, conductive, and biocompatible are expected to find even broader

application in sensors, monitoring devices, and smart implants [450]. These systems can enable continuous health tracking and tailored therapeutic interventions, aligning well with the push toward personalized medicine. In wound care, for instance, infection remains one of the most critical challenges, and next-generation dressings are being developed to combine real-time monitoring, early diagnosis, and on-demand therapy. One recent design integrates flexible polydimethylsiloxane-encapsulated electronics with temperature sensors and ultraviolet (UV) light-emitting diodes on the upper layer, while the lower layer consists of a UV-responsive antibacterial hydrogel. This hybrid dressing not only enables continuous monitoring of wound temperature for early infection detection but also triggers localized antibiotic release under in situ UV irradiation, offering a dual therapeutic and diagnostic function [456]. Together, these advances signal that future bioelectronic systems based on biodegradable and biocompatible polymers could reshape both healthcare and environmental monitoring by merging adaptability, sustainability, and patient safety into a single material platform.

6.3. Clinical Translation and Industrial Scalability

Despite strong laboratory data, very few biodegradable and biocompatible polymers have progressed to routine clinical use. Future efforts must place greater emphasis on long-term biocompatibility studies, standardized degradation metrics, and scalable, cost-effective manufacturing practices. Regulatory strategies will also need to evolve, as the dynamic and responsive behavior of these advanced materials challenges the current medical device classification systems [457]. Translating the success of biomaterial-based delivery systems from laboratory prototypes to clinically available therapies will require overcoming logistical, economic, and technical barriers. Moving from bench-scale synthesis to industrial production involves not only process optimization but also ensuring consistent quality across large-scale manufacturing. Encouragingly, recent studies on nanoparticle formulations demonstrate that it is possible to maintain reproducibility (showing only about 10% variability in size across production scales that differed by more than 100-fold) when advanced methods such as high-pressure microfluidization are used [458]. In practice, successful scale-up will draw on cross-functional expertise in quality management, textile/process engineering, systems engineering, and regulatory affairs, to bridge experimental prototypes and clinical deployment [459].

At the same time, the manufacturing of biomaterials, particularly for protein and cell-based delivery, presents unique technical hurdles that will shape future directions. Sterilization choices (e.g., filtration or chemical methods) can compromise therapeutic integrity or alter polymer functionality, demanding sterilization-aware design of materials and processes [458]. Furthermore, performance can vary significantly between in vitro and in vivo settings: Resorbable polymers frequently degrade more intricately in vivo, where the tissue environment, surgical handling, and sterilization history can shift erosion mechanisms and kinetics; future designs should purposefully tune mechanics and degradation profiles to stimulate tissue regeneration, while recognizing that “simpler” legacy monomers and polymers still have untapped potential. [459]. Looking forward, ensuring safety and efficacy will demand rigorous preclinical testing, transparent evaluation frameworks, and close collaboration between scientists, industry, and regulatory bodies such as the FDA and EMA [458]. Non-destructive, in vivo-relevant monitoring approaches, such as fluorescence imaging to track polymer erosion (e.g., PLGA) in living or ex vivo models, are proposed to become important tools for reducing the risks of translation [443].

Ultimately, the future of clinical translation and industrial scalability rests on integrating material design with considerations of formulation, in vitro and in vivo testing,

regulatory compliance, and industrial processing [460]. By addressing these areas together, biodegradable and biocompatible polymers can move from niche laboratory innovations into reliable, widely accessible clinical and industrial products.

6.4. Circular Economy and Recyclability

Finally, the long-term sustainability of biodegradable polymers depends on embedding them within circular economy frameworks. Rather than relying solely on biodegradation, future strategies emphasize closed-loop recycling and upcycling. For example, PLA may be chemically depolymerized back into lactide monomers, and new enzymatic routes show promise for polyhydroxyalkanoates (PHAs) [431]. By developing polymers for regulated end-of-life scenarios, researchers can ensure both performance and environmental sustainability. The future also rests upon sustainable synthesis: polymers created from renewable feedstocks and manufactured utilizing ecologically friendly methods. Recent research highlights breakthroughs in combining lignin, starch, and bacterial fermentation to generate biopolyesters, while employing green solvents and catalysts to reduce energy input [461]. Green chemistry advancements and the use of circular economy ideas are becoming increasingly accepted as vital for the manufacture of low-carbon, sustainable polymer products [450]. These approaches are consistent with global aims for lowering carbon footprints and promoting material circularity.

Science is working to develop materials that can not only biodegrade but also be recycled or reused as part of an evolving circular economy. Such measures assist in closing the loop on waste and resource consumption, matching the larger sustainability goals [5,434]. This viewpoint places biopolymers within broader sustainability strategies, viewing them as enablers of closed-loop systems that reduce both environmental load and economic expense. As a result, the future of biodegradable polymers is linked to changing entire material life cycles rather than just addressing single-application difficulties. Revisions to identification standards and LCA practice are frequently advocated for to enable valid claims, better purchasing signals, and design criteria that reward managed end-of-life rather than nominal biodegradability [431].

Author Contributions: Conceptualization, L.A., S.A., I.P., A.A.L., S.U. (Shihab Uddin), S.U. (Saleem Ullah) and I.A.; data curation, and writing—original draft preparation, L.A., S.A., I.P., A.A.L. and I.A.; illustrations, L.A., S.A., I.P., A.A.L. and I.A.; writing—review and editing., S.U. (Shihab Uddin) and S.U. (Saleem Ullah); supervision, and funding acquisition, I.A. All authors have read and agreed to the published version of the manuscript.

Funding: This study was supported by project number INMW2410 by the Interdisciplinary Research Center for Membranes and Water Security (IRC-MWS), King Fahd University of Petroleum and Minerals (KFUPM), Dhahran, 31261, Saudi Arabia. The Authors also wish to express thanks for the financial support received from KFUPM, Dhahran 31261, Saudi Arabia.

Institutional Review Board Statement: Not applicable.

Informed Consent Statement: Not applicable.

Data Availability Statement: No new data were created or analyzed in this study. Data sharing is not applicable to this article.

Acknowledgments: The authors acknowledge King Fahd University of Petroleum and Minerals (KFUPM), Dhahran, 31261, Saudi Arabia, for financial support for the APC of this work.

Conflicts of Interest: Author Saleem Ullah was employed by VTT Technical Research Centre of Finland Ltd., Tekniikantie 21, 02150 Espoo, Finland, The remaining authors declare that the research

was conducted in the absence of any commercial or financial relationships that could be construed as a potential conflict of interest.

References

1. Plastics Europe: Enabling a Sustainable Future. Available online: https://plasticseurope.org/ (accessed on 24 September 2025).
2. Booth, J.-P.; Mozetič, M.; Nikiforov, A.; Oehr, C. Foundations of Plasma Surface Functionalization of Polymers for Industrial and Biological Applications. *Plasma Sources Sci. Technol.* **2022**, *31*, 103001. [CrossRef]
3. Plastic Pollution Is Growing Relentlessly as Waste Management and Recycling Fall Short, Says OECD. Available online: https://www.oecd.org/en/about/news/press-releases/2022/02/plastic-pollution-is-growing-relentlessly-as-waste-management-and-recycling-fall-short.html (accessed on 24 September 2025).
4. Andanje, M.N.; Mwangi, J.W.; Mose, B.R.; Carrara, S. Biocompatible and Biodegradable 3D Printing from Bioplastics: A Review. *Polymers* **2023**, *15*, 2355. [CrossRef]
5. Maurya, A.K.; de Souza, F.M.; Dawsey, T.; Gupta, R.K. Biodegradable Polymers and Composites: Recent Development and Challenges. *Polym. Compos.* **2024**, *45*, 2896–2918. [CrossRef]
6. Nalawade, S.P.; Picchioni, F.; Janssen, L.P.B.M. Supercritical Carbon Dioxide as a Green Solvent for Processing Polymer Melts: Processing Aspects and Applications. *Prog. Polym. Sci.* **2006**, *31*, 19–43. [CrossRef]
7. Kurowiak, J.; Klekiel, T.; Będziński, R. Biodegradable Polymers in Biomedical Applications: A Review—Developments, Perspectives and Future Challenges. *Int. J. Mol. Sci.* **2023**, *24*, 16952. [CrossRef] [PubMed]
8. Mukherjee, C.; Varghese, D.; Krishna, J.S.; Boominathan, T.; Rakeshkumar, R.; Dineshkumar, S.; Brahmananda Rao, C.V.S.; Sivaramakrishna, A. Recent Advances in Biodegradable Polymers—Properties, Applications and Future Prospects. *Eur. Polym. J.* **2023**, *192*, 112068. [CrossRef]
9. Nanda, H.S.; Yang, L.; Hu, J.; Jiang, S.; Mao, H. Editorial: Biodegradable Polymers for Biomedical Applications-Volume II. *Front. Mater.* **2023**, *10*, 1231445. [CrossRef]
10. Yao, X.; Yang, X.; Lu, Y.; Qiu, Y.; Zeng, Q. Review of the Synthesis and Degradation Mechanisms of Some Biodegradable Polymers in Natural Environments. *Polymers* **2024**, *17*, 66. [CrossRef]
11. Zaaba, N.F.; Jaafar, M. A Review on Degradation Mechanisms of Polylactic Acid: Hydrolytic, Photodegradative, Microbial, and Enzymatic Degradation. *Polym. Eng. Sci.* **2020**, *60*, 2061–2075. [CrossRef]
12. Kliem, S.; Kreutzbruck, M.; Bonten, C. Review on the Biological Degradation of Polymers in Various Environments. *Materials* **2020**, *13*, 4586. [CrossRef]
13. Rosa, V.; Silikas, N.; Yu, B.; Dubey, N.; Sriram, G.; Zinelis, S.; Lima, A.F.; Bottino, M.C.; Ferreira, J.N.; Schmalz, G.; et al. Guidance on the Assessment of Biocompatibility of Biomaterials: Fundamentals and Testing Considerations. *Dent. Mater.* **2024**, *40*, 1773–1785. [CrossRef]
14. Chen, Y.; Su, Y.-C.; Roffler, S.R. Polyethylene Glycol Immunogenicity in Nanomedicine. *Nat. Rev. Bioeng.* **2025**, *3*, 742–760. [CrossRef]
15. Liu, R.; He, T.; Li, R.; Wang, S.; Lai, C.; Zhang, K. Comparison of Different Types of Poly-L-Lactic Acid Microspheres In Vitro and In Vivo Studies. *Aesthetic Surg. J. Open Forum* **2024**, *6*, ojae091. [CrossRef]
16. Filippi, M.; Born, G.; Chaaban, M.; Scherberich, A. Natural Polymeric Scaffolds in Bone Regeneration. *Front. Bioeng. Biotechnol.* **2020**, *8*, 474. [CrossRef]
17. Farjaminejad, S.; Farjaminejad, R.; Hasani, M.; Garcia-Godoy, F.; Abdouss, M.; Marya, A.; Harsoputranto, A.; Jamilian, A. Advances and Challenges in Polymer-Based Scaffolds for Bone Tissue Engineering: A Path Towards Personalized Regenerative Medicine. *Polymers* **2024**, *16*, 3303. [CrossRef] [PubMed]
18. Shah, Y.A.; Bhatia, S.; Al-Harrasi, A.; Oz, F.; Khan, M.H.; Roy, S.; Esatbeyoglu, T.; Pratap-Singh, A. Thermal Properties of Biopolymer Films: Insights for Sustainable Food Packaging Applications. *Food Eng. Rev.* **2024**, *16*, 497–512. [CrossRef]
19. Kalva, S.N.; Zakaria, Y.; Velasquez, C.A.; Koç, M. Tailoring the Mechanical and Degradation Properties of 3DP PLA/PCL Scaffolds for Biomedical Applications. *Rev. Adv. Mater. Sci.* **2025**, *64*, 20250098. [CrossRef]
20. Omidian, H.; Wilson, R.L. PLGA Implants for Controlled Drug Delivery and Regenerative Medicine: Advances, Challenges, and Clinical Potential. *Pharmaceuticals* **2025**, *18*, 631. [CrossRef]
21. Arruda, T.R.; Machado, G.D.O.; Marques, C.S.; Souza, A.L.D.; Pelissari, F.M.; Oliveira, T.V.D.; Silva, R.R.A. An Overview of Starch-Based Materials for Sustainable Food Packaging: Recent Advances, Limitations, and Perspectives. *Macromol* **2025**, *5*, 19. [CrossRef]
22. Chouhan, A.; Tiwari, A. Production of Polyhydroxyalkanoate (PHA) Biopolymer from Crop Residue Using Bacteria as an Alternative to Plastics: A Review. *RSC Adv.* **2025**, *15*, 11845–11862. [CrossRef] [PubMed]
23. Vroman, I.; Tighzert, L. Biodegradable Polymers. *Materials* **2009**, *2*, 307–344. [CrossRef]

24. Biduski, B.; Silva, W.M.F.D.; Colussi, R.; Halal, S.L.D.M.E.; Lim, L.-T.; Dias, Á.R.G.; Zavareze, E.D.R. Starch Hydrogels: The Influence of the Amylose Content and Gelatinization Method. *Int. J. Biol. Macromol.* **2018**, *113*, 443–449. [CrossRef]
25. Perez-Rea, D.; Bergenståhl, B.; Nilsson, L. Development and Evaluation of Methods for Starch Dissolution Using Asymmetrical Flow Field-Flow Fractionation. Part I: Dissolution of Amylopectin. *Anal. Bioanal. Chem.* **2015**, *407*, 4315–4326. [CrossRef] [PubMed]
26. Modjarrad, K.; Ebnesajjad, S.; Plastics Design Library (Eds.) *Handbook of Polymer Applications in Medicine and Medical Devices*; Plastics Design Library Handbook Series; Elsevier Science: Oxford, UK, 2014; ISBN 978-0-323-22169-6.
27. Samir, A.; Ashour, F.H.; Hakim, A.A.A.; Bassyouni, M. Recent Advances in Biodegradable Polymers for Sustainable Applications. *Npj Mater. Degrad.* **2022**, *6*, 68. [CrossRef]
28. Karnwal, A.; Rauf, A.; Jassim, A.Y.; Selvaraj, M.; Al-Tawaha, A.R.M.S.; Kashyap, P.; Kumar, D.; Malik, T. Advanced Starch-Based Films for Food Packaging: Innovations in Sustainability and Functional Properties. *Food Chem. X* **2025**, *29*, 102662. [CrossRef]
29. Mohammed, A.A.B.A.; Hasan, Z.; Omran, A.A.B.; Elfaghi, A.M.; Khattak, M.A.; Ilyas, R.A.; Sapuan, S.M. Effect of Various Plasticizers in Different Concentrations on Physical, Thermal, Mechanical, and Structural Properties of Wheat Starch-Based Films. *Polymers* **2022**, *15*, 63. [CrossRef]
30. Menzel, C.; González-Martínez, C.; Vilaplana, F.; Diretto, G.; Chiralt, A. Incorporation of Natural Antioxidants from Rice Straw into Renewable Starch Films. *Int. J. Biol. Macromol.* **2020**, *146*, 976–986. [CrossRef]
31. Wang, H.; Yang, L.; Yang, Y.; Zhang, D.; Hao, G. Multifunctional Natural Starch-Based Hydrogels: Critical Characteristics, Formation Mechanisms, Various Applications, Future Perspectives. *Carbohydr. Polym.* **2025**, *357*, 123458. [CrossRef]
32. Alipournazari, P.; Pourmadadi, M.; Abdouss, M.; Rahdar, A.; Pandey, S. Enhanced Delivery of Doxorubicin for Breast Cancer Treatment Using pH-Sensitive Starch/PVA/g-C3N4 Hydrogel. *Int. J. Biol. Macromol.* **2024**, *265*, 130901. [CrossRef]
33. Koshenaj, K.; Ferrari, G. A Comprehensive Review on Starch-Based Hydrogels: From Tradition to Innovation, Opportunities, and Drawbacks. *Polymers* **2024**, *16*, 1991. [CrossRef] [PubMed]
34. Tebaldi, M.L.; Maia, A.L.C.; Poletto, F.; De Andrade, F.V.; Soares, D.C.F. Poly(-3-Hydroxybutyrate-Co-3-Hydroxyvalerate) (PHBV): Current Advances in Synthesis Methodologies, Antitumor Applications and Biocompatibility. *J. Drug Deliv. Sci. Technol.* **2019**, *51*, 115–126. [CrossRef]
35. Jin, A.; Del Valle, L.J.; Puiggalí, J. Copolymers and Blends Based on 3-Hydroxybutyrate and 3-Hydroxyvalerate Units. *Int. J. Mol. Sci.* **2023**, *24*, 17250. [CrossRef] [PubMed]
36. Oliver-Cuenca, V.; Salaris, V.; Muñoz-Gimena, P.F.; Agüero, Á.; Peltzer, M.A.; Montero, V.A.; Arrieta, M.P.; Sempere-Torregrosa, J.; Pavon, C.; Samper, M.D.; et al. Bio-Based and Biodegradable Polymeric Materials for a Circular Economy. *Polymers* **2024**, *16*, 3015. [CrossRef]
37. Shi, B.; Hao, Z.; Du, Y.; Jia, M.; Xie, S. Mechanical and Barrier Properties of Chitosan-Based Composite Film as Food Packaging: A Review. *BioResources* **2024**, *19*, 4001–4014. [CrossRef]
38. Zafar, W.; Tabassum, M.; Jia, X.; Yang, B.; Liu, H.; Xu, G.; Zafar, M.N. Chitosan-Based Bionanocomposites for Elimination of Hazardous Environmental Contaminants and Food Packaging: A Comprehensive Review. *Sustain. Mater. Technol.* **2025**, *45*, e01524. [CrossRef]
39. Liu, Y.; Gilchrist, A.E.; Heilshorn, S.C. Engineered Protein Hydrogels as Biomimetic Cellular Scaffolds. *Adv. Mater.* **2024**, *36*, 2407794. [CrossRef]
40. Johari, N.; Moroni, L.; Samadikuchaksaraei, A. Tuning the Conformation and Mechanical Properties of Silk Fibroin Hydrogels. *Eur. Polym. J.* **2020**, *134*, 109842. [CrossRef]
41. Jung, D.; Lee, J.; Park, T.Y.; Yang, Y.J.; Cha, H.J. Diverse Silk and Silk-like Proteins Derived from Terrestrial and Marine Organisms and Their Applications. *Acta Biomater.* **2021**, *136*, 56–71. [CrossRef]
42. Sionkowska, A. Collagen Blended with Natural Polymersv: Recent Advances and Trends. *Prog. Polym. Sci.* **2021**, *122*, 101452. [CrossRef]
43. Davison-Kotler, E.; Marshall, W.S.; García-Gareta, E. Sources of Collagen for Biomaterials in Skin Wound Healing. *Bioengineering* **2019**, *6*, 56. [CrossRef] [PubMed]
44. Sabarees, G.; Vishvaja, S.; Raghuraman, S.; Velmurugan, V.; Alagarsamy, V.; Raja Solomon, V.; Padmini Tamilarasi, G. Collagen-Based Nanofibers: Revolutionizing Therapeutics for Impaired Wound Healing. *Int. J. Polym. Mater. Polym. Biomater.* **2025**, *74*, 1128–1156. [CrossRef]
45. Farooq, S.; Ahmad, M.I.; Zheng, S.; Ali, U.; Li, Y.; Shixiu, C.; Zhang, H. A Review on Marine Collagen: Sources, Extraction Methods, Colloids Properties, and Food Applications. *Collagen Leather* **2024**, *6*, 11. [CrossRef]
46. Furtado, M.; Chen, L.; Chen, Z.; Chen, A.; Cui, W. Development of Fish Collagen in Tissue Regeneration and Drug Delivery. *Eng. Regen.* **2022**, *3*, 217–231. [CrossRef]

47. Ding, C.; Yi, Y.; Cheng, K.; Wang, Y.; Wang, S.; Zhang, M. Full Life Cycle Green Preparation of Collagen-Based Food Packaging Films Using Halocynthia Roretzi as Raw Material. *Food Chem.* **2024**, *455*, 139943. [CrossRef] [PubMed]
48. Wang, H.; Yang, L.; Yang, Y. A Review of Sodium Alginate-Based Hydrogels: Structure, Mechanisms, Applications, and Perspectives. *Int. J. Biol. Macromol.* **2025**, *292*, 139151. [CrossRef] [PubMed]
49. Kadri, H.J.; Ahmed, F.; Rahman, M.H.; Mondal, M.I.H. Synthesis and Characterisation of Starch-g-Polyacrylamide-Co-Polylactic Acid Hydrogel for the Potential Wound Dressing Application. *Polym. Bull.* **2025**, *82*, 7917–7941. [CrossRef]
50. Costa, T.B.; Matias, P.M.C.; Sharma, M.; Murtinho, D.; Rosa, D.S.; Valente, A.J.M. Recent Advances on Starch-Based Adsorbents for Heavy Metal and Emerging Pollutant Remediation. *Polymers* **2024**, *17*, 15. [CrossRef]
51. Junka, A.; Bartoszewicz, M.; Dziadas, M.; Szymczyk, P.; Dydak, K.; Żywicka, A.; Owczarek, A.; Bil-Lula, I.; Czajkowska, J.; Fijałkowski, K. Application of Bacterial Cellulose Experimental Dressings Saturated with Gentamycin for Management of Bone Biofilm In Vitro and Ex Vivo. *J. Biomed. Mater. Res. B Appl. Biomater.* **2020**, *108*, 30–37. [CrossRef]
52. Acharya, S.; Liyanage, S.; Parajuli, P.; Rumi, S.S.; Shamshina, J.L.; Abidi, N. Utilization of Cellulose to Its Full Potential: A Review on Cellulose Dissolution, Regeneration, and Applications. *Polymers* **2021**, *13*, 4344. [CrossRef]
53. Pawase, P.A.; Rout, S.; Tripathy, S.; Pathare, A.M.; Srivastav, P.P.; Bashir, O.; Panghal, A. Recent Advances in Cellulose, Chitosan, and Protein-Based Edible Films for Sustainable Food Packaging: A Comprehensive Review. *Int. J. Biol. Macromol.* **2025**, *321*, 146172. [CrossRef]
54. Shah, T.V.; Vasava, D.V. A Glimpse of Biodegradable Polymers and Their Biomedical Applications. *e-Polymers* **2019**, *19*, 385–410. [CrossRef]
55. Luckachan, G.E.; Pillai, C.K.S. Biodegradable Polymers- A Review on Recent Trends and Emerging Perspectives. *J. Polym. Environ.* **2011**, *19*, 637–676. [CrossRef]
56. Marinho, E. Cellulose: A Comprehensive Review of Its Properties and Applications. *Sustain. Chem. Environ.* **2025**, *11*, 100283. [CrossRef]
57. Dalton, B.; Bhagabati, P.; De Micco, J.; Padamati, R.B.; O'Connor, K. A Review on Biological Synthesis of the Biodegradable Polymers Polyhydroxyalkanoates and the Development of Multiple Applications. *Catalysts* **2022**, *12*, 319. [CrossRef]
58. Kumar, S.; Thakur, K. Bioplastics—Classification, Production and Their Potential Food Applications. *J. Hill Agric.* **2017**, *8*, 118. [CrossRef]
59. Lalonde, J.N.; Pilania, G.; Marrone, B.L. Materials Designed to Degrade: Structure, Properties, Processing, and Performance Relationships in Polyhydroxyalkanoate Biopolymers. *Polym. Chem.* **2025**, *16*, 235–265. [CrossRef]
60. Gautam, S.; Gautam, A.; Pawaday, J.; Kanzariya, R.K.; Yao, Z. Current Status and Challenges in the Commercial Production of Polyhydroxyalkanoate-Based Bioplastic: A Review. *Processes* **2024**, *12*, 1720. [CrossRef]
61. McAdam, B.; Brennan Fournet, M.; McDonald, P.; Mojicevic, M. Production of Polyhydroxybutyrate (PHB) and Factors Impacting Its Chemical and Mechanical Characteristics. *Polymers* **2020**, *12*, 2908. [CrossRef] [PubMed]
62. Suzuki, M.; Tachibana, Y.; Kasuya, K. Biodegradability of Poly(3-Hydroxyalkanoate) and Poly(ε-Caprolactone) via Biological Carbon Cycles in Marine Environments. *Polym. J.* **2021**, *53*, 47–66. [CrossRef]
63. Wang, C.; Venditti, R.A.; Zhang, K. Tailor-Made Functional Surfaces Based on Cellulose-Derived Materials. *Appl. Microbiol. Biotechnol.* **2015**, *99*, 5791–5799. [CrossRef]
64. Perveen, K.; Masood, F.; Hameed, A. Preparation, Characterization and Evaluation of Antibacterial Properties of Epirubicin Loaded PHB and PHBV Nanoparticles. *Int. J. Biol. Macromol.* **2020**, *144*, 259–266. [CrossRef]
65. Yeo, J.C.C.; Muiruri, J.K.; Thitsartarn, W.; Li, Z.; He, C. Recent Advances in the Development of Biodegradable PHB-Based Toughening Materials: Approaches, Advantages and Applications. *Mater. Sci. Eng. C* **2018**, *92*, 1092–1116. [CrossRef]
66. Moliner, C.; Badia, J.D.; Bosio, B.; Arato, E.; Lagazzo, A.; Capurro, M.; Ribes-Greus, A. Mechanical and Thermal Performance of Pla and Phbv-Based Biopolymers as Potential Alternatives to Pet. *Chem. Eng. Trans.* **2017**, *57*, 1417–1422. [CrossRef]
67. Keskin, G.; Kızıl, G.; Bechelany, M.; Pochat-Bohatier, C.; Öner, M. Potential of Polyhydroxyalkanoate (PHA) Polymers Family as Substitutes of Petroleum Based Polymers for Packaging Applications and Solutions Brought by Their Composites to Form Barrier Materials. *Pure Appl. Chem.* **2017**, *89*, 1841–1848. [CrossRef]
68. Ibrahim, H.M.; El-Zairy, E.M.R. Chitosan as a Biomaterial—Structure, Properties, and Electrospun Nanofibers. In *Concepts, Compounds and the Alternatives of Antibacterials*; Bobbarala, V., Ed.; InTechOpen: Rijeka, Croatia, 2015; ISBN 978-953-51-2232-6.
69. Morrow, B.H.; Payne, G.F.; Shen, J.K. Titration Properties and pH-Dependent Aggregation of Chitosan. *Biophys. J.* **2015**, *108*, 488a. [CrossRef]
70. Castro, J.I.; Valencia-Llano, C.H.; Valencia Zapata, M.E.; Restrepo, Y.J.; Mina Hernandez, J.H.; Navia-Porras, D.P.; Valencia, Y.; Valencia, C.; Grande-Tovar, C.D. Chitosan/Polyvinyl Alcohol/Tea Tree Essential Oil Composite Films for Biomedical Applications. *Polymers* **2021**, *13*, 3753. [CrossRef]

71. Chandarana, C.; Bonde, S.; Sonwane, S.; Prajapati, B. Chitosan-Based Packaging: Leading Sustainable Advancements in the Food Industry. *Polym. Bull.* **2025**, *82*, 5431–5462. [CrossRef]
72. Saheed, I.O.; Oh, W.D.; Suah, F.B.M. Chitosan Modifications for Adsorption of Pollutants—A Review. *J. Hazard. Mater.* **2021**, *408*, 124889. [CrossRef] [PubMed]
73. Schmuck, B.; Greco, G.; Pessatti, T.B.; Sonavane, S.; Langwallner, V.; Arndt, T.; Rising, A. Strategies for Making High-Performance Artificial Spider Silk Fibers. *Adv. Funct. Mater.* **2024**, *34*, 2305040. [CrossRef]
74. Gholipourmalekabadi, M.; Sapru, S.; Samadikuchaksaraei, A.; Reis, R.L.; Kaplan, D.L.; Kundu, S.C. Silk Fibroin for Skin Injury Repair: Where Do Things Stand? *Adv. Drug Deliv. Rev.* **2020**, *153*, 28–53. [CrossRef]
75. Senthilkumar, D.; Don, T.-M.; Liao, Y.-J.; Kuo, C.-Y. The Art of Biodegradable Polymer Design for the Treatments against Osteomyelitis. *Int. J. Biol. Macromol.* **2025**, *285*, 138347. [CrossRef]
76. Kanoujia, J.; Raina, N.; Kishore, A.; Kaurav, M.; Tuli, H.S.; Kumar, A.; Gupta, M. Revealing the Promising Era of Silk-Based Nanotherapeutics: A Ray of Hope for Chronic Wound Healing Treatment. *Naunyn. Schmiedebergs Arch. Pharmacol.* **2025**, *398*, 6617–6641. [CrossRef]
77. You, C.; Wang, C.; Ma, Z.; Yu, Q.; Liu, S. Review on Application of Silk Fibroin Hydrogels in the Management of Wound Healing. *Int. J. Biol. Macromol.* **2025**, *298*, 140082. [CrossRef] [PubMed]
78. Zhu, S.; Zhang, Q.; Xu, X.; Liu, Z.; Cheng, G.; Long, D.; Cheng, L.; Dai, F. Recent Advances in Silk Fibroin-Based Composites for Bone Repair Applications: A Review. *Polymers* **2025**, *17*, 772. [CrossRef]
79. Altman, G.H.; Farrell, B.D. Sericulture as a Sustainable Agroindustry. *Clean. Circ. Bioecon.* **2022**, *2*, 100011. [CrossRef]
80. Puerta, M.; Gomez-Maldonado, D.; Restrepo-Osorio, A.; Peresin, M.S. Self-Assembled Green Composites of Silk Fibroin and Microfibrillated Cellulose. *MRS Bull.* **2025**, *50*, 846–855. [CrossRef]
81. Wosicka-Frąckowiak, H.; Poniedziałek, K.; Woźny, S.; Kuprianowicz, M.; Nyga, M.; Jadach, B.; Milanowski, B. Collagen and Its Derivatives Serving Biomedical Purposes: A Review. *Polymers* **2024**, *16*, 2668. [CrossRef]
82. Ren, Y.; Wang, Q.; Xu, W.; Yang, M.; Guo, W.; He, S.; Liu, W. Alginate-Based Hydrogels Mediated Biomedical Applications: A Review. *Int. J. Biol. Macromol.* **2024**, *279*, 135019. [CrossRef]
83. Lai, J.; Azad, A.K.; Sulaiman, W.M.A.W.; Kumarasamy, V.; Subramaniyan, V.; Alshehade, S.A. Alginate-Based Encapsulation Fabrication Technique for Drug Delivery: An Updated Review of Particle Type, Formulation Technique, Pharmaceutical Ingredient, and Targeted Delivery System. *Pharmaceutics* **2024**, *16*, 370. [CrossRef]
84. Hariyadi, D.M.; Islam, N. Current Status of Alginate in Drug Delivery. *Adv. Pharmacol. Pharm. Sci.* **2020**, *2020*, 8886095. [CrossRef]
85. Metha, C.; Pawar, S.; Suvarna, V. Recent Advancements in Alginate-Based Films for Active Food Packaging Applications. *Sustain. Food Technol.* **2024**, *2*, 1246–1265. [CrossRef]
86. Dong, Z.; Xu, J.; Lun, P.; Wu, Z.; Deng, W.; Sun, P. Dynamic Cross-Linking, Self-Healing, Antibacterial Hydrogel for Regenerating Irregular Cranial Bone Defects. *ACS Appl. Mater. Interfaces* **2024**, *16*, 39035–39050. [CrossRef] [PubMed]
87. Shin, H.; Kim, H.; Lee, J.; Sadeghi, K.; Seo, J. PBAT/PGA Blend Films for Sustainable Packaging: Effect of PGA on Physicochemical and Morphological Changes during Abiotic Degradation. *Food Packag. Shelf Life* **2025**, *51*, 101589. [CrossRef]
88. Firoozi, N.; Rezayan, A.H.; Tabatabaei Rezaei, S.J.; Mir-Derikvand, M.; Nabid, M.R.; Nourmohammadi, J.; Mohammadnejad Arough, J. Synthesis of Poly(ε-Caprolactone)-Based Polyurethane Semi-Interpenetrating Polymer Networks as Scaffolds for Skin Tissue Regeneration. *Int. J. Polym. Mater. Polym. Biomater.* **2017**, *66*, 805–811. [CrossRef]
89. Deshpande, M.V.; Girase, A.; King, M.W. Degradation of Poly(ε-Caprolactone) Resorbable Multifilament Yarn under Physiological Conditions. *Polymers* **2023**, *15*, 3819. [CrossRef]
90. Gedik, B.; Erdem, M.A. Electrospun PCL Membranes for Localized Drug Delivery and Bone Regeneration. *BMC Biotechnol.* **2025**, *25*, 31. [CrossRef]
91. Jahani, A.; Nassira, H. Polyethylene Glycol-Based Materials: Transformative Applications in Biomedicine and the Food Industry. *Mater. Chem. Horiz.* **2024**, *3*, 1074. [CrossRef]
92. Jafri, N.H.S.; Jimat, D.N.; Wan Nawawi, W.M.F.; Ahmad Nor, Y.; Amid, A. Effect of Incorporating Cellulose Nanofibers and Lemongrass Essential Oil in Polyvinyl Alcohol-Polyethylene Glycol/Glycerin Hydrogel for Wound Dressing. *IIUM Eng. J.* **2024**, *25*, 99–115. [CrossRef]
93. Cui, M.; Chai, Z.; Lu, Y.; Zhu, J.; Chen, J. Developments of Polyurethane in Biomedical Applications: A Review. *Resour. Chem. Mater.* **2023**, *2*, 262–276. [CrossRef]
94. Akindoyo, J.O.; Beg, M.D.H.; Ghazali, S.; Islam, M.R.; Jeyaratnam, N.; Yuvaraj, A.R. Polyurethane Types, Synthesis and Applications—A Review. *RSC Adv.* **2016**, *6*, 114453–114482. [CrossRef]
95. Jayalath, P.; Ananthakrishnan, K.; Jeong, S.; Shibu, R.P.; Zhang, M.; Kumar, D.; Yoo, C.G.; Shamshina, J.L.; Therasme, O. Bio-Based Polyurethane Materials: Technical, Environmental, and Economic Insights. *Processes* **2025**, *13*, 1591. [CrossRef]

96. Rahman Khan, M.M.; Rumon, M.M.H. Synthesis of PVA-Based Hydrogels for Biomedical Applications: Recent Trends and Advances. *Gels* **2025**, *11*, 88. [CrossRef]
97. Hedayati, H.R.; Khorasani, M.; Ahmadi, M.; Ballard, N. Preparation of Well-Defined Poly(Vinyl Alcohol) by Hydrolysis of Poly(Vinyl Acetate) Synthesized by RAFT Suspension Polymerization. *Polymer* **2022**, *246*, 124674. [CrossRef]
98. Hedir, G.; Stubbs, C.; Aston, P.; Dove, A.P.; Gibson, M.I. Synthesis of Degradable Poly(Vinyl Alcohol) by Radical Ring-Opening Copolymerization and Ice Recrystallization Inhibition Activity. *ACS Macro Lett.* **2017**, *6*, 1404–1408. [CrossRef]
99. Vengadesan, E.; Morakul, S.; Muralidharan, S.; Pullela, P.K.; Alarifi, A.; Arunkumar, T. Enhancement of Polylactic Acid (PLA) with Hybrid Biomass-Derived Rice Husk and Biocarbon Fillers: A Comprehensive Experimental Study. *Discov. Appl. Sci.* **2025**, *7*, 161. [CrossRef]
100. Pullarkad Bharathan, S.; Johnsy, G.; Raju, A.P.; Guthige, M.R.; Gowdahalli Mantelingachar, C.; Vasudevan, V.; Madan, R.; Kumar, R. Sustainable Antimicrobial Packaging Films: Effectiveness of Epsilon-Poly-L-Lysine in PLA/PBAT Blend Films. *Sustain. Food Technol.* **2025**. [CrossRef]
101. Zhang, L.; Zhong, J.; Ren, X. Natural Fiber-Based Biocomposites. In *Green Biocomposites*; Jawaid, M., Sapuan, S.M., Alothman, O.Y., Eds.; Green Energy and Technology; Springer International Publishing: Cham, Switzerland, 2017; pp. 31–70, ISBN 978-3-319-46609-5.
102. Ghanbarzadeh, B.; Almasi, H. Biodegradable Polymers. In *Biodegradation—Life of Science*; Chamy, R., Ed.; InTechOpen: Rijeka, Croatia, 2013; ISBN 978-953-51-1154-2.
103. Chen, S.; Meng, X.; Xin, Z.; Gong, W.; Li, C.; Wen, W. Preparation of Nonlinear Structure Poly(Glycolic Acid) with High Toughness, Excellent Hydrolysis Stability, and Foaming Performance. *Ind. Eng. Chem. Res.* **2024**, *63*, 9058–9069. [CrossRef]
104. Qiu, X.; Li, S.; Li, X.; Xiao, Y.; Li, S.; Fen, Q.; Kang, X.; Zhen, P. Experimental Study of β-TCP Scaffold Loaded with VAN/PLGA Microspheres in the Treatment of Infectious Bone Defects. *Colloids Surf. B Biointerfaces* **2022**, *213*, 112424. [CrossRef] [PubMed]
105. Tu, S.; Mai, S.; Shu, D.; Huang, Y.; Nie, Z.; Wang, Y.; Yang, W. Microfluidic-Based Preparation of PLGA Microspheres Facilitating Peptide Sustained-Release. *Mater. Lett.* **2024**, *368*, 136675. [CrossRef]
106. Jiang, L.; Zhang, J. Biodegradable Polymers and Polymer Blends. In *Handbook of Biopolymers and Biodegradable Plastics*; Elsevier: Amsterdam, The Netherlands, 2013; pp. 109–128, ISBN 978-1-4557-2834-3.
107. D'souza, A.A.; Shegokar, R. Polyethylene Glycol (PEG): A Versatile Polymer for Pharmaceutical Applications. *Expert Opin. Drug Deliv.* **2016**, *13*, 1257–1275. [CrossRef]
108. Verma, V.S.; Pandey, A.; Jha, A.K.; Badwaik, H.K.R.; Alexander, A. Ajazuddin Polyethylene Glycol–Based Polymer-Drug Conjugates: Novel Design and Synthesis Strategies for Enhanced Therapeutic Efficacy and Targeted Drug Delivery. *Appl. Biochem. Biotechnol.* **2024**, *196*, 7325–7361. [CrossRef]
109. Liu, Y.; Wang, S.; Lan, W. Fabrication of Antibacterial Chitosan-PVA Blended Film Using Electrospray Technique for Food Packaging Applications. *Int. J. Biol. Macromol.* **2018**, *107*, 848–854. [CrossRef] [PubMed]
110. Trigui, K.; Magnin, A.; Putaux, J.-L.; Boufi, S. Poly(Vinyl Alcohol)/Oxidized Cellulose Nanofibril Composite Films with High Nanofiller Content for Enhanced Packaging Applications. *J. Ind. Eng. Chem.* **2025**, *148*, 602–613. [CrossRef]
111. Narin, S.; Sahin, S.B.; Demir, E.; Cetinel, S. Electrospun Poly (Glycerol Sebacate) (PGS) Membranes for Corneal Tissue Engineering. *Macromol. Mater. Eng.* **2025**, e00163. [CrossRef]
112. Wang, Z.; Zhang, M.; Liu, L.; Mithieux, S.M.; Weiss, A.S. Polyglycerol Sebacate-Based Elastomeric Materials for Arterial Regeneration. *J. Biomed. Mater. Res. A* **2024**, *112*, 574–585. [CrossRef]
113. Rai, R.; Tallawi, M.; Grigore, A.; Boccaccini, A.R. Synthesis, Properties and Biomedical Applications of Poly(Glycerol Sebacate) (PGS): A Review. *Prog. Polym. Sci.* **2012**, *37*, 1051–1078. [CrossRef]
114. Andrä-Żmuda, S.; Chaber, P.; Martinka Maksymiak, M.; Musioł, M.; Adamus, G. Poly(Glycerol Sebacate): A Comparative Study of Various Synthesis Methods. *Biomacromolecules* **2025**. [CrossRef]
115. Risley, B.B.; Ding, X.; Chen, Y.; Miller, P.G.; Wang, Y. Citrate Crosslinked Poly(Glycerol Sebacate) with Tunable Elastomeric Properties. *Macromol. Biosci.* **2021**, *21*, 2000301. [CrossRef] [PubMed]
116. Yu, L.; Zeng, G.; Xu, J.; Han, M.; Wang, Z.; Li, T.; Long, M.; Wang, L.; Huang, W.; Wu, Y. Development of Poly(Glycerol Sebacate) and Its Derivatives: A Review of the Progress over the Past Two Decades. *Polym. Rev.* **2023**, *63*, 613–678. [CrossRef]
117. Martín-Cabezuelo, R.; Vilariño-Feltrer, G.; Vallés-Lluch, A. Influence of Pre-Polymerisation Atmosphere on the Properties of Pre- and Poly(Glycerol Sebacate). *Mater. Sci. Eng. C* **2021**, *119*, 111429. [CrossRef] [PubMed]
118. Godinho, B.; Gama, N.; Ferreira, A. Different Methods of Synthesizing Poly(Glycerol Sebacate) (PGS): A Review. *Front. Bioeng. Biotechnol.* **2022**, *10*, 1033827. [CrossRef]
119. Ning, Z.; Lang, K.; Xia, K.; Linhardt, R.J.; Gross, R.A. Lipase-Catalyzed Synthesis and Characterization of Poly(Glycerol Sebacate). *Biomacromolecules* **2022**, *23*, 398–408. [CrossRef]

120. Yousefi Talouki, P.; Tamimi, R.; Zamanlui Benisi, S.; Goodarzi, V.; Shojaei, S.; Hesami tackalou, S.; Samadikhah, H.R. Polyglycerol Sebacate (PGS)-Based Composite and Nanocomposites: Properties and Applications. *Int. J. Polym. Mater. Polym. Biomater.* **2023**, *72*, 1360–1374. [CrossRef]
121. Martín Cabezuelo, R. Monitoring of the Parameters of Synthesis of Poly(Glycerol Sebacate) and Influence on the Physicochemical and Biological Properties of Its Elastomer. Ph.D. Thesis, Universitat Politècnica de València, Valencia, Spain, 2020.
122. Shukla, K.; Arunagiri, A.; Muthukumar, K. Synthesis and Hydrolytic Degradation of Poly (Glycerol Succinate) Based Polyesters. *J. Indian Chem. Soc.* **2023**, *100*, 100841. [CrossRef]
123. Godinho, B.; Nogueira, R.; Gama, N.; Ferreira, A. Synthesis and Characterization of Poly(Glycerol Sebacate), Poly(Glycerol Succinate) and Poly(Glycerol Sebacate-Co-Succinate). *J. Polym. Environ.* **2024**, *32*, 4330–4347. [CrossRef]
124. Nakiou, E.A.; Lazaridou, M.; Pouroutzidou, G.K.; Michopoulou, A.; Tsamesidis, I.; Liverani, L.; Arango-Ospina, M.; Beketova, A.; Boccaccini, A.R.; Kontonasaki, E.; et al. Poly(Glycerol Succinate) as Coating Material for 1393 Bioactive Glass Porous Scaffolds for Tissue Engineering Applications. *Polymers* **2022**, *14*, 5028. [CrossRef] [PubMed]
125. Kolbuk, D.; Jeznach, O.; Wrzecionek, M.; Gadomska-Gajadhur, A. Poly(Glycerol Succinate) as an Eco-Friendly Component of PLLA and PLCL Fibres towards Medical Applications. *Polymers* **2020**, *12*, 1731. [CrossRef]
126. Hetemi, D.; Pinson, J. Surface Functionalisation of Polymers. *Chem. Soc. Rev.* **2017**, *46*, 5701–5713. [CrossRef] [PubMed]
127. Aditya, T.; Allain, J.P.; Jaramillo, C.; Restrepo, A.M. Surface Modification of Bacterial Cellulose for Biomedical Applications. *Int. J. Mol. Sci.* **2022**, *23*, 610. [CrossRef]
128. Sun, W.; Liu, W.; Wu, Z.; Chen, H. Chemical Surface Modification of Polymeric Biomaterials for Biomedical Applications. *Macromol. Rapid Commun.* **2020**, *41*, 1900430. [CrossRef]
129. Gao, Y.; Joshi, M.; Zhao, Z.; Mitragotri, S. PEGylated Therapeutics in the Clinic. *Bioeng. Transl. Med.* **2024**, *9*, e10600. [CrossRef]
130. Veronese, F.M.; Mero, A. The Impact of PEGylation on Biological Therapies. *BioDrugs* **2012**, *22*, 315–329. [CrossRef] [PubMed]
131. Santhanakrishnan, K.R.; Koilpillai, J.; Narayanasamy, D. PEGylation in Pharmaceutical Development: Current Status and Emerging Trends in Macromolecular and Immunotherapeutic Drugs. *Cureus* **2024**, *16*, e66669. [CrossRef] [PubMed]
132. Hoang Thi, T.T.; Pilkington, E.H.; Nguyen, D.H.; Lee, J.S.; Park, K.D.; Truong, N.P. The Importance of Poly(Ethylene Glycol) Alternatives for Overcoming PEG Immunogenicity in Drug Delivery and Bioconjugation. *Polymers* **2020**, *12*, 298. [CrossRef] [PubMed]
133. Kurul, F.; Doruk, B.; Topkaya, S.N. Principles of Green Chemistry: Building a Sustainable Future. *Discov. Chem.* **2025**, *2*, 68. [CrossRef]
134. Godinho, B.M.D.C.; Ogier, J.R.; Quinlan, A.; Darcy, R.; Griffin, B.T.; Cryan, J.F.; O'Driscoll, C.M. PEGylated Cyclodextrins as Novel siRNA Nanosystems: Correlations between Polyethylene Glycol Length and Nanoparticle Stability. *Int. J. Pharm.* **2014**, *473*, 105–112. [CrossRef]
135. Carcao, M.D.; Chelle, P.; Clarke, E.; Kim, L.; Tiseo, L.; Morfini, M.; Hossain, T.; Rand, M.L.; Brown, C.; Edginton, A.N.; et al. Comparative Pharmacokinetics of Two Extended Half-life FVIII Concentrates (Eloctate and Adynovate) in Adolescents with Hemophilia A: Is There a Difference? *J. Thromb. Haemost.* **2019**, *17*, 1085–1096. [CrossRef]
136. Makharadze, D.; del Valle, L.J.; Katsarava, R.; Puiggalí, J. The Art of PEGylation: From Simple Polymer to Sophisticated Drug Delivery System. *Int. J. Mol. Sci.* **2025**, *26*, 3102. [CrossRef]
137. Robella, M.; Vaira, M.; Argenziano, M.; Spagnolo, R.; Cavalli, R.; Borsano, A.; Gentilli, S.; De Simone, M. Exploring the Use of Pegylated Liposomal Doxorubicin (Caelyx®) as Pressurized Intraperitoneal Aerosol Chemotherapy. *Front. Pharmacol.* **2019**, *10*, 669. [CrossRef]
138. Demirel, E.; Karaca, E.; Yuksel Durmaz, Y. Effective PEGylation Method to Improve Biocompatibility of Graphene Derivatives. *Eur. Polym. J.* **2020**, *124*, 109504. [CrossRef]
139. Zaky, M.F.; Hammady, T.M.; Gad, S.; Alattar, A.; Alshaman, R.; Hegazy, A.; Zaitone, S.A.; Ghorab, M.M.; Megahed, M.A. Influence of Surface-Modification via PEGylation or Chitosanization of Lipidic Nanocarriers on In Vivo Pharmacokinetic/Pharmacodynamic Profiles of Apixaban. *Pharmaceutics* **2023**, *15*, 1668. [CrossRef]
140. Kesharwani, P.; Kumar, V.; Goh, K.W.; Gupta, G.; Alsayari, A.; Wahab, S.; Sahebkar, A. PEGylated PLGA Nanoparticles: Unlocking Advanced Strategies for Cancer Therapy. *Mol. Cancer* **2025**, *24*, 205. [CrossRef]
141. Nemani, K.; Annavarapu, R.K.; Mohammadian, B.; Raiyan, A.; Heil, J.; Haque, M.; Abdelaal, A.; Sojoudi, H. Surface Modification: Surface Modification of Polymers: Methods and Applications (Adv. Mater. Interfaces 24/2018). *Adv. Mater. Interfaces* **2018**, *5*, 1870121. [CrossRef]
142. Kurhade, R.R.; Shaikh, M.S.; Nagulwar, V.; Kale, M.A. Advancements in Carboxymethyl Cellulose (CMC) Modifications and Their Diverse Biomedical Applications: A Comprehensive Review. *Int. J. Polym. Mater. Polym. Biomater.* **2025**, *74*, 1043–1067. [CrossRef]

143. Yang, Q.; Pan, X. Introducing Hydroxyl Groups as Cellulose-Binding Sites into Polymeric Solid Acids to Improve Their Catalytic Performance in Hydrolyzing Cellulose. *Carbohydr. Polym.* **2021**, *261*, 117895. [CrossRef] [PubMed]
144. Chen, J.; Garcia, E.S.; Zimmerman, S.C. Intramolecularly Cross-Linked Polymers: From Structure to Function with Applications as Artificial Antibodies and Artificial Enzymes. *Acc. Chem. Res.* **2020**, *53*, 1244–1256. [CrossRef] [PubMed]
145. Musa, A.A.; Bello, A.; Adams, S.M.; Onwualu, A.P.; Anye, V.C.; Bello, K.A.; Obianyo, I.I. Nano-Enhanced Polymer Composite Materials: A Review of Current Advancements and Challenges. *Polymers* **2025**, *17*, 893. [CrossRef]
146. Sharma, H.; Arora, G.; Singh, M.K.; Rangappa, S.M.; Bhowmik, P.; Kumar, R.; Debnath, S.; Siengchin, S. From Composition to Performance: Structural Insights into Polymer Composites. *Next Mater.* **2025**, *8*, 100852. [CrossRef]
147. Laurano, R.; Boffito, M.; Torchio, A.; Cassino, C.; Chiono, V.; Ciardelli, G. Plasma Treatment of Polymer Powder as an Effective Tool to Functionalize Polymers: Case Study Application on an Amphiphilic Polyurethane. *Polymers* **2019**, *11*, 2109. [CrossRef]
148. Primc, G.; Mozetič, M. Surface Modification of Polymers by Plasma Treatment for Appropriate Adhesion of Coatings. *Materials* **2024**, *17*, 1494. [CrossRef]
149. Bhatt, P.; Kumar, V.; Subramaniyan, V.; Nagarajan, K.; Sekar, M.; Chinni, S.V.; Ramachawolran, G. Plasma Modification Techniques for Natural Polymer-Based Drug Delivery Systems. *Pharmaceutics* **2023**, *15*, 2066. [CrossRef]
150. Koodaryan, R.; Hafezeqoran, A. Surface Modification of Dental Polymers by Plasma Treatment: A Review. *Biomed. Pharmacol. J.* **2016**, *9*. [CrossRef]
151. Pidhatika, B.; Widyaya, V.T.; Nalam, P.C.; Swasono, Y.A.; Ardhani, R. Surface Modifications of High-Performance Polymer Polyetheretherketone (PEEK) to Improve Its Biological Performance in Dentistry. *Polymers* **2022**, *14*, 5526. [CrossRef]
152. Sundriyal, P.; Sahu, M.; Prakash, O.; Bhattacharya, S. Long-Term Surface Modification of PEEK Polymer Using Plasma and PEG Silane Treatment. *Surf. Interfaces* **2021**, *25*, 101253. [CrossRef]
153. Hu, L.; Wan, Y.; Zhang, Q.; Serpe, M.J. Harnessing the Power of Stimuli-Responsive Polymers for Actuation. *Adv. Funct. Mater.* **2020**, *30*, 1903471. [CrossRef]
154. Ofridam, F.; Tarhini, M.; Lebaz, N.; Gagnière, É.; Mangin, D.; Elaissari, A. pH-Sensitive Polymers: Classification and Some Fine Potential Applications. *Polym. Adv. Technol.* **2021**, *32*, 1455–1484. [CrossRef]
155. Bratek-Skicki, A. Towards a New Class of Stimuli-Responsive Polymer-Based Materials—Recent Advances and Challenges. *Appl. Surf. Sci. Adv.* **2021**, *4*, 100068. [CrossRef]
156. Das, S.S.; Bharadwaj, P.; Bilal, M.; Barani, M.; Rahdar, A.; Taboada, P.; Bungau, S.; Kyzas, G.Z. Stimuli-Responsive Polymeric Nanocarriers for Drug Delivery, Imaging, and Theragnosis. *Polymers* **2020**, *12*, 1397. [CrossRef] [PubMed]
157. Zhang, Q.; Weber, C.; Schubert, U.S.; Hoogenboom, R. Thermoresponsive Polymers with Lower Critical Solution Temperature: From Fundamental Aspects and Measuring Techniques to Recommended Turbidimetry Conditions. *Mater. Horiz.* **2017**, *4*, 109–116. [CrossRef]
158. Yuan, Y.; Raheja, K.; Milbrandt, N.B.; Beilharz, S.; Tene, S.; Oshabaheebwa, S.; Gurkan, U.A.; Samia, A.C.S.; Karayilan, M. Thermoresponsive Polymers with LCST Transition: Synthesis, Characterization, and Their Impact on Biomedical Frontiers. *RSC Appl. Polym.* **2023**, *1*, 158–189. [CrossRef]
159. Sharker, K.K.; Shigeta, Y.; Ozoe, S.; Damsongsang, P.; Hoven, V.P.; Yusa, S. Upper Critical Solution Temperature Behavior of pH-Responsive Amphoteric Statistical Copolymers in Aqueous Solutions. *ACS Omega* **2021**, *6*, 9153–9163. [CrossRef] [PubMed]
160. Kotsuchibashi, Y. Recent Advances in Multi-Temperature-Responsive Polymeric Materials. *Polym. J.* **2020**, *52*, 681–689. [CrossRef]
161. Halligan, E.; Zhuo, S.; Colbert, D.M.; Alsaadi, M.; Tie, B.S.H.; Bezerra, G.S.N.; Keane, G.; Geever, L.M. Modulation of the Lower Critical Solution Temperature of Thermoresponsive Poly(N-Vinylcaprolactam) Utilizing Hydrophilic and Hydrophobic Monomers. *Polymers* **2023**, *15*, 1595. [CrossRef] [PubMed]
162. Xiang, N.; Lin, Y.; Qin, Z.; Su, T.; Xie, X.; Ji, H. Temperature-Responsive Gating Chitosan-Based Microcapsules for Controlled Release of Urea Fertilizers. *Carbohydr. Polym.* **2025**, *348*, 122929. [CrossRef] [PubMed]
163. Liu, Z.; Guo, Y.; Inomata, K. Lower Critical Solution Temperature Behavior of Poly(2-Chloroethyl Vinyl Ether-Alt-Maleic Anhydride) in Organic Media. *Polym. J.* **2010**, *42*, 901–904. [CrossRef]
164. Concilio, M.; Beyer, V.P.; Becer, C.R. Thermoresponsive Polymers in Non-Aqueous Solutions. *Polym. Chem.* **2022**, *13*, 6423–6474. [CrossRef]
165. Korpanty, J.; Wang, C.; Gianneschi, N.C. Upper Critical Solution Temperature Polymer Assemblies via Variable Temperature Liquid Phase Transmission Electron Microscopy and Liquid Resonant Soft X-Ray Scattering. *Nat. Commun.* **2023**, *14*, 3441. [CrossRef]
166. Le, M.; Huang, W.; Chen, K.-F.; Lin, C.; Cai, L.; Zhang, H.; Jia, Y.-G. Upper Critical Solution Temperature Polymeric Drug Carriers. *Chem. Eng. J.* **2022**, *432*, 134354. [CrossRef]

167. Stetsyshyn, Y.; Raczkowska, J.; Harhay, K.; Gajos, K.; Melnyk, Y.; Dąbczyński, P.; Shevtsova, T.; Budkowski, A. Temperature-Responsive and Multi-Responsive Grafted Polymer Brushes with Transitions Based on Critical Solution Temperature: Synthesis, Properties, and Applications. *Colloid Polym. Sci.* **2020**, *299*, 363–383. [CrossRef]
168. Yang, L.; Yuan, Q.-Y.; Li, T.-T.; Lou, C.-W.; Hung, C.; Lin, J.-H. Recent Developments and Applications of pH-Responsive Polymers. *Text. Res. J.* **2025**, *95*, 2248–2272. [CrossRef]
169. AlSawaftah, N.M.; Awad, N.S.; Pitt, W.G.; Husseini, G.A. pH-Responsive Nanocarriers in Cancer Therapy. *Polymers* **2022**, *14*, 936. [CrossRef]
170. Yu, Y.; Zhao, Y.; Zou, Y.; Lu, C.; Li, N.; Shi, Z.; Li, X.; Lai, X. Ultra-Sensitive pH Responsive Hydrogels with Injectable and Self-Healing Performance for Controlled Drug Delivery. *Int. J. Pharm. X* **2025**, *9*, 100334. [CrossRef]
171. Twal, S.; Jaber, N.; Al-Remawi, M.; Hamad, I.; Al-Akayleh, F.; Alshaer, W. Dual Stimuli-Responsive Polymeric Nanoparticles Combining Soluplus and Chitosan for Enhanced Breast Cancer Targeting. *RSC Adv.* **2024**, *14*, 3070–3084. [CrossRef]
172. Kim, T.M.; Subba, S.H.; Hwang, Y.K.; Kim, S.G.; Park, J.; Jin, E.-J.; Park, S.Y. Electrical and Fluorescence in Situ Monitoring of Tumor Microenvironment-Based pH-Responsive Polymer Dot Coated Surface. *Talanta* **2025**, *281*, 126840. [CrossRef] [PubMed]
173. Chu, S.; Shi, X.; Tian, Y.; Gao, F. pH-Responsive Polymer Nanomaterials for Tumor Therapy. *Front. Oncol.* **2022**, *12*, 855019. [CrossRef]
174. Iftikhar, I.; Barkat, K.; Badshah, S.F.; Ashraf, M.U.; Mehmood, Y.; Anjum, I.; Shazly, G.A.; Metouekel, A.; Younous, Y.A.; Bourhia, M. Formulation of pH Responsive Polymeric Hydrogels for Prolonged Delivery of Famciclovir with Biosafety Evaluation. *Sci. Rep.* **2025**, *15*, 18686. [CrossRef] [PubMed]
175. Liu, M.; Huang, T.; Liu, Y.; Chen, L.; Liao, S.; Gong, X.; Bello, M.G.; Zhu, W.; Huang, S.; Zhang, X. Loading Curcumin on Hyperbranched Polymers Functionalized Zein via the Phenol-Yne Click Reaction as pH-Responsive Drug Delivery System for Chemotherapy and Photodynamic Therapy. *Int. J. Biol. Macromol.* **2025**, *293*, 139750. [CrossRef] [PubMed]
176. Liu, X.; Hao, P.; Wang, W.; Guo, G.; Wu, C.; Ge, R. Development and Characterization of a Poly(Amino Acid)-Based pH-Responsive Dual-Mode Antibacterial Nanoparticles Dental Restorative Resin. *J. Appl. Polym. Sci.* **2025**, *142*, e57570. [CrossRef]
177. Jiao, X.; Chong, X.; Du, H.; Yang, M.; Zhu, Z.; Ma, Z.; Wen, Y. Development of pH and Enzyme Dual Responsive Chitosan/Polyaspartic Acid Nanoparticle-Embedded Nanofibers for Fruit Preservation. *Int. J. Biol. Macromol.* **2025**, *297*, 139903. [CrossRef]
178. Shin, S.; Kim, S.; Hong, S.; Kim, N.; Kang, J.; Jeong, J. Tuning the Swelling Behavior of Superabsorbent Hydrogels with a Branched Poly(Aspartic Acid) Crosslinker. *Gels* **2025**, *11*, 161. [CrossRef]
179. Huo, M.; Yuan, J.; Tao, L.; Wei, Y. Redox-Responsive Polymers for Drug Delivery: From Molecular Design to Applications. *Polym. Chem.* **2014**, *5*, 1519–1528. [CrossRef]
180. Xu, L.; Cao, Y.; Xu, Y.; Li, R.; Xu, X. Redox-Responsive Polymeric Nanoparticle for Nucleic Acid Delivery and Cancer Therapy: Progress, Opportunities, and Challenges. *Macromol. Biosci.* **2024**, *24*, 2300238. [CrossRef] [PubMed]
181. Kilic Boz, R.; Aydin, D.; Kocak, S.; Golba, B.; Sanyal, R.; Sanyal, A. Redox-Responsive Hydrogels for Tunable and "On-Demand" Release of Biomacromolecules. *Bioconjug. Chem.* **2022**, *33*, 839–847. [CrossRef]
182. Dabas, R.; Kamaly, N. Redox-Responsive Nanogels for Precision Protein Delivery. *Eur. Polym. J.* **2024**, *215*, 113183. [CrossRef]
183. Zhang, Z.; Xu, X.; Du, J.; Chen, X.; Xue, Y.; Zhang, J.; Yang, X.; Chen, X.; Xie, J.; Ju, S. Redox-Responsive Polymer Micelles Co-Encapsulating Immune Checkpoint Inhibitors and Chemotherapeutic Agents for Glioblastoma Therapy. *Nat. Commun.* **2024**, *15*, 1118. [CrossRef] [PubMed]
184. Tao, Y.; Dai, C.; Xie, Z.; You, X.; Li, K.; Wu, J.; Huang, H. Redox Responsive Polymeric Nanoparticles Enhance the Efficacy of Cyclin Dependent Kinase 7 Inhibitor for Enhanced Treatment of Prostate Cancer. *Chin. Chem. Lett.* **2024**, *35*, 109170. [CrossRef]
185. Cherri, M.; Stergiou, P.S.; Ahmadian, Z.; Povolotsky, T.L.; Thongrom, B.; Fan, X.; Mohammadifar, E.; Haag, R. Redox-Responsive Hydrogels Loaded with an Antibacterial Peptide as Controlled Drug Delivery for Healing Infectious Wounds. *Adv. Healthc. Mater.* **2024**, *13*, 2401289. [CrossRef]
186. Meng, X.; Shen, Y.; Zhao, H.; Lu, X.; Wang, Z.; Zhao, Y. Redox-Manipulating Nanocarriers for Anticancer Drug Delivery: A Systematic Review. *J. Nanobiotechnol.* **2024**, *22*, 587. [CrossRef]
187. Kaur, R.; Pathak, L.; Vyas, P. Biobased Polymers of Plant and Microbial Origin and Their Applications—A Review. *Biotechnol. Sustain. Mater.* **2024**, *1*, 13. [CrossRef]
188. Serra Sampaio, M.; Wojcieszak, R.; Itabaiana Junior, I. Synthesis of Bio-Based Polymers and Adjuvants through Biomass Valorization: Challenges and Opportunities. *ChemCatChem* **2024**, *16*, e202301126. [CrossRef]
189. Adetunji, A.I.; Erasmus, M. Green Synthesis of Bioplastics from Microalgae: A State-of-the-Art Review. *Polymers* **2024**, *16*, 1322. [CrossRef] [PubMed]
190. Beena Unni, A.; Muringayil Joseph, T. Enhancing Polymer Sustainability: Eco-Conscious Strategies. *Polymers* **2024**, *16*, 1769. [CrossRef]

191. Anastas, P.; Eghbali, N. Green Chemistry: Principles and Practice. *Chem. Soc. Rev.* **2009**, *39*, 301–312. [CrossRef]
192. Stavila, E.; Yuliati, F.; Adharis, A.; Arya Laksmono, J.; Iqbal, M. Recent Advances in Synthesis of Polymers Based on Palm Oil and Its Fatty Acids. *RSC Adv.* **2023**, *13*, 14747–14775. [CrossRef]
193. Yang, W.; Qiu, S.; Zhang, J.; Cheng, Z.; Song, L.; Hu, Y. Innovative Design and Green Synthesis of Bio-Based Non-Isocyanate Polyurethanes: Efficient Combination of Cardanol and Carbon Dioxide with High Fire Safety and Robust Adhesion. *Chem. Eng. J.* **2024**, *482*, 148846. [CrossRef]
194. Ma, C.; Zhang, Y.; Zhao, Z.; Wang, J.; Chen, Y.; Qian, L.; Fang, Z.; Song, R.; Song, P. Green Synthesis of Bio-Based Flame Retardant/Natural Rubber Inorganic-Organic Hybrid and Its Flame Retarding and Toughening Effect for Polylactic Acid. *Int. J. Biol. Macromol.* **2024**, *256*, 128378. [CrossRef]
195. Post, C.; Maniar, D.; Jongstra, J.A.; Parisi, D.; Voet, V.S.D.; Folkersma, R.; Loos, K. Enzymatic Bulk Synthesis, Characterization, Rheology, and Biodegradability of Biobased 2,5-Bis(Hydroxymethyl)Furan Polyesters. *Green Chem.* **2024**, *26*, 8744–8757. [CrossRef]
196. Almustafa, W.; Grishchuk, S.; Redel, M.; Schubert, D.W.; Grun, G. Solvent-Free Processing of i-P3HB Blends: Enhancing Processability and Mechanical Properties for Sustainable Applications. *Polymers* **2025**, *17*, 2231. [CrossRef]
197. Ramezani, M.; Getya, D.; Gitsov, I.; Browning Monroe, M.B. Solvent-Free Synthesis of Biostable Segmented Polyurethane Shape Memory Polymers for Biomedical Applications. *J. Mater. Chem. B* **2024**, *12*, 1217–1231. [CrossRef]
198. Pellis, A.; Weinberger, S.; Gigli, M.; Guebitz, G.M.; Farmer, T.J. Enzymatic Synthesis of Biobased Polyesters Utilizing Aromatic Diols as the Rigid Component. *Eur. Polym. J.* **2020**, *130*, 109680. [CrossRef]
199. Herrlé, C.; Fadlallah, S.; Toumieux, S.; Wadccccccccouachi, A.; Allais, F. Sustainable Mechanosynthesis of Diamide Tetraols Monomers and Their Enzymatic Polymerization. *Green Chem.* **2024**, *26*, 1462–1470. [CrossRef]
200. Kimura, H.; Ogura, Y. Biodegradable Polymers for Ocular Drug Delivery. *Ophthalmologica* **2001**, *215*, 143–155. [CrossRef]
201. Ha, C.-S.; Gardella, J.A. Surface Chemistry of Biodegradable Polymers for Drug Delivery Systems. *Chem. Rev.* **2005**, *105*, 4205–4232. [CrossRef] [PubMed]
202. Wu, H.-Q.; Wang, C.-C. Biodegradable Smart Nanogels: A New Platform for Targeting Drug Delivery and Biomedical Diagnostics. *Langmuir* **2016**, *32*, 6211–6225. [CrossRef] [PubMed]
203. Eckmann, D.M.; Composto, R.J.; Tsourkas, A.; Muzykantov, V.R. Nanogel Carrier Design for Targeted Drug Delivery. *J. Mater. Chem. B* **2014**, *2*, 8085–8097. [CrossRef]
204. Kapoor, D.N.; Bhatia, A.; Kaur, R.; Sharma, R.; Kaur, G.; Dhawan, S. PLGA: A Unique Polymer for Drug Delivery. *Ther. Deliv.* **2015**, *6*, 41–58. [CrossRef]
205. Yang, J.; Zeng, H.; Luo, Y.; Chen, Y.; Wang, M.; Wu, C.; Hu, P. Recent Applications of PLGA in Drug Delivery Systems. *Polymers* **2024**, *16*, 2606. [CrossRef]
206. Wu, L.; Zhang, J.; Jing, D.; Ding, J. "Wet-state" Mechanical Properties of Three-dimensional Polyester Porous Scaffolds. *J. Biomed. Mater. Res. A* **2006**, *76A*, 264–271. [CrossRef]
207. Giram, P.S.; Wang, J.T.-W.; Walters, A.A.; Rade, P.P.; Akhtar, M.; Han, S.; Faruqu, F.N.; Abdel-Bar, H.M.; Garnaik, B.; Al-Jamal, K.T. Green Synthesis of Methoxy-Poly(Ethylene Glycol)- *Block* -Poly(L -Lactide- *Co* -Glycolide) Copolymer Using Zinc Proline as a Biocompatible Initiator for Irinotecan Delivery to Colon Cancer in Vivo. *Biomater. Sci.* **2021**, *9*, 795–806. [CrossRef] [PubMed]
208. Li, J.; Kataoka, K. Chemo-Physical Strategies to Advance the in Vivo Functionality of Targeted Nanomedicine: The Next Generation. *J. Am. Chem. Soc.* **2021**, *143*, 538–559. [CrossRef]
209. Wen, P.; Ke, W.; Dirisala, A.; Toh, K.; Tanaka, M.; Li, J. Stealth and Pseudo-Stealth Nanocarriers. *Adv. Drug Deliv. Rev.* **2023**, *198*, 114895. [CrossRef] [PubMed]
210. Doppalapudi, S.; Jain, A.; Domb, A.J.; Khan, W. Biodegradable Polymers for Targeted Delivery of Anti-Cancer Drugs. *Expert Opin. Drug Deliv.* **2016**, *13*, 891–909. [CrossRef] [PubMed]
211. Nicolas, J.; Mura, S.; Brambilla, D.; Mackiewicz, N.; Couvreur, P. Design, Functionalization Strategies and Biomedical Applications of Targeted Biodegradable/Biocompatible Polymer-Based Nanocarriers for Drug Delivery. *Chem. Soc. Rev.* **2013**, *42*, 1147–1235. [CrossRef]
212. Pan, J.; Liu, Y.; Feng, S.-S. Multifunctional Nanoparticles of Biodegradable Copolymer Blend for Cancer Diagnosis and Treatment. *Nanomedicine* **2010**, *5*, 347–360. [CrossRef] [PubMed]
213. Calzoni, E.; Cesaretti, A.; Polchi, A.; Di Michele, A.; Tancini, B.; Emiliani, C. Biocompatible Polymer Nanoparticles for Drug Delivery Applications in Cancer and Neurodegenerative Disorder Therapies. *J. Funct. Biomater.* **2019**, *10*, 4. [CrossRef]
214. Sendil, D.; Bonney, I.M.; Carr, D.B.; Lipkowski, A.W.; Wise, D.L.; Hasirci, V. Antinociceptive Effects of Hydromorphone, Bupivacaine and Biphalin Released from PLGA Polymer after Intrathecal Implantation in Rats. *Biomaterials* **2003**, *24*, 1969–1976. [CrossRef]

215. Ozeki, T.; Kaneko, D.; Hashizawa, K.; Imai, Y.; Tagami, T.; Okada, H. Improvement of Survival in C6 Rat Glioma Model by a Sustained Drug Release from Localized PLGA Microspheres in a Thermoreversible Hydrogel. *Int. J. Pharm.* **2012**, *427*, 299–304. [CrossRef]
216. Ungaro, F.; d'Angelo, I.; Coletta, C.; d'Emmanuele Di Villa Bianca, R.; Sorrentino, R.; Perfetto, B.; Tufano, M.A.; Miro, A.; La Rotonda, M.I.; Quaglia, F. Dry Powders Based on PLGA Nanoparticles for Pulmonary Delivery of Antibiotics: Modulation of Encapsulation Efficiency, Release Rate and Lung Deposition Pattern by Hydrophilic Polymers. *J. Control. Release* **2012**, *157*, 149–159. [CrossRef]
217. Tahara, K.; Miyazaki, Y.; Kawashima, Y.; Kreuter, J.; Yamamoto, H. Brain Targeting with Surface-Modified Poly(d,l-Lactic-Co-Glycolic Acid) Nanoparticles Delivered via Carotid Artery Administration. *Eur. J. Pharm. Biopharm.* **2011**, *77*, 84–88. [CrossRef]
218. Lloyd, A.W. Interfacial Bioengineering to Enhance Surface Biocompatibility. *Med. Device Technol.* **2002**, *13*, 18–21.
219. Huang, S.; Chen, H.-J.; Deng, Y.-P.; You, X.; Fang, Q.; Lin, M. Preparation of Novel Stable Microbicidal Hydrogel Films as Potential Wound Dressing. *Polym. Degrad. Stab.* **2020**, *181*, 109349. [CrossRef]
220. Bačáková, L.; Novotná, K.; Pařízek, M. Polysaccharides as Cell Carriers for Tissue Engineering: The Use of Cellulose in Vascular Wall Reconstruction. *Physiol. Res.* **2014**, *63*, S29–S47. [CrossRef]
221. Song, Y.; Xu, L.; Xu, L.; Deng, L. Radiation Cross-Linked Gelatin/Sodium Alginate/Carboxymethylcellulose Sodium Hydrogel for the Application as Debridement Glue Paste. *Polym. Bull.* **2022**, *79*, 725–742. [CrossRef]
222. Oh, G.-W.; Kim, S.-C.; Kim, T.-H.; Jung, W.-K. Characterization of an Oxidized Alginate-Gelatin Hydrogel Incorporating a COS-Salicylic Acid Conjugate for Wound Healing. *Carbohydr. Polym.* **2021**, *252*, 117145. [CrossRef]
223. Ozdil, D.; Aydin, H.M. Polymers for Medical and Tissue Engineering Applications: Polymers for Medical and Tissue Engineering Applications. *J. Chem. Technol. Biotechnol.* **2014**, *89*, 1793–1810. [CrossRef]
224. Liu, X.; Holzwarth, J.M.; Ma, P.X. Functionalized Synthetic Biodegradable Polymer Scaffolds for Tissue Engineering. *Macromol. Biosci.* **2012**, *12*, 911–919. [CrossRef]
225. Ma, P.X.; Zhang, R. Synthetic Nano-Scale Fibrous Extracellular Matrix. *J. Biomed. Mater. Res.* **1999**, *46*, 60–72. [CrossRef]
226. Schofer, M.D.; Fuchs-Winkelmann, S.; Gräbedünkel, C.; Wack, C.; Dersch, R.; Rudisile, M.; Wendorff, J.H.; Greiner, A.; Paletta, J.R.J.; Boudriot, U. Influence of Poly(L-Lactic Acid) Nanofibers and BMP-2–Containing Poly(L-Lactic Acid) Nanofibers on Growth and Osteogenic Differentiation of Human Mesenchymal Stem Cells. *Sci. World J.* **2008**, *8*, 1269–1279. [CrossRef] [PubMed]
227. Chang, P.; Liu, B.; Liu, C.; Chou, H.; Ho, M.; Liu, H.; Wang, D.; Hou, L. Bone Tissue Engineering with Novel rhBMP2-PLLA Composite Scaffolds. *J. Biomed. Mater. Res. A* **2007**, *81A*, 771–780. [CrossRef]
228. Ma, Z.; Wang, Q.; Xie, W.; Ye, W.; Zhong, L.; Huge, J.; Wang, Y. Performance of 3D Printed PCL/PLGA/HA Biological Bone Tissue Engineering Scaffold. *Polym. Compos.* **2021**, *42*, 3593–3602. [CrossRef]
229. Lin, C.-C.; Fu, S.-J.; Lin, Y.-C.; Yang, I.-K.; Gu, Y. Chitosan-Coated Electrospun PLA Fibers for Rapid Mineralization of Calcium Phosphate. *Int. J. Biol. Macromol.* **2014**, *68*, 39–47. [CrossRef] [PubMed]
230. Fujita, M.; Kinoshita, Y.; Sato, E.; Maeda, H.; Ozono, S.; Negishi, H.; Kawase, T.; Hiraoka, Y.; Takamoto, T.; Tabata, Y.; et al. Proliferation and Differentiation of Rat Bone Marrow Stromal Cells on Poly(Glycolic Acid)–Collagen Sponge. *Tissue Eng.* **2005**, *11*, 1346–1355. [CrossRef] [PubMed]
231. Jayabalan, M.; Shalumon, K.T.; Mitha, M.K.; Ganesan, K.; Epple, M. Effect of Hydroxyapatite on the Biodegradation and Biomechanical Stability of Polyester Nanocomposites for Orthopaedic Applications. *Acta Biomater.* **2010**, *6*, 763–775. [CrossRef] [PubMed]
232. Zamora, I.; Alfonso Morales, G.; Castro, J.I.; Ruiz Rojas, L.M.; Valencia-Llano, C.H.; Mina Hernandez, J.H.; Valencia Zapata, M.E.; Grande-Tovar, C.D. Chitosan (CS)/Hydroxyapatite (HA)/Tricalcium Phosphate (β-TCP)-Based Composites as a Potential Material for Pulp Tissue Regeneration. *Polymers* **2023**, *15*, 3213. [CrossRef]
233. Wang, Z.; Wang, Y.; Yan, J.; Zhang, K.; Lin, F.; Xiang, L.; Deng, L.; Guan, Z.; Cui, W.; Zhang, H. Pharmaceutical Electrospinning and 3D Printing Scaffold Design for Bone Regeneration. *Adv. Drug Deliv. Rev.* **2021**, *174*, 504–534. [CrossRef]
234. Liu, P.S. Mechanical Relation for Porous Metal Foams under Complex Loads of Triaxial Tension and Compression. *Mater. Des.* **2010**, *31*, 2264–2269. [CrossRef]
235. Jiang, N.; Qi, B.; Fan, X.; Yao, L.; Wang, Y.; Zhao, Z.; Xu, Y.; Razali, M.H. Fabrication of Biocompatible and Biodegradable Polyvinyl Alcohol/Sodium Alginate Blend Polymers Incorporating Ca^{2+} Doped TiO^2 Nanocomposite 3D Scaffold for Biomedical Applications. *J. Saudi Chem. Soc.* **2023**, *27*, 101758. [CrossRef]
236. Sadowska, J.M.; Power, R.N.; Genoud, K.J.; Matheson, A.; González-Vázquez, A.; Costard, L.; Eichholz, K.; Pitacco, P.; Hallegouet, T.; Chen, G.; et al. A Multifunctional Scaffold for Bone Infection Treatment by Delivery of microRNA Therapeutics Combined with Antimicrobial Nanoparticles. *Adv. Mater.* **2024**, *36*, 2307639. [CrossRef]
237. Müller, W.E.; Neufurth, M.; Wang, S.; Tolba, E.; Schröder, H.C.; Wang, X. Morphogenetically Active Scaffold for Osteochondral Repair (Polyphosphate/Alginate/N,O-Carboxymethyl Chitosan). *Eur. Cell Mater.* **2016**, *31*, 174–190. [CrossRef]

238. Mahapatra, C.; Jin, G.-Z.; Kim, H.-W. Alginate-Hyaluronic Acid-Collagen Composite Hydrogel Favorable for the Culture of Chondrocytes and Their Phenotype Maintenance. *Tissue Eng. Regen. Med.* **2016**, *13*, 538–546. [CrossRef]
239. González-González, A.M.; Cruz, R.; Rosales-Ibáñez, R.; Hernández-Sánchez, F.; Carrillo-Escalante, H.J.; Rodríguez-Martínez, J.J.; Velasquillo, C.; Talamás-Lara, D.; Ludert, J.E. In Vitro and In Vivo Evaluation of a Polycaprolactone (PCL)/Polylactic-Co-Glycolic Acid (PLGA) (80:20) Scaffold for Improved Treatment of Chondral (Cartilage) Injuries. *Polymers* **2023**, *15*, 2324. [CrossRef] [PubMed]
240. Patrascu, J.M.; Krüger, J.P.; Böss, H.G.; Ketzmar, A.K.; Freymann, U.; Sittinger, M.; Notter, M.; Endres, M.; Kaps, C. Polyglycolic Acid-Hyaluronan Scaffolds Loaded with Bone Marrow-Derived Mesenchymal Stem Cells Show Chondrogenic Differentiation in Vitro and Cartilage Repair in the Rabbit Model. *J. Biomed. Mater. Res. B Appl. Biomater.* **2013**, *101*, 1310–1320. [CrossRef] [PubMed]
241. McCullen, S.D.; Autefage, H.; Callanan, A.; Gentleman, E.; Stevens, M.M. Anisotropic Fibrous Scaffolds for Articular Cartilage Regeneration. *Tissue Eng. Part A* **2012**, *18*, 2073–2083. [CrossRef]
242. Pulat, G.; Gökmen, O.; Özcan, Ş.; Karaman, O. Collagen Binding and Mimetic Peptide-Functionalized Self-Assembled Peptide Hydrogel Enhance Chondrogenic Differentiation of Human Mesenchymal Stem Cells. *J. Biomed. Mater. Res. A* **2025**, *113*, e37786. [CrossRef]
243. Biomaterials and Neural Regeneration: Neural Regeneration Research. Available online: https://journals.lww.com/nrronline/fulltext/2020/15070/biomaterials_and_neural_regeneration.8.aspx (accessed on 25 September 2025).
244. Durgam, H.; Sapp, S.; Deister, C.; Khaing, Z.; Chang, E.; Luebben, S.; Schmidt, C.E. Novel Degradable Co-Polymers of Polypyrrole Support Cell Proliferation and Enhance Neurite Out-Growth with Electrical Stimulation. *J. Biomater. Sci. Polym. Ed.* **2010**, *21*, 1265–1282. [CrossRef]
245. Lee, J.Y.; Bashur, C.A.; Goldstein, A.S.; Schmidt, C.E. Polypyrrole-Coated Electrospun PLGA Nanofibers for Neural Tissue Applications. *Biomaterials* **2009**, *30*, 4325–4335. [CrossRef]
246. Tarus, D.; Hamard, L.; Caraguel, F.; Wion, D.; Szarpak-Jankowska, A.; Van Der Sanden, B.; Auzély-Velty, R. Design of Hyaluronic Acid Hydrogels to Promote Neurite Outgrowth in Three Dimensions. *ACS Appl. Mater. Interfaces* **2016**, *8*, 25051–25059. [CrossRef]
247. Pinho, T.S.; Cunha, C.B.; Lanceros-Méndez, S.; Salgado, A.J. Electroactive Smart Materials for Neural Tissue Regeneration. *ACS Appl. Bio Mater.* **2021**, *4*, 6604–6618. [CrossRef] [PubMed]
248. Wang, Y.; Zhao, Y.; Sun, C.; Hu, W.; Zhao, J.; Li, G.; Zhang, L.; Liu, M.; Liu, Y.; Ding, F.; et al. Chitosan Degradation Products Promote Nerve Regeneration by Stimulating Schwann Cell Proliferation via miR-27a/FOXO1 Axis. *Mol. Neurobiol.* **2016**, *53*, 28–39. [CrossRef]
249. Jiang, M.; Cheng, Q.; Su, W.; Wang, C.; Yang, Y.; Cao, Z.; Ding, F. The Beneficial Effect of Chitooligosaccharides on Cell Behavior and Function of Primary Schwann Cells Is Accompanied by Up-Regulation of Adhesion Proteins and Neurotrophins. *Neurochem. Res.* **2014**, *39*, 2047–2057. [CrossRef]
250. Jin, J.; Ji, Z.; Xu, M.; Liu, C.; Ye, X.; Zhang, W.; Li, S.; Wang, D.; Zhang, W.; Chen, J.; et al. Microspheres of Carboxymethyl Chitosan, Sodium Alginate, and Collagen as a Hemostatic Agent in Vivo. *ACS Biomater. Sci. Eng.* **2018**, *4*, 2541–2551. [CrossRef]
251. Bhattarai, S.R.; Bhattarai, N.; Viswanathamurthi, P.; Yi, H.K.; Hwang, P.H.; Kim, H.Y. Hydrophilic Nanofibrous Structure of Polylactide; Fabrication and Cell Affinity. *J. Biomed. Mater. Res. A* **2006**, *78*, 247–257. [CrossRef]
252. Sharifi, F.; Irani, S.; Zandi, M.; Soleimani, M.; Atyabi, S.M. Comparative of Fibroblast and Osteoblast Cells Adhesion on Surface Modified Nanofibrous Substrates Based on Polycaprolactone. *Prog. Biomater.* **2016**, *5*, 213–222. [CrossRef]
253. Zhou, Z.; Chen, J.; Peng, C.; Huang, T.; Zhou, H.; Ou, B.; Chen, J.; Liu, Q.; He, S.; Cao, D.; et al. Fabrication and Physical Properties of Gelatin/Sodium Alginate/Hyaluronic Acid Composite Wound Dressing Hydrogel. *J. Macromol. Sci. Part A* **2014**, *51*, 318–325. [CrossRef]
254. Haidari, H.; Vasilev, K.; Cowin, A.J.; Kopecki, Z. Bacteria-Activated Dual pH- and Temperature-Responsive Hydrogel for Targeted Elimination of Infection and Improved Wound Healing. *ACS Appl. Mater. Interfaces* **2022**, *14*, 51744–51762. [CrossRef] [PubMed]
255. Soletti, L.; Hong, Y.; Guan, J.; Stankus, J.J.; El-Kurdi, M.S.; Wagner, W.R.; Vorp, D.A. A Bilayered Elastomeric Scaffold for Tissue Engineering of Small Diameter Vascular Grafts. *Acta Biomater.* **2010**, *6*, 110–122. [CrossRef]
256. Chen, X.; Wang, J.; An, Q.; Li, D.; Liu, P.; Zhu, W.; Mo, X. Electrospun Poly(l-Lactic Acid-Co-ε-Caprolactone) Fibers Loaded with Heparin and Vascular Endothelial Growth Factor to Improve Blood Compatibility and Endothelial Progenitor Cell Proliferation. *Colloids Surf. B Biointerfaces* **2015**, *128*, 106–114. [CrossRef]
257. Radisic, M. Biomaterials for Cardiac Tissue Engineering. *Biomed. Mater.* **2015**, *10*, 030301. [CrossRef] [PubMed]
258. Mihic, A.; Cui, Z.; Wu, J.; Vlacic, G.; Miyagi, Y.; Li, S.-H.; Lu, S.; Sung, H.-W.; Weisel, R.D.; Li, R.-K. A Conductive Polymer Hydrogel Supports Cell Electrical Signaling and Improves Cardiac Function After Implantation into Myocardial Infarct. *Circulation* **2015**, *132*, 772–784. [CrossRef]
259. Navaei, A.; Moore, N.; Sullivan, R.; Truong, D.; Migrino, R.; Nikkhah, M. Electrically Conductive Hydrogel-Based Micro-Topographies for the Development of Organized Cardiac Tissues. *RSC Adv.* **2017**, *7*, 3302–3312. [CrossRef]

260. Xiao, R.; Huang, W.M. Heating/Solvent Responsive Shape-Memory Polymers for Implant Biomedical Devices in Minimally Invasive Surgery: Current Status and Challenge. *Macromol. Biosci.* **2020**, *20*, 2000108. [CrossRef]
261. Sivaraman, S.; Amoroso, N.; Gu, X.; Purves, J.T.; Hughes, F.M.; Wagner, W.R.; Nagatomi, J. Evaluation of Poly (Carbonate-Urethane) Urea (PCUU) Scaffolds for Urinary Bladder Tissue Engineering. *Ann. Biomed. Eng.* **2019**, *47*, 891–901. [CrossRef] [PubMed]
262. Liang, S.L.; Cook, W.D.; Thouas, G.A.; Chen, Q.Z. The Mechanical Characteristics and in Vitro Biocompatibility of Poly(Glycerol Sebacate)-Bioglass Elastomeric Composites. *Biomaterials* **2010**, *31*, 8516–8529. [CrossRef]
263. Full, S.M.; Delman, C.; Gluck, J.M.; Abdmaulen, R.; Shemin, R.J.; Heydarkhan-Hagvall, S. Effect of Fiber Orientation of Collagen-Based Electrospun Meshes on Human Fibroblasts for Ligament Tissue Engineering Applications. *J. Biomed. Mater. Res. B Appl. Biomater.* **2014**, *103*, 39. [CrossRef]
264. Sensini, A.; Gualandi, C.; Focarete, M.L.; Belcari, J.; Zucchelli, A.; Boyle, L.; Reilly, G.C.; Kao, A.P.; Tozzi, G.; Cristofolini, L. Multiscale Hierarchical Bioresorbable Scaffolds for the Regeneration of Tendons and Ligaments. *Biofabrication* **2019**, *11*, 035026. [CrossRef]
265. Khosravimelal, S.; Mobaraki, M.; Eftekhari, S.; Ahearne, M.; Seifalian, A.M.; Gholipourmalekabadi, M. Hydrogels as Emerging Materials for Cornea Wound Healing. *Small* **2021**, *17*, 2006335. [CrossRef]
266. Ahadian, S.; Khademhosseini, A. Smart Scaffolds in Tissue Regeneration. *Regen. Biomater.* **2018**, *5*, 125–128. [CrossRef] [PubMed]
267. Municoy, S.; Álvarez Echazú, M.I.; Antezana, P.E.; Galdopórpora, J.M.; Olivetti, C.; Mebert, A.M.; Foglia, M.L.; Tuttolomondo, M.V.; Alvarez, G.S.; Hardy, J.G.; et al. Stimuli-Responsive Materials for Tissue Engineering and Drug Delivery. *Int. J. Mol. Sci.* **2020**, *21*, 4724. [CrossRef]
268. Pilgrim, T.; Muller, O.; Heg, D.; Roffi, M.; Kurz, D.J.; Moarof, I.; Weilenmann, D.; Kaiser, C.; Tapponnier, M.; Losdat, S.; et al. Biodegradable- Versus Durable-Polymer Drug-Eluting Stents for STEMI. *JACC Cardiovasc. Interv.* **2021**, *14*, 639–648. [CrossRef] [PubMed]
269. The Development of Polymeric Biomaterials Inspired by the Extracellular Matrix. Available online: https://www.tandfonline.com/doi/epdf/10.1080/09205063.2017.1297285?needAccess=true (accessed on 25 September 2025).
270. Patel, B.B.; Chakraborty, S. Biodegradable Polymers: Emerging Excipients for the Pharmaceutical and Medical Device Industries. *J. Excip. Food Chem.* **2013**, *4*, 126–157.
271. Adeosun, S.O.; Lawal, G.I.; Gbenebor, O.P. Characteristics of Biodegradable Implants. *J. Miner. Mater. Charact. Eng.* **2014**, *2*, 88–106. [CrossRef]
272. Charles, L.F.; Shaw, M.T.; Olson, J.R.; Wei, M. Fabrication and Mechanical Properties of PLLA/PCL/HA Composites via a Biomimetic, Dip Coating, and Hot Compression Procedure. *J. Mater. Sci. Mater. Med.* **2010**, *21*, 1845–1854. [CrossRef]
273. Russias, J.; Saiz, E.; Nalla, R.K.; Gryn, K.; Ritchie, R.O.; Tomsia, A.P. Fabrication and Mechanical Properties of PLA/HA Composites: A Study of in Vitro Degradation. *Mater. Sci. Eng. C Biomim. Supramol. Syst.* **2006**, *26*, 1289. [CrossRef]
274. Kumar, A.; Mir, M.; Aldulijan, I.; Mahajan, A.; Anwar, A.; Leon, C.H.; Terracciano, A.; Zhao, X.; Su, T.-L.; Kalyon, D.M.; et al. Load-Bearing Biodegradable PCL-PGA-Beta TCP Scaffolds for Bone Tissue Regeneration. *J. Biomed. Mater. Res. B Appl. Biomater.* **2021**, *109*, 193–200. [CrossRef]
275. da Silva, D.; Kaduri, M.; Poley, M.; Adir, O.; Krinsky, N.; Shainsky-Roitman, J.; Schroeder, A. Biocompatibility, Biodegradation and Excretion of Polylactic Acid (PLA) in Medical Implants and Theranostic Systems. *Chem. Eng. J.* **2018**, *340*, 9. [CrossRef]
276. Elmowafy, E.M.; Tiboni, M.; Soliman, M.E. Biocompatibility, Biodegradation and Biomedical Applications of Poly(Lactic Acid)/Poly(Lactic-Co-Glycolic Acid) Micro and Nanoparticles. *J. Pharm. Investig.* **2019**, *49*, 347–380. [CrossRef]
277. Pérez-Davila, S.; Garrido-Gulías, N.; González-Rodríguez, L.; López-Álvarez, M.; Serra, J.; López-Periago, J.E.; González, P. Physicochemical Properties of 3D-Printed Polylactic Acid/Hydroxyapatite Scaffolds. *Polymers* **2023**, *15*, 2849. [CrossRef] [PubMed]
278. Peng, W.; Zheng, W.; Shi, K.; Wang, W.; Shao, Y.; Zhang, D. An in Vivo Evaluation of PLLA/PLLA-gHA Nano-Composite for Internal Fixation of Mandibular Bone Fractures. *Biomed. Mater.* **2015**, *10*, 065007. [CrossRef]
279. Tang, Y.; Singh, J. Biodegradable and Biocompatible Thermosensitive Polymer Based Injectable Implant for Controlled Release of Protein. *Int. J. Pharm.* **2009**, *365*, 34–43. [CrossRef] [PubMed]
280. Koutserimpas, C.; Alpantaki, K.; Chatzinikolaidou, M.; Chlouverakis, G.; Dohm, M.; Hadjipavlou, A.G. The Effectiveness of Biodegradable Instrumentation in the Treatment of Spinal Fractures. *Injury* **2018**, *49*, 2111–2120. [CrossRef]
281. Kukk, A.; Nurmi, J.T. A Retrospective Follow-up of Ankle Fracture Patients Treated with a Biodegradable Plate and Screws. *Foot Ankle Surg.* **2009**, *15*, 192–197. [CrossRef]
282. Amini, A.R.; Wallace, J.S.; Nukavarapu, S.P. Short-Term and Long-Term Effects of Orthopedic Biodegradable Implants. *J. Long-Term Eff. Med. Implants* **2011**, *21*, 93. [CrossRef] [PubMed]

283. Grayson, A.C.R.; Voskerician, G.; Lynn, A.; Anderson, J.M.; Cima, M.J.; Langer, R. Differential Degradation Rates in Vivo and in Vitro of Biocompatible Poly(Lactic Acid) and Poly(Glycolic Acid) Homo- and Co-Polymers for a Polymeric Drug-Delivery Microchip. *J. Biomater. Sci. Polym. Ed.* **2004**, *15*, 1281–1304. [CrossRef] [PubMed]
284. Zhang, W.; Chen, L.; Chen, J.; Wang, L.; Gui, X.; Ran, J.; Xu, G.; Zhao, H.; Zeng, M.; Ji, J.; et al. *Silk Fibroin Biomaterial Shows Safe and Effective Wound Healing in Animal Models and a Randomized Controlled Clinical Trial*; Semantic Scholar: Seattle, WA, USA, 2017.
285. Gore, M. Evaluation of Safety and Efficacy of Barrier Foam Dressing in Patients with Exuding Wounds. *Biomed. J. Sci. Tech. Res.* **2021**, *33*, 26292–26297. [CrossRef]
286. Haik, J.; Ullman, Y.; Gur, E.; Ad-El, D.; Egozi, D.; Kruchevsky, D.; Zissman, S.; Biros, E.; Nir, R.; Kornhaber, R.; et al. Advances in the Use of Electrospun Nanofibrous Polymeric Matrix for Dermal Healing at the Donor Site after the Split-Thickness Skin Graft Excision: A Prospective, Randomized, Controlled, Open-Label, Multicenter Study. *J. Burn Care Res.* **2021**, *43*, 889–898. [CrossRef] [PubMed]
287. Jamlang, J.; Marañon, M.T.; Rigor, G.J.; Tumolva, T. Developing a Physically Cross-Linked Hydroxyethyl Cellulose Hydrogel for Wound Dressing Applications. *Mater. Sci. Forum* **2019**, *947*, 3–12. [CrossRef]
288. Abulayzied, D.; Alturki, A.; Alatawi, A.; Bousbih, R.; Alamlah, R.; Abomostafa, H.; El Komy, G.; Abdel Aziz Taha, M.; Youness, R.A. Production of Polyvinyl Alcohol/Natural Hydroxyapatite/Magnesia/Silicon Carbide Hybrid Composites for Use in Orthopedic Applications: Optical, Electrical, and Mechanical Propertie. *Egypt. J. Chem.* **2024**, *67*, 397–409. [CrossRef]
289. Hong, Y.; Huber, A.; Takanari, K.; Amoroso, N.J.; Hashizume, R.; Badylak, S.F.; Wagner, W.R. Mechanical Properties and in Vivo Behavior of a Biodegradable Synthetic Polymer Microfiber–Extracellular Matrix Hydrogel Biohybrid Scaffold. *Biomaterials* **2011**, *32*, 3387–3394. [CrossRef]
290. Tripathi, S.; Dixit, P. Comparative Evaluation of Efficacy of Cyanoacrylate and Suture Material in The Management of Operative Skin Wounds. *Asian J. Pharm. Clin. Res.* **2022**, *15*, 59–61. [CrossRef]
291. Acharjee, S.A.; Bharali, P.; Gogoi, B.; Sorhie, V.; Walling, B. Alemtoshi PHA-Based Bioplastic: A Potential Alternative to Address Microplastic Pollution. *Water Air Soil Pollut.* **2023**, *234*, 21. [CrossRef]
292. Kubowicz, S.; Booth, A.M. Biodegradability of Plastics: Challenges and Misconceptions. *Environ. Sci. Technol.* **2017**, *51*, 12058–12060. [CrossRef]
293. Cheng, J.; Gao, R.; Zhu, Y.; Lin, Q. Applications of Biodegradable Materials in Food Packaging: A Review. *Alex. Eng. J.* **2024**, *91*, 70–83. [CrossRef]
294. Gupta, R.; Guha, P.; Srivastav, P. Natural Polymers in Bio-Degradable/Edible Film: A Review on Environmental Concerns, Cold Plasma Technology and Nanotechnology Application on Food Packaging—A Recent Trends. *Food Chem. Adv.* **2022**, *1*, 100135. [CrossRef]
295. Łupina, K.; Kowalczyk, D.; Drozłowska, E. Polysaccharide/Gelatin Blend Films as Carriers of Ascorbyl Palmitate—A Comparative Study. *Food Chem.* **2020**, *333*, 127465. [CrossRef] [PubMed]
296. Mirza, Z.S.; Chatta, A.M.; Shafi, J.; Waheed, K.N.; Saleem, S.; Hanif, M.M. The Effect of Natural Edible Coatings on Chemical, Microbial, and Sensory Quality of Tilapia during Frozen Storage. *J. Food Qual. Hazards Control* **2023**, *10*, 163–174. [CrossRef]
297. Uzundağ, D.; Can, Ö.P.; Saraç, M.G. Extending the Shelf Life of Unsalted White Cheese Produced for Special Dietary Preferences: Role of Essential Oils and Coating. *Harran Tarım Gıda Bilim. Derg.* **2025**, *29*, 191–204. [CrossRef]
298. Esmaeili, M.; Pircheraghi, G.; Bagheri, R. Optimizing the Mechanical and Physical Properties of Thermoplastic Starch via Tuning the Molecular Microstructure through Co-plasticization by Sorbitol and Glycerol. *Polym. Int.* **2017**, *66*, 809–819. [CrossRef]
299. Stelescu, M.D.; Oprea, O.-C.; Sonmez, M.; Ficai, A.; Motelica, L.; Ficai, D.; Georgescu, M.; Gurau, D.F. Structural and Thermal Characterization of Some Thermoplastic Starch Mixtures. *Polysaccharides* **2024**, *5*, 504–522. [CrossRef]
300. González Carmona, E.; Schlapp-Hackl, I.; Jääskeläinen, S.; Järvinen, M.; Nieminen, K.; Sawada, D.; Hummel, M.; Sixta, H. Development of Cellulose Films by Means of the Ioncell® Technology, as an Alternative to Commercial Films. *Cellulose* **2023**, *30*, 11633–11648. [CrossRef]
301. Yang, Q.; Saito, T.; Isogai, A. Transparent, Flexible, and High-strength Regenerated Cellulose/Saponite Nanocomposite Films with High Gas Barrier Properties. *J. Appl. Polym. Sci.* **2013**, *130*, 3168–3174. [CrossRef]
302. Zhao, S.; Bian, Y.; Zhang, G.; Yang, G.; Hou, X.; Gui, J.; Mu, S.; Liu, S.; Fang, Y. Shelf-life Extension of Pacific White Shrimp (*Litopenaeus Vannamei*) Using Sodium Alginate/Chitosan Incorporated with Cell-free Supernatant of *Streptococcus Thermophilus* FUA 329 during Cold Storage. *J. Food Sci.* **2024**, *89*, 1976–1987. [CrossRef]
303. Putranti, L.N.; Nugraheni, P.S. Effect of Carboxymethyl Cellulose Addition on the Characteristic of Chitosan-Based Bioplastic. *IOP Conf. Ser. Earth Environ. Sci.* **2023**, *1289*, 012038. [CrossRef]
304. Raghav, P.T.; Narayanapurapu; de Bellevue, S.A. Effect of Composite Edible Coatings and Abiotic Stress on Post Harvest Quality of Fruits. Available online: https://www.semanticscholar.org/paper/EFFECT-OF-COMPOSITE-EDIBLE-COATINGS-AND-ABIOTIC-ON-Raghav-Narayanapurapu/5badccb98be6ef0c40ca4309c1d21df125943eeb (accessed on 25 September 2025).

305. Tullo, A. A Biodegradable Polymer Hits the Big Time. *CEN Glob. Enterp.* **2021**, *99*, 26–27. [CrossRef]
306. Aversa, C.; Barletta, M.; Cappiello, G.; Gisario, A. Compatibilization Strategies and Analysis of Morphological Features of Poly(Butylene Adipate-Co-Terephthalate) (PBAT)/Poly(Lactic Acid) PLA Blends: A State-of-Art Review. *Eur. Polym. J.* **2022**, *173*, 111304. [CrossRef]
307. Chen, H.; Chen, F.; Chen, H.; Liu, H.; Chen, L.; Yu, L. Thermal Degradation and Combustion Properties of Most Popular Synthetic Biodegradable Polymers. *Waste Manag. Res. J. Sustain. Circ. Econ.* **2023**, *41*, 431–441. [CrossRef]
308. Auras, R.; Singh, S.; Singh, J. Performance Evaluation of PLA against Existing PET and PS Containers. *J. Test. Eval.* **2006**, *34*, 530–536. [CrossRef]
309. Ali, N. Effect of Polyethylene Terphalet (PET) on Mechanical and Optical Properties of Polylactic Acid (PLA) for Packaging Application. Available online: https://www.semanticscholar.org/paper/Effect-of-Polyethylene-Terphalet-(PET)-On-and-of-Ali/ad324e13added4d76d366a9c134b9df5d1172f29 (accessed on 25 September 2025).
310. Qi, Y.; Zhai, H.; Sun, Y.; Xu, H.; Wu, S.; Chen, S. Electrospun Hybrid Nanofibrous Meshes with Adjustable Performance for Potential Use in Soft Tissue Engineering. *Text. Res. J.* **2021**, *92*, 1537–1549. [CrossRef]
311. Klabukov, I.; Tenchurin, T.; Shepelev, A.; Baranovskii, D.; Mamagulashvili, V.; Dyuzheva, T.; Krasilnikova, O.; Balyasin, M.; Lyundup, A.; Krasheninnikov, M.; et al. Biomechanical Behaviors and Degradation Properties of Multilayered Polymer Scaffolds: The Phase Space Method for Bile Duct Design and Bioengineering. *Biomedicines* **2023**, *11*, 745. [CrossRef]
312. Nagy, B.; Miskolczi, N.; Eller, Z. Evaluation of the Effect of Castor Oil-Based Experimental Additives on Pla/Starch Foils. *Hung. J. Ind. Chem.* **2023**, *51*, 35–41. [CrossRef]
313. Wang, M.; Li, Z.; Zhao, W.; Huang, Z.; Liu, H.; Ma, L.; Yang, L. Preparation and Properties of Poly (Butylene-adipate-co-terephthalate) /Thermoplastic Hydroxypropyl Starch Films. *Polym. Int.* **2024**, *73*, 761–769. [CrossRef]
314. Alothman, O.Y.; Shaikh, H.M.; Alshammari, B.A.; Jawaid, M. Structural, Morphological and Thermal Properties of Nano Filler Produced from Date Palm-Based Micro Fibers (*Phoenix dactylifera* L.). *J. Polym. Environ.* **2022**, *30*, 622–630. [CrossRef]
315. Moustafa, H.; Guizani, C.; Dufresne, A. Sustainable Biodegradable Coffee Grounds Filler and Its Effect on the Hydrophobicity, Mechanical and Thermal Properties of Biodegradable PBAT Composites. *J. Appl. Polym. Sci.* **2017**, *134*, app.44498. [CrossRef]
316. Khan, A.; Asiri, A.M.; Jawaid, M.; Saba, N. Inamuddin Effect of Cellulose Nano Fibers and Nano Clays on the Mechanical, Morphological, Thermal and Dynamic Mechanical Performance of Kenaf/Epoxy Composites. *Carbohydr. Polym.* **2020**, *239*, 116248. [CrossRef]
317. Mandal, A.; Chakrabarty, D. Studies on Mechanical, Thermal, and Barrier Properties of Carboxymethyl Cellulose Film Highly Filled with Nanocellulose. *J. Thermoplast. Compos. Mater.* **2019**, *32*, 995–1014. [CrossRef]
318. Ma, F.; Chen, S.; Liu, P.; Geng, F.; Li, W.; Liu, X.; He, D.; Pan, D. Improvement of β-TCP/PLLA Biodegradable Material by Surface Modification with Stearic Acid. *Mater. Sci. Eng. C* **2016**, *62*, 407–413. [CrossRef]
319. De La Rosa-Ramírez, H.; Aldas, M.; Ferri, J.M.; Pawlak, F.; López-Martínez, J.; Samper, M.D. Control of Biodegradability Under Composting Conditions and Physical Performance of Poly (Lactic Acid) Based Materials Modified with Phenolic-Free Rosin Resin. *J. Polym. Environ.* **2023**, *31*, 5462–5476. [CrossRef]
320. Samorì, P.; Kinloch, I.A.; Feng, X.; Palermo, V. Graphene-Based Nanocomposites for Structural and Functional Applications: Using 2-Dimensional Materials in a 3-Dimensional World. *2D Mater.* **2015**, *2*, 030205. [CrossRef]
321. Drozdov, A.; Christiansen, J.; Klitkou, R. Volume Growth and Viscoplasticity of Polymer/Clay Nanocomposites. Available online: https://www.semanticscholar.org/paper/Volume-growth-and-viscoplasticity-of-polymer-clay-Drozdov-Christiansen/04a32ceebb37d07312ef4221fb2d24dae53776ad (accessed on 25 September 2025).
322. Rezvani, M.B.; Atai, M.; Hamze, F.; Hajrezai, R. The Effect of Silica Nanoparticles on the Mechanical Properties of Fiber-Reinforced Composite Resins. *J. Dent. Res. Dent. Clin. Dent. Prospect.* **2016**, *10*, 112–117. [CrossRef] [PubMed]
323. El-Shafai, N.; El-Khouly, M.E.; El-Kemary, M.; Ramadan, M.; Eldesoukey, I.; Masoud, M. Graphene Oxide Decorated with Zinc Oxide Nanoflower, Silver and Titanium Dioxide Nanoparticles: Fabrication, Characterization, DNA Interaction, and Antibacterial Activity. *RSC Adv.* **2019**, *9*, 3704–3714. [CrossRef]
324. Mandal, D.; Mualchin, M. Effects of Essential Oils on Post Harvest Quality and Shelf Life of Mango (*Mangifera indica* L.). *Bangladesh J. Bot.* **2021**, *50*, 1143–1149. [CrossRef]
325. Branciari, R.; Galarini, R.; Trabalza-Marinucci, M.; Miraglia, D.; Roila, R.; Acuti, G.; Giusepponi, D.; Dal Bosco, A.; Ranucci, D. Effects of Olive Mill Vegetation Water Phenol Metabolites Transferred to Muscle through Animal Diet on Rabbit Meat Microbial Quality. *Sustainability* **2021**, *13*, 4522. [CrossRef]
326. Miraglia, D.; Castrica, M.; Esposto, S.; Roila, R.; Selvaggini, R.; Urbani, S.; Taticchi, A.; Sordini, B.; Veneziani, G.; Servili, M. Quality Evaluation of Shrimp (*Parapenaeus longirostris*) Treated with Phenolic Extract from Olive Vegetation Water during Shelf-Life, before and after Cooking. *Foods* **2021**, *10*, 2116. [CrossRef]

327. Martinelli, M.; Bruner, M. The Effect of Cinnamon Extract on the Prevention of Fruit Spoilage via Delay in Microbial Growth. *J. Stud. Res.* **2024**, *13*, 1–8. [CrossRef]
328. Fiorentini, C.; Leni, G.; De Apodaca, E.D.; Fernández-de-Castro, L.; Rocchetti, G.; Cortimiglia, C.; Spigno, G.; Bassani, A. Development of Coated PLA Films Containing a Commercial Olive Leaf Extract for the Food Packaging Sector. *Antioxidants* **2024**, *13*, 519. [CrossRef] [PubMed]
329. Grabska-Zielińska, S.; Gierszewska, M.; Olewnik-Kruszkowska, E.; Bouaziz, M. Polylactide Films with the Addition of Olive Leaf Extract—Physico-Chemical Characterization. *Materials* **2021**, *14*, 7623. [CrossRef] [PubMed]
330. Alizadeh-Sani, M.; Mohammadian, E.; Rhim, J.; Jafari, S. pH-Sensitive (Halochromic) Smart Packaging Films Based on Natural Food Colorants for the Monitoring of Food Quality and Safety. *Trends Food Sci. Technol.* **2020**, *105*, 93–144. [CrossRef]
331. Ma, L.; Long, T.; Yuan, S.; Qi, P.; Han, L.; Hao, J. A pH-Indicating Smart Tag Based on Porous Hydrogel as Food Freshness Sensors. *J. Colloid Interface Sci.* **2023**, *647*, 32–42. [CrossRef] [PubMed]
332. Zhao, L.; Liu, Y.; Zhao, L.; Wang, Y. Anthocyanin-Based pH-Sensitive Smart Packaging Films for Monitoring Food Freshness. *J. Agric. Food Res.* **2022**, *9*, 100340. [CrossRef]
333. Shah, A.A.; Hasan, F.; Hameed, A.; Ahmed, S. Degradation of Plastics: A Comprehensive Review. *Biotechnol. Adv.* **2008**, *26*, 246–265. [CrossRef] [PubMed]
334. Arora, A.; Padua, G.W. Review: Nanocomposites in Food Packaging. *J. Food Sci.* **2010**, *75*, R43–R49. [CrossRef]
335. Reichert, C.L.; Bugnicourt, E.; Coltelli, M.-B.; Cinelli, P.; Lazzeri, A.; Canesi, I.; Braca, F.; Martínez, B.M.; Alonso, R.; Agostinis, L.; et al. Bio-Based Packaging: Materials, Modifications, Industrial Applications and Sustainability. *Polymers* **2020**, *12*, 1558. [CrossRef]
336. Saharan, N.; Wadhwa, N. A Comprehensive Review of Biodegradable Polymers in Sustainable Packaging Applications. *Res. Rev. J. Food Sci. Technol.* **2024**, *13*, 28–37. [CrossRef]
337. Avella, M.; De Vlieger, J.J.; Errico, M.E.; Fischer, S.; Vacca, P.; Volpe, M.G. Biodegradable Starch/Clay Nanocomposite Films for Food Packaging Applications. *Food Chem.* **2005**, *93*, 467–474. [CrossRef]
338. Brodhagen, M.; Goldberger, J.R.; Hayes, D.G.; Inglis, D.A.; Marsh, T.L.; Miles, C. Considerations for Limiting Unintended Residual Plastic in Agricultural Soils. *Environ. Sci. Policy* **2017**, *69*, 81–84. [CrossRef]
339. Kasirajan, S.; Ngouajio, M. Polyethylene and Biodegradable Mulches for Agricultural Applications: A Review. *Agron. Sustain. Dev.* **2012**, *32*, 501–529. [CrossRef]
340. Torquebiau, E.; Rosenzweig, C.; Chatrchyan, A.M.; Andrieu, N.; Khosla, R. Identifying Climate-Smart Agriculture Research Needs. *Cah. Agric.* **2018**, *27*, 26001. [CrossRef]
341. Cirujeda, A.; Pueyo, J.; Moreno, M.M.; Moreno, C.; Villena, J.; López-Marín, J.; Romero-Muñoz, M.; Pardo, G. Weed Control in Perennial Crops Using Hydromulch Compositions Based on the Circular Economy: Field Trial Results. *J. Crop Health* **2024**, *76*, 1101–1116. [CrossRef]
342. Alptekin, H.; Gürbüz, R. The Effect of Organic Mulch Materials on Weed Control in Cucumber (*Cucumis sativus* L.) Cultivation. *J. Agric.* **2022**, *5*, 68–79. [CrossRef]
343. Li, Y.-C.; Li, H.-P.; Wang, Y.-X.; Sun, Y.-P.; Wang, K.-R.; Yang, Q.-X. Pollution Status and Control Countermeasures of Polyethylene Mulch Film Residue in Farmland Soils of Qingdao City, China. Available online: https://www.semanticscholar.org/paper/Pollution-Status-and-Control-Countermeasures-of-in-Yan-chao-Hai-ping/45db99d64c7d02aa82aff8a53abcdf2edcafa113 (accessed on 25 September 2025).
344. Vargha, V.; Rétháti, G.; Heffner, T.; Pogácsás, K.; Korecz, L.; László, Z.; Czinkota, I.; Tolner, L.; Kelemen, O. Behavior of Polyethylene Films in Soil. *Period. Polytech. Chem. Eng.* **2016**, *60*, 60–68. [CrossRef]
345. Ramos, L.; Berenstein, G.; Hughes, E.A.; Zalts, A.; Montserrat, J.M. Polyethylene Film Incorporation into the Horticultural Soil of Small Periurban Production Units in Argentina. *Sci. Total Environ.* **2015**, *523*, 74–81. [CrossRef]
346. Halley, P.; Rutgers, R.; Coombs, S.; Kettels, J.; Gralton, J.; Christie, G.; Jenkins, M.; Beh, H.; Griffin, K.; Jayasekara, R.; et al. Developing Biodegradable Mulch Films from Starch-Based Polymers. *Starch-Stärke* **2001**, *53*, 362. [CrossRef]
347. Barragán, D.H.; Pelacho, A.M.; Martin-Closas, L. Degradation of Agricultural Biodegradable Plastics in the Soil under Laboratory Conditions. *Soil Res.* **2016**, *54*, 216–224. [CrossRef]
348. Xu, D.; Cheng, Y.; He, S.; Leng, W.; Chen, Y.; Dai, J.; Sun, M.; Wu, Z.; Li, J. Biomass-Derived Transparent Bamboo Composite Films with Europium-Based Photoconversion for Energy-Efficient Smart Agriculture. *Energy Environ. Mater.* **2025**, e70125. [CrossRef]
349. Popović, S.; Hromiš, N.; Šuput, D.; Bulut, S.; Vitas, S.; Savić, M.; Lazić, V. Pumpkin Seed Oil Cake/Polyethylene Film as New Food Packaging Material, with Perspective for Packing under Modified Atmosphere. *Packag. Technol. Sci.* **2021**, *34*, 25–33. [CrossRef]
350. Titova, L.M.; Nugmanov, A. Study of the Properties of Biodegradable Mulching Coating Obtained from Waste Water Treatment Waste. *Oil Gas Technol. Environ. Saf.* **2025**, *2025*, 35–42. [CrossRef]

351. Sham, I.N.; Yap, C.K.; Nulit, R.; Peng, S.H.T.; Chai, E.W. Nutrient Leaching in Oil Palm Plantation: A Review on Special Reference to Fertilization Application. *Pak. J. Life Soc. Sci. PJLSS* **2024**, *22*, 855–877. [CrossRef]
352. Albano, J.; Merhaut, D.; Blythe, E.; Newman, J. Nutrient Release from Controlled-Release Fertilizers in a Neutral-pH Substrate in an Outdoor Environment: II. Leachate Calcium, Magnesium, Iron, Manganese, Zinc, Copper, and Molybdenum Concentrations. *Hortscience* **2006**, *41*, 1674–1682. [CrossRef]
353. Jin, S.; Wang, Y.; He, J.; Yang, Y.; Yu, X.; Yue, G. Preparation and Properties of a Degradable Interpenetrating Polymer Networks Based on Starch with Water Retention, Amelioration of Soil, and Slow Release of Nitrogen and Phosphorus Fertilizer. *J. Appl. Polym. Sci.* **2013**, *128*, 407–415. [CrossRef]
354. Parvathy, P.C.; Jyothi, A.N.; John, K.S.; Sreekumar, J. Cassava Starch Based Superabsorbent Polymer as Soil Conditioner: Impact on Soil Physico-Chemical and Biological Properties and Plant Growth. *CLEAN–Soil Air Water* **2014**, *42*, 1610–1617. [CrossRef]
355. Iqbal, D.N.; Tariq, Z.; Philips, B.; Sadiqa, A.; Ahmad, M.; Al-Ahmary, K.M.; Ali, I.; Ahmed, M. Nanocellulose/Wood Ash-Reinforced Starch–Chitosan Hydrogel Composites for Soil Conditioning and Their Impact on Pea Plant Growth. *RSC Adv.* **2024**, *14*, 8652–8664. [CrossRef]
356. Akhter, M.; Shah, G.A.; Niazi, M.B.K.; Mir, S.; Jahan, Z.; Rashid, M.I. Novel Water-soluble Polymer Coatings Control NPK Release Rate, Improve Soil Quality and Maize Productivity. *J. Appl. Polym. Sci.* **2021**, *138*, 51239. [CrossRef]
357. Nooeaid, P.; Chuysinuan, P.; Pitakdantham, W.; Aryuwananon, D.; Techasakul, S.; Dechtrirat, D. Eco-Friendly Polyvinyl Alcohol/Polylactic Acid Core/Shell Structured Fibers as Controlled-Release Fertilizers for Sustainable Agriculture. *J. Polym. Environ.* **2021**, *29*, 552–564. [CrossRef]
358. Qiao, D.; Li, J.; Zhang, S.; Yang, X. Controlled Release Fertilizer with Temperature-Responsive Behavior Coated Using Polyether Polyol (PPG)/Polycaprolactone (PCL) Blend-Based Polyurethane Performs Smart Nutrient Release. *Mater. Today Chem.* **2022**, *26*, 101249. [CrossRef]
359. Dhanalakshmi, M.; Meena, S.; Janaki, P.; Karthikeyan, S.; Nalina, L. Effect of Addition of Biopolymer Coated DAP on Phosphorus Release Kinetics over an Incubation Time. *Res. Crops* **2022**, *23*, 781–786. [CrossRef]
360. An, T.; Qin, Y.; Cheng, H.; Wu, J.; Su, W.; Meng, G.; Wei, H.; Sun, C.; Liu, Z.; Guo, X. TiO_2-WO_3 Activated Weathered Lignite Coating Phosphate Fertilizer to Improve Longitudinal Migration Efficiency. *J. Clean. Prod.* **2022**, *351*, 131549. [CrossRef]
361. Firmanda, A.; Fahma, F.; Syamsu, K.; Suryanegara, L.; Wood, K. Controlled/Slow-Release Fertilizer Based on Cellulose Composite and Its Impact on Sustainable Agriculture: Review. *Biofuels Bioprod. Biorefin.* **2022**, *16*, 1909–1930. [CrossRef]
362. Kontárová, S.; Přikryl, R.; Škarpa, P.; Kriška, T.; Antošovský, J.; Gregušková, Z.; Figalla, S.; Jašek, V.; Sedlmajer, M.; Menčík, P.; et al. Slow-Release Nitrogen Fertilizers with Biodegradable Poly(3-Hydroxybutyrate) Coating: Their Effect on the Growth of Maize and the Dynamics of N Release in Soil. *Polymers* **2022**, *14*, 4323. [CrossRef]
363. Murphy, S.V.; Atala, A. 3D Bioprinting of Tissues and Organs. *Nat. Biotechnol.* **2014**, *32*, 773–785. [CrossRef]
364. Li, B.; Zhang, M.; Lu, Q.; Zhang, B.; Miao, Z.; Li, L.; Zheng, T.; Liu, P. Application and Development of Modern 3D Printing Technology in the Field of Orthopedics. *BioMed Res. Int.* **2022**, *2022*, 8759060. [CrossRef]
365. Veeman, D.; Sai, M.S.; Sureshkumar, P.; Jagadeesha, T.; Natrayan, L.; Ravichandran, M.; Mammo, W.D. Additive Manufacturing of Biopolymers for Tissue Engineering and Regenerative Medicine: An Overview, Potential Applications, Advancements, and Trends. *Int. J. Polym. Sci.* **2021**, *2021*, 1–20. [CrossRef]
366. Palaniappan, M.; Tirlangi, S.; Mohamed, M.J.S.; Moorthy, R.M.S.; Valeti, S.V.; Boopathi, S. Fused Deposition Modelling of Polylactic Acid (PLA)-Based Polymer Composites: A Case Study. In *Advances in Chemical and Materials Engineering*; Keshavamurthy, R., Tambrallimath, V., Davim, J.P., Eds.; IGI Global: Hershey, PA, USA, 2023; pp. 66–85, ISBN 978-1-6684-6009-2.
367. Raveverma, P.; Ibrahim, M.; Sa'ude, N.; Yarwindran, M. Mechanical Behaviour and Compatibility Analysis of Thermoplastic Polyurethane/ Polycaprolactone-Based New Fused Deposition Modelling Filament Composite. *J. Mech. Eng.* **2018**, *SI 5*, 116–128.
368. Banothu, D.; Kumar, P.; Ali, S.G.M.; Reddy, R.; Gobinath, R.; Dhanapalan, S. Design, Fabrication, and in Vitro Evaluation of a 3D Printed, Bio-Absorbable PLA Tibia Bone Implant with a Novel Lattice Structure. *Biomed. Phys. Eng. Express* **2025**, *11*, 055015. [CrossRef]
369. Kirmanidou, Y.; Chatzinikolaidou, M.; Michalakis, K.; Tsouknidas, A. Clinical Translation of Polycaprolactone-Based Tissue Engineering Scaffolds, Fabricated via Additive Manufacturing: A Review of Their Craniofacial Applications. *Biomater. Adv.* **2024**, *162*, 213902. [CrossRef]
370. Shao, X.X.; Hutmacher, D.W.; Ho, S.T.; Goh, J.C.H.; Lee, E.H. Evaluation of a Hybrid Scaffold/Cell Construct in Repair of High-Load-Bearing Osteochondral Defects in Rabbits. *Biomaterials* **2006**, *27*, 1071–1080. [CrossRef] [PubMed]
371. Wang, T.; Chow, L.C.; Frukhtbeyn, S.A.; Ting, A.H.; Dong, Q.; Yang, M.; Mitchell, J.W. Improve the Strength of PLA/HA Composite through the Use of Surface Initiated Polymerization and Phosphonic Acid Coupling Agent. *J. Res. Natl. Inst. Stand. Technol.* **2011**, *116*, 785. [CrossRef]

372. Leung, L.; DiRosa, A.; Naguib, H. Physical and Mechanical Properties of Poly(E-Caprolactone)–Hydroxyapatite Composites for Bone Tissue Engineering Applications. Available online: https://www.semanticscholar.org/paper/Physical-and-Mechanical-Properties-of-Composites-Leung-DiRosa/fa6093b2ab275c44d338143c8c390ddb234aa8dc (accessed on 25 September 2025).
373. Bondarenko, S.; Filipenko, V.; Ashukina, N.; Maltseva, V.Y.; Ivanov, G.; Lazarenko, I.; Sereda, D.; Schwarzkopf, R. World Journal of Orthopedics. Available online: https://www.semanticscholar.org/paper/World-Journal-of-Orthopedics-Bondarenko-Filipenko/65d0fc3ba86a6c5e931286161621e65a87468b62 (accessed on 25 September 2025).
374. Fujibayashi, S.; Takemoto, M.; Nakamura, T.; Matsushita, T.; Kokubo, T.; Sasaki, K.; Mori, S.; Matsuda, S. Stand-Alone Anterior Cervical Discectomy and Fusion Using an Additive Manufactured Individualized Bioactive Porous Titanium Implant without Bone Graft: Results of a Prospective Clinical Trial. *Asian Spine J.* **2021**, *15*, 373–380. [CrossRef] [PubMed]
375. Ragone, V.; Canciani, E.; Arosio, M.; Olimpo, M.; Piras, L.A.; Von Degerfeld, M.M.; Augusti, D.; D'Ambrosi, R.; Dellavia, C. In Vivo Osseointegration of a Randomized Trabecular Titanium Structure Obtained by an Additive Manufacturing Technique. *J. Mater. Sci. Mater. Med.* **2020**, *31*, 17. [CrossRef]
376. Åkerlund, E.; Diez-Escudero, A.; Grzeszczak, A.; Persson, C. The Effect of PCL Addition on 3D-Printable PLA/HA Composite Filaments for the Treatment of Bone Defects. *Polymers* **2022**, *14*, 3305. [CrossRef]
377. Dawood, R.M.; Mahdee, A.F. Fabrication and Characterization of 3D -printed Polymeric-based Scaffold Coated with Bioceramic and Naringin for a Potential Use in Dental Pulp Regeneration (in Vitro Study). *Int. Endod. J.* **2025**, *58*, 627–642. [CrossRef] [PubMed]
378. Moncal, K.K.; Heo, D.N.; Godzik, K.P.; Sosnoski, D.; Mrowczynski, O.D.; Rizk, E.B.; Ozbolat, V.; Tucker, S.; Gerhard, E.; Dey, M.; et al. 3D Printing of Poly(ε-Caprolactone)/Poly(D,L-Lactide-Co-Glycolide)/Hydroxyapatite Composite Constructs for Bone Tissue Engineering. *J. Mater. Res.* **2018**, *33*, 1972–1986. [CrossRef]
379. Lee, C.H.; Hajibandeh, J.; Suzuki, T.; Fan, A.; Shang, P.; Mao, J. Three-Dimensional Printed Multiphase Scaffolds for Regeneration of Periodontium Complex. *Tissue Eng. Part A* **2014**, *20*, 1342–1351. [CrossRef]
380. Im, G.-B.; Lin, R.-Z. Bioengineering for Vascularization: Trends and Directions of Photocrosslinkable Gelatin Methacrylate Hydrogels. *Front. Bioeng. Biotechnol.* **2022**, *10*, 1053491. [CrossRef]
381. Usme-Duque, L.K.; León-Campos, M.I.; Oyervides-Guajardo, V.G.; Gomez-Galicia, D.S.; Morales, M.A.M.; Flores-Guía, T.E.; Cano-Salazar, L.F.; Cabrera-Munguia, D.A.; Claudio-Rizo, J.A. The Bio-Envelope Revolution: Encapsulation Strategies for Stem Cell-Based Therapies. *Mediterr. J. Basic Appl. Sci.* **2025**, *9*, 204–227. [CrossRef]
382. Yue, K.; Trujillo-de Santiago, G.; Alvarez, M.M.; Tamayol, A.; Annabi, N.; Khademhosseini, A. Synthesis, Properties, and Biomedical Applications of Gelatin Methacryloyl (GelMA) Hydrogels. *Biomaterials* **2015**, *73*, 254–271. [CrossRef]
383. Levett, P.A.; Melchels, F.P.W.; Schrobback, K.; Hutmacher, D.W.; Malda, J.; Klein, T.J. A Biomimetic Extracellular Matrix for Cartilage Tissue Engineering Centered on Photocurable Gelatin, Hyaluronic Acid and Chondroitin Sulfate. *Acta Biomater.* **2014**, *10*, 214–223. [CrossRef]
384. Hernandez, I.; Kumar, A.; Joddar, B. A Bioactive Hydrogel and 3D Printed Polycaprolactone System for Bone Tissue Engineering. *Gels* **2017**, *3*, 26. [CrossRef]
385. Wang, J.-Y.; Wang, K.; Gu, X.; Luo, Y. Polymerization of Hydrogel Network on Microfiber Surface: Synthesis of Hybrid Water-Absorbing Matrices for Biomedical Applications. *ACS Biomater. Sci. Eng.* **2016**, *2*, 887–892. [CrossRef]
386. Das, M.; Sharabani-Yosef, O.; Eliaz, N.; Mandler, D. Hydrogel-Integrated 3D-Printed Poly(Lactic Acid) Scaffolds for Bone Tissue Engineering. *J. Mater. Res.* **2021**, *36*, 3833–3842. [CrossRef]
387. Basu, A.; Kunduru, K.R.; Doppalapudi, S.; Domb, A.J.; Khan, W. Poly(Lactic Acid) Based Hydrogels. *Adv. Drug Deliv. Rev.* **2016**, *107*, 192–205. [CrossRef] [PubMed]
388. Hassanien, M.; Alkhader, M.; Abu-Nabah, B.A.; Abuzaid, W. A Low-Cost Process for Fabricating Reinforced 3D Printing Thermoplastic Filaments. *Polymers* **2023**, *15*, 315. [CrossRef] [PubMed]
389. Zha, X.-J.; Wen, C.; Huang, X.; Ling, T.-X.; Li, J.-B.; Huang, J.-G. Digital Light Processing 3D Printing of High-Fidelity and Versatile Hydrogels via in Situ Phase Separation. *J. Mater. Chem. B* **2025**, *13*, 4630–4640. [CrossRef]
390. Viray, C.; Magill, B.V.; Zreiqat, H.; Ramaswamy, Y. Stereolithographic Visible-Light Printing of Poly(l-Glutamic Acid) Hydrogel Scaffolds. *ACS Biomater. Sci. Eng.* **2022**, *8*, 1115–1131. [CrossRef]
391. Zhang, Y.; Hao, L.; Savalani, M.M.; Harris, R.A.; Tanner, K.E. Characterization and Dynamic Mechanical Analysis of Selective Laser Sintered Hydroxyapatite-filled Polymeric Composites. *J. Biomed. Mater. Res. A* **2008**, *86A*, 607–616. [CrossRef] [PubMed]
392. Pawar, A.A.; Saada, G.; Cooperstein, I.; Larush, L.; Jackman, J.A.; Tabaei, S.R.; Cho, N.-J.; Magdassi, S. High-Performance 3D Printing of Hydrogels by Water-Dispersible Photoinitiator Nanoparticles. *Sci. Adv.* **2016**, *2*, e1501381. [CrossRef] [PubMed]
393. Armstrong, C.D.; Todd, N.; Alsharhan, A.T.; Bigio, D.I.; Sochol, R.D. A 3D Printed Morphing Nozzle to Control Fiber Orientation during Composite Additive Manufacturing. *Adv. Mater. Technol.* **2021**, *6*, 2000829. [CrossRef]

394. Oryan, A.; Hassanajili, S.; Sahvieh, S.; Azarpira, N. Effectiveness of Mesenchymal Stem Cell-Seeded onto the 3D Polylactic Acid/Polycaprolactone/Hydroxyapatite Scaffold on the Radius Bone Defect in Rat. *Life Sci.* **2020**, *257*, 118038. [CrossRef] [PubMed]
395. Rafiee, M.; Granier, F.; Therriault, D. Advances in Coaxial Additive Manufacturing and Applications. *Adv. Mater. Technol.* **2021**, *6*, 2100356. [CrossRef]
396. Goyal, R.; Sahu, S.; Mitra, S.; Niranjan, R.; Priyadarshini, R.; Yadav, R.; Lochab, B. Nanocellulose-Reinforced 4D Printed Hydrogels: Thermoresponsive Shape Morphing and Drug Release. *ACS Appl. Polym. Mater.* **2024**, *6*, 1348–1361. [CrossRef]
397. Li, H.; Darmawan, B.; Go, G.; Kim, S.; Nan, M.; Kang, B.; Kim, H.; Lee, S.B.; Bang, D.; Park, J.-O.; et al. Single-Layer 4D Printing System Using Focused Light: A Tool for Untethered Microrobot Applications. *Chem. Mater.* **2021**, *33*, 7703–7712. [CrossRef]
398. Cui, J.; Azzaroni, O.; Del Campo, A. Polymer Brushes with Phototriggered and Phototunable Swelling and pH Response. *Macromol. Rapid Commun.* **2011**, *32*, 1699–1703. [CrossRef]
399. Molina, B.G.; Ocón, G.; Silva, F.M.; Iribarren, J.I.; Armelin, E.; Alemán, C. Thermally-Induced Shape Memory Behavior of Polylactic Acid/Polycaprolactone Blends. *Eur. Polym. J.* **2023**, *196*, 112230. [CrossRef]
400. Gladman, A.S.; Matsumoto, E.A.; Nuzzo, R.G.; Mahadevan, L.; Lewis, J.A. Biomimetic 4D Printing. *Nat. Mater.* **2016**, *15*, 413–418. [CrossRef] [PubMed]
401. Ngah, W.S.W.; Fatinathan, S. Adsorption Characterization of Pb(II) and Cu(II) Ions onto Chitosan-Tripolyphosphate Beads: Kinetic, Equilibrium and Thermodynamic Studies. *J. Environ. Manag.* **2010**, *91*, 958–969. [CrossRef]
402. Papageorgiou, S.K.; Katsaros, F.K.; Kouvelos, E.P.; Nolan, J.W.; Le Deit, H.; Kanellopoulos, N.K. Heavy Metal Sorption by Calcium Alginate Beads from Laminaria Digitata. *J. Hazard. Mater.* **2006**, *137*, 1765–1772. [CrossRef]
403. Syarifuddin, A.; Haliza, N.; Izzah, N.; Tahir, M.M.; Dirpan, A. Physical, Mechanical, Barrier, and Optical Properties of Sodium Alginate/Gum Arabic/Gluten Edible Films Plasticized with Glycerol and Sorbitol. *Foods* **2025**, *14*, 1219. [CrossRef]
404. Azeem, B.; KuShaari, K.; Naqvi, M.; Kok Keong, L.; Almesfer, M.K.; Al-Qodah, Z.; Naqvi, S.R.; Elboughdiri, N. Production and Characterization of Controlled Release Urea Using Biopolymer and Geopolymer as Coating Materials. *Polymers* **2020**, *12*, 400. [CrossRef]
405. Shilpa, M.; Harisha, K.S.; Thripthi, S.; Arpitha, M.A.; Sangappa, Y. Eco-Friendly Magnetic Silk Fibroin Films for Heavy Metal Adsorption in Water Purification. *Next Mater.* **2025**, *9*, 101062. [CrossRef]
406. Griffin-LaHue, D.; Ghimire, S.; Yu, Y.; Scheenstra, E.J.; Miles, C.A.; Flury, M. In-Field Degradation of Soil-Biodegradable Plastic Mulch Films in a Mediterranean Climate. *Sci. Total Environ.* **2022**, *806*, 150238. [CrossRef]
407. Othman, N.A.F.; Selambakkannu, S.; Seko, N. Biodegradable Dual-Layer Polyhydroxyalkanoate (Pha)/Polycaprolactone (Pcl) Mulch Film for Agriculture: Preparation and Characterization. *Energy Nexus* **2022**, *8*, 100137. [CrossRef]
408. Wu, Q.; Shao, W.; Xia, N.; Wang, P.; Kong, F. A Separable Paper Adhesive Based on the Starch—Lignin Composite. *Carbohydr. Polym.* **2020**, *229*, 115488. [CrossRef] [PubMed]
409. Mansour, G.; Zoumaki, M.; Tsongas, K.; Tzetzis, D. Starch-Sandstone Materials in the Construction Industry. *Results Eng.* **2020**, *8*, 100182. [CrossRef]
410. Mustafa, P.; Niazi, M.B.K.; Jahan, Z.; Rafiq, S.; Ahmad, T.; Sikander, U.; Javaid, F. Improving Functional Properties of PVA/Starch-Based Films as Active and Intelligent Food Packaging by Incorporating Propolis and Anthocyanin. *Polym. Polym. Compos.* **2021**, *29*, 1472–1484. [CrossRef]
411. Alex, Y.; Divakaran, N.C.; Pattanayak, I.; Lakshyajit, B.; Ajay, P.V.; Mohanty, S. Comprehensive Study of PLA Material Extrusion 3D Printing Optimization and Its Comparison with PLA Injection Molding through Life Cycle Assessment. *Sustain. Mater. Technol.* **2025**, *43*, e01222. [CrossRef]
412. Hughes, J.; Thomas, R.; Byun, Y.; Whiteside, S. Improved Flexibility of Thermally Stable Poly-Lactic Acid (PLA). *Carbohydr. Polym.* **2012**, *88*, 165–172. [CrossRef]
413. Genovesi, A.; Aversa, C.; Barletta, M. Polyhydroxyalkanoates-Based Cast Film as Bio-Based Packaging for Fresh Fruit and Vegetables: Manufacturing and Characterization. *J. Polym. Environ.* **2023**, *31*, 4522–4532. [CrossRef]
414. Salama, H.E.; Abdel Aziz, M.S. Optimized UV-Barrier Carboxymethyl Cellulose-Based Edible Coatings Reinforced with Green Synthesized ZnO-NPs for Food Packaging Applications. *Polym. Bull.* **2024**, *81*, 16733–16755. [CrossRef]
415. Siew, Z.Z.; Chan, E.W.C.; Wong, C.W. Enhancing the Tearability and Barrier Properties of Cellulose Acetate Bioplastic Film with Polyethylene Glycol 1450 as an LDPE Replacement for Food Packaging. *Food Bioprocess Technol.* **2024**, *17*, 2265–2276. [CrossRef]
416. Xiong, W.; Chen, B.; Zhang, H.; Peng, J.; Pan, X.; Guo, M.; Luo, X.; Zhou, C.; Liu, Y. A Bio-Based Waterborne Polyurethane with High Toughness, Superior Wear Resistance, and Water Resistance Enabled by Sorbitol Monooleate. *Prog. Org. Coat.* **2023**, *185*, 107895. [CrossRef]
417. Lee, J.H.; Kim, S.H.; Oh, K.W. Bio-Based Polyurethane Foams with Castor Oil Based Multifunctional Polyols for Improved Compressive Properties. *Polymers* **2021**, *13*, 576. [CrossRef] [PubMed]

418. Oleksy, M.; Dynarowicz, K.; Aebisher, D. Advances in Biodegradable Polymers and Biomaterials for Medical Applications—A Review. *Molecules* **2023**, *28*, 6213. [CrossRef]
419. El-hadi, A.M. Increase the Elongation at Break of Poly (Lactic Acid) Composites for Use in Food Packaging Films. *Sci. Rep.* **2017**, *7*, 46767. [CrossRef]
420. Ncube, L.K.; Ude, A.U.; Ogunmuyiwa, E.N.; Zulkifli, R.; Beas, I.N. Environmental Impact of Food Packaging Materials: A Review of Contemporary Development from Conventional Plastics to Polylactic Acid Based Materials. *Materials* **2020**, *13*, 4994. [CrossRef]
421. Zhan, R.; Li, X.-L.; Zheng, Y.; Zeng, X.-R.; Shi, L.-Y.; Yang, K.-K.; Wang, Y.-Z. Fabrication of High-Strength and Tough PLA/PBAT Composites via in-Situ Copolymer Formation Using an Adaptable Epoxy Extender. *Int. J. Biol. Macromol.* **2025**, *302*, 140530. [CrossRef]
422. Wang, L.; Abenojar, J.; Martínez, M.A.; Santiuste, C. Degradation of Mechanical Properties of Flax/PLA Composites in Hygrothermal Aging Conditions. *Polymers* **2024**, *16*, 528. [CrossRef]
423. Regazzi, A.; Corn, S.; Ienny, P.; Bénézet, J.-C.; Bergeret, A. Reversible and Irreversible Changes in Physical and Mechanical Properties of Biocomposites during Hydrothermal Aging. *Ind. Crops Prod.* **2018**, *84*, 358–365. [CrossRef]
424. Al Abdallah, H.; Abu-Jdayil, B.; Iqbal, M.Z. Improvement of Mechanical Properties and Water Resistance of Bio-Based Thermal Insulation Material via Silane Treatment. *J. Clean. Prod.* **2022**, *346*, 131242. [CrossRef]
425. Li, F.; Chen, C.; Chen, X. Tremendous Advances, Multifaceted Challenges and Feasible Future Prospects of Biodegradable Medical Polymer Materials. *RSC Adv.* **2024**, *14*, 32267–32283. [CrossRef] [PubMed]
426. Wu, F.; Misra, M.; Mohanty, A.K. Challenges and New Opportunities on Barrier Performance of Biodegradable Polymers for Sustainable Packaging. *Prog. Polym. Sci.* **2021**, *117*, 101395. [CrossRef]
427. Makadia, H.K.; Siegel, S.J. Poly Lactic-Co-Glycolic Acid (PLGA) as Biodegradable Controlled Drug Delivery Carrier. *Polymers* **2011**, *3*, 1377–1397. [CrossRef]
428. Gentile, P.; Chiono, V.; Carmagnola, I.; Hatton, P. An Overview of Poly(Lactic-Co-Glycolic) Acid (PLGA)-Based Biomaterials for Bone Tissue Engineering. *Int. J. Mol. Sci.* **2014**, *15*, 3640–3659. [CrossRef]
429. Ma, S.; Feng, X.; Liu, F.; Wang, B.; Zhang, H.; Niu, X. The Pro-inflammatory Response of Macrophages Regulated by Acid Degradation Products of Poly(Lactide-co-glycolide) Nanoparticles. *Eng. Life Sci.* **2021**, *21*, 709–720. [CrossRef]
430. Kim, J.-K.; Go, E.-J.; Ko, K.-W.; Oh, H.-J.; Han, J.; Han, D.K.; Park, W. PLGA Microspheres Containing Hydrophobically Modified Magnesium Hydroxide Particles for Acid Neutralization-Mediated Anti-Inflammation. *Tissue Eng. Regen. Med.* **2021**, *18*, 613–622. [CrossRef]
431. Rosenboom, J.-G.; Langer, R.; Traverso, G. Bioplastics for a Circular Economy. *Nat. Rev. Mater.* **2022**, *7*, 117–137. [CrossRef]
432. Mansoor, Z.; Tchuenbou-Magaia, F.; Kowalczuk, M.; Adamus, G.; Manning, G.; Parati, M.; Radecka, I.; Khan, H. Polymers Use as Mulch Films in Agriculture—A Review of History, Problems and Current Trends. *Polymers* **2022**, *14*, 5062. [CrossRef]
433. Jha, S.; Akula, B.; Enyioma, H.; Novak, M.; Amin, V.; Liang, H. Biodegradable Biobased Polymers: A Review of the State of the Art, Challenges, and Future Directions. *Polymers* **2024**, *16*, 2262. [CrossRef] [PubMed]
434. Schick, S.; Heindel, J.; Groten, R.; Seide, G.H. Overcoming Challenges in the Commercialization of Biopolymers: From Research to Applications—A Review. *Polymers* **2024**, *16*, 3498. [CrossRef] [PubMed]
435. Wang, K.; Hobby, A.M.; Chen, Y.; Chio, A.; Jenkins, B.M.; Zhang, R. Techno-Economic Analysis on an Industrial-Scale Production System of Polyhydroxyalkanoates (PHA) from Cheese By-Products by Halophiles. *Processes* **2021**, *10*, 17. [CrossRef]
436. Faheem, M.; Khan, K.A. Harnessing Sustainable Biocomposites: A Review of Advances in Greener Materials and Manufacturing Strategies. *Polym. Bull.* **2025**, *82*, 8827–8870. [CrossRef]
437. Wrzecionek, M.; Kryszak, B.; Gadomska-Gajadhur, A. The Smart Way of Simultaneous Scaling up and Optimizing the Synthesis of PGS for Further Rapid Thermal Cross-Linking with the Use of Response Surface Methodology. *Polymer* **2025**, *336*, 128862. [CrossRef]
438. Dallaev, R.; Papež, N.; Allaham, M.M.; Holcman, V. Biodegradable Polymers: Properties, Applications, and Environmental Impact. *Polymers* **2025**, *17*, 1981. [CrossRef]
439. Sharma, V.P.; Singh, R.L.; Singh, R.P. Degradable Polymers and Plastics of the Future: Steps Toward Environmental Sustainability, Regulations, and Safety Aspects. In *Principles and Applications of Environmental Biotechnology for a Sustainable Future*; Singh, R.L., Ed.; Springer: Singapore, 2017; pp. 467–487, ISBN 978-981-10-1865-7.
440. Li, J.; Stachowski, M.; Zhang, Z. Application of Responsive Polymers in Implantable Medical Devices and Biosensors. In *Switchable and Responsive Surfaces and Materials for Biomedical Applications*; Elsevier: Amsterdam, The Netherlands, 2015; pp. 259–298, ISBN 978-0-85709-713-2.
441. Patel, S.; Sharma, S.; Suthar, J.; Suryawanshi, M. Regulatory Concern for Biomaterial and Its Toxicity. In *Design and Processing of Green Materials*; Faiyazuddin, M., Suryawanshi, M., Eds.; Biomaterials, Bioengineering and Sustainability; Springer Nature: Cham, Switzerland, 2025; Volume 4, pp. 433–458, ISBN 978-3-031-91789-9.

442. Xia, B.; Liu, Y.; Xing, Y.; Shi, Z.; Pan, X. Biodegradable Medical Implants: Reshaping Future Medical Practice. *Adv. Sci.* **2025**, *12*, e08014. [CrossRef]
443. Pappalardo, D.; Mathisen, T.; Finne-Wistrand, A. Biocompatibility of Resorbable Polymers: A Historical Perspective and Framework for the Future. *Biomacromolecules* **2019**, *20*, 1465–1477. [CrossRef]
444. Azeem, B. Stimuli-Responsive Starch-Based Biopolymer Coatings for Smart and Sustainable Fertilizers. *Gels* **2025**, *11*, 681. [CrossRef]
445. Yu, J.; Chen, R.; Liu, X.; Hileuskaya, K.; Kraskouski, A.; Shao, P. Advance of Stimulus-Responsive Materials in Food Packaging and Targeted Delivery of Bioactive Compounds: Insight of Discoloration and Deformation Mechanisms. *Trends Food Sci. Technol.* **2024**, *153*, 104732. [CrossRef]
446. Fu, X.; Hosta-Rigau, L.; Chandrawati, R.; Cui, J. Multi-Stimuli-Responsive Polymer Particles, Films, and Hydrogels for Drug Delivery. *Chem* **2018**, *4*, 2084–2107. [CrossRef]
447. Balcerak-Woźniak, A.; Dzwonkowska-Zarzycka, M.; Kabatc-Borcz, J. A Comprehensive Review of Stimuli-Responsive Smart Polymer Materials—Recent Advances and Future Perspectives. *Materials* **2024**, *17*, 4255. [CrossRef] [PubMed]
448. Li, C.; Deng, Z.; Gillies, E.R. Designing Polymers with Stimuli-Responsive Degradation for Biomedical Applications. *Curr. Opin. Biomed. Eng.* **2023**, *25*, 100437. [CrossRef]
449. Tariq, A.; Arif, Z.U.; Khalid, M.Y.; Hossain, M.; Rasool, P.I.; Umer, R.; Ramakrishna, S. Recent Advances in the Additive Manufacturing of Stimuli-Responsive Soft Polymers. *Adv. Eng. Mater.* **2023**, *25*, 2301074. [CrossRef]
450. Jiang, M.; Fang, H.; Tian, H. Latest Advancements and Trends in Biomedical Polymers for Disease Prevention, Diagnosis, Treatment, and Clinical Application. *J. Control. Release* **2025**, *380*, 138–174. [CrossRef]
451. Li, R.; Wang, L.; Kong, D.; Yin, L. Recent Progress on Biodegradable Materials and Transient Electronics. *Bioact. Mater.* **2018**, *3*, 322–333. [CrossRef] [PubMed]
452. Jose, M.; Vijjapu, M.T.; Neumaier, L.; Rauter, L.; Chakkunny, A.H.; Corzo, D.; Thoelen, R.; Picard, A.; Kosel, J.; Deferme, W. Convergence of Biocompatible Printed Electronics and Sensing in Wound Dressings: A Leap Forward in Sustainable Health Monitoring. *Npj Flex. Electron.* **2025**, *9*, 46. [CrossRef]
453. Zhu, J.; Wen, H.; Zhang, H.; Huang, P.; Liu, L.; Hu, H. Recent Advances in Biodegradable Electronics- from Fundament to the next-Generation Multi-Functional, Medical and Environmental Device. *Sustain. Mater. Technol.* **2023**, *35*, e00530. [CrossRef]
454. Khan, T.; Vadivel, G.; Ramasamy, B.; Murugesan, G.; Sebaey, T.A. Biodegradable Conducting Polymer-Based Composites for Biomedical Applications—A Review. *Polymers* **2024**, *16*, 1533. [CrossRef] [PubMed]
455. Liu, K.; Tran, H.; Feig, V.R.; Bao, Z. Biodegradable and Stretchable Polymeric Materials for Transient Electronic Devices. *MRS Bull.* **2020**, *45*, 96–102. [CrossRef]
456. Pang, Q.; Lou, D.; Li, S.; Wang, G.; Qiao, B.; Dong, S.; Ma, L.; Gao, C.; Wu, Z. Smart Flexible Electronics-Integrated Wound Dressing for Real-Time Monitoring and On-Demand Treatment of Infected Wounds. *Adv. Sci.* **2020**, *7*, 1902673. [CrossRef]
457. Dallaev, R. Smart and Biodegradable Polymers in Tissue Engineering and Interventional Devices: A Brief Review. *Polymers* **2025**, *17*, 1976. [CrossRef]
458. Gorantla, A.; Hall, J.; Troidle, A.; Janjic, J. Biomaterials for Protein Delivery: Opportunities and Challenges to Clinical Translation. *Micromachines* **2024**, *15*, 533. [CrossRef]
459. Zhang, F.; King, M.W. Biodegradable Polymers as the Pivotal Player in the Design of Tissue Engineering Scaffolds. *Adv. Healthc. Mater.* **2020**, *9*, 1901358. [CrossRef] [PubMed]
460. Jani, K.; Kaushal, N. Clinical Translation of PLGA Nanoparticles into Market—From Benchside to Breakthrough Therapy. In *Poly(Lactic-co-Glycolic Acid) (PLGA) Nanoparticles for Drug Delivery*; Elsevier: Amsterdam, The Netherlands, 2023; pp. 433–456, ISBN 978-0-323-91215-0.
461. Sternberg, J.; Sequerth, O.; Pilla, S. Green Chemistry Design in Polymers Derived from Lignin: Review and Perspective. *Prog. Polym. Sci.* **2021**, *113*, 101344. [CrossRef]

polymers

MDPI

Article

Effects of Steam Sterilization and Recycling on the Mechanical and Surface Properties of 3D-Printed Biodegradable PLA and Re-PLA Materials

Yunus Karayer [1], Şakir Altınsoy [1,*], Gökçe Koç [1,2], Diyadin Can [1] and Yunus Emre Toğar [3,4]

[1] Biomedical Engineering Department, Faculty of Engineering and Architecture, Istanbul Yeni Yuzyil University, Istanbul 34010, Turkey; bmm.yunuskarayer@gmail.com (Y.K.); gokce.koc@yeniyuzyil.edu.tr (G.K.); diyadin.can@yeniyuzyil.edu.tr (D.C.)
[2] Biomedical Engineering Department, Institute of Graduate Studies, Istanbul University-Cerrahpasa, Istanbul 34320, Turkey
[3] Mechatronics Program, Vocational School, Istanbul Beykent University, Istanbul 34500, Turkey; emretogar@beykent.edu.tr
[4] Mechanical Engineering Department, Faculty of Mechanical Engineering, Yıldız Technical University, Istanbul 34349, Turkey
* Correspondence: sakir.altinsoy@yeniyuzyil.edu.tr; Tel.: +90-534-720-32-81

Abstract

Polylactic acid (PLA) is an eco-friendly polymer known for its biodegradability and biocompatibility, yet its properties are sensitive to recycling and sterilization. These processes may cause chain scission and structural irregularities, leading to reduced strength, brittleness, or unpredictable deformation. In this study, PLA and recycled PLA (Re-PLA) specimens were produced by FDM 3D printing with different infill rates (25%, 50%, 75%), layer thicknesses (0.15, 0.20, 0.25 mm), and printing orientations (0°, 45°, 90°). Steam sterilization at 121 °C and 1 bar for 15 min simulated biomedical conditions. Mechanical, surface, degradation, and biocompatibility properties were examined using three-point bending, roughness measurements, SEM, and cell viability tests. Results showed that infill rate was the main parameter affecting flexural strength and surface quality, while orientation increased roughness. Sterilization and recycling made deformation less predictable, particularly in St-Re-PLA. SEM revealed stronger bonding at higher infill, but more brittle fractures in PLA and Re-PLA, while sterilized specimens showed ductile features. No visible degradation occurred at any infill level. Regression analysis confirmed that second-order polynomial models effectively predicted flexural strength, with layer thickness being most influential. These findings provide critical insights into optimizing PLA and Re-PLA processing for biomedical applications, particularly in the production of sterilizable and recyclable implantable devices.

Keywords: PLA; 3D printer; sterilization; recycling; mechanical properties; biocompatibility

1. Introduction

Advancements in medical technologies are closely linked to the continuous pursuit of innovative solutions aimed at improving patient care. One of the primary challenges in biomedical engineering is the design of safe and durable biomaterials for use in medical devices and implants. The development of medical implants is a highly complex process that requires extensive research, precision, and meticulous execution at every stage. In recent

years, additive manufacturing (AM) technologies have emerged as effective methods for implant production [1–3]. These techniques enable the fabrication of polymeric structures suitable for implantology while offering a high degree of design flexibility. Among the most common additive manufacturing techniques, Fused Deposition Modeling (FDM) is based on the controlled extrusion and bonding of thermoplastic materials in successive layers. Compared to conventional plastic processing technologies (e.g., extrusion, injection molding), AM enables the production of geometrically complex, fully customized products in a simple, rapid, and cost-effective manner [4]. Such personalized medical solutions present significant opportunities to improve patients' quality of life. In particular, 3D printing allows for the cost-effective and high-precision fabrication of patient-specific anatomical structures, implants, and surgical guides [5].

Biomedical materials are subject to increasingly stringent requirements in terms of biocompatibility and immune system tolerance, as the introduction of foreign substances into the body can invariably trigger defensive responses. Such interventions may lead to inflammation, allergic reactions, and even the onset of carcinogenic processes [6]. Polymeric materials can be used either temporarily or permanently within the human body, and many single-use surgical devices (e.g., screws) are designed specifically for use during a single surgical procedure before being discarded. In this context, technological progress and advances in materials science have made the use of biodegradable polymeric materials of either natural or synthetic origin particularly attractive for the 3D printing of implants [7,8].

One of the most widely used materials in 3D printing is polylactic acid (PLA), a sustainable thermoplastic that is biocompatible, biodegradable, and FDA-approved, making it highly suitable for medical applications. PLA's low glass transition temperature (~58 °C) and melting point (~175 °C) render it well-suited for 3D printing, and it has found widespread application in both engineering and biomedical fields [9]. Produced from renewable resources such as corn and sugarcane, PLA offers key advantages as an implant feedstock due to its non-toxicity, biocompatibility, and biodegradability [10,11]. Today, PLA is considered one of the most preferred sustainable polymers thanks to its bio-based origin, biodegradability, and recyclability [12,13]. However, the increasing adoption of 3D printing has also led to the generation of significant production waste, posing a notable environmental concern. Waste can result from the removal of support structures or from defective prints that cannot be reused, raising issues regarding environmental sustainability. According to the Plastics Europe (2022) report, approximately 20,000 tons of 3D printing waste are generated annually in Europe alone. This has necessitated the recycling and reuse of 3D printing materials, encouraging the adoption of recycled PLA (Re-PLA) [14]. Recycling waste filaments not only reduces environmental impact but also offers economic benefits. The recycling process involves collecting, shredding, remixing, homogenizing, and re-extruding waste material into filament form, thereby preventing raw material loss and reducing production costs. Many commercially available filaments suitable for 3D printing, including biocompatible polymers such as PLA and Re-PLA, are now widely accessible.

Nevertheless, for products such as implants or surgical devices that directly or indirectly come into contact with human tissue, compliance with sterilization requirements is critical [15]. Sterilization methods for effectively eliminating microorganisms in medical devices include chemical (e.g., ethylene oxide, hydrogen peroxide), mechanical (e.g., filtration), and physical (heat and radiation) techniques. Among these, heat sterilization is often preferred due to its ability to eradicate microorganisms without leaving toxic residues, its procedural simplicity, and its availability in most hospitals [16]. However, for polymeric

materials, the potential effects of sterilization on mechanical and surface properties must be carefully evaluated.

One of the main challenges during sterilization is maintaining the mechanical integrity of polymeric materials. Exposure to high temperature and humidity can induce structural changes, adversely affecting their performance in medical applications. Therefore, sterilization methods and process parameters must be carefully optimized within the material's processing window. Although PLA exhibits high strength and stiffness, it is inherently brittle. Consequently, its limited resistance to sterilization processes may restrict its widespread use in single-use surgical devices.

In this regard, Frizziero et al. reported that PLA-based 3D-printed components sterilized by moist heat in an autoclave largely retained their geometric integrity [17]. However, more pronounced deformations were observed in smaller or geometrically complex specimens. Notably, the study did not include direct mechanical testing, and assessments were based on thermal deformation and visual observations. Conversely, Zbyrad et al. demonstrated that changes in mechanical properties after steam sterilization vary depending on the type of polymer used, with certain materials such as PEEK and PET-G HT100 exhibiting high resistance to elevated temperatures [18].

While some studies have investigated only the effects of steam sterilization, others have examined the influence of manufacturing parameters (e.g., layer thickness, infill density, printing orientation) on mechanical properties without applying sterilization. For instance, Günay et al. analyzed the effects of parameters such as infill rate, printing speed, and raster angle on the tensile strength and surface quality of PLA specimens without sterilization [19]. Accordingly, Table 1 presents a comparative summary of studies that have investigated the effects of both steam sterilization and manufacturing parameters on the mechanical properties of PLA and Re-PLA.

An examination of Table 1 indicates that, in the current literature, not only the filament type but also various parameters associated with the printing process play a decisive role in determining the mechanical properties of 3D-printed components. These parameters include layer thickness, build orientation, printing speed, and infill density, with each variable either individually or in combination having a significant impact on the strength of the printed part. Although some studies have explored the influence of these parameters, analyses focusing specifically on recycled materials remain scarce. There is a clear need for research that evaluates recycled feedstocks in conjunction with manufacturing parameters. Moreover, despite the growing interest in 3D-printed products in recent years, studies investigating the structural and mechanical changes in Re-PLA-based 3D-printed parts after moist and dry heat sterilization are limited. Similarly, research that considers the combined effects of printing parameters such as layer thickness, build orientation, printing speed, and infill density together with sterilization is also limited.

Understanding the effects of sterilization on the properties of biomaterials used in implantology is critical to ensuring the safety, durability, and performance of these materials in clinical applications following sterilization. Therefore, in this study, both virgin polylactic acid (PLA) and recycled PLA (Re-PLA), which are biocompatible materials, were used to fabricate specimens via 3D printing under varying manufacturing parameters, and their mechanical performance was comprehensively analyzed before and after sterilization. In the experimental design, infill density, layer thickness, and build orientation were selected as the primary manufacturing parameters, and their effects on the flexural strength and surface quality of the specimens were examined in detail. To elucidate the microstructural origins of fracture behavior, scanning electron microscopy (SEM) analyses were performed on fracture surfaces, enabling the characterization of fracture modes at the microstructural

level. The experimental results were theoretically supported through statistical analyses and mathematical modeling, allowing for a direct comparison between experimental and predicted results to validate the model's accuracy. These modeling efforts facilitated the identification of optimal manufacturing parameters and contributed to reducing the number of required experimental trials.

Table 1. Comparative summary of studies on the effects of steam sterilization and manufacturing parameters on the mechanical properties of PLA and Re-PLA produced by 3D printing.

Ref. No	Material	Production Parameters	Sterilization Method	Characterization Studies
[19]	PLA, Re-PLA	Layer thickness and infill density.	-	Tensile, compression, bending, stress, strength and surface quality.
[20]	PLA	İnfill density, raster angle, and printing speed.	-	Optimization and ANOVA analysis.
[21]	PLA	Infill density.	-	Bending strength, tensile strength and mechanical properties.
[22]	Bronze/ PLA Composite	Printing orientation.	-	Mechanical properties, tensile strength, tribological behavior (friction, wear depth, stick-slip), surface roughness, and hardness.
[23]	Re- (PLA, ABS, PET, HDPE)	Manufacturing methods (FDM, HME, FPF) and recycling.	-	Tensile strength, flexibility, UV sensitivity, and biodegradability.
[17]	PLA	Thermomechanical behavior.	Steam	Deterioration and deformation.
[18]	PLA, PET-G, PEEK	Different polymer type.	Steam	Strength differences depending on material type.
[10]	PLA+ Hidroksiapatit	Surface treatment.	Steam s	FTIR, Gel Permeation Chromatography, and Differential scanning calorimetry (DSC).
[24]	PLA	Infill density.	Steam	Tensile strength (infill effect).
[25]	PLA	Layer thickness and build size.	Steam	Geometric deformation (axial deviation analysis), contamination test (sterility assessment by color change).
In this study	PLA, Re-PLA, St-PLA, St-Re-PLA	Infill rate, layer thickness, printing orientation, and recycling.	Steam	Bending strength, deformation, surface roughness, SEM, degradation and cytotoxic.

Furthermore, although PLA's biocompatibility is well established in the literature, it was hypothesized that melt extrusion-based recycling steps could affect the biocompatibility, degradation, and potential leaching behavior of Re-PLA through chain scission and the formation of low-molecular-weight species. Accordingly, biocompatibility, degradation, and leaching tests were conducted on Re-PLA. The results were comparatively analyzed alongside similar studies in the literature, and the findings from this research were interpreted to provide original contributions to the field. Overall, this study offers a comprehensive evaluation in which critical factors such as sterilization, recycling, and manufacturing parameters are jointly assessed to ensure the safe use of biodegradable and sustainable polymers in medical applications.

2. Materials and Methods

2.1. Materials and 3D Printing Process

The polylactic acid (PLA) material used in this study was the "PLA-PLUS" filament from the ELAS-3B brand. The recycled polylactic acid (Re-PLA) specimens were produced by recycling the same material. In the production of Re-PLA specimens, filaments obtained by recycling defective products produced in 3D printers with PLA PLUS filaments were used. The main properties of PLA are as follows: density 1500 kg/m^3, elastic modulus 5.9 GPa, Poisson's ratio 0.4, maximum tensile strength 60 MPa, and tensile elongation 2%. All specimens were manufactured using the Fused Deposition Modeling (FDM) method on a Creality CR-6 SE 3D printer (Shenzhen Creality-Chine, Shenzhen, China). Figure 1 shows the technical drawing of the test specimen used in the study. In the experimental study, infill rates (25%, 50%, and 75%), layer thicknesses (0.15 mm, 0.20 mm, and 0.25 mm), and printing orientations (0°, 45°, and 90°) were used as production parameters. In this study, a nozzle temperature of 200 °C, a bed temperature of 60 °C, a printing speed of 50 mm/s, and the cooling fan in the "on" mode were used. For each material, 27 parameter combinations were tested in triplicate (n = 81), yielding a total of 324 specimens across the four materials (81 × 4). Each parameter was systematically varied to examine its impact on the mechanical properties. Table 2 presents the list of materials, reagents, and their sources used in this study.

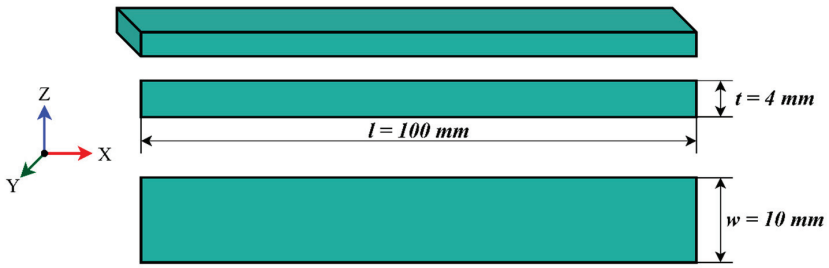

Figure 1. Technical drawing of the specimen.

Table 2. Materials and their sources used in the study.

Material	Purpose of Use	Origin
PLA-PLUS filament	3D printing (base material)	ELAS-3B (Kocaeli, Turkey)
Recycled PLA (Re-PLA)	Produced from defective PLA-PLUS parts	Extrusion via Rondol Microlab twin screw extruder.
NaOH (1%)	Cleaning of 3D printing waste	Kimyalab (Istanbul, Turkey)
Active surface solvent (3%)	Cleaning of 3D printing waste	Kimyalab (Istanbul, Turkey)
Eryiğit ERS 6613 D Autoclave	Sterilization process	Eryiğit (Istanbul, Turkey)
Phosphate-buffered saline (PBS)	Degradation tests	Sigma-Aldrich (Istanbul, Turkey)
L929 mouse fibroblast cells	Cytotoxicity tests	Merck (Istanbul, Turkey)
DMEM/F12 medium	Cell culture medium	Sigma-Aldrich (Istanbul, Turkey)
Dimethyl sulfoxide (DMSO)	Solubilization of formazan crystals	Merck

2.2. Recycling Steps

In this study, as part of the recycling process, defective parts generated during the production phase of 3D printers were collected and initially cleaned. Three-dimensional printing waste was cleaned by washing it under industrial conditions at 85 °C with a

solution containing 1% NaOH and 3% active surface solvent. Following the cleaning process, the materials were dried under vacuum. Recycled filament production was carried out in a Rondol Microlab twin screw extruder with an L/D ratio of 20 at a rotation speed of 60 rpm.

2.3. Sterilization Process

Sterilization is a fundamental step used in the production process of biomaterials or medical devices that will come into contact with the human body, as well as in the reuse of medical devices, to prevent complications such as infection or implant rejection [26]. Heat sterilization is based on the destruction of the vital metabolic and structural components of microorganisms through heat and oxidative processes. The most common protocol in clinical applications is autoclaving, which involves exposing materials to pressurized steam at temperatures between 121–136 °C for specific durations [27]. However, for biopolymers and many thermoplastics (e.g., PLA, PLGA, some bio-based polymers), this process may carry risks such as hydrolysis, chain scission, and physical degradation, leading to undesirable changes in mechanical, thermal, and morphological properties. Nevertheless, the literature reports that PLA can be sterilized by autoclaving under certain conditions and does not exhibit cytotoxicity. Although increases in hydrophilicity or changes in surface roughness have been observed, no significant inflammatory response has been reported [28,29].

A key challenge in sterilization is preserving the mechanical integrity of polymeric materials. Exposure to high temperatures and humidity can cause structural changes that may adversely affect the performance of materials in medical applications. Therefore, in order to ensure both sterility and mechanical stability, the sterilization method and process parameters must be carefully optimized within the material's processing window.

In this study, specimens were fabricated from PLA and recycled PLA (Re-PLA) using fused deposition modeling (FDM). For each parameter combination infill rate (25%, 50%, 75%), Layer Thickness (0.15, 0.20, 0.25 mm), and printing orientation (0°, 45°, 90°) specimens were autoclaved at 121 °C and 1 bar for 15 min in medical grade sterilization pouches. The sterilization process was performed using the ERYİĞİT ERS 6613 D (2020) autoclave device. After sterilization, PLA and Re-PLA specimens are denoted as St-PLA and St-Re-PLA, respectively. Figure 2 illustrates representative sterilization packages.

Figure 2. Specimen after the sterilization process.

2.4. Characterization Study

The three-point bending test is a standard mechanical testing method used to determine the flexural strength, modulus of elasticity, and fracture behavior of a material. In this test, the specimen is placed between two support points, and a single load is applied at

its center, causing it to fracture or deform. In this study, the tests were conducted using a Zwick Proline three-point bending tester, according to the ISO 178:2019 standard [30]. The distance between the supports was set to 64 mm, the bending speed to 2 mm/min, and the ambient temperature was maintained at 21 ± 3 °C. Three specimens were tested for each parameter.

Surface roughness is considered an important criterion for evaluating a material's surface quality and the effects of manufacturing process parameters on the surface. In this study, surface roughness measurements were performed using a Mitutoyo Surftest SJ-210 (Mitutoyo, Kawasaki, Japan) surface roughness device. The results were obtained using the "Surface Roughness Tester SJ-210/310/410" software. Previously tested three-point bending specimens were used in the surface roughness test. Ra (arithmetic mean deviation of the profile) values were measured to determine the surface roughness data of the test specimens. Before testing, the surfaces were thoroughly cleaned, and measurements were taken at five different points on each specimen to calculate the average Ra value. Scanning Electron Microscope (SEM) imaging was conducted with the FEI QUANTA 450 FEG ESEM device (Fei Company, Hillsboro, OR, USA), using FEG 450 model. SEM images were taken at Istanbul Arel University Polymer Technologies and Composite Application and Research Center (Arel POTKAM).

2.5. Degradation Tests

To study how PLA, Re-PLA, St-PLA, and St-Re-PLA behave in terms of degradation, it was prepared specimens with three different infill levels: 25%, 50%, and 75%. Each of these specimens was placed in 10 mL of phosphate-buffered saline (PBS) and kept in a shaking incubator set to 37 °C and 60 rpm, which helps mimic the conditions inside the human body. It was monitored the degradation over a period of one week. At specific time points 1, 2, 3, 4, 5, 24, 48, 72, 96, 120, 144, and 168 h we took 3 mL of solution from each container. To keep the volume stable, the removed liquid was replaced with 3 mL of fresh PBS. Each collected sample was then analyzed using a UV-Vis spectrophotometer, scanning between 200 and 800 nm, to check if any material had been degraded from the specimens over time.

2.6. Cytotoxic Tests

The biocompatibility testing was carried out using L929 mouse fibroblast cells with the MTT assay; this is the test where living cells convert a dye into colored crystals. The tested samples were made from PLA, recycled PLA (Re-PLA), sterilized PLA (St-PLA) and sterilized–recycled PLA (St-Re-PLA) at infill rates of 25%, 50%, and 75%. First, we sterilized all the specimens in an autoclave. After sterilization, 5 mL of serum-free DMEM F12 medium was placed over each sample and they were incubated at 37 °C for seven days. On days 1, 4, and 7, a portion of the medium was removed and stored in the fridge at 4 °C until the cytotoxicity tests were ready to run.

For the test itself, L929 cells were grown in 25 cm^2 flasks until they covered about 80% of the surface. Then the cells were counted and the total number was calculated with the following Equation (1).

$$\begin{gathered} \text{Total Cell Coun} = \text{Average Cell Count} \times \text{Dilution Factor} \times 10^4 \\ 2 \times 50 \times 10000 = 1000000\ Cell \end{gathered} \tag{1}$$

After that, 10,000 cells were seeded in 100 µL of medium into each well of a plate. The cells were left for 24 h to attach and grow. Once that time was up, the medium was removed, washed the cells with PBS, and added 100 µL of the stored sample medium from days 1, 4, or 7. Five replicates were performed for each sample to make sure the data was reliable. Then, the cells were incubated for another 24 h. Following this, 10 µL

of MTT reagent (Sigma M5655) was added to each well. The plates went into the dark for 3 h so the living cells could convert the MTT into formazan crystals. After incubation, 100 µL of DMSO (Merck) was added to dissolve the crystals, waited about 30 min, and then measured absorbance at 540 nm using a plate reader. The viability of the cells was calculated according to the equation given in Equation (2).

$$\%\ Viability = \frac{Experimental\ Group\ Absorbance}{Control\ Group\ Absorbance} \times 100 \quad (2)$$

2.7. Mathematical Modeling

The advancement of additive manufacturing technologies, particularly with biodegradable thermoplastics such as PLA and derivatives, has necessitated the use of mathematical modeling to rigorously analyze the effects of process parameters on mechanical and surface properties. Parameters such as infill density, layer thickness, and printing orientations exert complex, interdependent influences on material performance, and their evaluation requires robust statistical and mathematical formulations. In this context, correlation analysis and variance-based statistical methods such as ANOVA provide a foundation for identifying significant relationships among variables, while regression analysis enables the development of predictive models that capture both linear and nonlinear dependencies.

The correlation coefficient (r) is employed as a measure of the strength and direction of relationships between parameters, with values approaching +1 or -1 indicating strong positive or negative correlations, respectively, while values near zero suggest the absence of a meaningful statistical relationship. However, correlation alone cannot establish causality; thus, regression modeling becomes central in quantifying the extent to which independent variables contribute to variations in output responses such as bending strength (σ_{max}) or surface roughness (Ra).

The regression framework adopted in this study extends beyond simple linear relationships by incorporating higher-order and interaction terms, yielding a generalized polynomial form (Equation (3)):

$$Y = \beta_0 + \beta_1 X_1 + \beta_2 X_2 + \beta_3 X_3 + \beta_4 X_1^2 + \beta_5 X_2^2 + \beta_6 X_3^2 + \beta_7 X_1 X_2 + \beta_8 X_1 X_3 + \beta_9 X_2 X_3 \quad (3)$$

where Y represents the response variable of interest and X_i denote the process parameters under investigation. The estimation of regression coefficients was performed using Wolfram Mathematica, which provides both parameter values and statistical significance tests. The predictive capacity of the models was subsequently evaluated through established statistical metrics, including the coefficient of determination (R2), mean absolute error (MAE), and root mean square error (RMSE). Collectively, these measures provide a comprehensive assessment of the model's explanatory power, its average predictive deviation, and its sensitivity to larger discrepancies.

The application of this modeling framework to experimental datasets derived from PLA and its derivatives demonstrated that the interaction between material type and processing parameters is highly significant in determining deformation behavior. Regression-based models not only allowed for the quantification of individual parameter effects but also facilitated a broader understanding of interdependencies within the manufacturing process. Moreover, by averaging the regression coefficients obtained across different material systems, a composite predictive model was constructed. This pooled model representation was found to be effective in capturing general trends across diverse material classes, thereby offering a more holistic approach for the optimization of additive manufacturing processes.

3. Results and Discussion

In this section, the results of the bending test, deformation, surface roughness, SEM images, degradation test, cytotoxicity test, and mathematical modeling are presented in tables and graphs. These results are then discussed and compared with recent studies in the literature. In addition, statistical and parametric analyses are carried out to show how the printing parameters affect the mechanical and surface properties of the specimens. Finally, the most suitable printing conditions that improve mechanical strength and surface quality are identified. The experimental results of maximum flexural strength, maximum deformation, and surface roughness for PLA, Re-PLA, St-PLA, and St-Re-PLA specimens are given in Table 3.

Table 3. Experimental results of maximum flexural strength (σmax), maximum deformation (δ_{max}), and surface roughness (Ra) for PLA, Re-PLA, St-PLA, and St-Re-PLA specimens.

Production Parameters			Max. Flexural Strength, Mpa				Max. Deformation				Surface Roughness, μm			
Infill Rate, %	Layer Thickness, mm	Printing Orientation, °	PLA	Re-PLA	St-PLA	St-Re-PLA	PLA	Re-PLA	St-PLA	St-Re-PLA	PLA	Re-PLA	St-PLA	St-Re-PLA
25	0.15	0	53.4	65.0	65.4	68.4	10.1	9.6	6.1	8.6	4.1	6.5	3.7	7.4
		45	49.5	62.1	72.6	67.2	8.5	10.5	6.1	7.7	5.2	6.2	4.5	6.5
		90	65.4	76.2	57.0	64.8	24.0	18.2	4.8	6.6	4.9	8.0	7.6	7.0
	0.2	0	60.3	70.8	49.2	49.8	9.7	12.2	5.3	6.6	3.4	7.7	6.6	7.3
		45	60.9	70.5	57.6	63.0	9.6	12.9	5.1	7.8	6.5	5.4	3.7	11.5
		90	66.9	70.2	46.8	46.2	13.0	19.3	6.7	5.3	6.0	4.6	4.9	7.6
	0.25	0	65.7	72.6	46.2	57.6	9.8	13.4	7.5	6.9	4.0	3.5	5.4	7.8
		45	66.6	76.2	47.4	49.2	10.9	13.0	9.1	8.6	5.7	5.3	6.7	8.1
		90	65.1	66.6	42.6	45.6	13.3	12.6	6.2	9.1	5.8	8.6	5.9	5.4
50	0.15	0	57.6	63.9	71.4	70.8	12.1	11.7	6.9	8.3	3.2	7.7	4.4	3.7
		45	60.6	73.5	60.0	51.0	12.3	14.9	5.8	9.6	7.0	6.3	5.7	7.1
		90	65.7	69.3	58.2	61.2	24.4	18.4	5.5	8.7	4.8	4.2	6.7	7.3
	0.2	0	65.7	69.0	45.6	67.2	13.0	12.3	6.6	7.2	4.6	7.0	3.4	7.5
		45	56.7	72.0	39.0	69.0	9.2	13.9	9.3	7.1	5.1	5.7	6.7	8.6
		90	67.2	67.5	48.6	60.0	18.6	15.4	8.3	6.4	4.7	7.6	6.5	9.4
	0.25	0	70.5	87.9	51.6	55.2	12.8	14.3	9.1	12.0	5.3	6.6	6.3	6.7
		45	70.5	76.2	49.8	51.6	12.8	13.6	7.7	8.5	5.7	5.0	3.7	3.2
		90	67.8	78.9	39.0	65.4	24.7	14.4	9.3	7.2	2.9	7.1	4.9	7.6
75	0.15	0	75.0	80.1	75.6	53.4	13.1	13.2	5.9	8.8	4.8	3.3	5.6	5.8
		45	69.9	72.3	50.4	57.0	11.8	13.5	7.8	9.9	4.1	7.0	6.6	8.1
		90	75.3	75.9	61.8	66.6	16.1	17.7	5.4	6.4	3.6	4.9	3.7	6.4
	0.2	0	70.8	75.6	43.2	46.8	12.2	12.2	6.3	11.2	4.2	5.6	4.9	6.5
		45	70.5	76.8	46.2	56.4	11.2	12.2	6.7	8.3	4.1	6.3	5.4	3.0
		90	74.7	78.9	64.2	63.6	18.4	18.8	7.2	14.4	5.2	7.5	6.7	7.3
	0.25	0	73.8	90.0	60.6	58.2	12.1	17.0	6.9	9.9	5.5	6.7	3.9	5.5
		45	72.9	87.0	45.0	69.6	11.8	12.9	5.8	6.9	4.9	5.9	4.4	7.6
		90	75.6	69.0	60.0	59.4	22.2	30.1	5.8	7.1	5.9	6.3	6.7	6.8

3.1. Three-Point Bending Test Results

The three-point bending test is used to evaluate the flexural strength and elastic modulus of materials. Flexural strength indicates how well a material can resist breaking under applied force, while the elastic modulus reflects the material's stiffness and its ability to resist deformation when subjected to stress. Both parameters are critically important for assessing the strength of materials exposed to high mechanical loads, such as those

used in implant applications. The flexural strength test results for PLA, Re-PLA, St-PLA, and St-Re-PLA specimens, based on the experiments and measurements performed in this study, are presented in Table 3, as given above. Figures 3 and 4 show graphs created by averaging the relevant parameters, making it easier to interpret the results in Table 3.

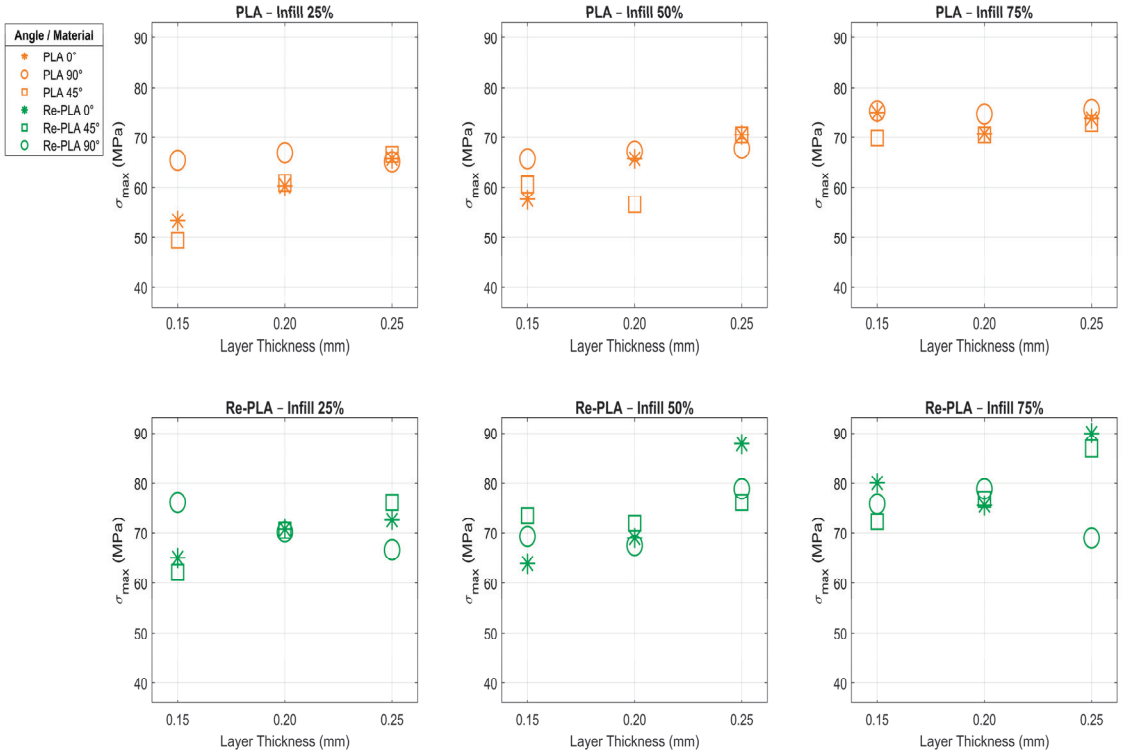

Figure 3. Effects of the same production parameters on the flexural strength of PLA and Re-PLA specimens.

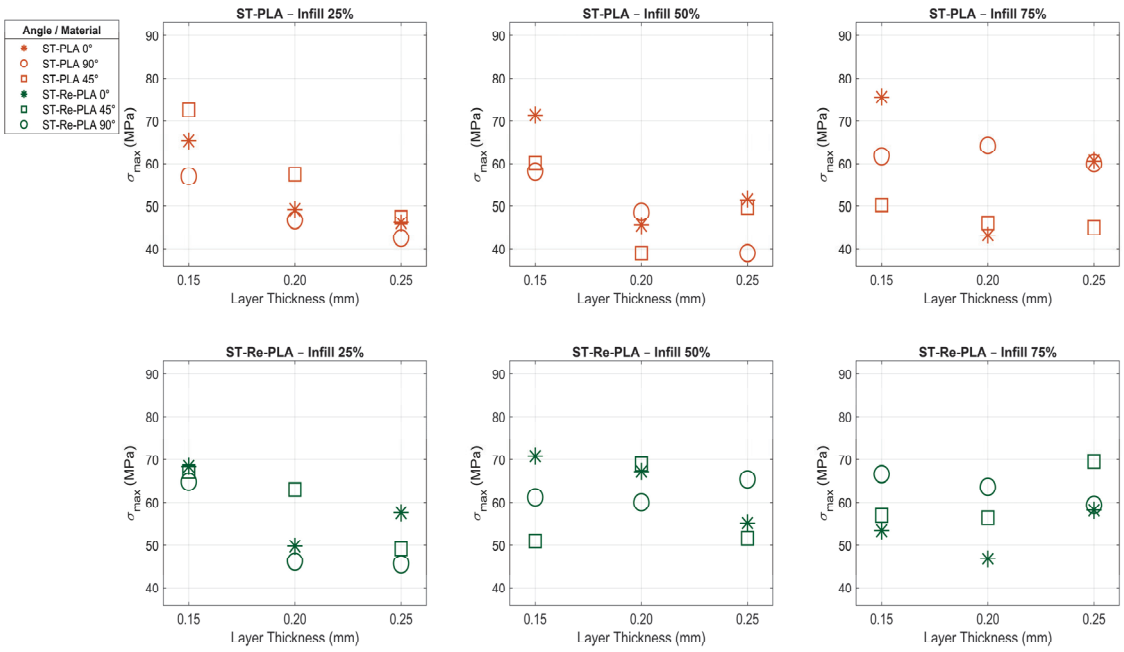

Figure 4. Effects of the same production parameters on the flexural strength of St-PLA and St-Re-PLA specimens.

Figure 3 shows how the same production parameters affect the flexural strength of PLA and Re-PLA specimens, while Figure 4 shows their effect on St-PLA and St-Re-PLA specimens.

When Table 3 and Figure 3 are examined, it is observed that flexural strength increases as the infill rate, printing orientation, and layer thickness of the PLA specimens increase. Increasing the infill rate from 25% to 50% led to a 5.146% increase in flexural strength, and increasing it from 50% to 75% resulted in a 13.086% increase. Increasing the layer thickness from 0.15 mm to 0.20 mm produced a 3.721% increase in flexural strength, and increasing it from 0.20 mm to 0.25 mm yielded a 5.862% increase. When evaluated according to printing orientation, increasing the angle from 0° to 45° resulted in a 2.48% decrease, while increasing it from 45° to 90° resulted in a 7.888% increase. The most influential parameter in PLA specimens was determined to be the infill rate. Because it directly alters the physical structure and internal strength of the material, it has been observed to have a more pronounced and powerful effect on flexural strength compared to other parameters [21,31,32]. The highest flexural strength was measured in a specimen with a 75% infill rate, a layer thickness of 0.25 mm, and a 90° printing orientation. In PLA, it is seen that the flexural strength values are almost the same in all printing orientations (0°, 45°, and 90°) at 75% infill rate and 2.0 mm layer thickness (Table 3, Figure 3). This can be explained by the minimisation of the internal porosity of the material at high infill rate and the formation of a more homogeneous structure. Thus, the differences in the printing orientation due to interlayer adhesion become insignificant, and the load transfer is more uniform regardless of the orientation. Similar results have been reported in the literature; it is emphasised that the effect of printing orientation on flexural strength is significantly reduced at high infill rates and the main determining parameter is the idolation ratio [33–35].

When the Re-PLA results presented in Table 3 and Figure 3 were examined, it was observed that flexural strength increased with higher infill rates and greater layer thicknesses, but decreased with increasing printing orientation (Table 3, Figure 3). Increasing the infill rate from 25% to 50% led to a 4.443% increase in flexural strength, and increasing it from 50% to 75% resulted in a 7.201% increase. Increasing the layer thickness from 0.15 mm to 0.20 mm yielded an approximate 2% increase in flexural strength, while increasing it from 0.20 mm to 0.25 mm led to an 8.153% increase. Regarding printing orientation, increasing the angle from 0° to 45° caused an approximate 1% decrease, and increasing it from 45° to 90° resulted in an approximate 2% decrease. It was determined that infill rate and layer thickness have a comparable impact on the flexural strength of Re-PLA specimens. Increasing the printing orientation is thought to negatively affect interlayer adhesion and the direction of load transmission, leading to a reduction in flexural strength [21,31,32]. The highest flexural strength was measured in the specimen with a 75% infill rate, a 0.25 mm layer thickness, and a 0° printing orientation.

The main reason why a similar increasing trend is observed in Re-PLA specimens at all infill rates (25, 50 and 75%) in Figure 3 is that as the infill rate increases, the internal porosity decreases, the adhesion between the layers strengthens and the load transfer becomes more homogeneous. Although chain shortening and crystallinity changes due to the recycling process limit the overall strength of the material, increasing infill rate and layer thickness compensate these negative effects and increase the flexural strength. However, since the increase in printing orientation makes load transfer difficult at the interface, it negatively affects the strength in Re-PLA [36,37].

In the St-PLA specimens, the infill rate, layer thickness, and printing orientation were observed to be effective parameters (Table 3, Figure 4). Increasing the infill rate from 25% to 50% resulted in a 4.455% decrease in flexural strength; however, increasing the infill rate

from 50% to 75% resulted in a 9.456% increase. Increasing the layer thickness from 0.15 mm to 0.20 mm resulted in a ≈23% decrease in flexural strength, while increasing it from 0.20 mm to 0.25 mm resulted in a ≈0.4% increase. This suggests that a thickness of 0.20 mm may be a critical threshold, and interlayer adhesion is minimal at this value. Regarding the printing orientation, increasing the printing orientation from 0° to 45° resulted in an ≈8% decrease in flexural strength, while increasing it from 45° to 90° resulted in a ≈2% increase. In St-PLA specimens, layer thickness has been determined to have a greater effect on flexural strength [21,31,32,38]. The highest flexural strength was measured in the specimen with a 75% infill rate, a 0.15 mm layer thickness, and a 0° printing orientation.

In the St-Re-PLA specimens, it was observed that infill rate, layer thickness, and printing orientation were the key parameters influencing flexural strength (Table 3, Figure 4). Increasing the infill rate from 25% to 50% led to a 7.737% increase in flexural strength; however, increasing it from 50% to 75% caused a 3.7% decrease. Increasing the layer thickness from 0.15 mm to 0.20 mm resulted in a 6.852% decrease in flexural strength, while increasing it from 0.20 mm to 0.25 mm led to a further approximate 2% decrease. When evaluated by printing orientation, increasing the angle from 0° to 45° produced an approximate 1% increase in flexural strength, while increasing it from 45° to 90° had virtually no effect. The highest flexural strength was recorded in the specimen with a 50% infill rate, 0.15 mm layer thickness, and 0° printing orientation. Overall, no consistent trend was observed in the figures. This irregularity is thought to be the result of the specimens undergoing both sterilization and recycling processes [21,32,39].

The irregular trends seen in the St-PLA and St-Re-PLA specimens in Figure 4 are due to the fact that the sterilisation and recycling processes disrupt the polymer chain structure, weakening interlayer bonding, increasing internal stresses, and making the microstructure heterogeneous. For this reason, even if the infill rate increased, the strength did not always increase, and in some cases, on the contrary, decreases were observed. In addition, critical threshold values occurred at certain layer thicknesses, minimising interface adhesion and causing fluctuations in mechanical performance; it has been reported in the literature that such processes can cause unpredictable strength losses in biopolymers [37].

A general evaluation of the flexural strength tests performed on PLA, Re-PLA, St-PLA, and St-Re-PLA specimens reveals that production parameters such as infill rate, layer thickness, and printing orientation have varying effects on each sample type. In general, increasing the infill rate increases flexural strength in PLA and Re-PLA specimens, while increasing the printing orientation has a limited effect on PLA specimens and decreases strength in Re-PLA specimens. Increasing layer thickness generally increases flexural strength in both material types, but this increase was limited in some cases.

In St-PLA specimens, increasing the infill rate initially reduces flexural strength, followed by an increase, revealing the complex interaction of this parameter with the material's microstructure. Furthermore, St-PLA specimens, which exhibit greater sensitivity to layer thickness, were determined to have a critical thickness of 0.20 mm. In St-Re-PLA specimens, both the infill rate and layer thickness caused a decrease in flexural strength within certain ranges. This was attributed to the negative effects of sterilization and recycling processes on material properties.

Increasing the printing orientation generally led to a slight decrease in flexural strength across all specimen types, although this effect was negligible in some cases. Based on these findings, it was determined that the most influential parameter in PLA-based specimens is the infill rate, whereas sterilization and recycling processes introduced greater variability in material behavior. Therefore, it was concluded that the production parameters

for recycled and sterilized biopolymers must be optimized with greater precision and care [21,23,31,32,38].

3.2. Deformation Test Results

Another important piece of information obtained from the three-point bending tests is the deformation behavior of the materials. Deformation tests are fundamental engineering analyses used to evaluate the mechanical performance of a material under external loading. The elastic, plastic, and fracture behaviors of a material are quantitatively assessed through strain and stress parameters, providing critical insights into properties such as service life, toughness, and suitability for engineering applications.

In recent years, the significance of deformation testing has grown, particularly in evaluating the performance of recycled and/or sterilized polymer materials produced using 3D printers. The deformation test results of PLA, Re-PLA, St-PLA and St-Re-PLA specimens are given in Table 3. The effects of the production parameters on the deformation of PLA and Re-PLA specimens are shown in Figure 5, while Figure 6 shows these effects for St-PLA and St-Re-PLA specimens.

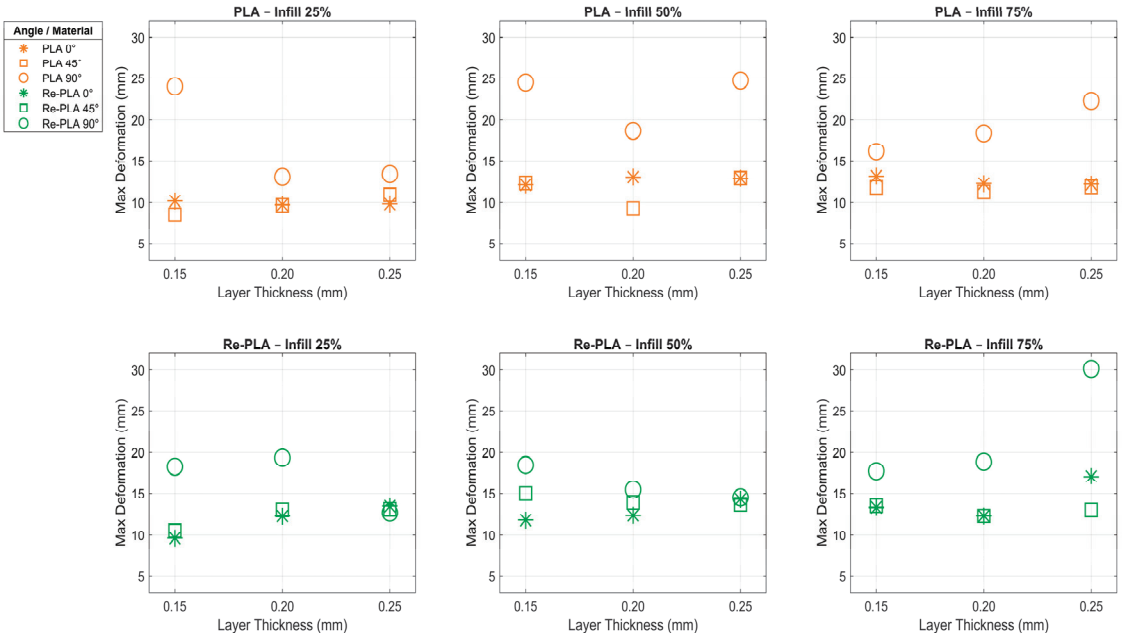

Figure 5. Effects of production parameters on deformation of PLA and Re-PLA specimens.

According to the deformation (ε) data presented in Table 3, Figures 5 and 6, the effects of the production parameters on the deformation of PLA, Re-PLA, St-PLA, and St-Re-PLA specimens were systematically evaluated. It was found that the infill rate, layer thickness, and printing orientation, which are considered production parameters, affect the deformation behavior at different rates and directions depending on the specimen type.

In PLA specimens, the deformation increased by 28.46% when the infill rate was increased from 25% to 50%, while a decrease of 7.89% was observed when the infill rate was increased from 50% to 75%. This can be attributed to the reduction in voids in the microstructure and the increase in the deformation capacity of the material under load. However, at a 75% infill rate, a decrease in deformation capacity may have occurred as the structure became more rigid. Similarly, in Re-PLA, the increase was limited to 5.88% from 25% to 50% and 14.53% from 50% to 75%. This shows that Re-PLA is not as sensitive to infill rate as PLA due to irregularities in its internal structure. There are two important

factors behind the deformation differences between PLA and Re-PLA materials. The first is how the production parameters shape the microstructural voids. When the infill rate in PLA increases up to a certain level, the voids between the layers are reduced, thereby increasing the deformation capacity of the material. However, when the infill rate reaches very high levels, the structure becomes overly rigid, and this becomes a factor limiting the deformation capacity. The second is the effect of recycling and sterilisation processes on polymer chains. In Re-PLA production, as recycled polymer chains undergo thermal and mechanical processes, breaks and irregularities occur in the chain structure. This leads to weakening of interlayer bonds, an increase in internal stresses, and heterogenisation of the microstructure. As a result, an increase in parameters such as infill rate or layer thickness does not always increase the mechanical strength of the material; in some cases, decreases in strength can be observed [23,32,38].

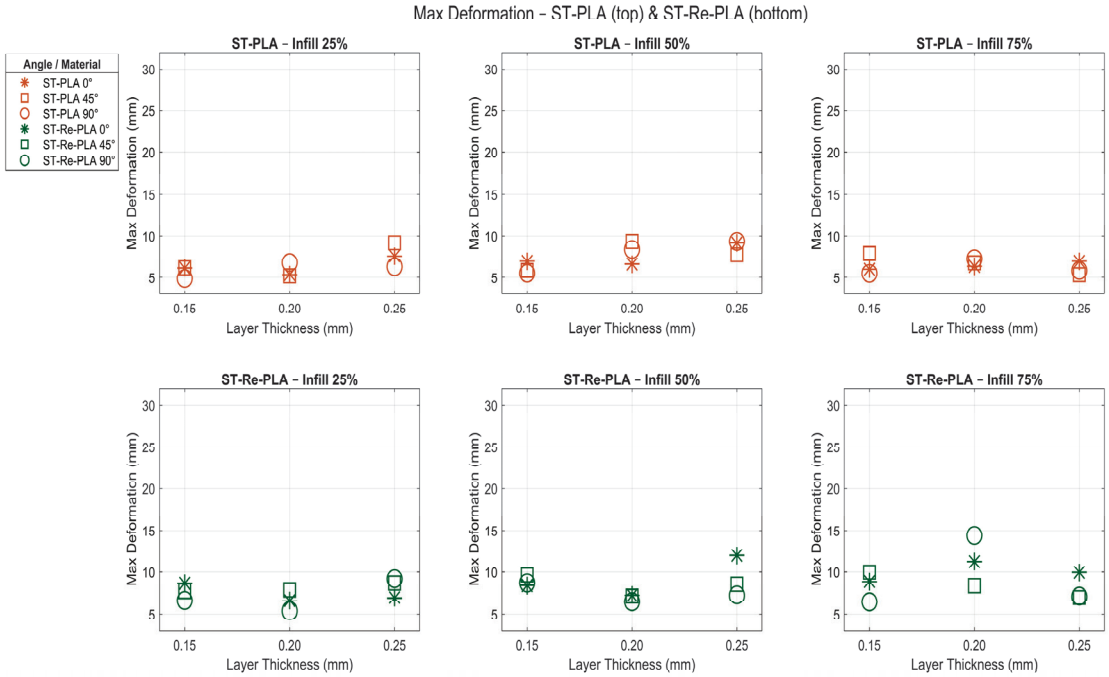

Figure 6. Effects of production parameters on deformation of St-PLA and St-Re-PLA specimens.

In the sterilized specimens (St-PLA and St-Re-PLA), the deformation increase was found to proceed more irregularly with the infill rate. In St-PLA, the deformation increased by 19.61% from 25% to 50%, while it decreased by 15.31% from 50% to 75%. This suggests that the microcracks formed in the internal structure after sterilization lose their effect with filling [39–42]. In St-Re-PLA, it was observed that the increase in deformation was irregular as the infill rate increased. When the deformation behaviours of St-PLA and St-Re-PLA specimens are examined, it is seen that the values do not increase steadily as the infill rate increases, and in some cases decrease. The main reason for this situation is that sterilisation and recycling processes cause breaks in polymer chains, weakening of interlayer bonds, and irregularities in the microstructure. While the structure is normally expected to become more durable when the infill rate increases, this effect is suppressed due to the microcracks caused by sterilisation and the heterogeneous structure caused by recycling, and in some cases, even the deformation capacity decreases.

When the deformation (ε) data presented in Table 3, Figures 5 and 6 are evaluated based on layer thickness, a clear trend is observed in PLA specimens. As the layer thickness

increases from 0.15 mm to 0.20 mm, deformation increases by 9.45%, and by an additional 11.84% as it increases from 0.20 mm to 0.25 mm.

This behavior indicates that thinner layers tend to make the structure more brittle, whereas thicker layers enhance the material's capacity to deform, even though the interlayer adhesion may become weaker due to reduced bonding between layers. In contrast, Re-PLA specimens exhibited much smaller changes, suggesting that they maintain a more stable structural response to changes in layer thickness. This could be related to altered molecular structure or stress relaxation effects introduced during the recycling process. For St-PLA and St-Re-PLA specimens, the deformation did not follow a regular pattern with increasing layer thickness. Particularly in St-PLA, deformation increased by 13.10% and 9.45% across the same thickness intervals, but these increases were inconsistent. This fluctuation is likely due to the weakening of interlayer bonding caused by the sterilization process, which may have degraded the surface properties of the layers or introduced microdefects. On the other hand, St-Re-PLA specimens showed a more consistent and limited change, indicating that the combined effects of sterilization and recycling resulted in a structure less sensitive to layer thickness variations.

When the same tables and figures are evaluated in terms of printing orientation, a 6.48% decrease in deformation was observed in PLA specimens as the printing orientation increased from 0° to 45°, whereas a substantial increase of 77.80% was recorded when the orientation increased from 45° to 90° (Table 3, Figures 5 and 6). This significant rise is attributed to the fact that at 90° printing orientation, the applied load is perpendicular to the interlayer bonds, making deformation easier due to weaker interfacial strength. In Re-PLA specimens, a similar trend was observed, with deformation increasing by 40.34% as the printing orientation changed, although the magnitude of change was lower than in PLA. This suggests that the effect of printing orientation on deformation is more limited in recycled materials, possibly due to altered microstructure or more uniform energy dissipation [21,23,31,32,38]. For St-PLA and St-Re-PLA specimens, deformation behavior showed fluctuating patterns depending on the printing orientation. Specifically, in St-PLA, deformation increased by 4.66% between 0° and 45°, but then decreased by 6.50% between 45° and 90°. In St-Re-PLA specimens, however, the variation in deformation was minimal, indicating that the influence of printing orientation diminished following the sterilization process [32,37,38,43–45].

3.3. Surface Roughness Results

Surface roughness is a basic parameter that has a direct impact on the quality level, functionality, and cost-efficiency of a product. Advances in manufacturing technologies and increased research and development activities allow the optimisation of production parameters in order to achieve higher surface quality. In this context, the investigation of the surface roughness of PLA- and Re-PLA-based materials manufactured by 3D printing technology provides important information about the surface characteristics of these materials. In this study, surface roughness measurements were performed on four different specimen types, namely PLA, St-PLA, Re-PLA, and St-Re-PLA, at five different points for each specimen, and the averages of the obtained values are presented. The surface roughness test results are summarized in Table 3. At the same time, Figures 7 and 8 illustrate the effects of production parameters on the surface roughness of PLA and Re-PLA specimens, and St-PLA and St-Re-PLA specimens, respectively.

When Table 3 and Figure 7 are analyzed, it is observed that the surface roughness decreases as the infill rate increases in PLA specimens, whereas it increases with increasing layer thickness. The surface roughness (Ra value) decreased by 5.143% when the infill rate

was increased from 25% to 50%, and by 2.3% when it was increased from 50% to 75%. This reduction is attributed to the fact that higher infill rates minimize internal voids, resulting in a more uniform and smoother surface texture. On the other hand, increasing the layer thickness from 0.15 mm to 0.20 mm led to a 4.926% rise in the Ra value, while a further increase from 0.20 mm to 0.25 mm caused an approximate increase of 4.5%. This can be explained by the fact that thicker layers lead to more pronounced transitions between layers, which adversely affect surface quality. In terms of printing orientation, surface roughness increased by approximately 23% when the orientation was changed from 0° to 45°, but decreased by about 9% when the orientation was further changed from 45° to 90°. This behavior is likely due to the way layer deposition aligns relative to the printing orientation, which directly influences the external surface profile. As a result, it was determined that the most effective parameter on the surface roughness of PLA specimens was the infill rate, while the most negative parameter affecting the surface quality was the printing orientation [31,32]. The lowest surface roughness was obtained in the specimen with 50% infill rate, 0.25 mm layer thickness, and 90° printing orientation, while the highest Ra value was obtained in the specimen with 50% infill rate, 0.15 mm layer thickness, and 45° printing orientation.

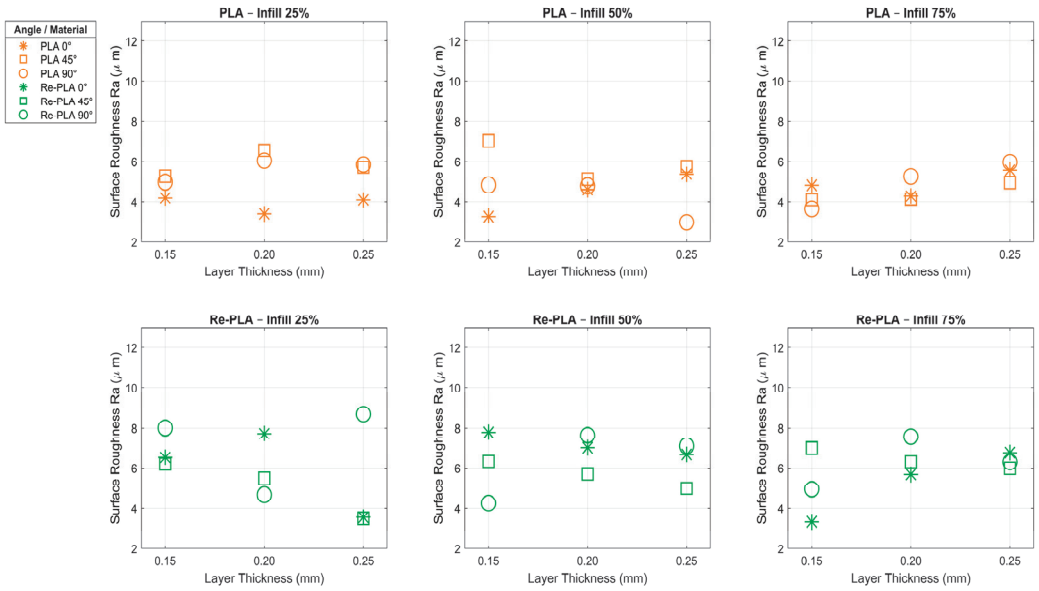

Figure 7. Effects of production parameters on surface roughness of PLA and Re-PLA specimens.

When the data presented in the same tables and figures were analyzed according to Re-PLA specimens, it was found that there was an initial increase in surface roughness and then a decreasing trend as the infill rate and layer thickness increased (Table 3, Figure 7). The surface roughness (Ra value) increased by 2.37% when the infill rate was increased from 25% to 50% and decreased by 6.22% when the infill rate was increased from 50% to 75%. This can be explained by the fact that the surface becomes rougher due to the irregularity of the internal structure at medium filling level, while at high filling level, the surface becomes smoother due to the reduction in voids [21,23]. Increasing the layer thickness from 0.15 mm to 0.20 mm resulted in an increase of 6.278% in the Ra value, while increasing the layer thickness from 0.20 mm to 0.25 mm resulted in a decrease of approximately 4.161%. This can be attributed to the fact that after a certain thickness, layer transitions become more harmonious and reduce surface roughness [31]. In terms of printing orientation, the surface roughness decreased by ≈3% by increasing the printing

orientation from 0° to 45° and increased by ≈11% by increasing the printing orientation from 45° to 90°. This increase can be explained by the fact that as the production angle reaches 90°, the layers accumulate in the vertical direction, causing more distinct surface marks [31]. The lowest surface roughness was obtained in the specimen with 75% infill rate, 0.15 mm layer thickness, and 0° printing orientation, while the highest Ra value was measured in the specimen with 25% infill rate, 0.25 mm layer thickness, and 90° printing orientation. As a result, it has been determined that the most negative parameter affecting the surface roughness of Re-PLA specimens is the printing orientation, while the infill rate and layer thickness can affect the surface quality both positively and negatively [23,31].

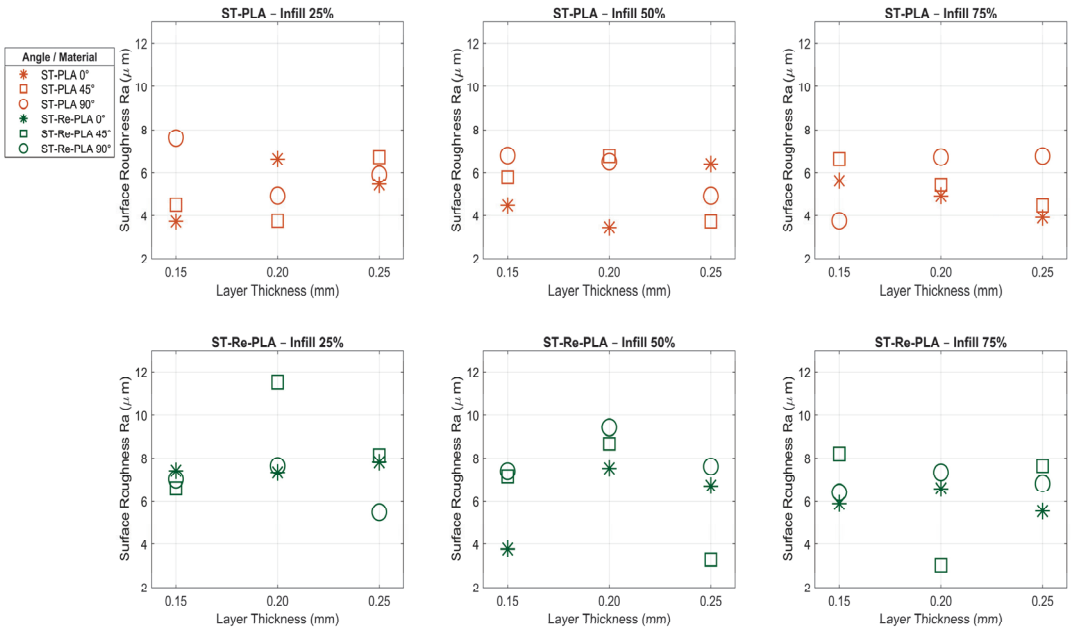

Figure 8. Effects of production parameters on surface roughness of St-PLA and St-Re-PLA specimens.

When the graphs and data presented in the table and figures are examined according to St-PLA specimens, it was found that the surface roughness decreased as the infill rate increased in the sterilised PLA (St-PLA) specimens, whereas the surface roughness first increased and then decreased as the layer thickness increased (Table 3, Figure 8). In addition, it has been observed that the surface roughness increases significantly with increasing printing orientation and adversely affects the surface quality [31,32]. The surface roughness (Ra value) decreased by ≈1% when the infill rate was increased from 25% to 50% and by ≈1.2% when the infill rate was increased from 50% to 75%. This can be explained by the fact that the increased infill rate makes the internal structure tighter and reduces the voids and distortions on the surface [32]. Increasing the layer thickness from 0.15 mm to 0.20 mm caused a slight increase of 0.44% in the Ra value, while increasing the layer thickness from 0.20 mm to 0.25 mm resulted in a decrease of approximately 1.98%. This may be related to the fact that after a certain thickness, the surface becomes smoother as the alignment between the layers becomes more uniform [31].

When evaluated in terms of printing orientation, the surface roughness increased by 7.3% when the angle was increased from 0° to 45°, while this increase reached 12.757% when the angle was increased from 45° to 90°. This increase is explained by the fact that as the printing orientation increases, the transition lines between the layers become more distinct and the printing direction forms a steeper angle with the surface [31]. The lowest surface roughness was obtained in the specimen with 50% infill rate, 0.2 mm layer thickness,

and 0° printing orientation, while the highest Ra value was measured in the specimen with 50% infill rate, 0.15 mm layer thickness, and 90° printing orientation. As a result, it has been determined that the parameter that most affects the surface roughness of St-PLA specimens is the printing orientation, while the infill rate contributes positively to the improvement of the surface quality [31,32].

When the results obtained are analyzed according to St-Re-PLA specimens, it is seen that the surface roughness decreases as the infill rate increases (Table 3, Figure 8). On the other hand, similar to Re-PLA and St-PLA specimens, the surface roughness increases as the layer thickness increases and decreases after a certain value. The surface roughness (Ra value) decreased by 10.735% when the infill rate was increased from 25% to 50% and by ≈7% when the infill rate was increased from 50% to 75%. Increasing the layer thickness from 0.15 mm to 0.20 mm increased the Ra value by 15.478% and increasing the layer thickness from 0.20 mm to 0.25 mm decreased the Ra value by ≈14.5%. In terms of printing orientation, it was found that it only increased similarly to St-PLA specimens, the surface roughness increased by 9.55% when increasing from 0° to 45°, and increased by 1.48% when increasing from 45° to 90°. The lowest surface roughness was obtained in the specimen with 75% infill rate, 0.2 mm layer thickness, and 45° printing orientation, while the highest Ra value was measured in the specimen with 25% infill rate, 0.2 mm layer thickness, and 45° printing orientation. As a result, it has been determined that the most effective parameter on the surface roughness of PLA specimens is the infill rate, while the most negative parameter affecting the surface quality is the printing orientation [23,32].

According to the general evaluation of the surface roughness (Ra) tests shown in the graphs given in Figures 7 and 8, increasing the infill rate had a decreasing effect on the surface roughness in all specimen types. The reason for this is that as the infill rate increases, the voids in the structure decrease, the material density increases, and the surface becomes smoother. Especially in St-Re-PLA specimens, this effect was much more pronounced, and a decrease of up to 10% in the roughness value was observed at high infill rates. In Re-PLA specimens, a short-term increase was observed at medium infill rates due to the more irregular internal structure, but at high infills, this situation was replaced by smooth surface formation [21,23,32].

The layer thickness parameter showed different effects depending on the specimen type. As the layer thickness increased, the surface roughness generally increased first and then started to decrease after a certain value. This can be explained as the smoothing of the surface at low thicknesses due to more precise and smoother transitions between layers, the increase in roughness at medium thicknesses as the transitions become more pronounced, and the decrease in surface fluctuations at high thicknesses as the layer alignment becomes harmonious again. Especially in St-Re-PLA specimens, an increase of 15.5% by increasing the layer thickness from 0.15 mm to 0.20 mm and a decrease of 14.5% by increasing the layer thickness from 0.20 mm to 0.25 mm provided a clear example of this trend [31].

The printing orientation was the parameter that had the most negative effect on the surface roughness in all specimen types examined. With the increase in the printing orientation, the layers are placed on the surface at a steeper angle, and this causes the layer traces to become more prominent on the surface. This increases the surface roughness and negatively affects the surface quality. Especially in PLA and St-PLA specimens, an increase of up to 23% in roughness was observed from 0° to 45°. In Re-PLA specimens, the surface roughness decreased when the printing orientation was increased from 0° to 45° and increased again when the printing orientation was increased from 45° to 90°. This indicates that the recycled material structure has a different and more complex response to the printing orientation [23,31].

When the results shown in the figures are evaluated in general, it is seen that the internal voids in the specimens decrease with the increase in the infill rate; as a result, a more homogeneous structure is obtained, and the surface quality improves. The layer thickness parameter shows a more complex effect: at low thicknesses, the more regular layer transitions contribute to the smoothing of the surface, while at medium thicknesses, the surface roughness increases due to the prominence of the transitions. However, at higher thicknesses, the roughness decreases again as the layer alignment becomes more harmonised. The printing orientation was the parameter that affected the surface quality most negatively in all specimen types. As the printing orientation increased, the layer traces became more prominent on the surface and increased the roughness. Especially in the specimens containing recycled material (Re-PLA and St-Re-PLA), more complex responses to the printing orientation were observed due to the irregular internal structure of the material.

3.4. SEM Analysis

The analysis of fracture surfaces resulting from mechanical tests is crucial for evaluating the material's microstructural properties and damage mechanisms. In this study, the fracture surfaces of PLA, Re-PLA, St-PLA, and St-Re-PLA specimens produced with 25%, 50%, and 75% infill rates were examined under fixed production parameters (0.2 mm layer thickness and 45° printing orientation) and analyzed using SEM imaging. Figures 9–12 present the SEM images of fracture surfaces obtained after bending tests on PLA, Re-PLA, St-PLA, and St-Re-PLA specimens, corresponding to the three infill rates.

When the SEM images between Figures 9 and 12 are examined, it is seen that the microstructural voids between the filaments (interlayer voids and trapped air gaps) are significantly reduced with the increase in the infill rate in the specimens. This is thought to be due to the more effective filling of the gaps between the extruded tracks due to the turbulent flow that occurs during the exit of the material from the nozzle [46].

The reduction in interlayer voids and air gaps has a significant impact on the mechanical performance of the material. It was observed that the fracture of PLA specimens has sharper edges and exhibits a typical brittle fracture behavior. It is also noteworthy that the inter-filament adhesion in these specimens is smooth and flawless. Similarly, in Re-PLA specimens, it was observed that the fracture was brittle and the air bubbles decreased with the increase in the infill rate and the inter-filament adhesion improved in parallel.

In St-PLA and St-Re-PLA specimens, clear signs of plastic deformation were observed on the fracture surfaces, indicating a ductile fracture behavior. Moreover, in these specimens, the filaments appeared to flatten from their original circular shape, and ductile fracture features were visible along the interlayer boundaries. This morphology suggests a reduction in surface quality. The surface roughness results were found to align well with the SEM observations. These findings are also consistent with previous studies in the literature [46–48].

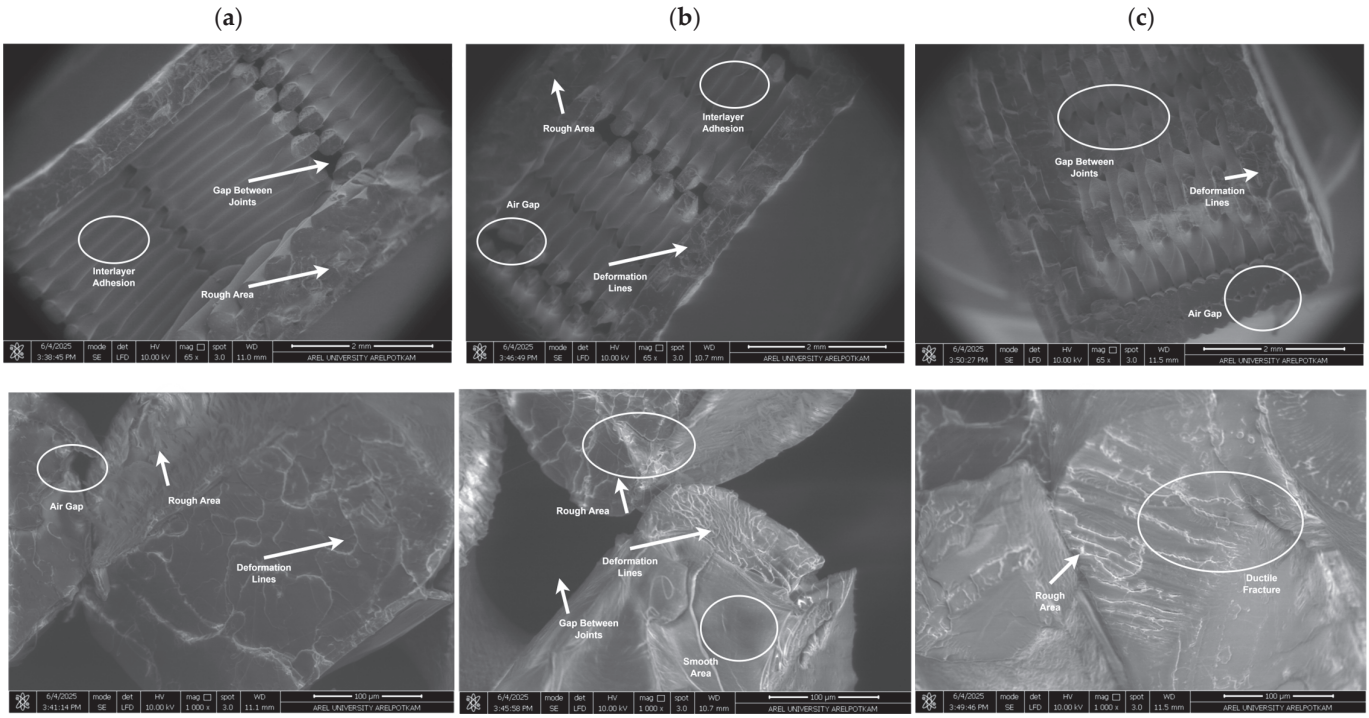

Figure 9. SEM images of PLA specimens with (**a**) 25%, (**b**) 50%, and (**c**) 75% infill rate.

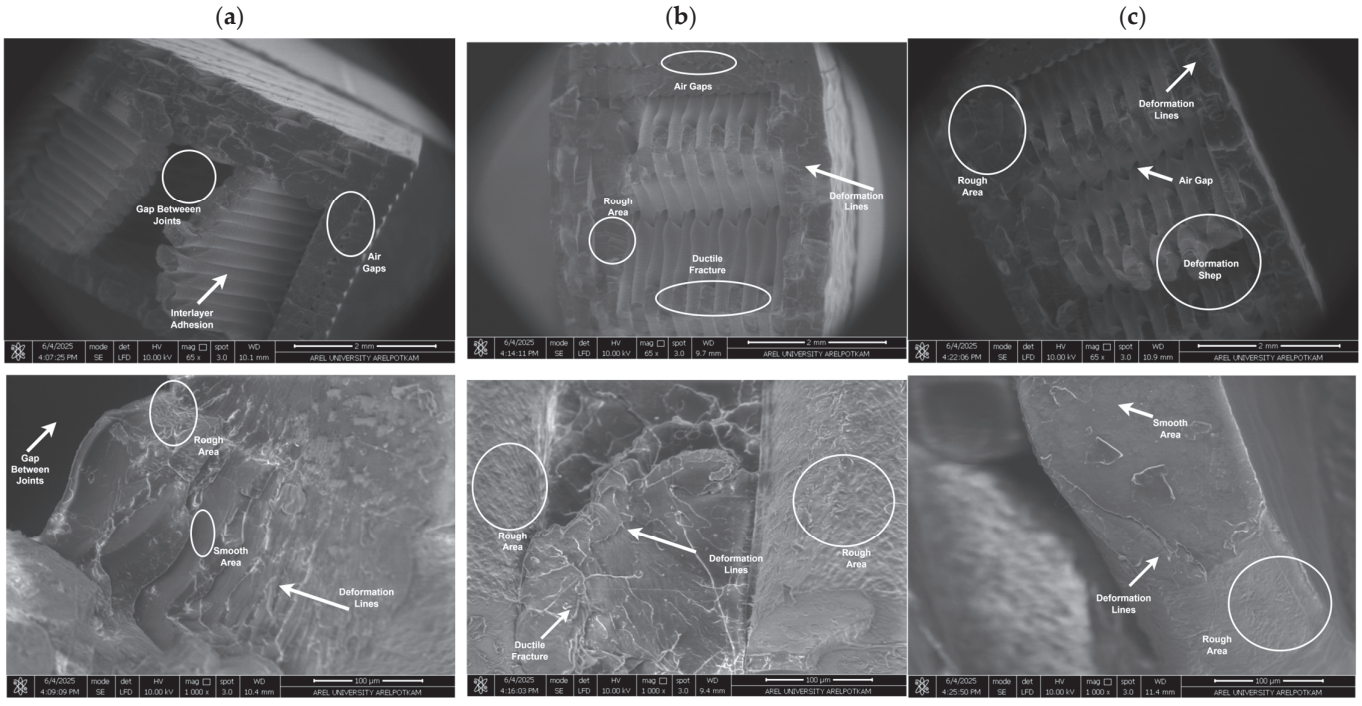

Figure 10. SEM images of Re-PLA specimens with (**a**) 25%, (**b**) 50%, and (**c**) 75% infill rate.

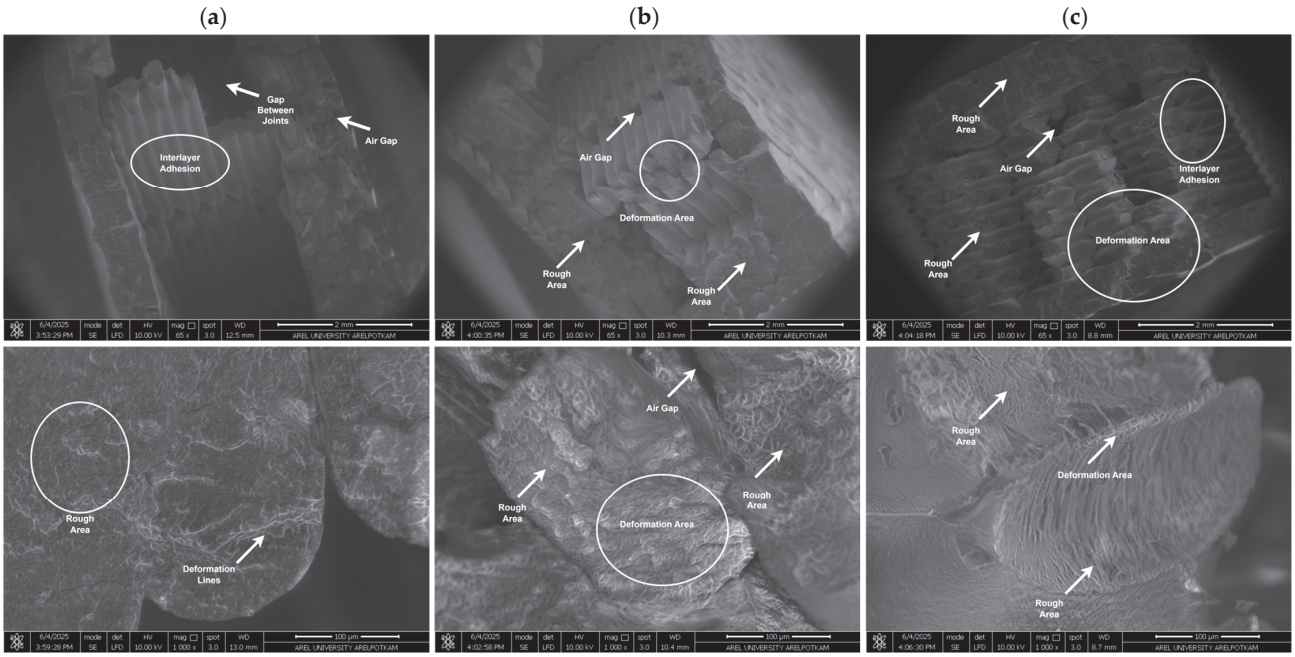

Figure 11. SEM images of St-PLA specimens with (**a**) 25%, (**b**) 50%, and (**c**) 75% infill rate.

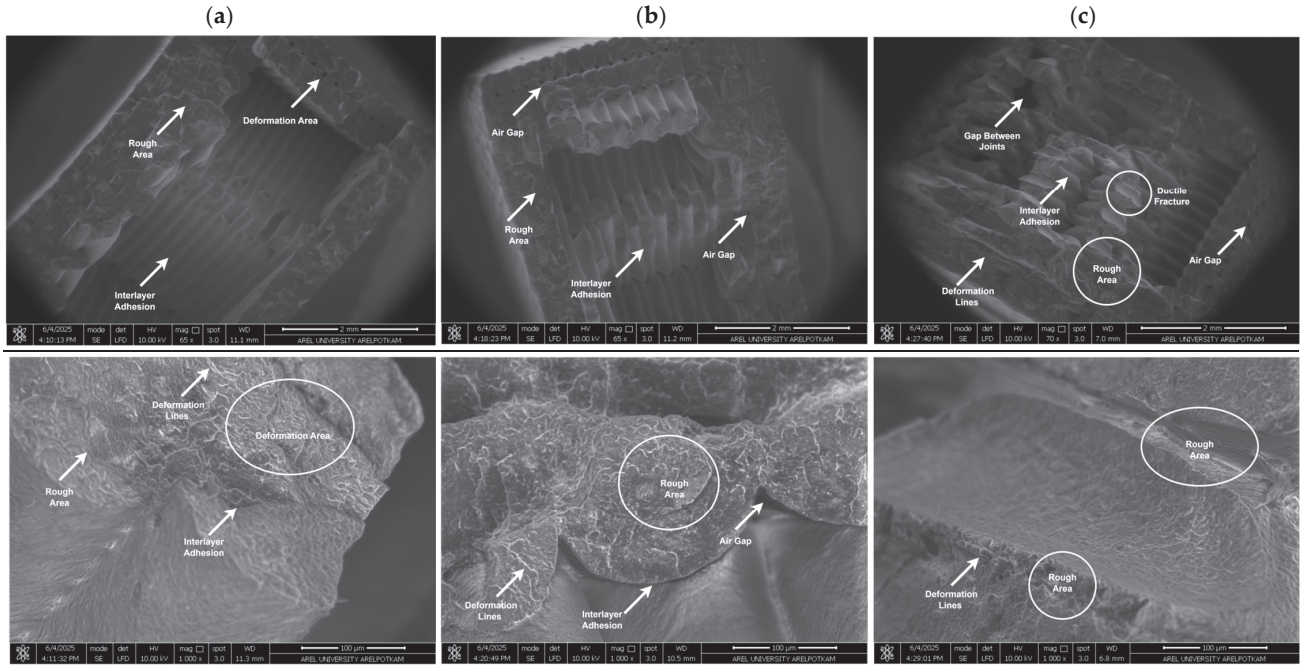

Figure 12. SEM images of St-Re-PLA specimens with (**a**) 25%, (**b**) 50%, and (**c**) 75% infill rate.

3.5. Degradation Tests Results

The degradation behavior of PLA, Re-PLA, St-PLA, and St-Re-PLA specimens was checked in PBS over a full week (168 h). Since these materials are meant to be used in living systems, PBS was used as it closely resembles the body's environment. The specimens with different infill rates (25%, 50%, and 75%) were examined using a UV-Vis spectrophotometer between 200 and 800 nm at various time points, from 1 h up to 7 days. Surprisingly, no detectable degradation was observed throughout the experiment. This likely happened because PLA is hydrophobic, so it does not dissolve in the PBS solution. This is expected, since PLA is widely used for implants due to its stability and resistance to breaking down in

aqueous environments. Overall, none of the specimens released any detectable substances, regardless of the infill rate, whether the PLA was recycled or not, or whether sterilization was applied [49].

3.6. Cytotoxic Tests Results

According to the measurement results of the obtained biocompatibility experiments, % viability values MTT test results are given in Figure 13 as a columnar graph. Viability percentages were determined according to the control group using the % cell viability formula. The cell viability of the control group was accepted as 100%.

The cell viability results from the MTT assay are shown in Figure 13. The control group was used as our baseline, setting their viability at 100%. Looking at the results, PLA specimens with 25% infill showed the highest values, reaching 105% on day 1, decreasing to 100% on day 4, and increasing again to 103% on day 7. Similarly, PLA at 75% infill also showed a recovery on the 7th day (90% → 85% → 88%). For PLA with 50% infill, values stayed lower (80% → 75% → 74%) without recovery.

For St-PLA, most groups decreased gradually, but at 75% infill, viability recovered from 88% on day 1, to 83% on day 4, and back up to 86% on day 7. At lower infills (25% and 50%), values continued to decline (e.g., 25% infill: 102% → 97% → 95%). For St-Re-PLA, only the 25% infill condition showed a small recovery (95% → 91% → 94%), while 50% and 75% infills continued to decline (e.g., 50% infill: 75% → 71% → 70%). For Re-PLA, all conditions showed a gradual decline with no significant recovery. For example, at 25% infill, viability decreased from 92% on day 1, to 89% on day 4, and 88% on day 7.

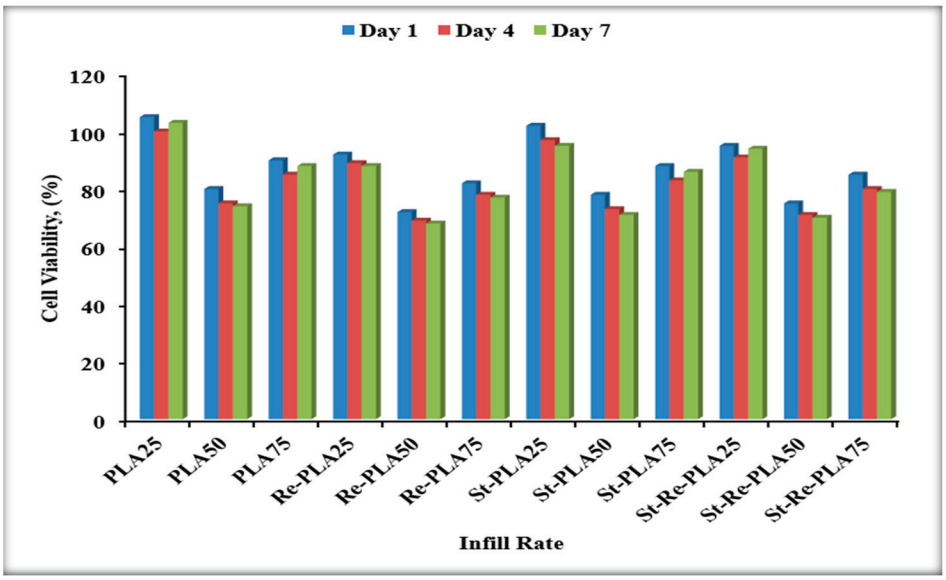

Figure 13. Comparison of MTT test results.

Overall, the ranking of materials in terms of biocompatibility was: 1. PLA > 2. St-PLA > 3. St-Re-PLA>4.Re-PLA. And the ranking of infill rates was: 25% > 75% > 50%. According to the ISO 10993-5 standard [50], if cell survival is above 70%, the material is not considered cytotoxic [50–52]. Based on this, all tested materials and conditions in this study can be considered non-cytotoxic and biocompatible, even though certain groups showed a decline while others exhibited recovery at the 7th day.

The different trends of the cytotoxicity tests are related to the structural changes resulting from the recycling and sterilization processes of the materials. In PLA and some St-PLA groups, cell viability tended to recover on day 7, whereas in Re-PLA, a continuous

decrease was observed due to chain shortening and structural deterioration. In St-Re-PLA, recovery was limited due to the negative effects of both processes. These differences are due to the porosity, surface properties, and the level of interaction with the biological environment, and all specimens are considered non-cytotoxic and biocompatible according to ISO 10993-5 standard, with cell viability above 70%.

3.7. Mathematical Analysis

This study investigates the mechanical properties of PLA-based polymer samples fabricated through the FDM method, focusing on flexural strength (σ_{max}) and surface roughness (Ra), and relates them to manufacturing parameters using multivariate regression models. By assessing both the individual and interactive effects of manufacturing variables, namely infill ratio (X_1, DO), layer thickness (X_2, KK), and printing angle (X_3, UA), the study explored how model behaviors varied across different material types.

The flexural strength (σ_{max}) and surface roughness (Ra) performances σ_{max} of PLA, Re-PLA, St-PLA, and St-Re-PLA specimens were related to the production parameters using X_1 multivariate regression models. When both individual and interactive contributions of production variables such as infill rate (X_1, DO), layer thickness (X_2, KK), and printing orientation (X_3, UA) were evaluated, different model behaviors were investigated according to the material type. Multivariate second-order polynomial regression models were developed depending on the three basic production parameters affecting flexural strength and surface roughness. Taking these models into account, general flexural strength (σ_{max}) and general surface roughness (Ra) models were also developed. The flexural strength (σ_{max}) models are given in Table 4, and the surface roughness (Ra) models are given in Table 5, along with performance evaluation and analysis comments.

Table 4. Flexural strength (σ_{max}) modeling study of PLA, Re-PLA, St -PLA and St -Re-PLA specimens and performance evaluation of the modeling study.

Model	Equation	R^2	MAE	RMSE	Analysis Comment
σ_{max} PLA	$Y = 0.2087 \cdot X_1 + 68.8333 \cdot X_2 + 0.0959 \cdot X_3 + 0.0042 \cdot X_1^2 - 1.8000 \cdot X_1 \cdot X_2 - 0.0009 \cdot X_1 \cdot X_3 + 300.0000 \cdot X_2^2 - 0.8111 \cdot X_2 \cdot X_3 + 0.0017 \cdot X_3^2$	0.87	1.92	2.41	The model has high explanatory power. The effect of layer thickness is evident.
σ_{max} Re-PLA	$Y = 0.0088 \cdot X_1 - 221.0000 \cdot X_2 + 0.4433 \cdot X_3 + 0.0017 \cdot X_1^2 + 0.3733 \cdot X_1 \cdot X_2 - 0.0020 \cdot X_1 \cdot X_3 + 891.1111 \cdot X_2^2 - 1.7926 \cdot X_2 \cdot X_3 - 0.0002 \cdot X_3^2$	0.69	3.30	3.81	For Re-PLA, the model is moderately explanatory; the $X_2{}^2$ effect is dominant.
σ_{max} St -PLA	$Y = -1.0900 \cdot X_1 - 1487.0000 \cdot X_2 - 0.3793 \cdot X_3 + 0.0058 \cdot X_1^2 + 2.4400 \cdot X_1 \cdot X_2 + 0.0016 \cdot X_1 \cdot X_3 + 2973.3333 \cdot X_2^2 + 0.6889 \cdot X_2 \cdot X_3 + 0.0014 \cdot X_3^2$	0.61	5.32	6.27	For St-PLA the $X_2{}^2$ effect is very high but the overall performance of the model is poor.
σ_{max} St -Re-PLA	$Y = -0.3680 \cdot X_1 - 497.6667 \cdot X_2 - 0.1563 \cdot X_3 + 0.0053 \cdot X_1^2 + 3.8800 \cdot X_1 \cdot X_2 + 0.0037 \cdot X_1 \cdot X_3 + 626.6667 \cdot X_2^2 - 0.0222 \cdot X_2 \cdot X_3 + 0.0002 \cdot X_3^2$	0.46	4.53	5.68	The St-Re-PLA model shows greater uncertainty and higher variance.
Unified PLA	$Y = -0.3101 \cdot X_1 - 534.2083 \cdot X_2 + 0.0009 \cdot X_3 + 0.0016 \cdot X_1^2 + 1.2233 \cdot X_1 \cdot X_2 + 0.0006 \cdot X_1 \cdot X_3 + 1197.7778 \cdot X_2^2 - 0.4843 \cdot X_2 \cdot X_3 + 0.0007 \cdot X_3^2$	0.64	1.93	2.51	The generalized model is balanced but has lower explanatory power than the individual PLA models.

Table 5. Surface roughness (Ra) modeling study of PLA, Re-PLA, St-PLA and St-Re-PLA specimens and performance evaluation of the modeling study.

Model	Equation	R^2	MAE	RMSE	Analysis Comment
Ra PLA	$Y = -0.0388 \cdot X_1 - 1.5439 \cdot X_2 + 0.0677 \cdot X_3 + 0.0001 \cdot X_1^2 + 0.1785 \cdot X_1 \cdot X_2 - 0.0004 \cdot X_1 \cdot X_3 + 1.2667 \cdot X_2^2 - 0.0517 \cdot X_2 \cdot X_3 - 0.0004 \cdot X_3^2$	0.34	0.62	0.80	The model has very limited explanatory power. Layer thickness has a negative effect.
Ra Re-PLA	$Y = -0.0529 \cdot X_1 + 20.3478 \cdot X_2 - 0.0526 \cdot X_3 + 0.0004 \cdot X_1^2 + 0.4667 \cdot X_1 \cdot X_2 - 0.0000 \cdot X_1 \cdot X_3 + 129.4222 \cdot X_2^2 + 0.2047 \cdot X_2 \cdot X_3 + 0.0002 \cdot X_3^2$	0.21	0.95	1.17	Low explanatory power; Re- PLA has high variance, X_2 effect is dominant. Variance increased substantially due to recycling. Model is weak.
Ra St-PLA	$Y = 0.0392 \cdot X_1 + 23.0367 \cdot X_2 + 0.0226 \cdot X_3 + 0.0000 \cdot X_1^2 - 0.2042 \cdot X_1 \cdot X_2 - 0.0000 \cdot X_1 \cdot X_3 + 23.3111 \cdot X_2^2 - 0.0931 \cdot X_2 \cdot X_3 + 0.0001 \cdot X_3^2$	0.16	0.93	1.12	The effect of X_2 is in the opposite direction.
Ra St-Re-PLA	$Y = -0.0595 \cdot X_1 + 180.0972 \cdot X_2 + 0.0301 \cdot X_3 + 0.0003 \cdot X_1^2 - 0.0587 \cdot X_1 \cdot X_2 - 0.0004 \cdot X_1 \cdot X_3 + 428.8444 \cdot X_2^2 - 0.1442 \cdot X_2 \cdot X_3 - 0.0001 \cdot X_3^2$	0.25	1.11	1.50	Highest variance. (highest deviation here) The combined effect reduces model performance.
Unified PLA	$Y = -0.0280 \cdot X_1 + 55.4844 \cdot X_2 + 0.0170 \cdot X_3 + 0.0000 \cdot X_1^2 + 0.0956 \cdot X_1 \cdot X_2 - 0.0000 \cdot X_1 \cdot X_3 + 145.7111 \cdot X_2^2 - 0.0211 \cdot X_2 \cdot X_3 - 0.0001 \cdot X_3^2$	0.29	0.51	0.62	The generalized PLA model can predict average behavior more stably across variants (lower MAE), but is weaker than the PLA model in explaining the internal variance of PLA (lower R^2).

Table 4 shows that the performance evaluations of the flexural strength models of PLA, Re-PLA, St-PLA, and St-Re-PLA specimens were carried out using the coefficient of determination (R^2), mean absolute error (MAE), and root mean square error (RMSE) criteria. The highest explanatory power (R^2 = 0.87) was observed in the PLA model, whereas the St-Re-PLA model exhibited lower fit and higher variance (R^2 = 0.46). The combined model obtained by averaging all PLA types provided a balanced generalization with a value of R^2 = 0.64. The regression models obtained successfully demonstrated the effect of production parameters on mechanical behavior; layer thickness, in particular, stood out as the most significant influencing variable among all variants.

When Table 5 is examined, it is observed that the St-PLA group provided the highest explanatory power with R^2 = 0.68, while the St-Re-PLA group had the lowest fit with R^2 = 0.12. Layer thickness (X_2) was the most decisive parameter for surface roughness in almost all variants, and the surface was observed to be wavier and irregular, especially in thicker layers.

The predictability of surface roughness decreased in recycled and sterilized PLA specimens. This is consistent with the literature that recycling weakens the polymer chain structure and thermal degradation causes microscopic defects on the surface.

In conclusion, although the modeling of Ra values was not as successful as that of mechanical strength, regression models yielded statistically reliable results, especially for certain groups such as the St-PLA variant. These findings demonstrate the influence of

production parameters on surface quality and, in agreement with the literature, show that surface behavior can be quite variable [53].

When the mechanical and surface roughness modeling studies for PLA, Re-PLA, St-PLA and St-Re-PLA were evaluated, the flexural strength (σ_{max}) and surface roughness (Ra) properties of PLA, Re-PLA, St-PLA, and St-Re-PLA specimens were investigated with multivariate second order regression models depending on the production parameters. While the explanatory power of the flexural strength models was observed ($R^2 \geq 0.69$), the surface roughness models had a lower explanatory power ($R^2 \leq 0.34$). This can be explained by the fact that while the mechanical properties show more direct and regular relationships with the production parameters, Ra is more susceptible to microstructural defects and external effects. In particular, layer thickness (X_2) was the most decisive parameter for both strength and surface quality, while the printing orientation (X_3) had an impact on bending strength but limited its effect on Ra. Recycling and sterilization processes increased variance, which in turn increased the margin of error, particularly in the Ra models. The results indicate that the mechanical strength of PLA-based parts produced with FDM can be predicted through parametric modeling, but surface roughness requires more complex modeling approaches.

In conclusion, because flexural strength in PLA specimens exhibits strong relationships with manufacturing parameters, regression modeling allowed for higher accuracy than surface roughness data. However, because surface roughness has more complex micro-level effects, more advanced, nonlinear approaches may be necessary.

The unstable response of recycled or sterilized polymer materials to the forming angle can be explained by orientation-dependent structural weaknesses. The deformation trends observed with increasing forming angle may be a result of internal structural irregularities in these materials [11,45]. Therefore, models developed should consider not only linear variables but also the thermomechanical history and anisotropic behavior of the material.

Surface roughness models have shown that classical regression techniques are inadequate with low R^2 and high variance. In this context, spline regression, Random Forest (RF), Support Vector More flexible models such as Machines (SVM) are recommended [54].

The findings demonstrate the impact of FDM process parameters on both the mechanical and surface properties of polymer-based samples using a multivariate approach. The study makes a significant contribution to literature by providing a model-based comparative analysis of the responses of different material types to post-production processes (recycling, sterilization).

4. Conclusions

This conclusion synthesizes the experimental and analytical results spanning flexural strength, deformation, surface roughness, SEM morphology, degradation/cytotoxicity, and regression modeling to elucidate how infill rate, layer thickness, and printing orientation govern the performance of PLA, Re-PLA, St-PLA, and St-Re-PLA.

- It was observed that the infill rate, layer thickness, and printing orientation had significant effects on the flexural strength of PLA, Re-PLA, St-PLA, and St-Re-PLA specimens. As the infill rate increased in PLA and Re-PLA, the flexural strength values increased, while sterilization and recycling processes made the behavior of the materials more wavy. In St-PLA specimens, layer thickness was found to establish a critical threshold, while in St-Re-PLA, recycling and sterilization together led to negative outcomes. Overall, it was concluded that production parameters must be adjusted more carefully, particularly in recycled and sterilized biopolymers.

- In PLA specimens, the infill rate, layer thickness, and printing orientation had uniform and significant effects on deformation, while these effects were more limited in Re-PLA. In St-PLA and St-Re-PLA specimens, the results were more variable, with the effects of layer thickness and printing orientation becoming irregular. In general, sterilization and recycling processes make the deformation behavior of materials more unpredictable, while the most regular and high deformation was obtained in PLA specimens.
- Surface roughness tests showed that the surface became smoother in all specimen types as the infill rate increased. It was observed that the layer thickness first increased the surface roughness and then decreased it after a certain value. Printing orientation was the parameter with the most negative effect on all specimens, with surface marks becoming more pronounced at 45° and 90° angles. In general, the increase in roughness was more noticeable in PLA and St-PLA, while in St-Re-PLA, surface quality reached its best level at high infill rates.
- SEM images showed that as the infill rate increased, the voids in the specimens decreased and the adhesion between filaments improved. While a more brittle fracture behavior was observed in PLA and Re-PLA specimens, plastic deformation traces became more pronounced, and ductile fracture properties became more prominent in St-PLA and St-Re-PLA. These findings are consistent with the surface roughness results and reveal that sterilization and recycling processes significantly affect the fracture morphology of the material.
- In our tests, none of the PLA, Re-PLA, St-PLA, or St-Re-PLA specimens, whether filled at 25%, 50%, or 75%, showed any degradation at all. When we checked how well the materials worked with cells, PLA gave the best results, St-PLA was very close, St-Re-PLA was slightly lower, and Re-PLA showed the lowest values, but still remained non-cytotoxic.
- The regression analyses demonstrated that second-order polynomial models provide robust predictive capability for mechanical properties, particularly bending strength, with layer thickness emerging as the dominant process parameter for PLA. By contrast, surface roughness exhibited lower predictability and higher error margins, underscoring the limitations of classical regression approaches in capturing microstructural complexities. These findings affirm the adequacy of polynomial regression for mechanical performance prediction, while simultaneously indicating the necessity of more advanced modeling strategies for surface quality assessment.
- Considering that steam sterilization adversely affected the performance of recycled specimens, future studies may investigate alternative sterilization methods such as ethylene oxide, gamma irradiation, or plasma treatment, which could potentially preserve the mechanical integrity and surface quality of PLA-based biomaterials.

Author Contributions: Conceptualization, Ş.A., D.C. and G.K.; methodology, Ş.A., G.K., Y.E.T. and Y.K.; validation, Ş.A. and G.K.; formal analysis, Ş.A., G.K., D.C. and Y.K.; investigation, Ş.A. and Y.K.; writing—original draft preparation, Ş.A., G.K., D.C., Y.E.T. and Y.K.; writing—review and editing, Ş.A., D.C. and G.K.; supervision, Ş.A.; project administration, Ş.A., D.C., Y.E.T. and G.K.; funding acquisition, Ş.A. and Y.K. All authors have read and agreed to the published version of the manuscript.

Funding: This work was supported by the Scientific Research Projects Coordination Unit of Istanbul Yeni Yuzyil University, project number: İYYÜ-BAP-AP-2025-22. The authors would like to thank the Scientific Research Projects Coordination Unit of Istanbul Yeni Yuzyil University for their support in

this matter. This publication was supported by the Scientific Research Projects Coordination Unit of Istanbul Yeni Yuzyil University.

Institutional Review Board Statement: Not applicable.

Data Availability Statement: The original contributions presented in this study are included in the article. Further inquiries can be directed to the corresponding author(s).

Acknowledgments: We would like to thank the Scientific Research Projects Coordination Unit of Istanbul Yeni Yuzyil University for supporting this study under project number İYYÜ-BAP-AP-2025-22.

Conflicts of Interest: The authors declare no conflicts of interest.

References

1. Vaz, V.M.; Kumar, L. 3D Printing as a Promising Tool in Personalized Medicine. *AAPS PharmSciTech* **2021**, *22*, 49. [CrossRef] [PubMed]
2. Kantaros, A. 3D Printing in Regenerative Medicine: Technologies and Resources Utilized. *Int. J. Mol. Sci.* **2022**, *23*, 14621. [CrossRef] [PubMed]
3. Okolie, O.; Stachurek, I.; Kandasubramanian, B.; Njuguna, J. 3D Printing for Hip Implant Applications: A Review. *Polymers* **2020**, *12*, 2682. [CrossRef] [PubMed]
4. Tofail, S.A.; Koumoulos, E.P.; Bandyopadhyay, A.; Bose, S.; O'Donoghue, L.; Charitidis, C. Additive Manufacturing: Scientific and Technological Challenges, Market Uptake and Opportunities. *Mater. Today* **2018**, *21*, 22–37. [CrossRef]
5. Buj-Corral, I.; Tejo-Otero, A.; Fenollosa-Artés, F. Development of Am Technologies for Metals in the Sector of Medical Implants. *Metals* **2020**, *10*, 686. [CrossRef]
6. Ratner, B.D.; Hoffman, A.S.; Schoen, F.J.; Lemons, J.E. Biomaterials Science: An Introduction to Materials in Medicine. *MRS Bull.* **2004**, *5*, 162–164.
7. Pugliese, R.; Beltrami, B.; Regondi, S.; Lunetta, C. Polymeric Biomaterials for 3D Printing in Medicine: An Overview. *Ann. 3D Print. Med.* **2021**, *2*, 100011. [CrossRef]
8. Haryńska, A.; Carayon, I.; Kosmela, P.; Brillowska-Dąbrowska, A.; Łapiński, M.; Kucińska-Lipka, J.; Janik, H. Processing of Polyester-Urethane Filament and Characterization of FFF 3D Printed Elastic Porous Structures with Potential in Cancellous Bone Tissue Engineering. *Materials* **2020**, *13*, 4457. [CrossRef]
9. Abdullah, K.A.; Reed, W. 3D Printing in Medical Imaging and Healthcare Services. *J. Med. Radiat. Sci.* **2018**, *65*, 237–239. [CrossRef]
10. Kucharska-Jastrząbek, A.; Chmal-Fudali, E.; Rudnicka, D.; Kosińska, B. Effect of Sterilization on Bone Implants Based on Biodegradable Polylactide and Hydroxyapatite. *Materials* **2023**, *16*, 5389. [CrossRef]
11. Fuentes, J.M.; Arrieta, M.P.; Boronat, T.; Ferrándiz, S. Effects of Steam Heat and Dry Heat Sterilization Processes on 3D Printed Commercial Polymers Printed by Fused Deposition Modeling. *Polymers* **2022**, *14*, 855. [CrossRef]
12. Beltrán, F.R.; Arrieta, M.P.; Moreno, E.; Gaspar, G.; Muneta, L.M.; Carrasco-Gallego, R.; Yáñez, S.; Hidalgo-Carvajal, D.; de la Orden, M.U.; Martínez Urreaga, J. Evaluation of the Technical Viability of Distributed Mechanical Recycling of PLA 3D Printing Wastes. *Polymers* **2021**, *13*, 1247. [CrossRef]
13. Balart, R.; Garcia-Garcia, D.; Fombuena, V.; Quiles-Carrillo, L.; Arrieta, M.P. Biopolymers from Natural Resources. *Polymers* **2021**, *13*, 2532. [CrossRef]
14. PlasticsEurope. *Plastics—The Facts 2019. An Analysis of European Plastics Production, Demand and Waste Data*; Plastic Europe: Brussels, Belgium, 2019; pp. 1–42.
15. Perez, M.; Block, M.; Espalin, D.; Winker, R.; Hoppe, T.; Medina, F.; Wicker, R. Sterilization of FDM-Manufactured Parts. In Proceedings of the 2012 International Solid Freeform Fabrication Symposium, Austin, TX, USA, 6–8 August 2012.
16. Rogers, W.J. Steam and Dry Heat Sterilization of Biomaterials and Medical Devices. In *Sterilisation of Biomaterials and Medical Devices*; Elsevier: Amsterdam, The Netherlands, 2012; pp. 20–55.
17. Frizziero, L.; Santi, G.M.; Leon-Cardenas, C.; Ferretti, P.; Sali, M.; Gianese, F.; Crescentini, N.; Donnici, G.; Liverani, A.; Trisolino, G. Heat Sterilization Effects on Polymeric, FDM-Optimized Orthopedic Cutting Guide for Surgical Procedures. *J. Funct. Biomater.* **2021**, *12*, 63. [CrossRef]
18. Zbyrad, B.; Zaborniak, M.; Kochmański, Ł.; Jasik, K.; Kluczyński, J.; Budzik, G.; Turek, P. Evaluation of High-Temperature Sterilization Processes: Their Influence on the Mechanical Integrity of Additively Manufactured Polymeric Biomaterials. *Materials* **2025**, *18*, 1356. [CrossRef] [PubMed]

19. Atakok, G.; Kam, M.; Koc, H.B. Tensile, Three-Point Bending and Impact Strength of 3D Printed Parts Using PLA and Recycled PLA Filaments: A Statistical Investigation. *J. Mater. Res. Technol.* **2022**, *18*, 1542–1554. [CrossRef]
20. Günay, M.; Gündüz, S.; Yılmaz, H.; Yaşar, N.; Kaçar, R. PLA Esaslı Numunelerde Çekme Dayanımı Için 3D Baskı Işlem Parametrelerinin Optimizasyonu. *Politek. Derg.* **2020**, *23*, 73–79. [CrossRef]
21. Kaptan, A.; Kartal, F. The Effect of Fill Rate on Mechanical Properties of PLA Printed Samples. *J. Inst. Sci. Technol.* **2020**, *10*, 1919–1927. [CrossRef]
22. Hanon, M.M.; Dobos, J.; Zsidai, L. The Influence of 3D Printing Process Parameters on the Mechanical Performance of PLA Polymer and Its Correlation with Hardness. *Procedia Manuf.* **2021**, *54*, 244–249. [CrossRef]
23. Maraveas, C.; Kyrtopoulos, I.V.; Arvanitis, K.G. Evaluation of the Viability of 3D Printing in Recycling Polymers. *Polymers* **2024**, *16*, 1104. [CrossRef]
24. Garnica-Bohórquez, I.; Güiza-Argüello, V.R.; López-Gualdrón, C.I. Effect of Sterilization on the Dimensional and Mechanical Behavior of Polylactic Acid Pieces Produced by Fused Deposition Modeling. *Polymers* **2023**, *15*, 3317. [CrossRef] [PubMed]
25. Neijhoft, J.; Henrich, D.; Kammerer, A.; Janko, M.; Frank, J.; Marzi, I. Sterilization of PLA after Fused Filament Fabrication 3D Printing: Evaluation on Inherent Sterility and the Impossibility of Autoclavation. *Polymers* **2023**, *15*, 369. [CrossRef] [PubMed]
26. Lerouge, S. Introduction to Sterilization: Definitions and Challenges. In *Sterilisation of Biomaterials and Medical Devices*; Elsevier: Amsterdam, The Netherlands, 2012; pp. 1–19.
27. Dai, Z.; Ronholm, J.; Tian, Y.; Sethi, B.; Cao, X. Sterilization Techniques for Biodegradable Scaffolds in Tissue Engineering Applications. *J. Tissue Eng.* **2016**, *7*, 1–13. [CrossRef] [PubMed]
28. Frizziero, L.; Santi, G.M.; Leon-Cardenas, C.; Donnici, G.; Liverani, A.; Papaleo, P.; Napolitano, F.; Pagliari, C.; Di Gennaro, G.L.; Stallone, S. In-House, Fast FDM Prototyping of a Custom Cutting Guide for a Lower-Risk Pediatric Femoral Osteotomy. *Bioengineering* **2021**, *8*, 71. [CrossRef]
29. Ferràs-Tarragó, J.; Sabalza-Baztán, O.; Sahuquillo-Arce, J.M.; Angulo-Sánchez, M.Á.; De-La-Calva Ceinos, C.; Amaya-Valero, J.V.; Baixauli-García, F. Autoclave Sterilization of an In-House 3D-Printed Polylactic Acid Piece: Biological Safety and Heat-Induced Deformation. *Eur. J. Trauma Emerg. Surg.* **2022**, *48*, 3901–3910. [CrossRef]
30. *ISO 178:2019*; Plastics-Determination of Flexural Properties. ISO: Geneva, Switzerland, 2019. Available online: http://www.iso.org/standard/70513.html (accessed on 20 August 2025).
31. Jaya Christiyan, K.G.; Chandrasekhar, U.; Venkateswarlu, K. Flexural Properties of PLA Components Under Various Test Condition Manufactured by 3D Printer. *J. Inst. Eng. India Ser. C* **2018**, *99*, 363–367. [CrossRef]
32. Özsoy, K.; Erçetin, A.; Çevik, Z.A. Comparison of Mechanical Properties of PLA and ABS Based Structures Produced by Fused Deposition Modelling Additive Manufacturing. *EJOSAT* **2021**, *27*, 802–809. [CrossRef]
33. Tymrak, B.M.; Kreiger, M.; Pearce, J.M. Mechanical Properties of Components Fabricated with Open-Source 3-D Printers Under Realistic Environmental Conditions. *Mater. Des.* **2014**, *58*, 242–246. [CrossRef]
34. Rajpurohit, S.R.; Dave, H.K. Effect of Process Parameters on Tensile Strength of FDM Printed PLA Part. *Rapid Prototyp. J.* **2018**, *24*, 1317–1324. [CrossRef]
35. Alafaghani, A.; Qattawi, A.; Alrawi, B.; Guzman, A. Experimental Optimization of Fused Deposition Modelling Processing Parameters: A Design-for-Manufacturing Approach. *Procedia Manuf.* **2017**, *10*, 791–803. [CrossRef]
36. Torres, J.; Cotelo, J.; Karl, J.; Gordon, A.P. Mechanical Property Optimization of FDM PLA in Shear with Multiple Objectives. *JOM* **2015**, *67*, 1183–1193. [CrossRef]
37. Lanzotti, A.; Grasso, M.; Staiano, G.; Martorelli, M. The Impact of Process Parameters on Mechanical Properties of Parts Fabricated in PLA with an Open-Source 3-D Printer. *Rapid Prototyp. J.* **2015**, *21*, 604–617. [CrossRef]
38. Arefin, A.M.E.; Khatri, N.R.; Kulkarni, N.; Egan, P.F. Polymer 3D Printing Review: Materials, Process, and Design Strategies for Medical Applications. *Polymers* **2021**, *13*, 1499. [CrossRef]
39. Berg, M.C.; Stump, B.A. Effect of Sterilization on the Properties of Polylactide Materials. *J. Biomed. Mater. Res. Part B Appl. Biomater.* **2009**, *88*, 129–137.
40. Gleadall, A.; Pan, J.; Kruft, M. Effects of Sterilization on 3D Printed Polymer Medical Devices. *Addit. Manuf.* **2019**, *26*, 138–145.
41. Mazzanti, V.; Malagutti, L.; Mollica, F. Fused Deposition Modelling (FDM) Process Parameters Optimization to Maximize the Mechanical Properties of Printed Parts Using a Design of Experiment Approach. *Materials* **2019**, *12*, 1861.
42. Pallari, J.; Dalgarno, K.; Woodburn, J. Mass Customization of Foot Orthoses for Rheumatoid Arthritis Using Selective Laser Sintering. *IEEE Trans. Biomed. Eng.* **2010**, *57*, 1750–1756. [CrossRef]
43. Scaffaro, R.; Maio, A.; Gulino, E.F.; Morreale, M. Recycling of PLA for 3D Printing: The Effect of Thermal-Mechanical Degradation on Printed Part Performance. *Polym. Degrad. Stab.* **2019**, *165*, 110–116.
44. Tao, Y.; Wang, Y.; Deng, Y.; Wang, Z. Effect of Sterilization on Mechanical and Thermal Properties of 3D Printed Polymers. *Addit. Manuf.* **2020**, *34*, 101192.

45. Spoerk, M.; Holzer, C.; Gonzalez-Gutierrez, J. Anisotropic Mechanical Properties of Fused Filament Fabricated Parts Described by Classical Laminate Theory. *Compos. Part A Appl. Sci. Manuf.* **2017**, *105*, 35–45.
46. Diederichs, E.; Picard, M.; Chang, B.P.; Misra, M.; Mohanty, A. Extrusion Based 3D Printing of Sustainable Biocomposites from Biocarbon and Poly(Trimethylene Terephthalate). *Molecules* **2021**, *26*, 4164. [CrossRef] [PubMed]
47. Benabderazag, K.; Belouadah, Z.; Guebailia, M.; Toubal, L. Characterization of Thermomechanical Properties and Damage Mechanisms Using Acoustic Emission of Lygeum Spartum PLA 3D-Printed Biocomposite with Fused Deposition Modelling. *Compos. Part A Appl. Sci. Manuf.* **2024**, *186*, 108426. [CrossRef]
48. Liu, H.; He, H.; Peng, X.; Huang, B.; Li, J. Three-Dimensional Printing of Poly(Lactic Acid) Bio-Based Composites with Sugarcane Bagasse Fiber: Effect of Printing Orientation on Tensile Performance. *Polym. Adv. Technol.* **2019**, *30*, 910–922. [CrossRef]
49. Hajilou, N.; Mostafayi, S.S.; Yarin, A.L.; Shokuhfar, T.A. Comparative Review on Biodegradation of Poly (Lactic Acid) in Soil, Compost, Water, and Wastewater Environments: Incorporating Mathematical Modeling Perspectives. *AppliedChem* **2024**, *5*, 1. [CrossRef]
50. Wallin, R.F.; Arscott, E.F. *A Practical Guide to ISO 10993-5: Cytotoxicity*; Medical Device and Diagnostic Industry: Santa Monica, CA, USA, 1998; Volume 20, pp. 96–98.
51. Altınsoy, Ş.; Erkan, S.; Üllen, N.B.; Ateş, S.C.; Evcil, N. Evaluation of Surface Properties of Modified Ti6Al4V Alloy with Copper Nanoparticles Organic Nanostructure for Biomedical Applications: Dependency on Anticorrosive, Antibacterial, and Biocompatibility. *Corros. Rev.* **2024**, *43*, 361–380. [CrossRef]
52. Altınsoy, Ş.; Kızılbey, K.; İlim, H.B. Green Synthesis of Ag and Cu Nanoparticles Using E. Telmateia Ehrh Extract: Coating, Characterization, and Bioactivity on PEEK Polymer Substrates. *Materials* **2024**, *17*, 5501. [CrossRef]
53. Keşkekçi, A.B.; Özkahraman, M.; Bayrakçı, H.C. A Review on the Impact of Polylactic Acid (PLA) Material on Products Manufactured Using Fused Deposition Modeling (FDM) Additive Manufacturing Method. *Gazi Mühendislik Bilim. Derg.* **2023**, *9*, 158–173. [CrossRef]
54. Li, B.; Yang, J.; Gu, H.; Jiang, J.; Zhang, J.; Sun, J. Surface Roughness of PLA Parts by FDM with Chemical Treatment. *J. Phys. Conf. Ser.* **2021**, *1948*, 012199. [CrossRef]

polymers

MDPI

Article

Cross-Linked Poly(methyl methacrylate) Nanocomposites' Synthesis, Characterization, and Antibacterial Effects

Nazeeha S. Alkayal [1,*] and Mashail A. Al Ghamdi [2]

[1] Chemistry Department, Faculty of Science, King Abdulaziz University, P.O. Box 80203, Jeddah 21589, Saudi Arabia
[2] Biological Department, Faculty of Science, King Abdulaziz University, P.O. Box 80200, Jeddah 21589, Saudi Arabia
* Correspondence: nalkayal@kau.edu.sa

Abstract: Polymer networks were synthesized using the condensation method between PMMA and melamine as cross-linkers. CuO nanoparticles (NPs) and activated carbon (AC) were used as a filler. The final products PMMA/Mel, PMMA/Mel-CuO, and PMMA/Mel-AC were tested for antibacterial activities against *E.coli* and *S. aureus.* The chemical structure and composition, thermal properties, and surface morphology of the new PMMA/Mel-based nanocomposites were investigated by various techniques. The XRD and EDX results showed the successful incorporation of CuO NPs and AC into the polymer matrix. Also, the thermal stability of the PMMA/Mel polymer was significantly enhanced after adding CuO nanoparticles. This finding showed that the PMMA/Mel-CuO and PMMA/Mel-AC nanocomposites have greater activity against both bacteria than PMMA/Mel. The PMMA/Mel-CuO and PMMA/Mel-AC polymers showed high activity against *S. aureus* bacteria, with inhibition zones of 22.6 mm and 11.3 mm, respectively. This confirms that small-sized nanoparticles have an effective role in killing bacterial cells.

Keywords: cross-linked PMMA; melamine; CuO nanoparticle; activated carbon; antibacterial; *E. coli*; *S. aureus*

1. Introduction

Microorganisms have an important role in regulating all living things, including humans, via biogeochemical processes. Infection occurs when a microbe escapes or impairs the host's defense mechanisms; such germs are termed pathogenic bacteria [1,2]. Bacterial resistance to antibacterial drugs occurs as a result of genetic changes caused by the misuse and overuse of antibiotics [3]. As a result, there is a compelling need to create novel critical antibacterial agents to combat antibiotic resistance.

PMMA (poly methyl methacrylate) has been utilized as an antibacterial substance in the medical industry over the last three-quarters of a century. Nonetheless, its antibacterial properties remain insufficient; when carrying out anatomical restoration and tissue implanting for tissue regeneration, biomaterial-derived infections can occur once the materials are attached to the body [4,5]. The development of biomaterials using nanotechnology is seen as a strong option that has lately been used to overcome this barrier.

To treat bacterial infections, different nanoparticles with antibacterial properties have emerged as a new class of biological chemicals, which have a strong influence on bacterial proliferation [6]. As part of this trend, PMMA was combined with metals, metal oxides, and carbon-based nanoparticles to create nanocomposites with enhanced antibacterial

properties [7]. In this regard, PMMA was treated with cross-linking agents to generate a porous skeleton, which was then filled with nanoparticles. Antibacterial drugs hinder cell wall and protein production, DNA damage, and bacterial metabolism, all of which end in bacterial death [8].

According to the literature, copper oxide (CuO) has several functions, including antibacterial capabilities [9–18]. Copper oxide nanostructures have been shown to have higher antibacterial activity than other metal oxides [19,20]. Furthermore, they are less costly than other metals such as Ag, may be readily disseminated in polymeric materials, and are used as implant substances [21]. In the same vein, low-cost activated carbon has outstanding antibacterial action and can be simply produced from biowaste-derived compounds [22–25]. It has a greater surface area, homogenous particle size, biocompatibility, and environmental friendliness, all of which contribute to its excellent bacterial adsorption efficiency [26].

Research studies have revealed the antibacterial effects of several nanoparticles. For example, Giti et al. discovered that adding CuO nanoparticles at concentrations of 2.5% and 7.5% to PMMA resin improves its antibacterial efficacy against *S. salivarius*, *S. sanguis*, and *C. dubliniensis* bacterial strains [27]. Sathya et al. created a PMMA nanocomposite with 0.1% *w*/*v* copper oxide NPs (PMMA-CuO), which showed antibacterial efficacy against *E. coli*. Meanwhile, a cetyl trimethyl ammonium bromide-capped CuO (PMMA-CuO (CTAB)) nanocomposite (0.1% *w*/*v*) was extremely effective against *S. aureus* [28]. Glazkova et al. created a 5 wt.% $CuFe_2O_4/Cu_2O/CuO$/PMMA nanocomposite, which showed 100% and 99.94% antibacterial effectiveness against *E. coli* and MRSA bacterial strains, respectively [29]. Varghese et al. investigated the synthesis of activated carbon from kitchen soot as a biowaste [30]. In their work, the antibacterial activity of AC nanoparticles was tested against both Gram-negative and Gram-positive bacterial strains with inhibition zones ranging from 19 to 29 mm. In another study, AC was produced from the Passiflora foetida plant and evaluated against twelve different bacterial strains using an agar-well diffusion technique. The data showed that AC has effective antibacterial action against practically all microorganisms [31].

In the present research, we prepared PMMA/Mel-CuO and PMMA/Mel-AC nanocomposites using a polycondensation reaction, and their structural and morphological characteristics were investigated by TGA, FT-IR, SEM, XRD, and elemental analysis to confirm the chemical distribution. The biological properties of the two nanocomposites were studied and compared with the cross-linked PMMA/Mel without NPs. All of the previous research findings were considered in our investigation, exploration, and implementation of the composite when exposed to *E. coli* as a Gram-negative and resistant bacteria. Our findings suggest that this is the optimum polymer composite to apply against *E. coli* gastrointestinal tract infections.

2. Experimental Section

2.1. Materials

Alfa Aesar (Haverhill, MA, USA) provided poly (methyl methacrylate) (PMMA, M_{wt} = 300 k), while BDH laboratory reagents supplied dimethyl sulfoxide (DMSO 99%) and melamine (97.5%). The Nano Center provided activated carbon and copper oxide nanoparticles (CuO < 100 nm). All compounds were utilized without additional purification.

2.2. Instrumentation

Thermogravimetric analysis (TGA) was carried out using a TGA4724 at a heating rate of 10 °C/min between 25 and 500 °C in a N_2 environment. The Nicolet Magna 6700 FT spectrometer (Thermo Fisher Scientific, Waltham, MA, USA) was used to examine the Fourier

transform infrared spectra (FTIR) in the 400–4000 cm^{-1} range. X-ray diffraction (XRD) patterns were analyzed using a Bruker D8 Advance and Cu Kα radiation (wavelength 1.5418 Å) at 40 kV and 40 Ma (Bruker, Billerica, MA, USA). The patterns were gathered between 2θ of 10° and 60°, with a scan speed of 1.5°/min. Imaging was performed using an FEI TENEO VS microscope with an EDAX detector (Thermo Fisher Scientific, Waltham, MA, USA). To prevent sample charging during imaging, the polymer sample was attached to an aluminum stub with sticky carbon tape and sputter coated with 3 nm iridium.

2.3. Synthesis of PMMA/Mel, PMMA/Mel-CuO, and PMMA/Mel-AC Nanocomposites

PMMA/Mel was created in accordance with the prior work [32], whereby 1 g of PMMA and 20% w/w melamine were added to 30 mL DMSO and heated to 175 °C for 72 h. After cooling, the product was filtered and washed with methanol, THF, and dichloromethane, yielding 85%.

PMMA/Mel-CuO and PMMA/Mel-AC nanocomposites were created utilizing in situ polymerization. Here, 1 g of PMMA was dissolved in 30 mL DMSO, and 0.1 g of CuO nanoparticles was stirred into the PMMA solution before being ultrasonically agitated for 10 min. Melamine was then added as a cross-linker, and the mixture was refluxed for 72 h at 175 °C with constant shaking. Following cooling, the product was filtered and washed with methanol, THF, and di-chloromethane, yielding 87%. The assay of each drug/antibiotic's loaded content was performed using UV-spectroscopy on the suitable Lambda max (Shimadzu, Kyoto, Japan).

2.4. The Antibacterial Activities of PMMA/Mel-CuO and PMMA/Mel-AC Nanocomposites and PMMA/Mel

2.4.1. Preparation of the Inoculums

Two fresh strains of bacteria were used in the experiments; one was *Staphylococcus aureus* as a Gram-positive bacterium, and the other was *Escherichia coli* as a Gram-negative bacterium. These were cultured on Muller–Hinton agar plates, and inoculums were prepared from a 24 h old culture and then incubated overnight at 37 °C. The inoculums from both strains were inoculated and suspended in 2 different 50 mL sterile Muller–Hinton broths by sterile cotton swapping. The absorbance (at 540 nm) was determined and measured for the 2 cultures after the incubation period at 37 °C. Then, the OD was adjusted to reach 1.5×10^8 CFU/mL of bacterial cells [33].

2.4.2. Determination of the Antibacterial Activity of (PMMA) Polymers Using the Agar-Well Diffusion Method

Evaluation of the antibacterial activity of three polymer solutions was performed with the agar-well diffusion method [33]. In a sterile water McFarland tube, 100 µL of each previous fresh bacterial culture was suspended to reach 1.5×10^8 CFU/mL as the standard value of the bacterial count. The bacterial suspension was spread over an MHA plate using a sterilized swab. Three holes with a diameter of 6 mm were punched by a sterile cork-borer in every bacterial culture plate. Then, 0.1 g of each polymer was suspended in 0.5 mL of DMSO and vortexed for 5 min. About 50 µL of each polymer was added to each well. After 18–24 h of incubation at 37 °C, the halo (clear) zones of inhibition of bacterial growth were then measured in millimeters. The above technique was performed in triplicate for the suggested replications. Lastly, we inoculated a plate of *E. coli* and *S. aureus* and applied different antibiotics to determine their resistance to the bacteria in MHA media when incubated for 24 h at 37 °C.

2.4.3. Antibiotics

CPM: Cefepime, GM: Gentamycin, C: Chloramphenicol, OX: Oxacillin, VA: Vancomycin, FC: Fusidic Acid, TS: Trimethoprim/Sulfamethoxazole, CD: Clindamycin, KF: Cephalothin, AP: Amoxicillin/Clavulanic Acid, E: Erythromycin, PG: Penicillin.

2.4.4. Antibiotic Sensitivity Assay for Bacteria

E. coli pathogenic bacteria was tested against twelve antibiotics to determine their susceptibility. The bacteria were cultured overnight in nutritional broth for activation, determined by measuring the optical density (OD) at 600 nm with a UV-visible spectrophotometer, and, subsequently, standardized to 0.1 McFarland standards (3107 CFU/mL). Later, the bacterial suspension was dispersed on MHA. The agar was then covered with antibiotic discs and incubated at 37 °C for 24 h. Later, the sizes of the zones of inhibition were measured and reported [34].

2.4.5. Determination of the Antibacterial Activity of (PMMA) Polymers Using the Colony Count Method

The antibacterial activity levels of the PMMA/Mel nanocomposite polymers were studied by the viable cell colony count method (CFU) against *E. coli*. Firstly, all sample of polymers were immersed in 4 mL nutrient broth containing $\sim 10^6$–10^7 colony-forming units per mL (CFU/mL). Then, the solution was shaken at 37 °C. A flask containing bacteria and no sample was used as the control. After 2 h of incubation, 0.2 mL of bacterial culture was removed from the flask, and serial dilutions were repeated with each initial sample. Then, 50 µL diluent of the sample was spread on MHA plates and incubated at 37 °C for 24 h. The number of viable microorganism colonies was counted manually using a pen and a click-counter and multiplied by the dilution factor. The percentage of inhibition of each film was calculated with the following equation (ASTM E2149-20) [35]:

$$\text{Mortality}(\%) = \text{B} - \text{A}/\ \text{B} \times 100$$

where B and A are the mean numbers of bacteria in the control samples (CFU/sample) and treated samples after 24 h of incubation (CFU/sample), respectively. The above technique was performed in triplicate for the suggested replications [36].

3. Results and Discussion

3.1. Structural Investigation

As described in our previous research article [32], the linear PMMA was chemically reacted using the polycondensation reaction with melamine as a cross-linking agent to form a cross-linked PMMA/Mel polymer network. Then, the prepared PMMA/Mel was incorporated by adding CuO and activated carbon nanoparticles to produce PMMA/Mel-CuO and PMMA/Mel-AC nanocomposites. Figure 1 gives a schematic representation of the methods for preparing the PMMA/Mel-CuO and PMMA/Mel-AC nanocomposites.

The FT-IR spectrum was investigated in the range of 600–4000 cm^{-1} and is presented in Figure 2a. The formation of PMMA/Mel cross-linked polymer was confirmed by the appearance of a band at 1700 cm^{-1} of amide carbonyl functional groups. Also, other bands at around 3000 cm^{-1} and 1100 cm^{-1} were noted, which are related to the N-H bond of the stretching and bending vibrations of the secondary amide, as illustrated in our previous work. This indicates successful condensation between melamine monomers (the cross-linker) and the linear PMMA. After the addition of nanoparticles, i.e., CuO and AC, no

obvious change was observed in the FT-IR spectra, suggesting that there are no covalent bonds formed between PMMA/Mel and NPs [29].

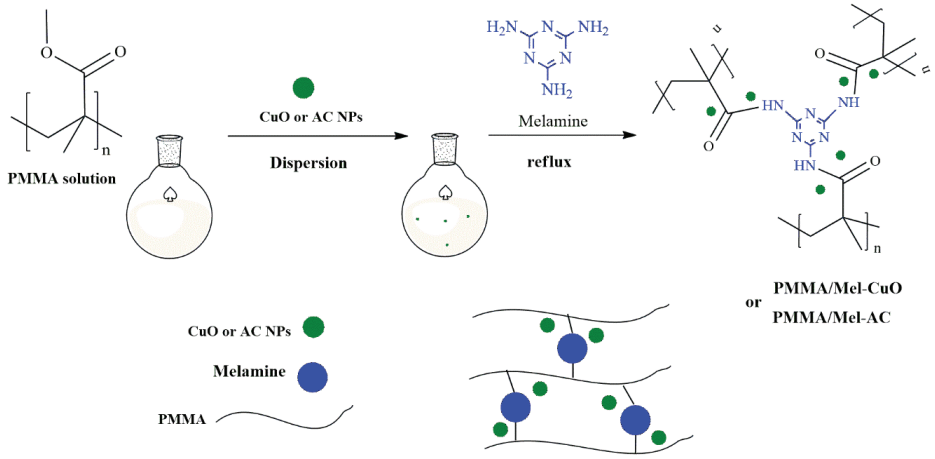

Figure 1. Preparation of PMMA/Mel-CuO and PMMA/Mel-AC nanocomposites.

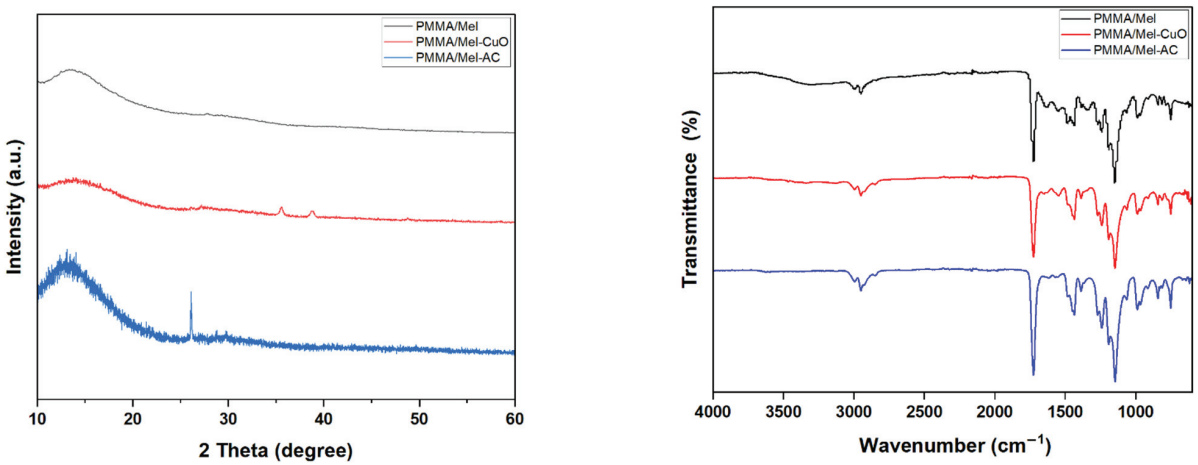

(**a**) (**b**)

Figure 2. (**a**) FTIR spectra and (**b**) XRD patterns of PMMA/Mel, PMMA/Mel-CuO, and PMMA/Mel-AC.

The X-ray diffraction patterns of PMMA/Mel were analyzed before and after the addition of CuO and AC nanoparticles, and the findings are shown in Figure 2b. The XRD diffractograms of the samples were studied in the 2-theta range between 10° and 60°. For all samples, a broad peak was observed at around 13° related to the PMMA/Mel matrix. The absence of any sharp peaks in the PMMA/Mel pattern showed that the polymer matrix is amorphous. New sharp peaks appeared in the PMMA/Mel-CuO curve at 35.5°, 38.7°, and 48.8°, which match the XRD pattern of standard copper oxide (JCPDS 48–1548), confirming the incorporation of CuO NPs into polymer segments to form a semicrystalline nanocomposite [37]. The XRD pattern of PMMA/Mel-AC showed an intense and sharp peak at 26°, which could be assigned to a particular crystal phase of the activated carbon nanoparticles, indicating the successful attachment of AC NPs with the polymer.

3.2. Thermal Study

As presented in Figure 3, the thermal stability levels of the cross-linked PMMA/Mel, PMMA/Mel-CuO, and PMMA/Mel-AC polymers were studied using the TGA technique. The TGA curve for PMMA/Mel showed that degradation takes place primarily in a

single step at temperatures ranging from 270 °C to 350 °C. The results demonstrated a significant improvement in the thermal stability of the PMMA/Mel-CuO and PMMA/Mel-AC nanocomposites compared to PMMA/Mel, with degradation occurring at 300 °C. The addition of metal oxides to the polymer network has a positive impact in increasing thermal stability [38]. Table 1 illustrates the decomposition percentages (T_{50}, T_{30}, and T_{10}), which define the temperatures for mass losses of 50%, 30%, and 10%, respectively. T_{50}, T_{30}, and T_{10} of PMMA/Mel-CuO were higher than those of the cross-linked PMMA/Mel and PMMA/Mel-AC.

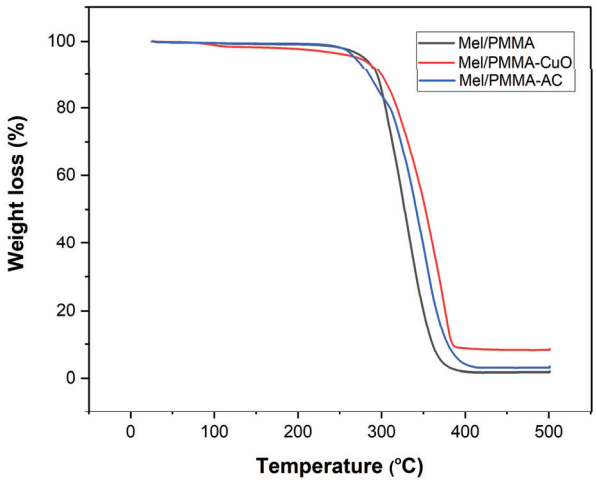

Figure 3. TGA micrograph of cross-linked PMMA/Mel, PMMA/Mel-CuO, and PMMA/Mel-AC.

Table 1. Thermal properties of cross-linked PMMA/Mel, PMMA/Mel-CuO, and PMMA/Mel-AC.

Sample	T_{10}	T_{30}	T_{50}
PMMA/Mel	305	311	326
PMMA/Mel-CuO	315	340	360
PMMA/Mel-AC	298	330	345

3.3. Morphological Investigation

The surface morphologies of PMMA/Mel, PMMA/Mel-CuO, and PMMA/Mel-AC were investigated using the SEM method, as displayed in Figure 4. In the micrometer range, the cross-linked PMMA/Mel polymer was revealed to have a rough, porous surface containing small, disorganized particles (Figure 4a,b). After surface modifications with NPs, the surface structure of PMMA/Mel was preserved (Figure 4c–f).

EDX analysis was conducted for elemental mapping of the nanocomposites, as shown in Figure 4 and Table 2. The elemental contents of the PMMA/Mel-CuO spectrum, given in Figure 4f, showed peaks for the O, C, and Cu elements, and the PMMA/Mel-AC spectrum (Figure 4e) exhibited peaks for the N, O, and C elements, confirming the formation of the nanocomposite.

Table 2. The elemental composition of PMMA/Mel-CuO and PMMA/Mel-AC samples.

Sample	PMMA/Mel-CuO				PMMA/Mel-AC			
Element	**C K**	**O K**	**S K**	**Cu L**	**C K**	**N K**	**O K**	**S K**
Weight%	63.69	28.33	0.51	7.47	59.34	20.07	19.99	0.60
Atomic%	73.58	24.57	0.22	1.63	64.66	18.75	16.35	0.24

3.4. Antibacterial Activity of Polymers Determined with the Agar-Well Diffusion Method

The antibacterial activity for the three polymers was measured with agar-well diffusion methods. In Table 3, the figures demonstrate that PMMA/Mel-CuO NP polymers had great antibacterial activity, with a clear zone from 8.3 ± 0.09 to 22.6 ± 0.1 mm against the tested bacteria. Meanwhile, the cross-linked PMMA/Mel, with a clear zone from 9.6.0 ± 0.02 to 8.3 ± 0.09 mm, showed the lowest antibacterial effect against the tested bacteria. Similarly, PMMA/Mel-AC produced the same result, with a clear zone measured from 8.6 ± 0.1 to 11.3 ± 0.1 mm. In this study, all tested polymers showed efficient activity against both *E. coli* and *S. aureus* strains. The PMMA/Mel-CuO polymer showed high activity against *S. aureus* (22.6 mm), followed by PMMA/Mel-AC with a 11.3 mm zone.

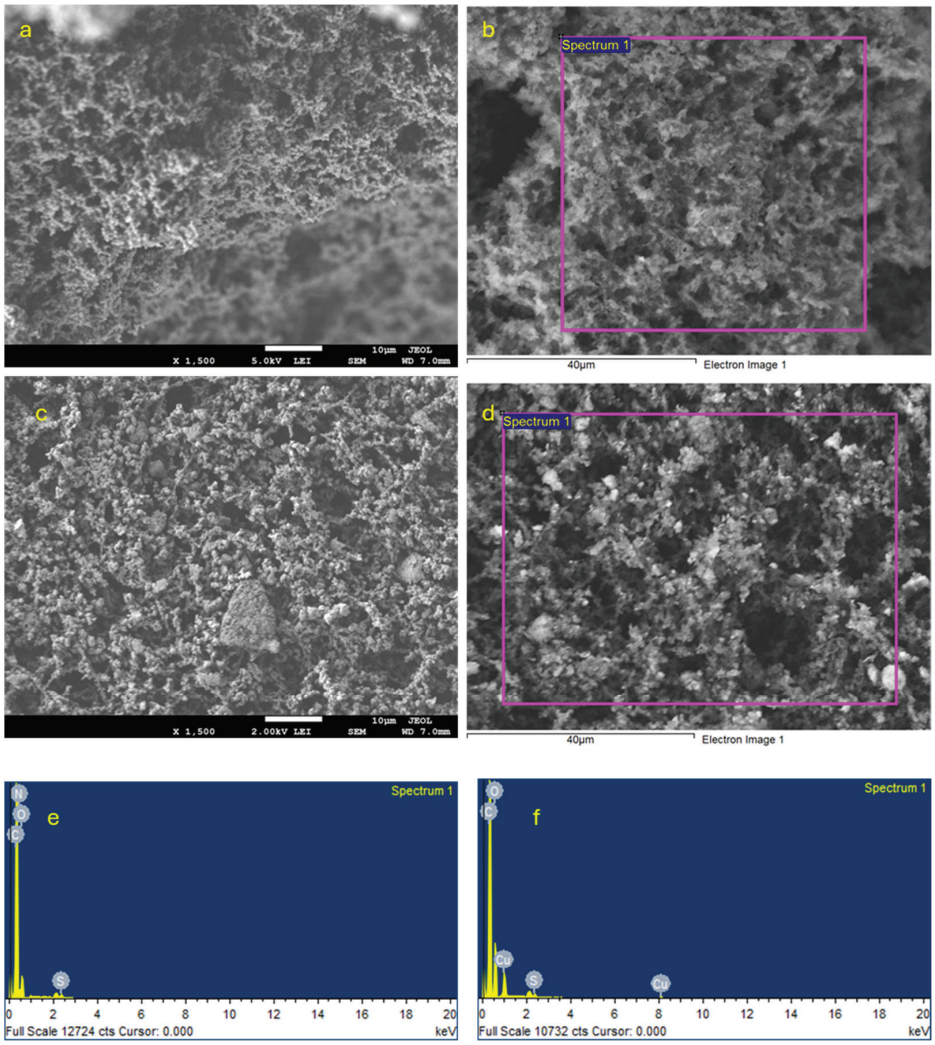

Figure 4. SEM micrographs for (**a**,**b**) PMMA/Mel-AC and (**c**,**d**) PMMA/Mel-CuO, and EDX elemental mapping of (**e**) PMMA/Mel-AC and (**f**) PMMA/Mel-CuO.

In the present study, through a suitable diffusion method, PMMA polymers and their activity were tested as antibacterial agents against *S. aureus* as a Gram-positive bacterium and *E.coli* as a Gram-negative bacterium. In Figure 5, it can be seen that PMMA/Mel showed antimicrobial efficient activity against the two different bacterial strains, which was promoted by increasing the integration with NPs. The PMMA/Mel polymer, with the incorporation of CuO and activated carbon NPs, had greater activity against the bacteria than PMMA/Mel without the integration with NPs, as shown in Figure 5. This

enhancement in the antibacterial activity arises from the very small size of CuO NPs, which can enter the cell wall of the bacterium and then kill it via denaturation of the cell permeability, or from the contact of CuO with many enzymes.

Table 3. Antimicrobial activity (mm) of polymers determined using the agar-well diffusion method.

Polymers	Inhibition Zone (mm)	
	E. coli	*S. aureus*
PMMA/Mel	9.6	8.3
PMMA/Mel-CuO	8.3	22.6
PMMA/Mel-AC	8.6	11.3

Data are expressed as the mean ± SD (n = 3).

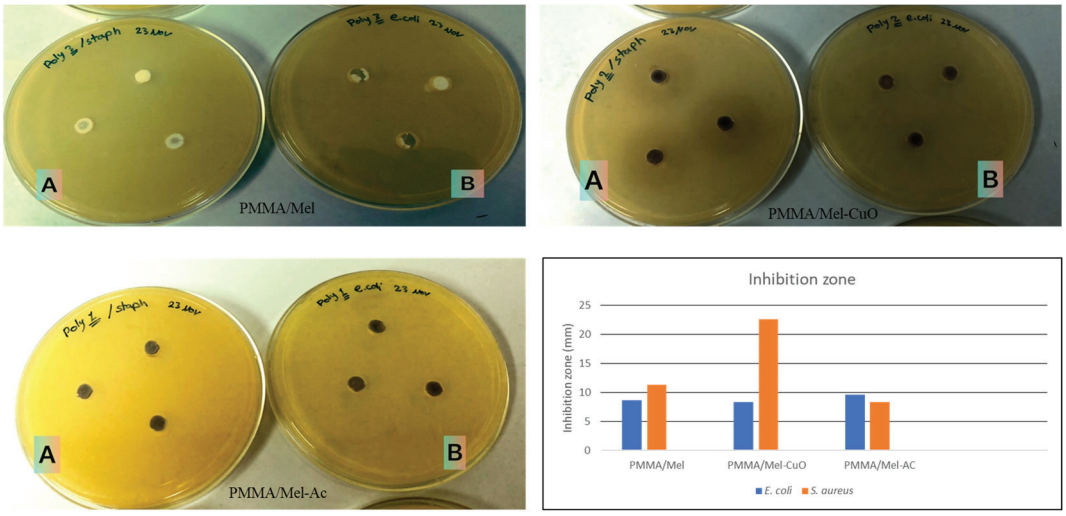

Figure 5. The antibacterial activity of cross-linked PMMA/Mel, PMMA/Mel-CuO, and PMMA/Mel-AC against (**A**) *S. aureus* and (**B**) *E. coli*.

In alignment with previous studies [39,40], microbial adhesion on PMMA-included biomaterial was reduced when PMMA was incorporated with activated carbon, and PMMA nanofibers showed good antibacterial activity against some pathogenic bacterial strains. In regard to the stability of polymers and their difficult solubility in media, PMMA/Mel incorporation with NPs increased the clear zone of bacterial growth. In another study, PMMA incorporated with metronidazole and chlorhexidine showed promising antibacterial activity against *Enterococcus faecalis* but not against *Porphyromonas gingivalis* [41].

3.5. Antibiotic Sensitivity Assay of Pathogenic E. coli Strain

In the present study, when we applied pathogenic *E. coli*, a positive result was observed as an inhibitory zone surrounding the bacterial colonies. The disc diffusion susceptibility test was carried out to determine the sensitivity or resistance of pathogenic microorganisms to various antimicrobial agents. On Mueller–Hinton agar, the pathogenic bacteria were cultivated in the presence of antimicrobial-impregnated filter paper discs. The presence or absence of bacterial growth around the discs is regarded as an indirect sign of the compound's ability to inhibit the organism. The results of the antibiotic sensitivity assay revealed a significant disparity between antibiotic resistance and sensitivity among the tested bacterial strains. Several antibiotics demonstrated resistance, including OX, VA, FC, CD, KF, AP, E, and P. In contrast, certain antibiotics showed measurable sensitivity, with TS exhibiting the highest sensitivity at 23 mm, followed by CPM at 20 mm, GM at 15 mm,

and C at 4 mm. These findings indicate that while some antibiotics are ineffective against these bacterial strains, others may still hold therapeutic potential. Table 4 and Figure 6A,B illustrate the antibiotic resistance characteristics of the pathogenic bacterial strain. The antibiotics TS and CPM produced inhibitory regions, indicating their effectiveness in halting bacterial growth. However, it is also evident that some compounds exhibited resistance when tested against *E. coli*. This resistance highlights the adaptive mechanisms of *E. coli*, necessitating further investigation into the factors contributing to such resistance and the potential development of alternative therapeutic strategies [42].

Table 4. Susceptibility of the *E. coli* strain used in the present study to different antibiotics.

Antibiotic	Resistance or Inhibitory Zone (mm) Produced by Antibiotics
CPM	20
GM	15
C	4
OX	R *
VA	
FC	
TS	23
CD	R
KF	
AP	
E	
PG	R

* R: Resistance. Antibiotic compounds used; CPM: Cefepime, GM: Gentamycin, C: Chloramphenicol, OX: Oxacillin, VA: Vancomycin, FC: Fusidic Acid, TS: Trimethoprim/Sulfamethoxazole, CD: Clindamycin, KF: Cephalothin, AP: Amoxicillin/Clavulanic Acid, E: Erythromycin, PG: Penicillin.

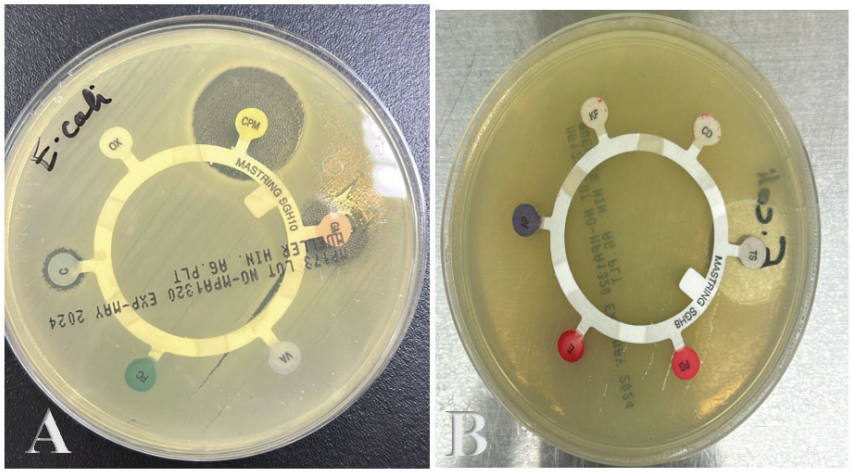

Figure 6. (**A**,**B**) Antibiotic resistance profiles of *E. coli* pathogenic bacteria. Antibiotic compounds used; CPM: Cefepime, GM: Gentamycin, C: Chloramphenicol, OX: Oxacillin, VA: Vancomycin, FC: Fusidic Acid, TS: Trimethoprim/Sulfamethoxazole, CD: Clindamycin, KF: Cephalothin, AP: Amoxicillin/Clavulanic Acid, E: Erythromycin, PG: Penicillin.

3.6. Antibacterial Activity of Polymers Determined with the Colony Count Method

The antibacterial activities of the three polymers were also tested by the CFU counting method to confirm the results obtained by the well diffusion method. The results showed that polymers impacted the number of *E. coli* colonies, leading to different numbers com-

pared to the control, as can be seen in Table 5 and Figure 7. The results showed decreases in the average number of colonies compared to the control dish's 27.33 CFU. The average colony number in the sample treated with PMMA and Mel was approximately 1.67 CFU, with a high killing mortality of 90%. Meanwhile, the mean in the sample treated with PMMA, Mel, and CuO was approximately 17.33 CFU, with 37% mortality. In the sample treated with PMMA, Mel, and Ac, it was approximately 8.33 CFU, with 70% mortality.

Table 5. Antimicrobial activity of polymers on *E. coli* determined using the colony count method.

	CFU	**Mortality%**
Control	27.33 ± 16	-
PMMA/Mel	1.6 ± 1.5	94%
PMMA/mel/CuO	17.3 ± 18	37%
PMMA/Mel/Ac	8.3 ± 10.11	70%

Control: *E. coli.*

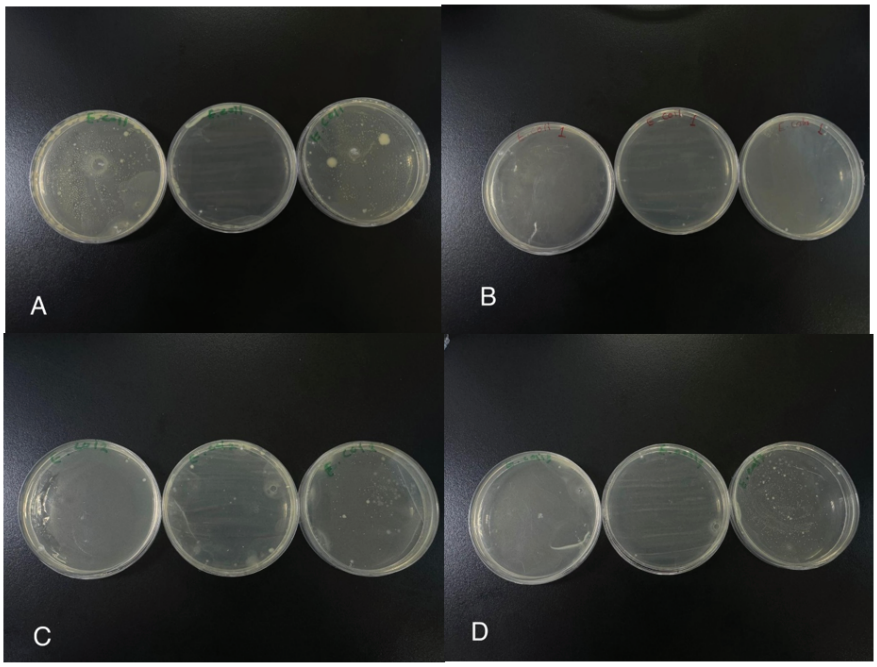

Figure 7. (**A**–**D**): The antibacterial activity of cross-linked (**B**) PMMA/Mel, (**C**) PMMA/Mel-CuO, and (**D**) PMMA/Mel-AC against *E. coli* according to the colony-forming units compared to (**A**) *E.coli* as a control.

A culture medium without any sample was used as a control. The antibacterial activity of polymers against Gram-negative bacteria may arise from interaction between active groups of polymers and anionic lipopolysaccharides of the Gram-negative cells, causing cell wall destruction, leakage of intracellular components, and inhibited transport of nutrients into the cells, finally leading to cell death [29]. The addition of polymethyl methacrylate (PMMA) to nanoparticles (NPs) reduces their efficiency in killing bacteria. This is because PMMA tends to encapsulate nanoparticles, preventing direct contact with bacterial cells and diminishing antibacterial mechanisms like reactive oxygen species (ROS) generation and ion release. Additionally, PMMA can cause nanoparticles to agglomerate [29], reducing their effective surface area for interaction with bacteria. The polymer matrix may also weaken the nanoparticles' effects, making it harder for them to penetrate bacterial membranes or disrupt vital biochemical processes. In another study, PMMA incorporation

with vancomycin and gentamicin reduced the number of colony-forming units per mL ($p < 0.05$). Gentamicin-loaded PMMA could inhibits the growth of sessile cells ($p < 0.05$), and the group with vancomycin 4 g + gentamicin 500 mg presented the best results [43].

4. Conclusions

In this work, the PMMA/Mel polymer network was incorporated with CuO and AC NPs through polycondensation reactions, and the products were employed as antibacterial agents against *S. aureus* as a Gram-positive bacterium and *E. coli* as a Gram-negative bacterium. The chemical structure and composition, thermal properties, and surface morphology of the new PMMA/Mel-based nanocomposites were investigated by various techniques. The XRD and EDX results showed the successful incorporation of CuO and AC NPs into the polymer matrix. Also, the thermal stability of the PMMA/Mel polymer was significantly enhanced after adding CuO nanoparticles. The finding showed that the PMMA/Mel-CuO and PMMA/Mel-AC nanocomposites had greater activity against both bacteria than PMMA/Mel. PMMA/Mel-CuO and PMMA/Mel-AC polymers showed high activity against *S. aureus* bacteria, with inhibition zones of 22.6 mm and 11.3 mm, respectively. This confirms that small-sized nanoparticles have an effective role in killing bacterial cells.

Author Contributions: Methodology, N.S.A. and M.A.A.G.; Formal analysis, M.A.A.G.; Investigation, N.S.A.; Writing—original draft, N.S.A. and M.A.A.G.; Supervision, M.A.A.G.; Project administration, N.S.A. All authors have read and agreed to the published version of the manuscript.

Funding: This project was funded by the Deanship of Scientific Research (DSR) at King Abdulaziz University, Jeddah, under grant no. GPIP-1728-247-2024.

Data Availability Statement: Data are contained within the article.

Acknowledgments: The authors acknowledge the support provided by Samaa Abdullah. The authors acknowledge the DSR for its technical and financial support.

Conflicts of Interest: The authors declare that they do not have any conflicts of interest.

References

1. Lakshmi, S.; Avti, P.K.; Hegde, G. Activated carbon nanoparticles from biowaste as new generation antimicrobial agents: A review. *Nanostructures Nano-Objects* **2018**, *16*, 306–321. [CrossRef]
2. Luksiene, Z. Nanoparticles and their potential application as antimicrobials in the food industry. In *Food Preservation*; Academic Press: Cambridge, MA, USA, 2017; pp. 567–601. [CrossRef]
3. Moellering, R.C. Introduction: Problems with Antimicrobial Resistance in Gram-Positive Cocci. *Clin. Infect. Dis.* **1998**, *26*, 1177–1178. [CrossRef] [PubMed]
4. Wen, J.; Jiang, F.; Yeh, C.K.; Sun, Y. Controlling fungal biofilms with functional drug delivery denture biomaterials. *Colloids Surf. B Biointerfaces* **2016**, *140*, 19–27. [CrossRef] [PubMed]
5. Matsuo, H.; Suenaga, H.; Takahashi, M.; Suzuki, O.; Sasaki, K.; Takahashi, N. Deterioration of polymethyl methacrylate dentures in the oral cavity. *Dent. Mater. J.* **2015**, *34*, 234–239. [CrossRef]
6. Slane, J.; Vivanco, J.; Rose, W.; Ploeg, H.L.; Squire, M. Mechanical, material, and antimicrobial properties of acrylic bone cement impregnated with silver nanoparticles. *Mater. Sci. Eng.* **2015**, *48*, 188–196. [CrossRef]
7. Rao, S.; Nandish, B.T.; Ginjupalli, K.; Jayaprakash, K. A review on poly (methyl methacrylate) denture base materials with antimicrobial properties. *Trends Biomater. Artif. Organs.* **2021**, *35*, 316–322.
8. Neu, H.C. The Crisis in Antibiotic Resistance. *Science* **1992**, *257*, 1064–1073. [CrossRef]
9. Salah, N.; Alfawzan, A.M.; Allafi, W.; Baghdadi, N.; Saeed, A.; Alshahrie, A.; Al-Shawafi, W.M.; Memic, A. Size-controlled, single-crystal CuO nanosheets and the resulting polyethylene–carbon nanotube nanocomposite as antimicrobial materials. *Polym. Bull.* **2021**, *78*, 261–281. [CrossRef]
10. Taran, M.; Rad, M.; Alavi, M. Antibacterial activity of copper oxide (CuO) nanoparticles biosynthesized by bacillus sp. FU4: Optimization of experiment design. *Pharm. Sci.* **2017**, *23*, 198–206. [CrossRef]

11. Mary, A.P.A.; Ansari, A.T.; Subramanian, R. Caffeine-mediated synthesis of CuO nanoparticles: Characterization, morphology changes, and bactericidal activity. *Inorg. Nano-Metal Chem.* **2020**, *51*, 174–181. [CrossRef]
12. Sutradhar, P.; Saha, M.; Maiti, D. Microwave synthesis of copper oxide nanoparticles using tea leaf and coffee powder extracts and its antibacterial activity. *J. Nanostructure Chem.* **2014**, *4*, 4–9. [CrossRef]
13. Wang, G.; Zhao, K.; Gao, C.; Wang, J.; Mei, Y.; Zheng, X.; Zhu, P. Green synthesis of copper nanoparticles using green coffee bean and their applications for efficient reduction of organic dyes. *J. Environ. Chem. Eng.* **2012**, *9*, 105331. [CrossRef]
14. Applerot, G.; Lellouche, J.; Lipovsky, A.; Nitzan, Y.; Lubart, R.; Gedanken, A.; Banin, E. Understanding the Antibacterial Mechanism of CuO Nanoparticles: Revealing the Route of Induced Oxidative Stress. *Small* **2012**, *8*, 3326–3337. [CrossRef] [PubMed]
15. Pandiyarajan, T.; Udayabhaskar, R.; Vignesh, S.; James, R.A.; Karthikeyan, B. Synthesis and concentration dependent antibacterial activities of CuO nanoflakes. *Mater. Sci. Eng. C* **2013**, *33*, 2020–2024. [CrossRef] [PubMed]
16. Khalaji, A.D.; Pazhand, Z.; Kiani, K.; Machek, P.; Jarosova, M.; Mazandarani, R. CuO nanoparticles: Preparation, characterization, optical properties, and antibacterial activities. *J. Mater. Sci. Mater. Electron.* **2022**, *31*, 11949–11954. [CrossRef]
17. Rajamma, R.; Nair, S.G.; Khadar, F.A.; Baskaran, B. Antibacterial and anticancer activity of biosynthesised CuO nanoparticles. *IET Nanobiotechnology* **2020**, *14*, 833–838. [CrossRef]
18. Ghasemi, N.; Jamali-Sheini, F.; Zekavati, R. CuO and Ag/CuO nanoparticles: Biosynthesis and antibacterial properties. *Mater. Lett.* **2017**, *196*, 78–82. [CrossRef]
19. Baek, Y.W.; An, Y.J. Microbial toxicity of metal oxide nanoparticles (CuO, NiO, ZnO, and Sb_2O_3) to Escherichia coli, Bacillus subtilis, and Streptococcus aureus. *Sci. Total Environ.* **2011**, *409*, 1603–1608. [CrossRef]
20. Ramazanzadeh, B.; Jahanbin, A.; Yaghoubi, M.; Shahtahmassbi, N.; Ghazvini, K.; Shakeri, M.; Shafaee, H. Comparison of Antibacterial Effects of ZnO and CuO Nanoparticles Coated Brackets against Streptococcus Mutans. *J. Dent.* **2015**, *16*, 200–205.
21. Ren, G.; Hu, D.; Cheng, E.W.C.; Vargas-Reus, M.A.; Reip, P.; Allaker, R.P. Characterisation of copper oxide nanoparticles for antimicrobial applications. *Int. J. Antimicrob.* **2009**, *33*, 587–590. [CrossRef]
22. Das Purkayastha, M.; Manhar, A.K.; Mandal, M.; Mahanta, C.L. Industrial Waste-Derived Nanoparticles and Microspheres Can Be Potent Antimicrobial and Functional Ingredients. *J. Appl. Chem.* **2014**, *2014*, 171427. [CrossRef]
23. Gonçalves, S.P.C.; Strauss, M.; Delite, F.S.; Clemente, Z.; Castro, V.L.; Martinez, D.S.T. Activated carbon from pyrolysed sugarcane bagasse: Silver nanoparticle modification and ecotoxicity assessment. *Sci. Total Environ.* **2016**, *565*, 833–840. [CrossRef] [PubMed]
24. Sekaran, G.; Karthikeyan, S.; Gupta, V.K.; Boopathy, R.; Maharaja, P. Immobilization of Bacillus sp. in mesoporous activated carbon for degradation of sulphonated phenolic compound in wastewater. *Mater. Sci. Eng. C Mater. Biol. Appl.* **2013**, *33*, 735–745. [CrossRef] [PubMed]
25. Saravanan, A.; Kumar, P.S.; Karthiga Devi, G.; Arumugam, T. Synthesis and characterization of metallic nanoparticles impregnated onto activated carbon using leaf extract of Mukia maderasapatna: Evaluation of antimicrobial activities. *Microb. Pathog.* **2016**, *97*, 198–203. [CrossRef]
26. Devi, T.B.; Mohanta, D.; Ahmaruzzaman, M. Biomass derived activated carbon loaded silver nanoparticles: An effective nanocomposites for enhanced solar photocatalysis and antimicrobial activities. *J. Ind. Eng. Chem.* **2019**, *76*, 160–172. [CrossRef]
27. Giti, R.; Zomorodian, K.; Firouzmandi, M.; Zareshahrabadi, Z.; Rahmannasab, S. Antimicrobial Activity of Thermocycled Polymethyl Methacrylate Resin Reinforced with Titanium Dioxide and Copper Oxide Nanoparticles. *Int. J. Dent.* **2021**, *2021*, 6690806. [CrossRef]
28. Sathya, S.; Murthy, P.S.; Devi, V.G.; Das, A.; Anandkumar, B.; Sathyaseelan, V.; Doble, M.; Venugopalan, V. Antibacterial and cytotoxic assessment of poly (methyl methacrylate) based hybrid nanocomposites. *Mater. Sci. Eng.* **2019**, *100*, 886–896. [CrossRef]
29. Glazkova, E.; Bakina, O.; Rodkevich, N.; Mosunov, A.; Evstigneev, M.; Evstigneev, V.; Klimenko, V.; Lerner, M. Antibacterial Properties of PMMA Functionalized with $CuFe_2O_4/Cu_2O/CuO$ Nanoparticles. *Coatings* **2022**, *12*, 957. [CrossRef]
30. Varghese, S.; Kuriakose, S.; Jose, S. Antimicrobial Activity of Carbon Nanoparticles Isolated from Natural Sources against Pathogenic Gram-Negative and Gram-Positive Bacteria. *J. Nanosci.* **2013**, *2013*, 457865. [CrossRef]
31. Shankar, D.; Krishnasamy, K.; Selvaraj, K. In vitro Evaluation of Antibacterial Efficacy using Passiflora foetida Activated Carbon. *Res. Pharm.* **2016**, *6*, 2986. [CrossRef]
32. Alkayal, N.S. Highly Efficient and Selective Capture of Pb(II) by New Crosslinked Melamine-Based Polymethyl Methacrylate for Water Treatment. *Adsorpt. Sci. Technol.* **2022**, *2022*, 5257960. [CrossRef]
33. Balouiri, M.; Sadiki, M.; Koraichi Ibnsouda, S. Methods for in vitro evaluating antimicrobial activity: A review. *J. Pharm. Anal.* **2016**, *6*, 71–79. [CrossRef] [PubMed]
34. Alghamdi, M.A.; Al-Sarraj, F.; Alamshani, W.H.; Alotibi, I.; Al-Zahrani, M.; Albiheyri, R.; Nass, N.M.; Sajer, B.H.; Bataweel, N.M.; Al-Matary, M.A.; et al. Antibacterial power of Pomegranate extracts against Beta-Lactamase producing *Escherichia coli*. *Caryologia* **2024**, *77*, 83–99. [CrossRef]

35. *ASTM E2149-20*; Standard Test Method for Determining the Antimicrobial Activity of Antimicrobial Agents Under Dynamic Contact Conditions. ASTM: West Conshohocken, PA, USA, 2020.
36. Nouri, F.; Yaraki, M.T.; Ghorbanpour, M.; Agarwal, S.; Gupta, V.K. Enhanced Antibacterial effect of chitosan film using Montmorillonite/CuO nanocomposite. *Int. J. Biol. Macromol.* **2018**, *109*, 1219–1231. [CrossRef]
37. Siddiqui, H.; Parra, M.R.; Qureshi, M.S.; Malik, M.M.; Haque, F.Z. Studies of structural, optical, and electrical properties associated with defects in sodium-doped copper oxide (CuO/Na) nanostructures. *J. Mater.* **2018**, *53*, 8826–8843. [CrossRef]
38. Salavati-Niasari, M.; Ghanbari, D. *Polymeric Nanocomposite Materials*; IntechOpen: London, UK, 2011.
39. Elashnikov, R.; Lyutakov, O.; Ulbrich, P.; Svorcik, V. Light-activated polymethylmethacrylate nanofibers with antibacterial activity. *Mater. Sci. Eng. C* **2016**, *64*, 229–235. [CrossRef]
40. Rani, G.V.; Singh, R.N. Hydrophobic coating of polymethylmetha-crylate (PMMA) on glass substrate for reduced bacterial adhesion. *J. Polym. Mat.* **2015**, *32*, 512.
41. Moffa, E.B.; Malheiros, S.S.; Silva, L.T.S.; Branco, D.I.; Junior, R.C.F.G.; Brandt, W.C.; Goncalves, F.; Barao, V.A.R.; Boaro, L.C.C. Antimicrobial activity of PMMA enriched with nano-clay loaded with metronidazole and chlorhexidine. *Braz. Oral Res.* **2024**, *38*, e110. [CrossRef]
42. Adaikalam, K.; Vikraman, D.; Lee, D.; Cho, Y.-A.; Kim, H.S. Optical and UV Shielding Properties of Inorganic Nanoparticles Embedded in Polymethyl Methacrylate Nanocomposite Freestanding Films. *Polymers* **2024**, *16*, 1048. [CrossRef]
43. Pedroni, M.A.; Ribeiro, V.S.; Cieslinski, J.; Lopes, A.P.; Kraft, L.; Suss, P.H.; Felipe, F.F. Different concentrations of vancomycin with gentamicin loaded PMMA to inhibit biofilm formation of Staphylococcus aureus and their implications. *J. Orthop. Sci.* **2024**, *29*, 334–340. [CrossRef]

polymers

MDPI

Article

Biodegradable PLA/PHB Composites with Inorganic Fillers and Modifiers

Jozef Feranc [1,*], Martina Repiská [2], Roderik Plavec [1], Katarína Tomanová [1], Michal Ďurfina [1], Zuzana Vanovčanová [1], Ida Vašková [1], Leona Omaníková [1], Mária Fogašová [1], Slávka Hlaváčiková [1], Ján Kruželák [1], Zuzana Kramárová [1], Eduard Oswald [1] and Pavol Alexy [1]

[1] Institute of Natural and Synthetic Polymers, Faculty of Chemical and Food Technology, Slovak University of Technology in Bratislava, Radlinského 9, 812 37 Bratislava, Slovakia; roderik.plavec@stuba.sk (R.P.); katarina.tomanova@stuba.sk (K.T.); michal.durfina@stuba.sk (M.Ď.); zuzana.vanovcanova@stuba.sk (Z.V.); ida.vaskova@stuba.sk (I.V.); leona.omanikova@stuba.sk (L.O.); maria.fogasova@stuba.sk (M.F.); slavka.hlavacikova@stuba.sk (S.H.); jan.kruzelak@stuba.sk (J.K.); zuzana.kramarova@stuba.sk (Z.K.); eduard.oswald@stuba.sk (E.O.); pavol.alexy@stuba.sk (P.A.)

[2] Audia Plastics s.r.o., Voderady 426, 919 42 Voderady, Slovakia; martina.repiska@audia.com

* Correspondence: jozef.feranc@stuba.sk

Abstract

The work is focused on the study of the influence of different types of inorganic fillers, in combination with modifiers, on the rheological, thermal, and mechanical properties of a biodegradable mixture based on PLA/PHB. Ten types of inorganic fillers based on talc, magnesium hydroxide, aluminum hydroxide, calcium carbonate, and silicon dioxide were used in the study, along with three types of modifiers. It was concluded that fillers containing reactive OH groups on their surface act as strong pro-degradants in PLA/PHB blends, and their degrading effect can be suppressed by the addition of reactive modifiers. Each modifier acts specifically with different types of fillers. Therefore, it is necessary to select a suitable filler/modifier combination not only for fillers with different chemical compositions but also for fillers with different morphologies within the same chemical type. Moreover, the preparation of PLA/PHB/magnesium hydroxide blends with suitable processing and application properties opens the possibility of developing environmentally friendly polymeric materials with a reduced flammability. The addition of talc, which has a platelet structure, can increase the barrier properties of the mixture.

Keywords: biodegradable polymer blend; polyhydroxybutyrate; polylactic acid; inorganic filler; modifier; degradation

1. Introduction

In recent years, there has been an increase in interest in biodegradable polymers due to the inevitable and impending depletion of fossil resources, the processing of which places a burden on the environment, and due to technologically and financially demanding recycling methods [1,2]. Biodegradable polymers derived from renewable raw materials represent a new generation of materials that reduce the impact on the environment (energy consumption, emissions and greenhouse gases, less dependence on fossil fuels, and others). Their development is currently at its peak, but for successful applications on the market there are some limitations in use and processing (high price). Many polymeric materials have been developed based on renewable resources [3].

In the field of biopolymers, polylactic acid (PLA) and polyhydroxybutyrate (PHB) and its blends are extensively studied biomaterials. PLA is a linear, thermoplastic, aliphatic biopolyester with many advantageous properties such as biodegradability, biocompatibility, high transparency, strength, relatively low flammability, easy processing, and commercial availability, making it one of the most widely used biodegradable polyesters. Despite these advantages, PLA also has some disadvantages, such as brittleness, high gas and vapor permeability, low melt strength, and limited thermal stability [3–6]. Moreover, its biodegradation rate is slower compared to other common natural organic wastes, such as food or garden residues, which significantly limits its adoption in industrial food and yard composting facilities and its widespread use in general [7]. PHB is a biodegradable, biocompatible, thermoplastic, semicrystalline linear polyester, which is formed as an intracellular product of microorganisms (Bacillus safensis, Bacillus megaterium, and others) in the form of granules [8,9]. PHB is relatively resistant to abiotic hydrolytic degradation and is insoluble in water. The physical properties of polyhydroxybutyrate are related to its stereochemistry. The temperature characteristics of polyhydroxybutyrate include a high melting point (173–180 °C), a glass transition temperature of about 1–5 °C, and a thermal degradation temperature of about 200 °C, which is close to the melting point and causes a processing problem [9–13].

Blending PLA with PHB has been widely explored as a modification of the brittleness of PLA with the stiffness of PHB. However, although these two polyesters are only partially miscible, they can form blends with improved performances when appropriate compatibilization strategies are applied [14–16]. The PLA/PHB mixture (75/25 weight percent (wt%)) has better mechanical and barrier properties than pure polylactic acid. As the amount of polyhydroxybutyrate in this mixture increases, there is a decrease in the mechanical properties (tensile strength, Young's modulus), but also a decrease in the glass transition temperature. The crystallization of the polyhydroxybutyrate in the mixture produces small spherulites which can act as nucleating agents for polylactic acid, leading to an increase in crystallinity [10,11]. Polylactic acid is more stable against enzymatic hydrolysis than polyhydroxybutyrate, so during biodegradation polyhydroxybutyrate primarily degrades in this mixture. In the manufacture of films from such a blend, the addition of plasticizers is necessary to reduce their brittleness, improve ductility and processability, and facilitate surface hydrolysis during biodegradation [10]. Biodegradable polylactic acid and polyhydroxybutyrate can be mixed with materials from natural sources such as starch, cellulose, cellulose derivatives, or chitin. Such preparation of the polymer mixture will ensure a reduction in the financial costs associated with their production and is an excellent alternative to the development of new materials with better properties [10,11]. The existence of weak van der Waals interactions between macromolecules in the polymer is often the reason for their immiscibility, so their compatibilization is necessary [17]. Compatibility is the specific way in which the stability of a polymer blend is achieved. The most important task is to reduce the size of the dispersed component (phase) by reducing the interphase voltage and preventing the coalescence of the dispersed particles, thereby stabilizing the system [18]. The compatibility can be improved by the interactions between dispersed components and the matrix resulting from the use of compatibilizers, which are mostly macromolecular substances with interphase activity in heterogeneous mixtures [10].

The utilization of natural origin inorganic fillers is possible as well. Calcium carbonate is an inorganic filler example that is widely used in the filling of biodegradable polymer composites, with the aim of increasing their strength, stiffness, and durability. It also reduces the overall costs of composite production and improves biodegradability, which is why its use to produce disposable products and packaging is so developed. Other

investigated inorganic fillers in connection with PLA include metal oxides such as zinc oxide and titanium dioxide. These, in addition to improving strength and hardness, can add antibacterial properties. Because of this property, this type of PLA composite is being investigated for biomedical applications. Also, the addition of TiO_2 to PHB increases its resistance to ultraviolet (UV) radiation, which is important for outdoor applications and packaging. The addition of this filler to PLA promotes crystallization, thereby improving the thermal stability of the matrix. An increase in the glass transition temperature and a slight increase in melting temperature supports the thermal resistance of the PLA composite [19–21]. The dimensional thermal stability of PLA can also be improved by the addition of TiO_2 nanoparticles, which influence its crystallization. However, mechanical tests reveal that this filler contributes to a decrease in the tensile strength and an increased brittleness of the PLA material. Results also indicate that the addition of TiO_2 leads to more intense photodegradation compared to pure PLA, which may be a useful property for regulating biodegradation [22]. Magnesium oxide (MgO) has similar effects on the PLA matrix as the previously mentioned oxides. Up to 2 wt%, there is a gradual increase in the Young's modulus and tensile strength of the PLA composite. An adequate surface interaction between PLA and the filler ensures a stress transfer from the matrix to the filler, leading to improved mechanical properties [23]. The magnesium oxide also affects the processability of PLA through extrusion and injection molding. In addition, it reduces the brittleness, increases the thermal stability, and improves the mechanical strength and stiffness of PLA and PHB and has antibacterial properties [19,20]. The addition of silicon dioxide (SiO_2) in polymer blends presents suitable properties, such as abrasion, optical ultraviolate (UV) filtering, luminescence, and biocompatibility, which have never been observed in their bulk state. It has a low refractive index and a high degree of thermal and mechanical stability [24]. Prapruddivongs et al. [25] studied the biodegradation behavior of PLA. They crosslinked PLA filled with precipitated SiO_2 (commercial SiO_2) and SiO_2 from rice husk ash and found that SiO_2 incorporation has a direct effect on the composites' stability. According to Opaprakasit et al. [26], PLA/silica composites can improve gas permeability and selectivity. Materials had a strong potential to be used as biodegradable packaging films with a tunable gas permeability. The study of [24] aimed to improve the understanding of how PLA and nano-SiO_2 interact, resulting in the specific morphology and surface properties of the blends. It was found that the mechanical properties of the blends were improved by the addition of nanoparticles. In addition, the results showed that nanoparticles have a positive influence on thermal stability as well as the thermal degradation of the blends obtained.

Among many others, talc is a filler that improves the thermal stability, mechanical properties, and processability of PLA and PHB. It reduces their brittleness, which is very important for packaging materials and industrial products. It was observed that talc acted as a nucleating agent and increased the crystallinity in polymers, and, thereby, the oxygen permeability (OTR) and the water vapor transmission rate (WVTR) were similarly reduced by talc [27,28]. The study of [29] found that the addition of talc increased the miscibility of PLA and the polyester while acting as a nucleating agent that improved PLA crystallinity. Jain et al. [30] reported that the oxygen and water vapor barrier properties of composite films were improved by 33 and 25%, respectively, at a 3 wt% talc loading. When talc was only emended in PLA, the tensile strength and modulus increased with the amount of talc, whereas Young's modulus decreased. It was also observed that talc improved the oxygen resistance by 72% in poly(3-hydroxybutyrate-co-3-hydroxyvalerate) (PHBV), and by 62% in PLA matrices. Compared to PLA itself, PLA/talc films also displayed a better barrier to water vapor (up to 55% improvement). Similarly, oxygen permeability is also reduced with

talc addition [30,31]. With the blending of 20 wt% PHBV, an overall further improvement of about 80% in both properties was achieved. In addition, it has been reported that mixing 20–35 wt% of PHBV with PLA is a suitable combination to achieve high barrier properties to both oxygen and water vapor, while maintaining the biocompatibility of the material [32].

In addition to improving mechanical properties, fillers can also impart a certain level of flame-retardant properties. These fillers include organically modified montmorillonite (OMMT), metal hydroxides such as magnesium hydroxide ($Mg(OH)_2$) and aluminum hydroxide ($Al(OH)_3$), phosphorus derivatives, etc. However, while these fillers can enhance the flame-retardant characteristics of PLA, they may also induce negative effects, such as a loss of mechanical and thermal properties and degradation of the PLA matrix [33–36]. The metal hydroxides have advantages such as non-toxicity, reducing the acidity of the combustion products and reducing the temperature of the polymer due to their ability to act as a smoke suppressant. However, they need to be added in large amounts (more than 30 wt% to 60 wt%) to make them effective as flame-retardant agents, which may affect the deterioration of the mechanical properties of the final products [37,38].

To avoid this negative phenomenon, the utilization of reactive modifiers in blends was our focus. Reactive modifiers are widely used in biodegradable polyesters to improve melt stability, rheology, and toughness by counteracting chain scission, inducing branching, and enhancing interfacial compatibility. They also promote stronger polymer–filler interactions by introducing functional groups into the matrix and blocking reactive filler surfaces. In PLA, reactive extrusion with Joncryl has been shown to increase molecular weight and induce long-chain branching, leading to a higher melt viscosity, improved melt strength, and enhanced foamability [39]. In neat PHB and PHB-based composites, Joncryl suppressed chain scission, raised the molecular weight, reduced the melt flow index, and extended the extrusion processing window [40]. In systems containing inorganic fillers, the incorporation of Joncryl ADR-4368F into PLA/talc composites during reactive extrusion reduced degradation and improved the filler–matrix adhesion, resulting in an enhanced mechanical performance and processability [41]. Similar effects were observed in PLA/nanoclay nanocomposites, where Joncryl promoted finer clay dispersion, improved rheological behavior, and enhanced mechanical performance [42]. In systems involving other polymers or biopolymers, phthalic anhydride (PhA) directly incorporated into polylactic acid/poly(butylene adipate-co-terephthalate) (PLA/PBAT) markedly improves phase morphology and overall toughness relative to uncompatibilized blends [43]. Maleic anhydride has also been used in hybrid PLA composites reinforced with short natural fibers and talc, where it improved interfacial adhesion and tensile strength compared to the uncompatibilized system, although its effect was less pronounced than that of multifunctional epoxide chain extenders such as Joncryl® ADR 4368 [41]. In neat PLA, blocked (latent) multifunctional isocyanates have been successfully employed to increase molecular weight and, more importantly, to enhance melt strength: a methanol-blocked polyisocyanate used in the extrusion foaming of PLA enabled the formation of a denser, finer cell structure and markedly improved foam processability, i.e., melt strength and cell morphology [44]. In addition, conventional diisocyanates (particularly hexamethylene diisocyanate (HDI)/methylene diphenyl diisocyanate (MDI)) function as efficient chain extenders in PLA, leading to significant increases in molecular weight (Mw) and stabilization against thermal degradation even in low-molecular-weight prepolymers [45,46]. In PHB matrices (or PHBV as a more processable PHB form), isocyanate chemistry has been applied to link hydroxyl-terminated chains to high-molecular-weight multi-block structures; both urethane and secondary allophanate linkages were reported, increasing molar mass and altering rheology and processability [47]. In PLA/PHBV blends, diisocyanates (HDI,

poly(HDI), 1,4-phenylene diisocyanate (PDI)) act as in situ compatibilizers: they refine the phase dispersion, increase the interfacial adhesion, and improve both the mechanical properties and processing windows [48].

Based on the literature review, it can be stated that only a limited number of studies have addressed the application of inorganic fillers in polymer blends based on PLA/PHB. The selection of fillers used in this study was motivated by their availability, the generally recognized lower cost compared to PLA and PHB, and their potential to improve properties, as reported in the literature above, which is of practical importance for extending the application window of PLA/PHB blends. Since the tested fillers may influence the stability of the polymer matrix, three types of modifiers with different mechanisms of action were also included in the study with the aim of further optimizing the properties. The focus was placed on evaluating the potential of these modifiers to enhance thermal stability by preventing chain scission and slowing down degradation. In addition, the modifiers are expected to improve interfacial compatibility, either between the filler and the matrix or between polymer phases.

2. Materials and Methods

2.1. Materials

Polymers: Polylactic acid (PLA) (Luminy® L130, TotalEnergies Corbion, Gorinchem, The Netherlands, ≥99% L-isomer, MFI 10 g/10 min, 190 °C/2.16 kg) and Poly(3-hydroxybutyrate) (PHB) (ENMAT™ Y3000 powder, TianAn Biologic Materials Co., Ltd., Ningbo, China).

Plasticizer: CITROFOL® BII (tributyl O-acetylcitrate; Jungbunzlauer Ladenburg GmbH, Ladenburg, Germany).

Fillers:

Aluminum hydroxide: Alfrimal 104 (Alpha Calcit Füllstoff Gesellschaft mbH & Co. KG, Cologne, Germany, density 2.4 g/cm^3, specific surface area 10 m^2/g, average particle size 10 μm) and Alfrimal 106 (Alpha Calcit Füllstoff Gesellschaft mbH & Co. KG, Cologne, Germany, density 2.4 g/cm^3, specific surface area 7 m^2/g, average particle size 5.5 μm); *Talc*: HTP3 (IMI Fabi, LLC, Benwood, WV, USA, density 2.8 g/cm^3, specific surface area 7 m^2/g, average particle size 17.5 μm), HTP4 (IMI Fabi, LLC, Benwood, WV, USA, density 2.8 g/cm^3, specific surface area 3.5 m^2/g, average particle size 30 μm), and HTP05c (IMI Fabi, LLC, Benwood, WV, USA, density 2.8 g/cm^3, specific surface area 11 m^2/g, average particle size 7 μm); *Calcium carbonate*: Omyacarb 1T-VA (Omya International AG, production site Vápenná, Czech Republic, specific surface area 4 m^2/g, average particle size 8 μm) and Calprec PR (Cales de Llierca S.A., Argelaguer, Spain, density 2.7 g/cm^3, specific surface area 2 m^2/g, average particle size 0.05 μm); *Magnesium hydroxide*: Securoc B (Sibelco Specialty Minerals Europe, Maastricht, The Netherlands, density 2.4 g/cm^3, specific surface area 7 m^2/g, average particle size 2.8 μm), Duhor C-043/S (Duslo a.s., Šaľa, Slovakia, density 2.4 g/cm^3, specific surface area 6 m^2/g, average particle size 1.5 μm), and Duhor N-PL/S (Duslo a.s., Šaľa, Slovakia, density 2.4 g/cm^3, specific surface area 6–10 m^2/g, average particle size 1.5 μm); *Silica*: Ultrasil 7000GR (Evonik Industries AG, Hanau, Germany, density 2 g/cm^3, specific surface area 175 m^2/g, average particle size 0.014 μm).

Modifiers: Phthalic anhydride (PhA) (produced by DEZA a.s., Valašské Meziříčí, Czech Republic), IsoQure TT (toluene diisocyanate (TDI) dimer, Acima AG, Buchs, Switzerland), and Joncryl ADR-4368 (multi-functional reactive epoxy-based chain extender, BASF Nederland B.V., Heerenveen, The Netherlands).

2.2. Methods

2.2.1. Blend Preparation

All blends were prepared using a laboratory twin screw extruder (Labtech Engineering Co., Ltd., Samutprakarn, Thailand), with a screw diameter of 16 mm and a length-to-diameter (L/D) ratio of 40. The screw geometry incorporated three kneading zones, and atmospheric venting was positioned at the 38 D mark on the barrel. The temperature profile of the device in the direction from the extruder hopper to extruder for all prepared mixtures was as follows: 160 °C, 170 °C, 175 °C, 180 °C, 180 °C, 180 °C, 180 °C, 180 °C, 175 °C, 170 °C. Extrusion was conducted at a screw speed of 140 RPM. The PLA/PHB ratio was 60/40 wt%. The plasticizer content was 9 wt% relative to the polymer blend. The filler was incorporated at 10 vol% into the blend, and the modifier was added at 1 wt% with respect to the blend.

2.2.2. Preparation of Test Films

The performance test films were prepared by attaching a chill-roll line head directly to the twin-screw extruder. The extruder head temperature was 170 °C. The melt emerging from the rectangular cross-sectional die was extruded onto a system of water-cooled rollers and subsequently wound under constant tension to a winding device. Testing specimens for measuring the physical–mechanical properties of the studied polymer mixtures according to ISO 527-3 [49] were prepared from the films. Strips 15 mm wide were cut from the foils by means of a precision cutter.

2.2.3. Rheological Characterization

The processing stability of the prepared polymer blends was evaluated on an RPA 2000 (Alpha Technologies, Hudson, OH, USA) oscillating rheometer using a timed test. The complex viscosity of each sample was measured following a controlled thermo-mechanical loading procedure using an oscillatory rheometer. The specimens were introduced into a biconical test chamber, which was subsequently sealed, and the system temperature was adjusted to 180 °C. A static preheating phase of 0.5 min was applied to ensure complete melting of the samples. Subsequently, oscillatory deformation was imposed at a frequency of 50 cycles per minute (cpm) with an oscillation angle of 30°, corresponding to a shear rate of 22 s^{-1}. Under these conditions, the evolution of the complex viscosity was monitored over 10 min. The viscosity value recorded at 5 min was considered a key indicator of processing stability. A lower complex viscosity at this stage was interpreted as indicative of reduced resistance to thermo-mechanical degradation and, consequently, lower processing stability. To eliminate the initial differences in viscosity of various blends, the relative complex viscosity was introduced, defined as follows:

$$\eta^*_{rel(t)} = \frac{\eta^*_{(t)}}{\eta^*_{(0)}} \quad (1)$$

where $\eta^*_{rel(t)}$ is the relative complex viscosity at time t, $\eta^*_{(t)}$ is the complex viscosity at time t, and $\eta^*_{(0)}$ is the complex viscosity at the beginning of the test.

2.2.4. Thermal Characterization

Differential scanning calorimetry (DSC) measurements were performed using a DSC 1 instrument (Mettler-Toledo Inc., Greifensee, Switzerland). The following thermal program was applied:

1. Isothermal hold at 30 °C for 1 min.

2. First heating from 30 to 190 °C at 10 °C/min.
3. Isothermal hold at 190 °C for 3 min.
4. Cooling from 190 to 30 °C at 10 °C/min.
5. Isothermal hold at 30 °C for 3 min.
6. Second heating from 30 to 190 °C at 10 °C/min.

The prepared sample was placed in the DSC chamber, and heat flow was recorded relative to an empty sealed aluminum pan used as reference, under nitrogen atmosphere (30 mL·min^{-1}). Data acquisition and analysis were performed using STARe evaluation software version 16.40 (Mettler-Toledo Inc., Greifensee, Switzerland). The enthalpy values obtained from DSC were recalculated per unit mass of polymer matrix, excluding the filler contribution, unless otherwise stated.

2.2.5. Tensile Test

Tensile tests were carried out on film strips prepared in accordance with ISO 527-3 [49]. For each polymer blend, five specimens were tested. The strips had a width of 15 mm, a gauge distance of 50 mm, and a thickness corresponding to the prepared films. Testing was performed on a universal testing machine (Zwick Roell, Ulm, Germany) equipped with a contact extensometer. The grip separation was set to 50 mm and the crosshead speed to 50 mm·min^{-1}. Tensile parameters, including yield stress, tensile strength at break, and elongation at break, were determined from the stress–strain curves.

2.2.6. Scanning Electron Microscopy (SEM)

Morphology of the tested specimens was examined using a JEOL JSM-7500F scanning electron microscope (JEOL Ltd., Tokyo, Japan). For SEM observation, the fracture surfaces of the polymer blend specimens were prepared by cryogenic fracturing in liquid nitrogen in order to obtain brittle fracture surfaces. Powder samples were deposited on double-sided adhesive tape for observation. Prior to observation, the samples were sputter-coated with a thin layer of gold/platinum alloy using a Balzers SCD 050 sputter coater (Balzers AG, Balzers, Liechtenstein).

2.2.7. Fourier Transform Infrared (FTIR) Spectroscopy

ATR-FTIR spectra of the solid-state samples were recorded using a Nicolet 5700 FTIR spectrometer (Thermo Scientific, Madison, WI, USA) in the range of 4000–400 cm^{-1} at room temperature. Each spectrum was collected with a resolution of 4 cm^{-1} by averaging 32 scans, using a diamond ATR crystal.

3. Results and Discussion

3.1. Rheological Properties

In polymer systems, the incorporation of fillers usually increases the melt viscosity, particularly when the fillers exhibit a high specific surface area or are surface-modified to promote interfacial compatibility with the polymer matrix, i.e., so-called active or reinforcing fillers. Conversely, the chemical nature of the filler surface may critically affect the processing stability of polymer matrices with a pronounced susceptibility to thermo-mechanical degradation. This is particularly relevant for PLA/PHB blends, which are prone to chain scission and molecular weight reduction under thermo-mechanical stress during melt processing [12,39]. The degradation pathways of these polyesters can be substantially influenced by other blend constituents, including the presence and chemistry of the filler. The processing stability of the prepared mixtures was measured as the dependence of the complex viscosity on time, during which the sample was loaded by shear stress in the

oscillating rheometer at 180 °C. The consequence of high temperature and shear stress during the processing of PLA/PHB blends in the melt is the degradation of the material, which causes a decrease in molecular weight following the decrease in viscosity of the mixture. The relative viscosity expresses the change in viscosity during thermomechanical stress over time compared to the flood viscosity value, and thus the degradation of the material itself. For a simple comparison of the influence of individual fillers on processing stability, the values of the viscosities in the 5th minute of the timed test in the oscillating rheometer were evaluated (Figures 1 and 2).

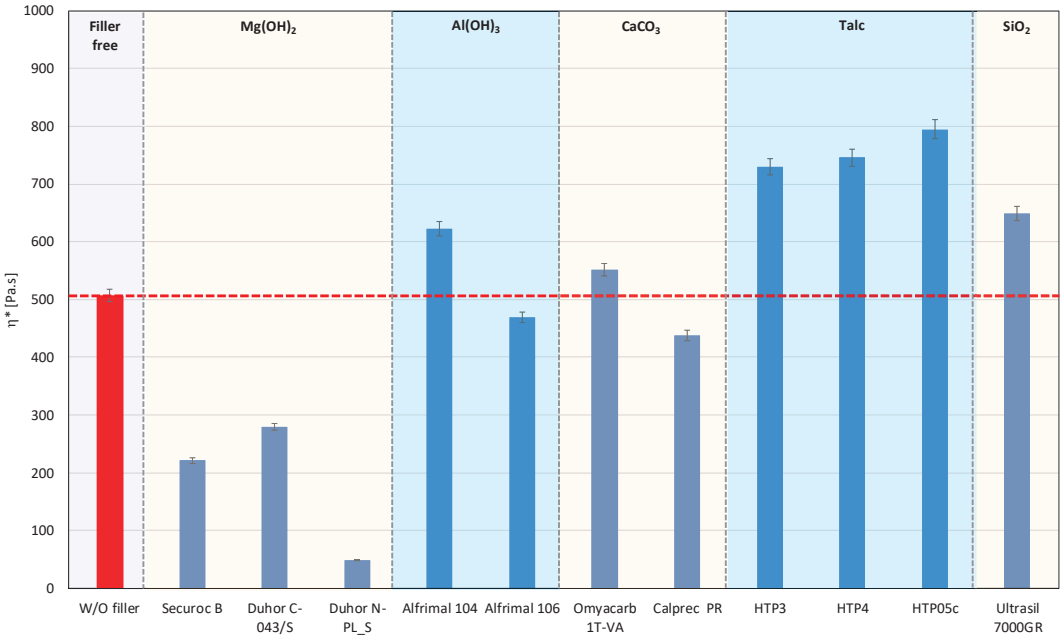

Figure 1. Complex viscosity at the 5th minute of testing for the polymer mixtures with fillers.

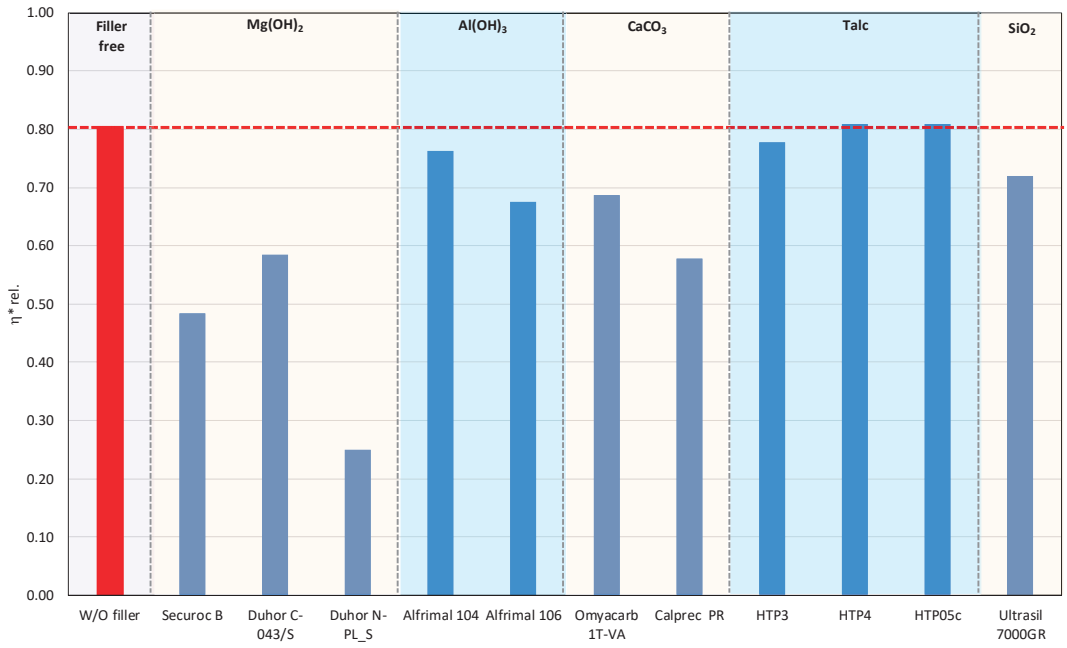

Figure 2. Relative complex viscosity at the 5th minute of testing for the polymer mixtures with fillers.

The addition of fillers to the blend led to an increase in viscosity for all tested fillers, except for magnesium hydroxide, one type of calcium carbonate, and one type of aluminum hydroxide, which resulted in a reduction in viscosity compared to the blend without fillers (Figure 1). The reason for the decrease in viscosity from the addition of particular fillers can be either because the fillers are not active or because the filler causes a degradation of the polymeric matrix or both. Considering the results of absolute complex viscosity (Figure 1) in conjunction with the relative complex viscosity evaluation (Figure 2), a conclusion emerges that all types of talc had no pro-degradation influence on the PLA/PHB matrix (relative viscosity after 5 min of melt processing in the rheometer is without changes in comparison to the filler-free blend), and all three tested talcs are active fillers (absolute values of viscosities are higher than the viscosity of the filler-free blend). The highest values of the viscosity among all the tested fillers were achieved with the talc-based mixtures. The HTP05c filler has the smallest particles, and the differences between the talc-based fillers are related to the particle size. Aluminum hydroxide is also an active filler (absolute viscosity of blend with Alfrimal 104 is higher than filler-free blend), but also this type of filler exhibits a moderate pro-degradation effect (slightly lower relative viscosity values). Calcium carbonate Omyacarb 1T-VA also exhibits a similar effect. The final effect on viscosity of the blend containing these fillers is given through the superposition of the reinforcing and degradation effects of fillers. The silica also acts as a pro-degradation substance in the studied PLA/PHB blend (lower relative viscosity), but, similarly to, for example, calcium carbonate Omyacarb 1T-VA, its reinforcing activity is higher; therefore, as a final effect, the viscosity of the blend filled with silica is higher than the unfilled blend. The strongest pro-degradation activity is exhibited by magnesium hydroxide as can be seen in Figure 2, and, due to this strong degradation of the polymeric matrix by the filler addition, the relative as well as the absolute viscosity of the blend is much lower than the viscosity of the unfilled blend. Magnesium hydroxide Duhor N-PL_S exhibits the strongest pro-degradation effect on the PLA/PHB blend, probably due to its very good dispersion in the matrix as will be shown later.

For the processability of PLA/PHB-based polymer composites using various technologies, such as extrusion or injection molding, and to achieve optimal mechanical properties, it will be crucial to minimize or eliminate the potential degradative effects of fillers. The strongest decrease in viscosity was recorded for fillers based on magnesium hydroxide. Thus, it can be stated that the degradation process of PLA/PHB mixtures will be significantly affected by the type of filler used, and especially by its chemical nature. Magnesium hydroxide fillers contain hydroxyl OH groups in their structures, and that is the reason why the mixtures that contain these fillers are the most sensitive to degradation. This conclusion is also supported by the results of work [50], where it has been proven that PHB can undergo an intensive degradation in the presence of two types of alcohol—ethylene glycol and glycerol. Alcoholysis with ethylene glycol is significantly faster than with glycerol, and the results show that degradation proceeds by random chain scission. This confirms that, not only OH presence, but also their reactivity has an influence on the degradation rate of the studied polymeric matrix. For both reactions, there was an observed decrease in the polydispersity index, which means that the degradation was caused by OH groups, which both alcohols contain [50]. An interesting situation is the case of aluminum hydroxide, where the presence of OH groups in this case causes a much lower degradation than magnesium hydroxide. This may be due to the fact that magnesium hydroxide is an ionic compound, while aluminum hydroxide exhibits stronger covalent forces, which may partially prevent the involvement of OH groups in degradation processes reactions.

The degradation of the polymeric matrix, in addition to decreasing the viscosity, can cause also the deterioration of other, mostly mechanical properties of the final material due to the decrease in the molecular weight of polymers created by the matrix.

In view of these facts, we have tried to eliminate the degradation process by the addition of suitable modifiers. We chose Joncryl (Figure 3a), a multifunctional styrene-acrylic-epoxy-based random oligomer which is the most common chain extender for polyesters including PLA due to its high functionality and chain-extending efficiency by reacting with terminal OH as well as terminal COOH groups of polyester chains [39,40]. We assumed that, in addition, epoxy groups could rapidly react with free OH groups on the filler surface, and, by this, they can protect the polyester against alcoholysis degradation. Phthalic anhydride (PhA) (Figure 3b) and diisocyanate (Figure 3c), which contain anhydride functional group and diisocyanate, respectively, also can rapidly react with OH groups on filler surfaces and, in this way, can protect polymers against the degradation described above. It should also be considered that the highly reactive isocyanate groups are capable of forming durable cross-linked structures, which complicates their straightforward classification as compatibilizers or chain extenders and may strongly affect the melt rheology and processing characteristics [51]. For the identification of the mechanisms of modifier action, it is important to understand how modifiers alone affect the rheological properties of a mixture without fillers; therefore, we measured the complex and relative complex viscosity of mixtures without added fillers. The results are presented in Figure 4.

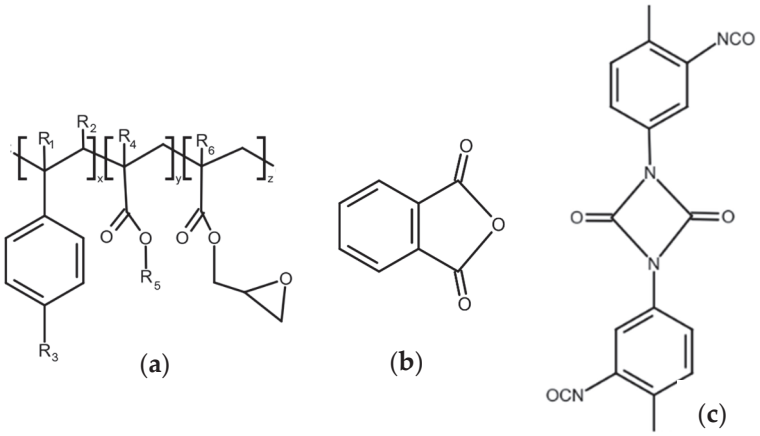

Figure 3. Chemical structure of (**a**) Joncryl 4368, (**b**) phthalic anhydride, and (**c**) IsoQure TT.

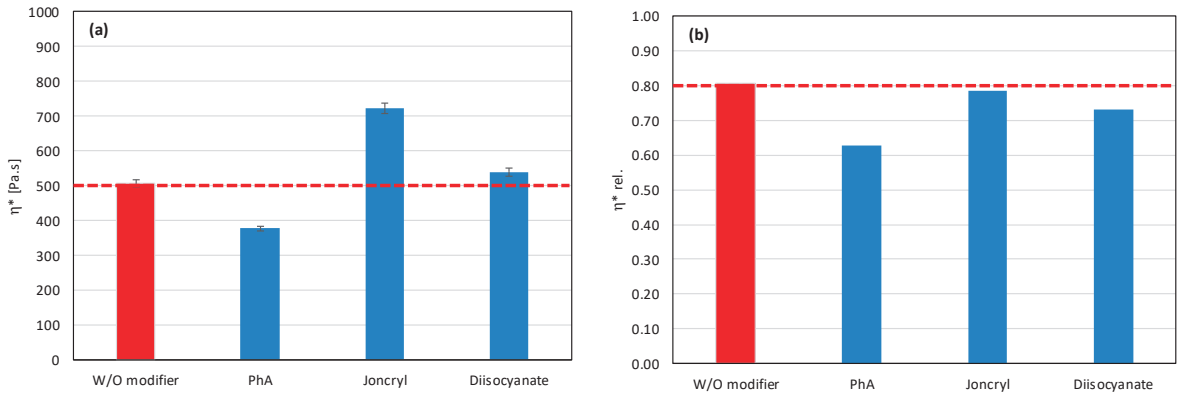

Figure 4. Effect of modifier on (**a**) complex and (**b**) relative complex viscosity at 5 min of testing for matrices without fillers.

Only Joncryl has no pro-degradation effect on the polyester matrix, and simultaneously acts as coupling agent (chain extender) (Figure 4). It causes no changes in the relative values of viscosity and increase in the absolute values of viscosity. Both anhydride and diisocyanate act as pro-degradants, but diisocyanate, in contrast to PhA, acts also as a coupling agent. The chemical nature (functional groups) of the modifier can initiate a degradation processes in the polymer matrix itself, so it is very important to find the right combination of filler and modifier, and finally a suitable amount of modifier added to the mixture, to obtain the best balance between all chemical reactions: the degradation of polymers, the endcupping of active OH groups of fillers, and the chain extending of polyesters. Therefore, a basic screening of modifier–filler combinations was realized to find the best option. In the first screening, all modifiers were applied at a concentration of 1 wt%, but it is clear that the quantitative acting of modifiers depends on the molar concentration of active groups in relation to the molar concentration of active OH groups on the filler surface.

As mentioned earlier, fillers with more reactive OH groups (Mg $(OH)_2$) have a significantly more pronounced effect on the degradation of the PLA/PHB blends than fillers with less reactive OH groups. Depending on the reactivity of OH groups and the intensity of degradation of the biopolyesters, the degrading effect of the tested potential modifiers is also manifested in various ways. Figures 5 and 6 show the complex viscosity and relative complex viscosity values in the 5th minute of testing for mixtures with aluminum hydroxide and magnesium hydroxide, respectively. Joncryl has practically no or a very weak effect on the processing stabilization of the blends with these two types of fillers (see relative viscosity values). On the other hand, a small increase in the absolute values of viscosity compared to the unmodified blend can be observed as a superposition of the chain extending, reinforcing, and degrading effects, together with the partial elimination of OH groups by a reaction with the epoxy groups. In contrast to Joncryl, more reactive modifiers react more rapidly with fillers' OH groups than Joncryl, and therefore they exhibit a more effective stabilizing effect. From this point of view, the most effective combination for aluminum hydroxide is Afrimal 104/diisocyanate. This blend has the same relative viscosity value as the unfilled blend and a much higher value of absolute viscosity than the unfilled and filled blends without modifiers. In this case, the modifier ensures a full protection of the matrix against degradation via the OH groups from the filler, and therefore the reinforcing effect of the filler can be developed. The same effect in the case of magnesium hydroxide can be observed in the combination of Duhor C-043/s as a filler and PhA as a modifier. Unmodified magnesium hydroxide (Duhor N-PL_S), which exhibited the strongest pro-degradation effect among all the tested fillers (Figures 1 and 2), was subsequently tested only with the PhA modifier based on the obtained results. Only this combination, out of all the tested filler/modifier alternatives, provides a higher relative viscosity in 5 min than the unfilled mixture, which means that the Duhor N-PL_S/PhA combination has a stabilizing effect on PLA/PHB melting and slows down the degradation rate of the mixture. This is probably due to the high reactivity of the OH groups, which, if unprotected, have a strong pro-degradation effect; on the other hand, in the presence of a bifunctional PhA-type reactive additive, this pro-degradation effect of the free OH groups is partially or fully eliminated.

To provide evidence for the interaction of the modifiers with the surface hydroxyl groups of the fillers, FTIR spectra of magnesium hydroxide and aluminum hydroxide in the presence of the additives were recorded. Dry mixtures were prepared using the same filler-to-modifier ratio as in the studied blends, and were subsequently mixed for five minutes at 180 °C to simulate the conditions of reactive processing. In the O–H stretching region,

a strong and sharp absorption band at 3687 cm^{-1} corresponding to the O–H stretching vibration of magnesium hydroxide was observed. The relative intensity of this absorption decreased compared with the pure magnesium hydroxide sample, providing evidence that some of the hydroxyl groups in the mixture samples reacted with the additives, which is reflected in the reduced intensity of the OH absorption signal (Figure S20). For aluminum hydroxide, the O–H stretching region is characterized by several broad absorption bands centered around 3620 cm^{-1}, together with a wider envelope extending from approximately 3550 to 3300 cm^{-1}. A clear decrease in the intensity of these OH-related bands was observed in the spectra of the mixtures, providing evidence of the interaction of the modifiers with the surface hydroxyl groups of aluminum hydroxide (Figure S19).

As a result, even the same type of filler (chemically) may require different types of modifiers to reduce the rate of degradation. All modifiers were tested also in combination with other tested fillers (talc, calcium carbonate, and silica) (Figures 7–9). The results confirmed the selectivity of modifiers for protection of the PLA/PHB matrix against processing degradation in the presence of various types of fillers. We could declare that Joncryl exhibited a positive effect in combination with calcium carbonate and silica.

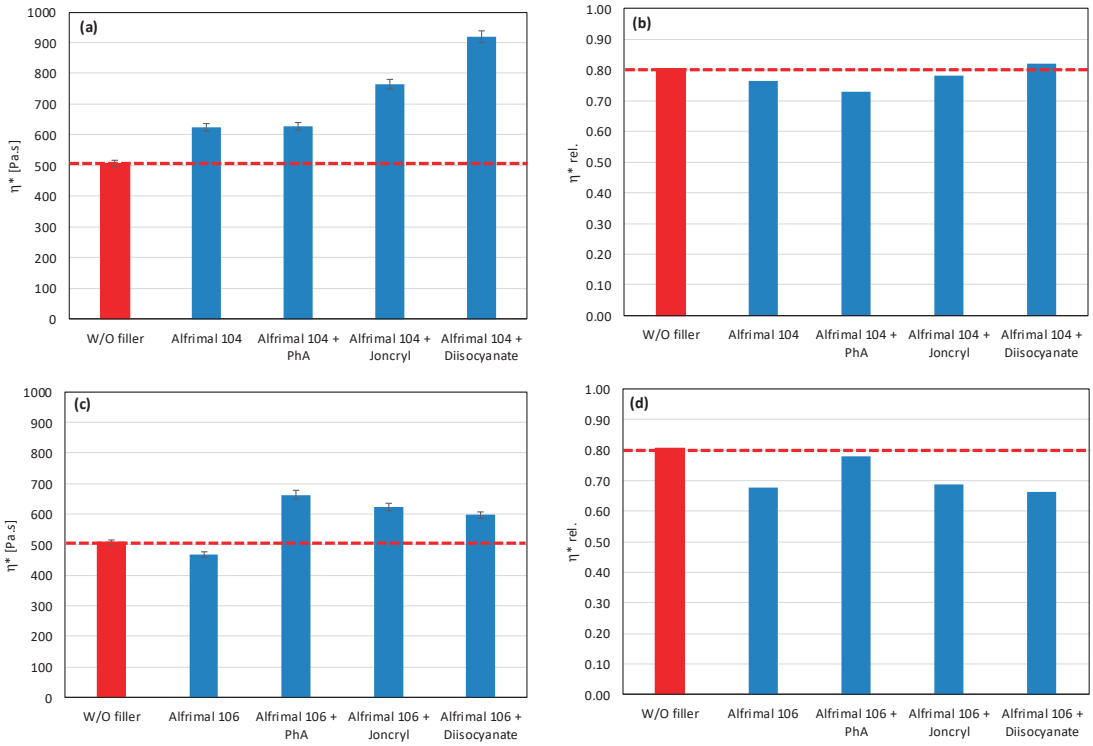

Figure 5. Effect of modifier on complex viscosity (**a**,**c**) and relative complex viscosity (**b**,**d**) at 5 min of testing for the polymer blend containing aluminum hydroxide.

3.2. Thermal Properties

Temperature and enthalpy of crystallization are very important parameters for the processing of semicrystalline polymeric materials like PLA/PHB blends. These parameters have a strong influence on the processing and application properties of polymeric materials. A high temperature of crystallization (T_c) indicates a fast and early crystallization during the cooling of a melt, which allows for a shorter injection molding cycle than in the case of materials with a lower T_c. The enthalpy of crystallization directly reflects the amount of crystalline phase which is created during the cooling of a melt. Based on DSC thermograms, the crystallization characteristics of the studied blends were evaluated. The influence of

fillers and modifiers on the temperature and enthalpy of crystallization is presented in Figure 10. The enthalpy values were recalculated relative to the polymer matrix, thereby eliminating the influence of filler mass and enabling a more accurate comparison of the crystallization behavior between neat and filled systems.

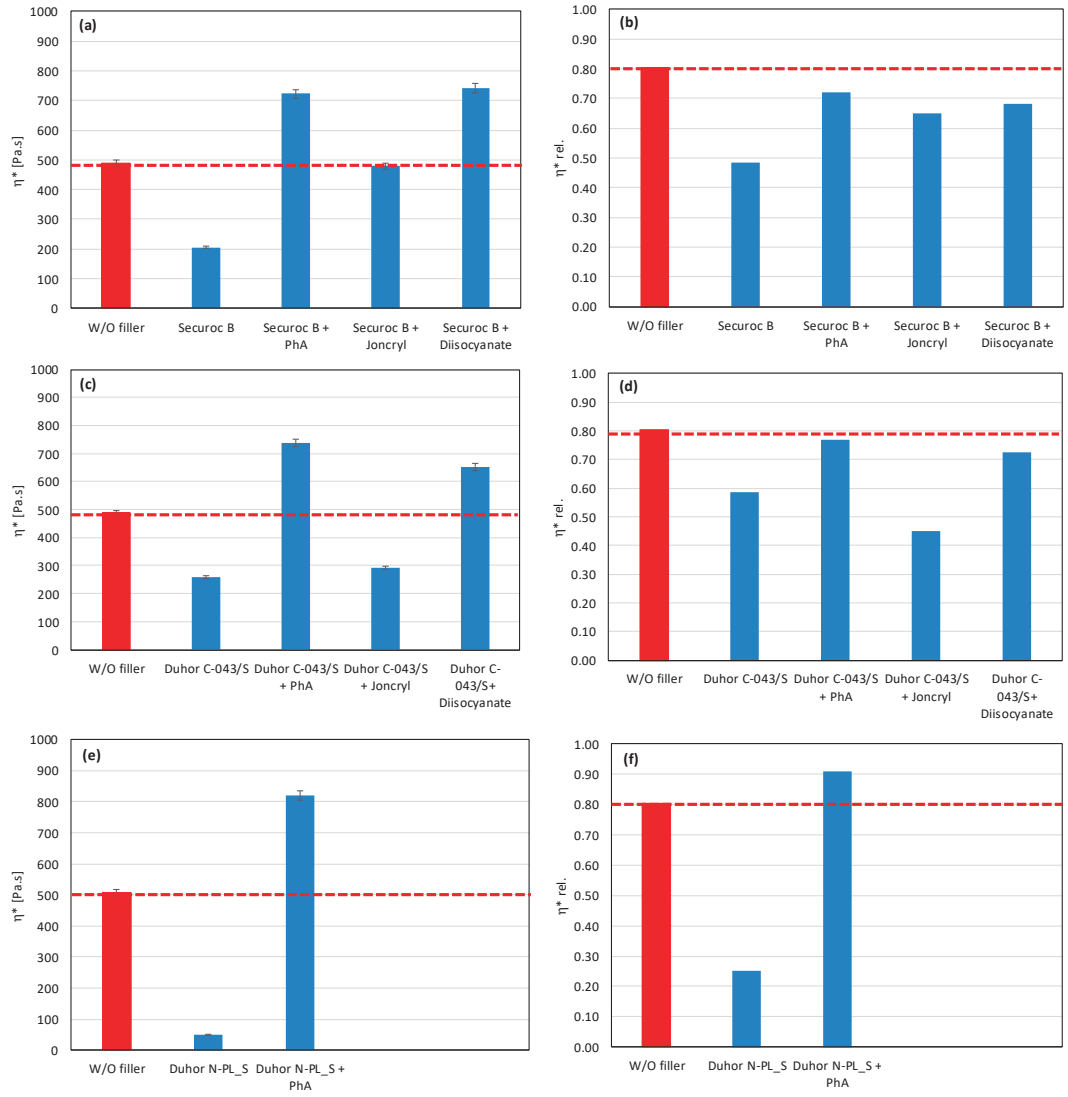

Figure 6. Effect of modifier on complex viscosity (**a**,**c**,**e**) and relative complex viscosity (**b**,**d**,**f**) at 5 min of testing for the polymer blend containing magnesium hydroxide.

The crystallization process is significantly affected by the presence of the filler. Talc in particular significantly increases Tc, which in turn allows for a higher content of crystallites in the final product, as documented by the increased enthalpy of crystallization (Figure 10). Talc clearly acts as the most effective nucleating agent among the tested fillers, while the effect of modifiers in the case of talc is negligible. However, as far as fillers that cause a degradation of the polymer matrix are concerned, then the modifiers have a significant effect on the crystallization process. A higher content of the crystalline phase is achieved for those modifiers which at the same time suppress degradation. For OH-functional fillers, these are mainly PhA and diisocyanate. Although Joncryl has a stronger influence on the neat matrix (showing the highest increase in viscosity in the matrix without filler, Figure 4), its modifying effect on either increasing the viscosity or influencing crystallization is usually

the lowest. This clearly confirms the correctness of the chosen approach—preventing the degradation of PLA/PHB/inorganic filler composites by modifying the filler surface (blocking pro-degrading OH groups) rather than subsequently reconstructing the degraded polymers by applying coupling agents. As shown in Figure 10, all mixtures with fillers without modifiers show a higher enthalpy of crystallization than the unfilled matrix alone, from which it is clear that the nucleation activity of the fillers is higher than their pro-degradative activity, while the application of suitable modifiers reduces the extent of matrix degradation by fillers containing $Mg(OH)_2$ and $Al(OH)_3$, subsequently slightly increasing the content of the crystalline phase.

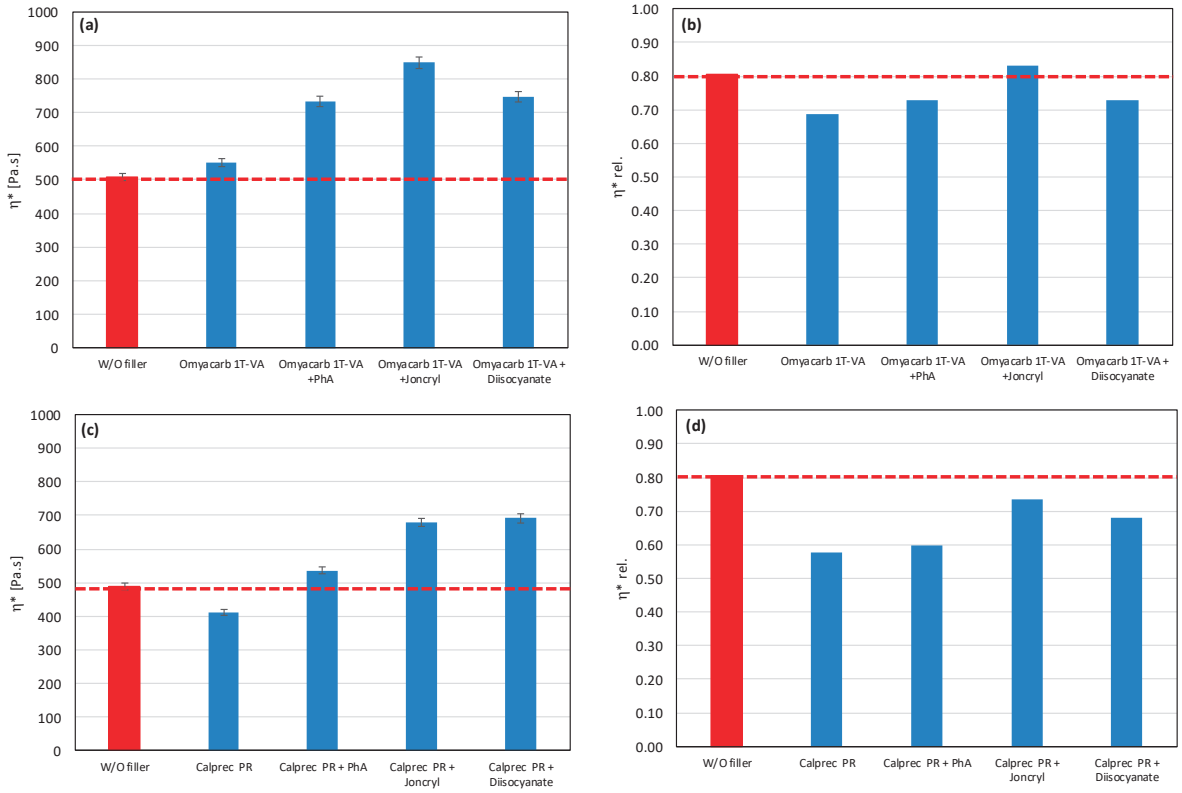

Figure 7. Effect of modifier on complex viscosity (**a**,**c**) and relative complex viscosity (**b**,**d**) at 5 min of testing for the polymer blend containing calcium carbonate.

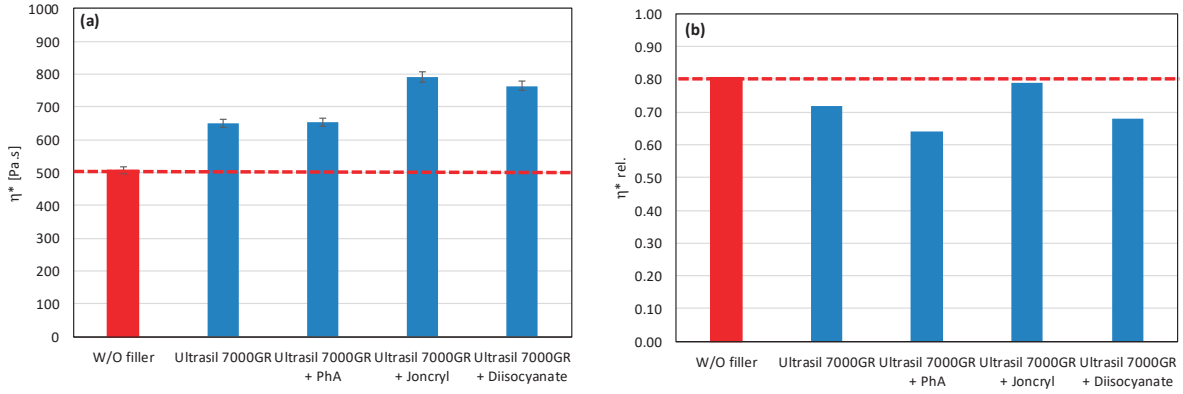

Figure 8. Effect of modifier on complex viscosity (**a**) and relative complex viscosity (**b**) at 5 min of testing for the polymer blend containing silica.

3.3. Mechanical Properties

As part of the assessment of the influence of the type of inorganic filler and modifier on the mechanical properties, in the basic screening part of the work, we used cast foils prepared by chill-roll technology at a lab scale. The relative elongation at break, tensile strength at break, and yield strength were monitored as basic mechanical parameters (Figure 11).

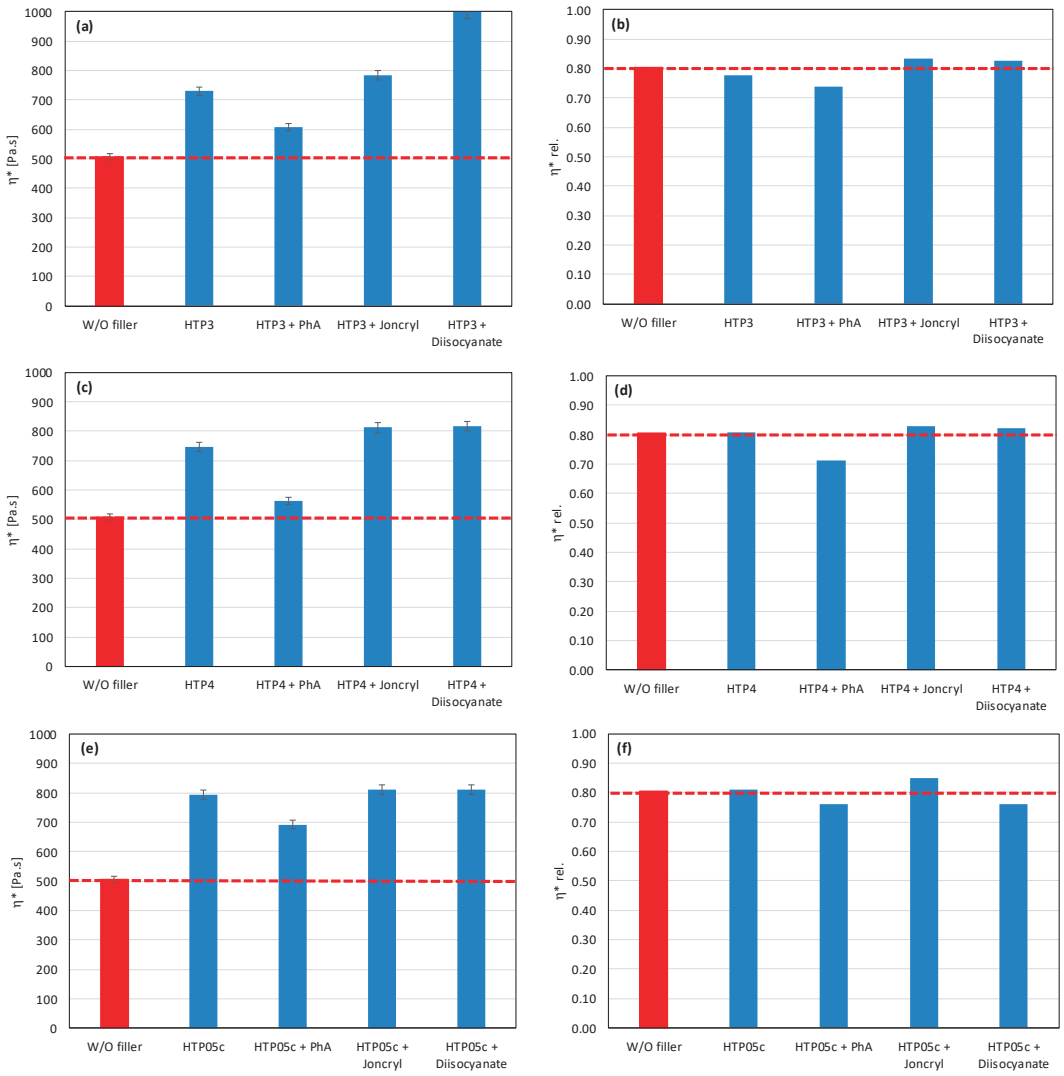

Figure 9. Effect of modifier on complex viscosity (**a**,**c**,**e**) and relative complex viscosity (**b**,**d**,**f**) at 5 min of testing for the polymer blend containing talc.

From the point of view of comparing the relative elongation at break for mixtures without modifiers, it can be stated that the highest values were logically reached for the unfilled mixture, at a level of approximately 30%. For filled mixtures without modifiers, the elongation was below 10%. A completely different situation can be observed after the application of the PhA modifier, which interacts with the polymer matrix the most. It can be observed that the relative elongation at break in mixtures without any filler was the highest with the PhA modifier, at approximately 300%. The PhA modifier seems to be the best for mixtures filled with HTP05c talc, HTP4 talc, and Alfirmal 106 as well. With the addition of another modifier (Joncryl), the situation changed completely when an elongation of the unfilled mixture below 10% was recorded; on the contrary, the values for the fillers Alfrimal 104, HTP3, and Omyacarb 1T increased. The changes in the case of extension for

mixtures with diisocyanate modifiers are negligible, and the modifying effect has not been confirmed for this property.

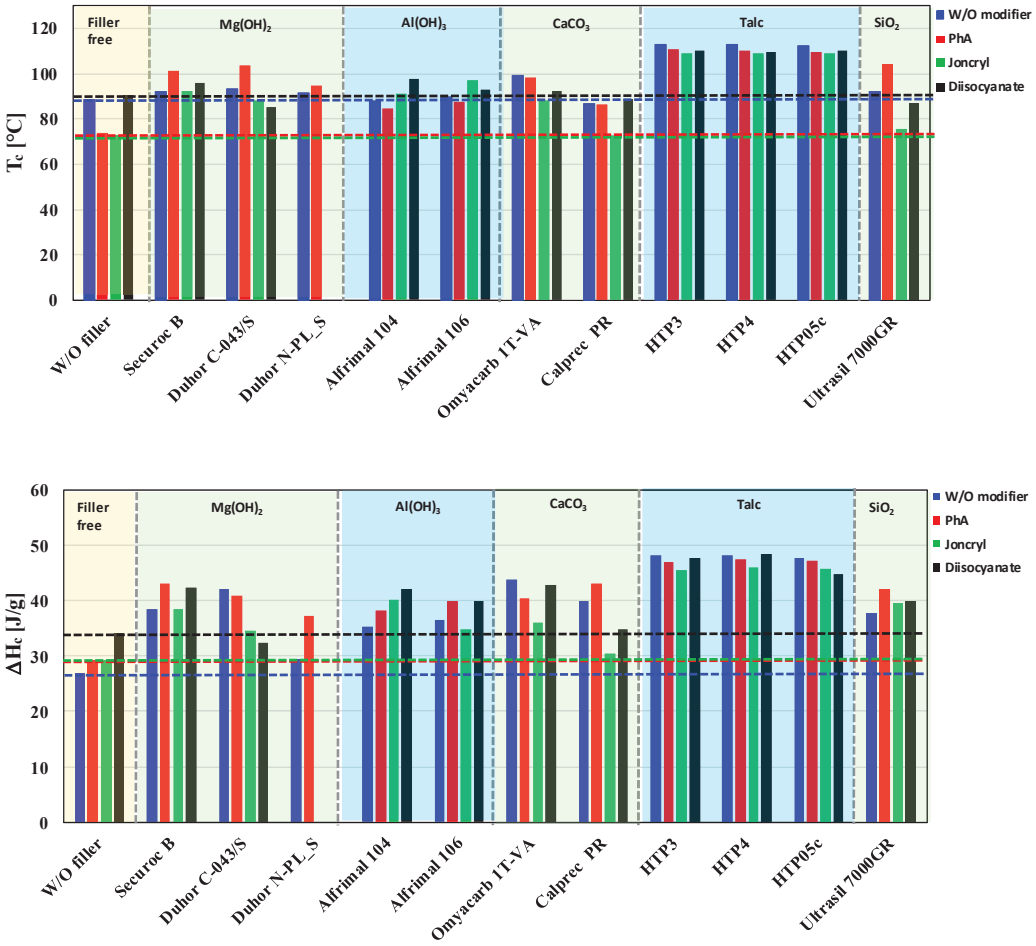

Figure 10. Effect of filler and modifier type on crystallization temperature (T_c) and enthalpy (ΔH_c).

It is more complicated to describe the influence of selected fillers and modifiers on the tensile strength at break. The positive effect of the modification on the monitored property can be clearly stated, but its improvement for a specific filler will be given by using the particle size of a filler and its surface treatment by a modifier. In this case, the chemical nature of the filler also plays a role, as the changes for groups of fillers (e.g., talc) are similar. However, in addition to improving the tensile strength at break of the filled mixtures, the selected modifiers also allow an increase in the case of a mixture without a filler. The highest values of tensile strength at break at the level of 58 MPa were achieved with talc (HTP05c), which has the smallest particle size of all types of talc used, in combination with the modifier diisocyanate. Other tested modifiers do not have such a pronounced effect on tensile strength, and their positive or negative effect depends on the type of filler. PhA was most positive in combination with Duhor C-043 and Omyacarb 1T. Joncryl either deteriorated or did not improve tensile strength for most fillers, with the exception of Duhor C-043, where there was a significant improvement. The last property evaluated was the yield strength. From the point of view of assessing the strength characteristics, it will be more important, as the absolute values were achieved higher than in the case of tensile strength at break. As was the case for tensile strength at break, the highest values of yield strength were achieved with HTP05c and Alfrimal 106 filler in combination with the diisocyanate modifier. Based on a summary of the previous considerations, it can be stated

that the resulting physical–mechanical properties will be determined not only by the type of filler, its chemical nature, and its particle size, but also by the type of modification. Based on the obtained results, it can be stated that there is no universal modifier to improve the mechanical properties for all types of fillers in the given PLA/PHB matrix. It turned out that, even within one class of fillers, e.g., talc, a given modifier can have a positive effect once and a negative effect depending on the specific properties of the filler, presence of functional groups, their density and reactivity, and also the specific surface area and the size of the particles.

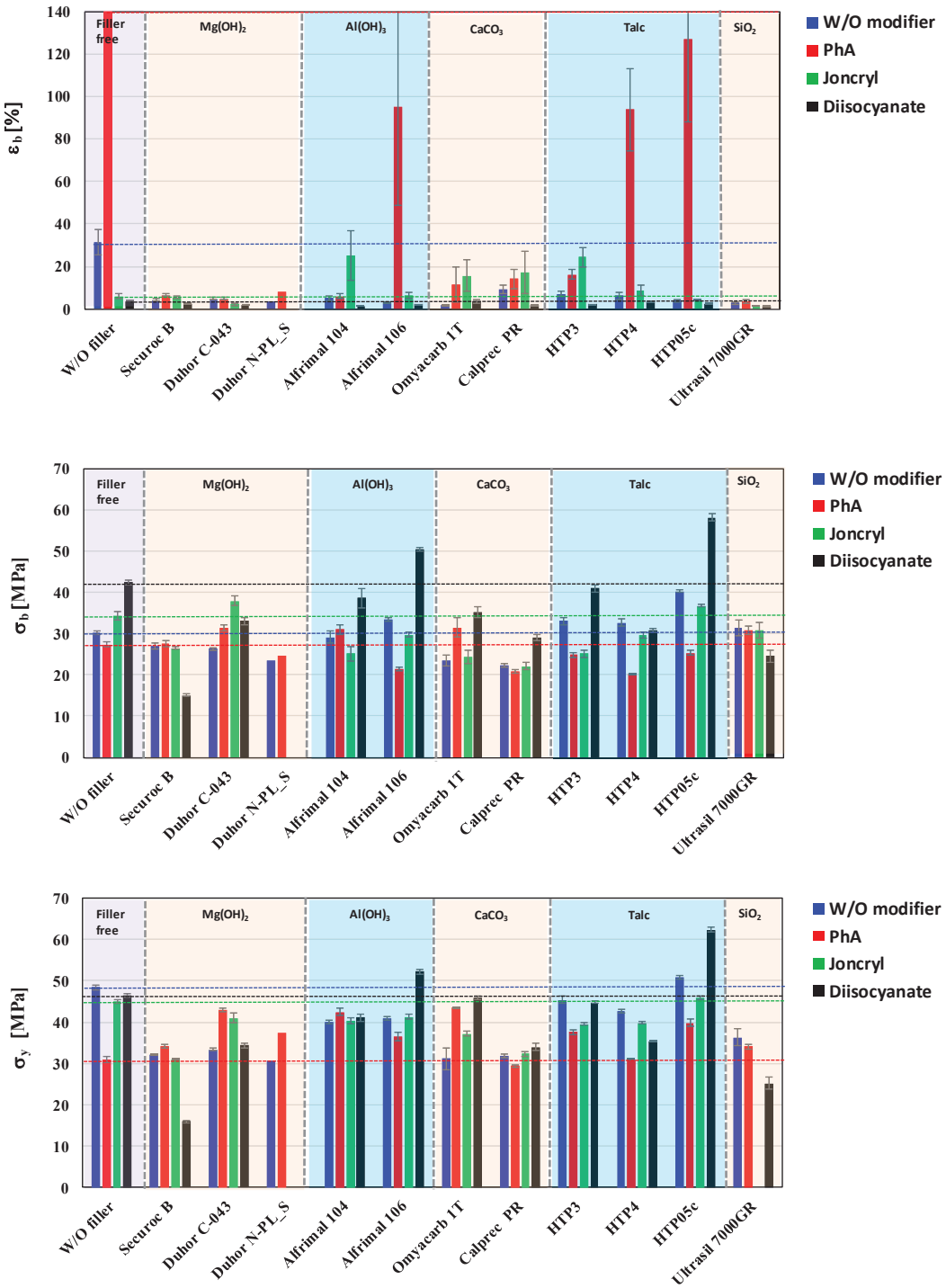

Figure 11. Effect of fillers and modifiers on mechanical properties of PLA/PHB blends.

3.4. Morphological Structure

Most properties, preferably mechanical, are closely related to the morphological structure of the blends. Important factors in this regard are the dispergation of the filler and the phase interface between the filler and the polymer matrix. A morphological study was conducted based on SEM images of fracture surfaces prepared in liquid nitrogen. SEM images at 5000× magnification are shown in Figure 12. The tested modifiers, regardless of their antidegradative activity in the mixture, have different effects on their morphologies.

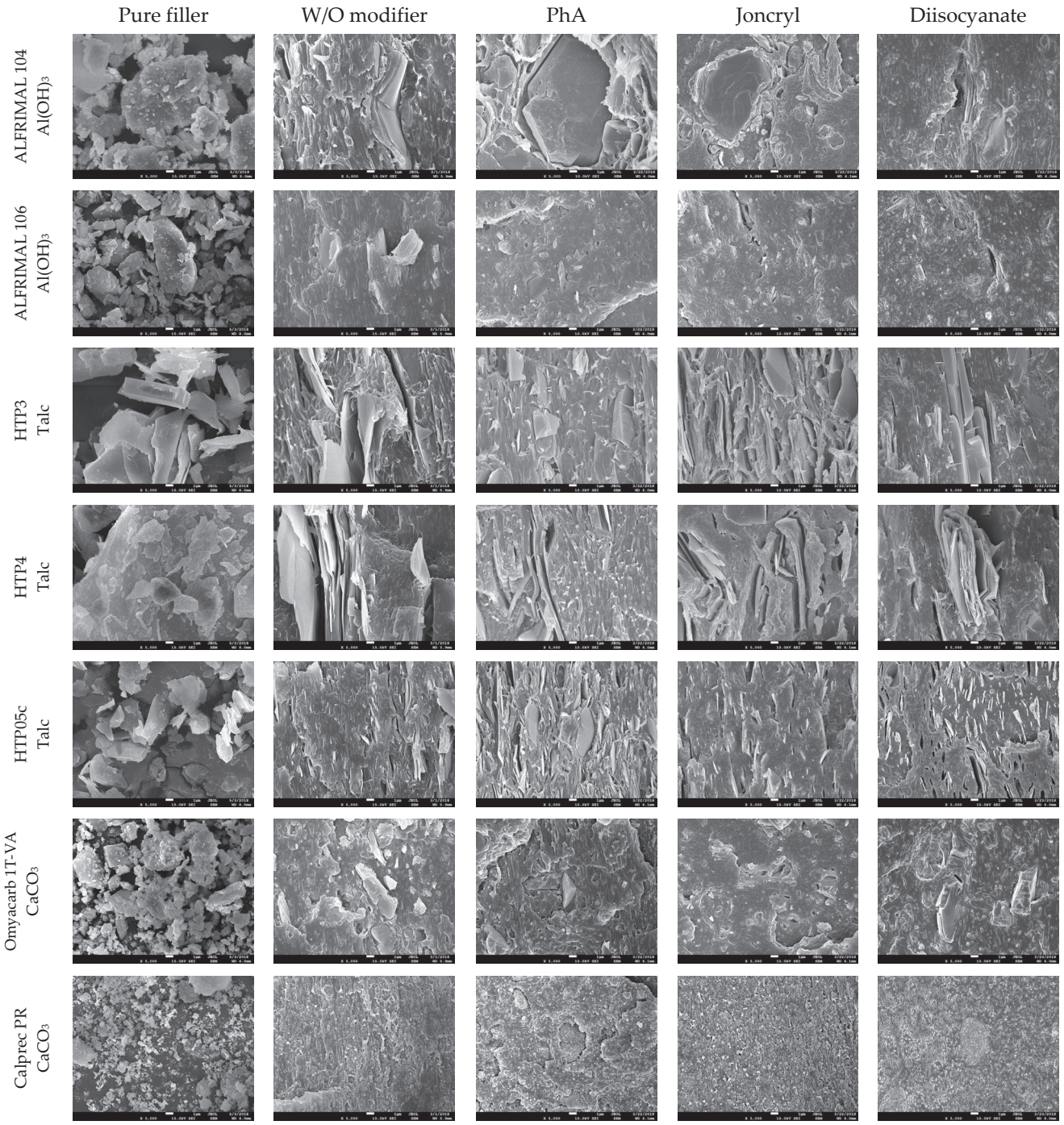

Figure 12. *Cont.*

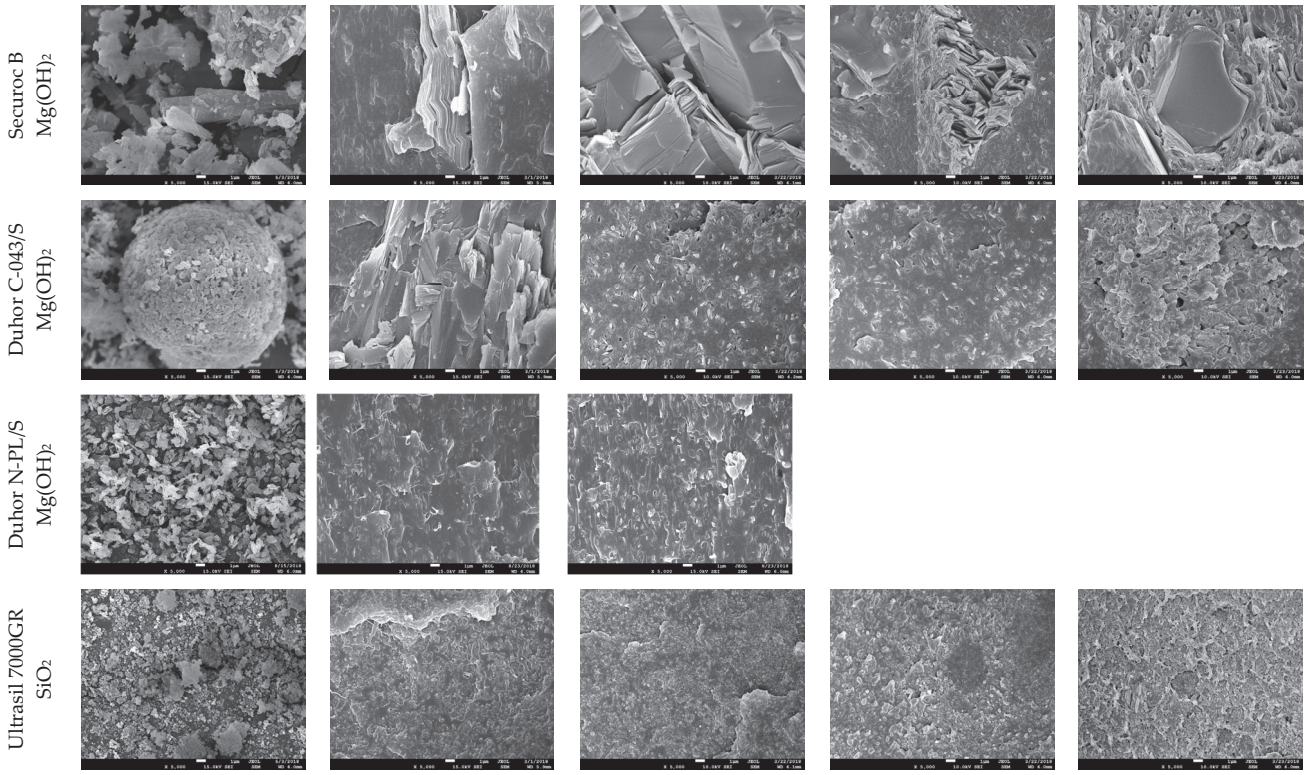

Figure 12. SEM images of the morphology of filled blends at 5000× magnification.

A comparison of the two types of aluminum hydroxide shows that Alfrimal 106 has smaller filler particles compared to Alfrimal 104. In the process of shear stress on a twin-screw extruder, in the case of the filler Alfrimal 104, the filler did not break into smaller particles; it can also be seen that, in the case of Alfrimal 104, after mixing into the mixture, the compatibility at the phase interface is worse than in the case of Alfrimal 106. At the same time, it can be seen that the addition of the modifier Joncryl and diisocyanate to the Afrimal 104 improved the compatibility between the filler and the polymer matrix at the phase interface in comparison to PhA, which corresponds to the following physical–mechanical properties: the highest elongation values for the modifier Joncryl and the highest values of tensile strength for the modifier diisocyanate. Smaller filler particles in the case of Alfrimal 106 and their better dispersion in the polymer matrix were responsible for a further increase in physical–mechanical properties compared to Alfrimal 104. In general, both tested aluminum hydroxide fillers have more potential as a filler for PLA/PHB blends with Afrimal 106, and, based on the morphology of the blends, the best results use PhA as a modifier. This also corresponds with mechanical properties, and this modifier offers the best processing stability of filled blends with Afrimal 106.

Talc-based fillers have a lamellar structure, where the decisive factor will be the ability to delaminate in the shear field during the blending. This effect is most pronounced in the case of talc HTP05c, and especially when applying the modifiers Joncryl and diisocyanate. This correlates with the obtained physical–mechanical properties, as the highest values of tensile strength at yield and tensile strength at break were achieved for all tested fillers. The other two types of talc (HTP3 and HTP4) show a significantly lower degree of delamination in the mixing process than HTP05c talc, regardless of the modifier applied.

If calcium carbonate, under the trade name Omyacarb 1T, was used as a filler, an improvement in compatibility with the polymer matrix could be observed on the fracture

surfaces as a result of the applied modifiers. In the case of the PhA and diisocyanate modifiers, this was reflected in higher values of tensile strength at break. A relatively wide particle size distribution can be observed in the images for the pure calcium carbonate filler Calprec PR. On the fracture surfaces of polymer mixtures, larger particles can be observed with the modifiers PhA and diisocyanate. Their comparison shows that a much better compatibility with the matrix is ensured by the addition of the diisocyanate modifier. On the other hand, Omyacarb particles, in general, are significantly larger than Calprec PR particles, which gives Calprec PR a greater application potential in PLA/PHB mixtures, but, compared to other types of fillers tested, mixtures tested with calcium carbonate can be assessed as mildly mixed.

In the case of magnesium hydroxide fillers (Securoc B, Duhor C-043 and Duhor N-PL_S), the modification was carried out mainly to suppress the degradation process during thermomechanical stress. Microscopy images show that there is a difference in the size and shape of the particles of these fillers. Securoc B has a much larger particle size compared to both Duhors, but, in the case of Duhor C-043, it is possible to observe relatively large spherical agglomerates of small elementary particles. Duhor N-PL_S is in the form of significantly smaller agglomerates than Duhor C-043/S. After mixing all three fillers into the mixture without modifiers, Duhor N-PL_S disperses very well; there is no significant dispersion of Duhor C-043/S, and the fracture surface structure contains relatively large areas of non-dispersed magnesium hydroxide. In the case of Securoc B, relatively large compact particles are present in the fracture area. Even the addition of modifiers does not result in a significant reduction in the Securoc B filler particle size, although PhA and Joncryl in particular visibly improve interfacial adhesion, resulting in the destruction of the filler particles themselves rather than delamination onto the particle surface during fracture. On the other hand, in the case of Duhor C-043/S, it can be seen that the modifiers, in particular PhA and Joncryl, ensure a very good dispersion of this filler down to the isolated primary particles. The diisocyanate has a significantly weaker dispersing efficiency, although it also improves adhesion at the phase interface. A good dispersion due to these modifiers probably also occurs due to the reaction between OH groups on the particle surface, which reduces the number of strong OH-OH interactions between the filler particles, which allows them to be more easily dispersed in a relatively low-viscosity less-polar PLA/PHB matrix. Duhor N-PL_S, as already mentioned, is very well dispersed, even without a modifier, and its dispersibility does not change with the addition of PhA. Also, due to the very good dispersibility and thus due to the large surface area of the filler available for the polymer matrix, the PLA/PHB mixture is highly sensitive to degradation due to this type of unmodified Duhor N-PL_S. After the elimination of OH groups through a reaction with PhA, the stability of the mixture is much better; even the relative viscosity, as previously described, is higher than the relative viscosity of the unfilled mixture, which means that this filler has a reinforcing effect in terms of the viscosity of the mixture. For these reasons, magnesium hydroxide Duhor N-PL_S, modified with PhA, seems to be the most promising filler for PLA/PHB mixtures.

The last monitored filler was silica, under the trade name Ultrasil 7000GR. This filler should have the smallest particle size and thus the largest specific surface area, since we expected that it could achieve good values for physical–mechanical properties. In addition, the observation of the morphological structure shows that the filler was very well dispersed in the polymer matrix during the mixing process, but only in small agglomerates, not as primary particles. The dimensions of the agglomerates depend on the applied modifier. However, on the fracture surfaces for modifier Joncryl and, in particular, modifier diisocyanate, a worse compatibilization effect of the modifier can be observed, which

would indicate a poorer adhesion to the polymer matrix. A problem with this filler may be the tendency to form agglomerates, which can be seen in the images for the pure filler as well as for the mixtures with the modifiers Joncryl and diisocyanate.

Based on the morphology evaluation, it can be stated that improving the compatibility between the filler and the polymer matrix can be achieved by adding modifiers, but the effect of a particular modifier will have to be assessed in relation to a particular filler, and it is not possible to generalize the effect of modifiers even within fillers of the same chemical nature.

4. Conclusions

The main objective of this work was to investigate the potential of applying inorganic fillers to bio-based and biodegradable PLA/PHB blends. For this purpose, commonly used commercial fillers were employed—calcium carbonate, talc, silica, magnesium hydroxide, and aluminum hydroxide—with different particle sizes and particle size distributions. In addition to these fillers, three types of modifiers (PhA, Joncryl ADR-4368, IsoQure TT diisocyanate) were also investigated to further adjust the material characteristics and enhance the overall performance of the blends.

Fillers containing reactive hydroxyl groups on their surface act as pronounced pro-degradants in PLA/PHB blends according to the executed rheological measurements. The results indicate that magnesium hydroxide exerts a stronger pro-degradation effect on the polymer matrix than aluminum hydroxide. The pro-degradative effect of fillers can be suppressed by introducing reactive modifiers capable of binding to the active hydroxyl groups on the filler surface during blend preparation, thereby preventing the degradation of PLA and PHB polyesters. The FTIR spectra of magnesium hydroxide and aluminum hydroxide mixed with modifiers indicate the interaction of modifiers with the surface hydroxyl groups of the fillers, which is reflected in the reduced intensity of the characteristic O–H absorption bands. The results also demonstrated that the efficiency of individual modifiers is highly specific to the type of filler, necessitating the selection of an appropriate filler/modifier combination not only between chemically distinct fillers but also among fillers of the same chemical nature with different morphologies. Among the tested alternatives, the most effective combinations were identified as magnesium hydroxide with phthalic anhydride and talc with diisocyanate. The crystallization behavior of PLA/PHB blends was strongly influenced by the presence of fillers, with talc acting as the most effective nucleating agent, significantly increasing Tc and the enthalpy of crystallization, while the effect of modifiers in this case was negligible. In contrast, for OH functional fillers such as $Mg(OH)_2$ and $Al(OH)_3$, modifiers played a decisive role, as PhA and diisocyanate suppressed matrix degradation and thereby promoted a higher crystallinity. The study confirmed that the effect of modifiers on the mechanical properties of PLA/PHB blends strongly depends on the type and morphology of the filler. While PhA significantly improved elongation at break, particularly in unfilled blends and in mixtures with talc HTP05c, Alfrimal 106, and HTP4, Joncryl enhanced this property only for Alfrimal 104, HTP3, and Omyacarb 1T, but reduced it in unfilled blends. In contrast, diisocyanate modifiers had a negligible effect on elongation at break, although they proved to be the most effective in enhancing tensile and yield strength in combination with talc HTP05c and Alfrimal 106. The morphological analysis revealed that the effectiveness of the modifiers strongly depends on the specific filler type: for some fillers, they enhance particle dispersion and interfacial adhesion, resulting in improved mechanical properties, while for others their effect is limited.

Supplementary Materials: The following supporting information can be downloaded at https://www.mdpi.com/article/10.3390/polym17202721/s1. Figure S1. Dependence of complex viscosity on time for the tested mixtures containing different fillers; Figure S2. Dependence of relative complex viscosity on time for the tested mixtures containing different fillers; Figure S3. Dependence of complex viscosity (A) and relative complex viscosity (B) on time for the tested mixtures containing different modifiers; Figure S4. Dependence of complex viscosity (A) and relative complex viscosity (B) on time for the tested mixtures containing Securoc B ($Mg(OH)_2$) filler with different modifiers; Figure S5. Dependence of complex viscosity (A) and relative complex viscosity (B) on time for the tested mixtures containing Duhor C-043/S ($Mg(OH)_2$) filler with different modifiers; Figure S6. Dependence of complex viscosity (A) and relative complex viscosity (B) on time for the tested mixtures containing Alfrimal 104 ($Al(OH)_3$) filler with different modifiers; Figure S7. Dependence of complex viscosity (A) and relative complex viscosity (B) on time for the tested mixtures containing Alfrimal 106 ($Al(OH)_3$) filler with different modifiers; Figure S8. Dependence of complex viscosity (A) and relative complex viscosity (B) on time for the tested mixtures containing Omyacarb 1T VA ($CaCO_3$) filler with different modifiers; Figure S9. Dependence of complex viscosity (A) and relative complex viscosity (B) on time for the tested mixtures containing Calprec PR ($CaCO_3$) filler with different modifiers; Figure S10. Dependence of complex viscosity (A) and relative complex viscosity (B) on time for the tested mixtures containing HTP3 (Talc) filler with different modifiers; Figure S11. Dependence of complex viscosity (A) and relative complex viscosity (B) on time for the tested mixtures containing HTP4 (Talc) filler with different modifiers; Figure S12. Dependence of complex viscosity (A) and relative complex viscosity (B) on time for the tested mixtures containing HTP05c (Talc) filler with different modifiers; Figure S13. Dependence of complex viscosity (A) and relative complex viscosity (B) on time for the tested mixtures containing Ultrasil 7000GR (SiO_2) filler with different modifiers; Figure S14. Heat flow as a function of temperature for the pure polymers (PLA and PHB); Figure S15. Heat flow as a function of temperature for mixtures with all fillers without modifier; Figure S16. Heat flow as a function of temperature for mixtures with all fillers with modifier PhA; Figure S17. Heat flow as a function of temperature for mixtures with all fillers with modifier Joncryl; Figure S18. Heat flow as a function of temperature for mixtures with all fillers with modifier diisocyanate; Table S1. Results of *t*-tests comparing mechanical properties (elongation at break, tensile strength at break, tensile stress at yield) of PLA/PHB composites with different fillers without and with modifiers (PhA, Joncryl, Diisocyanate); Figure S19. FTIR spectra of Alfrimal 104 ($Al(OH)_3$) powder and its mixtures with PhA, Joncryl, and diisocyanate after thermal treatment at 180 °C for 5 min; Figure S20. FTIR spectra of Duhor N-PL/S ($Mg(OH)_2$) powder and its mixtures with PhA, Joncryl, and diisocyanate after thermal treatment at 180 °C for 5 min.

Author Contributions: Conceptualization, J.F., M.R. and P.A.; Methodology, M.Ď., Z.V., I.V. and J.K.; Validation, K.T., M.F., S.H. and Z.K.; Formal analysis, L.O., J.K. and Z.K.; Investigation, M.R., K.T., L.O. and E.O.; Resources, J.K. and P.A.; Data curation, M.Ď., Z.V. and E.O.; Writing—original draft, J.F.; Writing—review & editing, R.P. and P.A.; Visualization, I.V. and S.H.; Supervision, R.P.; Project administration, J.F.; Funding acquisition, P.A. All authors have read and agreed to the published version of the manuscript.

Funding: This work was supported by the grant of Research and Development Agency APVV-20-0256 and APVV-23-0221.

Institutional Review Board Statement: Not applicable.

Data Availability Statement: The original contributions presented in this study are included in the article/supplementary material. Further inquiries can be directed to the corresponding author.

Conflicts of Interest: Author Martina Repiská was employed by the company Audia Plastics s.r.o. The remaining authors declare that the research was conducted in the absence of any commercial or financial relationships that could be construed as a potential conflict of interest.

References

1. Niaounakis, M. Recycling of biopolymers—The patent perspective. *Eur. Polym. J.* **2019**, *114*, 464–475. [CrossRef]
2. Samir, A.; Ashour, F.H.; Hakim, A.A.A.; Bassyouni, M. Recent advances in biodegradable polymers for sustainable applications. *npj Mater. Degrad.* **2022**, *6*, 68. [CrossRef]
3. Dutta, D.; Sit, N. A comprehensive review on types and properties of biopolymers as sustainable bio-based alternatives for packaging. *Food Biomacromolecules* **2024**, *1*, 58–87. [CrossRef]
4. McKeen, L. 13—Renewable Resource and Biodegradable Polymers. In *The Effect of Sterilization Methods on Plastics and Elastomers*, 4th ed.; McKeen, L., Ed.; William Andrew Publishing: Santa Rosa, CA, USA, 2018; pp. 417–435. [CrossRef]
5. Zeng, J.-B.; Li, K.-A.; Du, A.-K. Compatibilization strategies in poly(lactic acid)-based blends. *RSC Adv.* **2015**, *5*, 32546–32565. [CrossRef]
6. Utracki, L.A.; Mukhopadhyay, P.; Gupta, R.K. Polymer Blends: Introduction. In *Polymer Blends Handbook*; Utracki, L.A., Wilkie, C.A., Eds.; Springer Netherlands: Dordrecht, The Netherlands, 2014; pp. 3–170. [CrossRef]
7. Mayekar, P.C.; Castro-Aguirre, E.; Auras, R.; Selke, S.; Narayan, R. Effect of Nano-Clay and Surfactant on the Biodegradation of Poly(Lactic Acid) Films. *Polymers* **2020**, *12*, 311. [CrossRef]
8. Sakthiselvan, P.; Madhumathi, R. Kinetic evaluation on cell growth and biosynthesis of polyhydroxybutyrate (PHB) by Bacillus safensis EBT1 from sugarcane bagasse. *Eng. Agric. Environ. Food* **2018**, *11*, 145–152. [CrossRef]
9. Kessler, B.; Witholt, B. Poly(3-Hydroxyalkanoates). In *Encyclopedia of Bioprocess Technology*; John Wiley & Sons, Ltd.: Hoboken, NJ, USA, 2002. [CrossRef]
10. Yeo, J.C.C.; Muiruri, J.K.; Thitsartarn, W.; Li, Z.; He, C. Recent advances in the development of biodegradable PHB-based toughening materials: Approaches, advantages and applications. *Mater. Sci. Eng. C Mater. Biol. Appl.* **2018**, *92*, 1092–1116. [CrossRef] [PubMed]
11. Patel, M.K.; Hansson, F.; Pitkänen, O.; Geng, S.; Oksman, K. Biopolymer Blends of Poly(lactic acid) and Poly(hydroxybutyrate) and Their Functionalization with Glycerol Triacetate and Chitin Nanocrystals for Food Packaging Applications. *ACS Appl. Polym. Mater.* **2022**, *4*, 6592–6601. [CrossRef]
12. Turco, R.; Santagata, G.; Corrado, I.; Pezzella, C.; Di Serio, M. In Vivo and Post-synthesis Strategies to Enhance the Properties of PHB-Based Materials: A Review. *Front. Bioeng. Biotechnol.* **2021**, *8*, 619266. [CrossRef] [PubMed]
13. Iwata, T.; Fujita, M.; Aoyagi, Y.; Doi, Y.; Fujisawa, T. Time-Resolved X-ray Diffraction Study on Poly[(*R*)-3-hydroxybutyrate] Films During Two-Step-Drawing: Generation Mechanism of Planar Zigzag Structure. *Biomacromolecules* **2005**, *6*, 1803–1809. [CrossRef]
14. Zhang, L.; Xiong, C.; Deng, X. Miscibility, crystallization and morphology of poly(β-hydroxybutyrate)/poly(d,l-lactide) blends. *Polymer* **1996**, *37*, 235–241. [CrossRef]
15. D'anna, A.; Arrigo, R.; Frache, A. PLA/PHB Blends: Biocompatibilizer Effects. *Polymers* **2019**, *11*, 1416. [CrossRef]
16. Arrieta, M.P.; Samper, M.D.; Aldas, M.; López, J. On the Use of PLA-PHB Blends for Sustainable Food Packaging Applications. *Materials* **2017**, *10*, 1008. [CrossRef]
17. Imre, B.; Pukánszky, B. Compatibilization in bio-based and biodegradable polymer blends. *Eur. Polym. J.* **2013**, *49*, 1215–1233. [CrossRef]
18. Koning, C.; Van Duin, M.; Pagnoulle, C.; Jerome, R. Strategies for compatibilization of polymer blends. *Prog. Polym. Sci.* **1998**, *23*, 707–757. [CrossRef]
19. Sharif, A.; Mondal, S.; Hoque, M.E. Polylactic Acid (PLA)-Based Nanocomposites: Processing and Properties. In *Bio-Based Polymers and Nanocomposites: Preparation, Processing, Properties & Performance*; Sanyang, M.L., Jawaid, M., Eds.; Springer International Publishing: Cham, Switzerland, 2019; pp. 233–254. [CrossRef]
20. Ranakoti, L.; Gangil, B.; Mishra, S.K.; Singh, T.; Sharma, S.; Ilyas, R.; El-Khatib, S. Critical Review on Polylactic Acid: Properties, Structure, Processing, Biocomposites, and Nanocomposites. *Materials* **2022**, *15*, 4312. [CrossRef]
21. Wu, G.; Liu, S.; Jia, H.; Dai, J. Preparation and properties of heat resistant polylactic acid (PLA)/Nano-SiO_2 composite filament. *J. Wuhan Univ. Technol.-Mater. Sci. Ed.* **2016**, *31*, 164–171. [CrossRef]
22. Buzarovska, A. PLA Nanocomposites with Functionalized TiO_2 Nanoparticles. *Polym.-Plast. Technol. Eng.* **2013**, *52*, 280–286. [CrossRef]
23. Swaroop, C.; Shukla, M. Nano-magnesium oxide reinforced polylactic acid biofilms for food packaging applications. *Int. J. Biol. Macromol.* **2018**, *113*, 729–736. [CrossRef] [PubMed]
24. Mallakpour, S.; Naghdi, M. Polymer/SiO_2 nanocomposites: Production and applications. *Prog. Mater. Sci.* **2018**, *97*, 409–447. [CrossRef]
25. Prapruddivongs, C.; Apichartsitporn, M.; Wongpreedee, T. Effect of Commercial SiO_2 and SiO_2 from rice husk ash loading on biodegradation of Poly (lactic acid) and crosslinked Poly (lactic acid). *IOP Conf. Ser. Mater. Sci. Eng.* **2017**, *244*, 012007. [CrossRef]

26. Opaprakasit, P.; Boonpa, S.; Jaikaew, N.; Petchsuk, A.; Tangboriboonrat, P. Preparation of Surface-Modified Silica Particles from Rice Husk Ash and Its Composites with Degradable Polylactic Acid. *Macromol. Symp.* **2015**, *354*, 48–54. [CrossRef]
27. Rodriguez-Uribe, A.; Wang, T.; Pal, A.K.; Wu, F.; Mohanty, A.K.; Misra, M. Injection moldable hybrid sustainable composites of BioPBS and PHBV reinforced with talc and starch as potential alternatives to single-use plastic packaging. *Compos. Part C Open Access* **2021**, *6*, 100201. [CrossRef]
28. Huang, A.; Yu, P.; Jing, X.; Mi, H.-Y.; Geng, L.-H.; Chen, B.-Y.; Peng, X.-F. The Effect of Talc on the Mechanical, Crystallization and Foaming Properties of Poly(Lactic Acid). *J. Macromol. Sci. Part B* **2016**, *55*, 908–924. [CrossRef]
29. Helanto, K.; Talja, R.; Rojas, O.J. Talc reinforcement of polylactide and biodegradable polyester blends via injection-molding and pilot-scale film extrusion. *J. Appl. Polym. Sci.* **2021**, *138*, 51225. [CrossRef]
30. Jain, S.; Reddy, M.M.; Mohanty, A.K.; Misra, M.; Ghosh, A.K. A New Biodegradable Flexible Composite Sheet from Poly(lactic acid)/Poly(ε-caprolactone) Blends and Micro-Talc. *Macromol. Mater. Eng.* **2010**, *295*, 750–762. [CrossRef]
31. Tkirjoittaja Helanto, K. *Pilot-Scale Filler-Reinforced Biodegradable Coatings for Paperboard Packaging*; Aalto University: Helsinki, Finland, 2023.
32. Rivera-Briso, A.L.; Serrano-Aroca, Á. Poly(3-Hydroxybutyrate-co-3-Hydroxyvalerate): Enhancement Strategies for Advanced Applications. *Polymers* **2018**, *10*, 732. [CrossRef]
33. Bourbigot, S.; Fontaine, G.; Duquesne, S.; Delobel, R. PLA nanocomposites: Quantification of clay nanodis-persion and reaction to fire. *Int. J. Nanotechnol.* **2008**, *5*, 683–692. [CrossRef]
34. Kimura, K.; Horikoshi, Y. Bio-Based Polymers. *Fujitsu Sci. Tech. J.* **2005**, *41*, 173–180.
35. Réti, C.; Casetta, M.; Duquesne, S.; Bourbigot, S.; Delobel, R. Flammability properties of intumescent PLA including starch and lignin. *Polym. Adv. Technol.* **2008**, *19*, 628–635. [CrossRef]
36. Murariu, M.; Bonnaud, L.; Yoann, P.; Fontaine, G.; Bourbigot, S.; Dubois, P. New trends in polylactide (PLA)-based materials: "Green" PLA–Calcium sulfate (nano)composites tailored with flame retardant properties. *Polym. Degrad. Stab.* **2010**, *95*, 374–381. [CrossRef]
37. Taib, M.N.A.M.; Antov, P.; Savov, V.; Fatriasari, W.; Madyaratri, E.W.; Wirawan, R.; Osvaldová, L.M.; Hua, L.S.; Ghani, M.A.A.; Al Edrus, S.S.A.O.; et al. Current progress of biopolymer-based flame retardant. *Polym. Degrad. Stab.* **2022**, *205*, 110153. [CrossRef]
38. Mochane, M.J.; Mokhothu, T.H.; Mokhena, T.C. Synthesis, mechanical, and flammability properties of metal hydroxide reinforced polymer composites: A review. *Polym. Eng. Sci.* **2022**, *62*, 44–65. [CrossRef]
39. Al-Itry, R.; Lamnawar, K.; Maazouz, A. Improvement of thermal stability, rheological and mechanical properties of PLA, PBAT and their blends by reactive extrusion with functionalized epoxy. *Polym. Degrad. Stab.* **2012**, *97*, 1898–1914. [CrossRef]
40. Chagas, J.d.S.; Filho, J.E.S.; Silva, N.F.I.; Ueki, M.M.; de Medeiros, E.S.; Wellen, R.M.R.; de Oliveira, M.P.; Gois, G.d.S.; de Almeida, Y.M.B.; Santos, A.S.F. Effect of Concentration and Residence Time of Joncryl®ADR4368 on Melt Processability of Poly(3-hydroxybutyrate). *J. Renew. Mater.* **2024**, *12*, 2079–2094. [CrossRef]
41. Nanthananon, P.; Seadan, M.; Pivsa-Art, S.; Hamada, H.; Suttiruengwong, S. Facile Preparation and Characterization of Short-Fiber and Talc Reinforced Poly(Lactic Acid) Hybrid Composite with In Situ Reactive Compatibilizers. *Materials* **2018**, *11*, 1183. [CrossRef]
42. Grigora, M.-E.; Terzopoulou, Z.; Tsongas, K.; Bikiaris, D.N.; Tzetzis, D. Physicochemical Characterization and Finite Element Analysis-Assisted Mechanical Behavior of Polylactic Acid-Montmorillonite 3D Printed Nanocomposites. *Nanomaterials* **2022**, *12*, 2641. [CrossRef]
43. Dong, W.; Zou, B.; Ma, P.; Liu, W.; Zhou, X.; Shi, D.; Ni, Z.; Chen, M. Influence of phthalic anhydride and bioxazoline on the mechanical and morphological properties of biodegradable poly(lactic acid)/poly[(butylene adipate)-*co*-terephthalate] blends. *Polym. Int.* **2013**, *62*, 1783–1790. [CrossRef]
44. Xu, Z.; Lin, X.; Liu, H. The application of blocked polyfunctional isocyanate as a cross-linking agent in biodegradable extruded poly(lactic acid) foam. *Iran. Polym. J.* **2019**, *28*, 417–424. [CrossRef]
45. Tuominen, J.; Kylmä, J.; Seppälä, J. Chain extending of lactic acid oligomers. Increase of molecular weight with 1,6-hexamethylene diisocyanate and 2,2′-bis(2-oxazoline). *Polymer* **2002**, *43*, 3–10. [CrossRef]
46. Liu, C.; Jia, Y.; He, A. Preparation of Higher Molecular Weight Poly (L-lactic Acid) by Chain Extension. *Int. J. Polym. Sci.* **2013**, *2013*, 315917. [CrossRef]
47. Mai, J.; Pratt, S.; Laycock, B.; Chan, C.M. Synthesis and Characterisation of Poly(3-hydroxybutyrate-*co*-3-hydroxyvalerate)-*b*-poly(3-hydroxybutyrate-*co*-3-hydroxyvalerate) Multi-Block Copolymers Produced Using Diisocyanate Chemistry. *Polymers* **2023**, *15*, 3257. [CrossRef]
48. González-Ausejo, J.; Sánchez-Safont, E.; Lagarón, J.M.; Balart, R.; Cabedo, L.; Gámez-Pérez, J. Compatibilization of poly(3-hydroxybutyrate-*co*-3-hydroxyvalerate)–poly(lactic acid) blends with diisocyanates. *J. Appl. Polym. Sci.* **2017**, *134*, 44806. [CrossRef]

49. *ISO 527-3:2018*; Plastics—Determination of Tensile Properties—Part 3: Test Conditions for Films and Sheets. International Organization for Standardization: Geneva, Switzerland, 2018. Available online: https://www.iso.org/standard/70307.html (accessed on 25 August 2021).
50. Špitalský, Z.; Lacík, I.; Lathová, E.; Janigová, I.; Chodák, I. Controlled degradation of polyhydroxybutyrate via alcoholysis with ethylene glycol or glycerol. *Polym. Degrad. Stab.* **2006**, *91*, 856–861. [CrossRef]
51. Kim, S.J.; Kwak, H.W.; Kwon, S.; Jang, H.; Park, S.-I. Characterization of PLA/PBSeT Blends Prepared with Various Hexamethylene Diisocyanate Contents. *Materials* **2021**, *14*, 197. [CrossRef]

polymers

MDPI

Article

Solvent-Free Processing of i-P3HB Blends: Enhancing Processability and Mechanical Properties for Sustainable Applications

Wael Almustafa [1,*], Sergiy Grishchuk [1], Michael Redel [2], Dirk W. Schubert [2] and Gregor Grun [1]

[1] Department of Applied Logistics and Polymer Sciences, Kaiserslautern University of Applied Science, Schoenstr. 11, 67659 Kaiserslautern, Germany
[2] Institute of Polymer Materials, Department of Materials Science, Faculty of Engineering, Friedrich-Alexander University Erlangen-Nürnberg (FAU), Martensstr. 7, 91058 Erlangen, Germany
* Correspondence: wael.almustafa@hs-kl.de

Abstract

Poly(3-hydroxybutyrate) is a biobased and biodegradable polymer, produced via bacterial fermentation and characterized by an isotactic structure and mechanical properties similar to those of polyethylene and polypropylene. However, its brittleness—due to high crystallinity (~70%) and thermal degradation, starting at a temperature range of 180–190 °C near its melting point (175 °C)—makes its processing difficult and limits its applications. Most recent studies on modifying P3HB involved solution casting, typically using chloroform, which raises sustainability concerns. In this study blends of isotactic poly(3-hydroxybutyrate) (*i*-P3HB) with atactic poly(3-hydroxybutyrate) (*a*-P3HB) and poly(3-hydroxybutyrate-*co*-4-hydroxybutyrate) (P34HB) were prepared through solvent-free extrusion, and the thermal and mechanical properties of these blends were characterized. The obtained blends showed an extended processing window with reduced processing temperatures (150–160 °C), which were significantly lower than the onset of the decomposition temperature of *i*-P3HB, thereby avoiding thermal degradation. Furthermore, the crystallinity of these blends could be varied between 17 and 70%, depending on the polymer ratio, which allows for tailormade materials with tunable mechanical properties and an elongation at break up to 600%. Based on the results, the obtained blends in this study are promising candidates for various applications and processing techniques, such as injection molding, extrusion, and fiber spinning, offering a sustainable alternative to conventional plastics.

Keywords: poly(3-hydroxybutyrate); blend; crystallinity; biodegradable; polyester

1. Introduction

Poly(3-hydroxybutyrate) (P3HB) is a biobased, biocompatible, and biodegradable polymer belonging to the polyhydroxyalkanoates (PHAs) family. It was first discovered and characterized by Maurice Lemoigne [1]. Poly(3-hydroxybutyrate) is primarily produced biotechnologically through bacterial fermentation in an isotactic form (*i*-P3HB) and exhibits a high crystallinity of around 70% [2]. The desirable properties, such as eco-friendliness, a resistance to organic solvents, and gas barrier capabilities and, at the same time, similar mechanical characteristics to those of polyethylene (PE) and polypropylene (PP) made P3HB an attractive candidate to replace those conventional plastics (Table 1) [3–5]. However,

the high degree of crystallinity of neat *i*-P3HB also results in brittleness, and the onset of its thermal degradation, in terms of polymer chain scission, starting at a temperature range of 180–190 °C near its melting temperature (175 °C) complicates processing and hinders its application [6–11].

Table 1. Comparison of *i*-P3HB properties with PP/LDPE [12].

	***i*-P3HB**	**PP**	**LDPE**
Melting temperature [°C]	175	176	110
Glass transition temperature [°C]	4	−10	−30
Crystallinity [%]	70	50	50
E-modulus [GPa]	3.5	1.5	0.2
Tensile strength [MPa]	40	38	10
Elongation at break [%]	5	400	600

To address these challenges, improving the processability of *i*-P3HB and reducing its brittleness through chemical or physical modifications is crucial to facilitate its application in different sectors. For this approach, different strategies have been investigated in previous studies, such as the copolymerization with other hydroxy acids [13,14], the functionalization of *i*-P3HB with polyols followed by chain extension reactions [15–17], as well as blending *i*-P3HB with other polymers [18–21]. Among these strategies, blending *i*-P3HB with other polymers is particularly appealing, as it is industrially feasible without requiring significant investment [22–24].

Previous studies have explored blending *i*-P3HB with various polymers, including poly(ethylene oxide) [25,26], poly(vinyl alcohol) [27], poly(ε-caprolactone) [28,29], poly(butylene succinate) (PBS) [30,31], poly(ethylene succinate) (PES) [32], and poly[(butylene adipate)-*co*-terephthalate] (PBAT) [33]. However, these blends exhibited an incompatibility and phase separation, as indicated by thermal and mechanical analyses (e.g., distinct glass transition temperatures) [34].

An alternative strategy to improve the processability of *i*-P3HB involves its blending with other PHAs, PHA copolymers featuring varied chain lengths, or other polyesters with a similar chemical structure. Such polymers can be obtained biotechnologically, such as poly(3-hydroxybutyrate-*co*-3-hydroxyvalerate) (PHBV) and poly(3-hydroxybutyrate-*co*-4-hydroxybutyrate) (P34HB) [35–38], or chemically through methods like ring-opening polymerization (ROP) or the polycondensation of hydroxy acids and their esters, as in the case of poly(lactic acid) (PLA) and atactic poly(3-hydroxybutyrate) (*a*-P3HB) [39–44].

While blending *i*-P3HB with polylactic acid (PLA) and [45–47] poly(3-hydroxybutyrate-*co*-3-hydroxyvalerate) (PHBV) [48–50] has been thoroughly investigated in the literature, blending *i*-P3HB with *a*-P3HB and P34HB has still not been deeply explored. These two polymers—which, next to *i*-P3HB, are the focus of this study—are amorphous and have a similar chemical structure to that of *i*-P3HB. Therefore, it can be expected that they can be blended effectively with *i*-P3HB, resulting in interesting material properties. Figure 1 illustrates the structural differences between *i*-P3HB, *a*-P3HB, and P34HB.

A notable advantage of *i*-P3HB is its resistance to organic solvents, which facilitates its application in different media. However, its limited solubility in organic solvents (mainly soluble in chloroform) has led to the predominance of preparing blends by solution casting using chloroform, which reduces the sustainability of the obtained products.

To address this issue, it would be desirable to blend the polymers through extrusion, a solvent-free process, which, compared to solution casting, is environmentally friendly and compatible with high-throughput manufacturing.

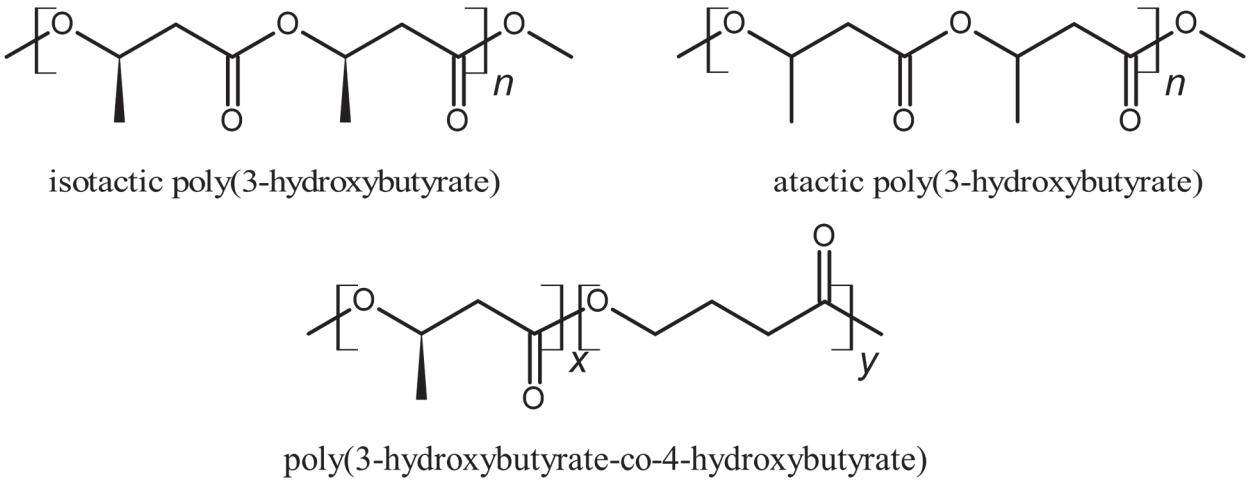

Figure 1. Chemical structure of *i*-P3HB, *a*-P3HB, and P34HB.

Unfortunately, the extrudability of *i*-P3HB is very limited due to the very small process window, resulting from a melting point of around 175 °C [12,51,52], for the onset of decomposition at a temperature range of 180–190 °C [6], making it difficult to achieve a stable extrusion process [53–57]. The narrow processing window of *i*-P3HB and the thermal degradation during processing present a significant challenge for the application of this biobased and biodegradable polymer. This highlights the urgent need to improve the processability of *i*-P3HB by extending its processing window, thereby avoiding thermal degradation during processing. The incorporation of amorphous *a*-P3HB and P34HB in these blends is expected to circumvent this, by influencing the crystalline phase in terms of lowering the melting point.

While similar blends were obtained in a previous study by solution casting [58], in this study, we aim to explore the potential of the solvent-free blending of *i*-P3HB with *a*-P3HB and P34HB to enhance processability and broaden the application potential of *i*-P3HB-based materials.

2. Materials and Methods

Isotactic poly (3-hydroxybutyrate) in powder form with a weight-average molecular weight of *M*w = 260,000 g·mol^{-1} ± 20,000 g·mol^{-1} and a polydispersity index of PDI = 2.7 was purchased from Biomer (Schwalbach/Germany). P34HB with *M*w = 196,000 g·mol^{-1} ± 26,000 g·mol^{-1}, (PDI = 2.3), was purchased from CJ Biomaterials (Seoul, Republic of Korea). *a*-P3HB was prepared by self-polycondensation as described in ref. [59]. *a*-P3HB was produced with titanium isopropoxide as catalyst and had a weight-average molecular weight of 2652 g·mol^{-1} ± 700 g·mol^{-1} (PDI = 2.3). Titanium isopropoxide (97%) was purchased from Sigma Aldrich (Darmstadt, Germany). The weight-average molecular weight of the polymers was determined with gel permeation chromatography (GPC) using an Agilent chromatograph (Waldbronn, Germany) conducted in chloroform and calibrated with polystyrene standards. The GPC results were evaluated using the DataApex Clarity Software (version 10.1) (Petrzilkova, Czech Republic).

2.1. i-P3HB Blends Preparation by Extrusion

To prepare the blends, binary mixtures of *i*-P3HB with either *a*-P3HB or P34HB were first produced separately, using proportions of 15, 30, and 50 wt.% of the second component. Additionally, binary blends of *i*-P3HB containing 30 wt.% and 50 wt.% of *a*-P3HB were

further mixed with P34HB in proportions of 15, 30, and 50 wt.%, having ternary blends containing all three polymers.

Sample labeling was conducted as described in Table 2, by noting the name of the second component in the blend next to *i*-P3HB, followed by their proportion in the blend.

Table 2. Sample designation and description.

Sample Designation	Description
i-P3HB	Neat *i*-P3HB
P34HB	Neat P34HB
a-P3HB	Neat *a*-P3HB
a-P3HB-15	Blend of i-P3HB with *a*-P3HB in 85:15 weight ratio
a-P3HB-30	Blend of i-P3HB with *a*-P3HB in 70:30 weight ratio
a-P3HB-50	Blend of *i*-P3HB with *a*-P3HB in 50:50 weight ratio
P34HB-15	Blend of *i*-P3HB with P34HB in 85:15 weight ratio
P34HB-30	Blend of *i*-P3HB with P34HB in 70:30 weight ratio
P34HB-50	Blend of *i*-P3HB with P34HB in 50:50 weight ratio
a-P3HB-30-P34HB-15	Blend of *a*-P3HB-30 with P34HB in 85:15 weight ratio
a-P3HB-30-P34HB-30	Blend of *a*-P3HB-30 with P34HB in 70:30 weight ratio
a-P3HB-30-P34HB-50	Blend of *a*-P3HB-30 with P34HB in 50:50 weight ratio
a-P3HB-50-P34HB-15	Blend of *a*-P3HB-50 with P34HB in 85:15 weight ratio
a-P3HB-50-P34HB-30	Blend of *a*-P3HB-50 with P34HB in 70:30 weight ratio
a-P3HB-50-P34HB-50	Blend of *a*-P3HB-50 with P34HB in 50:50 weight ratio

The specified amounts of each polymer were added into a mixing barrel and premixed for five minutes, 30 rpm, and the homogeneity was checked by visual inspection. The mixture was then processed by extrusion using a twin-screw Polylab extruder from Thermo Fisher (Kandel, Germany) equipped with three heating zones and co-rotating screws (16 mm diameter, 640 mm length). The processing temperature and screw rotation speed (rpm) were adjusted for each blend based on the results of the DSC analysis of the same blend obtained by solution casting, as well as observations of the extruder's torque and the optical homogeneity of the extruded blend.

The specific and optimized processing parameters are listed in Table 3. Once stable processing parameters were achieved, a throughput of 2 kg per hour was maintained for each blend in the laboratory setup.

Table 3. Extrusion parameters of *i*-P3HB blends.

Sample	Extrusion Temperature [°C]				Screw Speed [rpm]
	Zone 1	Zone 2	Zone 3	*T*M80 *	
a-P3HB-15	70	160	160	165	40
a-P3HB-30	70	155	155	160	40
a-P3HB-50	70	150	150	155	40
P34HB-15	70	165	170	175	50
P34HB-30	70	165	170	175	50
P34HB-50	70	165	170	175	55
a-P3HB-50-P34HB-15	70	155	155	160	40
a-P3HB-50-P34HB-30	70	155	150	155	40
a-P3HB-50-P34HB-50	70	155	150	155	40
a-P3HB-30-P34HB-15	70	155	155	160	40
a-P3HB-30-P34HB-30	70	155	150	155	40
a-P3HB-30-P34HB-50	70	155	150	155	40

* *T*M80: the temperature of the nozzle.

2.2. Preparing of Specimens for Tensile Tests

Specimens for tensile tests were prepared, as described in Figure 2, in the laboratory of Thermo Fisher (Karlsruhe, Germany). Each blend was plasticized by using the twin screw Minilab extruder, equipped with co-rotating conical screws (110 mm length). To avoid the building of voids, the melt was directly filled in the cylinder of the injection molding machine, HAAKE Minijet, and transferred to injection molding, where tensile specimens (Type 1A) were obtained. The extrusion temperature for all blends was 165 °C, with a screw speed of 60 rpm. The injection molding temperature was also 165 °C, with pressure of 200 bar for 10 s, while the mold temperature was 50 °C. These parameters produced the best results in this process.

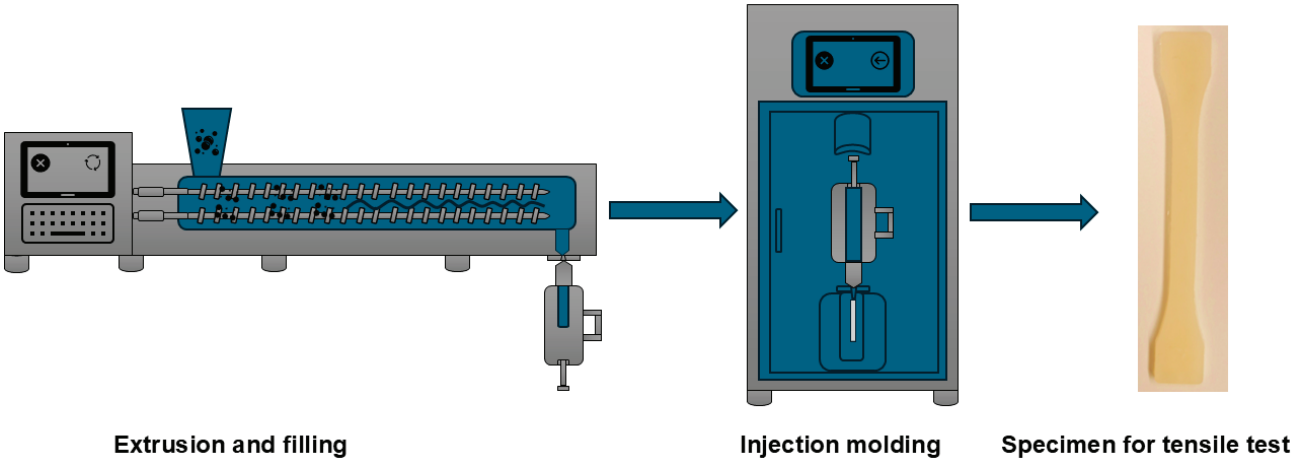

Figure 2. Preparation of specimen for tensile tests by extrusion and injection molding.

2.3. Differential Scanning Calorimetry (DSC)

Thermal parameters of the blends, including melting temperature (*T*m), glass transition temperature (*T*g), crystallization temperature (*T*c), their specific enthalpies, and crystalline ratio (*X*c), were determined with a Phoenix F1 204 DSC from NETZSCH (Selb, Germany) under nitrogen flow (20 mL·min^{-1}) and a heating/cooling rate of 10 °C·min^{-1} from −50 to 200 °C and also from −80 to 50 °C to determine the *T*g. The degree of crystallinity of *i*-P3HB blends was estimated from the melting enthalpy values (ΔHm) of the samples and the melting enthalpy of 100% crystalline *i*-P3HB (ΔH^0m = 146 J·g^{-1}) [60] using Equation (1).

$$x_c[\%] = \frac{\Delta H_m}{\Delta H_m^0 \times w_i} \times 100 \quad (1)$$

where w_i is the weight fraction of *i*-P3HB in the blends.

2.4. Thermogravimetric Analysis (TGA)

To determine the onset of degradation temperature (*T*d) of P3HB blends in terms of mass loss, thermogravimetric analysis was performed with a PerkinElmer TGA 4000 (Rodgau, Germany). The samples (10–30 mg) were heated from room temperature to 600 °C in nitrogen atmosphere (40 mL·min^{-1}) at a heating rate of 10 °C·min^{-1}. The onset of thermal degradation was also calculated using the software Pyris (version 11) of PerkinElmer (Rodgau, Germany).

2.5. Gel Permeation Chromatography (GPC)

The weight-average molecular weight (*M*w) of the obtained blends was determined by gel permeation chromatography (GPC) using an Agilent chromatograph (Waldbronn,

Germany) conducted in chloroform and calibrated with polystyrene standards. The GPC was equipped with a UV detector and a differential refractive index detector (1260 infinity) with two styrene–divinylbenzene columns (300 mm × 4.6 mm) connected in series with a flowrate of 0.3 mL·min^{-1} at 40 bar and 30 °C. The samples were prepared by dissolving in chloroform (HPLC grade), with concentration of 5 mg·ml^{-1}, and 20 µL of the solution was injected for the measurement.

2.6. Tensile Tests

Tensile tests were conducted according to DIN EN ISO 527-1 [61] at room temperature (23 °C, relative humidity: 50% ± 5%) using a ZwickRoell universal testing machine (Ulm, Germany). For each sample, 5 specimens (Type 1A), which were prepared by injection molding, were tested with a crosshead speed of 5 mm·min^{-1} and preload force of 1 Newton. The average values and the standard deviations for tensile strength and elongation at break were calculated using the Test Expert Software (version 1.4) of ZwickRoell.

3. Results and Discussion

Isotactic P3HB is an attractive candidate to replace petroleum-based plastics, due to its eco-friendliness, biodegradability, and favorable mechanical properties. However, its application is hindered by the brittleness caused by the high crystallinity and difficulties in melt processing, as thermal degradation occurs near its melting temperature. Recent studies aimed to modify *i*-P3HB and improve its processing window employed solution casting using chloroform, which reduces the sustainability of the obtained products [62–66].

Blending *i*-P3HB with *a*-P3HB and P34HB is expected to result in blends that can be processed by extrusion without solvents, at reduced temperatures below the melting point of *i*-P3HB. This is attributed to their amorphous nature, similar chemical structure, and the possible disruption of *i*-P3HB crystallization. Such an approach can extend the processing window of i-P3HB and prevent thermal degradation during processing.

In the following section, the thermal and mechanical properties of *i*-P3HB blends produced by melt extrusion with *a*-P3HB and P34HB will be examined, and their influence on the processing window of *i*-P3HB will be discussed.

3.1. Thermal Characterization

***a*-P3HB**: In the first step, *i*-P3HB was mixed with *a*-P3HB to produce binary blends by extrusion. It was expected that *a*-P3HB could improve the processing window of *i*-P3HB due to their similar chemical structures, facilitating extrusion at temperatures below the melting temperature of neat *i*-P3HB to mitigate thermal degradation.

Table 4 presents the thermal properties of *i*-P3HB blends with *a*-P3HB, as determined by DSC. The results of the obtained blends reveal a significantly lower glass transition temperature compared to the neat *i*-P3HB, which has a *T*g of 5.5 °C. Blends with 15 wt.% *a*-P3HB demonstrated a *T*g of −26 °C, while those with 50 wt.% *a*-P3HB demonstrated a *T*g of approximately −42 °C. This reduction indicates that *a*-P3HB acts as a plasticizer, due to its low molecular weight and chemical similarity to *i*-P3HB. This effect enhances the polymer chain mobility, facilitating extrusion processing [67–69]. However, similar blends obtained by solution casting in a recent study exhibited stable thermal and mechanical properties even after one month of storage, indicating no notable risk of migration over time [58]. Furthermore, in the present study, the mechanical tests of the obtained blends were carried out after one month of storage to evaluate the potential embrittlement due to post-crystallization.

While DSC curves show only one *T*g, the *T*g of *i*-P3HB may still be present but not detectable due to its high crystallinity (Figure 3). Therefore, further investigations are required to assess the miscibility between the two polymers.

Table 4. DSC results of *i*-P3HB blends.

Sample	*T*g [°C]	*T*m1 [°C]	*T*m2 [°C]	*T*c [°C]	*X*c (%)
P34HB	−15.4 ± 0.4				
i-P3HB	5.5 ± 0.3		175.5 ± 1.6	91.7 ± 3.34	68 ± 1.2
a-P3HB	−42.4 ± 1.2				
a-P3HB-15	−25.8 ± 0.9	166.3 ± 0.4	171 ± 0.1	101.2 ± 1.3	55 ± 0.2
a-P3HB-30	−42.1 ± 0.4	153.8 ± 0.2	165.5 ± 0.1	90.2 ± 0.2	48 ± 0.6
a-P3HB-50	−42.5 ± 1.3	130.8 ± 1.4	153 ± 0.6	71.4 ± 1.4	32 ± 0.1
P34HB-15	−16.9 ± 0.5	165.6 ± 0.7	175.4 ± 0.4	82 ± 0.6	54 ± 0.6
P34HB-30	−16.9 ± 0.3		173.9 ± 0.1	71.5 ± 1.2	46 ± 0.8
P34HB-50	−16.2 ± 0.1		173.7 ± 0.2	70.4 ± 3.6	32 ± 3.9
a-P3HB-50-P34HB-15	−39.6 ± 1.8	138.4 ± 0.2	159.4 ± 0.1	61.7 ± 0.1	29 ± 0.2
a-P3HB-50-P34HB-30	−33.4 ± 2.1	140.1 ± 1.1	162.1 ± 0.6	66.7 ± 0.2	25 ± 1.8
a-P3HB-50-P34HB-50	−29.2 ± 1.7		165.3 ± 0.5	58.5 ± 0.9	21 ± 0.4
a-P3HB-30-P34HB-15	−36.0 ± 1.6	154.4 ± 0.1	167.6 ± 0.1	87.6 ± 0.1	40 ± 0.8
a-P3HB-30-P34HB-30	−29.5 ± 1.4	151.7 ± 0.4	167.5 ± 0.2	84.1 ± 0.3	38 ± 0.1
a-P3HB-30-P34HB-50	−28.1 ± 0.4		167.7 ± 0.5	78.6 ± 3.3	31 ± 2.4

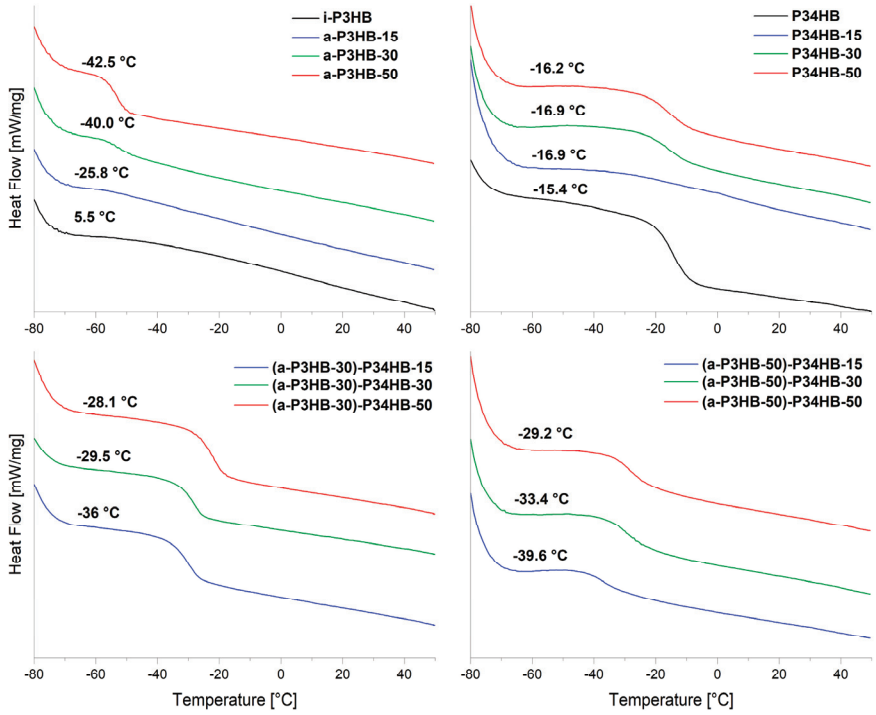

Figure 3. DSC curves (2. heating run) showing the *T*g values of the *i*-P3HB binary and ternary blend.

Additionally, blends with 30 and 50 wt.% *a*-P3HB exhibited a notable reduction in the melting temperature of *i*-P3HB, decreasing to approximately 165 °C and 150 °C, respectively. This represents a 10 to 25 °C reduction compared to the neat *i*-P3HB, which has a *T*m of 175 °C. The observed reduction in the *T*m is attributed to the good compatibility between *i*-P3HB and *a*-P3HB, due to their similar chemical structures, which strongly influences the crystallization of *i*-P3HB [70–72].

This change in crystallization behavior is also evident from the appearance of a second melting peak at lower temperatures, indicating the presence of crystals with a different

stability caused by the disruption of the *i*-P3HB crystallization (Figure 4) [73]. The impact of *a*-P3HB on the crystallization supports the feasibility of producing *i*-P3HB blends at lower temperatures, thereby reducing the risk of thermal degradation.

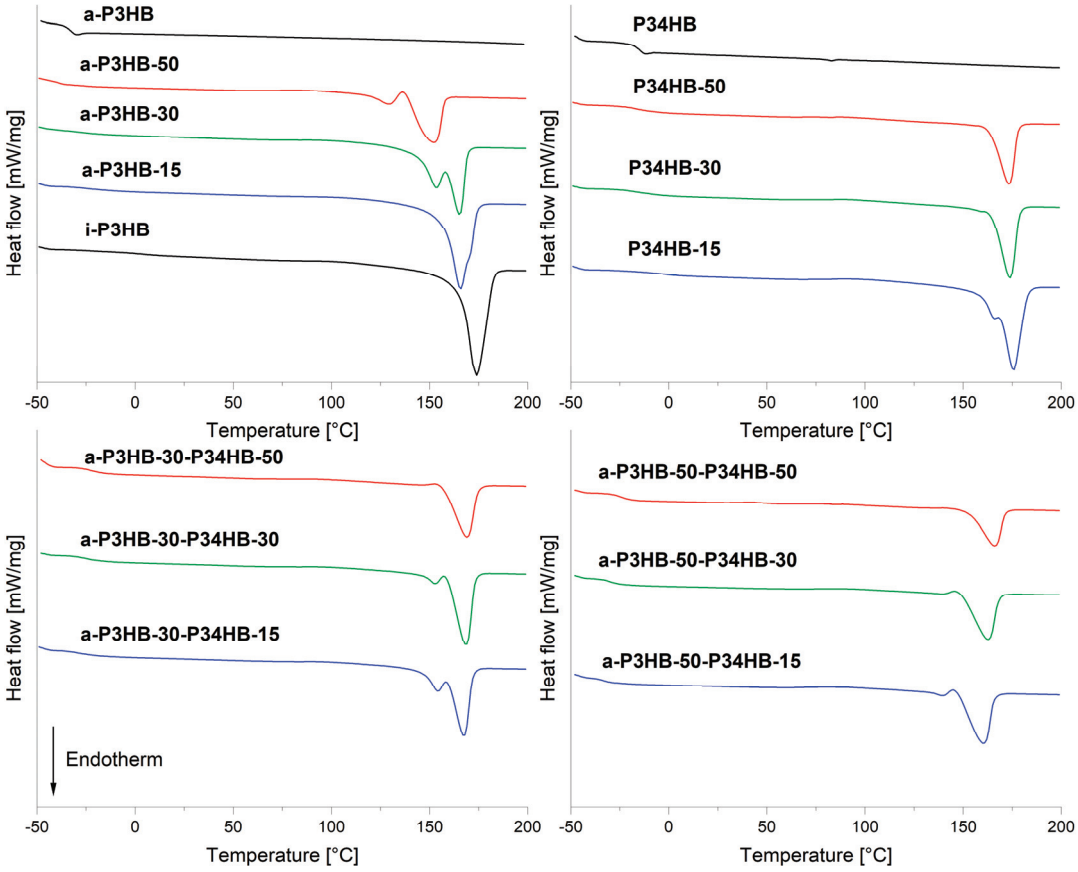

Figure 4. DSC curves (2. heating run) of *i*-P3HB blends.

The degree of crystallinity also decreased significantly from 68% in the neat *i*-P3HB to 30% in blends with 50 wt.% of *a*-P3HB (Table 4). This reduction is nearly proportional to the weight ratio of *a*-P3HB in the blends. Similarly, the crystallization temperature (*T*c) showed a comparable trend, decreasing to approximately 70 °C in blends with 50 wt.% *a*-P3HB. This shift reflects the increasing ratio of the amorphous polymer, which inhibits the formation of nuclei necessary for crystallization. However, the crystallization temperature can be adjusted by adding nucleating agents to the blends [58,74].

P34HB: *i*-P3HB was also mixed with the amorphous copolymer P34HB, and binary blends were produced by extrusion. Due to its amorphous nature and similar structure, P34HB was expected to have similar effects in terms of the crystallization behavior and lowering the melting temperature, thereby improving the processing window of *i*-P3HB.

DSC results of binary blends with P34HB, obtained by extrusion, showed *T*g values at around −16 °C, very close to the *T*g of the neat P34HB (−15.4 °C). This suggests the presence of a second *T*g. However, the DSC curves show only one *T*g, similar to the blends with *a*-P3HB, which can also be attributed to the limited amorphous phase of *i*-P3HB (Figure 3). Therefore, further investigations are required to assess the miscibility of the polymers.

In contrast to the blends with *a*-P3HB, the melting temperature of *i*-P3HB blends with P34HB did not exhibit any depression across all compositions. A second melting peak, appearing as a shoulder, was observed in blends with 15 wt.% P34HB but disappeared as

the P34HB content increased (Figure 4). This suggests a limited impact of P34HB on the crystallization of *i*-P3HB, compared with *a*-P3HB (Table 4).

The degree of crystallinity decreased proportionally with the P34HB content, reducing from 68% in the neat *i*-P3HB to 32% with the 50 wt.% P34HB. Similarly, the crystallization temperature showed a reduction, decreasing from approximately 98 °C for the neat *i*-P3HB to about 47 °C with the 50 wt.% P34HB (Table 4). This reduction is due to the increasing proportion of the amorphous polymer in the blend, which shifts the crystallization to lower temperatures.

Since the reduction in crystallinity was observed without any depression in the melting temperature, these blends are considered phase-separated blends. The reduced crystallinity is attributed to the presence of the amorphous P34HB rather than an alteration in the crystallization behavior of *i*-P3HB. The production of these blends by extrusion was only feasible at 175 °C, not, as expected, below the melting temperature of the neat *i*-P3HB. Therefore, no improvement in the processing window of *i*-P3HB was achieved by using only P34HB as the blend component.

***a*-P3HB-P34HB**: Blends containing 30 and 50 wt.% *a*-P3HB were further mixed with P34HB, to produce ternary blends via extrusion. This approach aimed to exploit the depression in the melting temperature and the disruption of the crystallization of *i*-P3HB induced by *a*-P3HB, along with the reduction in crystallinity due to the presence of P34HB. All blends were successfully extruded at temperatures between 150 and 160 °C, which is below the melting temperature of pure *i*-P3HB. This prevented thermal degradation and resulted in optical homogenous melts.

The DSC analysis of the obtained blends revealed that combining *i*-P3HB blends containing 30 and 50 wt.% of *a*-P3HB with P34HB allows for the production of blends with adjustable thermal properties and degrees of crystallinity. The *T*g values of the ternary blends increased with the P34HB content, ranging from approximately −40 to −28 °C. Similarly, the melting temperature of these blends also increased with the content of P34HB, from 160 °C to around 167. This increase in the *T*g and Tm is attributed to the decreasing proportion of *a*-P3HB. Nevertheless, all ternary blends showed significantly lower melting temperatures compared with the neat *i*-P3HB, confirming the improved processability (Table 4).

Among the ternary blends, the *a*-P3HB-50 with 50 wt.% P34HB showed the lowest crystallinity at 21%. This low crystallinity of ternary blends explains why the second melting peak, caused by *a*-P3HB and its disruption of the crystallization, was not detectable. Furthermore, the crystallization temperature *T*c of these blends ranged from 62 to 88 °C, a range that could be further controlled by incorporating nucleating agents as additives.

In summary, the DSC results highlight that blending with *a*-P3HB results in blends with lower melting temperatures and degrees of crystallinity compared to the neat *i*-P3HB (Figure 4). These blends can be processed by extrusion at reduced temperatures, safely below the thermal degradation temperature of *i*-P3HB, which begins at the temperature range of 180–190 °C. In contrast, binary blends with P34HB show reduced crystallinity but maintain the same melting temperature as the neat *i*-P3HB, indicating no improvement in its processing window.

By combining *a*-P3HB and P34HB with *i*-P3HB, ternary blends with adjustable thermal properties and crystallinity can be obtained. Importantly, these blends can be extruded at temperatures of 150–165 °C, which is 10–25 °C below the melting temperature of pure *i*-P3HB. This facilitates extrusion processing without solvents and avoids thermal degradation. Figure 5 illustrates the extended processing window of *i*-P3HB in a ternary diagram by showing the blends that are processable at reduced temperatures.

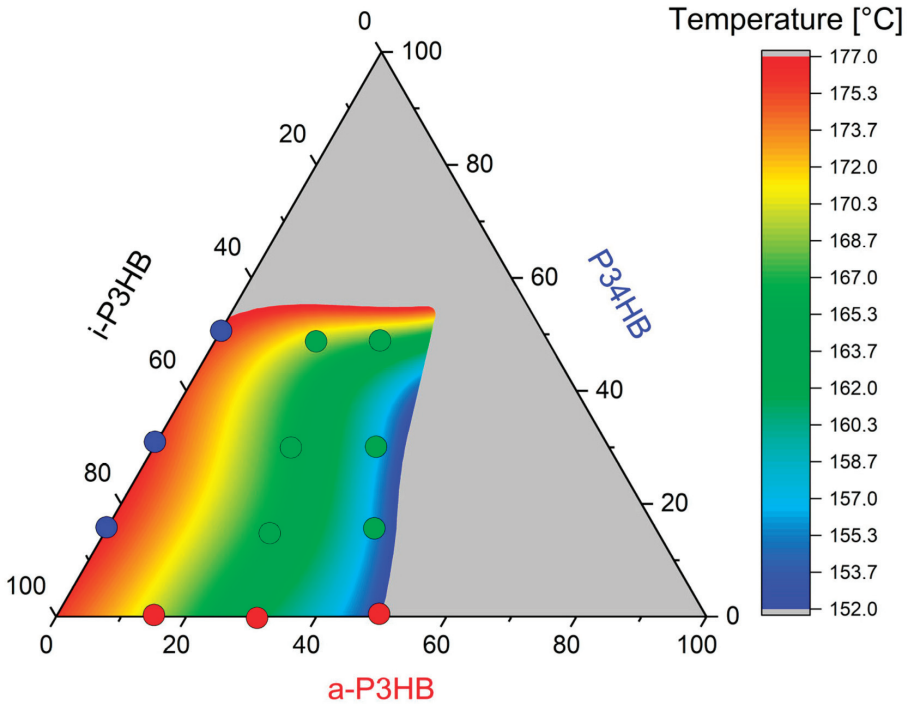

Figure 5. The improvement of the processing window of *i*-P3HB by blending with *a*-P3HB and P34HB.

The red points in the ternary diagram represent binary blends with *a*-P3HB, which are processable at temperatures between 150 and 165 °C. This is due to the depression of the melting temperature and the disruption of the crystallization induced by *a*-P3HB. In contrast, the blue points indicate binary blends with P34HB, which require higher processing temperatures, as P34HB appears to have no significant effect on the crystallization behavior of *i*-P3HB and its melting behavior. The green points represent ternary blends, which are also processable at reduced temperatures. This is attributed to the combined effects of a depressed melting temperature and reduced crystallinity, allowing for extrusion without requiring high shear rates to achieve a homogeneous melt.

Additionally, the gray zone in the ternary diagram delineates the limits of the proportion of amorphous polymers within the blends necessary to preserve the advantageous mechanical properties of *i*-P3HB and its tunable crystallinity.

3.2. Thermal Stability of i-P3HB Blends

The thermal analysis of *i*-P3HB blends showed that blending with *a*-P3HB and P34HB facilitates processing at reduced temperatures of 150–160 °C, which are 15–25 °C below the melting point of *i*-P3HB. To ensure that the extrusion process does not cause the extensive degradation of the molecular weight or affect the thermal stability of *i*-P3HB, both GPC and TGA analyses were performed on the starting polymers and the resulting blends. GPC results provided the weight-average molecular weight (*M*w) of the obtained blends and enabled the assessment of the potential reduction due to the degradation during processing. On the other hand, TGA results indicated the onset of thermal destructive degradation in terms of the mass loss.

Table 5 presents the *M*w values of the *i*-P3HB blends after extrusion, while the *M*w values of the neat *i*-P3HB and P34HB were determined from the unprocessed polymers. The *M*w of blends containing *a*-P3HB ranges between 260,000 and 270,000 g·mol^{-1}, which is very close to that of the *i*-P3HB used in this study. On the other hand, the *M*w of

binary and ternary blends containing P34HB ranges between 200,000 and 220,000 g·mol^{-1}. This shift is attributed to the presence of P34HB, which itself has an *M*w within this range (Figure 6). The variation in the *M*w among both binary and ternary blends was approximately 7000 g·mol^{-1}, which is negligible given that GPC is a relative measurement method. This indicates that there was no significant reduction in the *M*w of the polymers during extrusion.

Table 5. GPC and TGA results of *i*-P3HB blends.

Sample	*M*w [g·mol^{-1}]	*T*d [°C]
i-P3HB [1]	262,000 ± 20,000	285.6 ± 1.2
P34HB [2]	196,000 ± 26,000	280.9 ± 1.8
a-P3HB-15	270,000 ± 10,000	287.4 ± 3.0
a-P3HB-30	272,000 ± 18,000	284.9 ± 2.4
a-P3HB-50	255,000 ± 24,000	285.6 ± 1.7
P34HB-15	205,000 ± 35,000	284.5 ± 2.8
P34HB-30	216,000 ± 41,000	288.4 ± 1.7
P34HB-50	215,000 ± 16,000	283.2 ± 3.5
a-P3HB-50-P34HB-15	201,000 ± 25,000	283.2 ± 1.4
a-P3HB-50-P34HB-30	200,000 ± 13,000	283.6 ± 2.6
a-P3HB-50-P34HB-50	215,000 ± 29,000	277.5 ± 1.2
a-P3HB-30-P34HB-15	203,000 ± 30,000	286.4 ± 2.6
a-P3HB-30-P34HB-30	200,000 ± 38,000	284.8 ± 2.4
a-P3HB-30-P34HB-50	209,000 ± 25,000	284.4 ± 3.1

[1,2] Neat polymers without processing by extrusion.

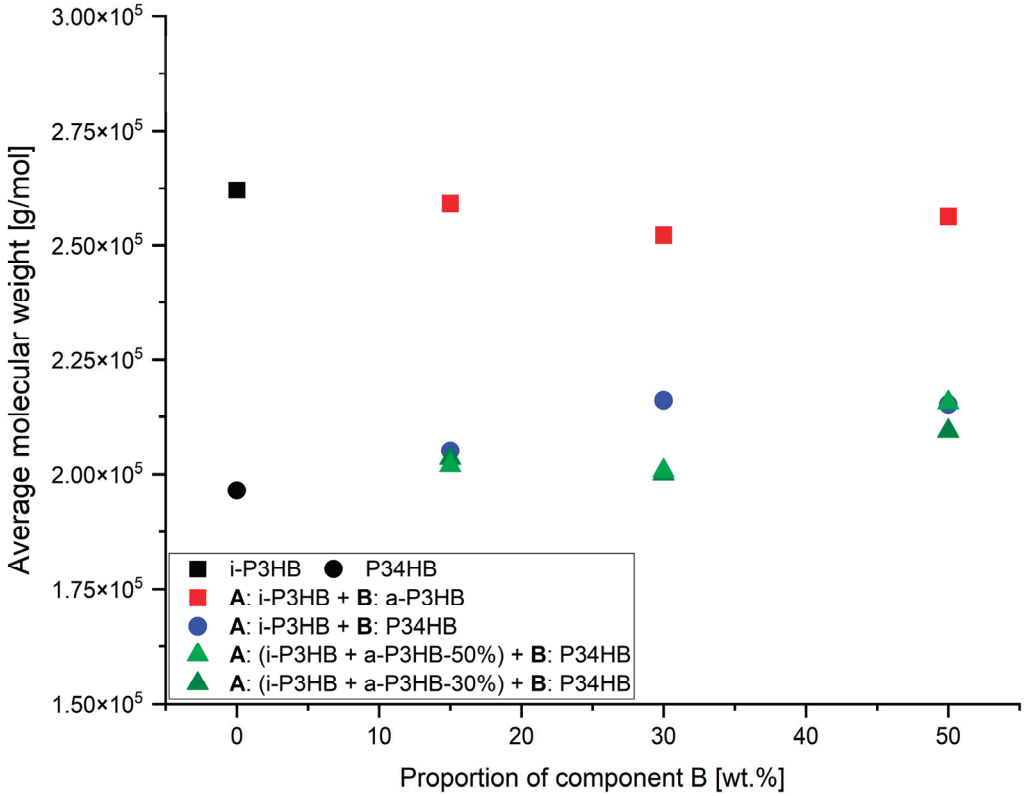

Figure 6. Weight-average molecular weight of *i*-P3HB blends.

While the thermal degradation of *i*-P3HB, in terms of chain scission, starts already at a temperature range of 180–190 °C [6,11], TGA results showed the onset of the thermal destructive degradation (*T*d), in terms of the mass loss, for unprocessed *i*-P3HB and P34HB

at 286 °C and 281 °C, respectively (Table 5). Binary blends with *a*-P3HB exhibited *T*d values between 284 °C and 287 °C, which are all closely comparable to that of the neat *i*-P3HB. Similarly, binary blends with P34HB and ternary blends containing all three polymers exhibited *T*d values between 277 °C and 288 °C, which are similarly close to that of the neat *i*-P3HB. These slight differences in the *T*d compared to *i*-P3HB across the samples demonstrate that blending with *a*-P3HB and P34HB does not impact the thermal stability, as the *T*d consistently remained within a narrow range (Figure 7).

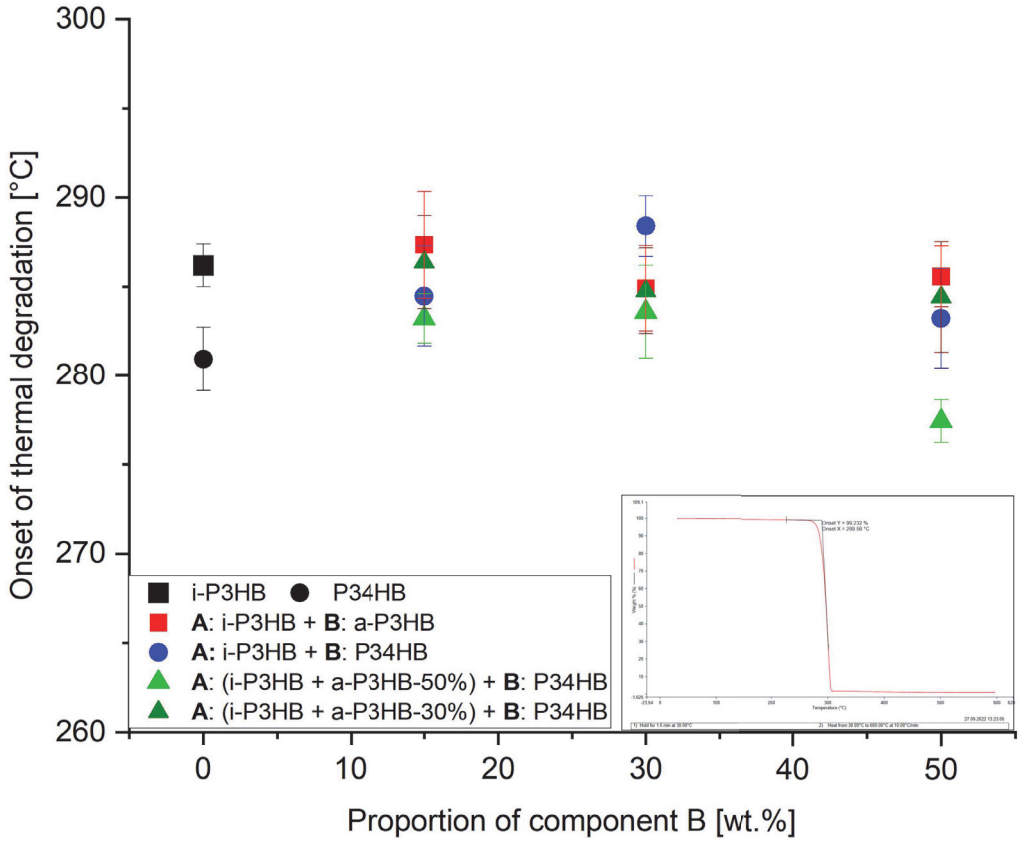

Figure 7. Onset of thermal degradation temperature of *i*-P3HB blends.

3.3. Mechanical Characterization

To determine the mechanical properties of *i*-P3HB blends, tensile test specimens were produced via injection molding. Prior to this, the blends underwent plastification through extrusion. However, producing pure *i*-P3HB samples via injection molding was not feasible. The material, in its powder form, melted only at 190 °C, leading to significant inhomogeneities and thermal degradation, as evidenced by strong smoke formation. Additionally, the direct injection molding of *i*-P3HB blends without prior extrusion-based plastification led to inhomogeneities in the specimen, indicating the relevance of prior plastification for further processing.

The results of tensile tests (Table 6) revealed distinct trends in the mechanical behavior of the *i*-P3HB blends. Blends with *a*-P3HB showed no significant improvement in the elongation at break compared to the pure i-P3HB, indicating that *a*-P3HB does not enhance flexibility but primarily influences thermal properties. For example, the elongation at break (εB) of the *a*-P3HB-15 blend was only 8.8%, and even at the higher *a*-P3HB content of 50 wt.%, the εB reached just 8.2%. Over time, these values remained relatively stable, suggesting that the secondary crystallization of *i*-P3HB was hindered. The reduction in

the tensile strength in these blends is attributed to the lower degree of crystallinity and the relatively low weight-average molecular weight of *a*-P3HB (Figures 8 and 9).

Table 6. Results of tensile tests of *i*-P3HB blends after production and after 30 days of storage.

	After Extrusion		After 30 Days	
Sample	**σB * [MPa]**	**εB ** [%]**	**σB [MPa]**	**εB [%]**
i-P3HB	40 [1]	5 [1]	-	-
a-P3HB-15	29.1 ± 1.8	8.8 ± 0.8	29.6 ± 2.4	6.4 ± 1.1
a-P3HB-30	17.6 ± 1.1	8.8 ± 2.3	18.6 ± 0.9	5.9 ± 0.5
a-P3HB-50	11.6 ± 0.2	8.2 ± 0.6	11.0 ± 1.1	6.6 ± 1.0
P34HB-15	43.0 ± 2.4	4.1 ± 1.0	49.0 ± 0.9	4.3 ± 0.5
P34HB-30	28.7 ± 3.6	23.0 ± 13	32.2 ± 3.4	17.0 ± 6.4
P34HB-50	22.5 ± 1.5	600.0 ± 23	18.3 ± 1.2	390.0 ± 45
a-P3HB-50-P34HB-15	8.8 ± 0.4	23.0 ± 5.6	8.8 ± 1.7	8.0 ± 4.5
a-P3HB-50-P34HB-30	7.2 ± 0.3	180.0 ± 68	6.9 ± 0.1	120.0 ± 18
a-P3HB-50-P34HB-50	7.3 ± 0.4	380.0 ± 36	6.3 ± 0.4	320.0 ± 36
a-P3HB-30-P34HB-15	13.0 ± 0.5	26.0 ± 4.2	17.1 ± 0.4	7.9 ± 0.9
a-P3HB-30-P34HB-30	12.1 ± 0.7	41.4 ± 20.4	14.2 ± 0.6	15.0 ± 3.2
a-P3HB-30-P34HB-50	12.3 ± 0.5	528.8 ± 69.3	11.1 ± 0.6	490.0 ± 51

* σB: tensile strength and ** εB: elongation at break; [1] values cited from ref. [12].

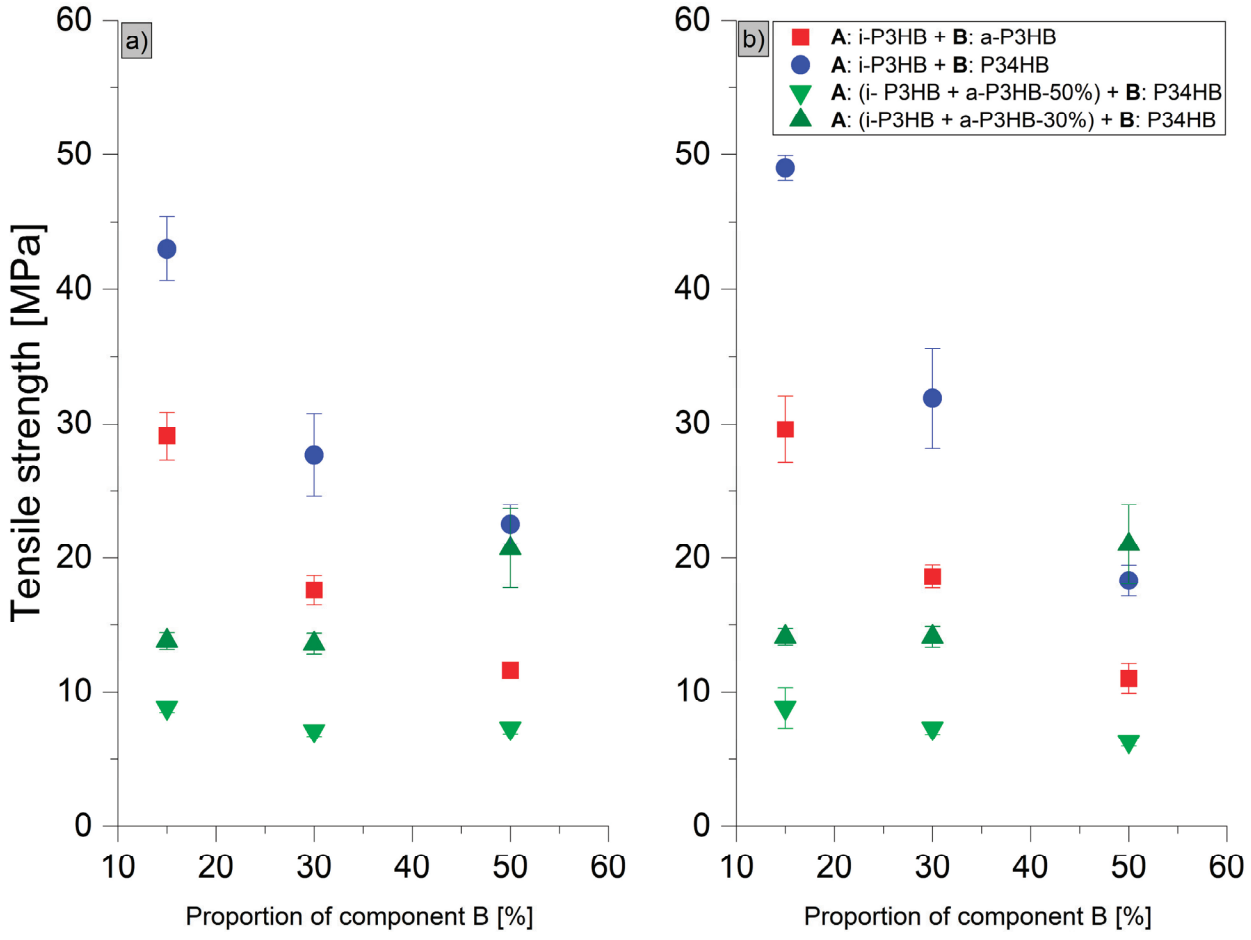

Figure 8. Tensile strength of *i*-P3HB blends (**a**) after production and (**b**) after 30 days of storage.

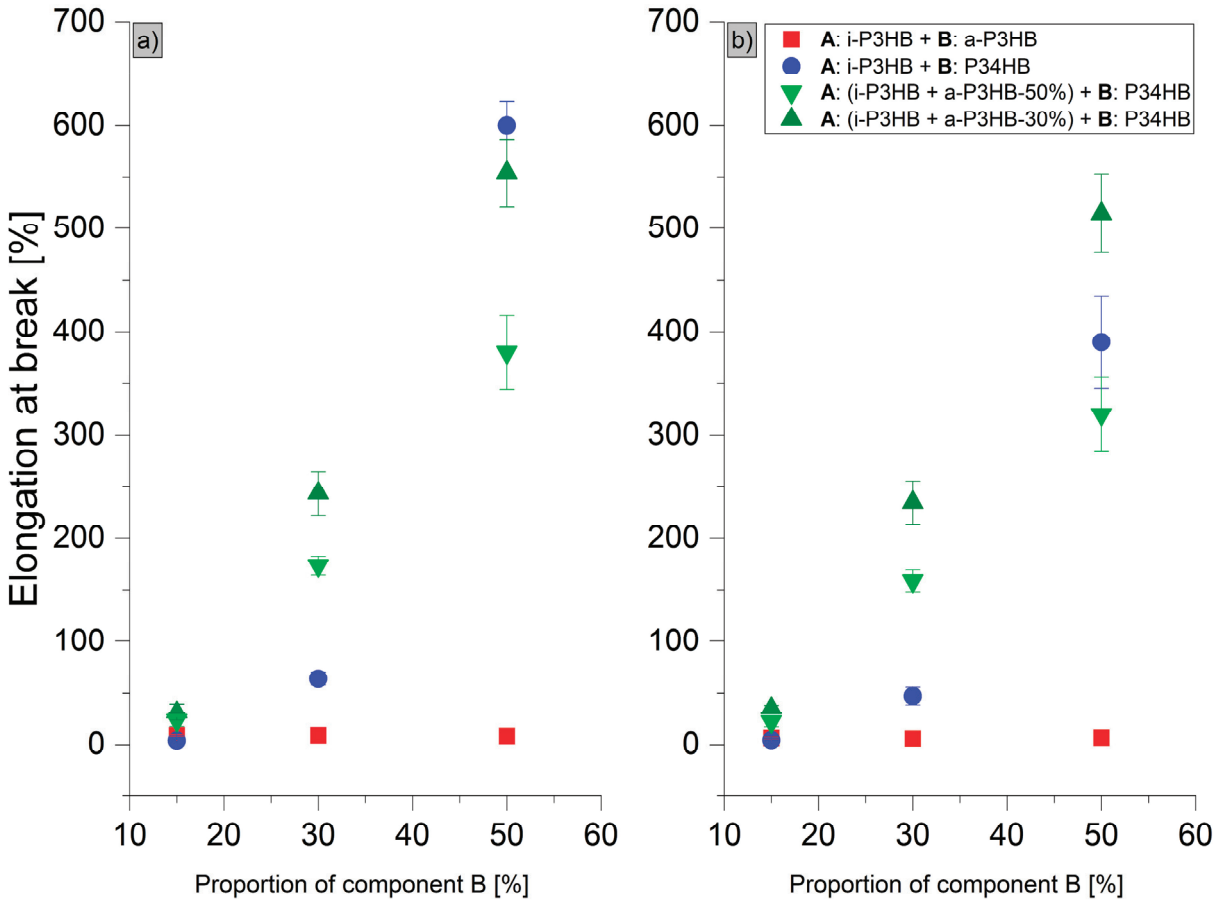

Figure 9. Elongation at break of *i*-P3HB blends (**a**) after production and (**b**) after 30 days of storage.

In contrast, blends with P34HB demonstrated a significant improvement in both the tensile strength and elongation at break, especially at higher P34HB contents. The P34HB-50 blend, for instance, achieved an elongation at break of 600%, which decreased to 390% after one month, indicating a reduction in ductility over time. Despite this decrease, the blend retained a high degree of flexibility. Additionally, the reduction in tensile strength was less pronounced compared to *a*-P3HB blends, due to the higher weight-average molecular weight of P34HB (Figures 8 and 9).

Blends containing both *a*-P3HB and P34HB exhibited a range of tensile strength values (8.8–13 MPa), depending on the polymer's ratio, and showed an enhanced elongation at break that remained relatively stable over time. For example, the *a*-P3HB-50-P34HB-50 blend achieved an initial εB of 380%, which decreased modestly to 320% after one month, demonstrating a better retention of mechanical properties. Similarly, the blend *a*-P3HB-30-P34HB-50 achieved an initial εB of 528.8%, maintaining a high value of 490% after one month, which is indicative of improved long-term mechanical stability (Figures 8 and 9).

These findings suggest that while *a*-P3HB has a limited impact on flexibility, blending with P34HB at higher concentrations (50 wt.%) enhances the elongation at break but does not preserve the enhanced mechanical properties over time. The combination of *a*-P3HB and P34HB creates a synergistic effect, resulting in a balanced enhancement of the mechanical performance, with an improved elongation at break and stable mechanical properties over time.

4. Conclusions

In this study, blends of *i*-P3HB with *a*-P3HB and P34HB were successfully prepared by a solvent-free method through extrusion. The influence of *a*-P3HB and P34HB on the processing behavior of *i*-P3HB was explored, along with an assessment of their thermal and mechanical properties using DSC, GPC, TGA, and tensile tests.

The DSC analysis indicated that the incorporation of *a*-P3HB led to a 15–25 °C decrease in the melting temperature compared to the neat *i*-P3HB and reduced crystallinity. Additionally, the appearance of a secondary melting peak suggested the presence of crystals with varying stabilities. In contrast, the addition of P34HB did not significantly affect the melting temperature but did contribute to a reduction in crystallinity. Ternary blends containing all three polymers exhibited both a lower crystallinity and decreased melting points. This demonstrates that blending *i*-P3HB with *a*-P3HB and P3HB facilitates its processing at reduced temperatures between 150 and 165 °C, thereby avoiding its thermal degradation.

Furthermore, the GPC analysis confirmed that the addition of *a*-P3HB and P34HB did not cause a significant reduction in the weight-average molecular weight of the extruded blends, supporting the conclusion that extrusion within the 150–165 °C range prevents thermal degradation.

In terms of mechanical properties, tensile tests revealed that blending with *a*-P3HB did not improve the elongation at break and slightly reduced the tensile strength. However, mechanical properties remained stable over 30 days, suggesting suppressed post-crystallization. In contrast, binary blends with P34HB exhibited an enhanced elongation at break, reaching up to 600% with 50 wt.% P34HB, although this effect decreased to around 400% after 30 days, probably due to the post-crystallization and lack of compatibility between *i*-P3HB and P34HB, which should be further investigated. Ternary blends of all three polymers demonstrated a tunable elongation at break (ranging from 23% to 529%) and tensile strength (7.2 to 13 MPa), with only minor reductions after 30 days.

In summary, blending *i*-P3HB with *a*-P3HB and P34HB significantly enhances its processability by expanding the processing window and enabling extrusion at reduced temperatures without inducing thermal degradation. The resulting ternary blends exhibit tunable and relatively stable thermal and mechanical properties, making them suitable for various processing techniques such as extrusion, injection molding, and fiber spinning.

This study presents a viable approach to process the biobased and biodegradable *i*-P3HB into blends with properties comparable to conventional plastics, with potential applications in the packaging, medicine, and textile industries.

Author Contributions: Conceptualization, W.A. and G.G.; methodology, W.A.; software, W.A.; validation, W.A.; formal analysis, W.A.; investigation, W.A.; resources, W.A. and S.G.; data curation, W.A.; writing—original draft preparation, W.A.; writing—review and editing, W.A., S.G., G.G., D.W.S. and M.R.; visualization, W.A.; supervision, G.G. and D.W.S.; project administration, G.G. and S.G.; funding acquisition, G.G. and S.G. All authors have read and agreed to the published version of the manuscript.

Funding: This work was supported by the European Union through the project Waste2BioComp, GA 101058654 and HORIZON-CL4-2021-TWIN-TRANSITION-01-05 of the Horizon Europe 2021—2027 program.

Institutional Review Board Statement: Not applicable.

Data Availability Statement: Data is contained within the article.

Conflicts of Interest: The authors declare no conflicts of interest. The funders had no role in the design of the study; in the collection, analyses, or interpretation of data; in the writing of the manuscript; or in the decision to publish the results.

References

1. Lemoigne, M. Products of dehydration and of polymerization of β-hydroxybutyric acid. *Bull. Soc. Chem. Biol.* **1926**, *8*, 770–782.
2. Gahlawat, G. *Polyhydroxyalkanoates Biopolymers*; Springer International Publishing: Cham, Switzerland, 2019; ISBN 978-3-030-33896-1.
3. Koller, M. (Ed.) *The Handbook of Polyhydroxyalkanoates: Microbial Biosynthesis and Feedstocks*; CRC Press: Boca Raton, FL, USA, 2020.
4. Dill, S. *Verarbeitung und Charakterisierung von Polyamid 6-Polyhydroxybutyrat-Blends: Verarbeitung und Charakterisierung von Polyamid 6-Polyhydroxybutyrat-Blends*; Universitätsverlag der TU Berlin: Berlin, Germany, 2020.
5. McAdam, B.; Fournet, M.B.; McDonald, P.; Mojicevic, M. Production of Polyhydroxybutyrate (PHB) and Factors Impacting Its Chemical and Mechanical Characteristics. *Polymers* **2020**, *12*, 2908. [CrossRef] [PubMed]
6. Türk, O. *Stoffliche Nutzung Nachwachsender Rohstoffe*; Springer Fachmedien Wiesbaden: Wiesbaden, Germany, 2014; ISBN 978-3-8348-1763-1.
7. Aoyagi, Y.; Yamashita, K.; Doi, Y. Thermal degradation of poly[(R)-3-hydroxybutyrate], poly[ε-caprolactone], and poly[(S)-lactide]. *Polym. Degrad. Stab.* **2002**, *76*, 53–59. [CrossRef]
8. Grassie, N.; Murray, E.J.; Holmes, P.A. The thermal degradation of poly(-(d)-β-hydroxybutyric acid): Part 1—Identification and quantitative analysis of products. *Polym. Degrad. Stab.* **1984**, *6*, 47–61. [CrossRef]
9. Ariffin, H.; Nishida, H.; Shirai, Y.; Hassan, M.A. Determination of multiple thermal degradation mechanisms of poly(3-hydroxybutyrate). *Polym. Degrad. Stab.* **2008**, *93*, 1433–1439. [CrossRef]
10. Yousefi, A.M.; Wnek, G.E.; Gomez Jimenez, H.; Ghassemi, H.; Zhang, J. Investigating the Effects of Temperature, Azodicarbonamide, Boron Nitride, and Multilayer Film/Foam Coextrusion on the Properties of a Poly(Hydroxyalkanoate)/Poly(Lactic acid) Blend. *J. Polym. Environ.* **2024**, *32*, 6349–6374. [CrossRef]
11. Janigová, I.; Lacék, I.; Chodák, I. Thermal degradation of plasticized poly(3-hydroxybutyrate) investigated by DSC. *Polym. Degrad. Stab.* **2002**, *77*, 35–41. [CrossRef]
12. Chodak, I. Polyhydroxyalkanoates: Properties and Modification for High Volume Applications. In *Degradable Polymers*; Scott, G., Ed.; Springer: Dordrecht, The Netherlands, 2002; pp. 295–319, ISBN 978-90-481-6091-4.
13. Luo, Z.; Wu, Y.L.; Li, Z.; Loh, X.J. Recent Progress in Polyhydroxyalkanoates-Based Copolymers for Biomedical Applications. *Biotechnol. J.* **2019**, *14*, e1900283. [CrossRef]
14. Sun, Y.; Jia, Z.; Chen, C.; Cong, Y.; Mao, X.; Wu, J. Alternating Sequence Controlled Copolymer Synthesis of α-Hydroxy Acids via Syndioselective Ring-Opening Polymerization of O-Carboxyanhydrides Using Zirconium/Hafnium Alkoxide Initiators. *J. Am. Chem. Soc.* **2017**, *139*, 10723–10732. [CrossRef]
15. Li, J.; Cheng, H.; Li, Y.; Wang, H.; Hu, H.; Liu, J. Effect of chain extender on the morphological, rheological and mechanical properties of biodegradable blends from PBAT and P34HB. *J. Polym. Res.* **2023**, *30*, 393. [CrossRef]
16. Samui, A.B.; Kanai, T. Polyhydroxyalkanoates based copolymers. *Int. J. Biol. Macromol.* **2019**, *140*, 522–537. [CrossRef]
17. Zhao, Q.; Cheng, G.X. Preparation of biodegradable poly(3-hydroxybutyrate) and poly(ethylene glycol) multiblock copolymers. *J. Mater. Sci.* **2004**, *39*, 3829–3831. [CrossRef]
18. Roy, I.; Visakh, P.M. (Eds.) *Polyhydroxyalkanoate (PHA) Based Blends, Composites and Nanocomposites*; Royal Society of Chemistry: Cambridge, UK, 2014; ISBN 978-1-84973-946-7.
19. Hamad, K.; Kaseem, M.; Ko, Y.G.; Deri, F. Biodegradable polymer blends and composites: An overview. *Polym. Sci. Ser. A* **2014**, *56*, 812–829. [CrossRef]
20. Rebia, R.A.; Rozet, S.; Tamada, Y.; Tanaka, T. Biodegradable PHBH/PVA blend nanofibers: Fabrication, characterization, in vitro degradation, and in vitro biocompatibility. *Polym. Degrad. Stab.* **2018**, *154*, 124–136. [CrossRef]
21. Mai, J.; Pratt, S.; Laycock, B.; Chan, C.M. Synthesis and Characterisation of Poly(3-hydroxybutyrate-co-3-hydroxyvalerate)-b-poly(3-hydroxybutyrate-co-3-hydroxyvalerate) Multi-Block Copolymers Produced Using Diisocyanate Chemistry. *Polymers* **2023**, *15*, 3257. [CrossRef] [PubMed]
22. Gabirondo, E.; Sangroniz, A.; Etxeberria, A.; Torres-Giner, S.; Sardon, H. Poly(hydroxy acids) derived from the self-condensation of hydroxy acids: From polymerization to end-of-life options. *Polym. Chem.* **2020**, *11*, 4861–4874. [CrossRef]
23. Nkrumah-Agyeefi, S.; Pella, B.J.; Singh, N.; Mukherjee, A.; Scholz, C. Modification of polyhydroxyalkanoates: Evaluation of the effectiveness of novel copper(II) catalysts in click chemistry. *Int. J. Biol. Macromol.* **2019**, *128*, 376–384. [CrossRef]
24. Utracki, L.A.; Wilkie, C.A. *Polymer Blends Handbook*; Springer: Dordrecht, The Netherlands, 2014; ISBN 978-94-007-6063-9.

25. Parra, D.F.; Fusaro, J.; Gaboardi, F.; Rosa, D.S. Influence of poly (ethylene glycol) on the thermal, mechanical, morphological, physical–chemical and biodegradation properties of poly (3-hydroxybutyrate). *Polym. Degrad. Stab.* **2006**, *91*, 1954–1959. [CrossRef]
26. Yang, H.; Ze-Sheng, L.; Qian, H.; Yang, Y.; Zhang, X.; Sun, C. Molecular dynamics simulation studies of binary blend miscibility of poly(3-hydroxybutyrate) and poly(ethylene oxide). *Polymer* **2004**, *45*, 453–457. [CrossRef]
27. Alata, H.; Hexig, B.; Inoue, Y. Effect of poly(vinyl alcohol) fine particles as a novel biodegradable nucleating agent on the crystallization of poly(3-hydroxybutyrate). *J. Polym. Sci. B Polym. Phys.* **2006**, *44*, 1813–1820. [CrossRef]
28. Chun, Y.S.; Kim, W.N. Thermal properties of poly(hydroxybutyrate-co-hydroxyvalerate) and poly(ϵ-caprolactone) blends. *Polymer* **2000**, *41*, 2305–2308. [CrossRef]
29. Qiu, Z.; Yang, W.; Ikehara, T.; Nishi, T. Miscibility and crystallization behavior of biodegradable blends of two aliphatic polyesters. Poly(3-hydroxybutyrate-co-hydroxyvalerate) and poly(ε-caprolactone). *Polymer* **2005**, *46*, 11814–11819. [CrossRef]
30. Qiu, Z.; Ikehara, T.; Nishi, T. Poly(hydroxybutyrate)/poly(butylene succinate) blends: Miscibility and nonisothermal crystallization. *Polymer* **2003**, *44*, 2503–2508. [CrossRef]
31. Qiu, Z.; Ikehara, T.; Nishi, T. Miscibility and crystallization behaviour of biodegradable blends of two aliphatic polyesters. Poly(3-hydroxybutyrate-co-hydroxyvalerate) and poly(butylene succinate) blends. *Polymer* **2003**, *44*, 7519–7527. [CrossRef]
32. Miao, L.; Qiu, Z.; Yang, W.; Ikehara, T. Fully biodegradable poly(3-hydroxybutyrate-co-hydroxyvalerate)/poly(ethylene succinate) blends: Phase behavior, crystallization and mechanical properties. *React. Funct. Polym.* **2008**, *68*, 446–457. [CrossRef]
33. Javadi, A.; Kramschuster, A.J.; Pilla, S.; Lee, J.; Gong, S.; Turng, L.-S. Processing and characterization of microcellular PHBV/PBAT blends. *Polym. Eng. Sci.* **2010**, *50*, 1440–1448. [CrossRef]
34. Ma, P.; Hristova-Bogaerds, D.G.; Lemstra, P.J.; Zhang, Y.; Wang, S. Toughening of PHBV/PBS and PHB/PBS Blends via In situ Compatibilization Using Dicumyl Peroxide as a Free-Radical Grafting Initiator. *Macro Mater. Eng.* **2012**, *297*, 402–410. [CrossRef]
35. Mai, J.; Kockler, K.; Parisi, E.; Chan, C.M.; Pratt, S.; Laycock, B. Synthesis and physical properties of polyhydroxyalkanoate (PHA)-based block copolymers: A review. *Int. J. Biol. Macromol.* **2024**, *263*, 130204. [CrossRef] [PubMed]
36. Zhang, L.; Ye, J.-W.; Zhang, X.; Huang, W.; Zhang, Z.; Lin, Y.; Zhang, G.; Wu, F.; Wang, Z.; Wu, Q.; et al. Effective production of Poly(3-hydroxybutyrate-co-4-hydroxybutyrate) by engineered Halomonas bluephagenesis grown on glucose and 1,4-Butanediol. *Bioresour. Technol.* **2022**, *355*, 127270. [CrossRef]
37. Policastro, G.; Panico, A.; Fabbricino, M. Improving biological production of poly(3-hydroxybutyrate-co-3-hydroxyvalerate) (PHBV) co-polymer: A critical review. *Rev. Environ. Sci. Biotechnol.* **2021**, *20*, 479–513. [CrossRef]
38. de Macedo, M.A.; Oliveira-Filho, E.R.; Taciro, M.K.; Piccoli, R.A.M.; Gomez, J.G.C.; Silva, L.F. Poly(3-hydroxybutyrate-co-4-hydroxybutyrate) [P(3HB-co-4HB)] biotechnological production: Challenges and opportunities. *Biomass Conv. Bioref.* **2024**, *14*, 26631–26650. [CrossRef]
39. Li, X.; Li, Y.; Zhang, G.; So, Y.-M.; Pan, Y. Recent Advances in Zinc Complexes for Stereoselective Ring-Opening Polymerization and Copolymerization. *Inorganics* **2025**, *13*, 185. [CrossRef]
40. Westlie, A.H.; Quinn, E.C.; Parker, C.R.; Chen, E.Y.-X. Synthetic biodegradable polyhydroxyalkanoates (PHAs): Recent advances and future challenges. *Prog. Polym. Sci.* **2022**, *134*, 101608. [CrossRef]
41. Grillo, A.; Rusconi, Y.; D'Alterio, M.C.; De Rosa, C.; Talarico, G.; Poater, A. Ring Opening Polymerization of Six- and Eight-Membered Racemic Cyclic Esters for Biodegradable Materials. *Int. J. Mol. Sci.* **2024**, *25*, 1647. [CrossRef] [PubMed]
42. Flory, P.J. *Principles of Polymer Chemistry*; Cornell University Press: Ithaca, NY, USA, 1953.
43. Odian, G. *Principles of Polymerization*, 4th ed.; John Willey & Sons: Hoboken, NJ, USA, 2004.
44. Rogers, M.E.; Long, T.E.; Turner, S.R. *Introduction to Synthetic Methods in Step-Growth Polymers*; John Willey & Sons: Hoboken, NJ, USA, 2003.
45. Arrieta, M.P.; López, J.; López, D.; Kenny, J.M.; Peponi, L. Development of flexible materials based on plasticized electrospun PLA–PHB blends: Structural, thermal, mechanical and disintegration properties. *Eur. Polym. J.* **2015**, *73*, 433–446. [CrossRef]
46. Vanovčanová, Z.; Alexy, P.; Feranc, J.; Plavec, R.; Bočkaj, J.; Kaliňáková, L.; Tomanová, K.; Perďochová, D.; Šariský, D.; Gálisová, I. Effect of PHB on the properties of biodegradable PLA blends. *Chem. Pap.* **2016**, *70*, 1408–1415. [CrossRef]
47. Arrieta, M.P.; Samper, M.D.; Aldas, M.; López, J. On the Use of PLA-PHB Blends for Sustainable Food Packaging Applications. *Materials* **2017**, *10*, 1008. [CrossRef]
48. Langford, A.; Chan, C.M.; Pratt, S.; Garvey, C.J.; Laycock, B. The morphology of crystallisation of PHBV/PHBV copolymer blends. *Eur. Polym. J.* **2019**, *112*, 104–119. [CrossRef]
49. Avella, M.; Martuscelli, E.; Raimo, M. Review Properties of blends and composites based on poly(3-hydroxy)butyrate (PHB) and poly(3-hydroxybutyrate-hydroxyvalerate) (PHBV) copolymers. *J. Mater. Sci.* **2000**, *35*, 523–545. [CrossRef]

50. Zhao, H.; Cui, Z.; Wang, X.; Turng, L.S.; Peng, X. Processing and characterization of solid and microcellular poly(lactic acid)/polyhydroxybutyrate-valerate (PLA/PHBV) blends and PLA/PHBV/Clay nanocomposites. *Compos. Part. B Eng.* **2013**, *51*, 79–91. [CrossRef]
51. Koller, M.; Braunegg, G. Polyhydroxyalkanoates: Experience of the past and prospects for the future. In *Handbook of Biopolymer-Based Materials*; Springer: Berlin/Heidelberg, Germany, 2015.
52. Sudesh, K.; Abe, H.; Doi, Y. Synthesis, structure and properties of polyhydroxyalkanoates: Biological polyesters. *Prog. Polym. Sci.* **2000**, *25*, 1503–1555. [CrossRef]
53. Costa, A.R.M.; Reul, L.T.; Sousa, F.M.; Ito, E.N.; Carvalho, L.H.; Canedo, E.L. Degradation during processing of vegetable fiber compounds based on PBAT/PHB blends. *Polym. Test.* **2018**, *69*, 266–275. [CrossRef]
54. Gonzalez, A.; Irusta, L.; Fernández-Berridi, M.J.; Iriarte, M.; Iruin, J.J. Application of pyrolysis/gas chromatography/Fourier transform infrared spectroscopy and TGA techniques in the study of thermal degradation of poly (3-hydroxybutyrate). *Polym. Degrad. Stab.* **2005**, *87*, 347–354. [CrossRef]
55. Roy, S.; Robert, J.W. Thermal Degradation of Bacterial Poly(hydroxybutyric acid): Mechanisms from the Dependence of Pyrolysis Yields on Sample Thickness. *Macromolecules* **1994**, *27*, 3782–3789. [CrossRef]
56. Kabe, T.; Tsuge, T.; Hikima, T.; Takata, M.; Takemura, A.; Iwata, T. Processing, Mechanical Properties, and Structure Analysis of Melt-Spun Fibers of P(3HB)/UHMW-P(3HB) Identical Blend. In *Green Polymer Chemistry: Biobased Materials and Biocatalysis*; Cheng, H.N., Gross, R.A., Smith, P.B., Eds.; American Chemical Society: Washington, DC, USA, 2015; pp. 63–75, ISBN 9780841230651.
57. Pachekoski, W.M.; Dalmolin, C.; Agnelli, J.A.M. The influence of the industrial processing on the degradation of poly(hidroxybutyrate)-PHB. *Mat. Res.* **2013**, *16*, 237–332. [CrossRef]
58. Almustafa, W.; Grishchuk, S.; Sebastian, J.; Schubert, D.W.; Grun, G. Improving i-P3HB Processing Window: Solution-Casting Blends With a-P3HB and P34HB. *J. Appl. Polym. Sci.* **2025**, *142*, e56805. [CrossRef]
59. Almustafa, W.; Schubert, D.W.; Grishchuk, S.; Sebastian, J.; Grun, G. Chemical Synthesis of Atactic Poly-3-hydroxybutyrate (a-P3HB) by Self-Polycondensation: Catalyst Screening and Characterization. *Polymers* **2024**, *16*, 1655. [CrossRef]
60. Barham, P.J.; Keller, A.; Otun, E.L.; Holmes, P.A. Crystallization and morphology of a bacterial thermoplastic: Poly-3-hydroxybutyrate. *J. Mater. Sci.* **1984**, *19*, 2781–2794. [CrossRef]
61. Deutsches Institutut für Normung. *DIN EN ISO 527-1: Plastics—Determination of Tensile Properties—Part 1: General Principles*; Beuth Verlag: Berlin, Germany, 2019.
62. Dawin, T.P.; Ahmadi, Z.; Taromi, F.A. Bio-based solution-cast blend films based on polylactic acid and polyhydroxybutyrate: Influence of pyromellitic dianhydride as chain extender on the morphology, dispersibility, and crystallinity. *Prog. Org. Coat.* **2018**, *119*, 23–30. [CrossRef]
63. Reis, K.C.; Pereira, J.; Smith, A.C.; Carvalho, C.; Wellner, N.; Yakimets, I. Characterization of polyhydroxybutyrate-hydroxyvalerate (PHB-HV)/maize starch blend films. *J. Food Eng.* **2008**, *89*, 361–369. [CrossRef]
64. UZUN, G.; AYDEMIR, D. Biocomposites from polyhydroxybutyrate and bio-fillers by solvent casting method. *Bull. Mater. Sci.* **2017**, *40*, 383–393. [CrossRef]
65. Adorna, J.A.; Ventura, R.L.G.; Dang, V.D.; Doong, R.; Ventura, J.S. Biodegradable polyhydroxybutyrate/cellulose/calcium carbonate bioplastic composites prepared by heat-assisted solution casting method. *J. Appl. Polym. Sci.* **2022**, *139*, 51645. [CrossRef]
66. Bayarı, S.; Severcan, F. FTIR study of biodegradable biopolymers: P(3HB), P(3HB-co-4HB) and P(3HB-co-3HV). *J. Mol. Struct.* **2005**, *744*, 529–534. [CrossRef]
67. Mascia, L.; Xanthos, M. An overview of additives and modifiers for polymer blends: Facts, deductions, and uncertainties. *Adv. Polym. Technol.* **1992**, *11*, 237–248. [CrossRef]
68. Bodaghi, A. An overview on the recent developments in reactive plasticizers in polymers. *Polym. Adv. Techs* **2020**, *31*, 355–367. [CrossRef]
69. Frone, A.N.; Nicolae, C.A.; Eremia, M.C.; Tofan, V.; Ghiurea, M.; Chiulan, I.; Radu, E.; Damian, C.M.; Panaitescu, D.M. Low Molecular Weight and Polymeric Modifiers as Toughening Agents in Poly(3-Hydroxybutyrate) Films. *Polymers* **2020**, *12*, 2446. [CrossRef] [PubMed]
70. Bonnet, M.; Buhk, M.; Trögner, G.; Rogausch, K.-D.; Petermann, J. Compatibility of syndiotactic with atactic polystyrene. *Acta Polym.* **1998**, *49*, 174–177. [CrossRef]
71. Nishi, T.; Wang, T.T. Melting Point Depression and Kinetic Effects of Cooling on Crystallization in Poly(vinylidene fluoride)-Poly(methyl methacrylate) Mixtures. *Macromolecules* **1975**, *8*, 909–915. [CrossRef]
72. Qiu, Z.; Ikehara, T.; Nishi, T. Melting behaviour of poly(butylene succinate) in miscible blends with poly(ethylene oxide). *Polymer* **2003**, *44*, 3095–3099. [CrossRef]

73. Schawe, J. Analysis of melting processes using TOPEM: Analysis of melting processes using TOPEM. *Anal. Melting Process. Using TOPEM* **2007**, *25*, 13–17.
74. Dong, T.; Mori, T.; Aoyama, T.; Inoue, Y. Rapid crystallization of poly(3-hydroxybutyrate-co-3-hydroxyhexanoate) copolymer accelerated by cyclodextrin-complex as nucleating agent. *Carbohydr. Polym.* **2010**, *80*, 387–393. [CrossRef]

polymers

MDPI

Article

The Lipid- and Polysaccharide-Rich Extracellular Polymeric Substances of *Rhodococcus* Support Biofilm Formation and Protection from Toxic Hydrocarbons

Anastasiia Krivoruchko [1,2,*], Daria Nurieva [1,2], Vadim Luppov [2], Maria Kuyukina [1,2] and Irina Ivshina [1,2]

[1] Perm Federal Research Center, 13a Lenin Street, 614990 Perm, Russia; daranurieva0@gmail.com (D.N.); kuyukina@iegm.ru (M.K.); ivshina@iegm.ru (I.I.)
[2] Microbiology and Immunology Department, Perm State National Research University, 15 Bukirev Street, 614990 Perm, Russia; onewayride@vk.com
* Correspondence: nast@iegm.ru; Tel.: +7-342-280-8114

Abstract

Extracellular polymeric substances (EPS) are multifunctional biopolymers that have significant biotechnological potential. In this study, forty-seven strains of *Rhodococcus* actinomycetes were screened for EPS production and the content of its main components: carbohydrates, lipids, proteins, and nucleic acids. The *Rhodococcus* strains produced lipid-rich EPS (15.6 mg·L^{-1} to 71.7 mg·L^{-1}) with carbohydrate concentrations varying from 0.6 mg·L^{-1} to 58.2 mg·L^{-1} and low amounts of proteins and nucleic acids. Biofilms of *R. ruber* IEGM 231 were grown on nitrocellulose filters in the presence of *n*-hexane, *n*-hexadecane, or diesel fuel. The distribution of β-polysaccharides, glycoconjugates, and proteins between cells and the extracellular matrix was examined using fluorescence microscopy. The observed release of β-polysaccharides into the biofilm matrix in the presence of *n*-hexane and diesel fuel was regarded as an adaptation to the assimilation of these toxic hydrocarbons by *Rhodococcus* cells. Atomic force microscopy of the dried EPS film revealed adhesion forces between 1.0 and 20.0 nN, while some sites were highly adhesive ($F_a \geq 20.0$ nN). EPS biosynthetic genes were identified, with two glycosyltransferases correlating with an increase in carbohydrate production. The production of EPS by *Rhodococcus* cells exhibited strain-specific rather than species-specific patterns, reflecting a high genetic diversity of these bacteria.

Keywords: extracellular polymeric substances; *Rhodococcus* actinomycetes; biofilms; cell aggregates; bacterial adhesion; tolerance to hydrocarbons; glycosyltransferases

1. Introduction

Extracellular polymeric substances (EPS) are biopolymers produced by microorganisms into the surrounding media. A large proportion of EPS are considered to be polysaccharides. As a major component of the biofilm matrix, EPS exhibit significant ecological and physiological functions. Furthermore, microbial EPS are multifunctional, biotechnologically valuable compounds. Due to their biodegradability, non-toxicity, water-absorbing capacity, chelating properties, and biological activities, they are used as sources of prebiotics, bioprinting materials, thickeners, emulsifiers, flocculants, stabilizing agents, hydrogels, anti-adhesion preparations, antioxidants, anti-cancer and anti-inflammatory drugs, metal ion binders, plant protectors, and plant growth stimulators. They can be used in medicine,

pharmaceuticals, cosmetics, the food industry, remediation, and agriculture [1–4]. The search for novel producers and the expansion of the range of microbial EPS are deemed key priorities.

Actinomycetes of the genus *Rhodococcus* (domain *Bacteria*, kingdom *Bacillati*, phylum *Actinomycetota*, class *Actinomycetes*, order *Mycobacteriales*, family *Nocardiaceae*, https://lpsn.dsmz.de/genus/rhodococcus, last accessed 16 June 2025) are well-known stress-tolerant biodegraders of a wide range of emergent ecopollutants, mainly hydrocarbons and their derivatives. They are also promising producers of various biotechnologically important metabolites, including amino acids, fatty acids, proteins, carotenoids, biosurfactants, and polysaccharides [5,6]. In comparison with well-characterized polysaccharide EPS, such as alginate produced by *Pseudomonas aeruginosa*, xanthan produced by *Xanthomonas* spp., levan produced by *Paenibacillus polymyxa*, dextran produced by lactic acid bacteria, succinoglycan produced by *Ensifer meliloti* (former *Sinorhizobium meliloti*), and EPS produced by *Bacillus* spp. and various proteobacteria [3,7–9], *Rhodococcus* EPS remain poorly characterized.

It is known that EPS produced by *Rhodococcus* bacteria affect their colony morphology, cell-surface hydrophobicity/hydrophilicity, aggregation, flocculation, growth rates, and resistance to toxicants [10–13]. In particular, EPS in the biofilm matrix enable *Rhodococcus* to resist chlorine-based disinfectants and quinoline, and to dominate in microbial communities in the presence of these compounds [14,15]. Increased EPS production has also been observed in *Rhodococcus* biofilms in the presence of the toxic, hydrophobic dibenzofuran [13]. The protective mechanism of EPS is universal. They trap (absorb) organic xenobiotics and act as a buffer zone between toxicants and cells while increasing adhesion to hydrophobic organic matter [13,14]. However, overproduction of EPS prevents flocculation and cell aggregation, but stimulates cell growth, as demonstrated for *Rhodococcus ruber* TH3 cells of the S- and R-types [12]. Cells of the tetrahydrofuran-degrading strain *R. ruber* YYL with a deleted *gmhD* gene (which encodes D-glycero-D-manno-heptose 1-phosphate guanosyltransferase) do not produce capsule lipopolysaccharides and are able to aggregate with each other [16]. Furthermore, EPS can play a key role in horizontal gene transfer by preventing binding with exogenous DNA. This has been demonstrated in the *R. ruber* YYL Δ*gmhD* mutant. This mutant does not form mushroom-like EPS extrusions, but exhibits high electrotransformation efficiency towards the plasmid pRESQ, with 2.38×10^7 transformed cells per μg DNA. Meanwhile, wild-type cells are surrounded by mushroom-like, translucent EPS and have an electrotransformation ability of less than 10^3 pRESQ-transformed cells per μg DNA [16].

EPS from *Rhodococcus* show promise as antiflocculants [12], thickeners [17,18], emulsifiers of edible oils [19], antioxidants [19], and cytotoxic agents [18]. They can also be used in bioremediation processes for the biosorption of heavy metals, as well as for use as biosurfactants. These activities have been confirmed for EPS produced by other actinomycetes. EPS produced by marine *Streptomyces* trap Sr^{2+} ions, EPS produced by *Nocardiopsis* trap Cs^{+} ions, and EPS produced by *Arthrobacter* trap Cu^{2+}, Pb^{2+}, and Cr^{6+} ions. EPS produced by *Streptomyces* exhibit washing and emulsifying activities towards motor oil, various hydrocarbons, and vegetable oils. EPS produced by *Gordonia polyisoprenivorans* emulsify benzene, toluene, and *o*-xylene [20]. EPS from *Rhodococcus opacus* affect the induced mineralization of calcium carbonate and participate in biomineralization. Therefore, they show promise in technologies for conserving stone artwork, the controlled synthesis of inorganic nanophases, crystal engineering of bulk solids, and the assembly of organized composite and ceramic materials [21]. Due to the presence of specific antigens, extracellular polysaccharides isolated from various *Rhodococcus* species (*Rhodococcus coprophilus*, *Rhodococcus equi*, *Rhodococcus*

erythropolis, *Rhodococcus rhodnii*, and *Rhodococcus rhodochrous*) bind viral-like particles of the GII.4 and GII.6 genotypes of human norovirus. This seems promising for the development of innovative antiviral strategies to prevent and treat norovirus infections in children [22].

Rhodococcus actinomycetes produce various types of EPS. These substances can be fatty acid-containing extracellular polysaccharides [11], acidic polysaccharides [11], or complex mixtures of various polymers [13,21]. The chemical composition of EPS polysaccharides in *Rhodococcus* is well described. These compounds are frequently acidic heteropolysaccharides, with compositions that vary significantly between species and strains. Details of the monomer composition of *Rhodococcus* exopolysaccharides can be found in the literature [11,13,17–19,21]. Less is known about the other components of *Rhodococcus* EPS. Non-carbohydrates can prevail or constitute a significant proportion. For instance, lipids account for 5.4% (*w*/*w*) of the fatty acid-containing EPS produced by *R. rhodochrous*. The yield of crude EPS in *R. erythropolis* HX-2 is 6.365 $g \cdot L^{-1}$, with a maximum of 8.957 $g \cdot L^{-1}$, but the yield of exopolysaccharides after multistep purification through the DEAE Cellulose DE-52 and Sepharose CL-6B columns is only 3.736 $g \cdot L^{-1}$. Losses are unavoidable during purification, but it appears that a significant proportion of crude EPS are non-carbohydrates [18]. Saturated fatty acids, such as stearic and palmitic acids, dominate the lipids in *Rhodococcus* EPS [12,23]. A large proportion of proteins are found in EPS produced by *Rhodococcus* sp. p52. These compounds account for 20–33% of total EPS and dominate polysaccharides by 1.5–3.0 times in a fraction of loosely cell-bound EPS [13]. The water-soluble fraction of EPS from *R. opacus* consists of 64.6% polysaccharides and 9.4% proteins, with the remainder being other compounds [21,24]. These proteins may be cytoplasmic molecules that are released into EPS via general secretory pathways and membrane vesicles. Electron transfer (ferredoxin, rubredoxin), toxin–antitoxin, and stress response proteins account for a greater proportion of the proteins present in EPS produced by *Rhodococcus* sp. p52 in the presence of dibenzofuran [13]. Large amounts of proteins are not unique to *Rhodococcus* actinomycetes. For example, the percentage of proteins in the EPS of quinoline-degrading microbial biofilms is fixed at 25–43% [14].

Polysaccharides are typically separated from the other components of EPS and further purified. This is necessary for analyzing their chemical composition and for applications requiring a high level of quality, such as in the fields of (bio)medicine, the food industry, and cosmetology. However, it is crude EPS, rather than their individual components, that determine the true physical-chemical properties of the cell surface. They affect the zeta potential and hydrophobicity of cells, and participate in cell-to-cell contact, as well as contact with substrates, nanoparticles, and surfaces for colonization. They also determine how processes of protection, anti-toxicity, flocculation, and dissolution of contaminants occur [13,14,21]. The hydrolysis of total EPS, including all their components, may affect passive cellular motility, as demonstrated in [13]. The viscosity of EPS (an important characteristic of thickeners and water-holding agents) depends on the combination of the individual components [14].

This study focuses on the crude, loosely cell-bound fraction of EPS produced by various species of the *Rhodococcus* genus, as this is the most cost-efficient fraction for biotechnological purposes. *Rhodococcus* EPS have been studied in terms of their chemical composition, concentrations of major biopolymers, their role in adhesion and formation of biofilms and cell aggregates, and the possible genetic mechanisms of their biosynthesis.

2. Materials and Methods

2.1. Chemicals

The mineral salts, solvents, Luria–Bertani (LB) broth, D-glucose, crystal violet, Bradford reagent, agar, and Calcofluor White Stain were >97% pure and were purchased from Sigma-Aldrich, Inc. (St. Louis, MO, USA). Phenol was of molecular biology grade and was also purchased from Sigma-Aldrich, Inc. (St. Louis, MO, USA). Concentrated (98%) sulphuric acid was >99.99% pure and was purchased from Chimregionsnab (Ufa, Russia). *n*-Hexane and *n*-hexadecane were >99% pure and were purchased from Cryochrom (St. Petersburg, Russia) and Ekos-1 (Moscow, Russia), respectively. Winter diesel fuel ECTO grade was purchased from Lukoil-Permnefteorgsintez (Perm, Russia). Wheat Germ Agglutinin Alexa Fluor® 350 Conjugate and FilmTracer SYPRO® Ruby Biofilm Matrix Stain were purchased from Thermo Fisher Scientific (Waltham, MA, USA).

2.2. Bacterial Strains and Growth Conditions

A total of 47 strains belonging to the following species were used: *Rhodococcus aetherivorans* (2 strains), *Rhodococcus cerastii* (3 strains), *Rhodococcus cercidiphylli* (1 strain), *Rhodococcus corynebacterioides* (1 strain), *R. erythropolis* (8 strains), *Rhodococcus fascians* (1 strain), *Rhodococcus globerulus* (1 strain), *Rhodococcus jostii* (2 strains), *R. opacus* (3 strains), *Rhodococcus pyridinivorans* (2 strains), *Rhodococcus qingshengii* (3 strains), *R. rhodochrous* (8 strains), *R. ruber* (7 strains), *Rhodococcus wtarislaviensis* (1 strain), and *Rhodococcus* sp. (4 strains) (Table S1). These strains were obtained from the Regional Specialised Collection of Alkanotrophic Microorganisms (acronym IEGM, WDCM number 768, http://www.iegmcol.ru/, last accessed 17 June 2025). The bacteria were grown in 100 mL of LB medium at 160 rpm and 28 °C for 48 h, at an initial cell concentration of 10^6 colony forming units (CFU) per mL.

2.3. Extraction of EPS and Quantitative Analysis of Biopolymers

The fraction of loosely cell-bound EPS was extracted from *Rhodococcus* cells according to [25]. The bacterial cultures were centrifuged at 6000 rpm for 15 min. The supernatant was discarded and the cells were washed with the same volume of phosphate-buffered saline (PBS) at 6000 rpm for 15 min. The PBS contained the following concentrations: NaCl—8.0 g·L^{-1}, KCl—2.0 g·L^{-1}, Na_2HPO_4—1.4 g·L^{-1}, KH_2PO_4—0.3 g·L^{-1}, and pH = 7.4. The cells were then resuspended in 10 mL of PBS and centrifuged at 13,600 rpm for 30 min. The EPS were then precipitated from the supernatant with three volumes of 96% ethanol. The mixture was then left to stand at 4 °C for 24 h before being separated from the solvent at 6000 rpm for 15 min. The EPS were then dried in air and dissolved in 1 mL of Milli-Q® water for subsequent analysis.

The total carbohydrate content of the crude EPS was determined using the phenol-sulphuric acid method [25]. One volume of dissolved EPS was mixed with one volume of 5% phenol and five volumes of concentrated sulphuric acid. The mixture was then incubated in a water bath Elma S10H (Elmasonic, Singen, Germany) at 30 °C for 20 min to produce a red (yellow) color. The color intensity was then measured in quartz cuvettes at 490 nm using a Lambda EZ201 spectrophotometer (Perkin Elmer, Shelton, CO, USA). The protein estimation was performed using the Bradford method. For this, 600 µL of the Bradford reagent was mixed with 60 µL of a sample (EPS dissolved in 1 mL of Milli-Q® water) thoroughly and incubated in the dark at room temperature for 10 min. A color change due to protein binding was observed, and the absorbance was measured at 595 nm. Calibration curves between $A_{490\,nm}$ and D-glucose concentration (Figure S1) and between $A_{595\,nm}$ and bovine serum albumin concentration (Figure S2) were used to calculate the polysaccharide and protein content, respectively. The nucleic acid content (total DNA and RNA) of the EPS

was determined by measuring 1 µL of the EPS samples at 260 nm using a NanoPhotometer N50 (Implen, Munich, Germany), according to the manufacturer's instructions.

To determine the lipid content of the EPS, a chloroform:methanol 3:1 (*v*/*v*) extraction was conducted [18,26]. For this analysis, dried EPS were used. They were mixed with 4 mL of the solvent mixture, heated at 60 °C for 4 h, and then centrifuged at 5000 rpm for 15 min. The liquid phase was transferred to the pre-weighed tubes and evaporated in a fume cupboard at 45 °C for 2 h, followed by overnight evaporation at room temperature. The dried extracted lipids were allowed to reach constant weight, after which they were weighed using Mettler AC 100 balances (Mettler Toledo, Columbus, OH, USA).

Blank samples (PBS without cells, treated in the same way as samples with EPS) were used as controls in all the quantitative analyses.

2.4. Adhesion Tests and Biofilm Growth

Adhesive activity tests were performed in the round-bottom 96-well polystyrene microplates (Medpolymer, St. Petersburg, Russia). A 150 µL suspension of cells in 0.5% NaCl at a concentration of $1 \cdot 10^8$ CFU·mL^{-1} was transferred to the microplates and incubated in a Titramax 1000 incubator (Heidolph Instruments, Schwabach, Germany) at 600 min^{-1}, 28 °C for 24 h. The liquid was then removed and the plates were washed twice with 0.5% NaCl. Next, 150 µL of 1% (*w*/*v*) aqueous crystal violet solution was added. After staining for 20 min at room temperature, the dye was removed and the plates were washed twice with 0.5% NaCl. The crystal violet was then extracted using a 1:4 (*v*/*v*) acetone: ethanol mixture, and the absorbance at 630 nm was measured using a Multiscan Ascent photometer (Thermo Electron Corporation, Vantaa, Finland) [27,28]. A calibration curve between A_{630nm} and CFU was used to quantify the number of adherent cells (Figure S3). Adhesive activities were expressed as the attached cell numbers per unit area (CFU·cm^{-2}). Uninoculated 0.5% NaCl was used as an abiotic control.

Biofilms were obtained using nitrocellulose membrane filters with a diameter of 25 mm and pore sizes of 0.22 µm (Millipore, Burlington, MA, USA). Then, 200 µL of a *Rhodococcus* cell suspension with a concentration of 10^6 CFU·mL^{-1} was dropped onto the filters, which were then placed onto LB agar or mineral agar K plates. Agar K contained the following (http://www.iegmcol.ru/medium/med05.html, last accessed 17 June 2025): KH_2PO_4—1.0 g·L^{-1}, K_2HPO_4—1.0 g·L^{-1}, NaCl—1.0 g·L^{-1}, KNO_3—1.0 g·L^{-1}, $MgSO_4$—0.2 g·L^{-1}, $CaCl_2$—0.02 g·L^{-1}, $FeCl_3$—0.001 g·L^{-1}, and agar—15.0 g·L^{-1}. Paper discs saturated with 200 µL of *n*-hexane, *n*-hexadecane, or diesel fuel were placed under the Petri dish lids and used as co- or growth substrates during cultivation on LB agar or mineral agar K plates, respectively. The plates with inoculated filters were incubated at 28 °C; for 6 days. Petri dishes containing sterile, non-inoculated filters were used as abiotic controls. Inoculated filters placed on LB agar without hydrocarbons were used as a biotic control. The density of the grown biofilms was determined after staining with crystal violet, according to the procedure described above, with modifications. Specifically, the biomass was collected from the membrane filters, resuspended in a 0.5% NaCl solution, and then centrifuged at 6000 rpm for 5 min. The cell pellet was then resuspended in a 1% water solution of crystal violet for staining. The cells were then washed twice with 0.5% NaCl and the crystal violet was extracted from the pellet for subsequent photometric analysis.

2.5. Fluorescence Microscopy of Biofilms and Aggregates

The following fluorescent dyes were used to visualize different components in biofilms and cell aggregates: Calcofluor White Stain for β-polysaccharides; Wheat Germ Agglutinin Alexa Fluor® 350 Conjugate for glycoconjugates; and FilmTracer SYPRO® Ruby Biofilm

Matrix Stain for proteins. Biofilms were obtained as described above. Their fragments were placed on microscope slides and stained with 20 μL of Calcofluor White in the dark for 1 min. Aggregates formed spontaneously in some flasks. *R. aetherivorans* IEGM 1250 was the only strain that grew in the form of aggregates. A 1 mL of bacterial suspension containing visible aggregates was centrifuged at 4000 rpm for 10 min. The precipitate was suspended in 50 μL of SYPRO Ruby and 50 μL of Wheat Germ Agglutinin, mixed gently and stained in the dark for 20 min. Then, 30 μL of the sample was applied to a microscope slide and 10 μL of Calcofluor White was added. The mixture was then incubated for 1 min in the dark. The cells were then observed using an Axio Imager 2 fluorescence microscope (Carl Zeiss, Oberkochen, Germany) with an excitation wavelength of 380 nm and an emission wavelength of 475 nm.

2.6. Atomic Force Microscopy (AFM)

To estimate the adhesion force of EPS, an MFP-3D-BIO™ atomic force microscope (Asylum Research, Santa Barbara, CA, USA) equipped with IgorPro 6.38B01 software (WaveMetrics, Lake Oswego, OR, USA) was used. Dried EPS were dissolved in 100 μL of Milli-Q® water. Then, 10 μL of this 10× concentrated solution was dropped onto a cover glass or a cantilever, after which the drop was left to dry in the air. OMCL-AC24OTS-R3 cantilevers (Olympus, Tokyo, Japan) with a spring constant of 2 N/m and a resonance frequency of 70 kHz, made from silicon, were used. Scanning was performed in contact mode with the following parameters: ForceDist = 2 μm, SpeedScan = 2 Hz and TriggerPoint = 1 V. Height and adhesion force maps measuring 15 × 15 μm, comprising 1024 force curves per sample, were produced.

2.7. Bioinformatics Analysis

To identify genes potentially involved in the EPS production, the draft genome sequences of the studied strains, which are available in DDBJ/ENA/GenBank databases (Table S1), were examined. The genomes were annotated using the NCBI Prokaryotic Genome Annotation Pipeline [29] and RAST 2.0 [30,31]. Specific genes were obtained from the KEGG database (https://www.genome.jp/kegg/pathway.html, last accessed 17 June 2025) and searched in the annotated genome sequences. Paired and multiple nucleotide and amino acid sequence alignments were performed using the NCBI Basic Local Alignment Search Tool (BLAST) (https://blast.ncbi.nlm.nih.gov/Blast.cgi, last accessed 17 June 2025) and ClustalW (https://www.genome.jp/tools-bin/clustalw, last accessed 17 June 2025). Evolutionary analysis and construction of phylogenetic trees were conducted using MEGA12 (https://www.megasoftware.net/, last accessed 17 June 2025) [32]. The neighbor-joining method was used to construct the trees. Branch lengths reflecting evolutionary distances (similarities) were calculated using the maximum likelihood method. A search for biosynthetic gene clusters (BGCs) was performed using antiSMASH 7.0 [33].

2.8. Statistics

All experiments were performed in three independent trials, with 3–8 replicates. Statistica version 13.5.0.17 (TIBCO Software Inc., Palo Alto, CA, USA) and Julius (https://julius.ai, last accessed 4 June 2025) were used to calculate basic statistics, compare data, perform correlation analysis, and create heatmaps. IgorPro 6.38B01 and Claude Sonnet 4 AI model (Anthropic, San Francisco, CA, USA) were used to treat and analyze the AFM data.

3. Results

3.1. The Chemical Composition of EPS Produced by Rhodococcus spp.

The concentrations of the major biological polymers (polysaccharides, lipids, proteins, and nucleic acids) in loose EPS produced by *Rhodococcus* bacteria were estimated. A phenol-sulphuric acid reaction was used to detect polysaccharides. However, this reaction is not strictly specific to these compounds, determining the total content of carbohydrate residues, which could originate from polysaccharides, glycoconjugates (e.g., glycolipids and glycoproteins), lipopolysaccharides, nucleic acids, monosaccharides, disaccharides, and oligosaccharides present in the EPS. Furthermore, the term 'EPS carbohydrates' was used, essentially assuming that the carbohydrates originated predominantly from polysaccharides. As seen from Table 1 and Figure 1a, the studied *Rhodococcus* strains produced low amounts of EPS carbohydrates, ranging from 0.6 ± 0.2 mg·L^{-1} (*R. aetherivorans* IEGM 1250) to 58.2 ± 24.0 mg·L^{-1} (*R. ruber* IEGM 231). The median EPS carbohydrate production was as low as 8.9 mg·L^{-1}.

Table 1. Concentrations of the EPS carbohydrates produced by *Rhodococcus* spp.

Strain	EPS Carbohydrates, mg·L^{-1}	Strain	EPS Carbohydrates, mg·L^{-1}
R. ruber IEGM 231	58.2 ± 24.0	*R. cercidiphylli* IEGM 1184	8.8 ± 1.6
R. erythropolis IEGM 1399	32.2 ± 13.2	*R. opacus* IEGM 262	8.8 ± 1.9
R. globerulus IEGM 1203	31.9 ± 9.9	*R. rhodochrous* IEGM 1161	8.0 ± 3.5
R. rhodochrous IEGM 1298	27.6 ± 1.3	*R. erythropolis* IEGM 788	7.3 ± 1.8
R. qingshengii IEGM 1359	23.9 ± 3.5	*R. jostii* IEGM 68	6.7 ± 1.6
R. fascians IEGM 1233	23.7 ± 4.9	*R. qingshengii* IEGM 1270	6.3 ± 2.7
R. cerastii IEGM 1243	23.1 ± 9.2	*Rhodococcus* sp. IEGM 1414	5.7 ± 1.3
R. ruber IEGM 1263	21.8 ± 1.3	*R. pyridinivorans* IEGM 1142	5.6 ± 1.1
R. ruber IEGM 1135	20.2 ± 4.2	*R. corynebacterioides* IEGM 1202	5.3 ± 1.8
R. erythropolis IEGM 708	18.4 ± 7.7	*R. rhodochrous* IEGM 1362	3.8 ± 1.1
R. qingshengii IEGM 267	18.4 ± 8.8	*Rhodococcus* sp. IEGM 1409	2.9 ± 0.6
R. erythropolis IEGM 1348	16.8 ± 5.3	*Rhodococcus* sp. IEGM 1401	2.6 ± 0.1
R. wratislaviensis IEGM 1171	13.5 ± 1.7	*R. aetherivorans* IEGM 1367	2.5 ± 0.3
R. erythropolis IEGM 1321	13.2 ± 1.4	*R. cerastii* IEGM 1327	2.3 ± 0.7
R. opacus IEGM 249	12.8 ± 1.7	*R. ruber* IEGM 1391	2.3 ± 0.6
R. cerastii IEGM 1278	10.7 ± 1.3	*R. erythropolis* IEGM 1415	2.2 ± 0.8
R. ruber IEGM 1121	10.5 ± 4.6	*R. pyridinivorans* IEGM 66	1.9 ± 0.5
R. rhodochrous IEGM 107	9.9 ± 3.2	*Rhodococcus* sp. IEGM 1408	1.9 ± 0.3
R. jostii IEGM 60	9.6 ± 3.4	*R. rhodochrous* IEGM 64	1.6 ± 0.3
R. rhodochrous IEGM 1360	9.4 ± 3.7	*R. erythropolis* IEGM 1020	0.9 ± 0.4
R. rhodochrous IEGM 1162	9.2 ± 3.7	*R. erythropolis* IEGM 766	0.8 ± 0.3
R. rhodochrous IEGM 1363	8.9 ± 1.1	*R. aetherivorans* IEGM 1250	0.6 ± 0.2

Means ± standard deviations are shown.

The production of the EPS carbohydrates was independent of the taxonomic classification of the strains, as this parameter varied significantly between representatives of the same species (Figure 1a). Accurate correlation analysis was performed on species with ≥3 strains, including *R. erythropolis*/*R. qingshengii*, *R. cerastii*, *R. rhodochrous* and *R. ruber* (Figure 1b). The Kruskal–Wallis test revealed no statistically significant differences between species ($p = 0.61$). The correlation coefficient for the EPS carbohydrate production and *Rhodococcus* species was as low as $R_{Spearman} = 0.05$ at $p = 0.82$ (Figure 1b).

A subset of strains representatives of various *Rhodococcus* species was used to analyze other common biopolymers present in EPS, such as lipids, proteins, and nucleic acids (Table 2). High concentrations of lipids were detected, with production of these compounds varying from 15.6 ± 1.6 mg·L^{-1} (*Rhodococcus* sp. IEGM 1401) to 71.7 ± 7.2 mg·L^{-1}

(*R. erythropolis* IEGM 1415), with a median value of 32.0 mg·L^{-1}. This was four times higher than the median production of EPS carbohydrates (Table 2, Figure 2). Concentrations of proteins and nucleic acids in *Rhodococcus* EPS were negligible, consisting of no more than 1.131 ± 0.091 mg·L^{-1} for proteins and 2.735 ± 1.276 mg·L^{-1} for nucleic acids (Table 2). The highest values of total proteins and nucleic acids were found only in the EPS produced by *R. rhodochrous* IEGM 107. Other strains produced less than 0.5 mg·L^{-1} of these compounds (Table 2, Figure 2).

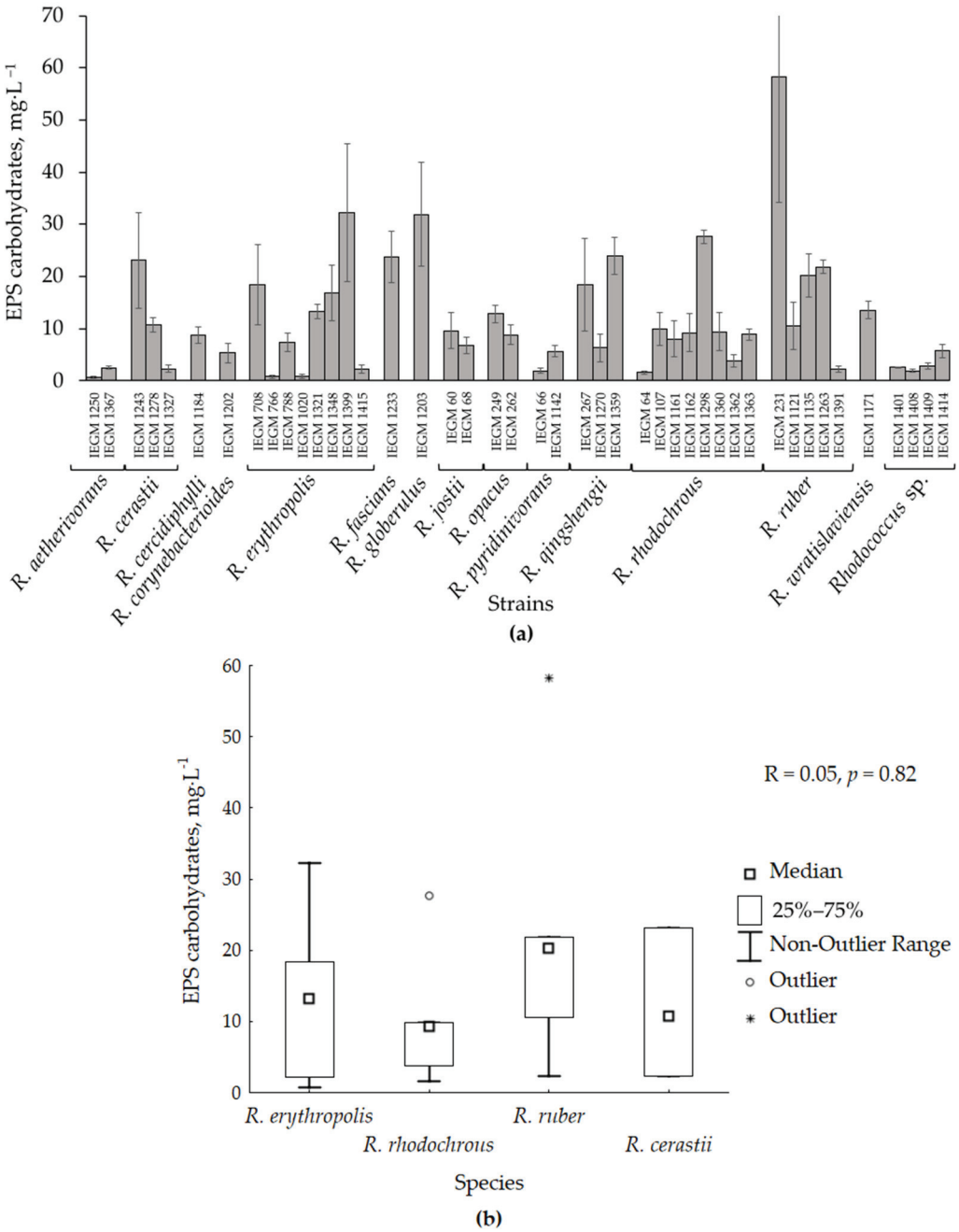

Figure 1. Production of EPS carbohydrates by various *Rhodococcus* species. Results are presented as: (**a**)—a diagram with strains grouped by species (means ± standard deviations are shown), (**b**)—box plots for EPS production by species (the total number of strains analyzed n = 26; the *R. erythropolis* box includes both *R. erythropolis* and *R. qinshengii* strains, https://lpsn.dsmz.de/species/rhodococcus-erythropolis, last accessed 17 June 2025). R—Spearman correlation coefficient; p—p-value.

The proportions of EPS biopolymers in individual *Rhodococcus* strains are shown in Figure 2. In one strain (*R. erythropolis* IEGM 1399), carbohydrates predominated over lipids by 56%. In three other strains—*R. globerulus* IEGM 1203, *R. wratislaviensis* IEGM 1171 and *R. opacus* IEGM 249—lipids did not significantly prevail over carbohydrates at 57%, 70%, and 48%, respectively. In seven strains, concentrations of EPS lipids exceeded those of EPS carbohydrates by 2–6 times. The EPS of other three strains (*R. erythropolis* IEGM 1415, *R. pyridinivoranss* IEGM 66 and *R. ceastii* IEGM 1327) consisted almost entirely of lipids. They predominated over carbohydrates by 15–33 times (Figure 2). Again, no relationship was observed between species and the composition of the studied EPS preparations.

Table 2. Concentrations of EPS biopolymers produced by *Rhodococcus* spp.

Strain	Lipids, mg·L^{-1}	Proteins, mg·L^{-1}	Nucleic Acids, mg·L^{-1}
R. erythropolis IEGM 1415	71.7 ± 7.2	Below detectable level	0.167 ± 0.019
R. qingshengii IEGM 1359	54.0 ± 8.5	0.112 ± 0.014	0.363 ± 0.199
R. globerulus IEGM 1203	50.0 ± 21.1	Below detectable level	0.126 ± 0.067
R. ruber IEGM 1122	43.3 ± 12.2	Below detectable level	0.077 ± 0.019
R. pyridinivorans IEGM 66	40.7 ± 11.2	Below detectable level	0.252 ± 0.086
R. cerastii IEGM 1327	34.0 ± 9.9	0.365 ± 0.164	0.151 ± 0.027
R. opacus IEGM 2226	34.0 ± 1.4	0.301 ± 0.091	0.254 ± 0.024
R. rhodochrous IEGM 107	32.0 ± 9.7	1.131 ± 0.091	2.735 ± 1.276
R. qingshengii IEGM 1270	31.3 ± 8.4	0.014 ± 0.002	0.111 ± 0.014
R. pyridinivorans IEGM 1142	26.3 ± 3.2	0.023 ± 0.004	0.177 ± 0.004
R. wratislaviensis IEGM 1171	23.0 ± 10.1	0.094 ± 0.008	0.308 ± 0.131
R. erythropolis IEGM 1399	20.7 ± 6.8	0.043 ± 0.003	0.287 ± 0.079
R. opacus IEGM 249	19.0 ± 7.9	Below detectable level	0.078 ± 0.018
R. jostii IEGM 68	17.3 ± 9.1	Below detectable level	0.062 ± 0.024
Rhodococcus sp. IEGM 1401	15.6 ± 1.6	0.244 ± 0.032	0.181 ± 0.013

Means ± standard deviations are shown.

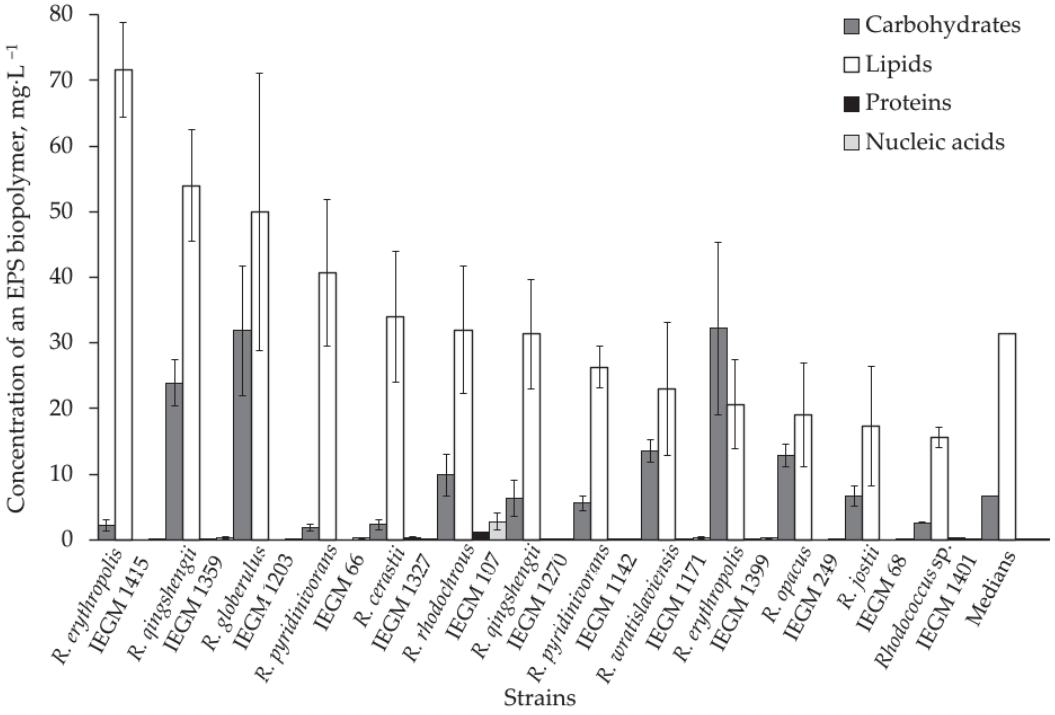

Figure 2. Comparison of major biopolymer concentrations in EPS produced by 13 *Rhodococcus* strains. Means ± standard deviations for individual strains are shown. The last set of columns shows the median biopolymer concentrations for all 13 strains.

3.2. EPS in Rhodococcus Biofilms and Cell Aggregates

The distribution of EPS between cells and the extracellular matrix was studied in *Rhodococcus* biofilms and cell aggregates using fluorescence microscopy. *R. ruber* IEGM 231 was selected as a model strain for biofilm formation. This strain is a known biodegrader of a wide range of hydrocarbons (http://www.iegmcol.ru/strains/rhodoc/ruber/r_ruber231.html, last accessed 17 June 2025) [34,35] and produces the highest amounts of EPS carbohydrates (Table 1). *R. ruber* IEGM 231 formed biofilms on all nitrocellulose membrane filters. As an oligotrophic microorganism [5], the IEGM 231 formed weak biofilms ($(0.9 \pm 0.1)\cdot10^9$ CFU·cm^{-2}) even in minimal media, such as mineral agar K without the supplementation of an external carbon source (Figure 3). The density of *R. ruber* IEGM 231 biofilms was affected by hydrocarbons. In particular, *n*-hexane, *n*-hexadecane, and diesel fuel resulted in a 2–8-fold increase in biofilm growth on mineral agar. This effect was observed in biofilms grown on mineral agar only, and was most notable for toxic hydrocarbons (e.g., *n*-hexane and diesel fuel), and least notable for *n*-hexadecane. No statistically significant differences were revealed between the biofilm densities of the biotic control and the hydrocarbon exposure on the LB agar (Figure 3).

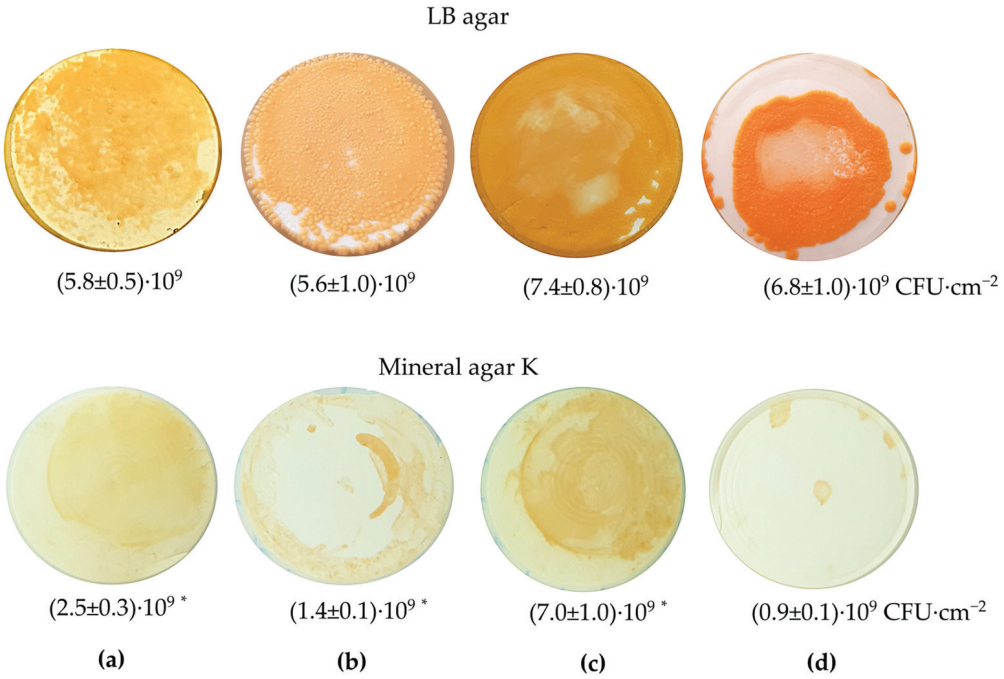

Figure 3. The *R. ruber* IEGM 231 biofilms grown on nitrocellulose filters placed on LB agar and mineral agar K in the presence of hydrocarbons. The hydrocarbons used: (**a**)—*n*-hexane, (**b**)—*n*-hexadecane, (**c**)—diesel fuel, (**d**)—control (no hydrocarbons). Biofilm densities are shown as means ± standard deviations, CFU·cm^{-2}. * Statistically different from the control at $p < 0.05$.

Staining of *R. ruber* IEGM 231 biofilms with Calcofluor White revealed that the β-polysaccharides were bound to and surrounded the cells, as well as constituting the extracellular matrix (Figure 4). The intensity of the fluorescence reflected the quantity of β-polysaccharides present on the cells and in the matrix. When exposed to *n*-hexadecane, *R. ruber* IEGM 231 cells exhibited a bright glow, indicating the presence of large quantities of β-polysaccharides bound to and surrounding the cells. The amounts of β-polysaccharides in the extracellular matrix were low. There was hardly any fluorescence, or only weak fluorescence, in the space between cells in the biofilms grown in the presence of *n*-hexadecane (Figure 4b,e).

When exposed to toxic hydrocarbons (e.g., *n*-hexane and diesel fuel), the *R. ruber* IEGM 231 cells appeared less bright, and the extracellular matrix appeared evidently white-blue (Figure 4c,f). Apparently, there were fewer cell-bound β-polysaccharides and more matrix-associated ones, indicating the release of β-polysaccharides into the extracellular space. In the presence of diesel fuel, as well as on LB agar without hydrocarbons, the cells were surrounded by loose, wide, fuzzy β-polysaccharide capsules. However, this effect was more pronounced at the diesel fuel exposure (Figure 4a,c). The formation of capsules was not observed in biofilms grown in the presence of individual *n*-alkanes or on mineral agar K without externally added growth substrates (Figure 4b,d–f). Cells in weak oligotrophic biofilms formed on agar K produced small amounts of the cell-bound β-polysaccharides and did not produce matrix β-polysaccharides, as evidenced by weak fluorescence (Figure 4d). This confirmed that no mature and functional rhodococcal biofilms were formed in this case. It is important to note that the effects of hydrocarbons on the distribution of β-polysaccharides between cells and the extracellular matrix were similar for biofilms grown on both LB agar and mineral agar K. However, their influence on the biofilm density was not registered on LB agar (Figure 3).

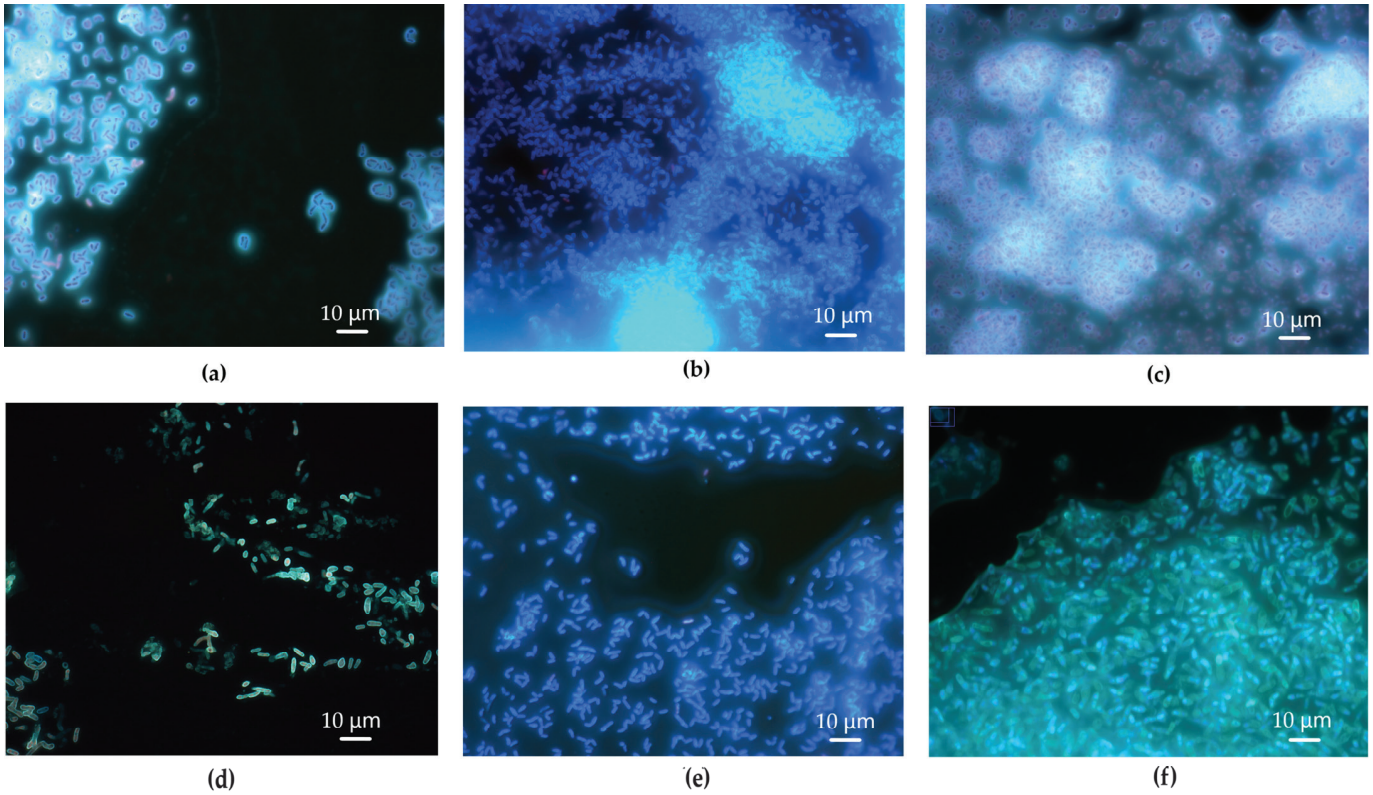

Figure 4. *R. ruber* IEGM 231 biofilms under a fluorescence microscope. Biofilms were obtained on: (**a**)—LB agar, (**b**)—LB agar in the presence of *n*-hexadecane, (**c**)—LB agar in the presence of diesel fuel, (**d**)—mineral agar K without externally added growth substrates, (**e**)—mineral agar K in the presence of *n*-hexadecane, and (**f**)—mineral agar K in the presence of *n*-hexane. Staining with Calcofluor White, which is specific to β-polysaccharides. Magnification ×1000.

The distribution of EPS was also examined in rhodococcal cell aggregates. One strain, *R. aetherivorans* IEGM 1250, grew in the form of aggregates. In other species, this process was more random and spontaneous, with typical growth occurring in the form of homogeneous suspensions. Aggregation was only rarely observed, specifically in *R. erythropolis* IEGM 1020 and *R. jostii* IEGM 68 (Figure 5). All three strains produced low amounts of EPS

carbohydrates (0.6–6.7 mg·L^{-1}) (Table 1). Furthermore, *R. jostii* IEGM 68 produced low amounts of EPS lipids (17.3 ± 9.1 mg·L^{-1}) (Table 2). Aggregation apparently did not affect the total EPS production, as no relationship was found between concentrations of EPS biopolymers and the formation of cell aggregates in particular flasks (i.e., replicates).

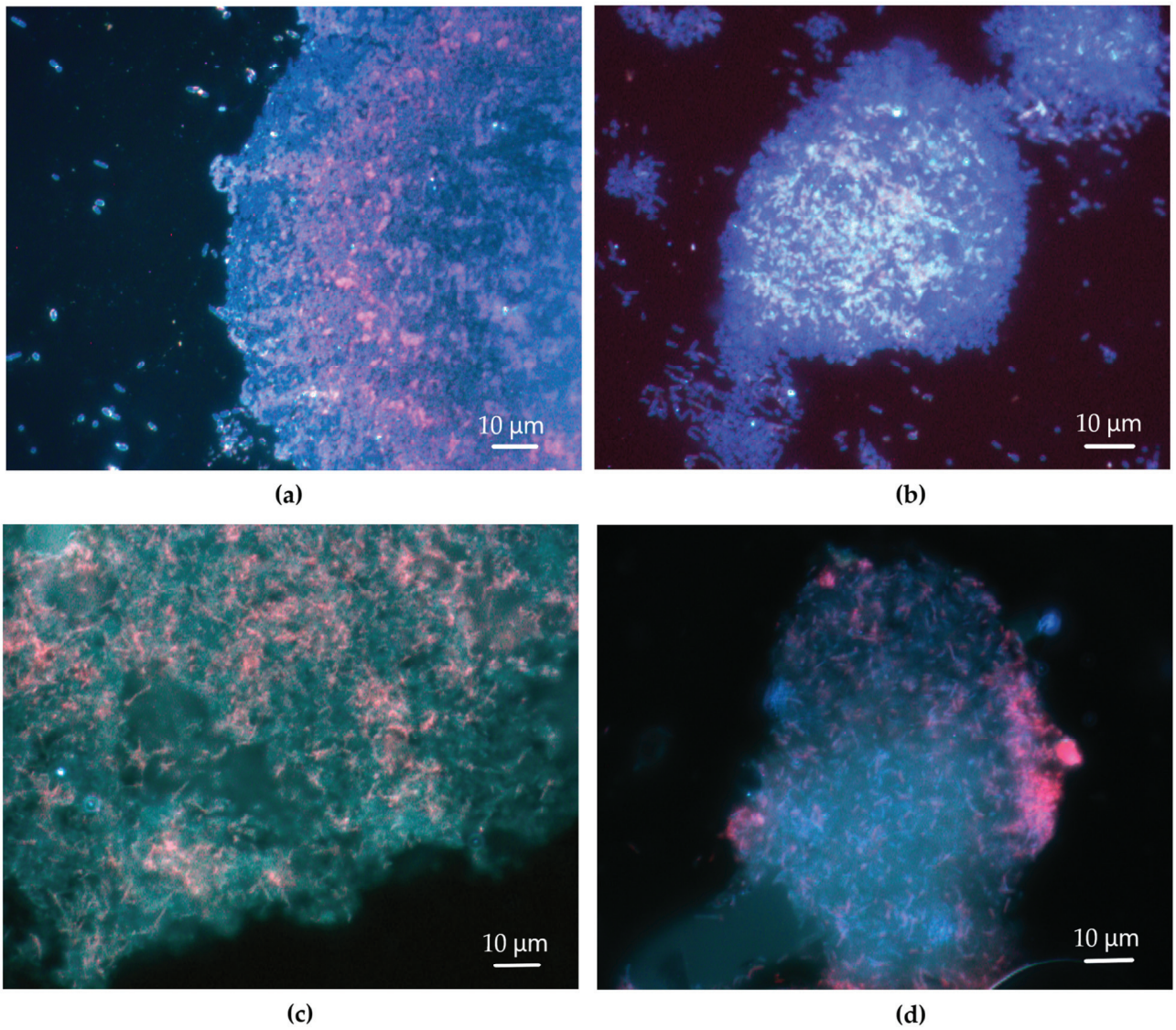

Figure 5. *Rhodococcus* cell aggregates under a fluorescence microscope. Strains: (**a**,**b**)—*R. aetherivorans* IEGM 1250, (**c**)—*R. erythropolis* IEGM 1020, (**d**)—*R. jostii* IEGM 68. Multi-component staining was performed using Calcofluor White Stain (specific to β-polysaccharides and exhibiting white-blue fluorescence), Wheat Germ Agglutinin Alexa Fluor® 350 Conjugate (specific to glycoconjugates and exhibiting blue fluorescence) and FilmTracer SYPRO® Ruby Biofilm Matrix Stain (specific to proteins and exhibiting red-orange, red or pink fluorescence). Magnification ×1000.

Aggregates of *Rhodococcus* cells were immersed in a matrix consisting of a complex mixture of β-polysaccharides and glycoconjugates, both of which produced a similar color when examined using fluorescence imaging. These compounds were found to be associated with the cells and the extracellular matrix in a manner similar to that observed in biofilms (Figure 5). *R. aetherivorans* IEGM 1250 cells formed dense aggregates with little free matrix (Figure 5a,b), whereas *R. erythropolis* IEGM 1020 cells (Figure 5c) and *R. jostii* IEGM 68 cells (Figure 5d) formed relatively loose aggregates with lower cell densities and

smaller amounts of cell-bound EPS and more extracellular matrix. The synthesis of cell-associated EPS differed between individual cells. Some cells were brighter and produced more EPS. Other cells were paler and produced fewer EPS. Some cells were unevenly stained, representing uneven distribution of EPS on the cell surface (Figure 5).

According to the multi-component staining data, the proteins were not part of the extracellular matrix of the *Rhodococcus* cell aggregates. Red, orange-red, and pink fluorescence associated with proteins was detected on the surface of bacterial cells rather than in the matrix (Figure 5). The proportion of cells synthesizing proteins differed between strains. Many red-orange cells were found in *R. erythropolis* IEGM 1020 aggregates (Figure 5c). *R. aetherivorans* IEGM 1250 aggregates predominantly consisted of cells with white/blue fluorescence that were actively synthesizing carbohydrate EPS. However, a proportion of cells producing surface proteins were also observed (Figure 5a,b). In the *R. jostii* IEGM 68 aggregates, protein-rich cells were localized at the poles of the aggregates (Figure 5d).

3.3. The Involvement of EPS in the Adhesion of Rhodococcus spp. To Solid Surfaces

The results of adhesion tests for *Rhodococcus* cells to polystyrene are shown in Table S2. No statistically significant correlation ($R_{Spearman} \leq 0.41$, $p > 0.05$) was revealed between the adhesive activity of rhodococci towards polystyrene and the amounts of carbohydrates and lipids in EPS. Two strains, *R. opacus* IEGM 249 and *R. rhodochrous* IEGM 1162, exhibited enhanced adhesive abilities. Some 63–64% of cells of these strains adhered to polystyrene, equivalent to 4.176–4.248·10^7 attached cells per cm^2 (Table S2). These strains produced low amounts of EPS lipids (19.0 ± 7.9 mg·L^{-1}) and median amounts of EPS carbohydrates (9.2–12.8 mg·L^{-1}) (Tables 1 and 2). Eight strains were unable to adhere to polystyrene (Table S2). Their synthesizing activities varied widely from 0.6 ± 0.2 mg·L^{-1} to 23.9 ± 13.5 mg·L^{-1} for the EPS carbohydrates and from 17.3 ± 9.1 mg·L^{-1} to 71.7 ± 7.2 mg·L^{-1} for the EPS lipids (Tables 1 and 2). The adhesive activities of the other *Rhodococcus* strains were between (0.153 ± 0.029)·10^7 CFU·cm^{-2} and (1.730 ± 0.380)·10^7 CFU·cm^{-2}, corresponding to 2% and 26% of the attached cells, respectively (Table S2). Their EPS production abilities also varied significantly (Tables 1 and 2).

The adhesive potential of the *Rhodococcus* EPS was additionally estimated by measuring the adhesion force F_a (nN) of the EPS produced by *R. ruber* IEGM 231. These EPS appeared to be inhomogeneous under an atomic force microscope. This could be seen on topographic maps of the EPS drop surface as a combination of dark and light spots, which corresponded to low- and high-relief areas, respectively (Figure 6c,d). This could be related to different densities and the formation of cords or strands consisting of more condensed EPS material [36]. The revealed heterogeneity was not associated with an arrangement of adhesion forces. Adhesive (light) and non-adhesive (dark) spots were sporadically located across the surface of EPS drops (Figure 6g). The median F_a for the EPS produced by *R. ruber* IEGM 231 was 7.0 nN, which was 2.8 nN (29%) lower than the median F_a of unmodified cover glass (Figure 6e–h). This could be due to electrostatic repulsion between the silicon cantilever and the charged EPS saturated with -OH groups. Most sites of EPS produced by *R. ruber* IEGM 231 exhibited adhesion forces between 1.0 and 20.0 nN. However, some rare sites were highly adhesive, with $F_a \geq 20.0$ nN (Figure 6h). Unmodified glass did not exhibit such adhesive spots, with its highest F_a values being around 13.2 nN (Figure 6e,f).

The adhesion force of the AFM cantilever modified with EPS towards the unmodified cover glass was 8.0 nN, which was 1.0 nN higher than that of the unmodified cantilever (Figure 7c). However, a bimodal distribution of adhesion forces was revealed. Some 80% of the measurements were >5.5 nN, with a median value of 8.2 nN; and 15% of the

measurements were ≤5.5 nN, with a median value of 3.2 nN (Figure 7d). The roughness of the cover glass when scanned with the EPS-modified cantilever was the same as when scanned with the unmodified cantilever (Figure 7a,b). This provided evidence that the scanning was correct. Additional topographic and adhesion force maps can be found in Figures S4 and S5.

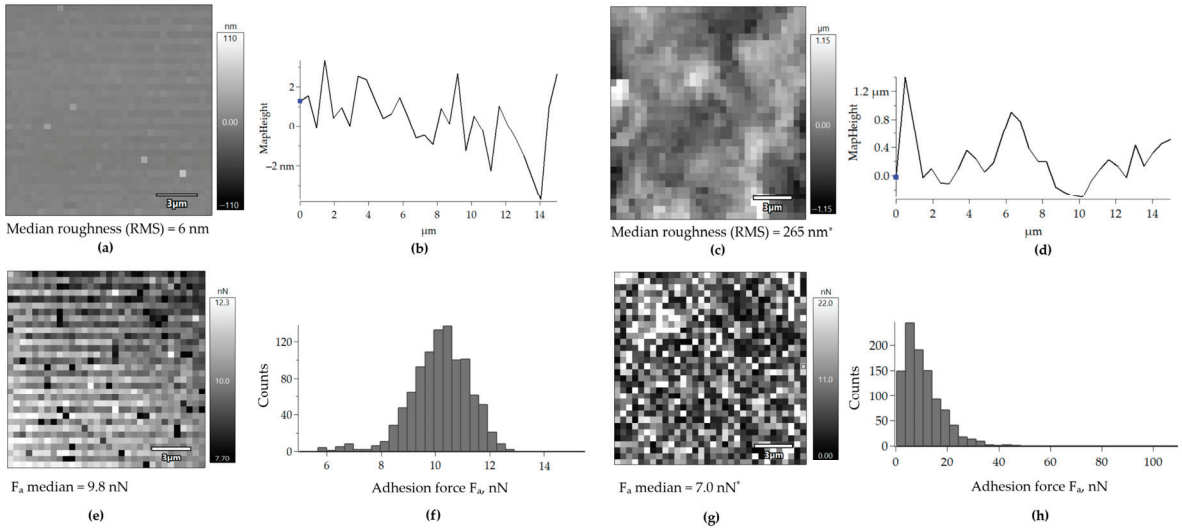

Figure 6. Distribution of adhesion forces F_a on the surface of unmodified cover glass (**a**,**b**,**e**,**f**) and of dried EPS extracted from the *R. ruber* IEGM 231 cells (**c**,**d**,**g**,**h**). The following data are shown: (**a**,**c**)—topographic maps, (**b**,**d**)—profiles of surfaces, (**e**,**g**)—adhesion force maps, and (**f**,**h**)—histograms showing the distribution of adhesion force values. RMS—root mean squared roughness. The slope of the topographic maps and surface profiles was eliminated using the Planefit function. * Significantly different from the control (unmodified cover glass) according to the Mann–Whitney U test at $p < 0.05$.

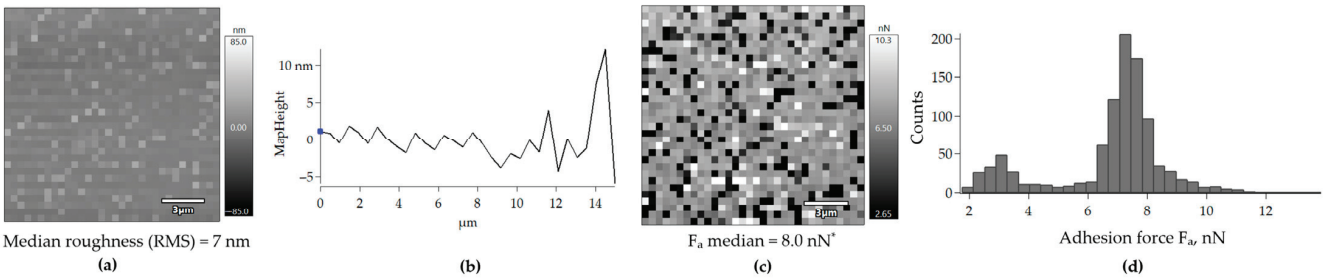

Figure 7. Distribution of adhesion forces F_a on the surface of an unmodified cover glass scanned with a cantilever modified with the *R. ruber* IEGM 231 EPS. The following data are shown: (**a**)—a topographic map, (**b**)—a profile of the scanned surface, (**c**)—an adhesion force map, and (**d**)—a histogram showing the distribution of adhesion force values. RMS—root mean squared roughness. The slope of the topographic maps and surface profiles was eliminated using the Planefit function. * Significantly different from the control (unmodified cantilever) according to the Mann–Whitney U test at $p < 0.05$.

3.4. Genes Involved in EPS Biosynthesis in Rhodococcus spp.

Genes likely involved in the biosynthesis of EPS polysaccharides in *Rhodococcus* spp. were analyzed. These genes coded for glycosyltransferases (gtfs), capsular polysaccharide biosynthesis proteins, undecaprenyl-phosphate galactose phosphotransferases, homoserine O-acetyltransferases, N-acetylglucosaminyl-diphospho-decaprenol L-rhamnosyltransferases, polysaccharide biosynthesis proteins, and acyl-CoA:1-acyl-sn-glycerol-3-phosphate acyltransferases. The latter two types of enzymes were rare, being

found only in two genomes: *Rhodococcus* sp. IEGM 1408 and *R. rhodochrous* IEGM 1360, respectively. The genes coding for glycosyltransferases were the most abundant and were found in all analyzed genomes (Figure 8, Table S3). The studied strains mainly harbored more than one glycosyltransferase gene. The largest number of glycosyltransferase genes detected was six, in three strains: *R. cerastii* IEGM 1243, *R. corynebacterioides* IEGM 1202 and *Rhodococcus* sp. IEGM 1408. The other three strains (*R. erythropolis* IEGM 1321, *R. ruber* IEGM 1391, and *Rhodococcus* sp. IEGM 1414) harbored five glycosyltransferases. Nine, nine, and eight strains had four, three, and two different glycosyltransferases, respectively. Only four strains (*R. rhodochrous* IEGM 107, IEGM 1161, IEGM 1362 and *Rhodococcus* sp. IEGM 1409) harbored one glycosyltransferase (Figure 8).

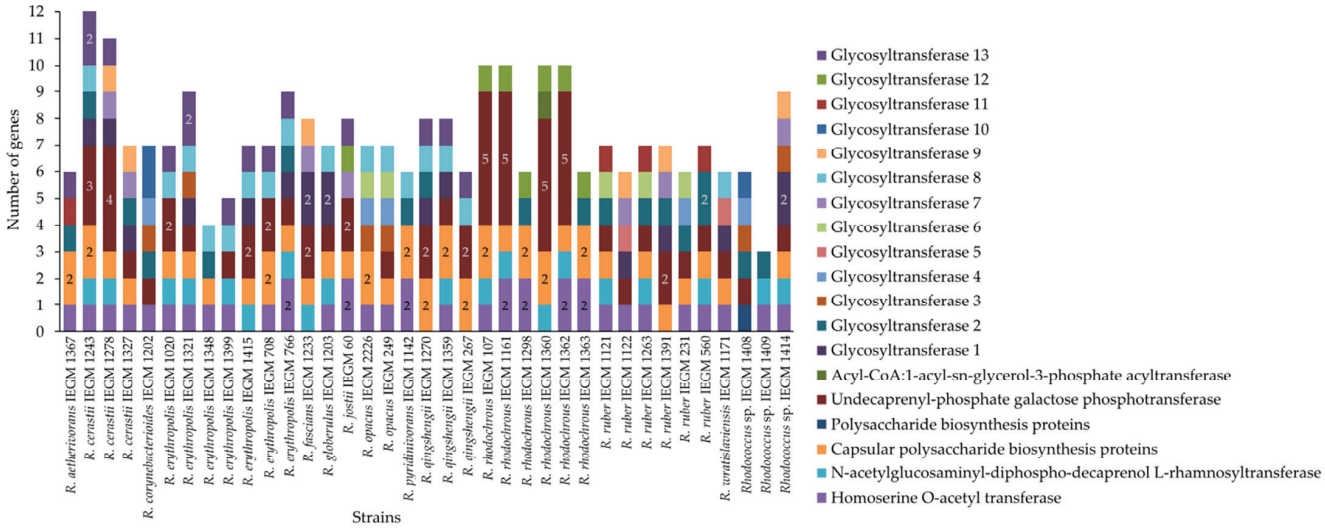

Figure 8. Combinations of genes that code for exopolysaccharide biosynthesis enzymes in *Rhodococcus* spp. If there is more than one copy of a gene in the genome, this is indicated by a number. IDs of glycosyltransferases (e.g., glycosyltransferase 1 and glycosyltransferase 2) correspond to the clades on the phylogenetic tree for genes (Figure 9).

As can be seen from the phylogenetic tree, the glycosyltransferases of *Rhodococcus* were diverse (Figure 9). Thirteen distinct clades could be identified based on bootstrap support. This parameter varied from 38% up to 99%. Most of these clades had a bootstrap support value of 94–99%. Four clades had lower support (38–58%), but these were further divided into low-rank peripheral groups with strong (98–99%) confidence. Therefore, glycosyltransferase-encoding genes within these confident clades were homologous and highly similar, sharing a common origin. However, they had no phylogenetic relationship with glycosyltransferases from other clades. Their divergence appears to have occurred long ago and could not be confirmed using sequence alignments. This can be seen from the very low ($\leq$13%) bootstrap support for nodes on deep branches (Figure 9).

The studied *Rhodococcus* strains harbored glycosyltransferase enzymes from different clades. Only some strains harbored two homologous enzymes from one clade. These strains were *R. cerastii* IEGM 1243 (gtfs 2 and 3), *R. corynebacterioides* IEGM 1202 (gtfs 1 and 2), *R. erythropolis* IEGM 1321 (gtfs 3 and 4), *R. fascians* IEGM 1233 (gtfs 2 and 4), *R. globerulus* IEGM 1203 (gtfs 1 and 2), *R. ruber* IEGM 560 (gtfs 1 and 2), and *Rhodococcus* sp. IEGM 1414 (gtfs 2 and 5). Their enzymes were not identical copies, except for gtfs 1 and 2 in *R. corynebacterioides* IEGM 1202 and gtfs 1 and 2 in *R. ruber* IEGM 560, which were completely identical to each other (Figure S6). Divergence was observed among glycosyltransferases within clades, as evidenced by the low (18–84%) support for some

peripheral groups (Figure 9) and the varying branch lengths on the amino acid similarity tree (Figure S6). The nucleotide sequence tree reflected the evolutionary and historical divergence of *Rhodococcus* species more accurately, although this was not necessarily reflected in divergence of glycosyltransferase functions. The amino acid sequences of glycosyltransferases were less diverse, and gtfs from various clades (particularly clades 8, 11 and 12) formed one large group with high similarity on the amino acid tree. This is the largest (32 gtfs) upper group in Figure S6. Differences in branch length within this group were no greater than 0.1, and at least one copy of the enzyme from this group was found in almost all of the strains studied.

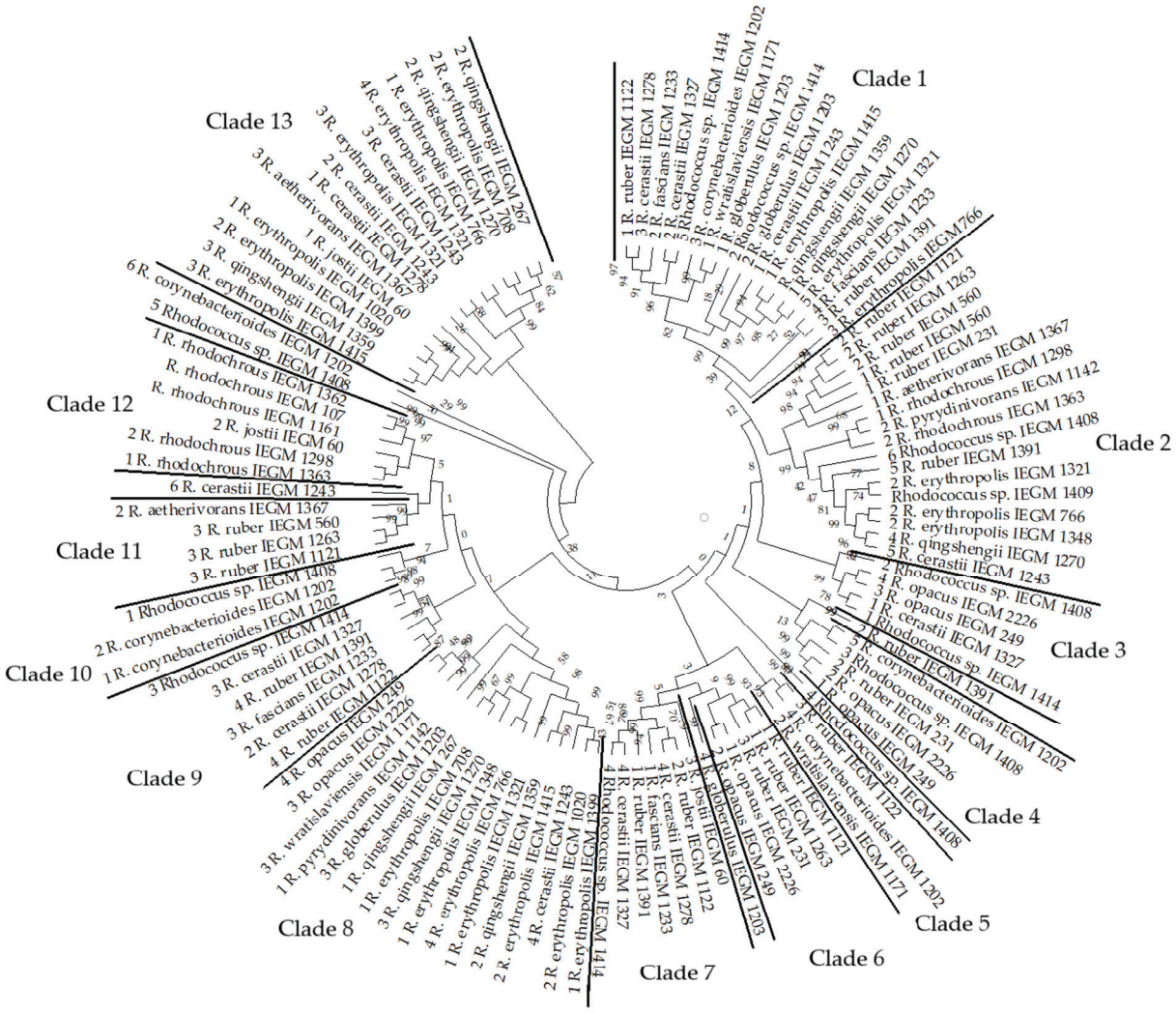

Figure 9. The phylogenetic tree of *Rhodococcus* glycosyltransferases, constructed using aligned nucleotide sequences. The tree was constructed using the neighbor-joining method of MEGA. The percentage of 500 bootstrap replicate support is shown for each node. The tree is rooted at the midpoint. Branch lengths reflect evolutionary distances (similarities) between genes.

Some patterns were observed among the species. Strains of *R. rhodochrous* had fewer glycosyltransferases (1–2), but harbored five undecaprenyl-phosphate galactose phosphotransferases. *R. cerastii* had the greatest number of glycosyltransferases (4–6) (Figures 8 and 9). The glycosyltransferases of *R. erythropolis* and *R. qingshengii* predominated in two large clades, 8 and 13. In other clades, these species were absent or present in lower numbers (Figure 9). The two *R. opacus* strains analyzed were highly similar and had identical sets of four different glycosyltransferases (Figures 9 and S6). *R. corynebacterioides*

IEGM 1202 and *Rhodococcus* sp. IEGM 1408 had unique combinations of glycosyltransferases. Their amino acid sequences were on separate branches and differed significantly from other gtfs (Figure S6).

A statistically significant correlation (R = 0.39, $p < 0.05$) was found between concentrations of EPS carbohydrates and the presence of the glycosyltransferase from clade 6 (C on the protein tree) (Figure 10). This glycosyltransferase was found in five strains, including two *R. opacus* strains (IEGM 249 and IEGM 2226) and three *R. ruber* strains (IEGM 231, IEGM 1121 and IEGM 1263). These strains produced EPS carbohydrates at a level of $\geq$10.5 mg·L^{-1}, which was higher than the median production level (Table 1). The most efficient producer of EPS carbohydrates, *R. ruber* IEGM 231, was among these five strains. Additionally, the IEGM 231 strain and the *R. opacus* strains harbored another glycosyltransferase from a clade 4 on the gene tree (Figure 9) and a distinct clade D on the protein tree (Figure S6). There was a strong correlation (R = 0.47, $p < 0.05$) between concentrations of EPS carbohydrates and the presence of this enzyme (Figure 10). Both glycosyltransferases were phylogenetically related and located in neighboring groups. The evolutionary distances between these glycosyltransferases in *R. opacus* and *R. ruber* were as low as 0.2 (Figures 9 and S6). The presence of other genes, as well as the number of glycosyltransferases, did not influence EPS carbohydrate production by *Rhodococcus* cells. This was evidenced by low correlation coefficients and *p*-values $\geq$ 0.05 (Figure 10).

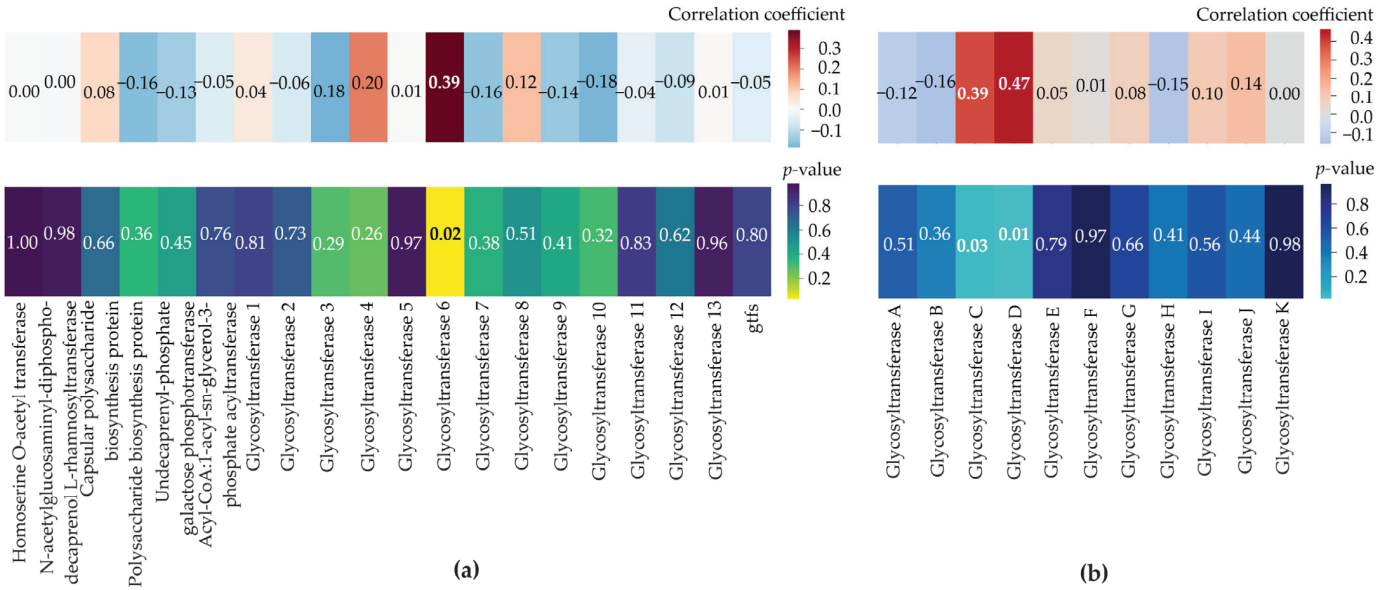

Figure 10. Correlation and *p*-value matrices (heatmaps) showing the dependence of EPS carbohydrate production by *Rhodococcus* cells on the presence and numbers of enzymes participating in exopolysaccharide biosynthesis. The glycosyltransferases are the same as those shown on the gene tree (Figure 9) (**a**) and on the protein tree (Figure S6) (**b**). Pearson correlation coefficients have been calculated and gtfs indicate the total number of glycosyltransferases in a given genome.

No BGCs specific to exopolysaccharide synthesis were found in the *Rhodococcus* genomes (Table 3). Only a cluster containing genes 75% similar to those for ectoine biosynthesis was found in the *R. rhodochrous* IEGM 107 genome. Clusters that are not polysaccharide-related or BGCs with very low ($\leq$27%) similarity were found in genomes of other strains. The annotated BGCs were related to the biosynthesis of osmoprotectants, siderophores, terpenes, antibiotics, alkaloids, and cell wall components (particularly glycopeptidolipids). These BGCs did not harbor specific genes for the biosynthesis of exopolysaccharides, but rather contained genes for the glycosylation of the major product or

its intermediates in the series of biochemical reactions connected with these BGCs (Table 3). Further details about the BGCs identified are summarized in Table S4.

Table 3. Putative exopolysaccharide-related biosynthetic gene clusters in *Rhodococcus* genomes.

Most Similar Known Cluster	Similarity, %	Type	Number of Strains	Strains
ectoine Other	75	ectoine	1	*R. rhodochrous* IEGM 107
coelichelin NRP	27	NRPS	1	*R. erythropolis* IEGM 1321
oxalomycin B NRP + Polyketide	12	NRPS	1	*R. wratislaviensis* IEGM 1171
acarbose Saccharide	7	PKS-like, amglyccycl	5	*R. cerastii* IEGM 1243, *R. erythropolis* IEGM 788, IEGM 1020, IEGM 1321, *R. ruber* IEGM 1391
glycopeptidolipid Saccharide	7	NRPS	1	*R. opacus* IEGM 2226
maduramicin Polyketide + Saccharide	7	NRPS	1	*R. wratislaviensis* IEGM 1171
SF2575 Polyketide: Type II polyketide + Saccharide: Hydrid/tailoring saccharide	6	NRPS, terpene	24	*R. aetherivorans* IEGM 1367, *R. cerastii* IEGM 1243, IEGM 1278, IEGM 1327, *R. corynebacterioides* IEGM 1202, *R. erythropolis* IEGM 708, IEGM 766, IEGM 1020, IEGM 1321, IEGM 1348, *R. globerulus* IEGM 1203, *R. opacus* IEGM 249, IEGM 2226, *R. pyridinivorans* IEGM 1142, *R. rhodochrous* IEGM 107, IEGM 1360, IEGM 1362, *R. ruber* IEGM 231, IEGM 1121, IEGM 1391, *R. wratislaviensis* IEGM 1171, *Rhodococcus* sp. IEGM 1408, IEGM 1409, IEGM 1414
Coumermycin A1 Saccharide: Hydrid/tailoring saccharide + Other: Aminocoumarin	6	T1PKS	1	*R. ruber* IEGM 1391
hydromycin A Saccharide	6	arylpolyene	1	*R. cerastii* IEGM 1278
kendomycin B Polyketide	6	NRPS	1	*R. rhodochrous* IEGM 107
K-252a Alkaloid	5	NRPS-like	1	*R. ruber* IEGM 1391
prejadomycin/rabelomycin/ gaudimycin C/gaudimycin D/UWM6/gaudimycin A Polyketide: Type II polyketide + Saccharide: Hydrid/tailoring saccharide	4	NRPS	1	*R. rhodochrous* IEGM 1362
Iomaiviticin A/Iomaiviticin C/Iomaiviticin D/Iomaiviticin E Polyketide: Type II polyketide + Saccharide: Hydrid/tailoring saccharide	3	NRPS	1	*R. qingshengii* IEGM 1359

Table 3. *Cont.*

Most Similar Known Cluster	Similarity, %	Type	Number of Strains	Strains
EPS-related biosynthetic gene clusters are not found			16	*R. aetherivorans* IEGM 1250, *R. cercidiphylli* IEGM 1184, *R. erythropolis* IEGM 1399, IEGM 1415, *R. fascians* IEGM 1233, *R. jostii* IEGM 60, IEGM 68, *R. opacus* IEGM 262, *R. qingshengii* IEGM 1270, *R. rhodochrous* IEGM 1161, IEGM 1162, IEGM 1298, IEGM 1363, *R. ruber* IEGM 560, IEGM 1122, IEGM 1263

Abbreviations: amglyccycl—aminoglycoside/aminocyclitol biosynthesis, NRP—non-ribosomal peptide, NRPS—non-ribosomal peptide synthetase, and T1PKS—type I polyketide synthase.

4. Discussion

The ability of 43 strains belonging to 14 known *Rhodococcus* species, as well as four *Rhodococcus* sp. isolates, to produce EPS, and the chemical composition of these EPS, were studied. In particular, the characteristics of crude, loosely cell-bound *Rhodococcus* EPS were examined. This fraction was selected for the analysis as it could be obtained routinely using only centrifugation steps. Our primary focus was on the EPS carbohydrates in this fraction. We assumed that the dominant compounds were exopolysaccharides. The *Rhodococcus* strains used produced low amounts of EPS carbohydrates. The median production of these components was 8.9 mg·L^{-1}, with the highest production being 58.2 mg·L^{-1} by the *R. ruber* IEGM 231 cells. This production level was similar to that of exopolysaccharides produced by mono- and dual-species biofilms of sludge bacteria and *Rhodococcus* sp. BH4, which ranged from 8 to 390 mg·L^{-1} [37]. However, other studies have shown that *Rhodococcus* strains can synthesize 10–1000 times more exopolysaccharides, with concentrations ranging from 3.7 to 9.0 g·L^{-1} [18,19]. The low biosynthetic abilities of IEGM strains may be due to underestimated carbohydrate content in the obtained EPS or non-optimal conditions for the EPS production. In studies [18,19], *Rhodococcus* cells were heated at 90 °C for 15–30 min prior to EPS separation. This preliminary procedure released additional EPS that were more tightly bound to the cell envelope. Heating at 60 °C for 30 min was also used to separate EPS from *Rhodococcus* sp. BH4 biofilms [37,38], which may account for the higher amounts of EPS observed in those studies. Fluorescence microscopy photographs of *R. ruber* IEGM 231 biofilms show that polysaccharides are concentrated on the surface of *Rhodococcus* cells rather than in the matrix (Figure 4). It is likely that polysaccharides constituted tightly bound EPS, as well as cell capsules, rather than the loose fraction. The bright coloring of *Rhodococcus* cells in biofilms after staining with Calcolfluor White, which is specific to β-polysaccharides, provides evidence of the widespread presence of these compounds among the *Rhodococcus* EPS carbohydrates.

The growth conditions in this study were optimal for *Rhodococcus* cells. They included a rich growth medium (LB), an optimal growth temperature of 28 °C, and good aeration on an orbital shaker. EPS typically exhibit protective functions and facilitate substrate assimilation [10,13,14,39]. This study confirmed these functions in dense *R. ruber* IEGM 231 biofilms formed in the presence of toxic *n*-hexane and diesel fuel. The release of β-polysaccharides into the extracellular matrix was stimulated in the dense biofilms (Figure 4). Exopolysaccharides were probably not essential for *Rhodococcus* cultures in LB but were necessary to enhance protection of *Rhodococcus* cells from toxic hydrocarbons. The optimization

of growth conditions to enhance EPS production by microbial cells is a separate step. It includes selecting multiple factors, such as pH, temperature, salt concentrations, aeration regimes, growth substrates, and nitrogen sources, as well as their concentrations, supported by mathematical modeling [18,40]. In this study, we compared various *Rhodococcus* strains, with optimization planned as the next step.

The most surprising result was the detection of large amounts of lipids in the EPS. It was already known that lipids were present in large quantities on the surface of the rhodococcal cell envelope [11,12,18,23]. In this study, however, they prevailed over EPS carbohydrates, and this disproportion was incredible: 15–33 times for certain strains. Lipids were not visualized in this study using fluorescent dyes. The *R. ruber* IEGM 231 biofilms were stained with Calcofluor White only, which is specific to β-polysaccharides, to highlight the distribution of these primary compounds of our interest between cells and the biofilm matrix. However, another study [41] showed that the extracellular matrix of *Rhodococcus* biofilms was saturated with lipids and had an intense red coloring after staining with Nile red. This confirmed our findings on the predominance of lipids in loose EPS. The mixture of solvents (chloroform:methanol, 3:1) used for lipid extraction could theoretically result in the extraction not only acylglycerols and free fatty acids, but also complex lipid components, particularly lipopolysaccharides, glycolipids, lipoproteins, and glycopeptidolipids. However, this assumption was not supported by data on the low concentrations of EPS carbohydrates and proteins, which could act as putative ligands for fatty acid residues.

The amounts of proteins in the EPS produced by the studied *Rhodococcus* strains were negligible and were below 1 mg·L^{-1} for most strains (Table 2, Figure 2). However, their notable presence in loose *Rhodococcus* EPS has been reported in other studies [13,21,24]. In study [13], the accumulation of proteins in the EPS produced by *Rhodococcus* sp. p52 was a response to the presence of dibenzofuran. However, rhodococci grew under optimal conditions in this study. Studies [21,24] analyzed concentrated, purified EPS from *R. opacus*, which could result in the overestimation of the true protein concentrations. Fluorescence microscopy images of *Rhodococcus* cell aggregates showed that proteins were localized on the surface of cells and were not present in the extracellular matrix (Figure 5). This was consistent with the results of multi-component staining of *R. rhodochrous* IEGM 1363 biofilms previously conducted. In those biofilms, proteins surrounded cells and were not present in the matrix [41].

The presence of large amounts of lipids and small amounts of proteins in loose EPS produced by the IEGM strains makes these EPS promising emulsifiers for removing hydrocarbons, and they are potentially suitable as food or cosmetic additives. Lipids can enhance the emollient properties of EPS preparations, while the minor presence of proteins reduces the risk of allergies. However, purification and detailed chemical analysis are certainly required, and will be carried out in subsequent studies.

No dependence of EPS production or adhesive activity on species was observed among the studied *Rhodococcus* strains. The strain-specific nature of functional traits is typical of *Rhodococcus* actinomycetes. This has been demonstrated with regard to their adhesive activities towards solid hydrocarbons, their abilities to degrade aromatic compounds, and their potential to accumulate heavy metals [34,42,43]. The reasons could be genetic versatility and redundancy, as well as the high genetic heterogeneity of *Rhodococcus* bacteria within species [44,45]. This has been clearly demonstrated for genes encoding enzymes of the exopolysaccharide biosynthesis. Although species patterns were found for these genes, they tended to be disarranged. Notably, *R. rhodochrous* strains had five undecaprenyl-phosphate galactose phosphotransferases, one glycosyltranferase from the

clade 12, 1–2 capsular polysaccharide biosynthesis proteins, and 1–2 homoserine O-acetyl transferases. However, two *R. rhodochrous* strains lacked undecaprenyl-phosphate galactose phosphotransferase genes, and one *R. rhodochrous* strain lacked homoserine O-acetyl transferase genes (Figure 8). Gene combinations in strains of other species were even more diverse. Notably, glycosyltransferases specific to *R. erythropolis* and *R. qingshengii* were found in clades 8 and 13. The gtf 8 was detected in all strains. The gtf 13 was absent in one strain and characterized by a high diversity in amino acid sequences (it was found in clades G, E, and F on the protein tree). Additionally, various combinations of other gtfs were found in *R. erythropolis* and *R. qingshengii* strains (Figures 8, 9 and S6).

The genetic diversity of *Rhodococcus* bacteria could be related to horizontal gene transfer (HGT) events and the possible localization of genes on megaplasmids [46,47]. *Rhodococcus* strains within one species exhibit significant genomic diversity. Large fragments of DNA can be lost or transferred, and these events are specific to individual strains, rather than species. This has been demonstrated in the case of soluble di-iron monooxygenases (SDIMOs) responsible for propane oxidation in *R. ruber*. It is known that a set of genes (operon) codes for one molecular complex of SDIMO. *R. ruber* has two SDIMO sets, one of which is linked with mobile elements and lost in some strains [6]. Intrinsic gene diversity, in combination with the existence of alleles and differences in the gene expression levels, can lead to significant variations in degrading and biosynthetic activities between strains within one *Rhodococcus* species.

The gene combinations did not influence the production of EPS carbohydrates. Only the presence of two glycosyltransferases specific to *R. opacus* and *R. ruber* enhanced the biosynthesis of EPS carbohydrates (Figure 10). These gtfs could be used in the future to identify and predict promising EPS producers. As previously mentioned, this could be related to differences in gene expression. Another possible reason is the relationship between the genes and amounts of tightly bound EPS, which were not assessed in this study. The combinations of genes may be more important for the chemical composition of the exopolysaccharides produced by *Rhodococcus* bacteria. Genetic variability could explain differences in composition of *Rhodococcus* EPS reported in the literature. In particular, the exopolysaccharides produced by *R. erythropolis* HX-2 are composed of glucose, mannose, galactose, glucuronic acid, and fucose, with mass ratios of 27%, 27%, 25%, 16%, and 5%, respectively [18]. The exopolysaccharide mucoidan produced by another strain of the same species, *R. erythropolis* PR4, was different, consisting of a pentasaccharide repeating unit of two β-D-glucose, one β-D-N-acetylglucosamine, one α-D-glucuronic acid, and one α-L-fucose residue [11]. This highlights the importance of in-depth studies of the genetic mechanisms responsible for EPS biosynthesis in *Rhodococcus* in order to select strains that produce specific EPS. It has also been shown that genetic modifications and the molecular engineering of EPS biosynthesis could present a challenge in *Rhodococcus* cells. No genes involved in (exo)polysaccharide biosynthesis were found to be connected with BGCs in the IEGM strains (Table 3). These genes probably participate in multiple biosynthetic pathways and are responsible not only for the biosynthesis of polysaccharide chains, but also for the glycosylation of various monomeric and polymeric metabolites, e.g., antibiotics, terpenes, amino acids, nucleotides, lipids, proteins, etc. Their modification or regulation of their expression levels can affect cell physiology in unpredictable ways.

The lack of association between putative polysaccharide biosynthetic genes and BGCs suggests that other regulatory mechanisms may govern exopolysaccharide biosynthesis in *Rhodococcus*. Analyzing the surrounding area of the studied biosynthetic genes revealed the presence of a few genes coded for transcriptional regulators. These belong to the AraC, PhoU, XRE (xenobiotic response element), and OmpR families. The AraC

(https://www.ncbi.nlm.nih.gov/Structure/sparcle/archview.html?archid=13263893, last accessed 8 July 2025), XRE (https://www.ebi.ac.uk/interpro/entry/cdd/CD02209/, last accessed 8 July 2025), and OmpR (https://www.uniprot.org/uniprotkb/P0AA18/entry, last accessed 8 July 2025) participate in the response of bacterial cells to stress, particularly the presence of xenobiotics in the case of XRE and osmotic stress in the case of OmpR. AraC is responsible for the metabolism of L-arabinose and the control of the degradation of several sugars. PhoU regulates the metabolism of phosphorus [48], which, in the form of phosphates, is required for the transfer of glycosyl residues. We hypothesize that these transcriptional regulators can control the expression of (exo)polysaccharide biosynthetic genes in *Rhodococcus*. Additionally, their proximity to the studied genes, which mainly encode glycosyltransferases, capsular polysaccharide biosynthesis proteins, and undecaprenyl-phosphate galactose phosphotransferases, suggest a role for EPS in protecting *Rhodococcus* cells from toxic hydrocarbons. For example, OmpR is part of a two-component sensor regulatory system. This system is responsible for the adaptation of bacteria to osmotic stress and reacts to the changes in the cell microenvironment. It can sense the disruptive effects on the cell wall and cytoplasmic membrane caused by toxicants such as *n*-hexane or diesel fuel. Further, it can impact the expression of genes involved in glycosylation and the transfer of glycosylated substances. This can result in the release of EPS components into the extracellular matrix, similar to the release of β-polysaccharides in the *R. ruber* IEGM 231 biofilms.

Other genes in proximity to the putative genes coded for (exo)polysaccharide biosynthesis in *Rhodococcus* are connected with various processes. These genes encode transporters and enzymes that are likely to be involved in oxidation/degradation (oxidoreductases), resistance (e.g., chloramphenicol acetyltransferase), and the metabolism of lipids, terpens, steroids, carbohydrates, amino acids, and nucleotides (various transferases, synthetases, dehydrogenases, dehydratases, etc.). Many genes are annotated as hypothetical proteins. This supports the hypothesis that EPS biosynthesis genes in *Rhodococcus* are involved in diverse metabolic processes and are not specific to the biosynthesis of (exo)polysaccharides. Genes coded for capsular polysaccharide biosynthesis proteins are always located next to any glycosyltransferase. Genes encoding undecaprenyl-phosphate galactose phosphotransferases are located in one sector, with one or a few glycosyltransferases. These genes may be in direct proximity or separated by several other genes. We also hypothesize that these gtfs transfer galactose. The revealed gene distribution provides evidence for their coupling and involvement in one chain of metabolic reactions. Mobile elements were not detected in genome segments with polysaccharide biosynthesis genes. It appears that the diversity of rhodococcal gtfs is the result of evolutionary changes, e.g., divergence and convergence.

Controversial results were obtained regarding the role of EPS in *Rhodococcus* cell adhesion and biofilm growth. On the one hand, EPS were found to be important in protecting rhodococci from toxic hydrocarbons. This was evident from the increased biofilm density and more pronounced extracellular matrix, as well as from the formation of polysaccharide-wrapped cells, and the release of exo-β-polysaccharides into the biofilm matrix when exposed to *n*-hexane and diesel fuel (Figures 3 and 4). These reactions seem to be protective rather than facilitating hydrocarbon utilization. No differences were observed in biofilm density on LB agar, either with or without hydrocarbons. However, β-polysaccharides were released into the matrix of biofilms grown on LB in the presence of toxic *n*-hexane and diesel fuel. β-Polysaccharides were apparently required for cell protection, but they did not induce hydrocarbon assimilation. The release of β-polysaccharides did not occur in the presence of non-toxic *n*-hexadecane in either medium, as no enhancement of matrix buffer functions was apparently required. However, some involvement of EPS in the utilization

of hydrocarbons cannot be ruled out. A synergetic effect was probably observed on agar K in the presence of *n*-hexane and diesel fuel, on which rhodococcal cells formed the 3–8-fold denser biofilms compared to the control and the 2–5-fold denser biofilms compared to *n*-hexadecane. The resistant cells were apparently able to effectively assimilate *n*-hexane and diesel fuel. This may be related to the accumulation of hydrocarbon molecules in the matrix and the optimized rate at which they were transported to the cells.

On the other hand, the adhesion of *Rhodococcus* cells to polystyrene did not depend on the production of EPS carbohydrates; the adhesion forces of *Rhodococcus* EPS towards glass and the AFM cantilever were weaker than those in the control measurements (without EPS), and cell aggregation was detected in strains with a low production of EPS carbohydrates. The latter was not surprising. In study [12], R-type cells of *R. ruber* TH3 produced low amounts of EPS and formed aggregates, whereas S-type cells produced large amounts of EPS and remained suspended. The *R. ruber* YYL cells, which had lost their ability to synthesize a capsule, aggregated easily. This can be explained by the presence of many negatively charged -OH and -COOH groups in the composition of the EPS polysaccharides, resulting in cell retraction [16]. Apparently, EPS were not key factors in the adhesion of *Rhodococcus* cells to solid surfaces in the first step of the biofilm formation. However, they (particularly EPS polysaccharides) were important for biofilm growth and tolerance to toxicants. An increase in polysaccharide amounts in the extracellular matrix has been observed in microbial biofilms in pipes treated with chlorine [15], as well as in quinoline-degrading biofilms in a membrane aerated biofilm reactor [14]. Cultivating *Rhodococcus* bacteria in the presence of pollutants can be an effective and economical way to increase the production of loose EPS by these microorganisms.

The EPS produced by *Rhodococcus* cells contains a high proportion of lipids. These lipids can play a significant role in the assimilation of hydrocarbons by rhodococcal cells. Lipids attract hydrocarbons, which are trapped and dissolved in the lipid-rich matrix. This probably facilitates their diffusion and transport to the cells. A depository for hydrocarbon molecules is also formed, where the rate of hydrocarbon assimilation can be regulated to be optimal. The participation of lipids in promoting hydrocarbon assimilation applies to both the non-toxic *n*-hexadecane and the toxic *n*-hexane and diesel fuel. However, an increase in biofilm density, the formation of a more pronounced extracellular matrix, and the release of polysaccharides were only observed in the presence of *n*-hexane and diesel fuel. In this case, the relatively hydrophobic, lipid-rich matrix is 'diluted' by hydrophilic β-polysaccharides, resulting in the formation of a buffer zone with an optimal hydrophilic–lipophilic balance. The increased extracellular matrix acts as a thick barrier that prevents the rapid infusion of toxic hydrocarbons. Small molecules of *n*-hexane and small diesel fuel compound slowly move within the porous, viscous, multi-channel β-polysaccharide-saturated matrix. Such a matrix is neither required nor favorable in the case of *n*-hexadecane.

Lipids are thought to enable bacterial adhesion. As hydrophobic substances, these compounds reduce the total surface energy and facilitate the approach of cells to the support for further multi-point adhesion [49]. Unfortunately, the adhesion potential of EPS lipids could not be confirmed by direct measurements of adhesion forces using AFM. This method cannot distinguish between the EPS components (lipids or carbohydrates) that facilitate or prevent *Rhodococcus* cells adhesion to polystyrene. The adhesion forces were uniformly distributed along the EPS layer on the glass surface. Some highly adhesive spots with adhesion forces ranging from 22 to 116 nN were present on this layer, but their chemical composition was unknown (Figures 6 and S5). Contact of the EPS-modified AFM cantilever with either the lipid or carbohydrate component could explain the bimodal distribution of F_a values (Figure 7). The adhesion force of the EPS was lower than that of

the unmodified cover glass. This was consistent with the results of the adhesive activity tests towards polystyrene. The adhesion of rhodococci was independent of the production of EPS carbohydrates and lipids by the cells. Apparently, EPS are not involved in the adhesion process of the studied IEGM strains to both relatively hydrophilic (cover glass and silicon cantilever) and relatively hydrophobic (polystyrene) surfaces. Lipids and polysaccharides were apparently proportionally mixed with each other within the EPS. Consequently, lipids had no significant effect on the adhesion of *R. ruber* IEGM 231 cells, which produce carbohydrate-rich EPS (Table 1, Figure 1a). Other factors must therefore be responsible for the adhesion of *Rhodococcus* cells to solid surfaces, such as the roughness of interacting surfaces and the presence of specific cytoadhesive structures on the cell surface [42]. Additionally, the manner in which the EPS cover the cell surfaces and form adhesive chains, as observed with the EPS produced by *Rhodococcus* sp. RC291 in the study [36], remains unclear.

5. Conclusions

For the first time, a large number of *Rhodococcus* strains belonging to well-known and ecologically significant species (*R. erythropolis*, *R. fascians*, *R. globerulus*, *R. jostii*, *R. opacus*, *R. rhodochrous* and *R. ruber*) and to less common species (*R. aetherivorans*, *R. cerastii*, *R. cercidiphylli*, *R. corynebacterioides*, *R. pyridinovorans*, *R. qingshengii* and *R. wratislaviensis*), as well as several unidentified *Rhodococcus* sp. isolates, were screened for their production of major EPS biopolymers, including polysaccharides, lipids, proteins, and nucleic acids. Loosely cell-bound EPS were characterized. The presence of large amounts of lipids, prevailing over or similar to the carbohydrate content, and low levels of proteins and nucleic acids in this fraction were detected. This chemical profile was consistent across all the *Rhodococcus* strains studied. Previous studies have mainly focused on the total fraction of loosely (separated by centrifugation only) and tightly (separated after heating) bound EPS, and this study properly characterized the loose fraction of *Rhodococcus* EPS. The chemical composition is important for estimating the biotechnological potential of EPS. Notably, *R. qingshengii* QDR4-2 produced non-acidic exopolysaccharides saturated with mannose residues, enhancing the antioxidant properties of these EPS [19]. The large amounts of lipids indicate the potential applications of crude EPS produced by the IEGM strains in the fields of hydrocarbon emulsification, bioremediation, and the development of emollient additives.

Another important finding was the strain-specific nature of the chemical composition and production of EPS. This relates to the genetic diversity of *Rhodococcus* strains within species. Further detailed analysis of EPS produced by individual strains is required, as is the identification of genes that code for EPS biosynthesis enzymes and an array of strains-producers for specific purposes. Future work will focus on purifying *Rhodococcus* EPS, identifying specific monomers, and screening functional characteristics. The aim is also to optimize growth conditions to increase the EPS yield, scale up production, and develop biotechnological products composed of EPS produced by *Rhodococcus* strains from the IEGM Collection.

Supplementary Materials: The following supporting information can be downloaded at: https://www.mdpi.com/article/10.3390/polym17141912/s1, Table S1: *Rhodococcus* strains used in this study; Figure S1: A calibration curve showing the relationship between the A_{490nm} absorbance and the concentration of D-glucose in the phenol-sulphuric acid reaction, used for the quantitative analysis of carbohydrates; Figure S2: A calibration curve showing the relationship between the A_{595nm} absorbance and the concentration of bovine serum albumin in Bradford analysis; Figure S3: A

calibration curve showing the relationship; Table S2: Adhesive activities of *Rhodococcus* spp. towards polystyrene; Figure S4: Topographic maps of an unmodified (**a**) and an EPS-coated (**b**) cover glass surface, scanned with an unmodified cantilever, and an unmodified cover glass surface scanned with a cantilever coated with the EPS (**c**). EPS produced by *R. ruber* IEGM 231 were used. The slope of the topographic maps was eliminated using the Planefit function; Figure S5: Adhesion force maps and distribution of F_a values for an unmodified (**a**) and an EPS-coated (**b**) cover glass surface, scanned with an unmodified cantilever, and for an unmodified cover glass surface, scanned with a cantilever coated with the EPS (**c**). EPS produced by *R. ruber* IEGM 231 were used; Table S3: Annotated genes and enzymes that are likely to be involved in the biosynthesis of exopolysaccharides in *Rhodococcus*; Figure S6: Phylogenetic tree of *Rhodococcus* glycosyltransferases constructed using aligned amino acid sequences. It was created using the neighbor-joining method in MEGA. The tree is rooted at the midpoint. Branch lengths reflect similarities between proteins; Table S4: Biosynthetic gene clusters probably related to the synthesis of exopolysaccharides in *Rhodococcus* spp.

Author Contributions: Conceptualization, I.I.; methodology, I.I., M.K. and A.K.; software, A.K., D.N. and V.L.; validation, A.K., D.N. and V.L.; formal analysis, A.K., D.N. and V.L.; investigation, A.K., D.N. and V.L.; resources, I.I. and M.K.; data curation, A.K.; writing—original draft preparation, A.K. and D.N.; writing—review and editing, I.I. and M.K.; visualization, A.K. and D.N.; supervision, I.I. and A.K.; project administration, I.I. and A.K.; funding acquisition, I.I. and M.K. All authors have read and agreed to the published version of the manuscript.

Funding: Physiological and biochemical studies of the lipid-rich EPS produced by the IEGM strains, as well as analysis of bacterial genomes, were funded by the Ministry of Science and Higher Education of the Russian Federation, state task 124020500028-4. Studies on cell adhesion and biofilm and aggregate formation, as well as EPS carbohydrate production, were funded by the Ministry of Science and Higher Education of the Russian Federation, state task 122031400671-1. Visualization of bacterial cells was funded by the Ministry of Science and Higher Education of the Russian Federation, state task FSNF-2025-0013.

Institutional Review Board Statement: Not applicable.

Data Availability Statement: The raw data supporting the conclusions of this article will be made available by the authors upon request.

Acknowledgments: This study was carried out using equipment from the Core Facilities Centers "Regional Specialised Collection of Alkanotrophic Microorganisms" and "Research of Materials and Matter" at the Perm Federal Research Center of the Ural Branch of the Russian Academy of Sciences.

Conflicts of Interest: The authors declare no conflicts of interest.

References

1. Decho, A.W.; Gutierrez, T. Microbial extracellular polymeric substances (EPS) in ocean systems. *Front. Microbiol.* **2017**, *8*, 922. [CrossRef]
2. Costa, O.Y.A.; Raaijmakers, J.M.; Kuramae, E.E. Microbial extracellular polymeric substances: Ecological function and impact on soil aggregation. *Front. Microbiol.* **2018**, *9*, 1636. [CrossRef]
3. Jeong, J.; Kim, Y.; Hu, Y.; Jung, S. Bacterial succinoglycans: Structure, physical properties, and applications. *Polymers* **2022**, *14*, 276. [CrossRef]
4. Wei, X.; Chen, Z.; Liu, A.; Yang, L.; Xu, Y.; Cao, M.; He, N. Advanced strategies for metabolic engineering of *Bacillus* to produce extracellular polymeric substances. *Biotechnol. Adv.* **2023**, *67*, 108199. [CrossRef]
5. Ivshina, I.B.; Kuyukina, M.S.; Krivoruchko, A.V. Extremotolerant *Rhodococcus* as an important resource for environmental biotechnology. In *Actinomycetes in Marine and Extreme Environments: Unexhausted Sources for Microbial Biotechnology*; Kurtböke, I., Ed.; Science Publishers, CRC Press: Boca Raton, FL, USA, 2024; pp. 209–246. [CrossRef]
6. Ivshina, I.B.; Kuyukina, M.S.; Krivoruchko, A.V.; Tyumina, E.A. The *Rhodococcus ruber* actinomycetes, key and universal biooxidizers of C_2-C_4 gaseous alkanes. *Microbiology* **2025**, *94*, 145–171. [CrossRef]

7. More, T.T.; Yadav, J.S.S.; Yan, S.; Tyagi, R.D.; Surampalli, R.Y. Extracellular polymeric substances of bacteria and their potential environmental applications. *J. Environ. Manage.* **2014**, *144*, 1–25. [CrossRef]
8. Ahuja, V.; Bhatt, A.K.; Banu, J.R.; Kumar, V.; Kumar, G.; Yang, Y.H.; Bhatia, S.K. Microbial exopolysaccharide composites in biomedicine and healthcare: Trends and advances. *Polymers* **2023**, *15*, 1801. [CrossRef]
9. Vandana; Priyadarshanee, M.; Das, S. Bacterial extracellular polymeric substances: Biosynthesis and interaction with environmental pollutants. *Chemosphere* **2023**, *332*, 138876. [CrossRef]
10. Iwabuchi, N.; Sunairi, M.; Anzai, H.; Morisaki, H.; Nakajima, M. Relationships among colony morphotypes, cell-surface properties and bacterial adhesion to substrata in *Rhodococcus*. *Colloids Surf. B Biointerfaces* **2003**, *30*, 51–60. [CrossRef]
11. Urai, M.; Yoshizaki, H.; Anzai, H.; Ogihara, J.; Iwabuchi, N.; Harayama, S.; Sunairi, M.; Nakajima, M. Structural analysis of mucoidan, an acidic extracellular polysaccharide produced by a pristane-assimilating marine bacterium, *Rhodococcus erythropolis* PR4. *Carbohydr. Res.* **2007**, *342*, 927–932. [CrossRef]
12. Jiao, S.; Chen, J.; Yu, H.; Shen, Z. Tuning and elucidation of the colony dimorphism in *Rhodococcus ruber* associated with cell flocculation in large scale fermentation. *Appl. Microbiol. Biotechnol.* **2017**, *101*, 6321–6332. [CrossRef]
13. Chen, Y.; Wei, Q.; Wang, X.; Wu, Y.; Fu, C.; Wang, X.; Xu, H.; Li, L. Characterizing the contaminant-adhesion of a dibenzofuran degrader *Rhodococcus* sp. *Microorganisms* **2025**, *13*, 93. [CrossRef]
14. Tian, H.; Li, Y.; Chen, H.; Zhang, J.; Hui, M.; Xu, X.; Su, Q.; Smets, B.F. Aerobic biodegradation of quinoline under denitrifying conditions in membrane-aerated biofilm reactor. *Environ. Pollut.* **2023**, *326*, 121507. [CrossRef]
15. Zheng, S.; Lin, T.; Chen, H.; Zhang, X.; Jiang, F. Impact of changes in biofilm composition response following chlorine and chloramine disinfection on nitrogenous disinfection byproduct formation and toxicity risk in drinking water distribution systems. *Water Res.* **2024**, *253*, 121331. [CrossRef]
16. Huang, H.; Liu, Z.; Qiu, Y.; Wang, X.; Wang, H.; Xiao, H.; Lu, Z. Efficient electrotransformation of *Rhodococcus ruber* YYL with abundant extracellular polymeric substances via a cell wall-weakening strategy. *FEMS Microbiol. Lett.* **2021**, *368*, fnab049. [CrossRef]
17. Urai, M.; Anzai, H.; Iwabuchi, N.; Sunairi, M.; Nakajima, M. A novel viscous extracellular polysaccharide containing fatty acids from *Rhodococcus rhodochrous* ATCC 53968. *Actinomycetologica* **2004**, *18*, 15–17. [CrossRef]
18. Hu, X.; Li, D.; Qiao, Y.; Wang, X.; Zhang, Q.; Zhao, W.; Huang, L. Purification, characterization and anticancer activities of exopolysaccharide produced by *Rhodococcus erythropolis* HX-2. *Int. J. Biol. Macromol.* **2020**, *145*, 646–654. [CrossRef]
19. Li, F.; Hu, X.; Li, J.; Sun, X.; Luo, C.; Zhang, X.; Li, H.; Lu, J.; Li, Y.; Bao, M. Purification, structural characterization, antioxidant and emulsifying capabilities of exopolysaccharide produced by *Rhodococcus qingshengii* QDR4-2. *J. Polym. Environ.* **2023**, *31*, 64–80. [CrossRef]
20. Behera, S.; Das, S. Potential and prospects of Actinobacteria in the bioremediation of environmental pollutants: Cellular mechanisms and genetic regulations. *Microbiol. Res.* **2023**, *273*, 127399. [CrossRef]
21. Szcześ, A.; Czemierska, M.; Jarosz-Wilkołazka, A. calcium carbonate formation on mica supported extracellular polymeric substance produced by *Rhodococcus opacus*. *J. Solid State Chem.* **2016**, *242*, 212–221. [CrossRef]
22. Santiso-Bellón, C.; Randazzo, W.; Carmona-Vicente, N.; Peña-Gil, N.; Cárcamo-Calvo, R.; Lopez-Navarro, S.; Navarro-Lleó, N.; Yebra, M.J.; Monedero, V.; Buesa, J.; et al. *Rhodococcus* spp. interacts with human norovirus in clinical samples and impairs its replication on human intestinal enteroids. *Gut Microbes* **2025**, *17*, 2469716. [CrossRef]
23. Sutcliffe, I.C.; Brown, A.K.; Dover, L.G. The rhodococcal cell envelope: Composition, organisation and biosynthesis. In *Biology of Rhodococcus*; Alvarez, H.M., Ed.; Springer: Berlin/Heidelberg, Germany, 2010; pp. 29–71. [CrossRef]
24. Czemierska, M.; Szcześ, A.; Pawlik, A.; Wiater, A.; Jarosz-Wilkołazka, A. Production and characterisation of exopolymer from *Rhodococcus opacus*. *Biochem. Eng. J.* **2016**, *112*, 143–152. [CrossRef]
25. Khan, S.T.; Ahamed, M.; Alhadlaq, H.A.; Musarrat, J.; Al-Khedhairy, A. Comparative effectiveness of $NiCl_2$, Ni- and NiO-NPs in controlling oral bacterial growth and biofilm formation on oral surfaces. *Arch. Oral Biol.* **2013**, *58*, 1804–1811. [CrossRef]
26. Zhang, X.; Yan, S.; Tyagi, R.D.; Surampalli, R.Y.; Valéro, J.R. Wastewater sludge as raw material for microbial oils production. *Appl. Energy* **2014**, *135*, 192–201. [CrossRef]
27. Huber, B.; Riedel, K.; Hentzer, M.; Heydorn, A.; Gotschlich, A.; Givskov, M.; Molin, S.; Eberl, L. The *cep* quorum-sensing system of *Burkholderia cepacia* H111 controls biofilm formation and swarming motility. *Microbiology* **2001**, *147*, 2517–2528. [CrossRef]
28. Krivoruchko, A.V.; Iziumova, A.Y.; Kuyukina, M.S.; Plekhov, O.A.; Naimark, O.B.; Ivshina, I.B. Adhesion of *Rhodococcus ruber* IEGM 342 to polystyrene studied using contact and non-contact temperature measurement techniques. *Appl. Microbiol. Biotechnol.* **2018**, *102*, 8525–8536. [CrossRef]
29. Tatusova, T.; Dicuccio, M.; Badretdin, A.; Chetvernin, V.; Nawrocki, E.P.; Zaslavsky, L.; Lomsadze, A.; Pruitt, K.D.; Borodovsky, M.; Ostell, J. NCBI Prokaryotic Genome Annotation Pipeline. *Nucleic Acids Res.* **2016**, *44*, 6614–6624. [CrossRef]

30. Overbeek, R.; Olson, R.; Pusch, G.D.; Olsen, G.J.; Davis, J.J.; Disz, T.; Edwards, R.A.; Gerdes, S.; Parrello, B.; Shukla, M.; et al. The SEED and the Rapid Annotation of Microbial Genomes Using Subsystems Technology (RAST). *Nucleic Acids Res.* **2014**, *42*, 206–214. [CrossRef]
31. Brettin, T.; Davis, J.J.; Disz, T.; Edwards, R.A.; Gerdes, S.; Olsen, G.J.; Olson, R.; Overbeek, R.; Parrello, B.; Pusch, G.D.; et al. RASTtk: A modular and extensible implementation of the RAST algorithm for building custom annotation pipelines and annotating batches of genomes. *Sci. Rep.* **2015**, *5*, 8365. [CrossRef]
32. Kumar, S.; Stecher, G.; Suleski, M.; Sanderford, M.; Sharma, S.; Tamura, K. MEGA12: Molecular Evolutionary Genetic Analysis version 12 for adaptive and green computing. *Mol. Biol. Evol.* **2024**, *41*, msae263. [CrossRef]
33. Blin, K.; Shaw, S.; Augustijn, H.E.; Reitz, Z.L.; Biermann, F.; Alanjary, M.; Fetter, A.; Terlouw, B.R.; Metcalf, W.W.; Helfrich, E.J.N.; et al. AntiSMASH 7.0: New and improved predictions for detection, regulation, chemical structures and visualisation. *Nucleic Acids Res.* **2023**, *51*, W46–W50. [CrossRef] [PubMed]
34. Krivoruchko, A.; Kuyukina, M.; Peshkur, T.; Cunningham, C.J.; Ivshina, I. *Rhodococcus* strains from the Specialized Collection of Alkanotrophs for biodegradation of aromatic compounds. *Molecules* **2023**, *28*, 2393. [CrossRef]
35. Ivshina, I.; Kuyukina, M.; Krivoruchko, A.; Elkin, A.; Peshkur, T.; Cunningham, C.J. Resistant *Rhodococcus* for biodegradation of diesel fuel at high concentration and low temperature. *Microorganisms* **2024**, *12*, 2605. [CrossRef]
36. Pen, Y.; Zhang, Z.J.; Morales-García, A.L.; Mears, M.; Tarmey, D.S.; Edyvean, R.G.; Banwart, S.A.; Geoghegan, M. Effect of extracellular polymeric substances on the mechanical properties of *Rhodococcus*. *Biochim. Biophys. Acta-Biomembr.* **2015**, *1848*, 518–526. [CrossRef]
37. Maddela, N.R.; Meng, F. Discrepant roles of a quorum quenching bacterium (*Rhodococcus* sp. BH4) in growing dual-species biofilms. *Sci. Total Environ.* **2020**, *713*, 136402. [CrossRef]
38. Maddela, N.R.; Zhou, Z.; Yu, Z.; Zhao, S.; Meng, F. Functional determinants of extracellular polymeric substances in membrane biofouling: Experimental evidence from pure-cultured sludge bacteria. *Appl. Environ. Microbiol.* **2018**, *84*, e00756-18. [CrossRef]
39. Pátek, M.; Grulich, M.; Nešvera, J. Stress response in *Rhodococcus* strains. *Biotechnol. Adv.* **2021**, *53*, 107698. [CrossRef]
40. El-Shanshoury, A.E.-R.R.; Allam, N.G.; Basiouny, E.M.; Azab, M.M. Optimization of exopolysaccharide production by soil actinobacterium *Streptomyces plicatus* under submerged culture conditions. *Egypt. J. Exp. Biol.* **2022**, *18*, 151–160. [CrossRef]
41. Kuyukina, M.S.; Bayandina, E.A.; Kostrikina, N.A.; Sorokin, V.V.; Mulyukin, A.L.; Ivshina, I.B. Adaptations of *Rhodococcus rhodochrous* biofilms to oxidative stress induced by copper(II) oxide nanoparticles. *Langmuir* **2025**, *41*, 1356–1367. [CrossRef]
42. Ivshina, I.B.; Krivoruchko, A.V.; Kuyukina, M.S.; Peshkur, T.A.; Cunningham, C.J. Adhesion of *Rhodococcus* bacteria to solid hydrocarbons and enhanced biodegradation of these compounds. *Sci. Rep.* **2022**, *12*, 21559. [CrossRef]
43. Ivshina, I.B.; Kuyukina, M.S.; Litvinenko, L.V.; Golysheva, A.A.; Kostrikina, N.A.; Sorokin, V.V.; Mulyukin, A.L. Bioaccumulation of molybdate ions by alkanotrophic *Rhodococcus* leads to significant alterations in cellular ultrastructure and physiology. *Ecotoxicol. Environ. Saf.* **2024**, *274*, 116190. [CrossRef] [PubMed]
44. Cappelletti, M.; Zampolii, J.; Zannoni, D. Genomics of *Rhodococcus*. In *Biology of Rhodococcus, Microbiology Monographs 16*; Alvarez, H.M., Ed.; Springer Nature: Cham, Switzerland, 2019; pp. 23–60. [CrossRef]
45. Garrido-Sanz, D.; Redondo-Nieto, M.; Martín, M.; Rivilla, R. Comparative genomics of the *Rhodococcus* genus shows wide distribution of biodegradation traits. *Microorganisms* **2020**, *8*, 774. [CrossRef] [PubMed]
46. Zou, B.; Huang, Y.; Zhang, P.-P.; Ding, X.-M.; Op den Camp, H.J.M.; Quan, Z.-X. Horizontal gene transfer of genes encoding copper-containing membrane-bound monooxygenase (CuMMO) and soluble di-iron monooxygenase (SDIMO) in ethane- and propane-oxidizing *Rhodococcus* bacteria. *Appl. Environ. Microbiol.* **2021**, *87*, e00227-21. [CrossRef] [PubMed]
47. Ferrari, E.; Di Benedetto, G.; Firrincieli, A.; Presentato, A.; Frascari, D.; Cappelletti, M. Unravelling the role of the group 6 soluble di-iron monooxygenase (SDIMO) SmoABCD in alkane metabolism and chlorinated alkane degradation. *Microb. Biotechnol.* **2024**, *17*, e14453. [CrossRef]
48. Baek, S.; Lee, E.-J. PhoU: A multifaceted regulator in microbial signaling and homeostasis. *Curr. Opin. Microbiol.* **2024**, *77*, 102401. [CrossRef]
49. Carniello, V.; Peterson, B.W.; van der Mei, H.C.; Busscher, H.J. Physico-chemistry from initial bacterial adhesion to surface-programmed biofilm growth. *Adv. Colloid Interface Sci.* **2018**, *261*, 1–14. [CrossRef]

polymers

MDPI

Article

Synthesis and Characterization of PLA/Biochar Bio-Composites Containing Different Biochar Types and Content

Katerina Papadopoulou [1], Panagiotis A. Klonos [1,2], Apostolos Kyritsis [2], Evangelia Tarani [3], Konstantinos Chrissafis [3], Ondrej Mašek [4], Konstantinos Tsachouridis [5], Antonios D. Anastasiou [5] and Dimitrios N. Bikiaris [1,*]

[1] Laboratory of Polymer Chemistry and Technology, Department of Chemistry, Aristotle University of Thessaloniki, 54124 Thessaloniki, Greece; katerina_1991papa@hotmail.com (K.P.); pklonos@central.ntua.gr (P.A.K.)
[2] Department of Physics, National Technical University of Athens, Zografou Campus, 15780 Athens, Greece; akyrits@central.ntua.gr
[3] Laboratory of Advanced Materials and Devices, Department of Physics, Aristotle University of Thessaloniki, GR-54124 Thessaloniki, Greece; etarani@physics.auth.gr (E.T.); hrisafis@physics.auth.gr (K.C.)
[4] UK Biochar Research Centre, School of GeoSciences, University of Edinburgh, Alexander Crum Brown Road, Edinburgh EH9 3FF, UK; ondrej.masek@ed.ac.uk
[5] Department of Chemical Engineering, University of Manchester, Manchester M1 9PL, UK; konstantinos.tsachouridis@manchester.ac.uk (K.T.); antonios.anastasiou@manchester.ac.uk (A.D.A.)
* Correspondence: dbic@chem.auth.gr; Tel.: +30-231-099-7812

Abstract: A series of poly(lactic acid) (PLA)/biochar (BC) bio-composites filled with low amounts (1–5 wt%) of BC were prepared and characterized. The synthesis involved the in situ ring-opening polymerization (ROP) of lactide in the presence of two different types of BC named SWP550 and SWP700, having been produced by pyrolysis of softwood pellets at two different temperatures, 550 and 700 °C, respectively. The bio-composites were characterized by complementary techniques. The successful synthesis of PLA and PLA/BC bio-composites was directly demonstrated by the formation of new bonds, most probably between PLA and BC. Indirect evidence for that was obtained by the systematic molar mass reduction in the presence of BC. BC was found by transmission electron microscopy (TEM) micrographs to be well dispersed at the nanosize level, indicating that in situ polymerization is a technique quite efficient for producing bio-composites with finely dispersed BC additive. The molecular dynamics mapping is performed here via dielectric spectroscopy, moreover, for the first time in these PLA/BC systems. The strong PLA/BC interactions (due to the grafting) led to a systematic deceleration of segmental mobility (elevation of the T_g) in the bio-composites despite the opposite effect expected by the decrease in molar mass with the BC content increasing. In addition, the same interactions and chain-length reduction are responsible for the slight suppression of the PLA's crystallizability. The effects are slightly stronger for SWP700 as compared to SWP550. The crystal structure is rather similar between the unfilled matrix and the bio-composites, whereas, based on the overall data, the semicrystalline morphology is expected to be tighter in the bio-composites. The thermal stability and decomposition kinetics were also thoroughly studied. All materials exhibit good resistance to thermal degradation. Additionally, the mechanical properties of bio-composites were evaluated by tensile testing and found slightly enhanced at low biochar contents and decreasing thereafter due to the low molecular weight of bio-composites with the larger BC contents.

Keywords: poly(lactic acid); biochar; bio-composites; in situ polymerization; mechanical properties; segmental mobility; thermal properties; enzymatic hydrolysis

1. Introduction

Global plastics production was estimated at 150 million metric tons in 2023. This is expected to rise in the following decades, reaching approximately 590 million metric tons by 2050 [1]. Therefore, the establishment of a bio-economy, as well as a circular economy, is related, among others, to the development of biobased and biodegradable plastics, i.e., alternative plastics made of renewable resources and eco-friendly in order to contribute towards the progressive independence from fossil-derived sources.

The urge to replace petroleum-based polymers has expectedly increased the interest in eco-friendly and sustainable materials. Poly(lactic acid) (PLA) is a very highly promising material for a wide range of applications, such as in medicine, packaging, agriculture, electronics, automotive, etc. [2–4], due to its biobased origin. PLA is an aliphatic polyester, which is produced through the fermentation of sugars obtained from sugarcane, corn starch, or potato starch and then converted to lactic acid [2,3]. PLA is typically synthesized by ring-opening polymerization (ROP) of L-lactide utilizing organometallic catalysts and organic solvents [2,5]. Over recent years, PLA has been one of the most produced and used biobased plastics in the world [6]. Moreover, depending on its structure, namely molar mass, and stereoisomerism (L-/D-lactide ratio), PLA is semicrystalline [7]. This presents both advantages and disadvantages, as crystallinity can be a severe parameter on many aspects regarding the polymer performance (mechanical strength, permeation of small molecules [8], thermal conductivity [9,10], compostability [11], etc.). However, PLA presents some drawbacks, such as low melt strength, fragility, and, thus, limited mechanical properties, moisture, and gas sensitivity [12,13]. These drawbacks can be overcome by using several fillers and nano additives [14].

The addition of organic/inorganic fillers provides a potential solution to the limitations of PLA, with notable enhancements in mechanical, thermal, and many other physical properties. In recent years, biochar (being introduced below) has been used as a biobased filler in order to improve the aforementioned properties of polymers. In particular, the thermomechanical properties of PLA-biochar composites were investigated with two different process methods (melt mixing and solvent casting) by Arrigo et al. [15]. In that study, the processing method indicated a remarkable influence on the thermal behavior of the bio-composites, and the addition of biochar decreased their thermal stability. Furthermore, Hernandez-Charpak et al. studied the effect of two different biochar feedstocks on the morphological, thermal, and mechanical properties of three polymeric matrixes, one of them being PLA [16]. Therein, it was investigated that different types of biochar affected mechanical and thermal properties in various ways. The effect was found to be different depending on the polymeric matrix and the biochar feedstock.

The bio-derived carbon, which is well known as biochar (BC), is a promising replacement for conventional carbonaceous non-renewable fossil-based fillers, such as carbon tubes, carbon black, carbon nanotubes, and graphene [17–19]. BC is a byproduct of biomass pyrolysis at high temperatures (300–800 °C). It is an abundant material prepared from many types of biomass plants. It is an actual cost-effective, non-toxic, eco-friendly, and sustainable material [20]. BC is characterized by a large surface area and stable structure with, obviously, high carbon contents [21]. The structure as well as the properties of BC are determined by numerous factors, including the type of feedstock, conditions of pyrolysis, and particle size [22]. For instance, with the increase in pyrolysis temperature from 550 to 750 °C, the carbon percentage of biochar is increased, the number/concentration of car-

boxylic groups is reduced, its hygroscopicity can be altered, and its total surface area can be increased [23,24]. In general, mechanical properties, thermal stability, electrical conductivity, and hydrophilicity or hydrophobicity of the materials could be affected by the type of biomass and the pyrolysis conditions [25–28]. The effect of BC on the mechanical, rheological, and morphological properties of PLA and poly(butylene adipate-co-terephthalate) (PBAT) blends has been carried out by Giulia Infurna et al. [29]. Also in our previous studies, we found that the addition of low amounts of biochar (1 and 2.5 wt%) in poly(butylene succinate) improved significantly the tensile and impact strengths [30] and enhanced its resistance against UV irradiation [31]. Moreover, we revealed that the BC effects of the polymer can be both direct and indirect, for example, via altering crystallinity.

The aim of the present study is to study the incorporation of different types and amounts of biochar in the PLA polymeric matrix. For this reason, we synthesized PLA/BC bio-composites with biochar's feedstock softwood pellet (SWP), having been produced at two different pyrolysis temperatures (550 °C and 700 °C), employing the in situ ring-opening polymerization technique. Biochar was incorporated for the first time by in situ ROP procedure into PLA at different weight contents (1, 2.5, and 5 wt%), aiming at evaluating the effect of different biochar types and loadings on the chemical structure, mechanical properties, molecular mobility, enzymatic hydrolysis, and thermal stability of PLA.

2. Materials and Methods

2.1. Materials

L-lactide (LA) monomer Purlact B3 (purity 99% *w*/*w*, stereochemical purity in L-isomer 95%) was purchased from Corbion N.V. (Gorinchem, The Netherlands). Tin(II) 2-ethylhexanoate ($Sn(Oct)_2$) (purity > 92.5%) was purchased from Merck KGaA (Darmstadt, Germany). The biochar (BC) used in this work was produced by intermediate pyrolysis of pelleted softwood pellets at 550 and 700 °C in a pilot-scale rotary kiln at the UK Biochar Research Centre, referred to as SWP550 and SWP700, respectively [32]. Prior to its use, the BC was dried overnight in the oven at 80 °C under vacuum. All other reagents were of analytical grade.

2.2. Synthesis of PLA and Its Bio-Composites

PLA and its bio-composites with biochar were synthesized by in situ ROP of lactide in the presence of $Sn(Oct)_2$. The catalyst was added as a 400 ppm solution in toluene. Dodecanol (0.05 g/mL acetone) was added as a co-initiator. The polymerization was carried out at 160 °C for 1.5 h with a 200 rpm screw speed and with a flow of dry N_2 in order to minimize the presence of air in the reaction chamber (250 mL round-bottom flask). After 1.5 h, the temperature increased to 180 °C, and the polymerization was continued for an additional 15 min under vacuum to remove untreated lactide monomer. The polymerization was terminated by rapid cooling of the flask to room temperature. Similarly, PLA/BC bio-composites were prepared to contain 1, 2.5, and 5 wt% biochar using the two different types, SWP550 and SWP700, which were added at the beginning of the reaction with lactide in the batch reactor. In total, 7 samples were synthesized.

2.3. Intrinsic Viscosity

Intrinsic viscosity [η] measurements were carried out using an Ubbelohde viscometer capillary 0c at 25 °C in chloroform. The solutions were filtered through a disposable membrane filter (Teflon). The average value was calculated after three different measure-

ments. The intrinsic viscosity value of the polymer was calculated by the Solomon–Ciuta Equation (1):

$$[\eta] = \frac{\left[2\left\{\frac{t}{t_0} - ln\left(\frac{t}{t_0}\right) - 1\right\}\right]^{1/2}}{C} \quad (1)$$

where c is the solution concentration, t is the flow time of the solution and t_0 is the flow time of pure solvent.

2.4. Gel Permeation Chromatography-Size Exclusion Chromatography (GPC/SEC)

The molecular weight of the materials was determined using GPC/SEC analysis. The analysis was conducted on an Agilent 1260 Infinity II LC system (Agilent Technologies, Santa Clara, CA, USA), which included an isocratic G7110B pump, an automatic vial sampler G7129A, a refractive index detector (RID) G7162A, a PLgel 5 μM (50 × 7.5 mm) guard column, and two PLgel 5 μM (300 × 7.5 mm) MIXED-C columns. Calibration was performed using poly(methyl methacrylate) (PMMA) standards with molecular weights ranging from 0.535 to 1591 kg/mol. Samples were prepared by dissolving them in $CHCl_3$ at a concentration of 3 mg/mL and filtering the solution through a 0.45 μm PTFE microfilter to eliminate any solid residues. Each sample was injected in a 20 μL volume, with a total elution time of 30 min. Both the column and RID temperatures were maintained at 40 °C throughout the analysis.

2.5. Nuclear Magnetic Resonance (NMR)

NMR spectra of aliphatic polyesters were recorded in deuterated chloroform. An Agilent 500 spectrometer (Agilent Technologies, Santa Clara, CA, USA) was used for the structural study of the bio-composites at room temperature. Spectra were calibrated using the residual solvent peaks.

2.6. Fourier-Transformed Infra-Red Spectroscopy (FTIR)

The FTIR spectra for the two types of biochar and the produced materials were obtained by FTIR-2000 (Perkin Elmer, Waltham, MA, USA). All spectra were collected in the wavenumber range from 450 to 4000 cm^{-1} using a resolution of 4 cm^{-1} and 32 co-added scans. The presented spectra were further baseline corrected, normalized, and converted into an absorbance mode.

2.7. Transmission Electron Microscopy (TEM)

TEM analysis was conducted using an FEI Tecnai G2 20 microscope (FEI, Hillsboro, OR, USA) operating at an accelerating voltage of 200 kV. For sample preparation, thin films of neat PLA and its bio-composites were sectioned using an ultramicrotome equipped with a DiATOME 45° diamond knife (DiATOME Ltd., Nidau, Switzerland) to achieve a thickness of 80 nm. The resulting sections, which floated on the water surface of the knife, were subsequently transferred onto carbon-coated grids and allowed to air dry overnight.

2.8. X-Ray Diffraction (XRD)

The XRD measurements were performed using a MiniFlex II XRD system (Rigaku Co., Tokyo, Japan) in the angle 2θ range from 5° to 45° with a scanning speed of 1°/min with CuKα radiation (λ = 0.154 nm). All samples were in the form of films.

2.9. Differential Scanning Calorimetry (DSC)

The thermal transitions of PLA (glass transition, crystallization, melting) were studied using a TA Q200 DSC instrument (TA Instruments, New Castle, DE, USA), priorly calibrated

with Indium for temperature and enthalpy and with sapphires for heat capacity. The measurements were performed in a gas nitrogen atmosphere of high purity (99.9995%) and within the temperature range from −20 to 190 °C on sample pieces of ~7–9 mg in mass closed in TA Tzero aluminum pans. In order to erase the thermal history of the sample, a first heating scan up to 190 °C was performed. Subsequently, the sample was cooled from 190 °C (melt state) (scan 1) down to −20 °C at the fastest achievable rate (~100 K/min), stayed there for 5 min, and heated up to 190 °C at 10 K/min; then, (scan 2) the sample was cooled from 190 °C (a, scan 1) down to −25 °C at 20 K/min, stayed there for 2 min, and, finally, heated to 190 °C at 10 K/min.

2.10. Dielectric Relaxation Spectroscopy (DRS)

Segmental mobility was studied employing the advanced technique of DRS [33]. The measurements were performed using a Novocontrol DRS setup (Novocontrol GmbH, Montabaur, Germany) in a nitrogen atmosphere on samples in the form of sandwich-like capacitors of 15 mm in diameter and ~100 μM in thickness (silica spacers employed). The samples were melted at ~180–190 °C between the finely polished brash electrodes (disks) and were subsequently cooled rapidly in order to produce PLA in the amorphous state. For this study, we recorded and evaluated the imaginary part of dielectric permittivity, ε'', related to the dielectric losses, as a function of frequency in the range from 10^{-1} to 10^{6} Hz and in the temperature range between 10 and 120 °C, upon heating at steps of 5 or 10 K.

2.11. Mechanical Properties

Tensile tests of PLA and its composites were performed using a Shimadzu EZ Test Tensile Tester (Kyoto, Japan), Model EZ-LX, with a 2 kN load cell, in accordance with ASTM D882 using a crosshead speed of 5 mm/min. Dumbbell-shaped tensile test specimens (central portions 5 × 0.5 mm thick, 22 mm gauge length) were prepared by compression molding in a thermopress at 170 °C, cooled rapidly, and cut in a Wallace cutting press. At least five measurements were conducted for each sample, and the results were averaged to obtain the mean values of Young's modulus, tensile strength at yield and breakpoint, and elongation at break.

2.12. Color Measurement

A Datacolor Spectraflash SF600 plus CT UV reflectance colorimeter (Datacolor, Marl, Germany) using the D65 illuminant was used for color measurements, including a 10° standard observer with the UV component excluded and the specular component. The coloration of the bio-composites was analyzed using the CIEL*a*b* color system. In this system, the L* axis represents luminosity or lightness, with values ranging from 0 (black) to 100 (white). The a* coordinate indicates redness when positive and greenness when negative, while the b* coordinate signifies yellowness when positive and blueness when negative. Additionally, C* denotes chroma, and H* refers to the hue angle. To evaluate the color concentration in the bio-composites, the K/S ratio was calculated [34].

2.13. Enzymatic Hydrolysis

Film samples, each measuring 1.5 cm × 1.5 cm with an approximate thickness of 1 mm, were prepared using an Otto Weber Type PW30 hydraulic press (Wuppertal, Germany). These films were placed in test tubes containing 10 mL of phosphate buffer solution (0.2 M, pH 7.2 ± 0.1) supplemented with 0.09 mg/mL of *Rhizopus delemar* lipase and 0.01 mg/mL of *Pseudomonas cepacia* lipase. The test tubes were incubated in an oven at 50 ± 1 °C for one month, with the buffer/enzyme solution being refreshed every three days. At

specified intervals (5, 10, 15, 20, 25, and 30 days), the films were retrieved from the solution, thoroughly washed with distilled water, and dried under vacuum at room temperature until a constant weight was achieved. Each measurement was conducted in triplicate. The rate and extent of enzymatic hydrolysis were determined based on the mass loss of the samples according to the following equation:

$$Mass\ loss\ \% = \frac{W_0 - W_i}{W_0} \quad (2)$$

Alterations of the morphology of the films after enzymatic hydrolysis were examined using SEM JEOL (JMS 760F).

2.14. Water Contact Angle

The water contact angle was measured with an Ossila contact angle goniometer L2004A1 at room temperature (25 °C). The contact angle was measured by gently placing a water droplet (5 μL) on the surface of the films of the samples prepared by in situ polymerization. At least three measurements were performed for each sample, and the mean value was reported.

2.15. Scanning Electron Microscopy (SEM)

The particle size of used BC and the surface morphology of enzymatically hydrolyzed materials were studied with a JEOL (Tokyo, Japan) JSM 7610F field emission scanning electron microscope operating at 5 kV. Pictures of thin films were also captured using a Jenoptik (Jena, Germany) ProgRes GRYPHAX Altair camera attached to a ZEISS (Oberkochen, Germany) SteREO Discovery V20 microscope.

2.16. Thermogravimetric Analysis (TGA)

Thermogravimetric analysis (TGA) of PLA/BC bio-composites was performed by a SETARAM SETSYS TG-DTA 16/18 instrument. The samples (10 ± 0.5 mg) were placed in alumina crucibles, while an empty alumina crucible was used as a reference. For the kinetic analysis study [35]. PLA composites were from 25 °C to 600 °C, and the N_2 at the rate of 50 mL/min flow for heating rates of 5, 10, 15, and 20 °C/min. Thermal degradation kinetic analysis of the PLA composites was achieved with the use of NETZSCH Kinetics Neo software (NETZSCH, Selb, Germany) [36]. Among the model-fitting kinetic approach algorithms is the deterministic one that seeks the best kinetic model by changing minimal parameters quantitatively describing the kinetics of the complete degradation reaction.

3. Results

3.1. Synthesis and Morphological Characterization of Biochar

Biochar from softwood pellets (SWP) was produced by intermediate pyrolysis at 550 and 700 °C in a pilot-scale rotary kiln [32]. After grinding, irregular particle sizes and shapes of biochar were formed. The SEM micrographs of Figure 1 show both large particles with sizes greater than 10 μm (10–15 μm) and much smaller particles with sizes at the nanoscale level (250–500 nm). These particles have been used as fillers for PLA/biochar bio-composites production.

3.2. Synthesis and Characterization of In Situ Prepared PLA/BC Bio-Composites

Neat PLA and its bio-composites were prepared by in situ ring-opening polymerization, yielding samples with high molecular weight. The number average molecular weight, M_n, values of neat PLA are evaluated by GPC as 109 kg/mol (Table 1), which

is high for aliphatic polyesters. However, as biochar content increases in the polymeric matrix, the M_n is reduced. Usually, when additives have some reactive groups, they can interact with the polymer matrix, affecting its molecular weight [16,18,37–39]. This can be attributed to the hydroxyl groups of biochar [19], which can act as co-initiators in ROP. The creation of new initiation sites can lead to lower molecular weight values. We recall that the thermochemical and time period parameters of ROP were kept fixed. Thus, compared to neat PLA, the drop in M_n is related to the simultaneous initiation of ROP at more sites in the presence of BC. Thus, M_n of PLA/SWP550 with 1, 2.5, and 5 wt% are about 40, 30, and 22 kg/mol, respectively, and M_n PLA/SWP700 with 1, 2.5, and 5 wt% are about 40, 31, and 20 kg/mol, respectively. This significant drop in M_n can be used as indirect, although strong, proof of the successful PLA grafting onto the BC entities. Interestingly, the smaller polydispersity indices (PDI) exhibited by the bio-composites (1.5–1.8), as compared to the unfilled PLA (2.2), suggest a moderate improvement in the bio-composites homogeneity. The intrinsic viscosity [η] was also calculated in order to confirm the M_n values alternations qualitatively. It can be seen that with the addition of biochar, the intrinsic viscosity values are decreased monotonically (Table 1), which is in good agreement with the M_n reduction trend calculated by GPC.

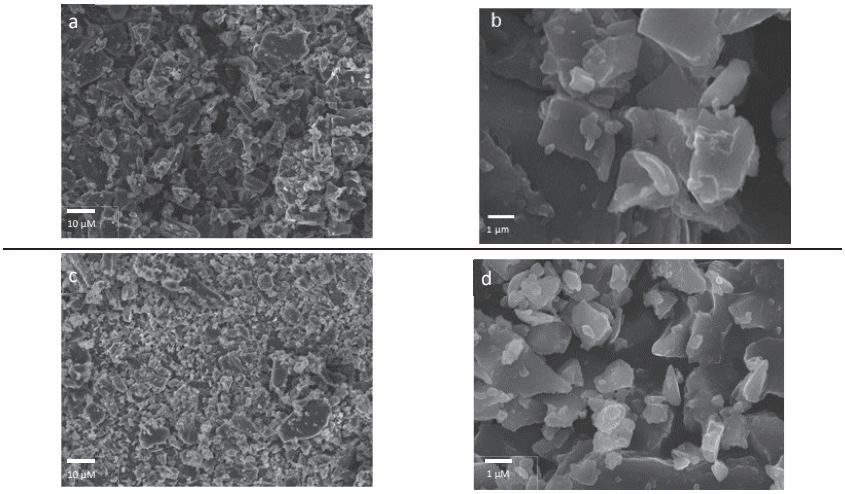

Figure 1. SEM micrographs of prepared biochar after pyrolysis at 550 and 700 °C and grinding in low (left) and high (right) magnification. Figures (**a**,**b**) depict biochar pyrolyzed at 550 °C, while figures (**c**,**d**) depict biochar pyrolyzed at 700 °C.

Table 1. Intrinsic viscosity and molecular weight of the prepared PLA and its bio-composites.

Sample	η (dL/g)	M_n (g/mol)	PDI
PLA neat	2.18	109,000	2.2
PLA/SWP550 1 wt%	1.26	40,200	1.53
PLA/SWP550 2.5 wt%	0.92	30,150	1.66
PLA/SWP550 5 wt%	0.8	22,500	1.71
PLA/SWP700 1 wt%	1.14	40,900	1.60
PLA/SWP700 2.5 wt%	0.99	30,800	1.81
PLA/SWP700 5 wt%	0.72	20,150	1.60

The NMR spectra were obtained in order to evaluate the successful synthesis of PLA and PLA/BC bio-composites. The chemical structure of the produced aliphatic polyesters was assessed by proton (^{1}H) and carbon (^{13}C) nuclear magnetic resonance spectroscopy. Scheme 1 presents the numbered structures of the studied polymers. The part of the structure corresponding to carbons 1–3 appears basically at the same shifts for all samples,

and the assigned chemical shift in ^{1}H and ^{13}C spectra remains at approximately the same positions (Figure 2). The ^{1}H-NMR resonance signal of neat PLA appears at 1.58 ppm (d, 3H, J = 7.1 Hz), is associated with the methylene protons (CH_3-), and at 5.16 ppm (q, 1H, J = 7.1 Hz) to methine protons (-CH-), Figure 2a,b. Figure 2c,d depicts the ^{13}C NMR spectra of the synthesized polymers. As mentioned above, the peaks of all samples corresponding to carbons 1–3 remain the same. At 16.1 ppm, the methyl carbons (1) are recorded, and at 68.9 ppm, the methine carbons (2). The carbons that are adjacent to the oxygen atom of the ester bond, carbonyl carbons, (3) give a peak at 169.6 ppm. The structural integrity of PLA is not compromised by the incorporation of biochar. Thus, the NMR spectra demonstrated successful synthesis of the PLA and PLA/BC composites. The results are in accordance with the literature [19,40]. The residual monomer in neat PLA and composites was also calculated by NMR, and in all cases is lower than 1 wt%. This is very important since the amount of residual lactide can affect the characteristics of the final polymer [41].

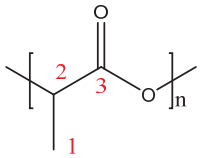

Scheme 1. Numbered structure of the prepared PLA and PLA/BC bio-composites.

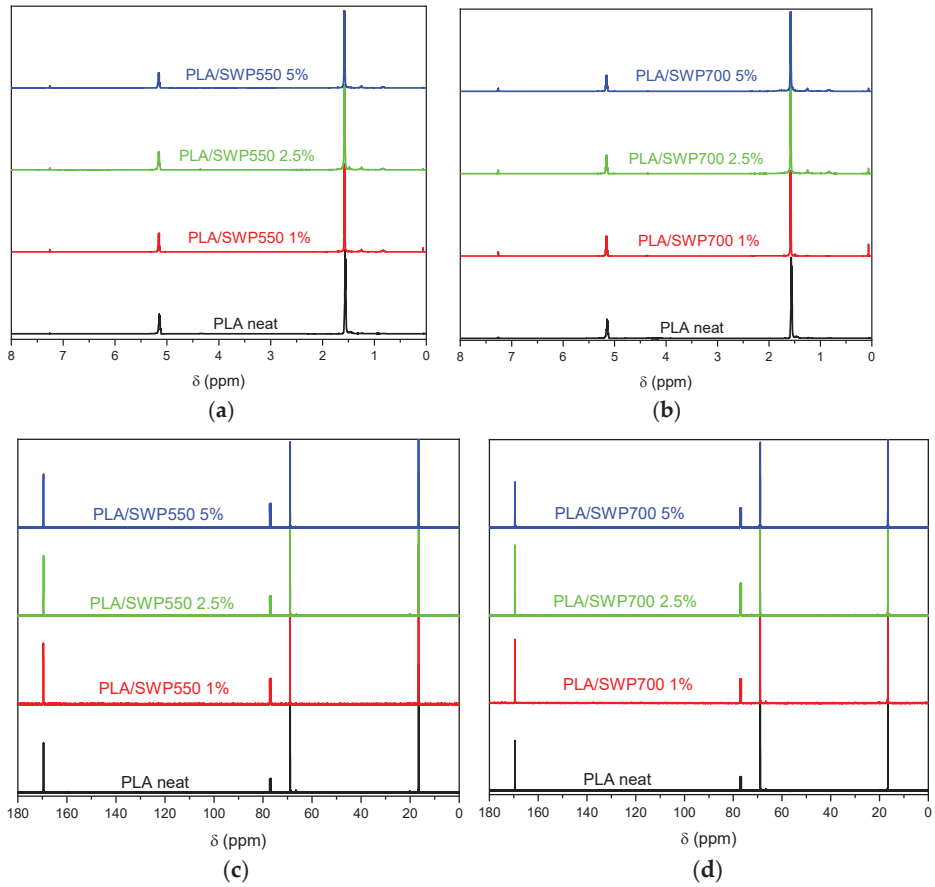

Figure 2. (**a**) ^{1}H NMR of PLA/SWP550, (**b**) ^{1}H NMR of PLA/SWP700, (**c**) ^{13}C NMR of PLA/SWP550, and (**d**) ^{13}C NMR of PLA/SWP700.

3.3. Structural Characterization of Biochar and PLA/BC Bio-Composites

From the FT-IR analysis of two different types of biochar (SWP550 and SWP700), their chemical structure can be seen in Figure 3. Examining the bands in the regions of interest,

a characteristic peak at 1620 cm^{-1} attributed to aromatic C=C stretching and two bands at around 1700 and 2900 cm^{-1} attributed to carbonyl groups and aliphatic C-H stretching vibrations, respectively, can be seen. Furthermore, a broad band at around 3400 cm^{-1}, which arises from the hydroxyl groups, indicates dehydration of cellulosic and ligneous components of softwood pellets [29,38,42,43].

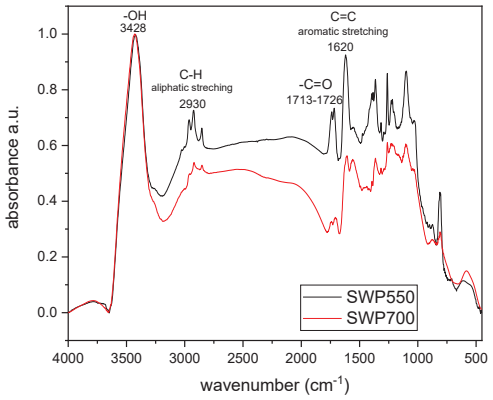

Figure 3. FT-IR spectra of biochar pyrolyzed at 550 °C and 700 °C.

Changes in the chemical structure upon the synthesis of PLA composites were evaluated through FT-IR spectroscopy. Figure 4a shows the FT-IR spectra of neat PLA and its bio-composites with SWP550 biochar, while Figure 4b displays the FT-IR spectra of PLA and its bio-composites with SWP700 biochar. In particular, the region for PLA and its bio-composites at around 1750 cm^{-1} of stretching vibration of ester groups provides information with respect to the relationship between PLA and biochar. Please note that the ester site (-C=O) is the most polar one for PLA; thus, it is the number one candidate for involvement in interactions. In the case of neat PLA spectrum, this peak at 1759 cm^{-1} is sharp, whereas, in the case of bio-composites, both SWP550 and SWP700 biochar are recording a broadening of the peak at smaller wavenumber sides. In particular, changes in the peak position and shape are recorded with the appearance of a split in the band. This is indicative of interfacial interactions between the biochar and PLA, probably due to the formation of new bonds between the -OH groups of biochar and the ester groups of PLA. Such broadening has been observed before in various polymer nanocomposites (including PLA) and has been interpreted in terms of the formation of more bound ester groups (polar sites) of the polymer due to their engagement by many polar groups of the nanofiller (e.g., -OH) [44,45]. By this result, we gain a first indication of the direct interaction-attachment of the PLA chains over the BCs, which is actually the idea behind the in situ synthesis. A small band at 3512 cm^{-1} is assigned to hydroxyl groups. This band, within all bio-composites, is increased when increasing the biochar content. It should be mentioned that the increase in the intensity of these peaks of the bio-composites may be assigned to the interactions between the fillers and the polymeric matrix. Additionally, this can be attributed to the reduced molecular weight of the bio-composites, since the smaller the molecular weight, the greater the carbonyl and hydroxyl end groups.

3.4. Biochar Dispersion Studied by TEM

From TEM micrographs taken of all of the composites (Figure 5), it seems that particles of BC are well dispersed throughout the PLA matrix; furthermore, in a nanosized form. Figure 5 shows dark, almost spherical particles with small sizes (100–200 nm) for the composites containing 1, 2.5, and 5 wt% of biochar with a 550 °C pyrolysis temperature. Especially for the sample of PLA/SWP550 with 5 wt% BC, there are several nanoparticulate

entities of ~20–30 nm in size. Furthermore, the composites containing 1 and 2.5 wt% of biochar with a 700 °C pyrolysis temperature have irregular shapes with sizes between 200 and 300 nm. In the case of the PLA/SWP700 5 wt% composite, the appearance of the nanoparticles is the same, with sizes of 100–200 nm. It seems that some aggregates were formed with the incorporation of BC content, though remaining in the range of nanoparticles. However, from these micrographs, it is clear that even though we started from BC particles with sizes greater than 10 μm, these broke down during the in situ polymerization at the nanosized level. In this regard, the achievement of a fine dispersion of BC nanoparticles is an additional advantage of the polymerization procedure. Similar results have been found also in our previous study with poly(butylene succinate)/biochar bio-composites [30]. This reduction could be attributed to the softness of BC particles, which during in situ polymerization are broken down into smaller particles. Thus, in all cases, BC is reduced to a nanosize level.

3.5. XRD

XRD patterns of PLA and its bio-composite films upon annealing at 100 °C for 1 h were recorded in order to evaluate the impact of biochar on the crystal organization of PLA chains (Figure 6). All initial taken samples after ROP synthesis were amorphous. The diffraction peaks at 2θ = 15.2°, 16.9°, and 19.2° have been recorded. Examining the position of these peaks, it can be seen that all PLA/BCs are in similar 2θ positions, as in the case of neat PLA, which is an indication that the addition of BC does not severely affect the crystalline structure of PLA. The bio-composites show sharp peaks at the same 2θ values.

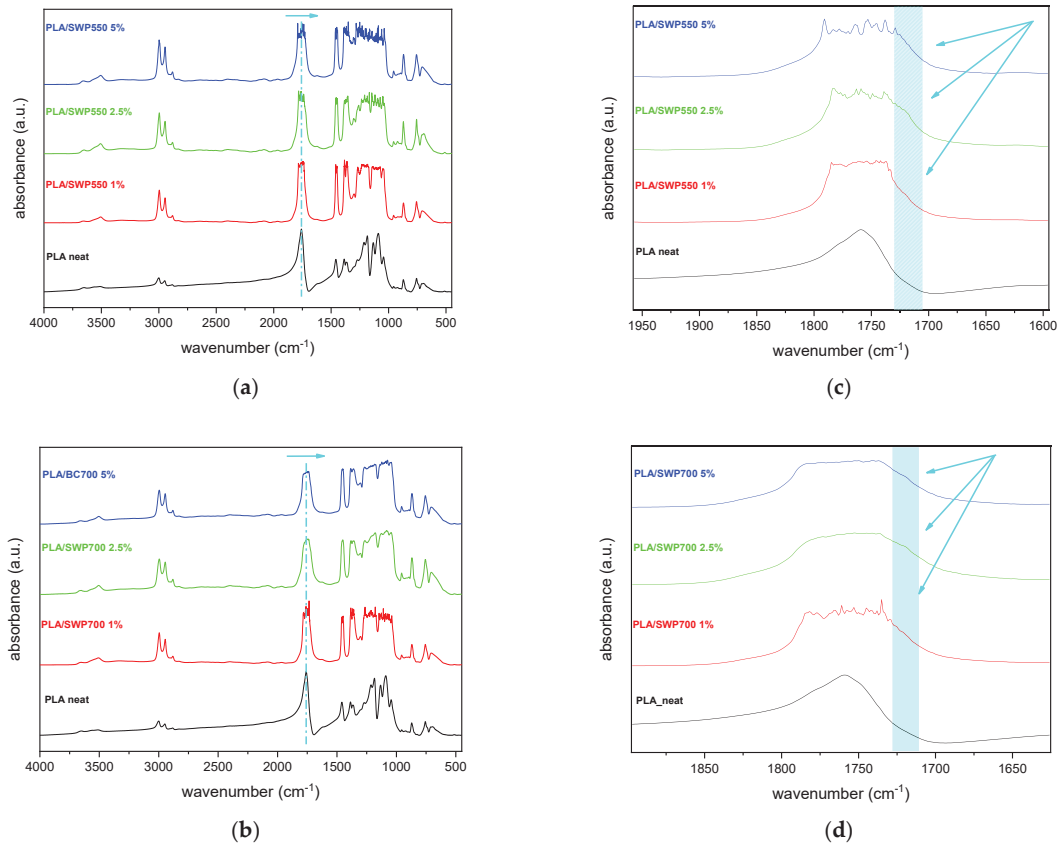

Figure 4. FT-IR spectra of neat PLA and its bio-composites with biochar pyrolyzed at (**a**) 550 °C and (**b**) 700 °C. Overlay of corresponding carbonyl peaks (**c**) for PLA/SWP550 bio-composites and (**d**) PLA/SWP700 bio-composites. The blue arrows mark the minor shift of bio-composite spectra toward lower wavenumbers.

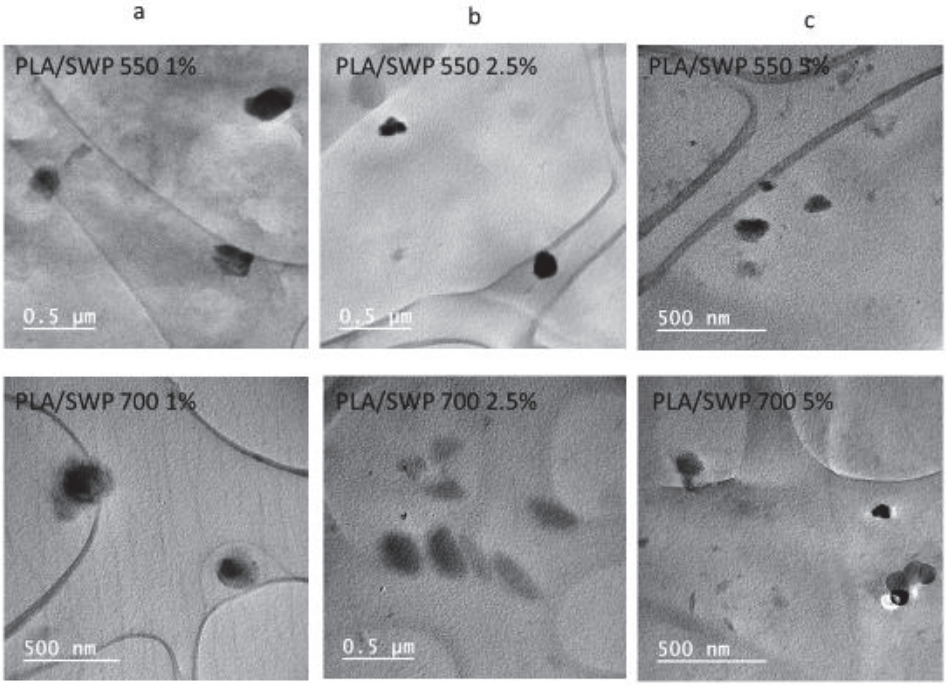

Figure 5. TEM micrographs of PLA/BC bio-composites with (**a**) 1 wt% biochar, (**b**) 2.5 wt% biochar, and (**c**) 5 wt% biochar.

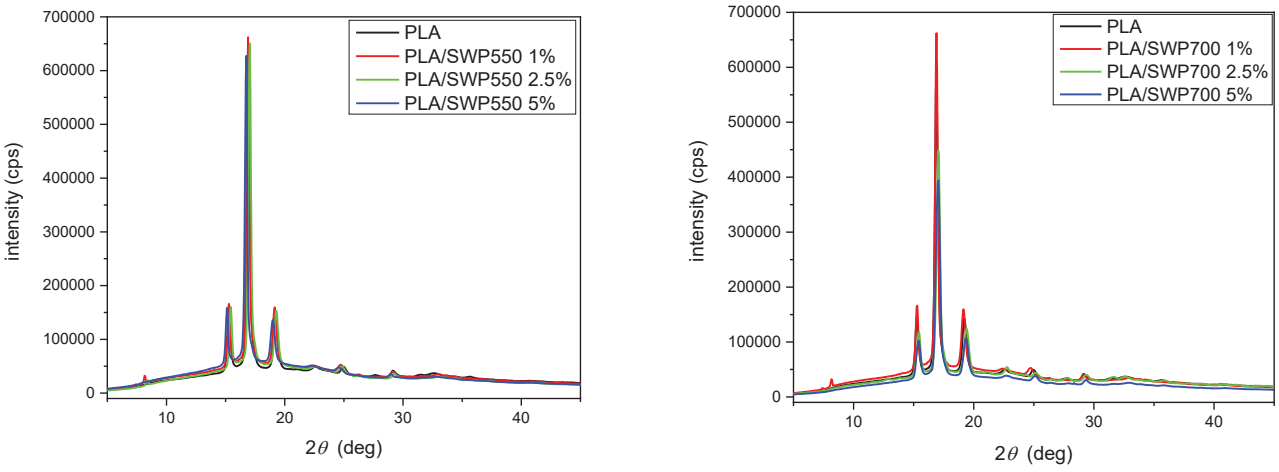

(**a**) (**b**)

Figure 6. XRD patterns of neat PLA and its bio-composites at different biochar loadings: (**a**) with biochar at 550 °C, (**b**) with biochar at 700 °C.

3.6. Thermal Transitions (DSC)

In Figure 7, we present the overall DSC data for both scans 1 and 2 in the form of comparative thermograms. During the fast cooling of initially amorphous samples (scan 1, not shown), no crystallization exothermal peak was recorded. Thus, the polymers are considered amorphous. During the subsequent heating (Figure 7), all samples exhibit sharp glass transition steps (35–55 °C), cold crystallization exothermal peaks (75–140 °C), as a result of the absence of melt crystallization during cooling, and melting endotherms (150–180 °C).

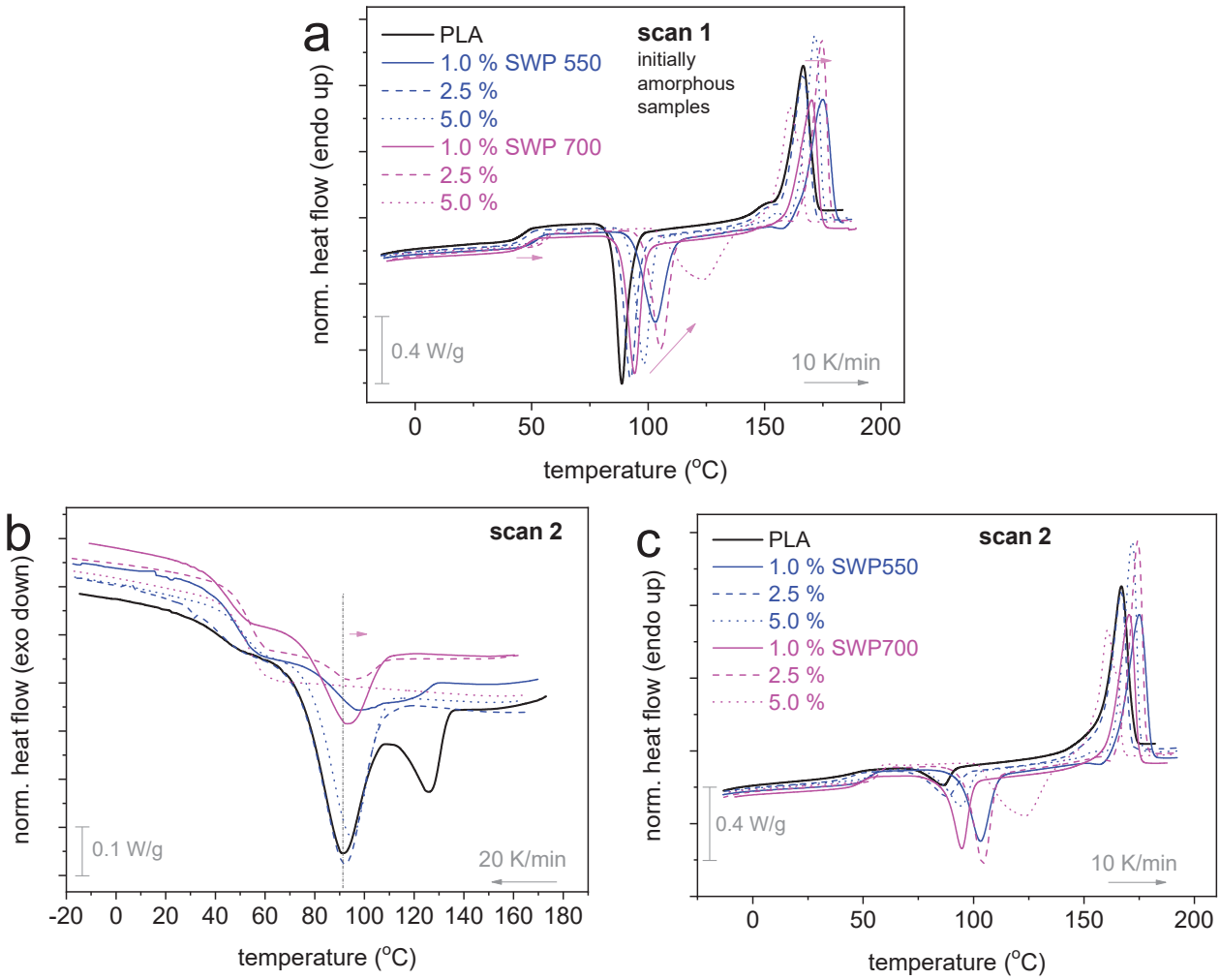

Figure 7. Comparative DSC traces during (**a**) the heating of scan 1 and (**b**,**c**) the cooling and heating of scan 2. The heat flow is shown upon normalization to the sample mass. The added arrows mark effects imposed by the filler addition.

Due to the amorphous character of the samples, at temperatures around the glass transition event, any alternations in the composites should be due to either the direct filler effects or/and the M_n alternation. The characteristic glass transition temperature, T_g, is estimated as the T at the half heat capacity change (Δc_p). The T_g values can be seen in Table 2. Compared to neat PLA, the T_g is increased in the composites by 1–10 K. The increase suggests the hindering of the segmental mobility of PLA. Such hindering is expected in polymer composites, especially in the implementation of strong attractive interfacial interactions [46]. The result supplements the previous discussion on FTIR (alteration in the ester group vibration). On the other hand, an opposite effect on T_g would be expected by the lowering of M_n. This effect may exist here; however, it seems to be compensated by the more dominant role of interactions (grafted polymer chains).

Regarding crystallization, in scan 1, there is an elevation of the cold crystallization temperatures (T_{cc}, Table 2) in PLA/BC, always comparing with neat PLA. During the melt crystallization of scan 2, the melt crystallization temperature, T_c, decreases. Also, the estimated crystalline fraction of neat PLA is 55% for cold crystallization and 35% for melt crystallization. Both values are suppressed in the presence of BC of both types. Taking together all these effects on crystallization, we conclude that there is a decrease in crystallizability in the composites, in both the terms of nucleation and crystal formation. Such effects

are compatible with previous recordings on nanocomposites with strong polymer-filler interactions [46,47]. In addition, the suppression in crystallizability is compatible as well with the reduced M_n. The effects on the melting temperature, T_m, (157–175 °C) are mainly minor, whereas there seems to be a tendency of T_m to drop for the higher BC loadings. Moreover, the endothermal event becomes complex (double peak). Comparing the two types of BC, in general, there is no severe difference in the imposed effects on the studied thermal events.

Table 2. The samples under investigation, values of interest: molar mass, M_n, glass transition temperature, T_g, change in heat capacity, Δc_p, melt/hot crystallization temperature and crystalline fraction, T_c and CF_c, cold crystallization temperature and crystalline fraction, T_{cc} and CF_{cc}, melting temperature(s), T_m. Note: CF_i was estimated by comparing the normalized enthalpy change ($\Delta H_{i,norm}$) with the heat of fusion for PLA, taken as $\Delta H_{100\%}$ = 93 J/g.

	Scan 1 (Fast Cooling ~100 K/min)							Scan 2 (Cooling at 20 K/min)					
Sample	M_n **(kg/mo)**	CF_c **(wt)**	T_g **(°C)**	Δc_p **(J/g·K)**	T_{cc} **(°C)**	CF_{cc} **(wt)**	T_c **(°C)**	CF_c **(wt)**	T_g **(°C)**	Δc_p **(J/g·K)**	T_{cc} **(°C)**	CF_{cc} **(wt)**	T_m **(°C)**
neat PLA	109	0	46	0.50	89	0.55	126/91	0.35	44	0.26	87	0.09	167
PLA/SWP550 1.0%	40	0	52	0.49	103	0.47	111/97	0.08	52	0.45	103	0.38	175
PLA/SWP550 2.5%	30	0	47	0.52	93	0.54	92	0.25	45	0.28	89	0.24	167
PLA/SWP550 5.0%	23	0	53	0.51	98	0.53	94	0.19	54	0.32	95	0.26	156/172
PLA/SWP700 1.0%	41	0	47	0.50	94	0.47	92	0.12	49	0.39	95	0.30	170
PLA/SWP700 2.5%	31	0	56	0.47	106	0.51	93	0.03	56	0.47	104	0.44	157
PLA/SWP700 5.0%	20	0	54	0.53	124	0.46	-	0	55	0.51	124	0.46	161/164

Regarding future applications and the PLA/BC performance, one would expect a significant role of BC via the alternations in the crystallizability of PLA. As discussed, the suppressed CF here is a result of the existence of strong interactions combined with the suppressed M_n [30,48]. It would be worth it to compare in the future the impact of BC on the crystallinity and corresponding macroscopic performance [49] of PLA or other polyesters in composites prepared by alternative mixing routes in order to bypass the change in the polymers' M_n recorded herein.

3.7. Molecular Mobility (DRS)

The advanced technique of DRS was employed to study the dynamics of glass transition, or else the so-called α dipolar relaxation, which is the dielectric analog of the calorimetric glass transition [33]. This process is recorded as a peak of the dielectric loss [ε''(f) and ε''(T)] at $T \geq T_g$, as shown in the selected isothermal recordings of Figure 8a and the isochronal representations of Figure 8b. Please note that in PLA/SWP550 an additional, faster process could be also resolved (named process I), resembling an additional local-like mobility. At the lower frequencies and higher temperatures, a significant signal uprise is recorded. This is due to the involvement of various ionic conductivity effects (ion transport, electrode polarization, interfacial charges, etc.). Interestingly, there is a special response of PLA/SWP700 1.0%, indicating high ionic conductivity even at $T < T_g$. The result was checked and found repeatable, precluding the evaluation of molecular dynamics (strong conductivity domination over the dipolar response).

Employing well-known methods involving fitting suitable model functions (here, the asymmetric Havriliak–Negami and the symmetric Cole–Cole models) [33], we performed an analysis of the complex ε''(f) spectra. Examples of the analysis-fitting process are shown in Figure 9.

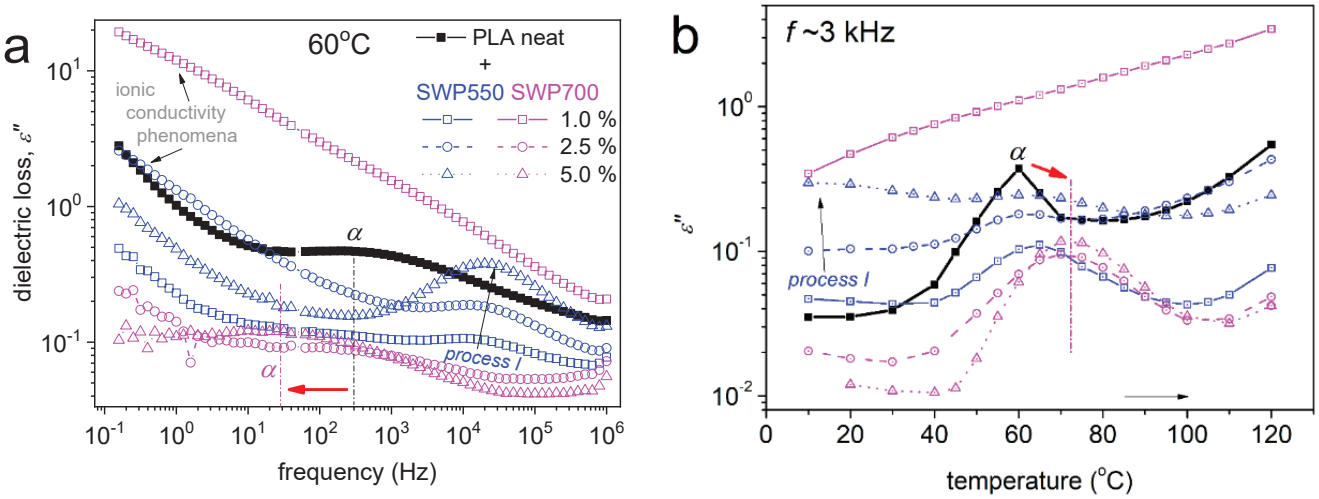

Figure 8. Comparative DRS results of ε'' in the form of ((**a**), raw data) isothermal curves at 60 °C and ((**b**), replotting) isochronal curves at f~3 kHz. Indicated are the main relaxation processes recorded. The added arrows mark the effects arising from the filler addition.

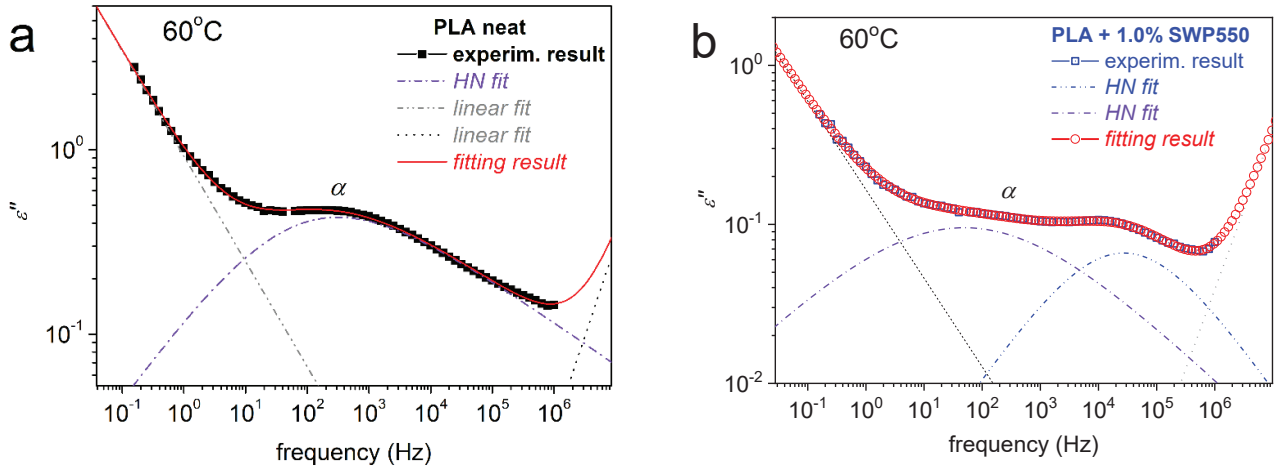

Figure 9. Examples of fitting of the ε''(f) spectra for the described samples [(**a**) neat PLA and (**b**) PLA + 1.0% SWP550] and temperatures, are given details in the text.

By the performed critical analysis, we were able to construct the segmental dynamics map in terms of the reciprocal temperature (1/T) dependence of the α relaxation maximum f (f_{max}). The map is presented in Figure 10a. Therein, the α relaxation exhibits, in all cases, the so-called Vogel–Tammann–Fulcher–Hesse behavior [i.e., a curved $f_{max}(1/T)$ trend], which is characteristic of segmental (cooperative) dynamics. Regarding the exceptional case of PLA/SWP550, the additional process I exhibit a linear time scale (Arrhenius-type) in Figure 10a, indicating a non-cooperative character. The estimated activation energy for process I is ~0.4 eV. Surprisingly, process I exhibits modes both 'faster' (at $T < T_g$) and 'slower' ($T > T_g$) than those of the α relaxation. This suggests not purely local dynamics of the polymer. Comparing with previous findings in polymers adsorbed on flat solid surfaces [50] and polyesters adsorbed on the solid surfaces of nanoparticles [51], wherein a similar dynamic view has been demonstrated, we may propose that process I arises from modified dynamics PLA chains being quite close to or adsorbed on the BC surfaces.

Coming back to segmental dynamics, all composites exhibit decelerated α dynamics, namely, migrating toward higher temperatures/lower frequencies. From these data, we evaluated the 'dielectric glass transition temperatures, $T_{g,diel}$' to vary between 40 and

49 °C (Figure 10b). In all cases, there is a systematic increase in $T_{g,diel}$ (i.e., dynamical deceleration) in the bio-composites. The effect provides additional support to the above-mentioned concept of strong chain grafting.

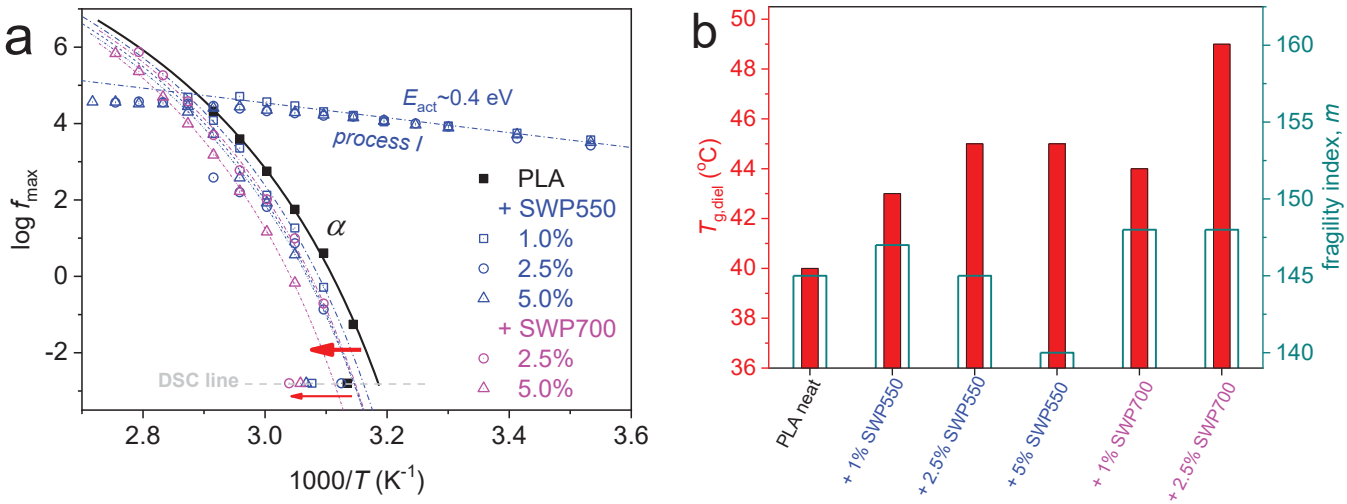

Figure 10. (**a**) Dielectric relaxation map in terms of time scale for all samples, described on the plot. The straight and curved lines connecting the experimental points are, respectively, fittings of the Arrhenius and Vogel–Tammann–Fulcher–Hesse equations. (**b**) The estimated dielectric T_g (left axis) and fragility index (right axis), from α relaxation, for the various samples.

The time-scale data of α relaxation enable also the evaluation of the dynamical fragility index [52]; m equals 145 for neat PLA; it slightly increases in the composites with 1 and 2.5% BC, whereas it drops for the 5% SWP550 (Figure 10b). The increase/decrease in m could be an indication of increasing/decreasing of the polymer chains degree of cooperativity or else narrowing/widening of the corresponding cooperativity lengths. Especially the drop of m here is compatible with the significant reduction of the chain lengths (M_n) in the bio-composites. More parameters are implemented within the cooperativity, such as any alternations in the free polymer volume and/or in the chain-chain associations (entanglements).

3.8. Mechanical Properties of PLA/BC Bio-Composites

Table 3 shows the results for the tensile properties of neat PLA and its bio-composites with SWP550 and SWP700 and with different biochar content, 1, 2.5, and 5 wt%. The tensile strength of neat PLA is about 30 MPa; PLA/SWP550 and PLA/SWP700 with 1 wt% BC are about 32 and 31 MPa, respectively. The tensile strength of PLA/SWP550 with 2.5 wt% BC is about 15 MPa, and PLA/SWP700 with 2.5 wt% BC is about 16 MPa, while PLA/BC bio-composites with 5 wt% biochar loading were brittle, and, thus, it was not technically possible to measure their mechanical properties. It appears that the tensile strength of PLA/BC composites, in both cases, is slightly increased in bio-composites with 1 wt% BC and decreased thereafter until 5 wt% biochar loading, at which point the specimens become brittle. The initial small increase could be attributed to the reinforcement effect of BC. A similar enhancement was also found in our previous study in poly(butylene succinate)/BC bio-composites [30], while the reduction thereafter could be attributed to the low molecular weight (Table 1). Incorporating biochar into a polymer matrix has been considered a method of improving its mechanical properties in the majority of the existing research that has been recently done [15,30,53]. More specifically, Mei Po et al. prepared PLA with bamboo charcoal composites with 2.5 wt%, 5 wt%, 7.5 wt%, and 10 wt% content. The increasing biochar content increases the mechanical properties, such as tensile strength

and Young's Modulus. Nevertheless, further addition of biochar content than 10 wt% results in decreasing the tensile strength [54]. Our results seem more compatible with the study of Mariem Zouari et al., wherein, adding biochar content leads to the reduction of tensile strength as well as young modulus, when biochar loading is more than 5 wt% [55].

Table 3. Mechanical properties of PLA and its bio-composites.

Sample	Tensile Strength at Break (MPa)	Elongation at Break (%)	Elastic Modulus (MPa)
PLA	30.08 ± 1.09	1.28 ± 0.07	3037 ± 231
PLA/SWP550 1 wt%	32.01 ± 0.34	1.51 ± 0.09	3143 ± 104
PLA/SWP550 2.5 wt%	15.25 ± 0.27	1.32 ± 0.02	2300 ± 111
PLA/SWP700 1 wt%	31.08 ± 0.72	1.12 ± 0.05	3187 ± 176
PLA/SWP700 2.5 wt%	16.82 ± 0.81	1.68 ± 0.03	1883 ± 59

For the samples PLA/SWP550 5 wt% and PLA/SWP700 5 wt% there are no available data.

Regarding the elongation at break, since PLA is a very brittle polymer with low elongation at break (about 1.3%), all bio-composites have similar values, as was expected. Furthermore, it was observed that the behavior of the elastic modulus of PLA/BC bio-composites has a similar trend as in the case of tensile strength. There is a negligible increase in PLA/BC bio-composites with 1 wt% BC and a significant reduction for PLA/BC when the concentration of BC is increased to 2.5 wt%.

3.9. Effect of Biochar Content on PLA Coloration

The increasing biochar content resulted in the coloration of PLA films. The color was measured with a colorimeter, and it is expressed with CIE coordinates in Table 4. PLA has an L* value of 88.98 and a* and b* values of −1.12 and 0.82, respectively, which is expected due to its white color. After the incorporation of both biochars, L* progressively decreased as expected due to their black color. The K/S fraction shows the concentration of the color on the composites, which increased with increasing biochar addition. PLA/SWP550 5% and PLA/SWP700 5% possess a higher concentration of the black color, 16.02 and 16.19, respectively. The color of composites changes due to the incorporation of biochar in a polymeric matrix. Similar findings were demonstrated by the study of Mariem Zouari et al., who investigated the addition of biochar to PLA and PLA/hemp fibers composites [18].

Table 4. Colorimetric data L*, a*, b*, C*, h°, and K/S values of PLA and PLA/BC samples.

Samples	L	a	b	C	h	K/S
PLA	88.98	−1.12	0.82	1.39	143.77	0.13
PLA/SWP550 1 wt%	30.40	0.44	1.34	1.16	64.17	9.02
PLA/SWP550 2.5 wt%	23.50	0.31	0.62	0.39	49.17	11.93
PLA/SWP550 5 wt%	19.81	0.15	0.13	0.22	321.62	16.02
PLA/SWP700 1 wt%	21.33	0.30	0	0.18	41.11	13.04
PLA/SWP700 2.5 wt%	20.34	0.36	−0.13	0.16	312.63	15.46
PLA/SWP700 5 wt%	19.91	0.12	0.04	0.14	347.69	16.19

3.10. Enzymatic Hydrolysis

As an aliphatic polyester, PLA occupies a relatively large number of ester bonds. For this reason, lipases, *Pseudomonas cepacian* (exotype) and *Rhizopus orizae* (endotype) can hydrolyze PLA and its bio-composites. The effect of enzymes on the mass loss of PLA and its bio-composites is presented in Figure 11. The mass loss of neat PLA is about 4% after 30 days of enzymatic hydrolysis. On the other hand, the incorporation of biochar

into the PLA matrix leads to a decrease in mass loss rate. More specifically, as biochar content increases, the mass loss of bio-composites decreases. Bio-composites containing 1, 2.5, and 5 wt% SWP550 lost about 3.9, 3.1, and 2% of their mass, respectively, after 30 days of enzymatic hydrolysis, while bio-composites containing 1, 2.5, and 5 wt% SWP700 lost about 3.8, 2.5, and 1.3% of their mass, respectively.

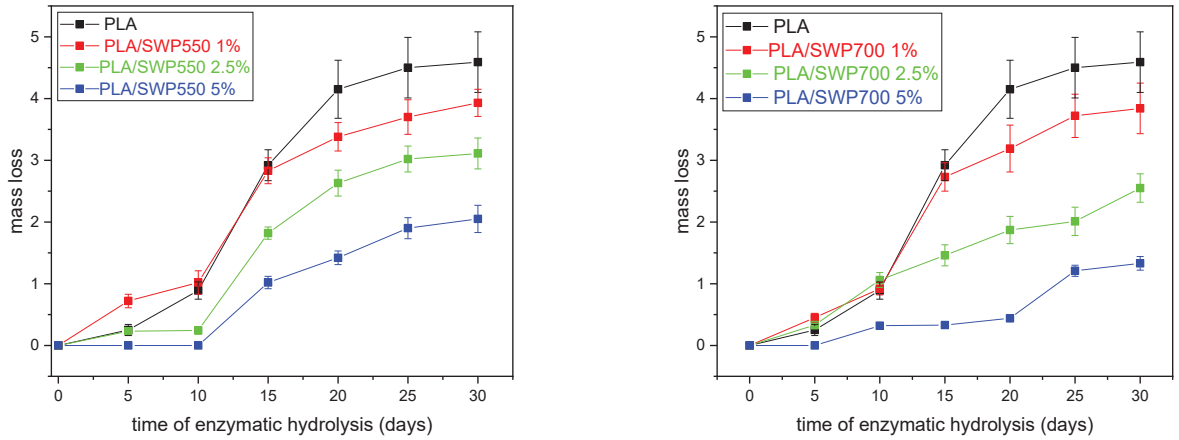

(**a**) (**b**)

Figure 11. Mass loss vs. time plot during enzymatic hydrolysis of neat PLA and PLA/BC bio-composites, (**a**) with biochar at 550 °C, (**b**) with biochar at 700 °C.

The effect of the hydrophilicity or hydrophobicity of the composites was explored by the measurement of their water contact angle (Table 5). The water contact angle of polymers depends on their surface properties, the preparation method, and the roughness, as well as the chemical composition and the temperature [56]. PLA displayed a water contact angle value of around 73°, whereas the addition of biochar increased this value. As the biochar content increased to 5 wt%, the water contact angle reached 82°. The reduced hydrophilicity of the bio-composites can be primarily attributed to the biochar's thermochemical conversion. Biochar loses the hydrophilic groups during the pyrolysis process, moving towards a more hydrophobic behavior. For this reason, its addition to PLA produces more hydrophobic bio-composites, which delay the enzymatic hydrolysis rate of PLA in all composites [18,55,57]. An increase in the content of both of the two types of biochar leads to a reduction in biodegradation time. Prolonged biodegradability of PLA can significantly increase the decomposition time and, thus, lead to the accumulation of this type of polymer in the environment, although it is a biobased and eco-friendly material. However, a longer biodegradability time may be useful for certain applications [58].

Table 5. Contact angle measurements of PLA and its bio-composites.

Sample	Contact Angle (Degree)
PLA	73.90 ± 0.40
PLA/SWP550 1 wt%	73.80 ± 0.39
PLA/SWP550 2.5 wt%	76.70 ± 0.44
PLA/SWP550 5 wt%	82.50 ± 0.42
PLA/SWP700 1 wt%	72.70 ± 0.42
PLA/SWP700 2.5 wt%	75.20 ± 0.36
PLA/SWP700 5 wt%	80.00 ± 0.39

The morphology of the sample's surfaces after 30 days of enzymatic hydrolysis was evaluated using SEM micrographs (Figure 12). The surfaces of neat PLA and its bio-

composites are smooth before the first days of enzymatic hydrolysis. The appearance of the surface's deterioration becomes apparent after 20 days of hydrolysis in both cases of two different biochar pyrolysis types (SWP550 and SWP700) with the presence of roughness, ridges, and holes. These observations are in agreement with the mass loss measurements.

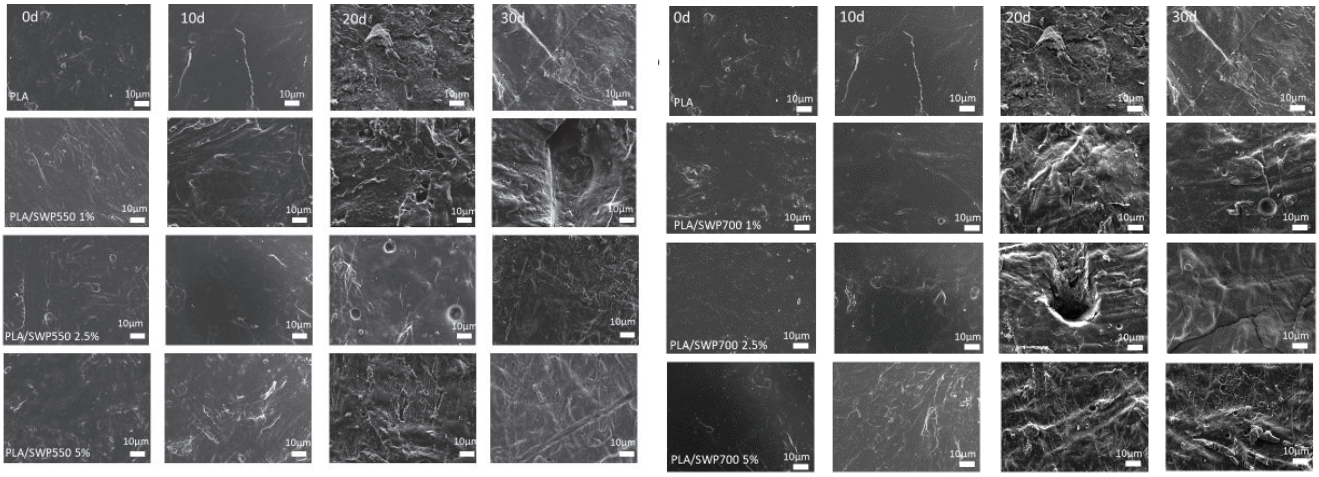

(**a**) (**b**)

Figure 12. SEM micrographs of PLA and its bio-composites: (**a**) with biochar at 550 °C, (**b**) with biochar at 700 °C throughout enzymatic hydrolysis (10, 20, and 30 days).

3.11. Thermal Degradation Studies of PLA/BC Bio-Composites

The thermal degradation of PLA/BC bio-composites was tested by TGA. The thermal graphs and the derivative thermogravimetry (dTG) curves of the two PLA_SWP550 and PLA_SWP700 bio-composites, which were filled with varying filler content (1 to 5 wt% of BC), are shown in Figure 13, being heated with a heating rate of 20 °C/min under a nitrogen atmosphere. The SWP550 and SWP700 results represented that BC was the sample with the most stable thermal behavior, with only 12% of the mass loss at temperatures below 600 °C. This seems logically consistent since biochar is the result of preparing organic waste-designated fly ash via thermal treatment [59]. The TGA curves indicate that neat PLA and PLA BC bio-composites show good resistance to thermal degradation. The literature shows that variations in biochar stemming from different feedstocks can influence the thermal stability of the polymer matrix in different ways. Some researchers emphasize that biochar has a nucleating role in PLA [60]. Conversely, there are also findings that report biochar's negative effect on thermal stability [15]. For example, Hernandez-Charpak et al. [16] found that the biochar produced from anaerobically digested dairy manure (DM) significantly decreased the crystallization and thermal stability of PLA, while biochar from eastern white pine wood chip (WC) had a much lesser impact on these properties. These variations have been associated with the moisture level of the DM and WC biochars, which facilitated the hydrolytic degradation of the polymer.

Table 6 shows the TGA results of neat PLA and PLA/BC composites with biochar of different contents, respectively. The temperatures corresponding to 1, 2.5, and 5 wt% mass loss and the maximum degradation temperatures ($T_{d,max1}$ and $T_{d,max2}$) indicate the effect of biochar and concentration on the thermal stability of PLA. The TGA results carry information that, in brief, neat PLA loses only 0.5% of the whole mass already at $T_{0.5}$ and after that breaks majorly at 343.0 °C and 374.5 °C, which means that PLA composites made of SWP550 and SWP700 show the efficiency of even small biochar concentrations with T0.5 even reaching a peak, as indicated by T0.5. When 5 wt% SWP550 is added, the $T_{0.5}$ slightly

decreases to 161.1 °C, but the thermal stability improves at later stages with $T_{2.5}$ and T_5 shifting to 274.8 °C and 293.0 °C, respectively. The maximum degradation temperatures ($T_{d,max1}$ and $T_{d,max2}$) are somewhat lower, at 335.9 °C and 368.3 °C, when compared to neat PLA.

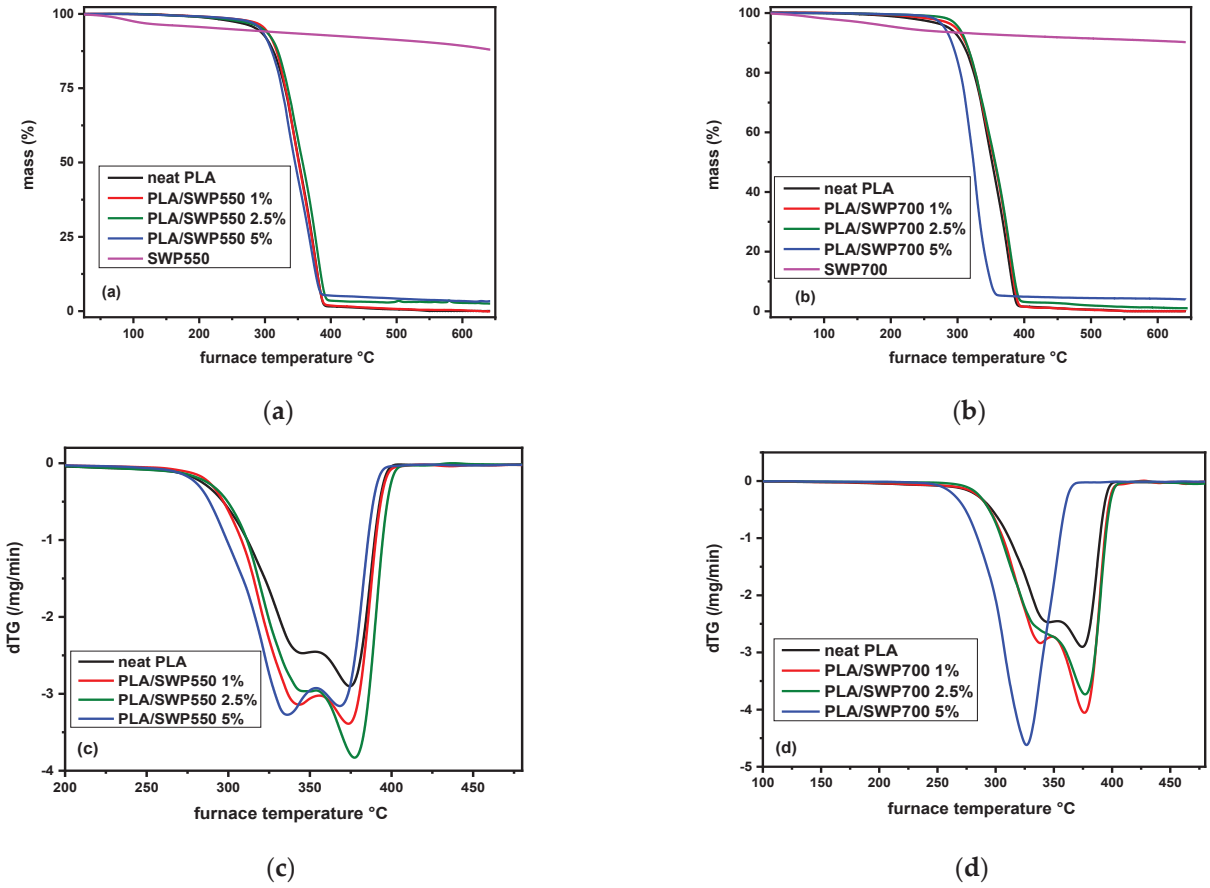

Figure 13. TGA thermograms and dTG curves of (**a**,**c**) PLA_SWP550 and (**b**,**d**) PLA_SWP700 at a heating rate of 20 °C/min under nitrogen flow.

Table 6. TGA results of all samples studied.

Sample	$T_{0.5}$ (°C)	$T_{2.5}$ (°C)	T_5 (°C)	$T_{d,max1}$ (°C)	$T_{d,max2}$ (°C)
Neat PLA	162.3	250.0	286.8	343.0	374.5
PLA/SWP550 1 wt%	172.4	276.9	297.2	343.2	373.5
PLA/SWP550 2.5 wt%	166.4	262.7	296.5	343.8	377.2
PLA/SWP550 5 wt%	161.1	274.8	293.0	335.9	368.3
PLA/SWP700 1 wt%	181.5	272.8	297.0	337.2	376.1
PLA/SWP700 2.5 wt%	210.8	290.8	302.0	332.4	376.7
PLA/SWP700 5 wt%	216.2	270.2	280.8	-	326.5

The initial thermal decomposition temperature of PLA/SWP700 5 wt% is 216.2 °C, and it indicates better early-stage thermal stability than the SWP550. However, in the case of T_5 (280.8 °C) and maximum degradation temperature (326.5 °C), they are found to be significantly less than those for the PLA/SWP550 5 wt% composite, implying that the decomposition process might be further expedited due to the SWP700 loading effect. The data suggests that the biochar (SWP700) ingrains early-stage thermal resistance in PLA but catalyzes faster degradation at higher temperatures. This variance clearly shows how biochar exhibits diverse effects on PLA's thermal properties, depending on its origin

and the amount of biochar used. However, when the biochar content is increased, the composite is more resilient against thermal degradation. The residual mass also increased with more biochar added. This is because, at higher temperatures, more char residues make the composite stable. Similarly, in a previous study [61], it was also found that when the BC was added to the system, it made the layer denser, and therefore, more mass was left as residual mass. Additionally, the obtained data indicates an accelerating influence on the thermal stability of PLA/BC composites as filler content increases; thus, a catalytic effect of biochar in the degradation together with a faster degradation rate can be deduced from the above explanation. In the study of Arrigo et al. [15], a gradual decrease in $T_{5\%}$ and $T_{10\%}$ (the temperatures corresponding to 5% and 10% mass loss values) with increasing filler content was accompanied by a change in the maximum temperature at which degradation occurred. This decrease is explained by the presence of potassium, the main component in biochar, that speeds up the degradation process of PLA and other bio-polyesters. The report of Haeldermans et al. [60] indicated that the onset and maximum degradation temperatures of PLA/biochar composites are diminished with the increment of biochar content. With 20% biochar, these temperatures drop to around 290 °C and 365 °C, respectively, and further decline to 275 °C and 350 °C with 50% biochar. This is likely due to a reduction in molecular weight during processing, accelerated by the presence of fillers, as well as the catalytic effect of carbonates from the biochar on PLA's ester bonds [18].

The degradation behavior of PLA biochar composites was analyzed by calculating the degree of conversion (α) and kinetic parameters using a combination of isoconversional methods and model-fitting approaches [35,61]. Following the kinetics of such a solid-state reaction may be defined as the mass left during the degradation process at the specific point that is assumed to be the result of the relationship between temperature and the conversion rate. Apart from that, another crucial parameter is the time in which the reaction model accounts for taking the reaction rate of arrival of gas species to fulfill the requirements, i.e., the rate of reaction constant (k) follows Arrhenius equation that describes the relation of the reaction speed with the temperature, the terms besides the Activation Energy (E in kJ/mol), gas constant (8.314 J/mol·K), and pre-exponential factor (A in s^{-1}) that also contribute. Isoconversional methods are a set of techniques that are used to examine reaction kinetics, especially in the thermal degradation of materials. They assume that for a constant conversion level, the reaction rate is only temperature-dependent. They enable the determination of activation energy in the absence of a specific reaction model. The most popular isoconversional methods include differential methods like the Friedman method and integral methods such as Ozawa–Flynn–Wall (OFW), Kissinger–Akahira–Sunose (KAS), and Vyazovkin methods [62–64]. The Friedman method directly calculates activation energy without approximation, while the Vyazovkin method uses a more accurate integral approach, making it well-suited for complex reactions.

Figure 14 illustrates the activation energy (E_α) values with error bars for PLA/SWP550 and PLA/SWP700 composites as a function of the degree of conversion (α), utilizing the previously mentioned isoconversional methods. The average E_α values obtained using the Vyazovkin method from TGA data closely matched those calculated by the Friedman method. In all cases, the variation in E_α suggests that the thermal degradation mechanism is complex, with different processes influencing the kinetics at various stages of degradation.

The E_α for all samples, except PLA/SWP700 5 wt%, shows an initial rise, followed by relatively stable values in the intermediate range and then another increase in the final stage, indicating a complex degradation mechanism. Using both the Friedman and Vyazovkin methods, noticeable differences in E_α were observed across the different ranges of α. For PLA/SWP550 2.5 wt%, the mean E_α is approximately 75.1 kJ/mol (Friedman)

and 78.3 kJ/mol (Vyazovkin) for $\alpha < 0.1$. In the mid-range ($0.1 < \alpha < 0.6$), the E_α increases to 109.9 kJ/mol (Friedman) and 108.1 kJ/mol (Vyazovkin), and for $\alpha > 0.6$, it further rises to 141.8 kJ/mol and 141.3 kJ/mol. For PLA/SWP550 5 wt%, the E_α starts at 73.4 kJ/mol (Friedman) and 72.0 kJ/mol (Vyazovkin) for $\alpha < 0.1$, rising to 93.8 kJ/mol (Friedman) and 94.1 kJ/mol (Vyazovkin) in the intermediate range, and increasing further to 129.7 kJ/mol (Friedman) and 128.5 kJ/mol for $\alpha > 0.6$. For PLA/SWP700 2.5 wt%, the E_α values are around 83.4 kJ/mol (Friedman) and 78.1 kJ/mol (Vyazovkin) for $\alpha < 0.1$, increasing to 100.4 kJ/mol (Friedman) and 98.8 kJ/mol (Vyazovkin) for the intermediate range, and reaching 140.7 kJ/mol (Friedman) and 139.2 kJ/mol for $\alpha > 0.6$. In contrast, PLA/SWP700 5 wt% exhibits higher initial E_α values, averaging 105.9 kJ/mol (Friedman) and 100.9 kJ/mol (Vyazovkin) across all ranges of conversion.

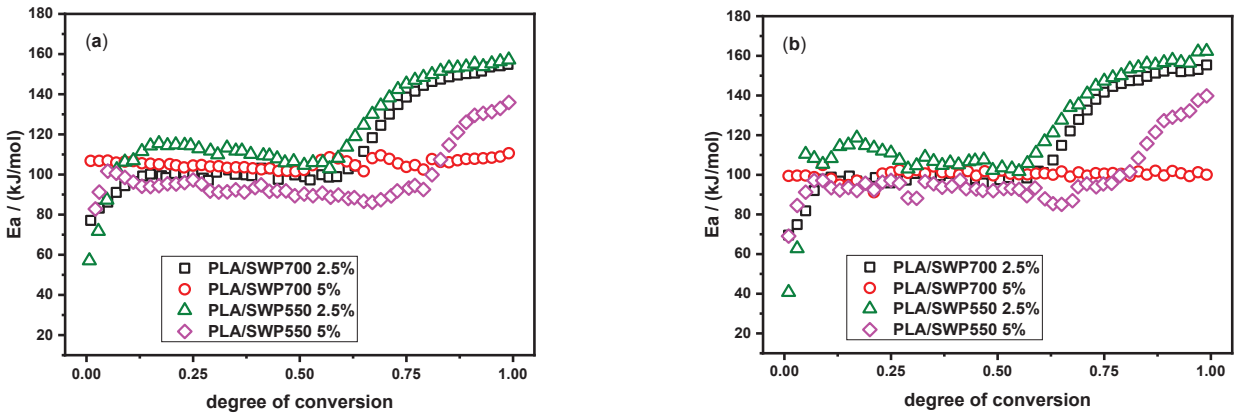

(**a**) (**b**)

Figure 14. The dependence of activation energy (E_α) on the degree of conversion (α) for the thermal degradation of PLA/SWP550 and PLA/SWP700 composites as calculated by (**a**) Friedman method and (**b**) Vyazovkin analysis.

PLA/SWP550 5 wt% shows a lower activation energy compared to PLA/SWP550 2.5 wt%, displaying a thermodynamic behavior that needs less E_α to start its thermal degradation response. The relatively lower activation energy indicates that the presence of SWP550 5 wt% particles impacts the degradation mechanism, which may promote higher susceptibility to thermal breakdown in a reinforced composite. PLA/SWP700 5 wt% shows a notably high activation energy, indicating strong thermal resistance, particularly in the early stages of degradation. The higher E_α suggests that more energy is required to initiate thermal breakdown, which implies that the composite is thermally stable in its initial phases. This stability is consistent with the TGA data in Table 1, where the onset degradation temperature (T0.5) for PLA/SWP700 5 wt% is 216.2 °C, significantly higher than other samples.

The E_α values for α ranges vary, indicating a mixed thermal degradation mechanism; however, it is highly interesting to note that the kinetics of degradation are determined by different mechanisms that are functional at different stages. A lot more importantly, the fact that E_α values went up at low and high levels while staying the same at intermediate levels and then going up again at the end shows that the degradation modes are very complexly connected during decomposition. In this sense, one of the principal contributions of isoconversional analysis is its influence on the selection of an appropriate multistep model.

An analytical model-fitting approach was applied in the study to determine the degradation mechanism and kinetic parameters, including the activation energy E_α, the pre-exponential factor A, and the reaction model $f(\alpha)$, by using multivariate non-linear

regression [61]. In addition, experimental data at four heating rates were compared with theoretical models and sixteen different reaction models were tested for compatibility with the experimental data. This was initially done in a one-step reaction model to account for the main mass loss, assuming average values as derived by isoconversional methods. Unless it fitted well, the methodology was extended by incorporating multiple reaction steps and refining the activation energy, drawing insight also from isoconversional methods, which gave much better results regarding the accuracy of the model.

The three consecutive Cn-Cn-Cn reaction models better described the thermal degradation behavior of PLA/SWP550 2.5 wt%, PLA/SWP550 5 wt%, and PLA/SWP700 2.5 wt%. Figure 15 shows results for selected samples PLA/SWP550 2.5 wt% and PLA/SWP700 2.5 wt%.

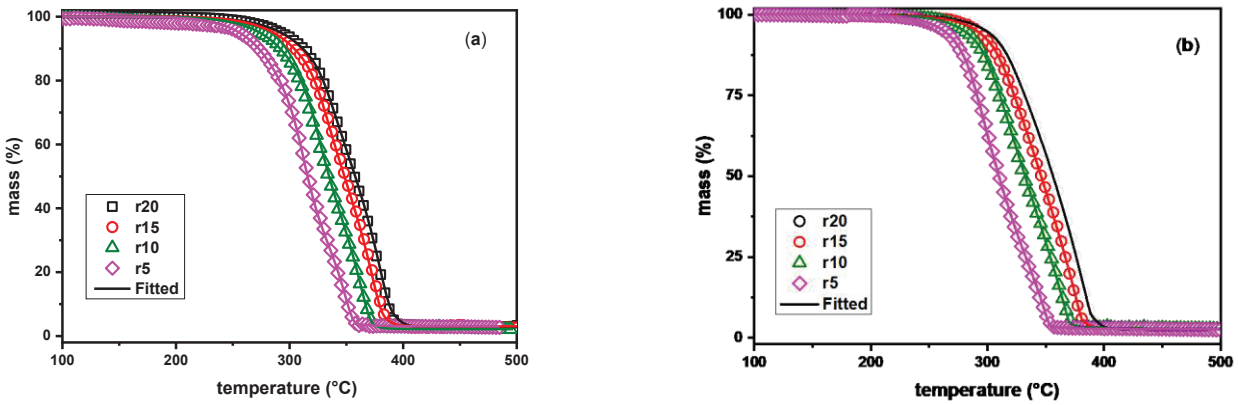

Figure 15. Mass (%) curves for selected (**a**) PLA/SWP550 2.5 wt% and (**b**) PLA/SWP700 2.5 wt% at heating rates of 5, 10, 15, and 20 °C/min in a nitrogen atmosphere (symbols) and corresponding fitted curves using the combination of Cn-Cn-Cn reaction models (Solid lines).

The autocatalytic mechanism n-order (Cn) is mathematically expressed as:

$$f(\alpha) = (1-\alpha)^n(1 + K_{cat}X) \quad (3)$$

where K_{cat} is the autocatalysis rate constant and X is the extent of conversion of the autocatalytic reactions. The three-step model effectively captures the degradation process, providing a more accurate representation of the conversion function compared to a single- or dual-step mechanism. The Cn-Cn-Cn model suggests that the degradation involves multiple stages where autocatalysis plays a key role, with each stage governed by its respective autocatalytic reaction. Using the consecutive Cn models reflects the gradual step-by-step break of the polymer chains in the presence of the biochar. In contrast, the PLA/SWP700 5 wt% sample is well described by a single Cn model, indicating that its degradation is less complex and can be effectively modeled by a simpler reaction mechanism. The PLA/SWP700 5 wt% sample presents one degradation step likely due to the increased carbon content and changes in biochar properties as a result of the higher pyrolysis temperature (700 °C). With the increase in pyrolysis temperature from 550 °C to 700 °C, the biochar undergoes significant structural transformations. During pyrolysis (especially at higher temperatures), biochar undergoes carbonization, which increases its carbon content. This process also reduces the presence of oxygen-containing functional groups like carboxylic acids, which are known to contribute to thermal instability due to their tendency to facilitate degradation reactions [65]. This single-step degradation suggests that the biochar produced at 700 °C creates a more stable interface with PLA, limiting multi-step breakdowns that are typically seen in composites with biochar produced at lower pyrolysis temperatures (like

550 °C). The differences in the number of Cn reactions required for each sample highlight the impact of biochar type and content on the degradation kinetics, with higher biochar content generally leading to more straightforward degradation behavior.

The experimentally determined parameters received in the tested models are listed in Table 7. On the one hand, composites in the PLA/BC data set showed high values of R^2, which means they are strongly correlated with the experiment results and, therefore, are a very good fit for the model. The E_α values inferred from the multi-step mechanism approach compare favorably with those obtained by isoconversional methods (Figure 2). The thermal degradation process of the PLA biochar composites, specifically PLA/SWP700 2.5 wt% and PLA/SWP550 5 wt%, can be conceived as a complex multi-step mechanism due to the variation in activation energy at different stages of degradation. According to the activation energy in the first step (89.8 kJ/mol), PLAB/SWP700 2.5 wt% degradation is associated with simpler processes, and it can be theorized to be the breakdown of weaker molecular bonds or the less stable components of the composite that are initiating the degradation. The second stage, with a higher activation energy of 109.5 kJ/mol and a greater contribution of 0.617, is the stage of more energy-intensive reactions, perhaps by the transformation of more stable polymer regions or the development of stronger interactions between PLA and biochar. The last stage, which has an activation energy of 137.9 kJ/mol, is the sign of the critical period when the most thermally stable parts of the composite are breaking down. In the case of PLA/SWP550 2.5 wt%, a similar sequence is found with a slightly lower activation energy in the first stage, which reflects the cruciality of biochar's low pyrolysis temperature. The first step (87.2 kJ/mol) is the one depicting the easiest initiation of degradation, whereas the second phase (108.3 kJ/mol) denotes the existence of considerable thermal resistance in the intermediate stages. The last step, with an activation energy of 140.4 kJ/mol, reveals a much higher breakdown of substances that demands the use of the most energy. The rising activation energy through the stages of degradation, along with higher Log Kcat values, highlights the role of autocatalysis in accelerating the reaction, especially in later stages. The autocatalytic effect is more pronounced in the biochar-biopolymer composites, where the biochar particles are the catalyst that catalyzes the breakdown of the PLA chains, particularly at higher temperatures. It is the relation between PLA and biochar as well as the properties of biochar itself (such as surface area, porosity, and the existence of functional groups) that alter the degradation way.

Table 7. Activation energy, pre-exponential factor, and reaction order of all studied samples.

Sample	Model	Activation Energy, $E/kJmol^{-1}$	Pre-Exponential Factor, $logA_1/s^{-1}$	Reaction Order/n	Log K_{cat}	Contribution	R^2
PLA/SWP700 2.5%	Cn	89.8	7.5	0.3	0.7	0.242	0.99996
	Cn	109.5	10.0	0.8	0.8	0.617	
	Cn	137.9	11.2	1.6	1.3	0.141	
PLA/SWP700 5%	Cn	104.9	6.9	1.2	0.9	1.000	0.99990
PLA/SWP550 2.5%	Cn	87.2	6.4	0.4	0.3	0.266	0.99973
	Cn	108.3	9.8	0.7	0.6	0.574	
	Cn	140.4	11.0	1.7	1.0	0.160	
PLA/SWP550 5%	Cn	79.0	5.3	0.3	0.7	0.251	0.99954
	Cn	103.6	9.2	0.6	0.9	0.501	
	Cn	133.64	10.2	1.3	1.1	0.248	

The introduction of 5 wt% biochar to the PLA composites has a much more evident change in the thermal degradation behavior, which is evident through low Eα values and a

corresponding increase in the decomposition rate constant. This accelerated decomposition might be referred to as the higher the biochar content, which acts as a catalyst for the easier thermal breakdown; due to the more BC particles, the quicker degradation starts. The A is also lower for PLA/BC 5 wt% composites in comparison to PLA/BC 2.5 wt%. This decrease in A is due to the reduced Eα and the fact that fewer energies are needed for the degradation reactions in the higher biochar content composite. Additionally, the larger rate constant for PLA/BC 5 wt% suggests that the degradation process is happening more rapidly. This comes from the fact that the extra biochar has led to a huge promoter in the surface area and thus more catalytic activity, permitting faster polymer chain scission and hence the acceleration of the overall thermal degradation process. The explanation for this is that the reduction in the activation energy additionally means that the energy barriers for degradation are removed, making the composite breakdown easier by thermal stress.

In comparison, PLA/BC 2.5 wt%, with higher Eα and pre-exponential factor values, demonstrates greater thermal stability. The higher energy barrier for degradation in this composite suggests that fewer polymer chains are breaking down at lower temperatures, resulting in slower overall thermal decomposition. This highlights the inverse relationship between biochar content and thermal stability, where increasing BC content enhances degradation but reduces the composite's resistance to thermal breakdown.

This behavior emphasizes the dual role of biochar in PLA composites: while it reinforces the material at lower concentrations, providing stability and improved thermal properties, higher concentrations act as catalysts, promoting quicker degradation by lowering the activation energy and increasing the rate constantly.

4. Conclusions

PLA bio-composites containing two different types of biochar, SWP550 and SWP700, which have been produced by pyrolysis of softwood pellets at 550 and 700 °C, were prepared by in situ ROP. From the TEM micrographs, it was found that this technique is appropriate for bio-composite preparation since it produces a sufficiently good dispersion of BC in the polymeric matrix. GPC measurements verified that PLA with high molecular weight can be synthesized, which has been progressively reduced in the bio-composites as biochar content increased. This reduction was attributed to the strong interactions between BC and PLA or due to the ability of BC's hydroxyl groups to act as initiators for ring-opening polymerization of lactide. The alteration in the ester group vibrations that are recorded in FTIR spectra indicates the interactions between BC and PLA polymeric matrix. These interactions led to a systematic deceleration of segmental mobility of bio-composites in combination with the elevation of the T_g. Furthermore, the aforementioned results are responsible for the slight suppression of the PLA bio-composites crystallizability. Bio-composites with SWP700 show a slightly stronger effect compared to SWP550. The different load of biochar and in different pyrolysis temperatures enhances slightly tensile strength at low BC content (1 wt%) while at higher loading, mechanical properties deteriorated. This could be attributed to the lower molar mass of the bio-composites. The loading of biochar, in both cases, reduced the hydrolysis rates of PLA bio-composites due to the slightly higher hydrophobicity of these samples. From TGA analysis, it was found that different types of biochar exhibit diverse effects on PLA bio-composite thermal properties.

Author Contributions: Methodology, validation, formal analysis, investigation, K.P., P.A.K., E.T., K.T., O.M, A.K., A.D.A., K.C. and D.N.B., writing—original draft preparation, K.P., P.A.K., E.T., K.T., O.M., A.K., A.D.A., K.C. and D.N.B., writing—review and editing, K.P., P.A.K., E.T., K.T., O.M., A.K.,

A.D.A., K.C. and D.N.B., supervision, D.N.B.; funding acquisition, O.M. and D.N.B. All authors have read and agreed to the published version of the manuscript.

Funding: This research was funded by the European Community's Horizon 2020 Framework Program H2020 (grant number 952941, Accessed on 1 January 2020, Project: BIOMAC, European Sustainable BIObased nanoMAterials Community; https://www.biomac-oitb.eu).

Institutional Review Board Statement: Not applicable.

Data Availability Statement: All the data of this study are included in the manuscript.

Acknowledgments: The authors would like to express their gratitude to both Eleni Pavlidou, School of Physics, AUTh, and Chrysanthi Papoulia, School of Physics, AUTh for the SEM observations, as well as to Nikolaos Nikolaidis of the Laboratory of Chemistry and Technology of Polymers and Dyes, Department of Chemistry AUTh for the color measurements. Furthermore, the authors gratefully acknowledge Alexandra Zamboulis, Department of Chemistry, AUTh for NMR measurements.

Conflicts of Interest: The authors declare no conflicts of interest.

References

1. Bachmann, M.; Zibunas, C.; Hartmann, J.; Tulus, V.; Suh, S.; Guillén-gosálbez, G.; Bardow, A. Towards Circular Plastics within Planetary Boundaries. *Nat. Sustain.* **2023**, *6*, 599–610. [CrossRef]
2. Balla, E.; Daniilidis, V.; Karlioti, G.; Kalamas, T.; Stefanidou, M.; Bikiaris, N.D.; Vlachopoulos, A.; Koumentakou, I.; Bikiaris, D.N. Poly(Lactic Acid): A Versatile Biobased Polymer for the Future with Multifunctional Properties-from Monomer Synthesis, Polymerization Techniques and Molecular Weight Increase to PLA Applications. *Polymers* **2021**, *13*, 1822. [CrossRef] [PubMed]
3. Bikiaris, N.D.; Koumentakou, I.; Samiotaki, C.; Meimaroglou, D.; Varytimidou, D.; Karatza, A.; Kalantzis, Z.; Roussou, M.; Bikiaris, R.D.; Papageorgiou, G.Z. Recent Advances in the Investigation of Poly(Lactic Acid) (PLA) Nanocomposites: Incorporation of Various Nanofillers and Their Properties and Applications. *Polymers* **2023**, *15*, 1196. [CrossRef]
4. Vlachopoulos, A.; Karlioti, G.; Balla, E.; Daniilidis, V.; Kalamas, T.; Stefanidou, M.; Bikiaris, N.D.; Christodoulou, E.; Koumentakou, I.; Karavas, E.; et al. Poly(Lactic Acid)-Based Microparticles for Drug Delivery Applications: An Overview of Recent Advances. *Pharmaceutics* **2022**, *14*, 359. [CrossRef] [PubMed]
5. Cheng, Y.; Deng, S.; Chen, P.; Ruan, R. Polylactic Acid (PLA) Synthesis and Modifications: A Review. *Front. Chem. China* **2009**, *4*, 259–264. [CrossRef]
6. Bioplastics Market Data. Available online: https://www.european-bioplastics.org/market/ (accessed on 3 September 2021).
7. Androsch, R.; Iqbal, H.M.N.; Schick, C. Non-Isothermal Crystal Nucleation of Poly (l-Lactic Acid). *Polymer* **2015**, *81*, 151–158. [CrossRef]
8. Armentano, I.; Bitinis, N.; Fortunati, E.; Mattioli, S.; Rescignano, N.; Verdejo, R.; Lopez-Manchado, M.A.; Kenny, J.M. Multifunctional Nanostructured PLA Materials for Packaging and Tissue Engineering. *Prog. Polym. Sci.* **2013**, *38*, 1720–1747. [CrossRef]
9. Mortazavi, B.; Hassouna, F.; Laachachi, A.; Rajabpour, A.; Ahzi, S.; Chapron, D.; Toniazzo, V.; Ruch, D. Experimental and Multiscale Modeling of Thermal Conductivity and Elastic Properties of PLA/Expanded Graphite Polymer Nanocomposites. *Thermochim. Acta* **2013**, *552*, 106–113. [CrossRef]
10. Saeidlou, S.; Huneault, M.A.; Li, H.; Park, C.B. Poly(Lactic Acid) Crystallization. *Prog. Polym. Sci.* **2012**, *37*, 1657–1677. [CrossRef]
11. Pradhan, R.; Misra, M.; Erickson, L.; Mohanty, A. Compostability and Biodegradation Study of PLA-Wheat Straw and PLA-Soy Straw Based Green Composites in Simulated Composting Bioreactor. *Bioresour. Technol.* **2010**, *101*, 8489–8491. [CrossRef]
12. Trivedi, A.K.; Gupta, M.K.; Singh, H. PLA Based Biocomposites for Sustainable Products: A Review. *Adv. Ind. Eng. Polym. Res.* **2023**, *6*, 382–395. [CrossRef]
13. Sha, L.; Chen, Z.; Chen, Z.; Zhang, A.; Yang, Z. Polylactic Acid Based Nanocomposites: Promising Safe and Biodegradable Materials in Biomedical Field. *Int. J. Polym. Sci.* **2016**, *2016*, 686915411. [CrossRef]
14. Bartoli, M.; Arrigo, R.; Malucelli, G.; Tagliaferro, A.; Duraccio, D. Recent Advances in Biochar Polymer Composites. *Polymers* **2022**, *14*, 2506. [CrossRef] [PubMed]
15. Arrigo, R.; Bartoli, M.; Malucelli, G. Poly(Lactic Acid)–Biochar Biocomposites: Effect of Processing and Filler Content on Rheological. *Polymers* **2020**, *12*, 892. [CrossRef] [PubMed]
16. Hernandez-Charpak, Y.D.; Trabold, T.A.; Lewis, C.L.; Diaz, C.A. Biochar-Filled Plastics: Effect of Feedstock on Thermal and Mechanical Properties. *Biomass Convers. Biorefinery* **2022**, *12*, 4349–4360. [CrossRef]

17. Kane, S.; Van Roijen, E.; Ryan, C.; Miller, S. Reducing the Environmental Impacts of Plastics While Increasing Strength: Biochar Fillers in Biodegradable, Recycled, and Fossil-Fuel Derived Plastics. *Compos. Part C Open Access* **2022**, *8*, 100253. [CrossRef]
18. Zouari, M.; Devallance, D.B.; Marrot, L. Effect of Biochar Addition on Mechanical Properties, Thermal Stability, and Water Resistance of Hemp-Polylactic Acid (PLA) Composites. *Materials* **2022**, *15*, 2271. [CrossRef] [PubMed]
19. Vidal, J.L.; Yavitt, B.M.; Wheeler, M.D.; Kolwich, J.L.; Donovan, L.N.; Sit, C.S.; Hatzikiriakos, S.G.; Jalsa, N.K.; MacQuarrie, S.L.; Kerton, F.M. Biochar as a Sustainable and Renewable Additive for the Production of Poly(ε-Caprolactone) Composites. *Sustain. Chem. Pharm.* **2022**, *25*, 100586. [CrossRef]
20. Aboughaly, M.; Babaei-Ghazvini, A.; Dhar, P.; Patel, R.; Acharya, B. Enhancing the Potential of Polymer Composites Using Biochar as a Filler: A Review. *Polymers* **2023**, *15*, 3981. [CrossRef]
21. Wang, J.; Wang, S. Preparation, Modification and Environmental Application of Biochar: A Review. *J. Clean. Prod.* **2019**, *227*, 1002–1022. [CrossRef]
22. Qambrani, N.A.; Rahman, M.M.; Won, S.; Shim, S.; Ra, C. Biochar Properties and Eco-Friendly Applications for Climate Change Mitigation, Waste Management, and Wastewater Treatment: A Review. *Renew. Sustain. Energy Rev.* **2017**, *79*, 255–273. [CrossRef]
23. Zhang, Q.; Khan, M.U.; Lin, X.; Cai, H.; Lei, H. Temperature Varied Biochar as a Reinforcing Filler for High-Density Polyethylene Composites. *Compos. Part B Eng.* **2019**, *175*, 107151. [CrossRef]
24. Das, C.; Tamrakar, S.; Kiziltas, A.; Xie, X. Incorporation of Biochar to Improve Mechanical, Thermal and Electrical Properties of Polymer Composites. *Polymers* **2021**, *13*, 2663. [CrossRef] [PubMed]
25. Zhang, Q.; Lei, H.; Cai, H.; Han, X.; Lin, X.; Qian, M.; Zhao, Y.; Huo, E.; Villota, E.M.; Mateo, W. Improvement on the Properties of Microcrystalline Cellulose/Polylactic Acid Composites by Using Activated Biochar. *J. Clean. Prod.* **2020**, *252*, 119898. [CrossRef]
26. She, D.; Dong, J.; Zhang, J.; Liu, L.; Sun, Q.; Geng, Z.; Peng, P. Development of Black and Biodegradable Biochar/Gutta Percha Composite Films with High Stretchability and Barrier Properties. *Compos. Sci. Technol.* **2019**, *175*, 1–5. [CrossRef]
27. Giorcelli, M.; Khan, A.; Pugno, N.M.; Rosso, C.; Tagliaferro, A. Biochar as a Cheap and Environmental Friendly Filler Able to Improve Polymer Mechanical Properties. *Biomass Bioenergy* **2019**, *120*, 219–223. [CrossRef]
28. Tengku Yasim-Anuar, T.A.; Yee-Foong, L.N.; Lawal, A.A.; Ahmad Farid, M.A.; Mohd Yusuf, M.Z.; Hassan, M.A.; Ariffin, H. Emerging Application of Biochar as a Renewable and Superior Filler in Polymer Composites. *RSC Adv.* **2022**, *12*, 13938–13949. [CrossRef] [PubMed]
29. Infurna, G.; Botta, L.; Ingargiola, I.; Maniscalco, M.; Caputo, G.; Dintcheva, N.T. Biochar from Digestate Pyrolysis as a Filler for Biopolymer Blends: Effect of Blend Composition. *J. Polym. Environ.* **2023**, *32*, 1921–1963. [CrossRef]
30. Papadopoulou, K.; Klonos, P.A.; Kyritsis, A.; Mašek, O.; Wurzer, C.; Tsachouridis, K.; Anastasiou, A.D.; Bikiaris, D.N. Synthesis and Study of Fully Biodegradable Composites Based on Poly(Butylene Succinate) and Biochar. *Polymers* **2023**, *15*, 1049. [CrossRef]
31. Papadopoulou, K.; Ainali, N.M.; Mašek, O.; Bikiaris, D.N. Biochar as a UV Stabilizer: Its Impact on the Photostability of Poly(Butylene Succinate) Biocomposites. *Polymers* **2024**, *16*, 3080. [CrossRef] [PubMed]
32. Mašek, O.; Wolfram, B.; Roy-Poirier, A.; Lowe, W.; Peters, C.; Brownsort, P.; Mignard, D.; Pritchard, C.; Masek, O.; Buss, W.; et al. Consistency of Biochar Properties over Time and Production Scales: A Characterisation of Standard Materials. *J. Anal. Appl. Pyrolysis* **2018**, *132*, 200–210. [CrossRef]
33. Herrmann, G. *Dynamics of Composite Materials*, 1st ed.; Schönhals, A., Szymoniak, P., Eds.; Springer: Berlin, Germany, 2022; Volume 5, ISBN 9783030897222.
34. Savvidis, G.; Karanikas, V.; Zarkogianni, M.; Eleftheriadis, I.; Nikolaidis, N.; Tsatsaroni, E. Screen-Printing of Cotton with Natural Pigments: Evaluation of Color and Fastness Properties of the Prints. *J. Nat. Fibers* **2017**, *14*, 326–334. [CrossRef]
35. Vyazovkin, S.; Burnham, A.K.; Criado, J.M.; Pérez-Maqueda, L.A.; Popescu, C.; Sbirrazzuoli, N. ICTAC Kinetics Committee Recommendations for Performing Kinetic Computations on Thermal Analysis Data. *Thermochim. Acta* **2011**, *520*, 1–19. [CrossRef]
36. Available online: https://kinetics.netzsch.com/en/ (accessed on 6 September 2018).
37. Papadopoulou, K.; Tarani, E.; Ainali, N.M.; Chrissafis, K.; Wurzer, C.; Mašek, O.; Bikiaris, D.N. The Effect of Biochar Addition on Thermal Stability and Decomposition Mechanism of Poly(Butylene Succinate) Bionanocomposites. *Molecules* **2023**, *28*, 5330. [CrossRef]
38. Jurczyk, S.; Andrzejewski, J.; Piasecki, A.; Musioł, M.; Rydz, J.; Kowalczuk, M. Mechanical and Rheological Evaluation of Polyester-Based Composites Containing Biochar. *Polymers* **2024**, *16*, 1231. [CrossRef]
39. Makri, S.P.; Xanthopoulou, E.; Valera, M.A.; Mangas, A.; Marra, G.; Ruiz, V.; Koltsakidis, S.; Tzetzis, D.; Zoikis Karathanasis, A.; Deligkiozi, I.; et al. Poly(Lactic Acid) Composites with Lignin and Nanolignin Synthesized by In Situ Reactive Processing. *Polymers* **2023**, *15*, 2386. [CrossRef] [PubMed]
40. Pérez, J.M.; Ruiz, C.; Fernández, I. Synthesis of a Biodegradable PLA: NMR Signal Deconvolution and End-Group Analysis. *J. Chem. Educ.* **2022**, *99*, 1000–1007. [CrossRef]

41. Inkinen, S.; Hakkarainen, M.; Albertsson, A.C.; Södergård, A. From Lactic Acid to Poly(Lactic Acid) (PLA): Characterization and Analysis of PLA and Its Precursors. *Biomacromolecules* **2011**, *12*, 523–532. [CrossRef] [PubMed]
42. Infurna, G.; Botta, L.; Maniscalco, M.; Morici, E.; Caputo, G.; Marullo, S.; D'Anna, F.; Dintcheva, N.T. Biochar Particles Obtained from Agricultural Carob Waste as a Suitable Filler for Sustainable Biocomposite Formulations. *Polymers* **2022**, *14*, 3075. [CrossRef] [PubMed]
43. de Jesus Duarte, S.; Glaser, B.; Paiva de Lima, R.; Pelegrino Cerri, C.E. Chemical, Physical, and Hydraulic Properties as Affected by One Year of *Miscanthus* Biochar Interaction with Sandy and Loamy Tropical Soils. *Soil Syst.* **2019**, *3*, 24. [CrossRef]
44. Füllbrandt, M.; Purohit, P.J.; Schönhals, A. Combined FTIR and Dielectric Investigation of Poly(Vinyl Acetate) Adsorbed on Silica Particles. *Macromolecules* **2013**, *46*, 4626–4632. [CrossRef]
45. Terzopoulou, Z.; Klonos, P.A.; Kyritsis, A.; Tziolas, A.; Avgeropoulos, A.; Papageorgiou, G.Z.; Bikiaris, D.N. Interfacial Interactions, Crystallization and Molecular Mobility in Nanocomposites of Poly(Lactic Acid) Filled with New Hybrid Inclusions Based on Graphene Oxide and Silica Nanoparticles. *Polymer* **2019**, *166*, 1–12. [CrossRef]
46. Wurm, A.; Ismail, M.; Kretzschmar, B.; Pospiech, D.; Schick, C. Retarded Crystallization in Polyamide/Layered Silicates Nanocomposites Caused by an Immobilized Interphase. *Macromolecules* **2010**, *43*, 1480–1487. [CrossRef]
47. Klonos, P.A.; Papadopoulos, L.; Papageorgiou, G.Z.; Kyritsis, A.; Pissis, P.; Bikiaris, D.N. Interfacial Interactions, Crystallization, and Molecular Dynamics of Renewable Poly(Propylene Furanoate) in Situ Filled with Initial and Surface Functionalized Carbon Nanotubes and Graphene Oxide. *J. Phys. Chem. C* **2020**, *124*, 10220–10234. [CrossRef]
48. Lin, Y.; Liu, L.; Xu, G.; Zhang, D.; Guan, A.; Wu, G. Interfacial Interactions and Segmental Dynamics of Poly(Vinyl Acetate)/Silica Nanocomposites. *J. Phys. Chem. C* **2015**, *119*, 12956–12966. [CrossRef]
49. Klonos, P.A.; Bikiaris, R.D.; Terzopoulou, Z.; Mouchlianiti, K.; Tsachouridis, K.; Anastasiou, A.D.; Kyritsis, A.; Kyzas, G.Z. Structure-Properties Relationships in New Polymer Nanocomposites Based on the Renewable Poly(Butylene Succinate) Filled with Low Amounts of Nanoparticles of 1-3D Geometries. *Polymer* **2024**, *296*, 126841. [CrossRef]
50. Madkour, S.; Szymoniak, P.; Heidari, M.; Von Klitzing, R.; Schönhals, A. Unveiling the Dynamics of Self-Assembled Layers of Thin Films of Poly(Vinyl Methyl Ether) (PVME) by Nanosized Relaxation Spectroscopy. *ACS Appl. Mater. Interfaces* **2017**, *9*, 7535–7546. [CrossRef] [PubMed]
51. Črešnar, K.P.; Zemljič, L.F.; Papadopoulos, L.; Terzopoulou, Z.; Zamboulis, A.; Klonos, P.A.; Bikiaris, D.N.; Kyritsis, A.; Pissis, P. Effects of Ag, ZnO and TiO_2 Nanoparticles at Low Contents on the Crystallization, Semicrystalline Morphology, Interfacial Phenomena and Segmental Dynamics of PLA. *Mater. Today Commun.* **2021**, *27*, 102192. [CrossRef]
52. Böhmer, R.; Ngai, K.; Angell, C.A.; Plazek, D.J. Nonexponential Relaxations in Strong and Fragile Glass Formers. *J. Chem. Phys.* **1993**, *99*, 4201–4209. [CrossRef]
53. Matykiewicz, D. Biochar as an Effective Filler of Carbon Fiber Reinforced Bio-Epoxy Composites. *Processes* **2020**, *8*, 724. [CrossRef]
54. Ho, M.P.; Lau, K.T.; Wang, H.; Hui, D. Improvement on the Properties of Polylactic Acid (PLA) Using Bamboo Charcoal Particles. *Compos. Part B Eng.* **2015**, *81*, 14–25. [CrossRef]
55. Zouari, M.; Mikuljan, M.; Schwarzkopf, M. Impact of Biochar on the Fungal Decay Resistance of Hemp-Polylactic Acid Composites against Wood Basidiomycetes. *Front. Mater.* **2023**, *10*, 1–10. [CrossRef]
56. Zaaba, N.F.; Jaafar, M. A Review on Degradation Mechanisms of Polylactic Acid: Hydrolytic, Photodegradative, Microbial, and Enzymatic Degradation. *Polym. Eng. Sci.* **2020**, *60*, 2061–2075. [CrossRef]
57. Botta, L.; Teresi, R.; Titone, V.; Salvaggio, G.; La Mantia, F.P.; Lopresti, F. Use of Biochar as Filler for Biocomposite Blown Films: Structure-Processing-Properties Relationships. *Polymers* **2021**, *13*, 3953. [CrossRef]
58. McKeown, P.; Jones, M.D. The Chemical Recycling of PLA: A Review. *Sustain. Chem.* **2020**, *1*, 1–22. [CrossRef]
59. Cappello, M.; Rossi, D.; Filippi, S.; Cinelli, P.; Seggiani, M. Wood Residue-Derived Biochar as a Low-Cost, Lubricating Filler in Poly(Butylene Succinate-Co-Adipate) Biocomposites. *Materials* **2023**, *16*, 570. [CrossRef]
60. Haeldermans, T.; Samyn, P.; Cardinaels, R.; Vandamme, D.; Vanreppelen, K.; Cuypers, A.; Schreurs, S. Poly(Lactic Acid) Bio-Composites Containing Biochar Particles: Effects of Fillers and Plasticizer on Crystallization and Thermal Properties. *Express Polym. Lett.* **2021**, *15*, 343–360. [CrossRef]
61. Tarani, E.; Chrissafis, K. Isoconversional Methods: A Powerful Tool for Kinetic Analysis and the Identification of Experimental Data Quality. *Thermochim. Acta* **2024**, *733*, 179690. [CrossRef]
62. Budrugeac, P.; Segal, E.; Pérez-Maqueda, L.A.; Criado, J.M. The Use of the IKP Method for Evaluating the Kinetic Parameters and the Conversion Function of the Thermal Dehydrochlorination of PVC from Non-Isothermal Data. *Polym. Degrad. Stab.* **2004**, *84*, 311–320. [CrossRef]
63. Friedman, H.L. Kinetics of Thermal Degradation of Char-Forming Plastics from Thermogravimetry. Application to a Phenolic Plastic. *J. Polym. Sci. Part C Polym. Symp.* **2007**, *6*, 183–195. [CrossRef]

64. Vyazovkin, S. Evaluation of Activation Energy of Thermally Stimulated Solid-State Reactions under Arbitrary Variation of Temperature. *J. Comput. Chem.* **1997**, *18*, 393–402. [CrossRef]
65. Tomczyk, A.; Sokołowska, Z.; Boguta, P. Biochar Physicochemical Properties: Pyrolysis Temperature and Feedstock Kind Effects. *Rev. Environ. Sci. Biotechnol.* **2020**, *19*, 191–215. [CrossRef]

polymers

MDPI

Article

Avocado Seed Starch-Based Films Reinforced with Starch Nanocrystals

Pedro Francisco Muñoz-Gimena [1], Alejandro Aragón-Gutiérrez [2], Enrique Blázquez-Blázquez [1], Marina Patricia Arrieta [3], Gema Rodríguez [1], Laura Peponi [1,*] and Daniel López [1,*]

[1] Instituto de Ciencia y Tecnología de Polímeros (ICTP-CSIC), C/Juan de la Cierva 3, 28006 Madrid, Spain; pfmunoz@ictp.csic.es (P.F.M.-G.); enrique.blazquez@ictp.csic.es (E.B.-B.); gema@ictp.csic.es (G.R.)
[2] Grupo de Tecnología de Materiales y Envases, Instituto Tecnológico del Embalaje, Transporte y Logística, ITENE, Unidad Asociada Al CSIC, C/Albert Einstein 1, Paterna, 46980 Valencia, Spain; alejandro.aragon@itene.com
[3] Departamento de Ingeniería Química Industrial y del Medio Ambiente, Escuela Técnica Superior de Ingenieros Industriales, Universidad Politécnica de Madrid (ETSII-UPM), C/José Gutiérrez Abascal 2, 28006 Madrid, Spain; m.arrieta@upm.es
* Correspondence: lpeponi@ictp.csic.es (L.P.); daniel.l.g@csic.es (D.L.); Tel.: +34-915-622-900 (L.P. & D.L.)

Abstract: Biopolymers derived from biomass can provide the advantages of both biodegradability and functional qualities from a circular economy point of view, where waste is transformed into raw material. In particular, avocado seeds can be considered an interesting residue for biobased packaging applications due to their high starch content. In this work, avocado seed starch (ASS)-based films containing different glycerol concentrations were prepared by solvent casting. Films were also reinforced with starch nanocrystals (SNCs) obtained through the acid hydrolysis of ASS. The characterization of the extracted starch and starch nanocrystals by scanning electron microscopy, X-ray diffraction, and thermogravimetric analysis has been reported. Adding 1% of SNCs increased elastic modulus by 112% and decreased water vapor permeability by 30% with respect to neat matrix. Interestingly, the bioactive compounds from the avocado seed provided the films with high antioxidant capacity. Moreover, considering the long time required for traditional plastic packaging to degrade, all of the ASS-based films disintegrated within 48 h under lab-scale composting conditions. The results of this work support the valorization of food waste byproducts and the development of reinforced biodegradable materials for potential use as active food packaging.

Keywords: starch; nanocrystals; avocado; seed; antioxidant; biobased films; active packaging

1. Introduction

Plastics are synthetic polymeric materials derived from fossil hydrocarbons. These lightweight, strong, durable, and low-cost materials have become an integral part of everyday life. However, the durability that makes them so appealing becomes a problem as they are highly resistant to degradation in open environments. In this respect, biopolymers are a promising solution as they are obtained from renewable resources and, if disposed of properly, reduce the environmental impact compared to synthetic polymers. Their use can therefore contribute to sustainable development [1]. Of the over 400 million tons of plastic currently produced annually, biopolymers represent approximately 0.5%, with production capacity set to increase from around 2.18 million tons in 2023 to approximately 7.43 million tons in 2028 [2].

The food industry produces large volumes of waste, which results in potential disposal and severe pollution problems. These wastes are also rich in carbon content and can be attractive renewable substrates for the production of added-value products [3]. Avocado (*Persea americana*) is a fruit belonging to the *Lauraceae* family, native to Mexico

and Latin America, with Mexico currently being the largest producer worldwide [4]. Avocado peel and seeds are commonly discarded as waste during the processing of avocado pulp. An estimated 520,000–720,000 metric tons of avocado seeds are produced annually worldwide, accounting for 13–18% of the fruit produced annually, estimated to be more than 4 million metric tons [5]. In general, avocado seeds are composed of water (51–58%), starch (27.5–29.8%), sugars (2.2–3.5%), proteins (2.3–2.4%), ash (1.2–1.3%), and crude fiber (3.6–4.1%) [6] and several bioactive compounds such as β-sitosterol and octadecenoic acid. The valorization of these seeds can be performed by the extraction of starch, protein, and phytochemicals, which can be utilized in different industrial applications, including biomaterials, regenerated fibers, pharmaceutical and cosmetic products, animal feed, and biofertilizers [5].

Over recent decades, starch has been actively researched as a potential biopolymer in food packaging applications. Several associated advantages include abundance, biocompatibility, non-toxicity, low cost, biodegradability, and air stability [7]. Native starch granules, upon their botanical source, exhibit a broad range of sizes, size distributions, forms, starch extraction conditions, and chemical composition [8]. Moreover, starch sources can influence films' properties, enhancing their conceivable applications. However, the brittleness and crystallinity of native starch films greatly limit their application in food packaging [9]. This can be overcome using plasticizers such as glycerol, sorbitol, and urea, frequently incorporated into starch-based bioplastics [10]. To create thermoplastic starch (TPS), the molecular structure should become disordered and the granules gelatinized. During the thermoplastic starch production process, water contained in starch and the addition of plasticizers decreases the internal starch hydrogen bonding, increasing the flexibility of the films [11]. Moreover, plasticizers lower the glass transition temperature and can effectively restrain starch retrogradation, resulting in better packaging qualities [12]. TPS can be achieved via (i) casting from an aqueous system after starch gelatinization, (ii) thermocompression directly from a starch/plasticizer premixture, and (iii) extrusion, i.e., mixing and shear force action at high temperatures [13]. While the latter methods are especially preferred when processing large quantities of material, like on an industrial scale, solvent casting offers a simple and cost-effective method for film preparation, making it more suitable for small laboratory-scale production.

However, starch exhibits some limitations as a stand-alone film material, such as inferior barrier, thermal, and mechanical properties compared to other commercial polymeric counterparts [14]. Common strategies used to enhance starch-based film performance and processability include creating polymeric blends, coating with high-barrier materials, employing multilayered films containing high-barrier films, chemically modifying natural biopolymers, or adding fillers to form composites [15]. In this context, the addition of mineral or organic fillers can be used to create novel, low-cost, biodegradable polymers with reinforced properties. Starch nanocrystals (SNCs) constitute crystalline fragments produced through the disintegration of the amorphous sections in starch granules. The crystalline lamellae, which are more resistant to hydrolysis, can be subjected to extended-time hydrolysis resulting in nanocrystals with dimensions in the nanometer scale (<100 nm) in at least one dimension [16]. Therefore, SNCs can be obtained through the acid hydrolysis (typically using sulfuric acid) of native starch granules by strictly monitoring the temperature, acid and starch concentrations, hydrolysis duration, and stirring speed [17].

Oxidation is one of the main degradative processes that lowers food quality. Packaging with a regulated low-oxygen atmosphere or adding antioxidants to food products are two popular methods for reducing oxidation [18]. Active packaging offers an alternative to these traditional approaches, as it allows the packaging material itself to release antioxidants into the foodstuff. These additives thereby extend shelf life, improve product safety, and can perform additional functions, such as flavor enhancement and gas scavenging [19]. For example, essential oils have a high popularity in film production as the migration of their active compounds can provide improved barrier and optical properties and antioxidant and antibacterial activities [20]. On this note, avocado seeds have been found to exhibit

high antioxidant activity attributed to the high content of phenolic compounds and ascorbic acid [21].

Current research on starch-based film production has shifted from traditional starches (i.e., potato, maize, and rice) to non-conventional starch sources such as avocado seeds. Although the use of starch from traditional sources is well established, starch obtained from avocado seeds has two important advantages, which are intended to be highlighted in this study: on the one hand, the use of a waste product from the food industry that is constantly growing; on the other hand, and more importantly, the composition of the avocado seeds allows the incorporation of intrinsic antioxidant and antimicrobial compounds into the developed films.

The main aim of this study was to produce plasticized starch-based films using avocado seeds as the starch source and to reinforce them with starch nanocrystals. Before processing the films, a preliminary study was carried out to determine the properties of ASS and SNCs. While increasing the plasticizer concentration increases film flexibility, elastic modulus, and elongation, it also decreases the film's barrier properties. Therefore, ASS was combined with varying glycerol concentrations to compare the properties of the films in search of a compromise between all properties. As reinforcing agents, SNCs obtained through acid hydrolysis were added in different amounts to the preferred TPS formulation (Gly35) to reduce film permeability. Finally, the mechanical, morphological, thermal, antioxidant, barrier, and biodegradation properties of all of the developed films were studied and evaluated to establish the best composition.

2. Materials and Methods

2.1. Reagents and Materials

The avocado seeds obtained from avocado (*Persea americana Miller*, cv. Hass) fruits were purchased in a local grocery store in Madrid, Spain. Glycerol (purity $\geq$ 99%, CAS 56-81-5), sodium bisulfite (CAS 7631-90-5) and iodine (CAS 7553-56-2) were acquired from Sigma-Aldrich (St. Louis, MO, USA). Potassium iodide was purchased from Quimicen SA (Madrid, Spain), 2,2-difenil-1-picrylhydrazyl (DPPH), and sulfuric acid (CAS 76664-93-9) was obtained from Scharlau (Barcelona, Spain).

2.2. Avocado Starch Production

Starch was extracted from avocado (*Persea americana Miller*, cv. Hass) seeds, based on a modified procedure described by Chel-Guerrero et al. [22]. Briefly, seeds were removed from fresh avocados and washed with water. Then, 100 g of seeds were peeled, cut into small pieces, and introduced in a sodium bisulfite solution ($NaHSO_3$) (1500 ppm) 1:5 (v/w) to prevent oxidation. The seeds were milled in $NaHSO_3$ solution using an IKA Multidrive blender (Staufen, Germany) at 10,000 rpm for 1 min followed by 3 min at 3000 rpm (10 s running and 5 s rest). The resultant suspension was filtered using a 50 μm mesh sieve. The starch was washed with distilled water and dried using vacuum filtration. The resulting avocado seed starch (ASS) was stored in a sealed container at room temperature.

2.3. Avocado Starch Nanocrystal Elaboration

Avocado starch nanocrystals were produced by the acid hydrolysis of the previously prepared ASS, using a modified version of the procedure described by Angellier et al. [23]. The starch (10 g) was dispersed in 200 mL of 3.16 M H_2SO_4 solution inside a 250 mL glass tank reactor equipped with a magnetic stirrer. The reaction was left stirring for 5 days at 40 °C and 250 rpm, to hydrolyze the amorphous fraction. The reactor temperature was kept lower than the gelatinization temperature and argon was bubbled into the suspension to reduce oxidation. After 5 days, the suspension was diluted with 2 L of distilled water, stirred, and left to decant. The precipitate was re-suspended in distilled water and centrifuged for 10 min at 10,000 rpm. The washing process was repeated until it reached a neutral pH (5.5). The nanocrystals were freeze-dried and stored in a dry chamber at room temperature.

2.4. Avocado-Starch-Based Film Formation

ASS-based films were all prepared from a film-forming solution of 1% wt. avocado starch powder (0.3 g starch in 30 mL distillate water). The additives were added in relation to the mass of avocado starch and expressed in parts per hundred resin/rubber (phr). The glycerol content was 0, 15, 25, 35, and 45 phr, as seen in Table 1. The solution was heated in a silicone bath with mechanical stirring for 15 min at 95 °C for complete gelatinization. Then, the films were obtained by solvent casting in a polystyrene Petri dish in an oven at 37 °C for 24 h. SNC concentrations (1, 3, and 5 phr) were added to the Gly35 solution after the mixture had cooled down to 40 °C. The SNCs were dispersed using an Ultra-Turrax T25 (IKA, Staufen, Germany) at 8000 rpm for 5 min before casting.

Table 1. Avocado-starch-based film compositions.

Film	Water (g)	ASS (g)	Glycerol (g)	SNCs (g)
Gly0	30	0.3	-	-
Gly15	30	0.3	0.045	-
Gly25	30	0.3	0.075	-
Gly35	30	0.3	0.105	-
Gly45	30	0.3	0.135	-
Gly35-1SNC	30	0.3	0.105	0.003
Gly35-3SNC	30	0.3	0.105	0.009
Gly35-5SNC	30	0.3	0.105	0.015

2.5. Avocado Starch and Starch Nanocrystal Characterization

The chemical structure of ASS and SNC was studied by Fourier-transform infrared (FTIR) spectroscopy, using a Spectrum One FTIR spectrometer (Perkin Elmer instruments, Madrid, Spain). The samples were analyzed at room temperature in the spectral range of 400–4000 cm^{-1} at a resolution of 4 cm^{-1}.

The percentage of amylose in the starch was determined following the total amylose content method [24]. Briefly, the starch was placed in a cellulose extraction thimble inside a Soxhlet extractor. Lipids were removed with 200 mL of a 75% (v/v) n-propanol solution in water heated at 110 °C for 24 h. The thimble was air-dried for 12 h before removing the lipid-free starch. The starch was placed in an oven at 37 °C for 24 h. Triplets of the dried starch sample (20 mg) were dissolved in 8 mL 90% DMSO–water solution and heated at 85 °C for 15 min with intermittent mixing. The samples were diluted to 25 mL with deionized water, of which 1 mL was diluted in 50 mL dilution with 5 mL of iodine solution. Similarly, 20 mg mixtures of pure amylose and amylopectin standards (0%, 10%, 20%, 40%, 50%, 60%, 80%, 90%, and 100% amylose) were prepared. The absorbance of samples and standards were measured in a UV-Vis Varian Cary 1E UV-Vis spectrophotometer (Madrid, Spain) at 600 nm against a reagent blank as a reference.

The crystallographic structure was analyzed using a Bruker D8 Advance instrument (Madrid, Spain) with a CuK as source (0.154 nm) and a Detector Vantec1. The operating conditions were X-ray line (λ = 1.5406 Å), voltage 40 kV, and current 40 mA. The samples were loaded on an aluminum plate and X-ray diffractions were recorded from 0° to 60° for 2θ with a scanning rate of 0.02°/min.

The thermal stability of the starch, starch-based films, and nanocrystals were studied using a TA Instruments TGA Q500 analyzer (Waters, Madrid, Spain). Samples (~10 mg) were heated from 30 to 800 °C at a heating rate of 10 °C min^{-1} under a nitrogen atmosphere. Previously, the samples were introduced into a desiccator with phosphorus pentoxide to minimize the water content. The maximum degradation temperature (Tmax) was calculated from the first derivative of the TGA curves. Dynamic DSC measurements were performed in a Mettler Toledo DSC822e instrument (Barcelona, Spain). The starch gelatinization process was studied under a nitrogen atmosphere: samples of around 2 mg were sealed in aluminum pans in an excess of water and heated from 25 °C to 100 °C at a heating rate of 10 °C/min.

2.6. Film Characterization

Film thickness was determined using a digital micrometer (0.001 mm, Hangzhou United Bridge Tools Co., Ltd., Hangzhou, China). For each formulation, ten random points were measured on three different films. The color properties of the films were evaluated by measuring the color coordinates in the CIELab color space: L* (lightness), a* (red-green) and b* (yellow-blue) employing a KONICA CM-2500d (Konica Minolta Sensing Americas, Inc.,Wayne, NJ, USA). The instrument was calibrated using a white and black standard tile and the measurements were taken at random locations over the surface of the TPS-based films. The results are expressed as the average values of at least five measurements.

The morphology of cryo-fractured cross-sections of films was studied using a SEM (PHILIPS XL30 Scanning Electron Microscope, FEI Philips, Hillsboro, OR, USA). All of the samples were previously gold-coated (≈5 nm thickness) in a Polaron SC7640 Auto/Manual Sputter. SEM images were acquired with an accelerating voltage of 25.0 kV and a working distance of 20 mm.

The mechanical properties of the films were studied using an Instron Universal Machine (Barcelona, Spain) at a strain rate of 10 mm min^{-1}. Tensile test measurements were performed on dog bone specimens with a width of 2 mm, leaving a 20 mm separation between the clamps. The strips were preconditioned at 40% relative humidity (RH) for 24 h inside a sealed container at room temperature (25 ± 1 °C). The Young Modulus, the elongation at break, and the tensile strength were obtained.

The water permeability of the films was measured by determining the water vapor transmission rate (WVTR) by gravimetry. The films were placed in permeability cups exposed to an area (A) of 10 cm^2. The test cups were filled with 2 g of silica gel as a desiccant to produce a 0% RH below the film. The permeability cups were kept in a desiccator with a saturated KNO_3 solution at 23 ± 1 °C and under an RH higher than 75%. Three samples of each formulation film were weighed each hour for 8 h. WVTR (g $days^{-1}$ cm^{-2}) was calculated using Equation (1), where m_t is the mass of the cup at time t, m_0 is the initial mass of the cup, and A is the exposed area of the films.

$$WVTR = \frac{x(m_t - m_0) * 240}{A * t} \quad (1)$$

The water vapor permeability (WVP) was calculated according to Equation (2), where S is the saturation vapor pressure of water at 23 °C, R1 and R2 are the relative humidity in the desiccator and inside the cup, respectively, and ε is the thickness of the film.

$$WVP = \frac{WVTR * \varepsilon}{S * (R1 - R2)} \quad (2)$$

The oxygen transmission rates of the films were determined using an OX-TRAN Model 2/22 H OTR Analyzer Mocon (Lippke, Neuwied, Germany). Tests were carried out at 23 ± 1 °C and 0% relative humidity following the ASTM D3985 standard [25].

For fatty food products aimed to be stored in ambient conditions (temperatures between 20 °C and 40 °C for not more than 30 days), the legislation establishes that food packaging materials must be tested at contact temperature in the worst foreseeable use of 40 °C for 10 days. Therefore, double-sided total-immersion-specific migration tests were conducted via the total immersion of two of 15 × 15 mm film samples in a glass vial containing 7.5 mL of fatty food simulant (Simulant D1 = ethanol 50% v/v) at 40 °C for 10 days [26]. Simulant D1 was run simultaneously with the migration test and used as a control, and all samples were performed in triplicate. After 10 days, the film samples were removed and the radical scavenging activity (RSA) of the food simulant was determined to measure the antioxidant capacity of starch-based films by the reduction of the absorbance of a 2,2-difenil-1-picrylhydrazyl radical (2mM DPPH in ethanolic solution) at 526 nm using a

UV-Vis Varian Cary 1E UV-Vis spectrophotometer. The percentage of the radical scavenging activity (RSA) was determined using Equation (3).

$$RSA(\%) = \frac{A_{control} - A_{sample}}{A_{control}} \times 100\% \quad (3)$$

where $A_{control}$ is the absorbance of DPPH radical in simulant D1 and A_{sample} the absorbance of DPPH solution after 15 min in contact with each food simulant sample after 10 contact days with the starch-based films.

The analytical determination of antioxidants was carried out using a Hewlett Packard 6890 HRGC gas chromatograph equipped with an Agilent Technologies mass spectrometry detector model 5973 (GC-MS) (Santa Clara, CA, USA). The separation of the compounds was performed on a DB5-HT capillary column (15 m × 250 µm and 0.1 µm). The carrier gas used was helium with a flow rate of 1 mL/min. The electronic impact (70 eV) was the type of ionization selected for the mass spectrometer. The different samples were extracted taking 50 mg and adding dichloromethane at 40 °C for 24 h. The solvent was evaporated until dryness and the extracts were analyzed by GC-MS. The identification of compounds was carried out by matching their mass spectra vs. the NIST20 (US National Institute of Standards and Technology, Gaithersburg, MD, USA) commercial library, with a match above 900.

The films were disintegrated under industrial composting conditions at a laboratory scale following ISO 20200 standards [27]. The films were cut into 15 × 15 mm samples, placed in mosquito nets, and buried in a perforated plastic box with prepared compost soil. The mosquito net allowed direct contact with compost soil and facilitated the removal of degraded film. The compost soil consisted of a mixture containing approximately 40% sawdust, 30% rabbit food, 10% compost, 10% corn starch, 5% sugar, 4% corn oil, and 1% urea. Deionized water was added up to 55 wt.% of the total content. The boxes were kept under aerobic conditions at 58 °C. The samples were unburied after 1, 3, 6, 12, 24, 36, and 48 h, and dried in an oven at 37 °C for 24 h. Photographs of unburied samples were taken for visual comparison.

3. Results and Discussion

3.1. Starch Granule and Nanocrystal Characterization

The starch extracted from the avocado seeds (ASS) exhibited a light brown color. The starch nanocrystals (SNCs) showed a slightly darker brown color compared to the ASS granules. ASS extraction yielded about 13.1%, which is similar to the 20.1% reported using a similar sodium bisulfite solution [22] or the 16.5% (wet basis) obtained through a combined mechanical and ultrasonic extraction method [28]. The iodine method established that the amylose content of the extracted avocado starch was 31.4%, which is similar to the 29.7 ± 2.4% [29] reported for ASS from an unspecified avocado variety. In solvent casting, when comparing films obtained in the same conditions, starch matrices with higher amylose percentages are thicker and, thus, more opaque, while amylopectin content favors obtaining less heterogeneous and denser films and, thus, thinner films [30]. High amylose starches have a higher viscosity, making processing techniques challenging, resulting in TPS with higher stiffness, therefore increasing elastic modulus and tensile strength and decreasing elongation [31].

The FTIR spectra for ASS and SNCs and a description of their characteristic bands can be seen in Supplementary Figure S1. The similarity in the spectra suggests that the chemical bonds of the SNCs remained mostly unchanged after the acid hydrolysis. The absorption peak intensity of SNCs increased in the 3000–3600 cm^{-1} and 1635 cm^{-1} band compared to ASS; this is due to the increasing hydroxyl groups in the SNCs by acid hydrolysis. Similarly, the band at 2930 cm^{-1} was lower in SNCs, which is ascribed to decreased amylose content, which was also expected, since amylopectin is predominant in the crystalline fraction [32]. The small variations in the 1050–990 cm^{-1} region could be associated with the presence of more ordered structures and the disappearance of the amorphous fraction, respectively [33].

A thermogravimetric analysis of the ASS and SNCs was carried out to compare their thermal stability. As seen in Supplementary Figure S2, the TGyadaA curves show three stages. The initial weight loss (60–120 °C) corresponds to the water evaporation and low-molecular-weight compounds (approx. 7–8% of weight). The main weight loss (250–330 °C) refers to the thermal degradation of carbohydrates including amylose and amylopectin, as well as the eradication of lipid complexes, through an irreversible reaction, producing water, carbon monoxide, carbon dioxide, acetaldehyde, furan, and 2-methyl furan. The last stage (above 330 °C) is related to the carbonization decomposition of raw starch, which ends with the formation of carbon black.

The SNCs exhibited lower water content (3–4% of the weight) compared to the ASS. This reduction can be associated with the higher crystallinity, therefore being structurally more compact and organized, and the presence of sulfate groups that reduce the exposure of hydroxyl groups on the surface, reducing the water content, as reported by Velásques et al. [34]. Additionally, the thermal decomposition of SNCs began earlier than the ASS granules despite the hydrolysis treatment. This is consistent with relevant literature findings in which the depolymerization reaction of SNCs is catalyzed faster by the presence of sulfate groups produced during hydrolysis on the surface of SNCs [35]. Interestingly, LeCorre et al. [36] compared different starches and their SNCs, and suggested that larger SNCs have higher degradation temperatures, closer to the initial starch thermal behavior, as groups with less sulfate can catalyze the degradation reaction. Moreover, at 200–300 °C, the sulfonic acid groups are thermally decomposed and the depolymerization rate slows down, with no influence on the final weight. The earlier thermal decomposition of SNCs does not affect their application in solvent-casted film. However, the preparation of nanocomposite films using other thermal methods can result in the melting of SNCs, especially if water is present [37].

Starch suffers gelatinization in excess water. The DSC analysis showed a gelatinization curve of avocado starch, with a maximum peak centered at 71 °C. The recorded initial gelatinization temperature was 63 °C and the final gelatinization temperature was 82 °C (Supplementary Figure S3), in agreement with other literature results. For example, Lacerda et al. [38] reported a gelatinization range of 73.77 to 81.27 °C for an unspecified variety of avocado starch.

Wide-angle X-ray diffraction (XDR) was carried out on the ASS granules and SNCs, as shown in Figure 1. The XDR patterns for ASS showed a strong peak at 17.1° (2θ) and other peaks at 2θ 15.2°, 19.6°, and 22.4°, exhibiting a clear B-type pattern. This result matches the B-type patterns commonly described for Hass ASS, as described by De Dios-Ávila et al. [39]. SNCs presented changes in the crystallinity pattern after hydrolysis, mainly the strong peak at 17.1° unfolding into a double peak. Moreover, the SNCs showed an increased reflection peak intensity compared to the ASS. This is expected as a result of the selective hydrolysis of the amorphous regions of starch by the sulfuric acid, subsequently forming a more defined crystalline region.

The morphology of the ASS and SNCs was studied using a scanning electron microscope (SEM and FE-SEM). As seen in the SEM micrographs in Figure 2A, the ASS granules exhibited different forms including rounded, elliptical, and irregular shapes. Moreover, the granules exhibited a smooth surface with varying granular sizes, including small rounded 3–7 μm granules and larger elliptical and irregularly shaped granules, with lengths between 15 and 30 μm and widths of 5–20 μm. This matches the description reported by Esquivel-Fajardo et al. [28], whose ASS granules exhibited lenticular, spherical, and irregular morphologies, with a 5–30 μm size distribution, a mean length of 18.6 ± 5.2 μm, and a mean width of 10.9 ± 3.1 μm.

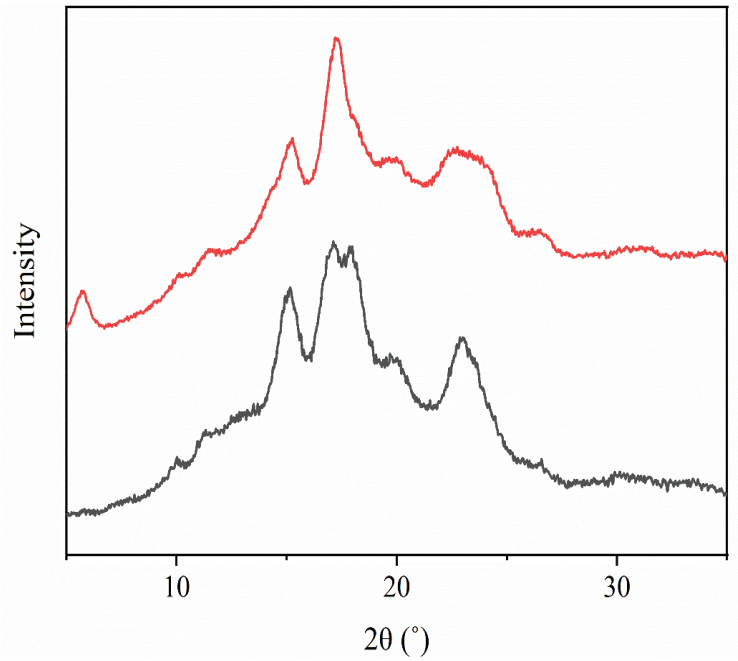

Figure 1. X-ray diffraction patterns of ASS (top) and SNCs (bottom).

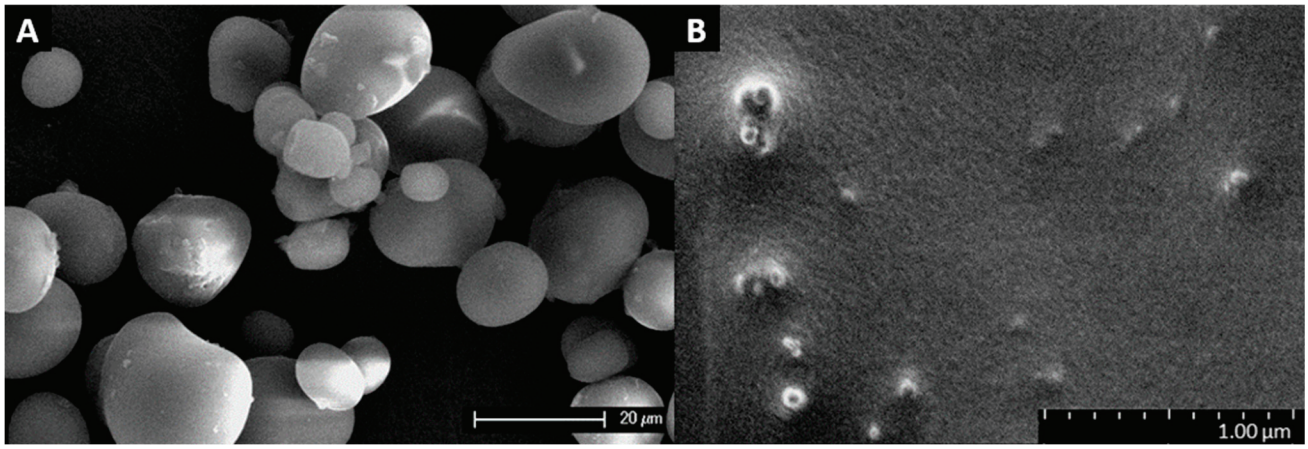

Figure 2. (**A**) SEM micrograph of avocado seed starch (ASS) granules. (**B**) FE-SEM micrograph of starch nanocrystals (SNCs).

The FE-SEM observation of SNCs showed crystals with differing dimensions and shapes, as seen in Figure 2B. Most SNCs exhibited a round shape with diameters smaller than 100 nm. This description would fit a study by LeCorre et al. [40], where they explained how B-type starches (e.g., high amylose maize, potato) produced round-shaped particles after acid hydrolysis. Moreover, the SNCs presented a strong tendency to self-aggregate, which could be explained by surface hydroxyl groups promoting hydrogen bonding interactions, as described by Bel Haaj et al. [41].

3.2. Film Characterization

Visual aspects of the avocado seed starch (ASS)-based films are presented in Figure 3. On the macroscopic scale, all of the films obtained were homogeneous, continuous, and odorless and exhibited a light orange/brown color. Glycerol and SNCs had no significant effect on film transparency and color, as seen in Table 2. The lightness (L*) of all of the examined films was higher than the 73.02 ± 0.48 reported by Jímenez et al. [42] for their plasticized ASS films. Moreover, the same films presented higher red (a*: 12.47) and yellow (b*: 31.58) values. All films exhibited a* y b* coordinate values closer to light white, similar

to those reported for banana starch [(L*) 81.33, (a*) 4.29, and (b*) 10.07] [43]. Despite the ultrasonic dispersion of SNCs before casting, small macroscale agglomerations were visible, mainly in the highest concentration (Gly35-5SNC). The films were easy to handle, except Gly0 and, to some extent, Gly15, which presented a fragile nature. The unplasticized film (Gly0) formed very brittle and cracked films, limiting possibilities to measure mechanical and barrier properties.

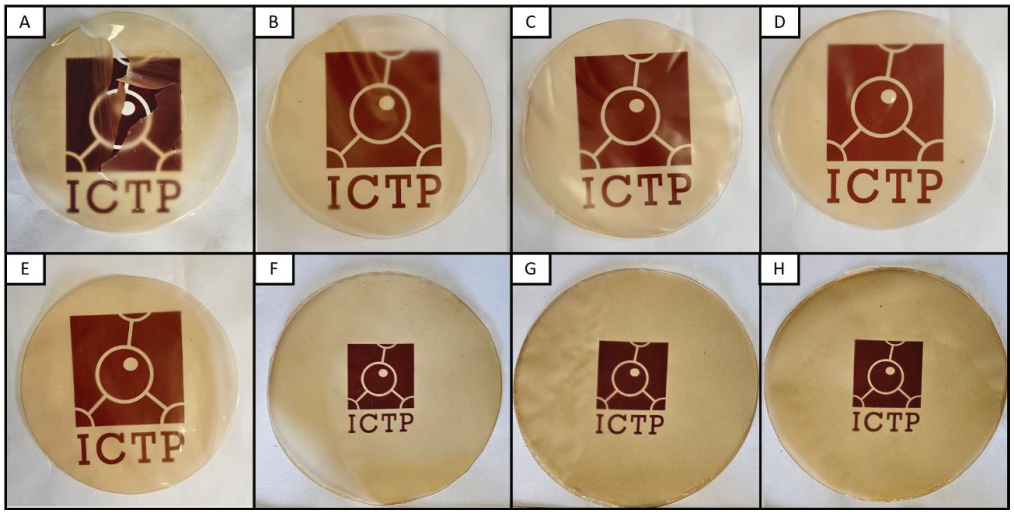

Figure 3. Visual aspect of avocado-starch-based films: (**A**) Gly0, (**B**) Gly15, (**C**) Gly25, (**D**) Gly35, (**E**) Gly45, (**F**) Gly35-1SNC, (**G**) Gly35-3SNC, (**H**) Gly35-5SNC.

Table 2. Film thickness and luminance (L*) and color coordinates (a*b*) of avocado-starch-based films.

Sample	Thickness (μm)	L	a	b
Gly0	46.0 ± 2.0	84.62 ± 0.32	0.82 ± 0.34	21.38 ± 0.68
Gly15	53.0 ± 1.2	84.70 ± 0.76	1.04 ± 0.33	21.77 ± 1.83
Gly25	57.8 ± 0.4	84.38 ± 0.64	1.04 ± 0.21	21.29 ± 0.76
Gly35	59.3 ± 1.7	84.37 ± 0.66	1.08 ± 0.28	21.96 ± 1.42
Gly45	61.0 ± 4.0	84.98 ± 0.31	0.68 ± 0.22	21.44 ± 1.43
Gly35-1SNC	53.7 ± 3.7	83.70 ± 1.16	0.58 ± 0.26	20.06 ± 1.26
Gly35-3SNC	56.6 ± 1.0	83.37 ± 0.31	1.01 ± 0.19	20.46 ± 1.34
Gly35-5SNC	61.4 ± 4.7	82.80 ± 0.89	1.24 ± 0.13	21.01 ± 0.72

Film thickness was significantly influenced by glycerol and SNC content, as seen in Table 2. Higher glycerol concentrations lead to thicker films. This is expected, as the matrix becomes less dense and the mobility of starch chains is facilitated with the increase in plasticizer [44]. Zaharia et al. [45] reported that glycerol concentration increased potato starch film thickness and moisture content while decreasing density. On the other hand, Gly35-1SNC films had significantly lower thicknesses compared to Gly35. Additionally, Gly35-3SNC and Gly35-5SNC displayed small increases in thickness compared to Gly35 despite the increment in total dry mass content. A possible explanation is that SNCs dispersed homogeneously in the starch matrix, making films with higher density. Fan et al. [46] reported similar behavior, where the average thickness of the control starch film was 160 μm compared to the 120 μm of the 1% SNC film.

The effect of glycerol and SNCs on the thermal properties of the ASS films was studied by thermogravimetric analysis, as seen in Figure 4. The initial stages of film thermal degradation originated at the 60–120 °C interval. This weight loss can be connected with moisture and the evaporation of loosely connected water and low-molecular-weight molecules in the film. The plasticized films presented lower $T_{10\%}$ than the unplasticized films (Gly0), which can be attributed to the reduction in inter- and intra-molecular bonds in the starch matrix as the concentration of glycerol increased. Similarly, the addition of SNCs

further reduced $T_{10\%}$, indicating a lower water absorption capacity. The strong hydrogen bond between SNCs and ASS probably prevented water absorption in the starch matrix.

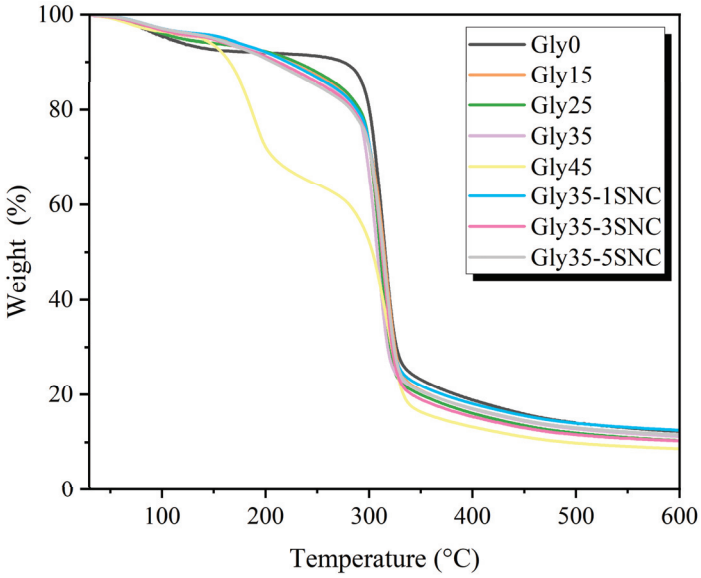

Figure 4. Thermogravimetric analysis of avocado seed starch (ASS)-based films with different glycerol and starch nanocrystal (SNC) content.

The main degradation process (250–330 °C) is linked to the loss of hydroxyl groups and depolymerization of carbon chains. The TGA analysis of the glycerol films showed a constant decreasing trend in Tmax as the plasticizer content increased. The lower thermal stability of glycerol compared to ASS can explain this phenomenon. Interestingly, Gly45 displayed two phases during the main degradation the first at 150–200 °C and a second at 250–320 °C, demonstrating a phase separation between the glycerol and the starch. The addition of SNCs resulted in lower initial decomposition temperatures, as seen in Figure 4, as nanocrystals exhibit lower initial thermal stability after the hydrolysis processing of the native starch granules. However, increasing the SNC concentrations also resulted in higher T_{max} with Gly35 (307.4 °C), Gly35-1SNC, (312.6 °C), Gly35-3SNC (313.5 °C), and Gly35-5SNC (314.2 °C), which evidenced that thermal stability of films was enhanced with the incorporation of SNC. Similarly, Kumari et al. [47] described how the addition of SNC increased the $T_{50\%}$ of their mung-bean-starch-based films by up to 7 °C and attributed it to the strong crystalline structure of SNC, which required more energy and time to melt the crystal. All films presented a similar mass residue at 600 °C, around 10% of the remaining mass, matching the previously described TGA pattern for ASS and SNCs.

The cryo-fractured cross-sections of all of the films were studied by scanning electron microscopy to assess the influence of the addition of glycerol and SNCs on their morphology. Noteworthy differences were spotted between films when comparing different glycerol content, as seen in Figure 5. The unplasticized film (Gly0) presented small cracks on the surface, indicating a fragile nature, which could explain the difficulties in forming a complete film. The addition of glycerol (Gly15) significantly decreased the number and size of the cracks, while an even higher glycerol content (Gly25, Gly35, and Gly45) resulted in smooth surfaces, confirming good gelatinization and the homogeneous mixing of ASS with glycerol. The small scale of glycerol molecules grants enhanced intercalation capabilities between the polymeric chains. The high compatibility permits glycerol to reduce the strong intramolecular attraction in the starch matrix and increase the H-bonding between the plasticizer and starch molecules. The homogeneity of these films, which can be attributed to this good synergy, results in better mechanical properties.

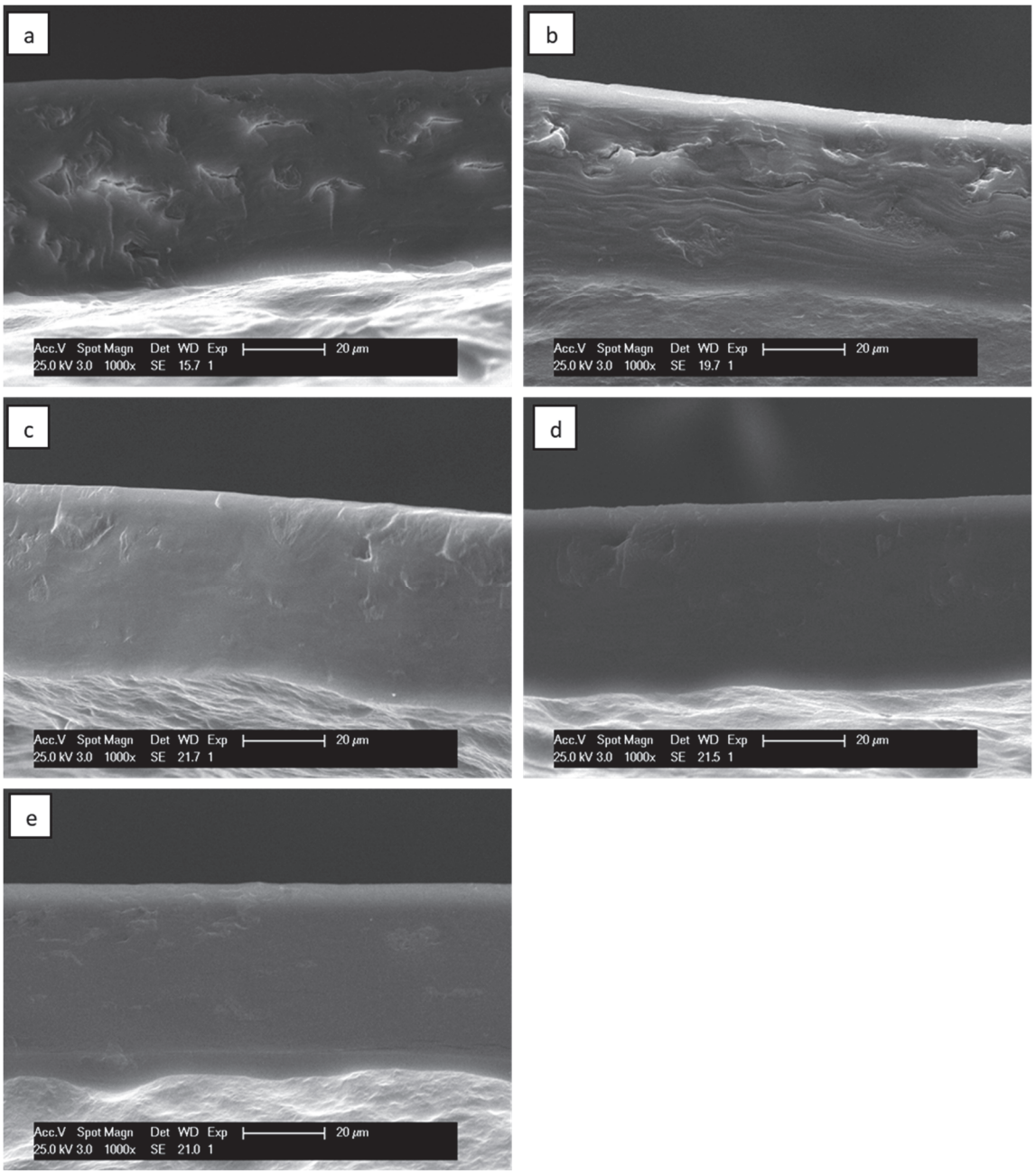

Figure 5. SEM micrographs (1000×) of the cross-section of avocado starch films with varying plasticizer content: (**a**) Gly0, (**b**) Gly15, (**c**) Gly25, (**d**) Gly35, (**e**) Gly45.

The influence of SNCs in the morphology was also studied, as seen in Figure 6. The smooth surface of the original Gly35 film can be seen in all SNC formulations. However, small agglomerations of SNCs can be perceived in Gly35-5NC and, to a lesser extent, in Gly35-3SNC. The tendency of SNCs to self-aggregate into microscale agglomerates is a common behavior, independent of the morphology of nanocrystals and botanical origin of the starch [37].

The wide-angle X-ray diffraction patterns of the ASS films are shown in Supplementary Figure S4. The films showed diffraction peaks and a broad amorphous halo, which is the typical behavior of semi-crystalline polymers with a low degree of crystallinity. Diffraction peaks can be identified at 2θ of 12.9°, 17.1°, and 19.9°. Although ASS presented a B-type crystallinity, the films obtained showed a pattern of VH-type crystallinity. This indicates that the crystalline structure of native starch was destroyed during gelatinization, and a

semi-crystalline structure was formed from the recrystallization of simple amylose helices (B-type crystallinity), as reported by Palluch et al. [48]. The VH-type crystallinity is induced during the heat treatment, where the interaction between the hydroxyl groups of the starch molecules is replaced by hydrogen bonds formed between the plasticizer and starch [49]. The trends of XDR analysis of the glycerol films showed a constant decrease in peak intensity at 13.0° as the plasticizer content increased. On the other hand, an increase in the peak intensity at 13.0° and 17.0° was observed mainly at Gly35-3SNC and Gly35-5NC. This could be the result of the macroscale SNC agglomerates formed in the nanocomposite at the highest SNC concentration.

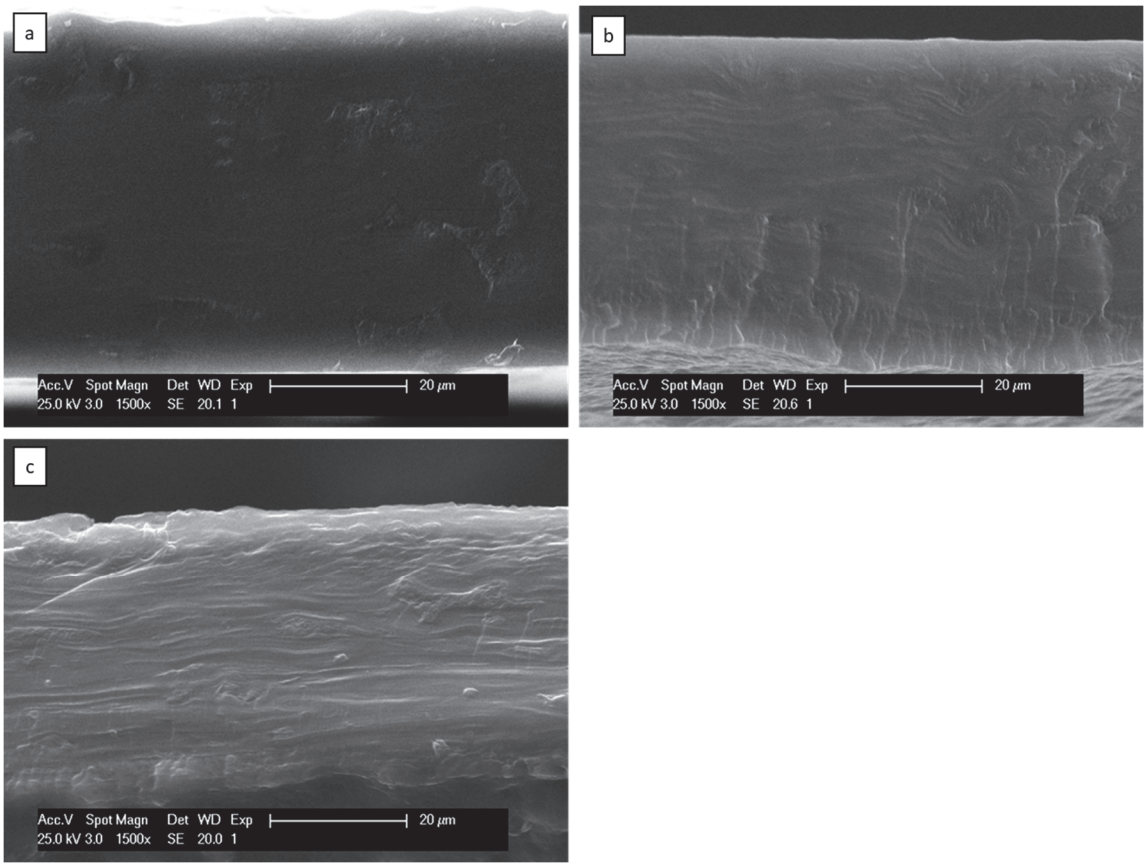

Figure 6. SEM micrographs of the cross-section of SNC-reinforced avocado starch films (1500×): (**a**) Gly35-1SNC, (**b**) Gly35-3SNC, (**c**) Gly35-5SNC.

The mechanical properties of starch films exhibit high sensitivity to multiple factors including botanical origin and humidity. A high relative humidity can provide a plasticizing effect, as water molecules enhance molecular mobility due to an increase in free volume. The unplasticized films (Gly0) were rigid and brittle; consequentially, no measures for mechanical properties could be taken. The plasticizing effect of glycerol can be seen in Table 3a. Films with increasing glycerol content exhibited a lower elastic modulus and tensile strength, while the elongation at break increased. The elastic modulus values decreased significantly from 1247 MPa to 109 MPa with glycerol incorporation, which translated into lower rigidity and stiffness in the films.

Table 3. Mechanical properties of avocado seed starch-based (ASS) films based on the effect of glycerol and starch nanocrystals (SNCs).

Film	Elastic Modulus (MPa)	Tensile Strength (MPa)	Elongation at Break (%)
(a) Mechanical properties of avocado seed starch (ASS)-based films based on the effect of glycerol.			
Gly15	1246.8 ± 172.8 [a]	17.5 ± 1.1 [a]	1.3 ± 0.7 [a]
Gly25	420.1 ± 269.8 [b]	4.8 ± 1.1 [b]	15.0 ± 7.5 [b]
Gly35	177.5 ± 42.7 [c]	4.5 ± 0.3 [b]	24.9 ± 1.7 [c]
Gly45	109.3 ± 89.9 [c]	3.7 ± 1.1 [b]	22.5 ± 5.9 [c]
F ratio	6.026	2.535	8.691
p-value	0.004 *	0.091 *	0.0005 *
(b) Mechanical properties of avocado seed starch (ASS)-based films based on the effect of starch nanocrystals (SNCs).			
Gly35	177.5 ± 42.7 [a]	4.5 ± 0.3 [a,b]	24.9 ± 1.7 [a]
Gly35-1SNC	376.6 ± 126.9 [b]	6.4 ± 1.4 [a]	16.7 ± 1.7 [b]
Gly35-3SNC	209.0 ± 113.6 [a]	4.8 ± 1.4 [a,b]	24.9 ± 4.2 [a]
Gly35-5SNC	133.4 ± 69.8 [a]	4.1 ± 1.3 [b]	24.9 ± 3.8 [a]
F ratio	1.264	4.014	2.97
p-value	0.312 *	0.021 *	0.065 *

Different letters in the column indicate significant differences according to Tukey's test ($p < 0.05$). * Values are significant at $p < 0.05$.

The addition of a small concentration of SNCs (Gly35-1SNC) led to an increase in the elastic modulus and tensile strength, and a decline in elongation at break, as seen in Table 3b. The high specific surface area provided by the SNCs caused stronger filler–matrix interfacial interactions, leading to the higher tensile strength (+112%) of the films reinforced with starch nanoparticles. However, the higher quantity of SNCs in Gly35-3SNC provided a smaller reinforcing effect compared to Gly35-1SNC, while Gly35-5SNC presented values similar to its neat counterpart (Gly35). This is to be expected, as high concentrations of SNCs tended to self-aggregate, decreasing the surface area for interactions with the matrix, resulting in decreases in tensile strength and modulus. Velásquez-Castillo et al. [33] reported that their cassava starch film tensile strength (TS) and Young's modulus (M) increased (+154% and +135%, respectively) when the quinoa SNC concentration increased from 0 to 5%, and then reduced at 7.5% of QSNC. Similarly, Li et al. [50] reported that higher SNC concentrations had a reduced reinforcing effect on their pea starch films and associated it with the linking of hydroxyl groups in the surface of the SNCs, leading to a micro-phase separation.

Since the main function of food packaging is often to avoid or at least to decrease moisture transfer between the food and the surrounding atmosphere, water vapor permeability (WVP) should be as low as possible. Therefore, the high water permeability of starch films limits their use in the food packaging industry. The WVP values of the ASS films increased with higher glycerol content, as seen in Table 4. Glycerol can easily penetrate the starch film structure, decrease the matrix density, and create active sites where water molecules can be absorbed. Therefore, rising glycerol content forms a hydrophilic film with poor moisture barrier properties, as it increases moisture content, water solubility, and water absorption.

Table 4. Barrier properties of avocado-starch-based films.

Reference	Gly0	Gly15	Gly25	Gly35	Gly45	Gly35-1SNC	Gly35-3SNC	Gly35-5SNC
WVP (g/mm.d.KPa)	-	5.1 ± 0.2	9.1 ± 1.7	13.5 ± 1.7	15.1 ± 0.8	8.8 ± 1.8	7.3 ± 1.2	10 ± 0.7
OTR(mL/m^2 day)	>4000 *	>4000 *	>4000 *	11.0 ± 4.3	18.7 ± 2.6	9.8± 0.8	8.2 ± 3.0	12.2 ± 3.1

* Above the upper measurement range of the equipment for the tested area.

On the contrary, the incorporation of SNCs significantly reduced the WVP of the starch films (Gly35), as seen in Table 4. Gly35-3SNC exhibited a 40% decrease in WVP compared to Gly35. It is well known that adding nanoparticles to composite films forms a tortuous path for water molecules to permeate, significantly decreasing WVP. However, the high amount of hydroxyl groups at the surface of starch nanocrystals can lead to an interaction with water and a consequent increase in WVP. In this work, the reduction in the WVP can be ascribed to the positive interaction between the polymeric matrix and the SNC that avoids the interaction with water. The strong interactions between the nanoparticles and the polymeric matrix enhance film compactness, reducing possible paths for water molecules trying to penetrate the polymeric matrix.

The oxygen transmission rate (OTR) results for the films are shown in Table 4. The brittle nature of non- or slightly plasticized films combined with the small measurement area (2.5 cm^2) resulted in small cracks that caused the OTR values to be above the upper measurement range of the equipment for the tested area. However, it is commonly recognized that adding plasticizers lowers the oxygen barrier properties of the matrix by increasing free volume. Therefore, OTR values should increase as glycerol content also increases. On the other hand, the addition of SNCs has been reported to lower OTR in films [51]. A decreasing pattern can be seen when comparing Gly35-1SNC and Gly35-3SNC to Gly35. However, for Gly35-5SNC films, a possible agglomeration of SNCs resulted in lower barrier properties. Nevertheless, compared to traditional plastics, the poor oxygen and water vapor barrier properties are still insufficient to serve as high-barrier packaging, greatly limiting the application of current biodegradable polymers. As a result, the current focus of biodegradable food packaging is mainly on dry food products for short shelf lives, or long shelf-life applications that do not require strong barrier properties.

Radical scavenging activity (RSA) was measured using the DPPH method after the materials were subjected to specific migration tests. In this technique, when antioxidant substances are present in the sample, the initial purple color of the solution changes to yellow. This color change is triggered by antioxidants donating hydrogens from their phenolic hydroxyl groups to DPPH free radicals, resulting in a more stable compound [52]. All of the films presented antioxidant activity, as seen in Figure 7, since the ASS polymeric matrix is rich in antioxidant compounds.

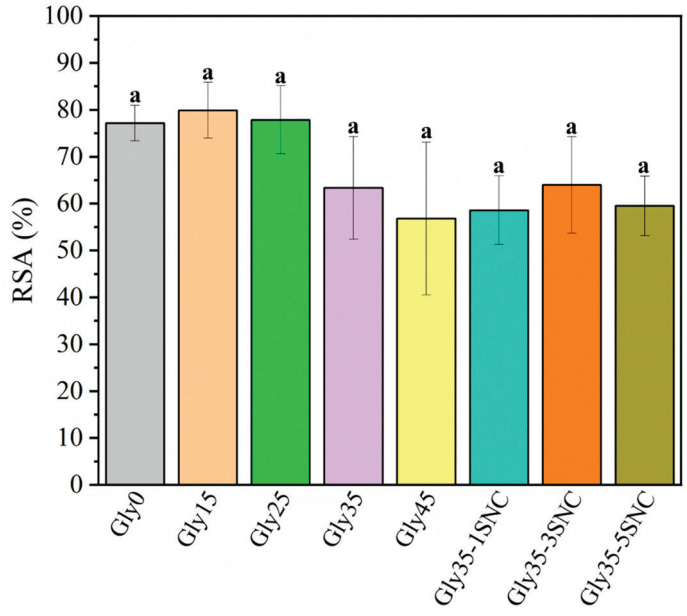

Figure 7. Radical scavenging assay (RSA) effect of glycerol and starch nanocrystal content on avocado starch films. Different letters in the column indicate significant differences according to Tukey's test ($p < 0.05$). F ratio: 1.208 and p-value > F: 0.353 (Values are significant at $p < 0.05$).

Although the RSA values were similar for all films, a downward tendency can be seen, meaning that the antioxidant ability decreased as the glycerol content increased. Thus, the lowest RSA% was presented by Gly45 as glycerol does not possess any antioxidant activity, while the highest value was seen for films containing lower amounts of glycerol (Gly0, Gly15, Gly25). Additionally, the antioxidant capacity of the ASS was probably further reduced due to interactions between the starch and glycerol. Similar results were reported by Merino et al. [53], in which pure avocado seed powder presented a higher antioxidant capacity than plasticized film. The presence of SNCs had no apparent effect on the film's antioxidant capacity, as the values remained comparable to Gly35. Hu et al. [54] developed cassava starch aldehyde functionalized with catechin conjugates reaching around 60% RSA values, similar to those obtained here. However, they required the incorporation of catechin conjugates in high amounts (between 18% and 62%) into the starchy structure. Meanwhile, the materials developed here intrinsically possess antioxidant activity.

Waste materials from the avocado processing industry (peels and seeds) have been proven to show intense antioxidant effects linked to polyphenols, which can vary between avocado varieties [55]. ASS, SNCs, and Gly35 film were analyzed by GC-MS to identify the source of the antioxidant properties of the films. A series of proposed compounds were identified in all three samples, as seen in Table 5. Furan and furanone derivatives isolated from avocados have notable insecticidal, cytotoxic, and antifungal activities [56]. n-Hexadecenoic acid is reported to have antioxidant, anti-inflammatory, hypocholesterolemic, and cancer-prevention properties [57]. Similarly, 9,12-octadecadienoic acid has been linked to anti-inflammatory, antibacterial, hypocholesterolemic, and hepatoprotective activities [57]. On another note, avocado fruits have been reported to be a good source of 4-desmethylsterols, with β-sitosterol representing around 89% of total sterol content [58]. β-sitosterol has anti-inflammatory, antibacterial, and antifungal effects [59].

Table 5. Proposed compounds identified using GC-MS in avocado seed starch (ASS) and starch nanocrystals (SNCs), and starch-based films (Gly35).

tr (Min)	Proposed Compound	*m*/*z*	Molecular Formula
9.53	Avocadynofuran	248.10	$C_{17}H_{26}O$
10.01	(E)-Avocadynofuran	246.20	$C_{17}H_{26}O$
10.39	Avocadynofuran	244.18	$C_{17}H_{24}O$
11.29	n-Hexadecenoic acid	256.24	$C_{16}H_{32}O_2$
11.55	2-(Pentadec-14-yn-1-yl)furan	274.23	$C_{19}H_{30}O$
11.59	(E)-2-(Pentadec-2-en-1-yl)furan	276.25	$C_{19}H_{32}O$
11.65	2-Pentadecylfuran	278.26	$C_{19}H_{34}O$
12.40	(E)-2-(Pentadeca-1,14-dien-1-yl)furan	274.23	$C_{19}H_{30}O$
12.46	(Z)-2-(Pentadec-1-en-1-yl)furan	276.25	$C_{19}H_{32}O$
13.18	9,12-Octadecadienoic acid (Z,Z)-	280.24	$C_{18}H_{32}O_2$
13.50	2-((8Z,11Z)-Heptadeca-8,11-dien-1-yl)furan	302.26	$C_{21}H_{34}O$
14.22	2-((1E,8Z,11Z)-Heptadeca-1,8,11-trien-1-yl)furan	300.25	$C_{21}H_{32}O$
23.12	β-Sitosterol	414.39	$C_{29}H_{50}O$

The disintegration test reproduces the humidity (about 55%) and heat (58 °C) conditions typical of the thermophilic phase of a composting plant at a lab scale. The degradation rate was studied under visual comparison, as seen in Figure 8. After 12 h, all films presented clear degradation as they had lost their initial appearance, shape, and structural integrity. Moreover, all of the starch films were fully degraded after 48 h. Sessini et al. [60] observed that starch films with a lower amount of glycerol disintegrated faster under lab-scale compost conditions (58 °C), explaining how the chain mobility of plasticized films allowed the water to infiltrate through the polymer matrix, leading to earlier hydrolysis. A lower degradation rate was observed in the nanocomposite films containing SNCs. These results could be related to the nucleation effect of SNCs on the films, since the ordered structures in the crystalline fractions decrease the action of microorganisms [61].

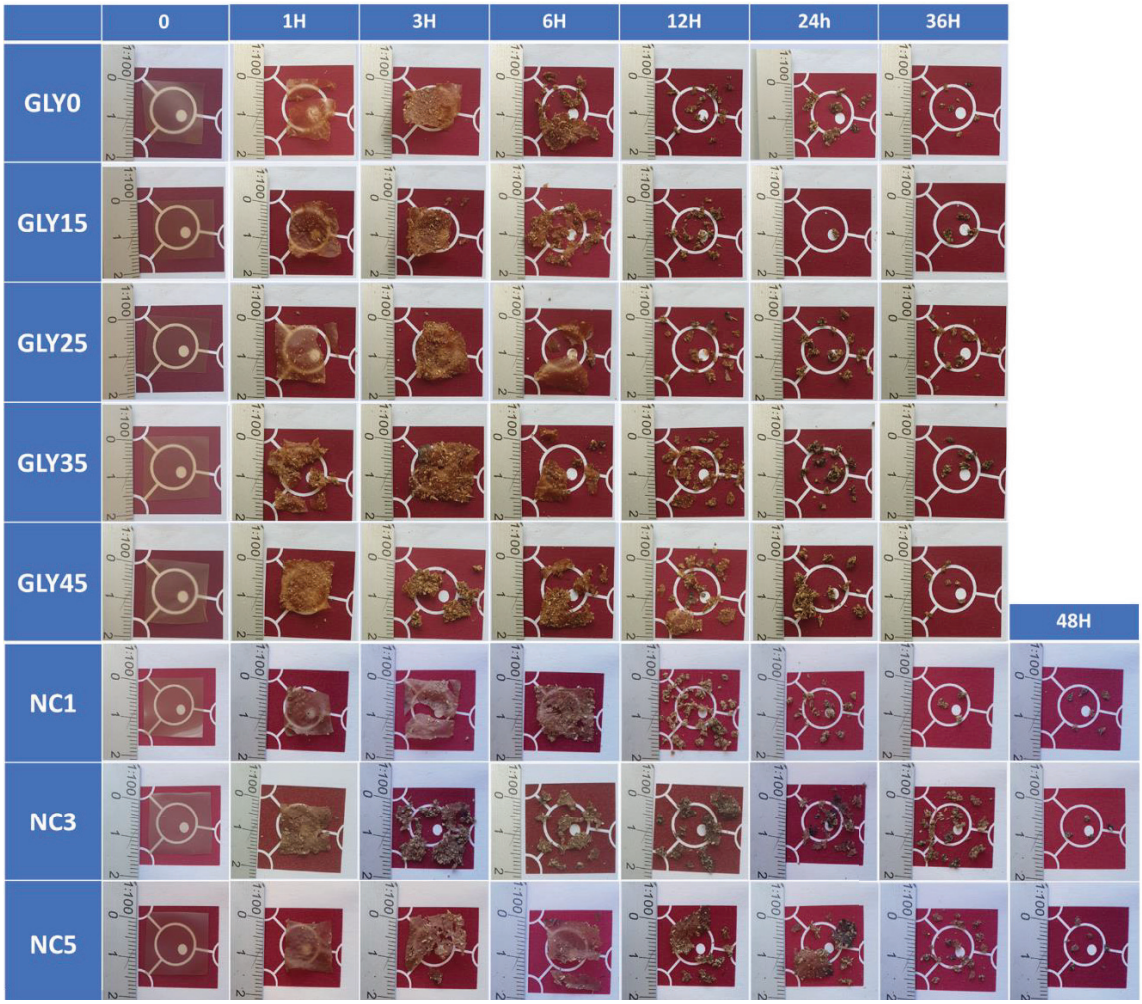

Figure 8. The visual appearance of avocado-starch-based films during disintegration.

4. Conclusions

Starch was successfully extracted from avocado seed and characterized. Starch-based films with intrinsic antioxidant properties were obtained through the addition of glycerol and starch nanocrystals. Increasing the glycerol content reduced the brittleness and tensile strength of the films, but lowered the barrier properties. The Gly35 film was found to be a good compromise between these properties and was therefore selected to incorporate the starch nanocrystals (SNCs) prepared via acid hydrolysis. The addition of SNCs created a tortuous path that lowered water vapor and oxygen permeability. The reinforcing effect was especially effective at lower SNC concentrations, as higher concentrations led to SNC agglomeration that hindered the interactions between the matrix and SNCs. Considering all of the studied properties comprehensively, Gly35-1SNC presented the best balance of properties: high tensile strength and modulus, and moderate elongation. Moreover, Gly35-1SNC preserved an intrinsically high antioxidant activity from reaming bioactive compounds of the seed and excellent biodegradability properties, as the films disintegrated in 48 h under lab-scale composting.

These findings suggest that avocado seed waste can be utilized to extract starch and develop films for active food packaging. The exploitation of avocado seeds, frequently treated as a byproduct, would contribute to the zero-waste and circular economy principles. However, more research is needed to enhance their mechanical and barrier qualities, as food packaging films typically demand sufficient stretchability and tensile strength to withstand external stress and retain their integrity, as well as high moisture and oxygen barrier properties. Solvent casting is a convenient laboratory-scale method for producing

food packaging films, yet future research should focus on industrial applications and further improve the properties of the films by exploring extrusion and other conventional polymer-processing techniques such as blending.

Supplementary Materials: The following supporting information can be downloaded at https://www.mdpi.com/article/10.3390/polym16202868/s1: Figure S1. FTIR spectra of avocado seed starch (ASS) and starch nanocrystals (SNCs). Figure S2. DSC of the avocado seed starch gelatinization. Figure S3. X-ray diffraction patterns of avocado-seed-starch-based films with different glycerol and SNC contents. Figure S4. Tensile properties of avocado-seed-starch-based films. Figure S5. Water vapor permeability of avocado-starch-based films.

Author Contributions: Conceptualization, D.L. and L.P.; methodology, P.F.M.-G., A.A.-G., E.B.-B., M.P.A. and G.R.; software, P.F.M.-G.; validation, M.P.A., L.P. and D.L.; investigation, P.F.M.-G.; resources, D.L. and L.P.; writing—original draft preparation, P.F.M.-G.; writing—review and editing, A.A.-G., M.P.A., G.R., D.L. and L.P.; supervision, D.L. and L.P.; project administration, D.L. and L.P., funding acquisition, D.L. and L.P. All authors have read and agreed to the published version of the manuscript.

Funding: This research was funded by the Agencia Estatal de Investigación (AEI, MICINN, Spain), Fondo Europeo de Desarrollo Regional (FEDER, EU), NextGenerationEU MRR TED2021-129335B-C21, and MCIN/AEI/10.13039/501100011033/ by "ERDF A way of making Europe" for the PID2021-123753NB-C31 and PID2021-123753NB-C32 projects.

Institutional Review Board Statement: Not applicable.

Data Availability Statement: The raw data supporting the conclusions of this article will be made available by the authors on request.

Acknowledgments: The authors would like to acknowledge the contribution made to this paper by Jaime Vaquerizo Gómez, Corentine Tamaya, and Elena Zubillaga Maharg during their internships at ICTP-CSIC. The authors also want to acknowledge MICIN for the PID2021-123753NB-C31 and TED2021-129335B-C21 projects.

Conflicts of Interest: The authors declare no conflicts of interest.

References

1. Davis, G.; Song, J.H. Biodegradable Packaging Based on Raw Materials from Crops and Their Impact on Waste Management. *Ind. Crops Prod.* **2006**, *23*, 147–161. [CrossRef]
2. Europian Bioplatics December 2023 Bioplastics Market Development Update 2023. Available online: https://www.european-bioplastics.org/market/ (accessed on 4 March 2024).
3. Lalnunthari, C.; Devi, L.M.; Amami, E.; Badwaik, L.S. Valorisation of Pumpkin Seeds and Peels into Biodegradable Packaging Films. *Food Bioprod. Process.* **2019**, *118*, 58–66. [CrossRef]
4. Segovia, F.J.; Hidalgo, G.I.; Villasante, J.; Ramis, X.; Almajano, M.P. Avocado Seed: A Comparative Study of Antioxidant Content and Capacity in Protecting Oil Models from Oxidation. *Molecules* **2018**, *23*, 2421. [CrossRef]
5. Tesfaye, T.; Ayele, M.; Gibril, M.; Ferede, E.; Limeneh, D.Y.; Kong, F. Beneficiation of Avocado Processing Industry By-Product: A Review on Future Prospect. *Curr. Res. Green Sustain. Chem.* **2022**, *5*, 100253. [CrossRef]
6. Kringel, D.H.; Dias, A.R.G.; Zavareze, E.d.R.; Gandra, E.A. Fruit Wastes as Promising Sources of Starch: Extraction, Properties, and Applications. *Starch/Staerke* **2020**, *72*, 1900200. [CrossRef]
7. Sharma, C.; Dhiman, R.; Rokana, N.; Panwar, H. Nanotechnology: An Untapped Resource for Food Packaging. *Front. Microbiol.* **2017**, *8*, 1735. [CrossRef] [PubMed]
8. Barbosa, S.E.; García, M.A.; Castillo, L.; Lopez, O.V.; Villar, M. *Starch-Based Materials in Food Packaging: Processing, Characterization and Applications*; Academic Press: Cambridge, MA, USA, 2017; Volume 4, ISBN 978-0-12-809439-6/0128094397.
9. Tarique, J.; Sapuan, S.M.; Khalina, A. Effect of Glycerol Plasticizer Loading on the Physical, Mechanical, Thermal, and Barrier Properties of Arrowroot (Maranta Arundinacea) Starch Biopolymers. *Sci. Rep.* **2021**, *11*, 13900. [CrossRef]
10. Pelissari, F.M.; Ferreira, D.C.; Louzada, L.B.; Dos Santos, F.; Corrêa, A.C.; Moreira, F.K.V.; Mattoso, L.H. *Starch-Based Edible Films and Coatings: An Eco-Friendly Alternative for Food Packaging*; Academic Press: Cambridge, MA, USA, 2018; ISBN 9780128094402.
11. Domene-López, D.; García-Quesada, J.C.; Martin-Gullon, I.; Montalbán, M.G. Influence of Starch Composition and Molecular Weight on Physicochemical Properties of Biodegradable Films. *Polymers* **2019**, *11*, 1084. [CrossRef]
12. Guo, A.; Li, J.; Li, F.; Xu, J. Comparison of Single/Compound Plasticizer to Prepare Thermoplastic Starch in Starch-Based Packaging Composites. *Medziagotyra* **2019**, *25*, 183–189. [CrossRef]

13. Zdanowicz, M.; Staciwa, P.; Jedrzejewski, R.; Spychaj, T. Sugar Alcohol-Based Deep Eutectic Solvents as Potato Starch Plasticizers. *Polymers* **2019**, *11*, 1385. [CrossRef]
14. Santhosh, R.; Ahmed, J.; Thakur, R.; Sarkar, P. Starch-Based Edible Packaging: Rheological, Thermal, Mechanical, Microstructural, and Barrier Properties—A Review. *Sustain. Food Technol.* **2024**, *2*, 307–330. [CrossRef]
15. Ghanbarzadeh, B.; Oleyaei, S.A.; Almasi, H. Nanostructured Materials Utilized in Biopolymer-Based Plastics for Food Packaging Applications. *Crit. Rev. Food Sci. Nutr.* **2015**, *55*, 1699–1723. [CrossRef] [PubMed]
16. Muñoz-Gimena, P.F.; Oliver-Cuenca, V.; Peponi, L.; López, D. A Review on Reinforcements and Additives in Starch-Based Composites for Food Packaging. *Polymers* **2023**, *15*, 2972. [CrossRef]
17. Xie, F.; Pollet, E.; Halley, P.J.; Avérous, L. Starch-Based Nano-Biocomposites. *Prog. Polym. Sci.* **2013**, *38*, 1590–1628. [CrossRef]
18. Kowalczyk, D.; Szymanowska, U.; Skrzypek, T.; Basiura-Cembala, M.; Materska, M.; Łupina, K. Corn Starch and Methylcellulose Edible Films Incorporated with Fireweed (*Chamaenerion angustifolium* L.) Extract: Comparison of Physicochemical and Antioxidant Properties. *Int. J. Biol. Macromol.* **2021**, *190*, 969–977. [CrossRef] [PubMed]
19. Fidelis, J.C.F.; Monteiro, A.R.G.; Scapim, M.R.S.; Monteiro, C.C.F.; Morais, D.R.; Claus, T.; Visentainer, J.V.; Yamashita, F. Development of an Active Biodegradable Film Containing Tocopherol and Avocado Peel Extract. *Ital. J. Food Sci.* **2015**, *27*, 468–475.
20. Vianna, T.C.; Marinho, C.O.; Marangoni Júnior, L.; Ibrahim, S.A.; Vieira, R.P. Essential Oils as Additives in Active Starch-Based Food Packaging Films: A Review. *Int. J. Biol. Macromol.* **2021**, *182*, 1803–1819. [CrossRef]
21. Bertling, I.; Tesfay, S.; Bower, J. Antioxidants in "Hass" Avocado. *S. Afr. Avocado Grow. Asoc.* **2007**, *30*, 17–19.
22. Chel-Guerrero, L.; Barbosa-Martín, E.; Martínez-Antonio, A.; González-Mondragón, E.; Betancur-Ancona, D. Some Physicochemical and Rheological Properties of Starch Isolated from Avocado Seeds. *Int. J. Biol. Macromol.* **2016**, *86*, 302–308. [CrossRef]
23. Angellier, H.; Choisnard, L.; Molina-Boisseau, S.; Ozil, P.; Dufresne, A. Optimization of the Preparation of Aqueous Suspensions of Waxy Maize Starch Nanocrystals Using a Response Surface Methodology. *Biomacromolecules* **2004**, *5*, 1545–1551. [CrossRef]
24. Hoover, R.; Ratnayake, W.S. Determination of Total Amylose Content of Starch. *Curr. Protoc. Food Anal. Chem.* **2001**, *1*, E2–E3. [CrossRef]
25. *ASTM D3985-17*; Standard Test Method for Oxygen Gas Transmission Rate Through Plastic Film and Sheeting Using a Coulometric Sensor. American Society for Testing and Materials: Philadelphia, PA, USA, 2024.
26. European Commission. Commission Regulation (Eu) No. 10, 2011 of 14, on Plastic Materials and Articles Intended to Come into Contact with Food. *Off. J. Eur. Union* **2011**, *L12*, 1–89.
27. *ISO 20200:2015*; Plastics—Determination of the Degree of Disintegration of Plastic Materials under Simulated Composting Conditions in a Laboratory-Scale Test. International Organization for Standardization: Geneva, Switzerland, 2015; pp. 1–8.
28. Esquivel-Fajardo, E.A.; Martinez-Ascencio, E.U.; Oseguera-Toledo, M.E.; Londoño-Restrepo, S.M.; Rodriguez-García, M.E. Influence of Physicochemical Changes of the Avocado Starch throughout Its Pasting Profile: Combined Extraction. *Carbohydr. Polym.* **2022**, *281*, 119048. [CrossRef]
29. Pires, J.B.; Santos, F.N.d.; Cruz, E.P.d.; Fonseca, L.M.; Siebeneichler, T.J.; Lemos, G.S.; Gandra, E.A.; Zavareze, E.d.R.; Dias, A.R.G. Starch Extraction from Avocado By-Product and Its Use for Encapsulation of Ginger Essential Oil by Electrospinning. *Int. J. Biol. Macromol.* **2024**, *254*, 127617. [CrossRef] [PubMed]
30. Basiak, E.; Lenart, A.; Debeaufort, F. Effect of Starch Type on the Physico-Chemical Properties of Edible Films. *Int. J. Biol. Macromol.* **2017**, *98*, 348–356. [CrossRef]
31. Montilla-Buitrago, C.E.; Gómez-López, R.A.; Solanilla-Duque, J.F.; Serna-Cock, L.; Villada-Castillo, H.S. Effect of Plasticizers on Properties, Retrogradation, and Processing of Extrusion-Obtained Thermoplastic Starch: A Review. *Starch-Stärke* **2021**, *73*, 2100060. [CrossRef]
32. Silva, A.P.M.; Oliveira, A.V.; Pontes, S.M.A.; Pereira, A.L.S.; Souza Filho, M.d.s.M.; Rosa, M.F.; Azeredo, H.M.C. Mango Kernel Starch Films as Affected by Starch Nanocrystals and Cellulose Nanocrystals. *Carbohydr. Polym.* **2019**, *211*, 209–216. [CrossRef] [PubMed]
33. Velásquez-Castillo, L.E.; Leite, M.A.; Ditchfield, C.; Sobral, P.J.d.A.; Moraes, I.C.F. Quinoa Starch Nanocrystals Production by Acid Hydrolysis: Kinetics and Properties. *Int. J. Biol. Macromol.* **2020**, *143*, 93–101. [CrossRef]
34. Velásquez-Castillo, L.E.; Leite, M.A.; Tisnado, V.J.A.; Ditchfield, C.; Sobral, P.J.d.A.; Moraes, I.C.F. Cassava Starch Films Containing Quinoa Starch Nanocrystals: Physical and Surface Properties. *Foods* **2023**, *12*, 576. [CrossRef]
35. Yogananda, K.C.; Ramasamy, E.; Vasantha Kumar, S.; Rangappa, D. Synthesis, Characterization, and Dye-Sensitized Solar Cell Fabrication Using Potato Starch– and Potato Starch Nanocrystal–Based Gel Electrolytes. *Ionics* **2019**, *25*, 6035–6042. [CrossRef]
36. LeCorre, D.; Bras, J.; Dufresne, A. Influence of Native Starch's Properties on Starch Nanocrystals Thermal Properties. *Carbohydr. Polym.* **2012**, *87*, 658–666. [CrossRef] [PubMed]
37. Kim, H.Y.; Park, S.S.; Lim, S.T. Preparation, Characterization and Utilization of Starch Nanoparticles. *Colloids Surf. B Biointerfaces* **2015**, *126*, 607–620. [CrossRef] [PubMed]
38. Lacerda, L.G.; Colman, T.A.D.; Bauab, T.; Da Silva Carvalho Filho, M.A.; Demiate, I.M.; De Vasconcelos, E.C.; Schnitzler, E. Thermal, Structural and Rheological Properties of Starch from Avocado Seeds (Persea Americana, Miller) Modified with Standard Sodium Hypochlorite Solutions. *J. Therm. Anal. Calorim.* **2014**, *115*, 1893–1899. [CrossRef]

39. De Dios-Avila, N.; Tirado-Gallegos, J.M.; Rios-Velasco, C.; Luna-Esquivel, G.; Isiordia-Aquino, N.; Zamudio-Flores, P.B.; Estrada-Virgen, M.O.; Cambero-Campos, O.J. Physicochemical, Structural, Thermal and Rheological Properties of Flour and Starch Isolated from Avocado Seeds of Landrace and Hass Cultivars. *Molecules* **2022**, *27*, 910. [CrossRef]
40. LeCorre, D.; Bras, J.; Dufresne, A. Influence of Botanic Origin and Amylose Content on the Morphology of Starch Nanocrystals. *J. Nanopart. Res.* **2011**, *13*, 7193–7208. [CrossRef]
41. Bel Haaj, S.; Thielemans, W.; Magnin, A.; Boufi, S. Starch Nanocrystals and Starch Nanoparticles from Waxy Maize as Nanoreinforcement: A Comparative Study. *Carbohydr. Polym.* **2016**, *143*, 310–317. [CrossRef]
42. Jiménez, R.; Sandoval-Flores, G.; Alvarado-Reyna, S.; Alemán-Castillo, S.E.; Santiago-Adame, R.; Velázquez, G. Extraction of Starch from Hass Avocado Seeds for the Preparation of Biofilms. *Food Sci. Technol.* **2022**, *42*, e56820. [CrossRef]
43. García-Tejeda, Y.V.; Zamudio-Flores, P.B.; Bello-Pérez, L.A.; Romero-Bastida, C.A.; Solorza-Feria, J. Oxidación Del Almidón Nativo De Plátano Para Su Uso Potencial En La Fabricación De Materiales De Empaque Biodegradables: Caracterización Física, Química, Térmica Y Morfológica. *Rev. Iberoam. Polim* **2011**, *12*, 125–135.
44. Tang, X.; Alavi, S.; Herald, T.J. Effects of Plasticizers on the Structure and Properties of Starch–Clay Nanocomposite Films. *Carbohydr. Polym.* **2008**, *74*, 552–558. [CrossRef]
45. Zakaria, N.H.; Muhammad, N.; Abdullah, M.M.A.B. Effect of Glycerol Content on Mechanical, Microstructure and Physical Properties of Thermoplastic Potato Starch Film. *AIP Conf. Proc.* **2018**, *2030*, 020230. [CrossRef]
46. Fan, H.; Ji, N.; Zhao, M.; Xiong, L.; Sun, Q. Characterization of Starch Films Impregnated with Starch Nanoparticles Prepared by 2,2,6,6-Tetramethylpiperidine-1-Oxyl (TEMPO)-Mediated Oxidation. *Food Chem.* **2016**, *192*, 865–872. [CrossRef] [PubMed]
47. Kumari, S.; Yadav, B.S.; Yadav, R. Development and Characterization of Mung Bean Starch–Based Composite Films Incorporated with Sweet Potato Starch Nanocrystals for Their Morphological and Thermo-Mechanical Properties. *Biomass Convers. Biorefin.* **2023**. [CrossRef]
48. Paluch, M.; Ostrowska, J.; Tyński, P.; Sadurski, W.; Konkol, M. Structural and Thermal Properties of Starch Plasticized with Glycerol/Urea Mixture. *J. Polym. Environ.* **2022**, *30*, 728–740. [CrossRef]
49. Mendes, J.F.; Paschoalin, R.T.; Carmona, V.B.; Sena Neto, A.R.; Marques, A.C.P.; Marconcini, J.M.; Mattoso, L.H.C.; Medeiros, E.S.; Oliveira, J.E. Biodegradable Polymer Blends Based on Corn Starch and Thermoplastic Chitosan Processed by Extrusion. *Carbohydr. Polym.* **2016**, *137*, 452–458. [CrossRef] [PubMed]
50. Li, X.; Qiu, C.; Ji, N.; Sun, C.; Xiong, L.; Sun, Q. Mechanical, Barrier and Morphological Properties of Starch Nanocrystals-Reinforced Pea Starch Films. *Carbohydr. Polym.* **2015**, *121*, 155–162. [CrossRef]
51. Dai, M.; Xiong, X.; Cheng, A.; Zhao, Z.; Xiao, Q. Development of Pullulan-Based Nanocomposite Films Reinforced with Starch Nanocrystals for the Preservation of Fresh Beef. *J. Sci. Food Agric.* **2023**, *103*, 1981–1993. [CrossRef] [PubMed]
52. Gomez-Caturla, J.; Ivorra-Martinez, J.; Quiles-Carrillo, L.; Balart, R.; Garcia-Garcia, D.; Dominici, F.; Puglia, D.; Torre, L. Improvement of the Barrier and Mechanical Properties of Environmentally Friendly Mango Kernel Flour/Glycerol Films by Varying the Particle Size of Mango Kernel Flour. *Ind. Crops Prod.* **2022**, *188*, 115668. [CrossRef]
53. Merino, D.; Bertolacci, L.; Paul, U.C.; Simonutti, R.; Athanassiou, A. Avocado Peels and Seeds: Processing Strategies for the Development of Highly Antioxidant Bioplastic Films. *ACS Appl. Mater. Interfaces* **2021**, *13*, 38688–38699. [CrossRef]
54. Hu, H.; Yong, H.; Yao, X.; Yun, D.; Huang, J.; Liu, J. Highly Efficient Synthesis and Characterization of Starch Aldehyde-Catechin Conjugate with Potent Antioxidant Activity. *Int. J. Biol. Macromol.* **2021**, *173*, 13–25. [CrossRef]
55. Rodríguez-Carpena, J.G.; Morcuende, D.; Andrade, M.J.; Kylli, P.; Estevez, M. Avocado (Persea Americana Mill.) Phenolics, in Vitro Antioxidant and Antimicrobial Activities, and Inhibition of Lipid and Protein Oxidation in Porcine Patties. *J. Agric. Food Chem.* **2011**, *59*, 5625–5635. [CrossRef]
56. Bhuyan, D.J.; Alsherbiny, M.A.; Perera, S.; Low, M.; Basu, A.; Devi, O.A.; Barooah, M.S.; Li, C.G.; Papoutsis, K. The Odyssey of Bioactive Compounds in Avocado (Persea Americana) and Their Health Benefits. *Antioxidants* **2019**, *8*, 426. [CrossRef] [PubMed]
57. Mazumder, K.; Nabila, A.; Aktar, A.; Farahnaky, A. Bioactive Variability and in Vitro and in Vivo Antioxidant Activity of Unprocessed and Processed Flour of Nine Cultivars of Australian Lupin Species: A Comprehensive Substantiation. *Antioxidants* **2020**, *9*, 282. [CrossRef] [PubMed]
58. Plaza, L.; Sánchez-Moreno, C.; De Pascual-Teresa, S.; De Ancos, B.; Cano, M.P. Fatty Acids, Sterols, and Antioxidant Activity in Minimally Processed Avocados during Refrigerated Storage. *J. Agric. Food Chem.* **2009**, *57*, 3204–3209. [CrossRef] [PubMed]
59. Lye, H.S.; Ong, M.K.; Teh, L.K.; Chang, C.C.; Wei, L.K. Avocado. In *Valorization of Fruit Processing By-Products*; Elsevier: Amsterdam, The Netherlands, 2020; pp. 67–93. ISBN 9780128171066.
60. Sessini, V.; Arrieta, M.P.; Kenny, J.M.; Peponi, L. Processing of Edible Films Based on Nanoreinforced Gelatinized Starch. *Polym. Degrad. Stab.* **2016**, *132*, 157–168. [CrossRef]
61. Zhang, G.; Xu, C.; Wu, D.; Xie, W.; Wang, Z. Crystallization of Green Poly(ε-Caprolactone) Nanocomposites with Starch Nanocrystal: The Nucleation Role Switching of Starch Nanocrystal with Its Surface Acetylation. *Ind. Eng. Chem. Res.* **2018**, *57*, 6257–6264. [CrossRef]

polymers

MDPI

Article

Valorization of Cellulosic Waste from Artichoke for Incorporation into Biodegradable Polylactic Acid Matrices

Alexandra Llidó Barragán *, Alejandro de la Calle Salas, Francisco Parres García and José Enrique Crespo Amorós

Department of Mechanical and Materials Engineering, Universitat Politècnica de València (UPV), Plz. Ferrándiz y Carbonell, s/n, 03801 Alcoy, Spain; aldel14a@epsa.upv.es (A.d.l.C.S.); fraparga@dimm.upv.es (F.P.G.); jocream@dimm.upv.es (J.E.C.A.)

* Correspondence: alexllidoupv@gmail.com; Tel.: +34-966528570

Abstract: This study presents the development of ecological compounds using polylactic acid (PLA) and artichoke flour with the aim of obtaining materials with properties like commercial PLA. PLA biocomposites with different concentrations of green artichoke (HV) and boiled artichoke (HH) (1, 3, 5, 7, 10 and 20% by weight) were manufactured through an extrusion and injection process. Structural, mechanical, physical and color tests were carried out to analyze the effect of lignocellulosic particles on the biopolymeric matrix. The Shore D hardness, elongation at break and heat deflection temperature (HDT) of the PLA/HV and PLA/HH samples showed similar values to pure PLA, indicating that high concentrations of both fillers did not severely compromise these properties. However, reductions in the tensile strength, impact strength and Young's modulus were observed, and both flours had increased water absorption capacity. FTIR analysis identified the characteristic peaks of the biocomposites and the ratio of the groups regarding the amount of added filler. The SEM revealed low interfacial adhesion between the polymer matrix and the filler. This study represents a significant advance in the valorization and application of circular economy principles to agricultural waste, such as artichoke waste. PLA/HV biocomposites make a substantial contribution to sustainable materials technology, aligning with the goals of the 2030 agenda to reduce environmental impacts and promote sustainable development.

Keywords: circular economy; artichoke; PLA; revaluation

1. Introduction

Artichoke, scientifically known as Cynara cardunculus var. Scolymus, has gained great relevance in agriculture in regions with temperate climates, with Spain being one of the main producing countries, producing 185.6 tons in 2023. Regarding the management of by-products, 60% of by-products from the total production process of artichoke is destined for the canning industry, while the remaining 40% is consumed fresh [1]. In the artichoke industry, the inner bracts are used along with the artichoke receptacle, while the leaves and stems are discarded. These wastes, which represent approximately 70% by weight of the artichoke flower, have been subject to transformation, revaluation and/or elimination. The aim of this study is to revalue these wastes, which contain a significant amount of crude fiber composed of cellulose (65%), hemicellulose (21%) and lignin (14%) [1]. Artichoke residues, especially the leaves, have a remarkable concentration of the enzyme ascorbate peroxidase (APX) along with kinarin and other phenolic compounds. These plant fibers are made up of cellulose, lignin, hemicellulose and pectin, each of which plays a crucial role in their structural properties.

Cellulose, for example, significantly influences the macroscopic characteristics of plant fibers, increasing their tensile strength and Young's modulus; this results in greater structural rigidity and stability. Lignin, on the other hand, provides an effective defense against attacks from microorganisms, contributing to the durability of the fibers. Pectin is

responsible for giving flexibility to the fibers, allowing them to maintain some elasticity. In addition, these two components act as adhesive agents [2]. In contrast, a higher hemicellulose content improves the moisture absorption capacity and accelerates the biodegradation process, thus facilitating faster and more efficient decomposition [3].

This knowledge of the properties of artichoke residues is essential in industry, where they are used in the production of polymer matrix compounds. By taking advantage of these characteristics, the strength and flexibility of the products are demonstrated, contributing to the reduction in waste and the development of more sustainable solutions.

The widespread use of plastics in various sectors has also given rise to concerns about their negative environmental impact, reaching a global figure of 400.3 million tons in 2022 with projections that it will continue growing. To address this problem, the exploration of more sustainable alternatives such as biopolymers derived from renewable and/or biodegradable sources has increased [4–6]. In response to growing environmental awareness, polylactic acid (PLA) has emerged as a biodegradable alternative to conventional plastics [7–9]. PLA is a synthetic thermoplastic polymer derived from renewable sources, such as corn starch or sugar cane, and it comes from the lactic acid generated by the iron–anaerobic digestion of carbonated materials [10]. The characteristics of commercial PLA are a tensile strength of 32.22 MPa, an elongation at break of 30.7% and a glass transition temperature (Tg) of 63.8 °C [11]. However, the physical properties and biodegradability of PLA depend on its stereochemistry and molecular weight. In the case of L-lactide, a semi-crystalline crystallinity of 37% is obtained, and it is a transparent and hard polymer which has a tensile strength of 4570 MPa and an elongation at break ranging from 85 to 105%. Between the thermal characteristics, it has a vitreous transition (Tg) of 53 °C and a melting point (Tm) of 170–180 °C [12,13]. PLA (DL-Lactida) is considered an amorphous polymer that has no melting point and achieves a glass transition (Tg) of 55 °C. Also, it has a low tensile strength [11,14]. However, PLA has drawbacks such as low thermal stability and brittleness [15]. In addition, its rapid degradation into the environment makes it more sustainable than conventional plastics. It is used in a wide range of applications, from packaging to the construction sector, due to its properties and renewable origin. Research continues to focus on improving the properties of PLA with lignocellulosic reinforcements, thus contributing to reducing the environmental impact of plastics in the future. For example, in a previous study, lignocellulose-rich biowaste with a booster charge (pecan nut (PNS)) and chemically modified polylactic acid were used, revealing an improvement in the behavior of PLA regarding biodegradation [16]. Another example is the work carried out by several authors on the biodegradation process of PLA and TPS, which are compounds used in the manufacture of packaging, in which the stages of biodegrading are detailed. The main features of this process are disintegrating, fragmentation and mineralization [17]. In addition, another study investigated the swelling and biodegradability properties of a biocomposite based on low-molecular-weight polylactic acid (ELP) combined with wheat straw and wood sawdust with the aim of using it as a soil conditioner. The results show that the incorporation of lignocellulosic material into the ELP improved the water retention capacity by 10% as well as its stability in the soil environment. Likewise, the rate of swelling of the biocomposite increased to 300% [18]. On the other hand, another recent investigation revealed that the incorporation of chemically modified rice straw improved the thermal and mechanical properties of PLA, such as its tensile strength, Young's modulus and glass transition temperature (Tg) [19]. Likewise, an additional study demonstrated that it has excellent mechanical properties due to the strong adhesion between the reinforcement of date palm fibers and low-molecular-weight polylactic acid (ELP) [20].

To sum up, the main objective of this study is to develop materials for industrial applications based on PLA (polylactic acid) with additives from artichoke waste. Research is carried out on the interaction between two types of waste, green artichoke (HV) and boiled artichoke (HH), with a PLA matrix in injection-molded tensile samples with different weight contents. The obtained materials were characterized mechanically by tensile tests.

In addition, a thermal analysis (TGA) and a structural analysis (FTIR) were performed. The morphology of the fracture surfaces was analyzed using scanning electron microscopy (SEM). Colorimetry and water absorption tests were also carried out.

2. Experimental

2.1. Materials

In this study, we used polylactic acid (PLA) RXP 7053 NATURAL (PLA/9/1000μ), manufactured by NatureWorks (Plymouth, MN, USA) and supplied by the Resinex Group (Tarragona, Spain). This commercial grade is characterized by being a completely amorphous polymer with a glass transition (Tg) of 55 °C that is obtained by polymerization of the racemic mixture D, L-LA [21] with a melt flow rate of 0.9 g/min (210 °C) and a density of 1.24 g/cm^3 [22]. Artichoke, provide by Conservas El Raal, S.L.U (Murcia, Spain), had a cellulose content of 21 wt.%, a hemicellulose content of 21 wt.% and a lignin content of 14 wt.% This residue was provided in green (HV) and boiled (HH) states.

2.1.1. Sample Preparation

First, the leaves of both types of artichoke were dried at 50 °C for 72 h in an oven to remove moisture. The leaves were then ground to obtain HV and HH powders.

After the processing, PLA powders and artichokes were manually pre-mixed in different containers according to the formulations described in Table 1 and left to dry in an oven at 50 °C for 12 h to prevent the hydrolysis of PLA. The extrusion process followed by injection molding was performed on an Xplore MC 15HT microcomponent and an Xplore IM12 microinjection molding machine, which were both supplied by Xplore Instruments BV (Sittard, The Netherlands). The temperature profile for the extrusion process was 145–160–155 °C with a speed of 100 rpm. The mixture was kept in the chamber for 1 min to ensure homogeneity. To produce 1BA type samples, the material mixed in the microinjector was introduced at a temperature of 170 °C (injection nozzle) and 30 °C in the mold with a pressure of 16 bar, and the injection and cooling time was 4 s.

Table 1. Summary of compositions according to the weight content (wt.%) of PLA and different proportions of raw artichoke (HV) and boiled artichoke (HH).

Code	PLA (wt.%)	Artichoke (wt.%)
PLA	100	0
PLA/1HV	99	1
PLA/3HV	97	3
PLA/5HV	95	5
PLA/7HV	93	7
PLA/10HV	90	10
PLA/20HV	80	20
PLA/1HH	99	1
PLA/3HH	97	3
PLA/5HH	95	5
PLA/7HH	93	7
PLA/10HH	90	10
PLA/20HH	80	20

2.1.2. Particle Size Measurement

To obtain the particle sizes, a Microtrac MRB particle analyzer with a Sync particle analyzer (Hann, Germany) was used. This equipment is characterized for analyzing the size and shape of particles from 0.01 to 4000 microns using the laser diffraction ISO 13320:2020 standard and dynamic image analysis ISO 13322-2:2006 standard.

2.1.3. Thermal Properties Measurement

To obtain the mass percentage during the material decomposition stages, the STA 449F5 Jupiter® thermobalance from NETZSCH, (Weimar, Germany) was used. The equipment offers high resolution, a wide temperature range, low balance drift and a highly sensitive DSC signal. The samples were placed in a standard 85 µL alumina (Al_2O_3) crucibles with an average weight between 7 and 9 mg. For the tests, mass flow controllers (MFCs) used oxygen and argon at rates of 252.5 mL/min and 249.3 mL/min, respectively. These were subjected to a heating program from 40 to 700 °C with a heating rate of 10 °C/min in air atmosphere.

2.1.4. Mechanical Properties Measurement

The mechanical properties of the samples were evaluated using an ELIB 30 universal electromechanical testing machine manufactured by Ibertest (Madrid, Spain) with a 5 kN load cell. All tests were carried out following the UNE-EN ISO 527 standard at a speed of 5 mm/min.

The impact test used a 6J Charpy pendulum from Metrotec S.A. (San Sebastián, Spain) in accordance with the ISO-179 standard.

To obtain a complete mechanical characterization, the Shore D hardness was measured with the JBA 673-D durometer from J. Bot S.A. (Barcelona, Spain) in the injection-molded samples with dimensions of 80 × 10 × 4 mm according to the ISO 868:2003 standard, applying a force of approximately 20 N, using an indenter with an angle of 30° and a tip radius of R0.1. In this test, measurements were made at five different points of the samples with a stabilization time of 15 s.

The values of all mechanical parameters were calculated as an average over 5 specimens for each composition. All tests were carried out at room temperature.

2.1.5. Electron Microscopy (SEM)

An analysis of the morphology of the fractured surfaces of the PLA/HV and PLA/HH tensile specimens was performed using a ZEISS ULTRA 55 field emission scanning electron microscope (FESEM) from Oxford Instruments (Abingdon, UK), operating at an accelerating voltage of 2 kV. Before observation, samples were coated with a 5–7 nm Au layer under vacuum conditions.

2.1.6. Colorimetry

To measure the color of the samples, a Hunter Diffuse model colorimeter (Hunterlab, Reston, VA, USA) was used. The color indices (L*, a* and b*) were measured according to the following criteria: L* is the luminosity and varies from 0 to 100; a* represents the chromatic variable from green (−a*) to red (+a*), and b* represents the chromatic variable from blue (−b*) to yellow (+b*). In the test, 3 measurements were taken, determining their average. The total color difference (AE) was studied using expression (1):

$$AE = \sqrt{(\Delta L^*)^2 + (\Delta a^*)^2 + (\Delta b^*)^2} \quad (1)$$

where ΔL*, Δa*, and Δb* are the differences in color parameters between the samples and the control film (L* = 30.9; a* = −0.4; b* = 3.8).

2.1.7. Water Uptake Characterization

The water absorption capacity was studied using injection-molded samples of 80 × 10 × 4 mm, which were immersed in distilled water at a temperature of 23.1 °C. Previously, all samples had been dried at 50 °C for 24 h. Samples were then cooled to room temperature, and the initial weight (Wi) of the samples was measured using the electronic analytical balance AG245 from Mettler Toledo Inc. (Schwerzenbach, Switzerland). After obtaining the initial weights, samples were immersed during the established time, and each time, the surface water of the samples was removed with a paper. This process was

repeated for a total of 7 weeks with weight change assessments performed every 24 h during the first 3 days and every 7 days for the rest.

2.1.8. FTIR Analysis

Attenuated total reflectance–Fourier transform infrared spectroscopy (FTIR-ATR) was carried out using a Perkin Elmer Spectrum Two FT-IR spectrometer (PerkinElmer, MA, USA) equipped with a universal ATR accessory to identify the functional groups of HV and HH and the different samples of PLA/HV and PLA/HH blends. For this test, FTIR spectra were recorded with a wavenumber range from 4000 to 600 cm^{-1} with a resolution of 4.0 cm^{-1} and an interval of 1.0 cm^{-1}.

3. Results and Discussion

3.1. Particle Size Measurement

The results of the analysis of the particle size distribution by laser diffraction and dynamic analysis are presented in Figures 1 and 2. These graphs show the size of the particles (μm) on the horizontal axis, while on the vertical axes, both the accumulated percentage of particles larger than or equal to that size in relation to the total particles, called Q3 (%P), and the accumulated percentage of particles smaller or equal to that size in relation to the total particles are represented, which are called q3 (%).

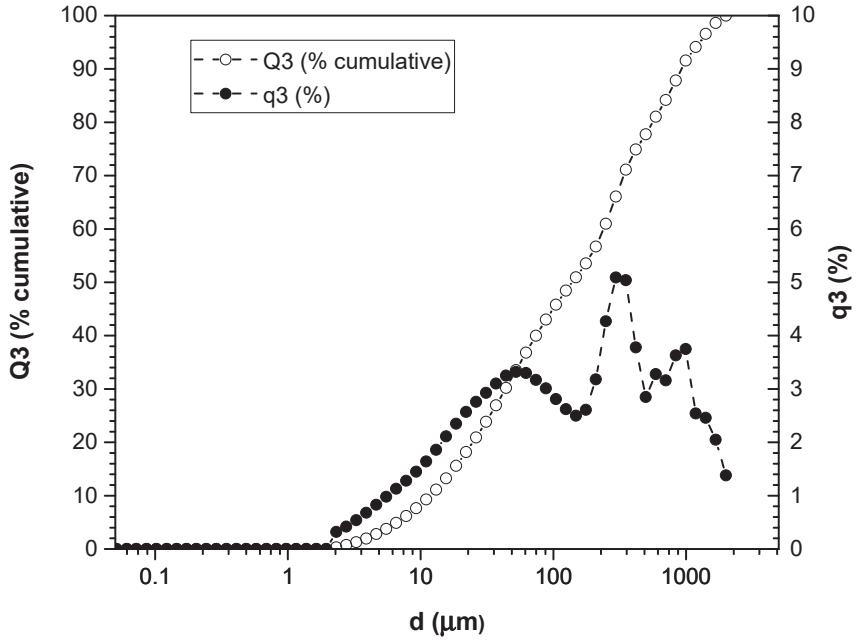

Figure 1. Particle size distribution of HV.

Analysis of the graph in Figure 1 provides a detailed understanding of how the particle size distribution changes in the green (HV) artichoke leaf sample. It is highlighted that the line representing the accumulated percentage of large particles (Q3 (%P)) shows a clear tendency to decrease as the particle size decreases, suggesting a reduction in the accumulation of larger particles in the distribution. For example, between 2000 and 500 μm, this reduction is gradual but constant, while for even smaller particles, this trend appears to be more pronounced. On the other hand, the curve that represents the accumulated percentage of small particles (q3 (%)) follows a different pattern: it is initially low and gradually increases with decreasing particle size. However, it reaches a point where it stabilizes at a lower value. For example, for particles of around 1000 μm, the percentage is relatively low, but as the particles become smaller, it increases significantly until it reaches approximately 3.5%, remaining stable thereafter. An inverse relationship between Q3 (%P)

and q3 (%) was observed at certain points on the graph, where while Q3 (%P) decreases, q3 (%) increases.

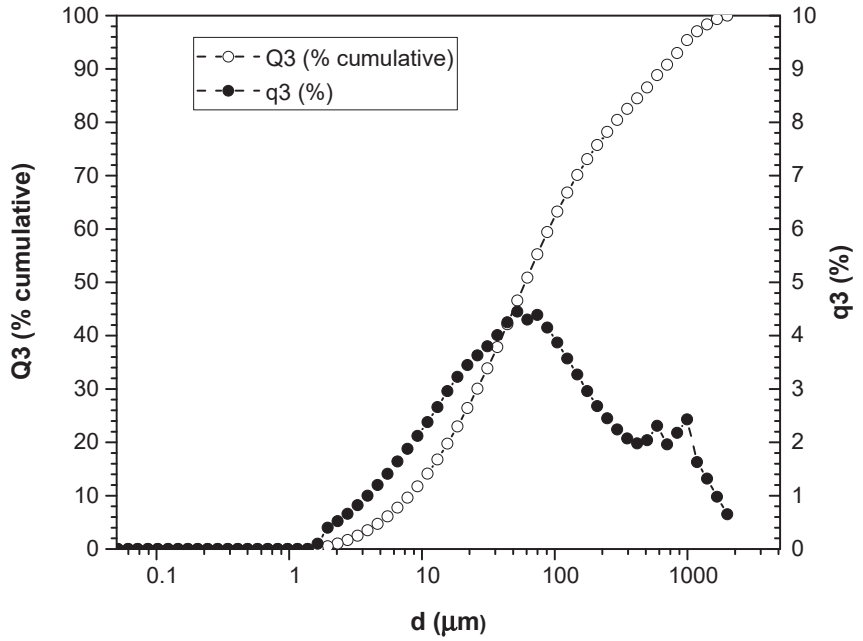

Figure 2. Particle size distribution of HH.

Analysis of boiled artichoke leaf (HH) shows a clear decrease in the accumulated percentage of large particles as its size decreases, indicating a trend toward a greater accumulation of larger particles in the distribution. On the other hand, the accumulated percentage of smaller particles initially increases with decreasing particle size, although it later stabilizes at low values. This trend suggests a more uniform distribution of small particles. Furthermore, an inversion is observed in the relationship between the cumulative percentages of large and small particles at certain points on the graph, which could indicate changes in the particle size distribution depending on their size.

The analysis of the particle size of artichoke leaves reveals a complex distribution ranging from 2.13 to 2000 μm for HV and from 1.635 to 2000 μm for HH. This difference indicates that leaves subjected to a boiling process are broken down into smaller particles. These differences therefore have significant implications for their application.

3.2. Thermal Properties

Thermogravimetric analysis is important to determine the mass percentage of samples. The degradation start temperatures ($T_{5\%}$) were obtained when a mass loss of 5% was reached. The maximum decomposition temperatures (T_{max}) were calculated from the first derivative of the thermal decomposition rate curves (DTG). The combustion characteristics of HV and HH flour are shown in Table 2.

Table 2. HV and HH combustion characteristics.

Material	Weight Loss (%) in a Temperature Range of 40–180	I Degradation Stage				II Degradation Stage				Lignin Decomposition (% by Weight)
		$T_{5\%}$ (°C)	$T_{90\%}$ (°C)	T_{max} (°C)	Weight Loss (%)	$T_{5\%}$ (°C)	$T_{90\%}$ (°C)	T_{max} (°C)	Weight Loss (%)	
HV	5.76	181.5	235.5	217.5	11.49	368.8	235.5	314.4	40.94	13.38
HH	3.50	181.7	265.1	222.7	17.38	373.5	262.7	309.4	37.04	11.49

In Figure 3, the different TGA curves for each type of artichoke leaf are presented. It can be observed that the degradation onset (T5%) takes place at almost identical temperatures: 181.5 °C for the leaf in the green state (HV) and 181.7 °C for the boiled leaf (HH) [22,23]. At

first glance, a difference is noticeable in the representation of the curves, where the boiled leaf shows a slightly lower percentage of lignin: 11.49% compared to 13.38% for the green leaf [24]. This is due to the process of citric acid addition to the artichoke leaf, which causes changes in the chemical composition, especially in the reduction in lignin content.

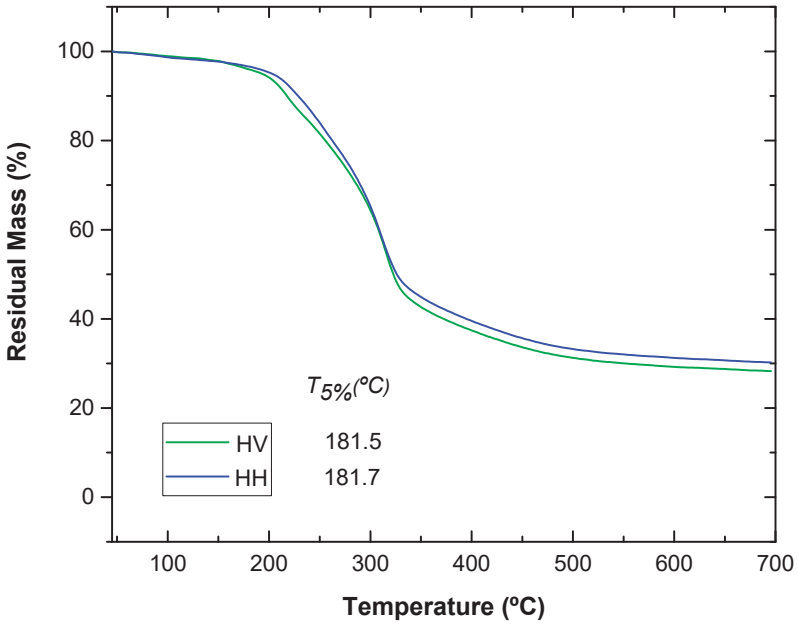

Figure 3. Comparison of TGA curves of HV and HH.

Figure 4 shows a comparison of the thermal decomposition rate (DTG) curves of various artichoke flours. In these curves, the decomposition stages associated with the peaks of hemicellulose, cellulose and lignin can be clearly distinguished. It is notable to highlight the maximum peaks for each type of artichoke flour examined. For example, artichoke leaf flour in the green state reaches a maximum peak of 314.4 °C, while the boiled leaf reaches a maximum peak of 309.3 °C [22,24,25]. The only significant difference is observed in the hemicellulose decomposition stage, where the boiled leaf presents a curve with two peaks due to the decomposition of citric acid at around 250 °C [26].

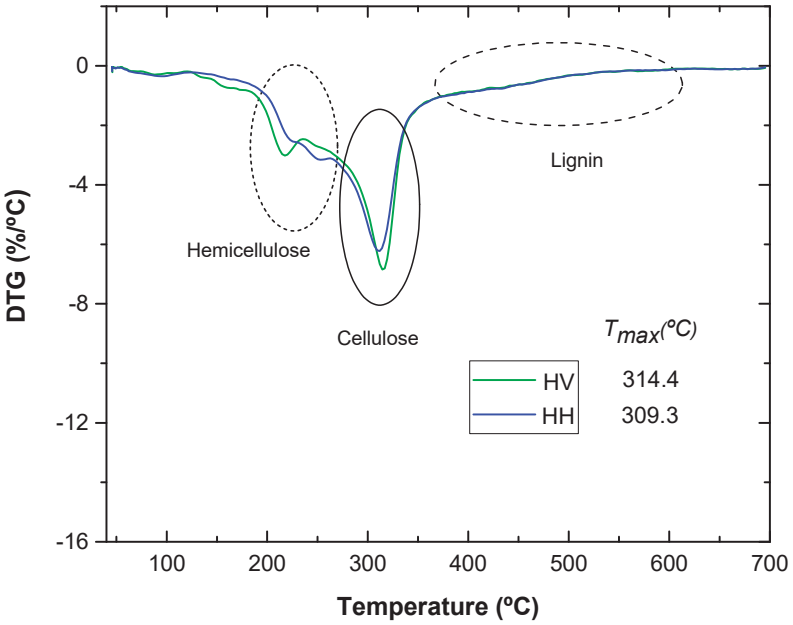

Figure 4. Comparison of DTG curves of HV and HH.

The last graph can be related to a previous study that is based on the thermal characterization of okra fibers as a reinforcement of polymeric compounds, in which TG and DTG curves with a similar pattern were obtained [22]. In Figure 5, the degradation onset of okra fibers (220 °C) and their different decomposition stages are shown. The first stage (220–310 °C) causes a weight loss of 16.1%; while the second stage at 310–390 °C produces a weight loss of 60.6% [27] and lignin decomposition (an extended range of temperatures).

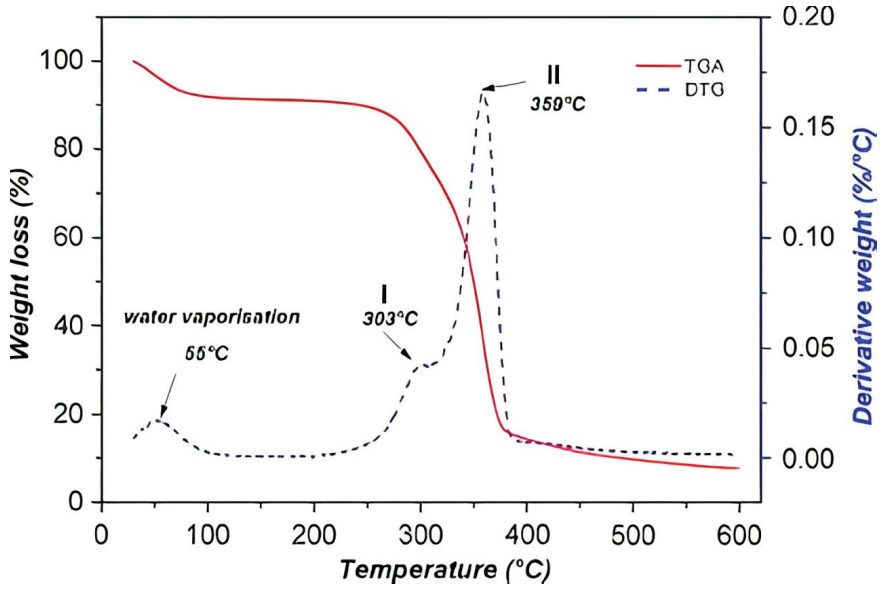

Figure 5. Curve TG and DTG of okra fibers.

In conclusion, in the present project, the thermal analysis curves reveal that the artichoke leaves are stable until around 180 °C in both cases. This is related to the values of natural fibers provided in the literature [28,29].

3.3. Mechanical Properties

The mechanical properties of a material are critical in determining its suitability for specific applications. Tensile and impact testing is essential, as it provides vital information on properties such as tensile strength, elongation at break and the ability to withstand impacts. These characteristics are detailed in Table 3.

Table 3. Mechanical characteristics of the PLA blends.

Code	τ_{max} (MPa)	ε_b (%)	E (MPa)	Shore D Hardness	Impact Strength (kJ/m^2)
PLA	60.9 ± 2.2	6.9 ± 0.3	1133.7 ± 129.4	77.0 ± 0.5	25.6 ± 5.0
PLA/1HV	59.6 ± 0.55	6.9 ± 0.3	1176.2 ± 58.3	79.0 ± 0.0	20.5 ± 3.1
PLA/3HV	58.2 ± 1.62	7.0 ± 0.9	1141.2 ± 54.2	79.2 ± 0.4	16.4 ± 1.2
PLA/5HV	56.4 ± 0.87	6.3 ± 0.5	1153.2 ± 43.3	79.6 ± 0.5	15.7 ± 0.7
PLA/7HV	55.9 ± 0.76	5.8 ± 0.2	1201.8 ± 7.8	78.8 ± 0.5	14.8 ± 0.4
PLA/10HV	52.8 ± 0.71	5.8 ± 0.3	1120.0 ± 23.2	80.2 ± 0.5	12.1 ± 1.2
PLA/20HV	43.2 ± 2.96	4.4 ± 0.4	1125.4 ± 38.5	80.6 ± 0.9	11.5 ± 0.9
PLA/1HH	57.6 ± 0.6	6.4 ± 0.3	1159.5 ± 36.9	78.6 ± 0.4	19.2 ± 2.9
PLA/3HH	56.3 ± 1.6	6.1 ± 0.3	1172.2 ± 24.6	79.2 ± 0.5	17.4 ± 1.2
PLA/5HH	52.4 ± 0.9	6.3 ± 1.0	1133.9 ± 32.7	79.8 ± 0.0	16.0 ± 2.3
PLA/7HH	50.7 ± 0.8	5.7 ± 0.3	1133.9 ± 34.7	80.0 ± 0.0	15.6 ± 0.7
PLA/10HH	43.9 ± 0.7	5.0 ± 0.2	1085.0 ± 46.7	80.2 ± 0.4	13.5 ± 1.0
PLA/20HH	40.6 ± 2.9	4.5 ± 0.3	1075.7 ± 34.5	80.4 ± 0.5	13.1 ± 1.3

PLA exhibits brittle behavior, with low elongation capacity but high tensile strength, with typical values of 60.9 MPa for tensile strength, 1134 MPa for Young's modulus (E) and

7% of elongation at break. The incorporation of HV into PLA clearly showed a significant reduction in the maximum stress as the filler content increased. Several investigations have examined the mechanical properties of natural flours in combination with a polymeric matrix [23]. One of these studies by Ki Wook Kim reveals that the tensile strength of PLA in biocomposites decreases as the amount of added cassava and pineapple flour increases [30]. In the current project, the incorporation of 20% by weight of artichoke in the green state decreased by 29.06%, and it decreased by 33.33% in the boiled state. This phenomenon could be attributed to the milling method applied, which affects the grain size of the different artichokes as well as their physical and morphological characteristics [31]. Likewise, a trend is observed toward a reduction in the elongation capacity with the incorporation of these flours up to 20%. As for the Young's modulus, in the case of HV, the stiffness increases up to a maximum of 1201.8 MPa at 7% by weight and decreases when raising the added load to a minimum value of 1120 MPa. On the other hand, in the case of HH, a slight increase in the Young's modulus is observed with the addition of 1 and 3% by weight; however, at higher load values, like 20%, Young's modulus values are obtained below that of the polymer matrix (1133.7 MPa). This makes sense, because by adding a charge to a polymer, its elasticity and ductility are reduced. Instead of acting as a reinforcement, the load mechanically weakens the sample, decreasing the tensile modulus. At higher concentrations, the particles cluster together, creating weak points and negatively affecting the stiffness of the material [32]. On the other hand, the differences in HV and HH are due to the boiling process that could alter the structure of the leaves, affecting how they disperse.

Among other mechanical characteristics are the hardness and impact strength. In relation to hardness, a slight increase is observed with the addition of the filler, which may be related to the reinforcing effect caused by the hard filler in the polymer matrix. Specifically, the initial hardness value of PLA is 77, and an increase of 4.41% in HV and 4.68% in HH has been experienced.

Finally, the impact strength values of pure PLA are between 28 and 34 kJ/m^2, which are values close to the one in this work, which was 26 kJ/m^2. The incorporation of this filler caused a notable decrease in the Charpy impact strength, which was initially 25.6 kJ/m^2 in the PLA, being reduced to values between 11.5 and 13.1 in the developed biocomposites. This reduction represents a decrease of 44.92% in HV and 51.17% in HH. This effect can be attributed to the high artichoke content (20% by weight), which possibly causes high tensile stresses and limited deformation along the sample [33]. As a result, a reduced ability to absorb impact energy is observed.

3.4. Morphology

Microscopic analysis is crucial to examine the failure surface of materials and understand their mechanical behavior. The image (Figure 6) of the PLA fracture is characterized by the presence of large areas of smooth appearance located at different planes of little unevenness, which is very typical of fragile breaks. Several studies support the low fracture toughness of the polymer [34].

Figures 7 and 8 show that the incorporation of artichoke particles, both green and boiled, causes a substantial change in the breaking surface as the particle percentage increases, being more abrupt as the particle percentage increases. This is a consequence of the presence of cavity particles generated by their removal. In addition, larger particles can be visualized. It is in this type of particles where the lack of adhesion between the matrix phase and the particles can be observed [35]. This phenomenon is seen in both green and boiled particles.

Fractured surfaces of the PLA mixtures with the addition of 20% of HV and HH are contrasted in Figure 9. In Figure 9a, a certain number of incrustations and voids generated by the material can be seen, as well as artichoke particles of various sizes, ranging from 2 to 10 μm. On the other hand, Figure 9b shows a torn surface with depressions, where holes are larger.

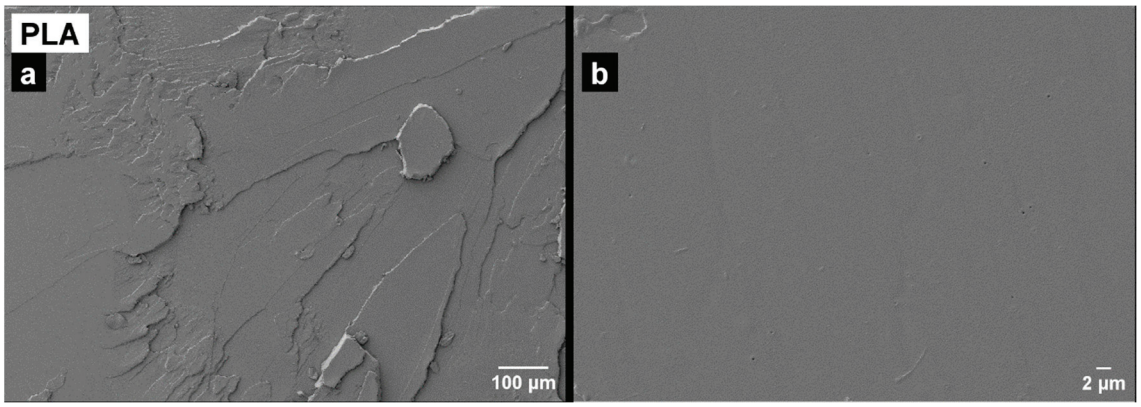

Figure 6. Field emission scanning electron microscopy (FESEM) images (**a**) at 100× and (**b**) at 1500× of the fracture surfaces of the PLA.

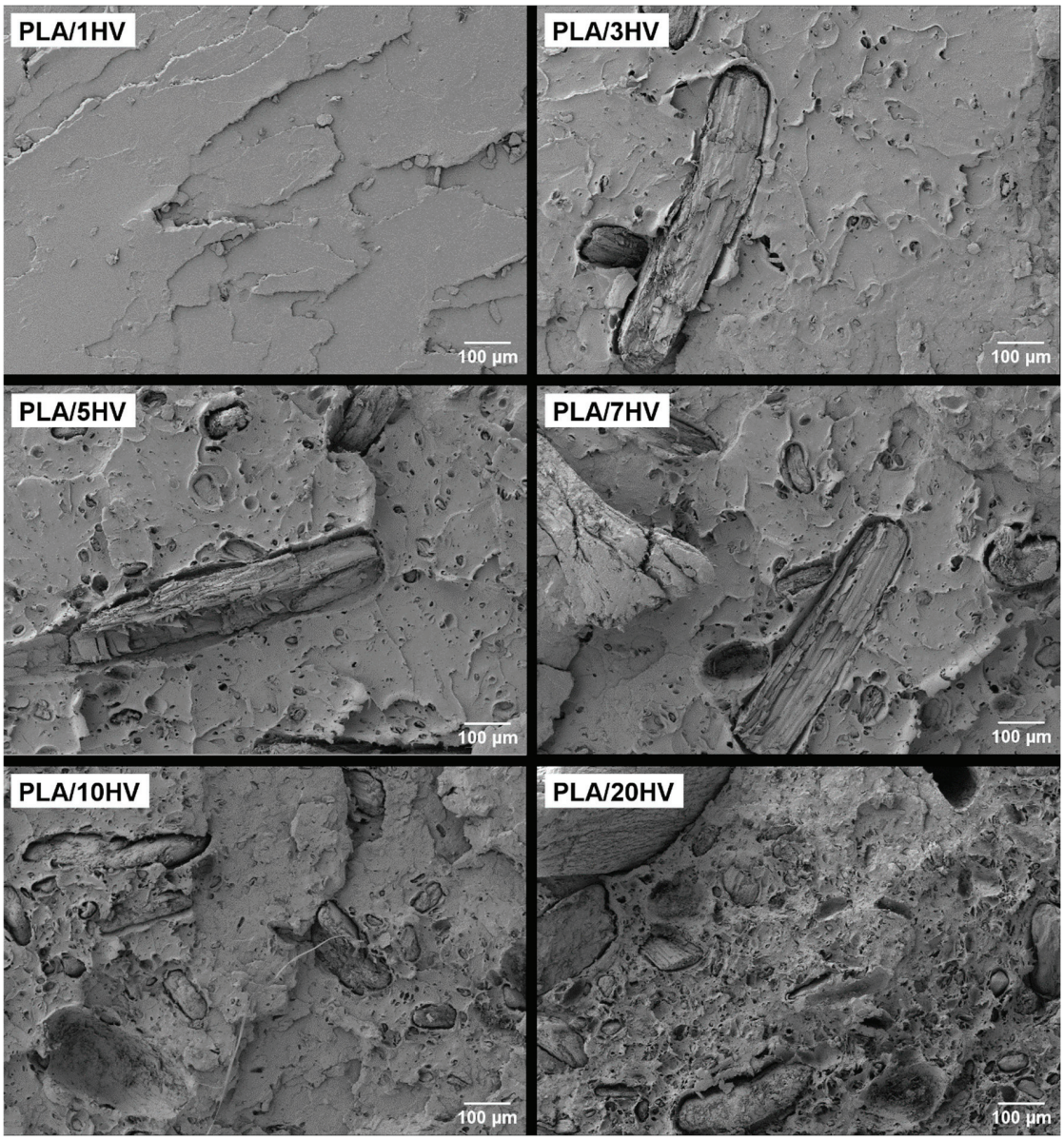

Figure 7. Field emission scanning electron microscopy (FESEM) images at 100× of the fracture surfaces of the PLA/HV composites.

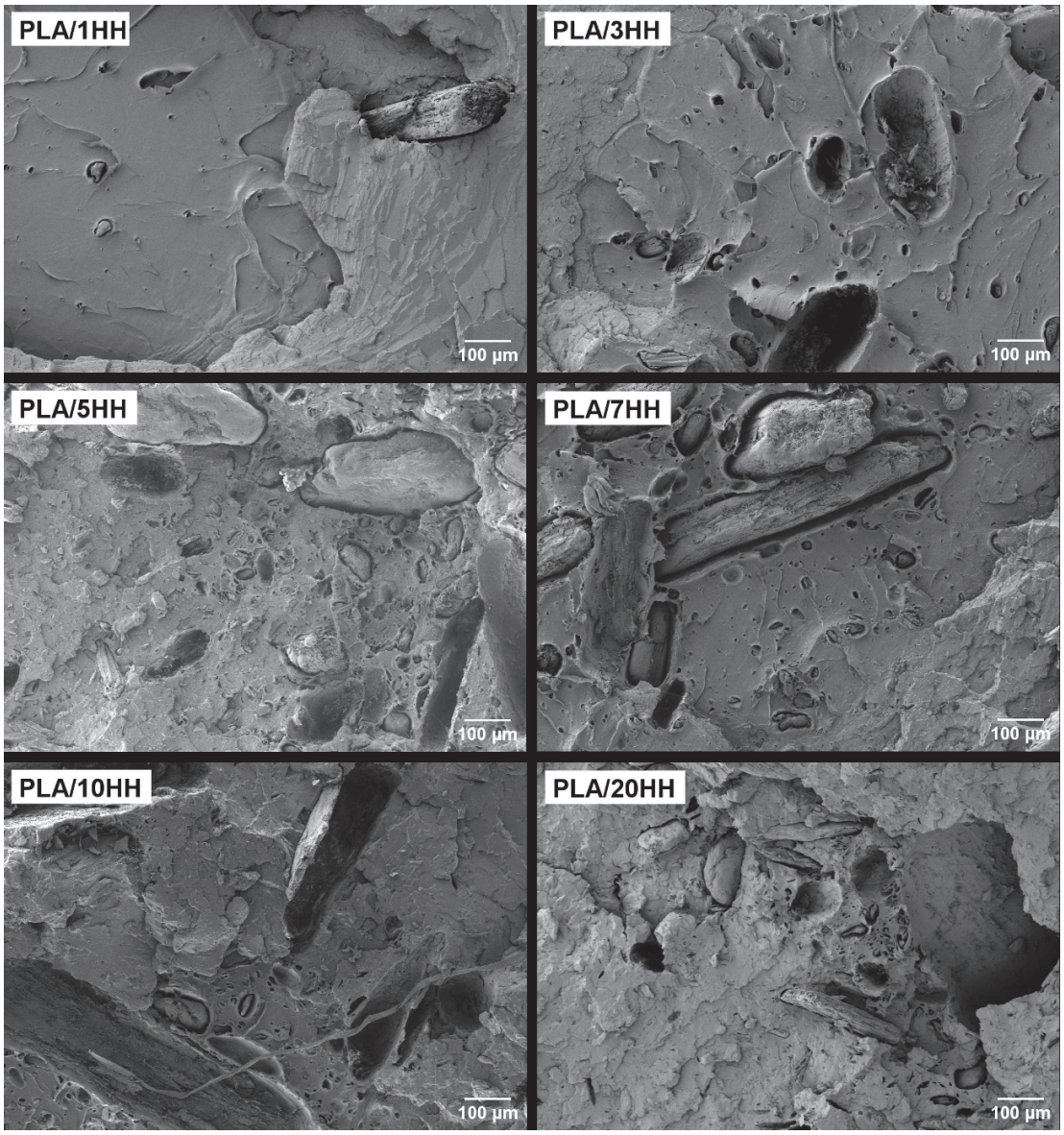

Figure 8. Field emission scanning electron microscopy (FESEM) images at 100× of the fracture surfaces of the PLA/HH composites.

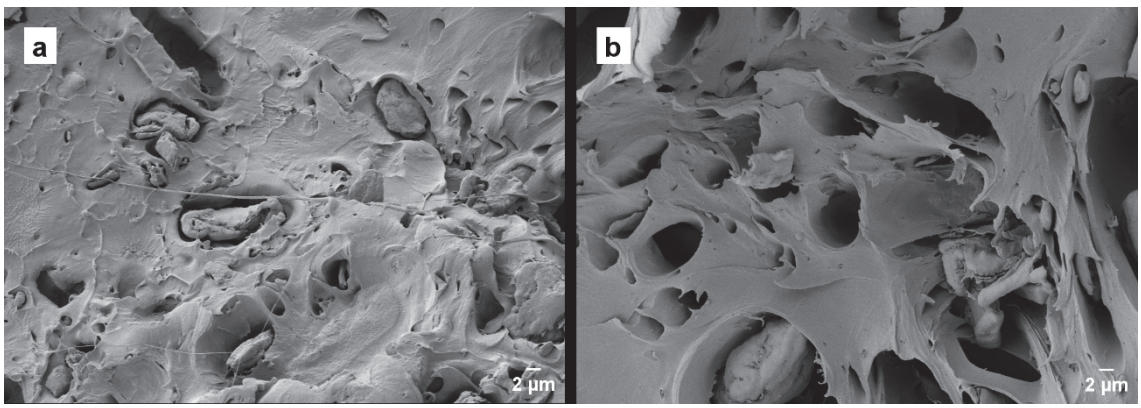

Figure 9. Comparative between field emission scanning electron microscopy (FESEM) images at 1500× of the comparison between composites with the 20% HV and HH. (**a**) PLA/20HV; (**b**) PLA/20HH.

The results obtained show that the PLA/HV biocomposites exhibit a clearer surface with more dispersed particles, while in the PLA/HH biocomposites, a greater presence of voids is easily seen. This fact reinforces the initial need to introduce a compatibilization agent in these mixtures to strengthen the adhesion between the PLA and the lignocellulosic filler of the different artichokes.

3.5. Color Tests

Figure 10 shows the visual appearance of pure PLA and PLA mixtures with both artichokes, HV and HH, which resembles the color of wood. The brown tone has been induced by the injection method due to the temperature reached to inject the PLA.

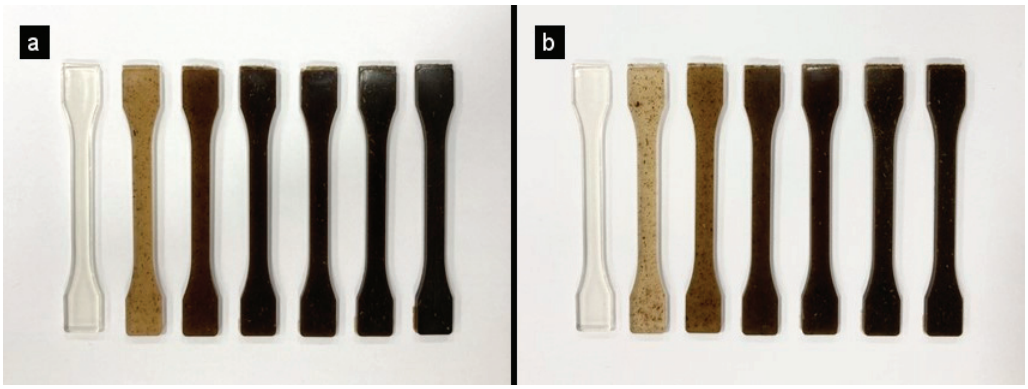

Figure 10. The visible physical appearance of the samples: (**a**) PLA and PLAHV; (**b**) PLA and PLA/HH.

In addition to the previous qualitative evaluation, color parameters have been studied using the CIELab* system and the total color difference (ΔE) found in Table 4. A marked difference is observed between the polylactic acid samples with and without fillers. Initially, the L* value for PLA is 30, which is considered average due to its natural transparency. With the increase in the loading percentage, the samples acquire a darker tone, going from a light brown tone to a darker one, which translates into a reduction in the luminance value (L*). Other investigations have confirmed these results, demonstrating that the brown color intensifies with the incorporation of more filler to the matrix [36]. Furthermore, the values of the parameters a* and b* are positive, indicating the presence of red and yellow tones, respectively. It is important to note that at the beginning, the different flours had visibly different colors: one was dark brown (HV), and the other was lighter with a yellowish tone (HH). When combined with the transparency of PLA, a similar color was created. This darker tone is confirmed by the L* values obtained for the loaded compounds, which vary between 27 and 29 for a 10% artichoke load.

Table 4. Optical parameters of pure PLA and the PLA/HV and PLA/HH blends.

Code	L*	a*	b*	ΔE (Control)
PLA	30.9	−0.4	3.8	-
PLA/1HV	25.6	0.4	3.0	5.4
PLA/3HV	24.6	1.5	3.5	6.6
PLA/5HV	25.2	2.4	3.4	6.4
PLA/7HV	25.4	1.7	3.9	5.9
PLA/10HV	26.9	1.9	3.3	4.6
PLA/20HV	29.4	2.4	3.5	3.2
PLA/1HH	25.1	1.9	5.4	6.4
PLA/3HH	27.6	1.7	5.0	4.1
PLA/5HH	27.9	2.1	4.7	4.0
PLA/7HH	27.8	2.1	4.6	4.1
PLA/10HH	28.9	2.6	4.6	3.7
PLA/20HH	28.2	2.9	4.1	4.5

3.6. Water Absorption

Polylactic acid is characterized for being a naturally hydrophobic material that could negatively affect water absorption. For example, several studies have been carried out on the water absorption characteristics of different biomaterials. In particular, the water absorption capacity of a Kenaf core has been examined as an animal bedding material and has shown promising results comparable to commercial materials such as straw and wood chips [37]. Cellulose, which is the most abundant material, shows a strong affinity for water due to the presence of numerous hydroxyl groups [38].

In an additional study, the use of oat husks as a bioabsorbent for natural gas dehydration was investigated, demonstrating a higher water absorption capacity than commercial adsorbents. The oat husk showed a water absorption capacity of 0.63 (g/g), while for molecular sieves, alumina and silica gel values were recorded in the ranges of 0.21–0.26, 0.25–0.33 and 0.35–0.5, respectively [39].

In this case, different artichoke flours were incorporated into the PLA to improve the hydrophobic nature of PLA and take advantage of the management of agricultural waste from artichokes. This by-product contains a high proportion of lignin, cellulose and hemicellulose.

Figure 11 illustrates the evolution of the water absorption capacity of the samples manufactured during 52 days of water immersion.

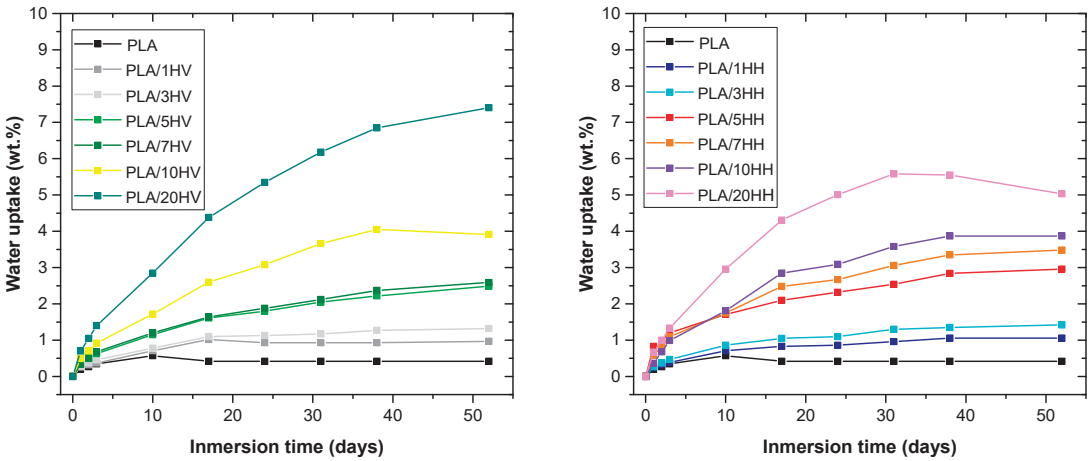

Figure 11. Water uptake of PLA/HV and PLA/HH composites.

It is evident that pure PLA experienced minimal water absorption, recording a value of 0.05% by weight. This can be attributed to the low affinity that PLA has with water, since it is a hydrophobic polymer. By adding the artichoke filler (HV) to the polymer matrix, the water absorption capacity of the biocomposites increases. Artichoke samples of 1%, 3%, 5% and 7% by weight recorded maximum absorption values of between 1% and 3.5% after 52 days. A 10% of HV and HH loading reached values close to 4% by weight, while the 20% sample increased the maximum water absorption capacity to values of 7.4% and 5.03% by weight. This increase is due to the artichoke's rich composition of cellulose, hemicellulose, pectin and lignin, which can bind functional groups (hydroxyls) with water molecules. However, the difference in water absorption values between HV and HH is because the HH load contains less hemicellulose, lignin and pectin due to the boiling process with citric acid. In summary, the increase in water absorption increases with the percentage of load per age and is most noticeable for HV. However, the incorporation of this residue could improve the water absorption capacity of the polymeric matrix. There was also a gradual degradation of PLA as the percentage of lignocellulosic fillers increased, as shown in Figure 12, which is considered beneficial to accelerate the degradation process of PLA. In addition, color changes and an increased porosity of the material are observed, which facilitates water absorption through the generated pores.

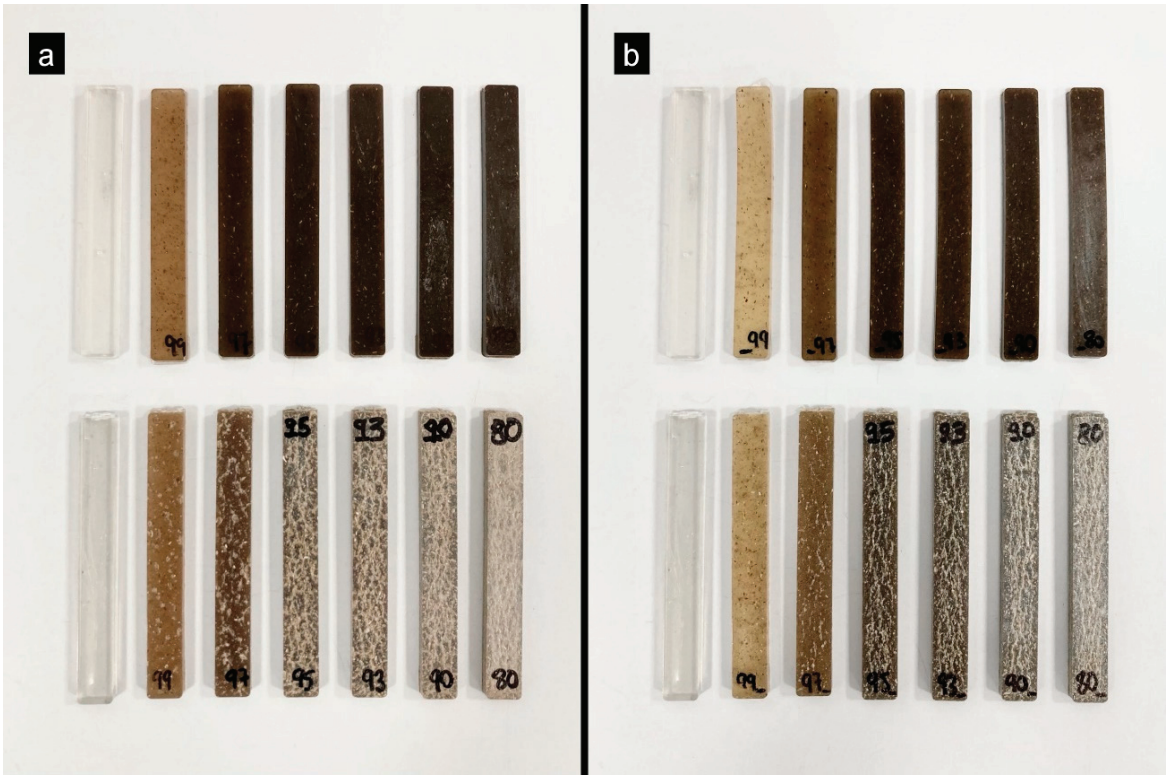

Figure 12. Test pieces obtained after immersion in water. (**a**) PLA/HV composites; (**b**) PLA/HH composites.

3.7. FTIR

The FTIR spectra of PLA, HV and HH chemical function assignments for each absorption band are listed in Table 5. Figure 13 shows the most relevant peaks of PLA. The absorption bands at 1747 cm^{-1} and 1090 cm^{-1} are related to the C=O and C-O groups, respectively. The peaks at 1452 cm^{-1} and 1360 cm^{-1} correspond to the characteristic bands of the symmetric and asymmetric vibrations of the groups [40].

Table 5. Characteristic peaks of PLA, HV and HH.

PLA		HV-HH	
Assignment	**Wavenumbers (cm^{-1})**	**Assignment**	**Wavenumbers (cm^{-1})**
CH_3	2997	OH	3500–3000
-C-CH_3	2947	CH	2918
-CH, -CH_3	2882	(Carbonyl, ketone and ester) C=O	1734
C=O	1747	OH hydroxyls	1645
CH_3	1452	C=O	1618
-CH_3, CH-CH_3	1360	CH	1430–1407
COC, -CO	1180	CH, polysaccharides	1370
COC, r_{as} CH_3	1130	CO	1318
COC	1090	COC of phenol ether bond	1239
CC, COC	1045	CO	1034
CH_3, C=O	760	CH	896

The FTIR spectra of the HV and HH materials are shown in Figure 14. Several significant peaks stand out: at 3303 cm^{-1}, corresponding to the stretching vibration of the O-H group and the hydrogen bonding of the hydroxyl groups [41]; at 2910 cm^{-1}, representing the C-H vibration of the aliphatic groups present in cellulose and hemicellulose [42]; at 1734 cm^{-1}, associated with the stretching of the carbonyl group of the ester groups [41];

and at 1608 cm^{-1}, related to the aromatic benzene of lignin [3]. Furthermore, peaks are observed at 1370 cm^{-1} and 1318 cm^{-1}, which are linked to the bending of the C-H and C-O groups of the aromatic ring in the polysaccharides, respectively [43]. The band at 1239 cm^{-1} is attributed to the stretching of the C-O group from the acetyl group of lignin [44]. On the other hand, the intense band centered at 1034 cm^{-1} can be associated with the stretching bond of C-O and O-H belonging to the ether and hydroxyl groups in the polysaccharides, while the peak at 896 cm^{-1} is attributed to the presence of β-glucosidics bonds in monosaccharides [22].

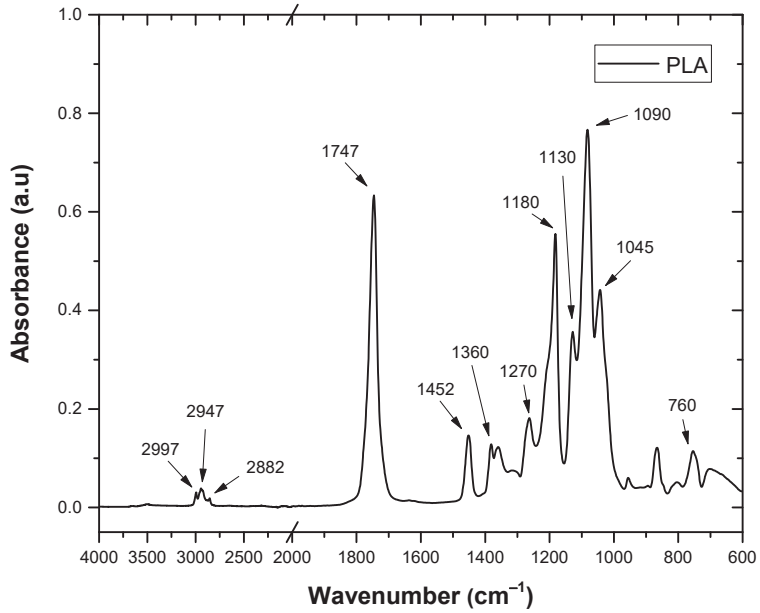

Figure 13. Fourier transform infrared spectrum of the PLA.

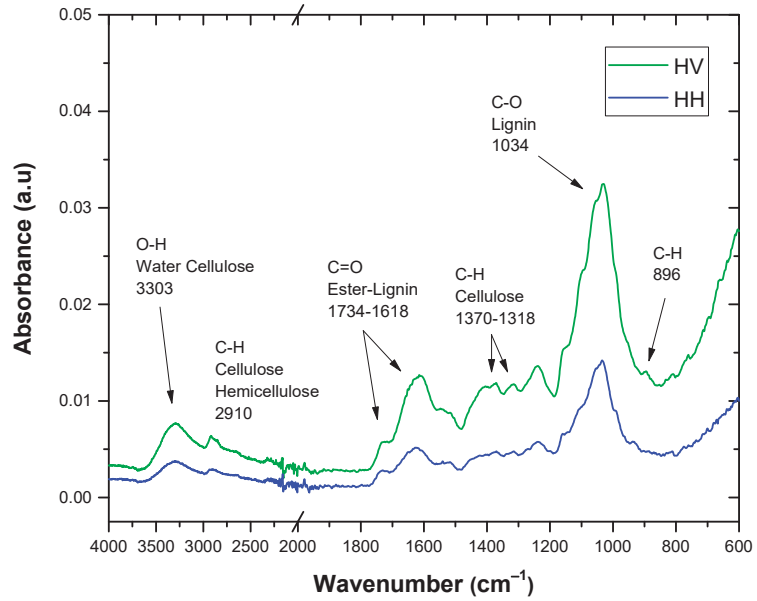

Figure 14. Fourier transform infrared spectrum of the HV and HH.

Observing these FTIR spectra, the height of the peaks in the spectrum of the boiled leaf is lower compared to that of the green leaf. This is due to the treatment of the boiled leaf with citric acid (C6H8O7), where similarities and differences between the characteristic bands are identified. Among these similarities and differences are the functional groups of hydroxyl groups (O-H) and carbonyl groups (C=O) [45].

Figures 15 and 16 show the FTIR spectra, like those of pure PLA, with the addition of HV and HH to the PLA matrix. In the range of 3500 to 3000 cm^{-1}, the O-H functional group was identified, which is possibly related to water absorption due to its hydrophilic nature. This peak was present in all samples but disappeared in pure PLA. Furthermore, stretching absorption peaks of C=O, which are associated with the interaction between the carbon groups of PLA and the ester groups of HV and HH, were observed at 1747 cm^{-1}, which is in agreement with previous research [43]. Two bands of asymmetric and symmetric bending of the methyl group (CH_3) were also detected at 1455 and 1382 cm^{-1}, respectively. Furthermore, an increase in the bands at 1129 and 1080 cm^{-1} was noted, which was possibly due to the presence of (C-O), (C=O) groups in hemicellulose and lignin. The O-H stretching vibration was also detected at 1040 cm^{-1}, which belongs to polysaccharides in cellulose [46,47]. The difference in the intensity of the peaks between the PLA/HV and PLA/HH samples is related to the content of both artichokes, while the slight shifts between the peaks could be attributed to the interactions between the carbon groups of PLA and the hydroxyl groups of the different artichokes.

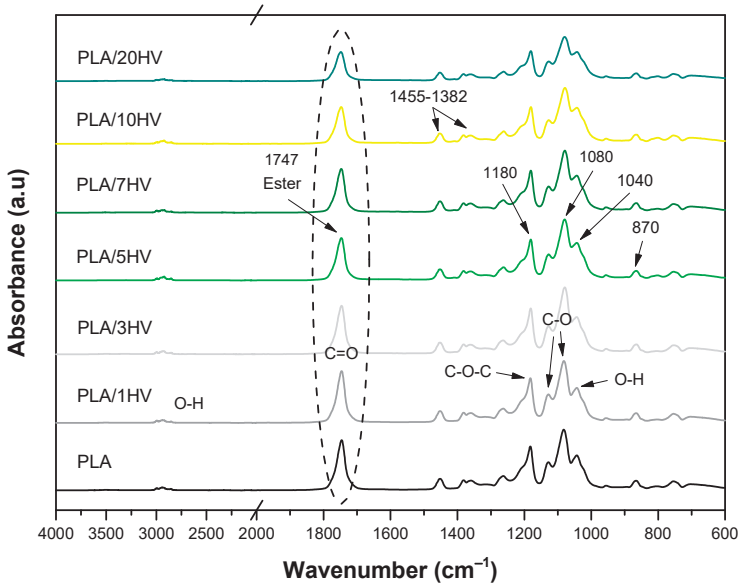

Figure 15. FTIR spectra of PLA formulations with HV.

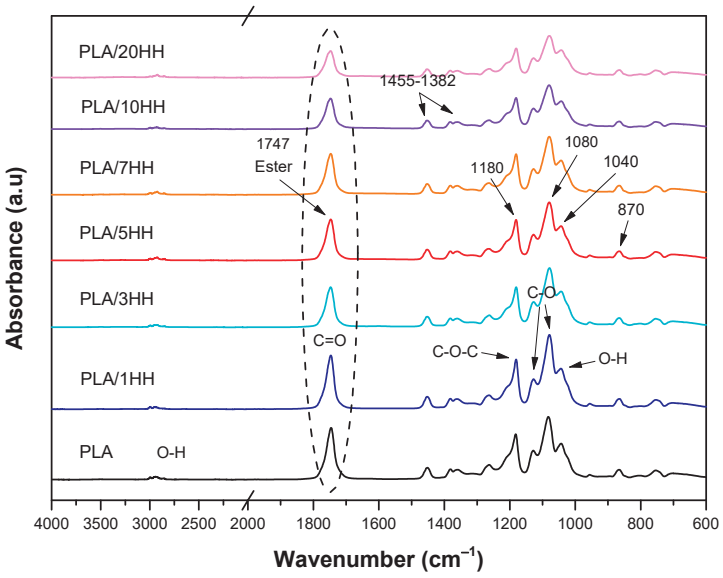

Figure 16. FTIR spectra of PLA formulations with HH.

4. Conclusions

Six different formulations of PLA/HV and PLA/HH mixtures were prepared with contents by weight of 1%, 3%, 5%, 7%, 10% and 20%. TGA revealed the stages of decomposition of each lignocellulosic load, highlighting a greater difference in the stage of decomposition of hemicellulose due to the process of boiling leaves in citric acid. Although these biocomposites showed elongation at break and Shore D hardness values comparable to those of pure PLA, decreases in the tensile strength, Young's modulus and impact resistance were observed, which were possibly due to low interfacial interaction. The SEM analysis revealed a low adhesion between PLA and artichoke powders, which caused tensile losses, especially in mixtures with HV artichoke powder. The first sample of this type was used in its natural state without further treatment but showed a clearer dispersion of the particles. The FTIR analysis highlighted the influence of the carbonyl group (C=O) and the improvement in leaf dispersion due to ethanol in HV and HH, emphasizing how the use of PLA compounds in plant-based materials, such as artichoke leaves, can affect the properties of materials. The particle size measurement showed that the sample particle size varies between 1.635 and 2000 μm. In the colorimetric test, both artichokes create biocompounds with a brown color degradation, resulting in a visual appearance like wood. The results of the water absorption capacity test indicate that PLA biocompounds with artichoke flour accelerate the degradation process. Despite the mechanical properties of the starting polymer and the antioxidant capacity of the artichoke residue, the process of boiling leaves does not improve the material properties. These results highlight the biocomposite PLA with a 5% load of HV, demonstrating that the HDT-TDF is a highly dynamic system that presents an optimum balance, combining a high load content with minimal losses in mechanical properties such as maximum stress of 7.3% and 6% in HDT. Without any damage, it improves the Young's modulus by 1.7% and the PLA hardness by 3.3%, in addition to accelerating its degradation with a water absorption of 2.5%. These biocomposites are especially useful in sectors that demand materials with low tensile strength and water degradability, such as biodegradable pots and disposable products. The use of lignocellulosic fillers reduces PLA costs, and the elimination of the boiling process reduces both production costs and time. In conclusion, PLA/5HV biocomposites represent a significant contribution toward sustainable materials, aligning with the 2030 agenda goals for minimizing environmental impacts and promoting sustainable development.

Author Contributions: Conceptualization, A.L.B., F.P.G. and J.E.C.A.; Data curation, F.P.G.; Funding acquisition, J.E.C.A.; Investigation, A.L.B., A.d.l.C.S. and J.E.C.A.; Methodology, J.E.C.A.; Project administration, J.E.C.A.; Resources, J.E.C.A.; Supervision, F.P.G. and J.E.C.A.; Visualization, A.d.l.C.S.; Writing—original draft, A.L.B.; Writing—review and editing, A.L.B., A.d.l.C.S., F.P.G. and J.E.C.A. All authors have read and agreed to the published version of the manuscript.

Funding: This research received no external funding.

Institutional Review Board Statement: Not applicable.

Data Availability Statement: The data presented in this study are available on request from the corresponding author due to privacy reasons.

Acknowledgments: To the Spanish Ministry of Education and Professional Training for the help granted to the scholarship-collaboration project in the Department of Mechanical and Materials Engineering at the Polytechnic University of Valencia during the first year of the Master's Degree (2022/2023).

Conflicts of Interest: The authors declare no conflicts of interest.

References

1. PINELLI; PATRIZIA. Proceso Para Producir Extractos Nutracéuticos Refinados a Partir de Residuos de Alcachofa y Otras Plantas Del Género Cynara. 2 401 203. ES2401203T3 Patent 12 December 2012.
2. Mohanty, A.K.; Misra, M.; Drzal, L.T. *Natural Fibers, Biopolymers, and Biocomposites*; CRC Press: Boca Raton, FL, USA, 2005; Volume 894, p. 274.

3. Calvo, A. *Determinación Experimental y Modelización de Isotermas de Absorción de Agua de Hojas de Alcachofa*; Universitat Politècnica de València: Valencia, Spain, 2013.
4. PlasticsEurope. Available online: https://plasticseurope.org/wp-content/uploads/2022/10/PE-PLASTICS-THE-FACTS_V7-Tue_19-10-1.pdf (accessed on 21 October 2022).
5. Malinconico, M.; Cerruti, P.; Santagata, G.; Immirzi, B. Natural polymers and additives in commodity and specialty applications: A challenge for the chemistry of future. *Macromol. Symp.* **2014**, *337*, 124–133. [CrossRef]
6. John, M.J.; Thomas, S. Biofibres and biocomposites. *Carbohydr. Polym.* **2008**, *71*, 343–364. [CrossRef]
7. Vilpoux, O.; Averous, L. Starch-based plastics. *Technol. Use Potentialities Lat. Am. Starchy Tubers* **2004**, *3*, 521–553. Available online: http://averousl.free.fr/fichiers/Starch-based_Plastics.pdf (accessed on 20 September 2024).
8. Yu, L.; Dean, K.; Li, L. Polymer blends and composites from renewable resources. *Prog. Polym. Sci.* **2006**, *31*, 576–602. [CrossRef]
9. Oliveira, R.B. Polímeros na obtenção de sistemas de liberação de fármacos. *Rev. Eletrônica De Farmácia* **2006**, *3*. [CrossRef]
10. Anugwom, I.; Lahtela, V.; Kallioinen, M.; Kärki, T. Lignin as a functional additive in a biocomposite: Influence on mechanical properties of polylactic acid composites. *Ind. Crops Prod.* **2019**, *140*, 111704. [CrossRef]
11. Briassoulis, D. Una descripción general del comportamiento mecánico de las películas agrícolas biodegradables. *J. Poli. Reinar* **2004**, *12*, 65–81.
12. VERT, M. Polymères de fermentation: Les poly (acide lactique) s et leurs précurseurs, les acides lactiques. *L'Actualité Chim. (Paris. 1973)* **2002**, *11–12*, 79–82. Available online: http://pascal-francis.inist.fr/vibad/index.php?action=getRecordDetail&idt=14372033 (accessed on 20 September 2024).
13. Mochizuki, M.; Hirami, M. Efectos estructurales sobre la biodegradación de poliésteres alifáticos. *Polimero. Adv. Tecnol.* **1197**, *8*, 203. [CrossRef]
14. Rutot, D.; Dubois, P. Les (bio) polymeres biodegradables: L'enjeu de demain? *Chim. Nouv.* **2004**, *86*, 66–74. Available online: http://pedagogie.ac-limoges.fr/physique-chimie/IMG/pdf/biopolymeres-2.pdf (accessed on 20 September 2024).
15. Weng, Y.X.; Jin, Y.J.; Meng, Q.Y.; Wang, L.; Zhang, M.; Wang, Y.Z. Biodegradation behavior of poly (butylene adipate-co-terephthalate) (PBAT), poly (lactic acid) (PLA), and their blend under soil conditions. *Polym. Test.* **2013**, *32*, 918–926. [CrossRef]
16. Sánchez-Acosta, D.; Rodriguez-Uribe, A.; Álvarez-Chávez, C.R.; Mohanty, A.K.; Misra, M.; López-Cervantes, J.; Madera-Santana, T.J. Physicochemical characterization and evaluation of pecan nutshell as biofiller in a matrix of poly (lactic acid). *J. Polym. Environ.* **2019**, *27*, 521–532. [CrossRef]
17. Camacho-Muñoz, R.; Villada-Castillo, H.S.; Solanilla-Duque, J.F. Anaerobic biodegradation under slurry thermophilic conditions of poly (lactic acid)/starch blend compatibilized by maleic anhydride. *Int. J. Biol. Macromol.* **2020**, *163*, 1859–1865. [CrossRef] [PubMed]
18. Cruz Fabian, D.R.; Durpekova, S.; Dusankova, M.; Cisar, J.; Drohsler, P.; Elich, O.; Borkova, M.; Cechmankova, J.; Sedlarik, V. Renewable Poly(Lactic Acid)Lignocellulose Biocomposites for the Enhancement of the Water Retention Capacity of the Soil. *Polymers* **2023**, *15*, 2243. [CrossRef] [PubMed]
19. Ghorbani Chaboki, M.; Mohammadi-Rovshandeh, J.; Hemmati, F. Poly (Lactic Acid)/Thermoplasticized Rice Straw Biocomposites: Effects of Benzylated Lignocellulosic Filler and Nanoclay. *Iran. Polym. J.* **2019**, *28*, 777–788. [CrossRef]
20. Ghanmi, I.; Slimani, F.; Ghanmi, S.; Guedri, M. Development and Characterization of a PLA Biocomposite reinforced with Date Palm Fibers. *Eng. Technol. Appl. Sci. Res.* **2024**, *14*, 13631–13636. [CrossRef]
21. Carrión, F.J.; Avilés, M.D.; Nakano, K.; Tadokoro, C.; Nagamine, T.; Bermúdez, M.D. Diprotic ammonium palmitate ionic liquid crystal and nanodiamonds in aqueous lubrication. Film thickness and influence of sliding speed. *Wear* **2019**, *418*, 241–252. [CrossRef]
22. De Rosa, I.M.; Kenny, J.M.; Puglia, D.; Santulli, C.; Sarasini, F. Morphological, Thermal and Mechanical Characterization of Okra (*Abelmoschus Esculentus*) Fibres as Potential Reinforcement in Polymer Composites. *Compos. Sci. Technol.* **2010**, *70*, 116–122. [CrossRef]
23. Fiore, V.; Valenza, A.; Di Bella, G. Artichoke (*Cynara Cardunculus* L.) Fibres as Potential Reinforcement of Composite Structures. *Compos. Sci. Technol.* **2011**, *71*, 1138–1144. [CrossRef]
24. Poletto, M.; Ornaghi, H.L.; Zattera, A.J. Native Cellulose: Structure, Characterization and Thermal Properties. *Materials* **2014**, *7*, 6105–6119. [CrossRef]
25. Ouajai, S.; Shanks, R.A. Composition, Structure and Thermal Degradation of Hemp Cellulose after Chemical Treatments. *Polym. Degrad. Stab.* **2005**, *89*, 327–335. [CrossRef]
26. Silva, N.T.; Nascimento, N.F.; Cividanes, L.S.; Bertran, C.A.; Thim, G.P. Kinetics of Cordierite Crystallization from Diphasic Gels. *J. Sol-Gel Sci. Technol.* **2008**, *47*, 140–147. [CrossRef]
27. Albano, C.; Gonzalez, J.; Ichazo, M.; Kaiser, D. Thermal stability of blends of polyolefins and sisal fiber. *Polym. Degrad. Stab.* **1999**, *66*, 179–190. [CrossRef]
28. Wielage, B.; Lampke, T.; Marx, G.; Nestler, K.; Starke, D. Thermogravimetric and differential scanning calorimetric analysis of natural fibres and polypropylene. *Thermochim. Acta* **1999**, *337*, 169–177. [CrossRef]
29. Spinacé, M.A.; Lambert, C.S.; Fermoselli, K.K.; De Paoli, M.A. Characterization of lignocellulosic curaua fibres. *Carbohydr. Polym.* **2009**, *77*, 47–53. [CrossRef]
30. Kim, K.-W.; Lee, B.-H.; Kim, H.-J.; Sriroth, K.; Dorgan, J.R. Thermal and Mechanical Properties of Cassava and Pineapple Flours-Filled PLA Bio-Composites. *J. Therm. Anal. Calorim.* **2012**, *108*, 1131–1139. [CrossRef]

31. Taşdemir, M. Effects of Olive Pit and Almond Shell Powder on Polypropylene. *Key Eng. Mater.* **2017**, *733*, 65–68. [CrossRef]
32. Quiles-Carrillo, L.; Montanes, N.; Jorda-Vilaplana, A.; Balart, R.; Torres-Giner, S. A comparative study on the effect of different reactive compatibilizers on injection-molded pieces of bio-based high-density polyethylene/polylactide blends. *J. Appl. Polym. Sci.* **2019**, *136*, 47396. [CrossRef]
33. Morreale, M.; Liga, A.; Mistretta, M.C.; Ascione, L.; Mantia, F.P. Mechanical, Thermomechanical and Reprocessing Behavior of Green Composites from Biodegradable Polymer and Wood Flour. *Materials* **2015**, *8*, 7536–7548. [CrossRef]
34. Chaiwutthinan, P.; Chuayjuljit, S.; Srasomsub, S.; Boonmahitthisud, A. Composites of poly (lactic acid)/poly (butylene adipate-co-terephthalate) blend with wood fiber and wollastonite: Physical properties, morphology, and biodegradability. *J. Appl. Polym. Sci.* **2019**, *136*, 47543. [CrossRef]
35. da Silva, W.A.; Luna, C.B.B.; de Melo, J.B.d.C.A.; Araújo, E.M.; Filho, E.A.d.S.; Duarte, R.N.C. Feasibility of Manufacturing Disposable Cups Using PLA/PCL Composites Reinforced with Wood Powder. *J. Polym. Environ.* **2021**, *29*, 2932–2951. [CrossRef]
36. Liminana, P.; Quiles-Carrillo, L.; Boronat, T.; Balart, R.; Montanes, N. The Effect of Varying Almond Shell Flour (ASF) Loading in Composites with Poly (Butylene Succinate (PBS) Matrix Compatibilized with Maleinized Linseed Oil (MLO). *Materials* **2018**, *11*, 2179. [CrossRef]
37. Lips, S.J.J.; Iñiguez de Heredia, G.M.; Op den Kamp, R.G.M.; van Dam, J.E.G. Water Absorption Characteristics of Kenaf Core to Use as Animal Bedding Material. *Ind. Crops Prod.* **2009**, *29*, 73–79. [CrossRef]
38. Al Abdallah, H.; Abu-Jdayil, B.; Iqbal, M.Z. Improvement of Mechanical Properties and Water Resistance of Bio-Based Thermal Insulation Material via Silane Treatment. *J. Clean. Prod.* **2022**, *346*, 131242. [CrossRef]
39. Ghanbari, S.; Niu, C.H. Characteristics of oat hull based biosorbent for natural gas dehydration in a PSA process. *J. Nat. Gas Sci. Eng.* **2019**, *61*, 320–332. Available online: https://www.sciencedirect.com/science/article/pii/S1875510018305079?casa_token=wFo0IaUsH7YAAAA:tylQM0TAlyodHd0-2qviXgCdSrzEuVogKwgTCfdu7OkfNO3u_vufmcuSPx_ybzivNbhgDl4CKk (accessed on 20 September 2024). [CrossRef]
40. Sánchez, C. Desarrollo, Caracterización y Propiedades de Nanofases, Nanofluidos y Nanomaterials. Ph.D. Thesis, Universidad Politécnica de Cartagena, Cartagena, Spain, 2023.
41. Yang, H.; Yan, R.; Chen, H.; Lee, D.H.; Zheng, C. Characteristics of Hemicellulose, Cellulose and Lignin Pyrolysis. *Fuel* **2007**, *86*, 1781–1788. [CrossRef]
42. Paiva, M.C.; Ammar, I.; Campos, A.R.; Cheikh, R.B.; Cunha, A.M. Alfa Fibres: Mechanical, Morphological and Interfacial Characterization. *Compos. Sci. Technol.* **2007**, *67*, 1132–1138. [CrossRef]
43. Le Troëdec, M.; Dalmay, P.; Patapy, C.; Peyratout, C.; Smith, A.; Chotard, T. Mechanical Properties of Hemp-Lime Reinforced Mortars: Influence of the Chemical Treatment of Fibers. *J. Compos. Mater.* **2011**, *45*, 2347–2357. [CrossRef]
44. Liu, W.; Mohanty, A.K.; Drzal, L.T.; Askel, P.; Misra, M. Effects of alkali treatment on the structure, morphology and thermal properties of native grass fibers as reinforcements for polymer matrix composites. *J. Mater. Sci.* **2004**, *39*, 1051–1054. Available online: https://www.academia.edu/45237217/Effects_of_alkali_treatment_on_the_structure_morphology_and_thermal_properties_of_native_grass_fibers_as_reinforcements_for_polymer_matrix_composites (accessed on 20 September 2024). [CrossRef]
45. Stuart, B. *Infrared Spectroscopy: Fundamentals and Applications*; John Wiley & Sons: Hoboken, NJ, USA, 2004.
46. Venkatesh, C.; Laurenti, M.; Bandeira, M.; Lanzagorta, E.; Lucherini, L.; Cauda, V.; Devine, D.M. Biodegradation and Antimicrobial Properties of Zinc Oxide–Polymer Composite Materials for Urinary Stent Applications. *Coatings* **2020**, *10*, 1002. [CrossRef]
47. Yang, S.; Wu, Z.-H.; Yang, W.; Yang, M.-B. Thermal and Mechanical Properties of Chemical Crosslinked Polylactide (PLA). *Polym. Test.* **2008**, *27*, 957–963. [CrossRef]

MDPI AG
Grosspeteranlage 5
4052 Basel
Switzerland
Tel.: +41 61 683 77 34

Polymers Editorial Office
E-mail: polymers@mdpi.com
www.mdpi.com/journal/polymers

Academic Open
Access Publishing

mdpi.com

ISBN 978-3-7258-6377-8